A.I.Ch.E. JOURNAL

CHEMICAL ENGINEERING RESEARCH AND DEVELOPMENT / SEPTEMBER 1958

ENGINEERING LIBRARY

CONTENTS

Kinetics of Nitrogen Tetroxide Absorption in Water	M. M. Wendel and R. L. Pigford
Viscosity: Reduced-State Correlation for the Inert Gases	Hiroshi Shimotake and George Thodos
Convergence Pressures for Close-boiling Nonideal Systems	J. M. Lenoir
Discharge Coefficients Through Perforated Plates at Reynolds Numbers of 400 to 3,000	P. L. Smith, Jr. and Matthew Van Winkle
Regular Solution Theory for Gas-liquid Solutions	J. M. Prausnitz
Drop Formation in Liquid-liquid Systems from Single Nozzles	Harold R. Null and Homer F. Johnson
Pulsations in Sieve-tray and Bubble-cap Distillation Towers	R. A. McAllister and C. A. Plank
Combined Laminar Free- and Forced-convection Heat Transfer in External Flows	Andreas Acrivos
Some Properties of the Poisson Distribution	A. S. Said
Phase Relations of Binary Systems that Form Azeotropes I. The Ammonia–*n*-Butane System	Webster B. Kay and Herbert A. Fisch
II. The Ammonia-Isooctane System	Webster B. Kay and F. Morgan Warzel
A Reactor-design Equation Based on a Proposed Distributed Boundary-layer Thickness	H. E. Hoelscher
Drainage of Packed Beds in Gravitational and Centrifugal-force Fields	Emile Nenniger, Jr., and J. Anderson Storrow
Freezing Points of Binary Mixtures of Methane	Jerome Brewer and Fred Kurata
Heat Transfer in Forced Convection with Internal Heat Generation	H. L. Toor
Generalized Correlation for Loading in Packed Towers with Countercurrent Gas-liquid Flow	J. E. Howkins and J. F. Davidson
Shape Factors for Conductive Heat Flow	Julian C. Smith, John E. Lind, Jr., and David S. Lermond
Local Shell-side Heat Transfer Coefficients in Baffled Tubular Heat Exchangers	T. W. Ambrose and J. G. Knudsen
Electrolytic Methods for Measuring Water Velocities	William E. Ranz
Diffusion in a Pore of Varying Cross Section	E. E. Petersen
The Formation of Interfacial Area in Immiscible Liquids by Orifice Mixers	L. S. Scott, W. B. Hayes, III, and C. D. Holland
An Improved Experimental Reactor for Applied Kinetic Studies	Thomas K. Perkins and Howard F. Rase
Critical Temperatures and Pressures of Hydrocarbons	J. Charles Forman and George Thodos
The Viscosity of Acetone-water Solutions up to their Normal Boiling Points	Katherine S. Howard and R. A. McAllister
Axial Dispersion of Mass in Flow Through Fixed Beds	J. J. Carberry and R. H. Bretton
Heat Transfer to a Liquid Fluidized Bed	Robert Lemlich and Isidoro Caldas, Jr.

YORKMESH® DEMISTERS

will improve PROCESS VESSEL PERFORMANCE

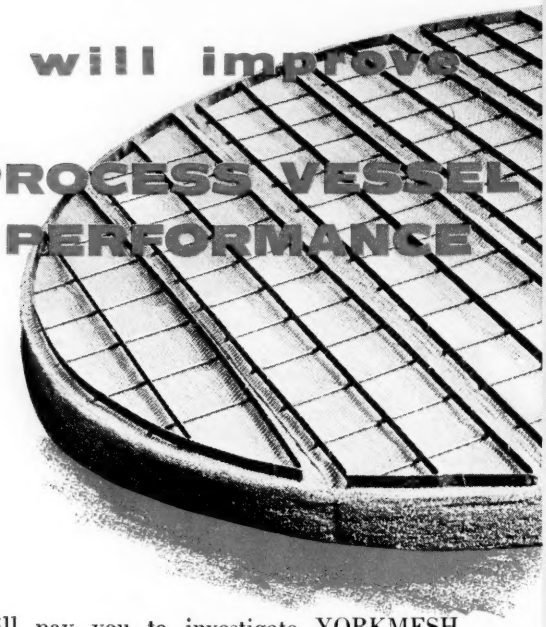

It will pay you to investigate YORKMESH DEMISTERS if your process vessels need a lift in efficiency. The versatile knitted wire-mesh pads are being used more and more throughout industry to *stop* liquid entrainment and improve the performance of:

Vacuum Towers, Distillation Equipment, Gas Absorbers, Scrubbers, Evaporators, Knock-Out Drums, Steam Drums and many others.

Here is what happens when YORKMESH DEMISTERS are installed:

1. As vapor disengages from liquid it carries with it fine liquid droplets.
2. When the vapor stream passes thru the fine wire mesh, the liquid droplets impinge on the wire surfaces, coalesce in to large drops, and fall.
3. The vapor is now dry and free from entrained liquid.

Send us details on your type of process vessel or operation, vapor flow rate, pressure, temperature, and density or molecular weight; approximate amount of entrained liquid, viscosity, and specific gravity . . . for existing equipment advise dimensions, indicate vertical or horizontal vessel and material of construction required for mesh and grids. Complete details will make it possible for us to present our recommendations and quotation.

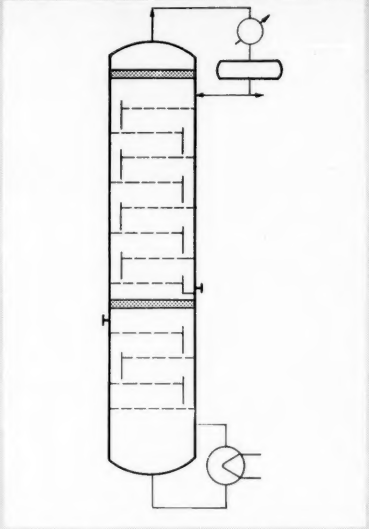

The efficiency of separation and thruput capacity of distillation equipment can be significantly improved by the use of YORKMESH DEMISTERS.

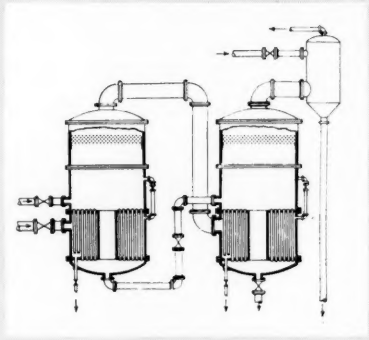

YORKMESH DEMISTERS installed in evaporators avoid product loss and provide clean condensate.

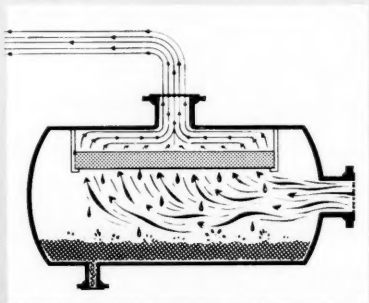

YORKMESH DEMISTERS installed in Knock-Out Drums result in high separation efficiency at low pressure drop.

YORK

OTTO H. YORK CO., INC.

6 CENTRAL AVE. • WEST ORANGE, N. J.

A.I.Ch.E. JOURNAL

SEPTEMBER 1958 · VOL. 4, NO. 3

PUBLISHER
F. J. Van Antwerpen
EDITOR
Harding Bliss
ADVERTISING MANAGER
L. T. Dupree

ADVISORY BOARD

C. M. Cooper, O. E. Dwyer, W. C. Edmister, E. R. Gilliland, A. N. Hixson, H. F. Johnstone, W. R. Marshall, Jr., R. H. Newton, R. L. Pigford, E. L. Piret, J. M. Smith, Theodore Vermeulen, R. R. White, R. H. Wilhelm

The A.I.Ch.E. Journal, an official publication of the American Institute of Chemical Engineers, is devoted in the main to theoretical developments and research in chemical engineering and allied branches of engineering and science. Manuscripts should be submitted to the New York office.

Federal Aid (?) to Education 247

Kinetics of Nitrogen Tetroxide Absorption in Water . . . . . *M. M. Wendel and R. L. Pigford* 249

Viscosity: Reduced-State Correlation for the Inert Gases . . . . . *Hiroshi Shimotake and George Thodos* 257

Convergence Pressures for Close-boiling Nonideal Systems . . . . . *J. M. Lenoir* 263

Discharge Coefficients Through Perforated Plates at Reynolds Numbers of 400 to 3,000 *P. L. Smith, Jr., and Matthew Van Winkle* 266

Regular Solution Theory for Gas-liquid Solutions . . . . . *J. M. Prausnitz* 269

Drop Formation in Liquid-liquid Systems from Single Nozzles . . . *Harold R. Null and Homer F. Johnson* 273

Pulsations in Sieve-tray and Bubble-cap Distillation Towers . . . . . *R. A. McAllister and C. A. Plank* 282

Combined Laminar Free- and Forced-convection Heat Transfer in External Flows . . . . *Andreas Acrivos* 285

Some Properties of the Poisson Distribution . . . . . *A. S. Said* 290

Phase Relations of Binary Systems That Form Azeotropes
I. The Ammonia–*n*-Butane System . . . . . *Webster B. Kay and Herbert A. Fisch* 293
II. The Ammonia-Isooctane System . . . . . *Webster B. Kay and F. Morgan Warzel* 296

A Reactor-design Equation Based on a Proposed Distributed Boundary-layer Thickness . *H. E. Hoelscher* 300

Drainage of Packed Beds in Gravitational and Centrifugal-force Fields *Emile Nenniger, Jr., and J. Anderson Storrow* 305

Freezing Points of Binary Mixtures of Methane . . . . . *Jerome Brewer and Fred Kurata* 317

Heat Transfer in Forced Convection with Internal Heat Generation . . . . . *H. L. Toor* 319

Generalized Correlation for Loading in Packed Towers with Countercurrent Gas-liquid Flow *J. E. Howkins and J. F. Davidson* 324

Shape Factors for Conductive Heat Flow . . . . *Julian C. Smith, John E. Lind, Jr., and David S. Lermond* 330

Local Shell-side Heat Transfer Coefficients in Baffled Tubular Heat Exchangers *T. W. Ambrose and J. G. Knudsen* 332

Electrolytic Methods for Measuring Water Velocities . . . . . *William E. Ranz* 338

Diffusion in a Pore of Varying Cross Section . . . . . *E. E. Petersen* 343

The Formation of Interfacial Area in Immiscible Liquids by Orifice Mixers *L. S. Scott, W. B. Hayes, III, and C. D. Holland* 346

An Improved Experimental Reactor for Applied Kinetic Studies . *Thomas K. Perkins and Howard F. Rase* 351

Critical Temperatures and Pressures of Hydrocarbons . . . . . *J. Charles Forman and George Thodos* 356

The Viscosity of Acetone-water Solutions up to their Normal Boiling Points *Katherine S. Howard and R. A. McAllister* 362

Axial Dispersion of Mass in Flow Through Fixed Beds . . . . . *J. J. Carberry and R. H. Bretton* 367

Heat Transfer to a Liquid Fluidized Bed . . . . . *Robert Lemlich and Isidoro Caldas, Jr.* 376

Flow Measurement with Ball Flow Meters . . . . . *K. L. Shulman and K. A. Van Wormer, Jr.* 380

Absorption into an Accelerating Film . . . . . *L. E. Scriven and R. L. Pigford* 382

Publication Office, Richmond, Virginia. Published quarterly in March, June, September, and December by the American Institute of Chemical Engineers, 25 West 45 Street, New York 36 New York. Manuscripts and other communications should be sent to the New York office. Correspondence with the editor may be addressed to him at Yale University, 225 Prospect Street, New Haven 11, Connecticut. Statements and opinions in the *A.I.Ch.E. Journal* are those of the contributors, and the American Institute of Chemical Engineers assumes no responsibility for them. Subscriptions: one year, member $4.50, nonmember $9.00; two years, member $7.50, nonmember $15.00; additional yearly postage, Canada 50 cents, Pan American Union $1.50, other foreign $2.00 (foreign subscriptions payable in advance). Single copies: $3.00. Second-class mail privileges authorized at Richmond, Virginia. Copyright 1958 by the American Institute of Chemical Engineers. National headquarters of A.I.Ch.E. is concerned about nondelivery of copies of the *A.I.Ch.E. Journal* and urgently requests subscribers to give prompt notification of any change of address. Sixty days must be allowed for changes to be made in the records.

SPECIAL PRE-PUBLICATION ANNOUNCEMENT

The United Nations announces . . . **the only complete & official**

PROCEEDINGS OF THE SECOND UNITED NATIONS INTERNATIONAL CONFERENCE ON THE PEACEFUL USES OF ATOMIC ENERGY (Geneva, September 1st to 13th, 1958) . . . AUTHORIZED ENGLISH EDITION.

More than 2,200 papers (double the number presented at the 1955 Conference) covering all aspects of the Peaceful Uses of Atomic Energy will be presented at the Conference in which approximately 70 countries will participate and discuss their latest achievements, both experimental and practical . . . to be published in the Only OFFICIAL UN EDITION.

The main subjects of the Conference are listed below:

Basic physics
Basic chemistry
Biology and medicine
Use of nuclear enegry for purposes other than generation of electricity
Thermonuclear developments
Possibility of controlled fusion
Raw materials
Production of nuclear materials
Research and power reactors
Reactor technology
Production and uses of isotopes
Training in nuclear sciences

The English edition is expected to consist of 34 volumes (approximately 500 pages each), which will become available beginning December, 1958; publication is expected to be completed by June, 1959.

A special pre-publication price of $435 (or equivalent in other currencies) for the complete set is now available, and orders will be accepted on this basis until November 30, 1958. The regular price for the full set will approximate $510.

Abridged editions in French and Spanish are planned for simultaneous publication. They will consist mainly of the papers presented orally at the Conference (approximately 500), the papers submitted in the language of the edition, and a selection of other papers. These editions are expected to be in 15 volumes, and a pre-publication price is available (up to November 30, 1958) of $190 or equivalent in other currencies.

For further details consult your local bookstore or

UNITED NATIONS : NEW YORK

Brochures giving further details available on request

A.I.Ch.E. JOURNAL

Federal Aid (?) to Education

The various proposals for Federal aid to education have been mulled over by Congress, and a bill has been made law. This law calls for the expenditure of vast sums for student loans, scientific equipment, graduate fellowships, guidance, teacher training, language centers, etc. Proposals apparently not enacted into law were for student scholarships, text books, audio-visual aids, etc.

These proposals seem to attack only the peripheral aspects of the problem. There is no shortage of students around most universities; there are certainly a great many (though assuredly not enough) scholarship funds from private, corporate, and governmental sources; and any shortage of text books has escaped the eye of this observer. As for audio-visual aids, the mind boggles at a serious consideration of such devices when one remembers how these were used by the military in recent years: tape recorders, projectors, and neophytes do not combine to make a teacher.

These proposals attack the periphery at a cost of several hundred million dollars but totally avoid the central problem. The crux of the whole crisis in education at all levels is the shortage of teachers, and particularly the lack of good ones. The present proposals will be of very little assistance in this problem; indeed they probably will make it all the worse by further overloading the present teaching staffs. Yet there is something the government could do about this critical aspect of the problem—and at no expense to the taxpayers.

Probably the greatest single obstacle to securing enough good teachers is the financial one. On the average, teachers are underpaid, and as the cost of living soars into space, they are left farther and farther behind, or they abandon teaching. Inflation, "the cruelest tax," is particularly hard on teachers because the funds which support them are either private benefactions or state taxes. There is a severe limitation on both of these; neither can keep up with a persistent inflation. And the inflation is due largely to the unbalanced budgets of the same Federal Government which proposes to "aid" education.

The best "aid" to education would be for the government to live within its income and to cease and desist from those policies which harm the teachers. And the beauty of this logical course of action is that it would also help many millions of Americans.

H.B.

PROCESS SIMULATION

Where is it used ?

In Research Studies—Process Simulation:

- Bridges the gap between empirical data and theoretical expressions.
- Accelerates the determination of the effect of possible parameter variations.
- Quickly defines missing data required for completion of the study.
- Provides quick and convenient evaluations of theoretical equations.

In Process Design—Process Simulation:

- Permits rapid selection of the best of several design concepts.
- Provides faster optimization of proposed design parameters.
- Assures design on a more fundamental basis.
- Facilitates more accurate scale-up of available pilot-plant data.
- Permits specifications of operating conditions for new designs that are closer to the safe, reasonable limits of the design.
- Applications include distillation columns, absorption beds, continuous reactors, catalytic reactors, heat exchangers, and many others.

In Control Instrumentation—Process Simulation:

- Is especially effective in the accurate representation of instrumentation systems to facilitate integration of control elements.
- Provides special advantages in studying multi-loop and unusual control systems.
- Permits reliable preconstruction specifications and performance requirements for instrumentation planning.
- Considerably reduces cut-and-try engineering.
- Facilitates establishment of pre-trial-run specifications of start-up procedures.

In Optimization of Existing Processes—Process Simulation:

- Permits economical exploration in operating conditions, equipment, and controls without expensive experimentation or production upsets.
- Safely and accurately locates adequate and reasonable safety limits.
- Evaluates proposed changes in process such as side-draws, reflux ratios, piping changes, pump performance, etc., without costly commitments of equipment.

The observations recorded are not guesswork. They represent the results of many hours of experimentation and study acquired by engineering groups of leading companies in the Chemical, Petro-Chemical, and Petroleum fields. These studies have been performed either on their own equipment or on analog computing equipment rented at any of EAI's completely staffed and equipped computation centers in Princeton, New Jersey; Los Angeles, California; or Brussels, Belgium.

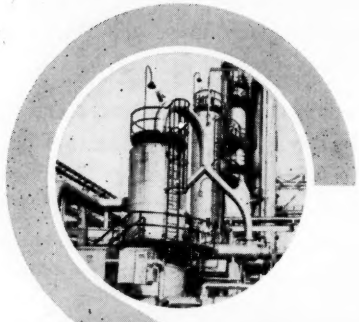

PROCESS SIMULATION COMES OF AGE

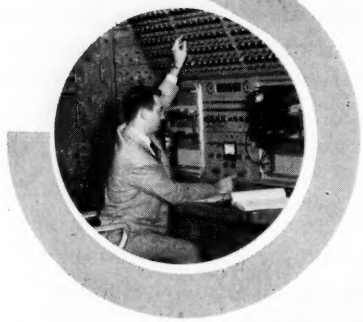

Detailed information can be obtained by mail, wire or telephone :

Electronic Associates, Inc.

Manufacturers of PACE *Precision Analog Computing Equipment*

LONG BRANCH, NEW JERSEY Dept. AI-9

Tel. CApital 9-1100

Kinetics of Nitrogen Tetroxide Absorption in Water

M. M. WENDEL and R. L. PIGFORD

University of Delaware, Newark, Delaware

The rate of absorption of nitrogen peroxide into water at 25° and 40°C. has been found to be a linear function of the concentration of nitrogen tetroxide in the gas phase and directly proportional to the interfacial partial pressure of the same species.

The rate of absorption is independent of gas velocity over a range of Re_G from 170 to 350. The results plotted as absorption rate divided by interfacial partial pressure of nitrogen tetroxide show no effect of liquid rate or contact time between gas and liquid over a tenfold range of contact time from 0.03 to 0.3 sec. This indicates that the rate-controlling step during nitrogen dioxide absorption into water is the rate of hydrolysis of nitrogen tetroxide.

The absorption rate decreases with increasing temperature from 25° to 40°C., owing to the shift of the equilibrium in the gas phase away from the reacting species nitrogen tetroxide toward nitrogen dioxide and owing to the decreased solubility of nitrogen tetroxide in water. The effect of these factors on absorption more than offsets the effect of the increase in reaction rate and higher diffusivity on absorption at 40°C.

The reaction rate constant for the hydrolysis of nitrogen tetroxide has been determined and the solubility of dissolved but unreacted nitrogen tetroxide in equilibrium with gaseous nitrogen tetroxide has been found.

Despite the large quantities of nitric acid made by the absorption of nitrogen oxides into water, the kinetics of the reactions involved are not yet fully explained. These reactions are commonly written as

$$2NO + O_2 \rightarrow 2NO_2 \qquad (1)$$

$$2NO_2 \rightleftharpoons N_2O_4 \qquad (2)$$

$$\left\{\begin{matrix} 3NO_2 \\ \text{or} \\ \frac{3}{2}N_2O_4 \end{matrix}\right\} + H_2O \rightleftharpoons 2HNO_3 + NO \qquad (3)$$

The reaction shown in Equation (3) is the least-understood step of the three.

Future efforts to improve the already high efficiency of absorption towers where reaction (3) is carried out will be based on a better understanding of the kinetics of this reaction. To add to the knowledge of this reaction, a study has been made of the kinetics of the absorption and reaction of nitrogen peroxide* with water. Others (*4, 6, 20*) who have studied this same problem have shown that nitrogen tetroxide is the reacting species in Equation (3) and that the rate-controlling step during absorption is the reaction between nitrogen tetroxide and water, although there is some disagreement as to whether this reaction occurs in the vapor or liquid phase or both. The two-film theory of absorption has been used in some cases (*3, 5, 7*) to analyze absorption results, while in others (*4, 6, 20*) the data have been interpreted in terms of chemical reaction kinetics alone. A different approach was taken in the present work. The results reported here were obtained with the aid of the penetration or unsteady state absorption plus reaction theory (*12*), which mathematically combines the effects on absorption of simultaneous diffusion and chemical reaction in the liquid phase.

*Nitrogen peroxide refers to the equilibrium mixture of nitrogen dioxide and nitrogen tetroxide.

M. M. Wendel is with E. I. du Pont de Nemours and Company, Inc., Wilmington, Delaware.

LITERATURE REVIEW

Studies of the absorption of nitrogen peroxide into aqueous solutions have been made in both short and long wetted-wall columns (*3* to *7* and *21*) and on bubble-cap plates (*20*). The results obtained in long wetted-wall columns (about 3 ft. long) by Bolshakoff (*3*) and Chambers and Sherwood (*5*) indicated that gas-film resistance controlled the absorption of nitrogen dioxide into aqueous solutions of nitric acid and sodium hydroxide. Eagleton, Langer, and Pigford (*7*) reported that the slow rate of reaction between dissolved nitrogen dioxide and liquid water limited the rate of nitrogen dioxide absorption into strong caustic solutions in long wetted-wall columns. Peters and Holman (*21*) studied the effects of temperature and water-vapor concentration on the absorption of nitrogen peroxide into aqueous solutions of sodium hydroxide and sodium chloride in long wetted-wall columns. They concluded that both gas- and liquid-phase reactions between nitrogen tetroxide and water occurred and that the rate of absorption was controlled by these reactions.

Denbigh and coworkers (*4, 6*), working with short wetted-wall columns (less than 7 in.), reported, before Peters and Holman (*21*), that the absorption rate of nitrogen peroxide into aqueous solutions of nitric acid, sodium hydroxide, and calcium chloride was proportional to nitrogen tetroxide concentration in the gas phase. They too had concluded that the speed of absorption was determined by the reaction of nitrogen tetroxide and water and not by diffusion.

Peters, Ross, and Klein (*20*) absorbed nitrogen peroxide into aqueous nitric acid in a bubble-cap–plate column and concluded that the rate-controlling step was the chemical reaction between nitrogen tetroxide and water in the gas phase.

The existence of a homogeneous vapor-phase reaction between nitrogen peroxide and water is an unsettled question of major importance in studies on the mechanism of nitrogen oxide absorption into water. If such a reaction does occur to an appreciable extent, the interpretation of absorption results must take it into consideration. The evidence in support of such a reaction is summarized:

1. Chambers and Sherwood (*5*) ob-

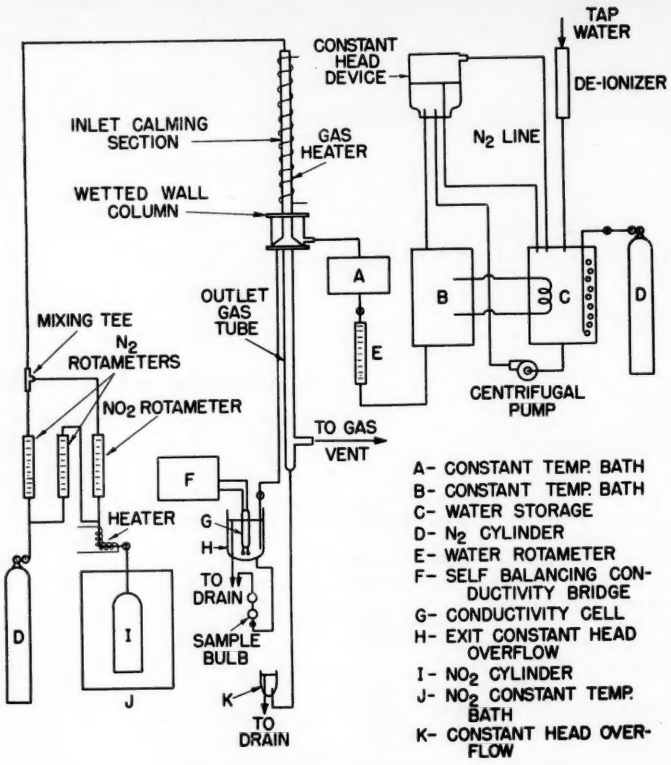

Fig. 1. Diagram of apparatus.

served a mist while absorbing nitrogen peroxide into aqueous solutions of sodium hydroxide and nitric acid. They postulated that this mist was caused by the condensation of the nitric acid produced by the vapor-phase reaction.

$$3NO_2 + H_2O \rightarrow 2HNO_3 + NO \quad (4)$$

They also observed nitric oxide in the exit gas from the absorbers during all runs, including those where sodium hydroxide solutions were used as the absorbents, and concluded that this nitric oxide could result only from the gas-phase reaction of Equation (4), since they believed that the dioxide, once absorbed, reacted with sodium hydroxide according to

$$2NO_2 + 2NaOH \rightarrow NaNO_2 + NaNO_3 + H_2O \quad (5)$$

from which no nitric oxide could be produced.

2. Eagleton, Langer, and Pigford (*7*) also detected nitric oxide in the gaseous effluent when absorbing nitrogen peroxide into sodium hydroxide solutions in a long wetted-wall column, and a mist was observed in the gas phase during one experiment.

3. Peters, Ross, and Klein (*20*) observed a mist during runs where nitrogen dioxide was absorbed into water on a bubble-cap plate.

4. Peters and Holman (*21*) found nitric oxide in the exit gas stream from their long wetted-wall–column absorber when absorbing nitrogen peroxide into aqueous solutions. Thus the hypothesis of a gas-phase reaction has always been based on the presence of a mist and nitric oxide in the exit gas from absorbers.

On the other hand, there is evidence that there is no homogeneous reaction between water and nitrogen peroxide in the vapor phase:

1. Kuzminikh and Udintseva (*14*) attempted to measure the pressure change which should occur in a constant-volume system if a homogeneous vapor-phase reaction took place between nitrogen peroxide and water. They found no change and concluded that no reaction had occurred in the vapor phase.

2. Harris (*11*) performed similar experiments and also observed no reaction. No mist was observed when nitrogen dioxide and water vapors were contacted.

3. Simon (*25*) studied the gaseous reaction over various catalysts, such as activated carbon and silica gel, and did observe a reaction. However in the absence of these catalysts he found no reaction between nitrogen dioxide and water. His experimental method included a qualitative analysis for nitric oxide in the exit gas stream from the reaction chamber. He also observed no mist in the reaction chamber in the absence of liquid water.

4. In direct contradiction to part of the evidence cited in support of a vapor-phase reaction, Denbigh and Prince (*6*) observed no mist during any of their runs while absorbing nitrogen peroxide into nitric acid solutions in a short column.

5. No mist was observed during any of Caudle and Denbigh's (*4*) experiments, and no nitric oxide was found in the exit gas stream during the absorption runs where sodium hydroxide solutions were used. This evidence excluded the possibility of a gas-phase reaction according to

$$N_2O_4 + H_2O \rightleftharpoons HNO_3 + HNO_2 \quad (6)$$

since the nitrous acid would have decomposed to yield nitric oxide by

$$2HNO_2 \rightleftharpoons H_2O + NO_2 + NO \quad (7)$$

6. During a few of his experiments on the oxidation of nitric oxide to nitrogen dioxide with oxygen, Bodenstein (*2*), adding water vapor to the NO–O_2 mixture, found no change in the course of the reaction from the case where water vapor was absent. If water vapor reacts with nitrogen dioxide, it should have affected his results.

Since the evidence on this question appears as strong for as against, it is difficult to conclude from past work whether or not a homogeneous gas-phase reaction does occur. In this research a fog appeared during a few absorption runs in which the concentration of nitrogen dioxide in the gas phase was large, but its presence had no effect on absorption rate since results obtained with and without fog present were in complete agreement. Therefore the data of this investigation were interpreted with the assumption that no gas-phase reaction occurred, and most of the experiments were carried out under conditions such that no fog could be seen.

THEORY

The penetration theory can be used to predict absorption rates or to interpret absorption experiments when absorption occurs under conditions which meet the restrictions of the theory: (1) the liquid phase is in laminar motion with no mixing taking place during absorption; (2) no concentration gradients exist in the liquid before exposure to the gas; (3) molecules of absorbed gas diffuse into the liquid only a very short distance compared with the total liquid depth; and (4) gas and liquid are in physical equilibrium at the interface. The differential equations which describe absorption under these conditions constitute the mathematical model of the penetration theory. These equations have been integrated for the cases of physical absorption of a gas and for absorption plus simultaneous reaction in the liquid phase where the reaction is first or second order (*19, 24*).

In the past the majority of the investigations where the penetration theory was involved have been concerned with establishing the validity of the theory by comparing measured absorption rates with those predicted from the theory. Since good agreement has been obtained (*8, 13, 16, 17, 18, 23, 29*), the validity of the theory was assumed in this study, and it was used, together with measured absorption rates of nitrogen peroxide into water, to calculate the reaction-rate constant for the hydrolysis of nitrogen tetroxide and the equilibrium solubility of this species in the unreacted form in water. Neither of these quantities can be obtained conveniently by other means.

APPARATUS

The apparatus, shown schematically in Figure 1, consisted of a short wetted-wall column and auxiliary apparatus for producing and measuring gas and liquid streams flowing to the column. Constant-temperature controllers were used to bring these streams to the desired operating temperatures.

One of the important features of a short wetted-wall column is that it produces a falling film of water which is contacted by a gas stream for a known period of time over a known area. Figure 2 shows a column assembled to do this. During operation water enters at the liquid inlet, fills the inlet liquid reservoir, passes through the inlet slot, and flows down the wetted-wall section in a smooth film. Near the exit slot some ripples always appear on the liquid surface. The water follows the flared portion of the glass and leaves the absorption section through the exit slot formed by the exit-gas tube and the glass, passes through the liquid outlet, and flows to the sampling bulb. The length of the interfacial area was measured with a millimeter scale beginning at the bottom edge of the inlet-gas tube and extending to the top edge of the exit-gas section. The inlet and exit slots were maintained completely full during all absorption experiments. The critical dimensions of the wetted-wall columns used are given in Table 1.

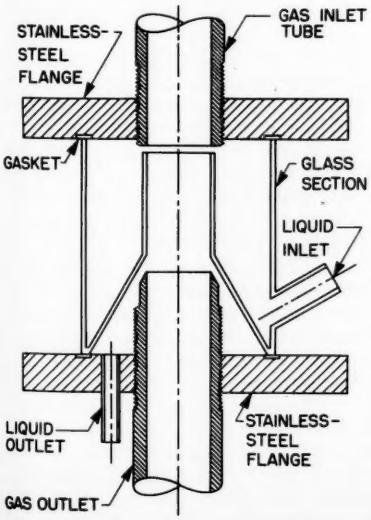

Fig. 2. Short wetted-wall column.

Table 1. Dimensions of Wetted-wall Columns

Column length,* cm.	Column I.D., cm.	Interfacial area, sq. cm.
1.61	2.54	12.9
4.15	2.41	31.4
8.72	2.54	69.4

*Length includes slots formed by inlet and exit gas tubes and column.

The auxiliary equipment for the gas-feed system was designed to give mixtures of nitrogen and nitrogen peroxide in known concentrations at the wetted-wall column. Gas and liquid flowed concurrently through the column to avoid contact before the wetted-wall section.

Nitrogen peroxide of purity reported greater than 99% was used without further purification, and nitrogen with less than 0.004% impurities was used for the carrier gas. Deionized water, purged of all gases except nitrogen, was used as the solvent in all experiments.

The solutions from the wetted-wall column absorber were analyzed for the total oxides of nitrogen absorbed. A sample of the solution was pipetted under the surface of a known volume of standard carbon dioxide–free sodium hydroxide solution containing 10 ml. of 1.5% hydrogen peroxide solution. This basic solution was then back-titrated with carbon dioxide–free standard hydrochloric acid to obtain the amount of base equivalent to all absorbed nitrogen oxides in whatever form, expressed as nitrogen dioxide. The results of the analysis in this form were sufficient for the purposes of this investigation.

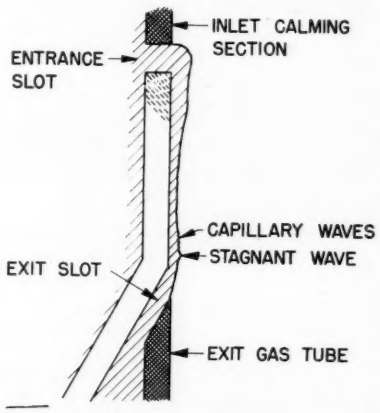

Fig. 3. Cross section of wetted-wall column.

SURFACE OF WATER LAYER

It was stated earlier that ripples appeared on the surface of the water in the wetted-wall column near the exit liquid slot. A qualitative study was made during this research of the liquid flow conditions in the 4.15-cm. column to determine what caused these ripples and what effect they had on the absorption rate of a gas.

Figure 3 is a cross section of one side of a column showing the shape of the liquid layer. The layer is thickest at the entrance slot and thins out as it proceeds down the column. Just above the exit slot a series of waves appears on the liquid surface. Their size and position depend on the liquid rate. These waves were always present despite changes in the exit slot width, variations in water rate, or the presence of a moving gas stream, as long as no liquid was allowed to spill over into the exit gas tube section. The waves are the result of the deceleration of the liquid surface to zero velocity by the top of the exit gas line. A similar phenomenon can be observed in front of a fish line submerged in a moving stream. A wave pattern is evident upstream of the line no matter what the liquid velocity. Lamb (*15*) discusses this situation at length and shows that the velocity of propagation depends on the interfacial tension.

Two types of waves were visible on the liquid surface. The first kind, labeled *capillary* waves in Figure 3, had a relatively small wave length, and the second, called *stagnant* waves, was of distinctly larger wave length and amplitude. Another difference between the waves was the speed with which they formed just after a spillover, that is, after a liquid overflow at the exit slot into the exit gas line ceased. The capillary waves appeared immediately thereafter, but the stagnant waves formed more slowly and progressed upstream from the exit slot at a low rate to a steady position which depended on the liquid velocity. This position varied from about 1 to 12 mm. from the top of the exit-gas tube section, the height being inversely related to the liquid rate. A small band of capillary waves riding on top of the stagnant wave extended another 2 or 3 mm. upstream.

Qualitative studies were made of liquid-surface conditions by introducing a very narrow dye streak onto the surface of the liquid and observing its behavior as it flowed down the column. The streak was undisturbed as it moved on the water surface through the capillary waves, but immediately on contacting the stagnant wave the dye streak broadened, indicating that the condition of the surface below the stagnant wave was different from that above it. When 320-mesh alundum powder was blown onto the surface of the moving liquid in the wetted-wall column, the particles

were swept rapidly through the area above the stagnant wave but were decelerated on the surface below the stagnant wave and sometimes moved in a direction opposite to the total water flow. The stagnation of this lower portion of the surface was probably due to the accumulation of a monomolecular layer of surface-active organic compounds which could be present in the water in trace amounts. A surface covered with a layer of this type would be expected to be only partially effective for gas absorption. Experimental observations of a decreased effectiveness of this type have been made by Lynn, Straatemeier, and Kramers (*16*) in a wetted-wall absorber and by Kennedy (*13*) in a rotating drum absorber. The carbon dioxide absorption studies of this investigation have confirmed their results. Therefore it was decided to remove the stagnant surface once every 30 sec. by causing a momentary spillover of liquid into the exit-gas tube section by pinching a rubber portion of the exit-liquid line for ½ sec. The stagnant area thus never had time to develop completely; yet only a negligible fraction of the solution containing absorbed gas was lost. A dye-streak test showed that intermittent spilling over maintained the stagnant wave at a position much lower than with no spillover. During the carbon dioxide–absorption experiments of this research, results obtained with and without spillover showed that operation with spillover resulted in less scatter and more proximity to the predictions of the penetration theory.

EXPERIMENTAL PLAN

Since a fog occurred during absorption when the total nitrogen peroxide concentration was greater than about 25 mole % and occasionally even as low as 5 mole %, the nitrogen peroxide concentration was always maintained below 25 mole % in the experiments reported here, and no fog was apparent during most of the runs. In those few cases where it did occur it was only barely visible and had no detectable effect on the absorption rate.

The gas-film resistance introduced by the inert carrier, N_2 was investigated by using ammonia as the solute to develop a correlation with which the gas-film resistance could be estimated when NO_2 was substituted for NH_3. Absorption studies of carbon dioxide into water were also made to check the operation of the column. The detailed results of the carbon dioxide experiments are reported elsewhere (*29*). It is sufficient to say here that the results showed excellent agreement with published data (*13, 17*), an indication that the columns were being operated properly. Following this the effects of gas rate, gas composition, water rate, or contact time between gas and liquid, and temperature on the absorption of nitrogen peroxide into water were studied. The nitrogen peroxide fraction of the gas stream, expressed as moles of $NO_2 + 2N_2O_4$ divided by total moles, was varied between 0.06 and 0.20. The range of gas rates covered Re_G from 170 to 350. Water rates were adjusted to give contact times between gas and liquid from 0.03 to 0.3 sec., and experiments were carried out at 25° and 40°C. The original data can be found in a thesis by one of the authors (*29*).

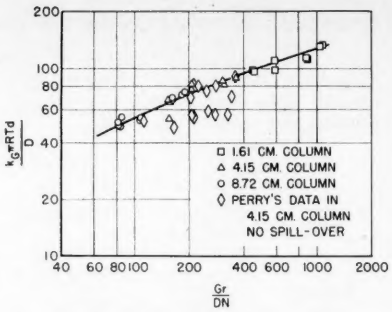

Fig. 4. Gas-film coefficient correlation based on ammonia absorption experiments.

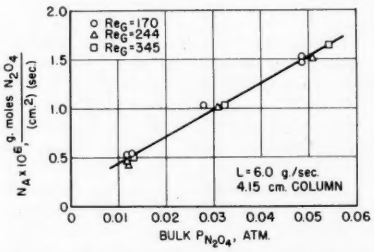

Fig. 5. Effect of gas rate and gas composition on N_2O_4 absorption.

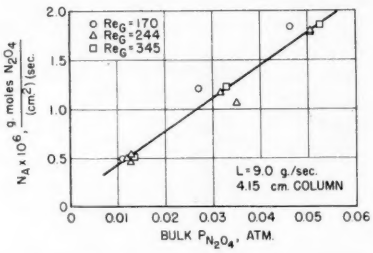

Fig. 6. Effect of gas rate and gas composition on N_2O_4 absorption.

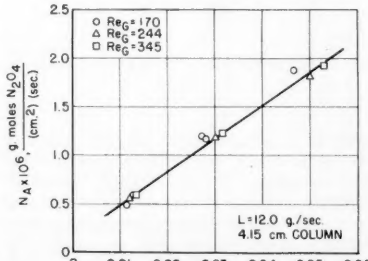

Fig. 7. Effect of gas rate and gas composition on N_2O_4 absorption.

AMMONIA ABSORPTION

A gas-film resistance correlation for short wetted-wall columns was obtained from a series of ammonia absorption experiments. The data, shown in Figure 4, were correlated on the basis of a material-balance equation which assumes no back pressure of ammonia at the liquid surface.

$$\frac{k_G \pi RTd}{D} = \left(\frac{2G_T p_{BM}}{DNP}\right)\left(\frac{p_{G_1} - p_{G_2}}{p_{G_1} + p_{G_2}}\right) \quad (8)$$

Perry's data (*18*) on a short wetted-wall column, included for comparison in Figure 4, fall below the best line through the data of this research and show greater scatter because Perry had no spillover at the exit slot of his column.

NITROGEN DIOXIDE–NITROGEN TETROXIDE ABSORPTION STUDIES

Effect of Gas Rate

Three levels of gas rate were examined: 0.11, 0.15, and 0.22 total g.-moles of gas/min., corresponding to Re_G of 170, 244, and 345. These rates were selected so that inordinate amounts of NO_2 and N_2 would not be consumed and the concentration of nitrogen oxides in the gas stream might still be varied over a moderate range. The gas-rate investigations were carried out in the 4.15-cm. column at 25°C. with liquid rates of 6.0, 9.0, and 12.0 g./sec. The absorption rates at the three gas velocities are plotted as a function of the average composition of the bulk gas phase in Figures 5, 6, and 7. It can be seen that the gas rate had no apparent effect on the quantity absorbed.

Effect of Gas Composition

The absorption rate was measured as a function of nitrogen peroxide composition in all three columns, with the result that the rate was proportional to nitrogen tetroxide partial pressure in the bulk gas stream at all gas rates and contact times, and at both temperatures of operation. The lower curves in Figures 8, 9, and 10 are plots of a portion of the data taken in the 8.72-cm. column at 25°C. This is representative of the remainder of the data from the 1.61- and 4.15-cm. columns in that the points for

bulk composition also fell on straight lines whose intercepts were not zero.

The linear relation between the absorption rate and nitrogen tetroxide bulk composition suggests very strongly that the rate-limiting step in the process is the reaction between 1 molecule of nitrogen tetroxide or 2 of nitrogen dioxide and water. The nitrogen dioxide concentration is related to the nitrogen tetroxide in the gas by the equilibrium constant

$$K_p = \frac{p_{N_2O_4}}{(p_{NO_2})^2} \qquad (9)$$

Hence the linear relation found between absorption rate and $p_{N_2O_4}$ means that a similar relation exists between the rate and the square of p_{NO_2}. The two reactions which could occur in solution are

$$N_2O_4 + H_2O \rightleftharpoons HNO_2 + HNO_3 \quad (10)$$

or

$$2NO_2 + H_2O \rightleftharpoons HNO_2 + HNO_3 \quad (11)$$

If liquid-phase diffusion of the oxide after absorption had any effect whatsoever on the absorption rate and if nitrogen dioxide were actually the reacting species according to Equation (11), the over-all rate would be proportional to some power of nitrogen dioxide concentration between 1 and 2. (The diffusion rate would be proportional to the first power of nitrogen dioxide concentration and the reaction rate probably to the square of the nitrogen dioxide concentration, giving an over-all effect of nitrogen dioxide concentration to somewhat smaller than the second power.) A similar line of reasoning for nitrogen tetroxide indicates that the absorption rate would be proportional to the first power of nitrogen tetroxide concentration, as found experimentally in this work. Therefore it was concluded that, at least under the conditions studied, nitrogen tetroxide is the compound which dissolves and reacts with water more rapidly. A less convincing argument also in favor of this conclusion is the greater likelihood of a bimolecular reaction occurring, according to Equation (10), rather than a termolecular one, as expressed by Equation (11).

To apply the concepts of the penetration theory to the results of this work, it was necessary to know the partial pressure of the material being absorbed at the point in the gas phase adjacent to the gas-liquid interface. The average value of this quantity through the column was used. To calculate it Herron's equation, as quoted by Eagleton *et al.* (*7*), for the simultaneous diffusion of nitrogen dioxide and nitrogen tetroxide through a stagnant gas film was used. [See Equation (12).] The equation was derived by assuming that the two substances are locally at chemical equilibrium everywhere in the gas film.

$$N_A = 2K_p(k_G)_{N_2O_4}[(p_{NO_2})^2 - (p_{iNO_2})^2] + (k_G)_{NO_2}[(p_{NO_2} - p_{iNO_2})] \quad (12)$$

The interfacial partial pressure of nitrogen tetroxide is related to that of nitrogen dioxide by Equation (9). With Equation (12) and the gas-film coefficient correlation developed during this work, the interfacial partial pressure of nitrogen tetroxide could be obtained. The upper curves in Figures 8, 9, and 10 are plots of absorption rate as a function of interfacial partial pressure of nitrogen tetroxide for the results obtained with the 8.72-cm. column. The interfacial concentration of nitrogen textroxide is appreciably less than the bulk nitrogen tetroxide. A straight line through these results passes through the origin, showing a direct proportionality between N_A and $(p_i)_{N_2O_4}$. Therefore nitrogen tetroxide is the species which dissolves and reacts more rapidly.

Effect of Liquid Rate

The change in absorption rate with contact time between gas and liquid was studied by varying the water rate through the columns. All three of the columns were employed to give as wide a variation of contact time as possible. Figure 11 shows the results plotted as absorption rate divided by interfacial partial pressure of nitrogen tetroxide vs. contact time. Each point on this graph represents the average of all the runs made at that particular contact time. The points were weighted, according to the number of runs making up the average, to locate the best line through the data. There is no trend of the data with time over the tenfold range covered. This independence of the rate and the contact time also means that end effects, such as partial stagnation of the liquid at the exit slot, which might change the contact time, probably had very little effect on the absorption rate of nitrogen tetroxide into water.

A series of runs was made at 40°C. to determine the effect of temperature on absorption rate. It was found, as seen in Figure 11, that a slight decrease of $N_A/(p_i)_{N_2O_4}$ with increased temperature occurred, even when runs were made at the same interfacial partial pressure. The decrease, which may not be significant because of the scatter in the data, is probably due to the lower solubility of nitrogen tetroxide in water at the higher temperature, which more than offsets the increase of diffusivity of nitrogen tetroxide in water once the molecule has been absorbed. If the data had been plotted as absorption rate vs. total nitrogen peroxide in the gas, the rate would have been found to be lower at the higher temperature.

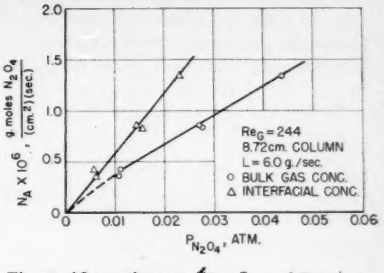

Fig. 8. Absorption results, L = 6.0 g./sec.

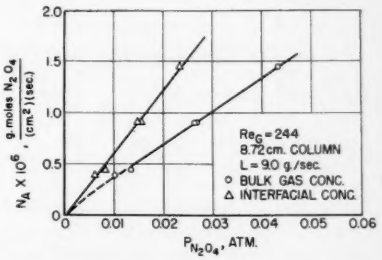

Fig. 9. Absorption results, L = 9.0 g./sec.

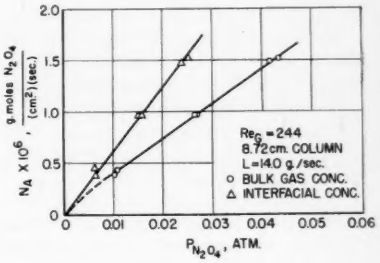

Fig. 10. Absorption results, L = 14.0 g./sec.

RESULTS IN TERMS OF THE PENETRATION THEORY

The controlling chemical step in the absorption process is the bimolecular reaction between dissolved nitrogen tetroxide and liquid water:

$$N_2O_{4(aq)} + H_2O_{(l)} \xrightarrow{k_c} HNO_{2(aq)} + HNO_{3(aq)} \quad (13)$$

The water concentration always greatly exceeds the tetroxide, and so the reaction can be considered a pseudo-first-order one. For a first-order chemical reaction accompanying absorption, Sherwood and Pigford (*24*) give the following equation derived on the basis of the penetration theory.

$$N_A = \sqrt{k_c D}[1 + \tfrac{1}{2}(k_c t) + \cdots]c_i \quad (14)$$

The fact that the absorption rate at constant interfacial concentration of

nitrogen tetroxide is not affected by the time of contact between gas and liquid t indicates that the reaction rate constant k_c is large. Equation (14) can be simplified to

$$N_A = \sqrt{k_c D}(c_i)_{N_2O_4} \quad (15)$$

where $(c_i)_{N_2O_4}$ is the concentration at the interface of the dissolved but unreacted nitrogen tetroxide in water. This equation can be rewritten in the form

$$\frac{N_A}{(p_i)_{N_2O_4}} = \sqrt{k_c D}\,\frac{(c_i)_{N_2O_4}}{(p_i)_{N_2O_4}} \quad (16)$$

For the physical solution of nitrogen tetroxide in water,

$$N_2O_{4(g)} \rightleftharpoons N_2O_{4(aq)} \quad (17)$$

the equilibrium constant

$$K_1 = \frac{(c_i)_{N_2O_4}}{(p_i)_{N_2O_4}} \quad (18)$$

is a measure of the solubility of unreacted nitrogen tetroxide in water. $N_A/(p_i)_{N_2O_4}$ has been measured in this research and found to depend only on the temperature. Although it cannot be measured directly, the diffusivity D of nitrogen tetroxide in water can be estimated from the Wilke correlation (*30*). Thus, on the basis of the experiments, there is a relation between the equilibrium constant for the physical solution of nitrogen tetroxide in water K_1 and the rate constant for hydrolysis of nitrogen tetroxide, k_c:

$$k_c = \left[\frac{N_A}{(p_i)_{N_2O_4}}\right]^2 \frac{1}{D}\left(\frac{1}{K_1}\right)^2 \quad (19)$$

Inserting the known quantities from Figure 11 in Equation (19) one obtains

$$k_c = 2.68 \times 10^{-4}\left(\frac{1}{K_1}\right)^2 \text{ at } 25°\text{C.} \quad (20)$$

$$k_c = 1.66 \times 10^{-4}\left(\frac{1}{K_1}\right)^2 \text{ at } 40°\text{C.} \quad (21)$$

To carry the analysis of the data further, one must resort to an independent source of physico-chemical data. Abel and Schmid (*1*), who have made an extensive study of the kinetics of nitrous acid formation and decomposition, showed that the decomposition of nitrous acid takes place by a sequence of steps stoichiometrically equivalent to the reaction

$$3HNO_2 \xrightarrow{k_1} H^+ + NO_3^- + 2NO + H_2O \quad (22)$$

and during the initial stages

$$-\frac{d(HNO_2)}{dt} = k_1\frac{(HNO_2)^4}{(p_{NO})^2} \quad (23)$$

Values of k_1 determined by Abel are quoted in Table 2.

Table 2. Rate Constants of Abel and Schmid For Nitrous Acid Decomposition

T, °C.	k_1, (liters)⁴/(g. moles)⁴(min.)(atm.)²
0	0.602
12	3.63
25	46
40	525

To explain the rate, Equation (23), Abel and Schmid proposed the mechanism

$$4HNO_{2(aq)} \rightleftharpoons N_2O_{4(aq)} + 2NO_{(g)} + 2H_2O_{(l)} \quad (24)$$

a relatively rapid equilibrium

$$N_2O_{4(aq)} + H_2O_{(l)} \xrightarrow{k_2} HNO_{2(aq)} + H^+ + NO_3^- \quad (25)$$

a slower, rate-determining step

For the equilibrium step, Equation (24), one writes

$$K_2 = \frac{(N_2O_4)(p_{NO})^2}{(HNO_2)^4} \quad (26)$$

or

$$\frac{(HNO_2)^4}{(p_{NO})^2} = \frac{(N_2O_4)}{K_2} \quad (27)$$

Thus from Equations (23) and (27)

$$-\frac{d(HNO_2)}{dt} = \frac{k_1(N_2O_4)}{K_2} \quad (28)$$

Since a net total of three molecules of nitrous acid decompose when one molecule of nitrogen tetroxide disappears and from Equation (25)

$$-\frac{d(N_2O_4)}{dt} = \frac{1}{3}\frac{k_1(N_2O_4)}{K_2} = k_c(N_2O_4) \quad (29)$$

$$k_c = \frac{1}{3}\left(\frac{k_1}{K_2}\right) \quad (30)$$

The concentration of dissolved but unreacted nitrogen tetroxide can be related to the partial pressure in the gas by the equilibrium constant K_1 as given in Equation (18). If K_1 is substituted into Equation (26), one obtains

$$K_2 = \frac{K_1(p_{N_2O_4})(p_{NO})^2}{(HNO_2)^4} \quad (31)$$

With

$$\frac{K_2}{K_1} = \frac{(p_{N_2O_4})(p_{NO})^2}{(HNO_2)^4} = K_3 \quad (32)$$

$$k_c = \frac{1}{3}\frac{k_1}{K_1K_3} \quad (33)$$

Abel, to find K_3, made use of the data of Pick (*22*), who measured standard electrode potentials at 25°C. for the reactions

$$2HNO_{2(aq)} + 2H^+ = 2NO_{(g)} + 2H_2O_{(l)} - 2e;\ E° = 0.98 \text{ volt} \quad (34)$$

$$N_2O_{4(g)} + 2H^+ = 2HNO_{2(aq)} - 2e;\ E° = 1.07 \text{ volts} \quad (35)$$

Subtracting (35) from (34) one obtains

$$4HNO_{2(aq)} = N_2O_{4(g)} + 2NO_{(g)} + 2H_2O_{(l)};\ E° = -0.09 \text{ volt} \quad (36)$$

from which $\Delta F° = 4{,}150$ cal./mole can be calculated. The equilibrium constant for reaction (36) is K_3; it can be obtained from the expression relating the free energy change and equilibrium constant.

$$\Delta F° = -RT \ln K_3 \quad (37)$$

$$K_3 = 9.1 \times 10^{-4}\frac{(\text{atm.})^3(\text{liter})^4}{(\text{g.-mole})^4} \text{ at } 25°\text{C.} \quad (38)$$

Equation (33) becomes

$$k_c = 361\,\frac{k_1}{K_1} \quad (39)$$

From Table 2 a value of 46 at 25°C. is available for k_1, where the units are in moles per liter and minutes. If this is converted to moles per cubic centimeter and seconds and substituted in Equation (39), one obtains

$$k_c = \frac{0.281}{K_1} \quad (40)$$

Equations (40) and (20) involve the rate constant for hydrolysis of nitrogen tetroxide k_c and the equilibrium constant K_1. With these simultaneous equations one finds at 25°C.

$$k_c = 290 \text{ sec.}^{-1}$$

$$K_1 = 9.55 \times 10^{-4} \text{ g.-moles/(cc.)(atm.)}$$

The solubility, expressed as a Henry's Law constant, is $H = 58$ atm./(g.-moles N_2O_4)/(g.-mole solution). For comparison, H for carbon dioxide is 1,640 at 25°C.; therefore nitrogen tetroxide is about thirty times more soluble than carbon dioxide. From the absorption runs made at 40°C. one can procure

$k_c = 1{,}340 \text{ sec.}^{-1}$

$K_1 = 3.52 \times 10^{-4}$ g.-moles/(cc.)(atm.) or

$H = 158$ atm./(g.-mole N_2O_4)/(g.-mole solution)

The energy of activation for the hydrolysis of nitrogen tetroxide and the heat of solution of nitrogen tetroxide in water can be estimated from the knowledge of k_c and K_1 at two temperatures.

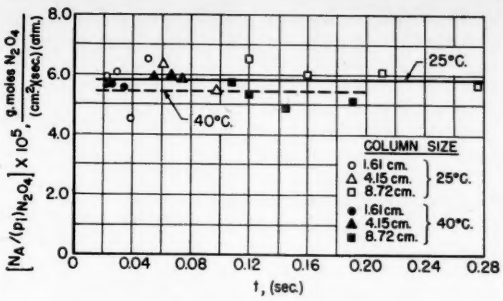

Fig. 11. Effect of absorption time on absorption rate.

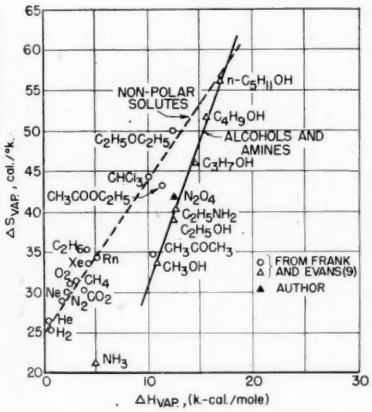

Fig. 12. Thermodynamic properties of nonionic solutes in water.

$$\Delta H_{act} = 18.8 \text{ k.-cal./g.-mole}$$

$$\Delta H_{soln} = -12.3 \text{ k.-cal./g.-mole}$$

This value of activation energy is a reasonable one for reactions in solution, and the heat of solution is of the same order of magnitude as an estimate of −14.1 k.-cal./g.-mole at 18°C. given for nitrogen tetroxide into water by Thomsen (*26*).

COMPARISON OF RESULTS WITH LITERATURE INFORMATION

The phenomenon of a white fog or mist during nitrogen dioxide absorption is not new. A mist is often visible in the absorption towers used to manufacture nitric acid. Previous authors specifically called attention to its occurrence in long wetted-wall columns (*5*, *7*). However Denbigh and co-workers (*4*, *6*) observed no mist, and Peters and Holman (*21*) state that they eliminated mist during NO_2 absorption by carefully filtering the inert carrier gas before using it. In most of the experiments made in this research, although the nitrogen was not filtered, no fog was visible even after nitrogen dioxide had contacted liquid water in the column. When hydrogen chloride was mixed with nitrogen and passed through the column, mist occurred similar in appearance to what was observed occasionally during nitrogen dioxide absorption. In addition the author (*28*) observed a mist when pure phosgene was absorbed into water and aqueous solutions of sodium hydroxide. This suggests a possible explanation for the mist phenomenon.

When a highly soluble gas is absorbed which has a large heat of solution and reaction with water, the temperature of the water surface rises, causing vaporization of some water. As this water vapor diffuses outward into the cooler gas stream condensation occurs in the form of minute droplets: a fog. Absorption of gas can take place into these droplets generating, in the case of nitrogen peroxide, nitric acid within them.

Further evidence in support of this hypothesis was found when a temperature gradient was deliberately imposed on the NO_2–H_2O system in the present research. The water in the wetted-wall column was held at 40°C. inlet temperature, and an NO_2–N_2O_4–N_2 gas stream 15° cooler was passed through the absorber. A very dense mist ensued, but as the gas temperature was increased the amount of mist decreased until only a trace was visible when both gas and liquid were at 40°C. According to the hypothesis the amount of water vapor condensing to form fog decreased as the gas temperature was increased.

For a nitrogen peroxide system absorption into water droplets would yield nitric oxide which would then escape into the gas stream because of its low solubility in nitric acid solutions. This could account for the occurrence of nitric oxide in the exit gas from Chambers' (*5*) column. The heat of reaction between nitrogen peroxide and water or sodium hydroxide solution could have caused some water to be vaporized which, condensed as described, absorbed nitrogen dioxide and desorbed nitric oxide. The heat of reaction between nitrogen dioxide and the water droplets would generate heat in the gas phase which would raise the temperature and account for a temperature rise in the gas stream, also reported by Chambers. Fog droplets escaping from the column with the exit gas would give an acid reaction, even though the liquid phase is alkaline, in agreement with observations. Thus neither the occurrence of a mist nor the presence of nitric oxide in the exit gas stream from an absorber should be used as conclusive evidence of a vapor-phase reaction between nitrogen dioxide and water.

The absence of a gas-rate effect on absorption rates is in complete agreement with Bolshakoff (*3*), as recalculated by Eagleton, *et al.* (*18*), who found no effect in the range of Re_g from 125 to 1,100 when the partial pressure of $NO_2 + 2N_2O_4$ was 0.04 atm. or greater. Bolshakoff used a long wetted-wall column and absorbed into aqueous solutions of sodium hydroxide. Denbigh and Prince (*17*), who were the only other investigators to use gas rates as low as those of this research, found only a small effect of gas velocity.

There is considerable support in the literature for the linear relationship found in this work between absorption rate and bulk gas-phase nitrogen tetroxide concentration. Denbigh and coworkers (*4*, *6*) and Peters, Ross, and Klein (*20*) concur and account for it by assuming that the reaction between nitrogen tetroxide and water is the rate-controlling chemical step in the process. The latter authors believed the reaction to occur in *both* gas and liquid phases, but Denbigh (*4*) stated only that it must occur near the gas-liquid interface. Denbigh and Prince (*6*) expressed the relation between rate of absorption of nitrogen peroxide and bulk nitrogen tetroxide concentration in the gas by the equation

$$N_A = k_a(p_{N_2O_4}) \qquad (41)$$

when absorbing into dilute nitric acid solutions in the absence of nitric oxide. This equation indicates that their plots of N_A vs. $p_{N_2O_4}$ passed through the origin, although a small intercept was found in every case in this research when plotting bulk $p_{N_2O_4}$. The use of interfacial $p_{N_2O_4}$ has been shown to eliminate this intercept in the present paper. The average values of k_a found by Denbigh and Prince at 25° and 40°C. are compared with the average slope of lines from plots of N_A vs. bulk N_2O_4 partial pressure for this investigation (for example, Figures 5, 6, and 7) in Table 3. The agreement is fair considering that the average for this research included results for all liquid rates. The influence of temperature on k_a, also shown in Table 3, is nearly the same in the two investigations.

In these experiments no effect of liquid rate (or time of contact between gas and liquid) on $N_A(p_i)_{N_2O_4}$ was found. This is in accord with the results of Denbigh and Prince (*6*) who found no effect of liquid rate on $N_A/(p_{N_2O_4})$ bulk and Caudle and Denbigh (*4*) who reported only a slight effect on a similar quantity.

TABLE 3. COMPARISON OF D. AND P. RESULTS WITH THIS WORK

Temp., °C.	k_a (D & P.), cm./sec.	$\frac{(k_a)\ 40°}{(k_a)\ 25°}$	k_a (this work), cm./sec.	$\frac{(k_a)\ 40°}{(k_a)\ 25°}$
25	1.8		0.71	
40	2.3		0.94	
		1.28		1.32

The small decrease in $N_A(p_i)_{N_2O_4}$ with a temperature rise from 25° to 40°C. means that at a constant value of total nitrogen peroxide in the gas the absorption rate for nitrogen peroxide decreased with an increase in temperature. This occurs because more nitrogen peroxide must be present at 40°C. to give the same nitrogen tetroxide concentration at the interface, owing to the shift in the NO_2–N_2O_4 equilibrium. Webb (*27*) and Denbigh and Prince (*7*) also found this decrease in absorption at higher temperatures.

Although the proposed mechanism of the absorption process is supported by all of the experimental evidence available, it may be reasonably asked whether another mechanism, possible involving other chemical species, may not also be able to account for the experimental facts. That many different compounds involving nitrogen and oxygen are possible and that many are chemically reactive toward water is obvious. Therefore is the proposed mechanism the true one? Are the chemical properties of dissolved nitrogen tetroxide molecules, inferred from the experimental data, those of a real or imaginary chemical substance? Although an unequivocal answer to such questions may not be possible, in view of the limitations of the data owing to experimental errors of observation, it can be stated that with a high degree of probability the suggested mechanism *is* the true one, since it can be shown that the derived thermodynamic properties of the tetroxide are reasonable values. Several independent pieces of experimental evidence, each independent of the other, have been employed, and each has assumed the existence of the tetroxide molecules. The numerical values of heat and entropy of solution derived from all the data through the chain of assumptions could hardly represent acceptable thermodynamic properties unless all the assumptions were essentially correct. If one of the mutually dependent results can be shown to be correct, all must be essentially true.

Frank and Evans (*10*) have plotted the entropy of vaporization of various nonionic solutes in water vs. the heat of vaporization of the gases from aqueous solution as shown in Figure 12. The points on this plot may be divided into two groups: (*a*) nonpolar solutes, and (*b*) alcohols and amines. An entropy of vaporization for dissolved but unreacted nitrogen tetroxide of −42.2 cal./°K. can be calculated from the values of K_1 and ΔH_{soln} at 25°C. to give the point for nitrogen tetroxide plotted on Figure 12. It is seen that this point falls close to the line for alcohols and amines, as might be expected on the basis of hydrogen bonding since alcohols, amines, and nitrogen tetroxide (which has four oxygen atoms available) have the opportunity to hydrogen bond in water solution. The fact that the observed values of ΔS and ΔH lie at a reasonable position in Figure 12 lends support to the validity of both thermodynamic properties and the rate data obtained for nitrogen tetroxide.

ACKNOWLEDGMENT

Grateful acknowledgment is made to E. I. du Pont de Nemours and Company and the Shell Oil Company whose postgraduate fellowships provided financial assistance for this investigation.

NOTATION

c_i = interfacial concentration of solute, g.-moles/cc.
d = wetted-wall column I.D., cm.
D = diffusivity, sq. cm./sec.
$\Delta F°$ = standard free energy change, cal./g.-mole
G_r = relative gas rate, cc./sec.
H = Henry's law constant, atm./(g.-mole N_2O_4)/(g.-mole solution)
ΔH_{act} = energy of activation, k.-cal./g.-mole
ΔH_{soln} = heat of solution, k.-cal./g.-mole
k = reaction rate constant, subscript denotes reaction
k_a = slope of curve of N_A vs. $p_{N_2O_4}$, g.-moles/(sq. cm.)(sec.)(atm.)
k_c = pseudo-first-order rate constant, sec.$^{-1}$
k_G = gas-film coefficient, g.-mole/(sq. cm.)(sec.)(atm.)
K = equilibrium constant, subscript denotes reaction
L = liquid flow rate, g./sec.
N = wetted-wall column length, cm.
N_A = average absorption rate, g.-moles N_2O_4/(sq. cm.)(sec.)
p = partial pressure of gas, atm.
P_{G_1} = partial pressure of solute at inlet to column, atm.
P_{G_2} = partial pressure of solute at exit from column, atm.
P = total pressure, atm.
p_{BM} = log mean partial pressure of inert gas, atm.
Re_G = gas Reynolds number
t = time of contact between phases, sec.
T = temperature, °K.

LITERATURE CITED

1. Abel, E., and H. Schmid, *Z. physik. Chem.* **132**, 56, 64 (1928); **134**, 279 (1928); **136**, 135, 419, 430 (1928).
2. Bodenstein, M., F., *Elektrochem.* **24**, 183 (1918).
3. Bolshakoff, P. E., S.M. thesis, Mass. Inst. Tech., Cambridge (1934).
4. Caudle, P. G., and K. G. Denbigh, *Trans. Faraday Soc.*, **49**, 39 (1953).
5. Chambers, F. S., and T. K. Sherwood, *Ind. Eng. Chem.*, **29**, 1415 (1937).
6. Denbigh, K. G., and A. J. Prince, *J. Chem. Soc.*, 790 (1947).
7. Eagleton, L. C., R. M. Langer and T. H. Pigford, S.M. thesis, Mass. Inst. Tech., Cambridge (1948).
8. Emmert, R. E., Ph.D. thesis, Univ. of Del., Newark (1954).
9. Emmert, R. E., and R. L. Pigford, *Chem. Eng. Progr.*, **50**, 87 (1954).
10. Frank, H. S., and M. W. Evans, *J. Chem. Phys.*, **6**, 40 (1938).
11. Harris, G. E., B.S. thesis, Univ. of Del., Newark (1951).
12. Higbie, R., *Trans. Am. Inst. Chem. Engrs.*, **31**, 365 (1935).
13. Kennedy, A. M., "Kinetics of Liquid-Film Processes in Gas Absorption," thesis, Cambridge Univ., Cambridge, Eng. (1954).
14. Kuzminykh, I. N., and V. S. Udintseva, *Khimstroi*, **6**, 523 (1954).
15. Lamb, H., "Hydrodynamics," 6 ed., p. 464, Dover Publications, New York (1945).
16. Lynn, S., J. R. Straatemeir, and K. Kramers, *Chem. Eng. Sci.*, **4**, 49 (1955).
17. Vivian, J. E., and D. W. Peaceman, *A.I.Ch.E. Journal*, **2**, 437 (1956).
18. Perry, R. H., Ph.D. thesis, Univ. of Del., Newark (1953).
19. Perry, R. H., and R. L. Pigford, *Ind. Eng. Chem.*, **45**, 1247 (1953).
20. Peters, M. S., C. P. Ross, and J. E. Klein, *A.I.Ch.E. Journal*, **1**, 105 (1955).
21. Peters, M. S., and J. L. Holman, *Ind. Eng. Chem.*, **47**, 2536 (1955).
22. Pick, H., *Z. Elektrochem.*, **26**, 182 (1920).
23. Scriven, L. E., Ph.D., Univ. of Del., Newark (1956).
24. Sherwood, T. K., and R. L. Pigford, "Absorption and Extraction," 2 ed., McGraw-Hill, New York (1952).
25. Simon, R. H. M., B.Ch.E., Univ. of Del., Newark (1948).
26. Thomsen, A., "Thermochemistry," trans. by K. A. Burke, Longmans, Green, and Co., London (1908).
27. Webb, H. W., "Absorption of Nitrous Gases," E. Arnold and Co., London (1923).
28. Wendel, M. M., M.Ch.E. thesis, Univ. of Del., Newark (1954).
29. Wendel, M. M., Ph.D. thesis, Univ. of Del., Newark (1956).
30. Wilke, C. R., *Chem. Eng. Prog.*, **45**, 218 (1949).

Manuscript received Jan. 20, 1958; revision received July 3, 1958; paper accepted July 7, 1958.

Viscosity: Reduced-State Correlation for the Inert Gases

HIROSHI SHIMOTAKE and GEORGE THODOS

The Technological Institute, Northwestern University, Evanston, Illinois

A reduced-state viscosity correlation has been constructed from the available data of the inert gases. For the development of this correlation, the fragmentary experimental data for argon were utilized along the lines proposed for thermal conductivities by Owens and Thodos (*21*) in order to determine the effect of pressure on viscosity. In addition, the only available low-pressure viscosity data for neon and helium have been incorporated in this correlation to produce for the first time the effect of subatmospheric pressures. This correlation covers the range of pressures included between $P_R = 40$ and $P_R = 0.015 \times 10^{-4}$ and extends up to temperatures of $T_R = 100$. It has been found that the effect of subatmospheric pressures on viscosity does not become significant above pressures of 1 mm. of mercury. However, at lower pressures, viscosity is found to decrease rapidly, particularly in the regions below absolute pressures of 0.01 mm. of mercury.

Viscosities calculated with the reduced state correlation produce an average over-all deviation of 0.93% for neon, argon, krypton, and xenon. In these comparisons the available viscosity data for the gaseous and liquid states of these substances have been included. Deviations of the same order of magnitude are produced for helium in the gaseous state; however, these deviations become excessive for viscosities of helium in the liquid state.

The application of the final reduced state correlation has been extended to a number of diatomic and polyatomic gases and found to apply well to the diatomic gases only.

The current advances in the field of transport properties by Hirschfelder, Curtiss, and Bird (*9*) through the use of quantum and statistical mechanic principles, in conjunction with the recent developments on thermal conductivities by Owens and Thodos (*21*), make possible the extension of studies for the establishment of reduced-state viscosity correlations. The thermal conductivity studies of Owens and Thodos were restricted to the inert gas family, to obtain a background representative of substances possessing the simplest molecular constitution. In their studies the effect of pressure on thermal conductivity was accounted for from the single continuous correlation resulting when the residual thermal conductivity $k - k^*$ was correlated with ρ, the corresponding density of the substance. This relationship proved unique in defining thermal conductivities for the gaseous and liquid states.

In 1943 Uyehara and Watson (*30*) developed a generalized reduced-state correlation for which they claimed expected deviations on viscosity of less than 20%. They used the available viscosity information for a large number of substances in order to develop their compromising generalized reduced-state correlation. Despite the fact that the Uyehara-Watson correlation has proved quite valuable in its present form, particularly for engineering calculations, the recent advances of concepts on transport properties make necessary an examination of this field to find whether viscosity can be treated along the same lines as thermal conductivity for the development of similar correlations. In this study, this objective has been achieved through the utilization of the available high-pressure viscosity data for argon. These permitted the establishment of the high-pressure and liquid regions of the reduced-state correlation for the inert gases. In addition, the available subatmospheric viscosity data for neon and helium made possible for the first time the extension of this reduced-state correlation in the low-pressure region.

VISCOSITY AT MODERATE PRESSURES

Atmospheric-pressure viscosity data available in the literature for the inert gases have been correlated with reduced temperature to produce the relationships presented in Figure 1. The critical temperatures of the inert gases (*16*) used to produce the reduced temperatures and literature sources of the viscosity data are presented in Table 1. The curved relationships of Figure 1 are essentially parallel to each other, with the exception of helium. This behavior strongly suggests that the theorem of corresponding states should apply alike for neon, argon, krypton, and xenon. The different behavior for helium is expected and is consistent with deviations found in the correlations of compressibility factors (*20*) and thermal conductivities (*21*).

By an approach comparable to that utilized for thermal conductivities (*21*), the viscosity ratio $\mu^*/\mu_{T_c}{}^*$ was correlated with the reduced temperature T_R to produce the single relationship presented in Figure 2. The value $\mu_{T_c}{}^*$ represents the viscosity at atmospheric pressure resulting from Figure 1 at the critical temperature $T_R = 1.0$. In order to bring the viscosity data of helium in line with the relationship of Figure 2, it becomes necessary to assign to it the pseudocritical temperatures $T_c' = 5.3 + 2.03 = 7.33$°K. for $T > 10$°K. and $T_c' = 5.3 - 0.54 = 4.76$°K. for temperatures below 10°K.

The relationship of Figure 2 is unique and applies to all the inert gases for moderate absolute pressures ranging from 1 mm. of mercury up to pressures well above 10 atm. In addition, this relationship is found to be linear for $T_R \leq 1.0$ and $T_R \geq 3.5$. Therefore, the viscosity ratio for these regions can be expressed in equation form as follows:

$$\frac{\mu^*}{\mu_{T_c}{}^*} = T_R{}^{0.917} \qquad \text{for } T_R \leq 1.0 \quad (1)$$

$$\frac{\mu^*}{\mu_{T_c}{}^*} = 1.276 T_R{}^{0.645} \qquad \text{for } T_R \geq 3.5 \quad (2)$$

For reduced temperatures, $1 \leq T_R \leq 3.5$, the viscosity ratios must be obtained directly from Figure 2.

The recent theoretical developments of

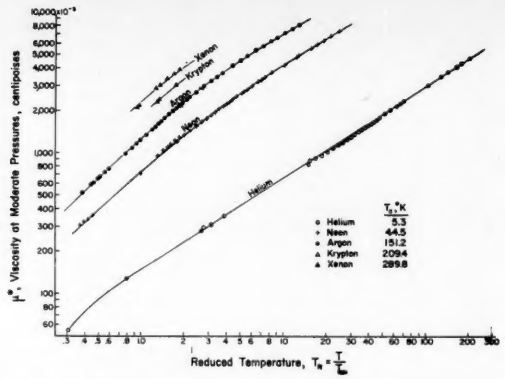

Fig. 1. Relationships of viscosity at moderate pressures and reduced temperature from literature data for the inert gases.

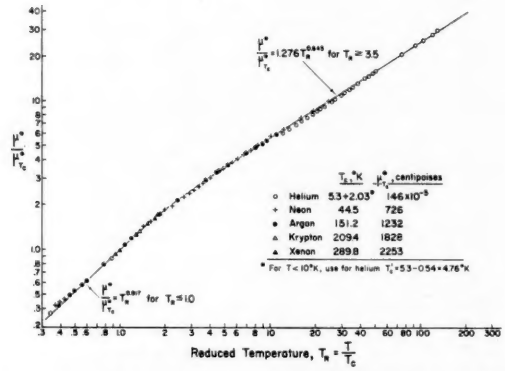
$\frac{\mu^*}{\mu_{T_c}^*} = 1.276 T_R^{0.645}$ for $T_R = 3.5$
$\frac{\mu^*}{\mu_{T_c}^*} = T_R^{0.967}$ for $T_R = 1.0$
$\frac{\mu^*}{\mu_{T_c}^*}$
T_c, °K
$\mu^*_{T_c}$, centipoises
Helium 5.3+2.03* 146×10⁻⁵
Neon 44.5 726
Argon 151.2 1232
Krypton 209.4 1828
Xenon 289.8 2253
* For T < 10°K, use for helium T_c = 5.3 − 0.54 + 4.76°K
Reduced Temperature, $T_R = \frac{T}{T_c}$

Fig. 2. Relationship of viscosity ratio and reduced temperature from the literature data for the inert gases at moderate pressures.

Hirschfelder, Curtiss, and Bird (*9*) in the field of transport properties utilize the Lennard-Jones potential parameters to define coefficients of thermal conductivity, viscosity, and self-diffusion. In this connection they propose for the first approximation of viscosity at moderate pressures,

$$[\mu]_1 = 2.6693 \times 10^{-5} \frac{\sqrt{MT}}{\sigma^2 \Omega^{(2,2)*}[T_N]} \quad (3)$$

Values of the constants σ and ϵ/κ for a number of substances are available (*9*). With these constants and the tabulated values of $\Omega^{(2,2)*}[T_N]$, the generalized collision integral function (*9*), the viscosity for the first approximation can be evaluated with Equation (3). For the kth approximation, the viscosity coefficient is given by

$$[\mu]_k = f_\mu^{(k)} [\mu]_1 \quad (4)$$

Values through the third approximation $f_\mu^{(3)}$ are presented by Hirschfelder, Curtiss, and Bird (*9*). Therefore, with Equations (3) and (4), the viscosity of gases for the third approximation $[\mu]_3$ can be calculated for any temperature and for the moderate pressures ranging from 1 mm. of mercury to 10 atm. The values of σ and ϵ/κ presented by Hirschfelder, Curtiss, and Bird (*9*) and appearing in Table 1 have been used with Equations (3) and (4) to produce the calculated viscosities μ^*. The viscosity at the critical temperature $\mu_{T_c}{}^*$ has been specifically calculated and used to produce the ratios $\mu^*/\mu_{T_c}{}^*$. These ratios, when correlated with reduced temperature, produced the relationship presented in Figure 3. The calculated values $\mu_{T_c}{}^*$ used to define these ratios are also presented in Table 1. The relationship of Figure 3 is similar to that presented in Figure 2 and also shows the existence of linear relationships for reduced temperatures $T_R \leq 1.0$ and $T_R \geq 3.5$. For these regions the viscosity ratio can be defined in equation form as

$$\frac{\mu^*}{\mu_{T_c}{}^*} = T_R \qquad \text{for } T_R \leq 1.0 \quad (5)$$

$$\frac{\mu^*}{\mu_{T_c}{}^*} = 1.276 T_R{}^{0.645} \text{ for } T_R \geq 3.5 \quad (6)$$

The striking resemblance between Figures 2 and 3 is significant and proves helpful

Table 1. Fundamental Constants for the Inert Gases and Literature Sources of Viscosity Data at Moderate Pressures

	Molecular wt.	T_c, °K.	P_c, atm.	Lennard-Jones potential parameters σ, Å.	ϵ/κ, °K.	$\mu_{T_c}{}^*$, centipoises Experimental, Figure 1	Calculated, Equation (3)	μ_c, centipoises	Literature sources
Helium	4.00	5.3	2.26	2.576	10.22	146×10^{-5}	113×10^{-5}	272×10^{-5}	*6, 8, 10, 12, 15, 22, 28, 29, 33*
Neon	20.18	44.5	26.9	2.789	35.7	726	723	1681	*4, 12, 15, 22, 27, 28, 33*
Argon	39.94	151.2	48.0	3.418	124	1232	1237	2852	*3, 11, 14, 15, 17, 22, 23, 24, 28, 31, 33*
Krypton	83.8	209.4	54.3	3.61	190	1828	1790	4232	*19, 22*
Xenon	131.3	289.8	58.0	4.055	229	2253	2238	5216	*19, 22, 26*

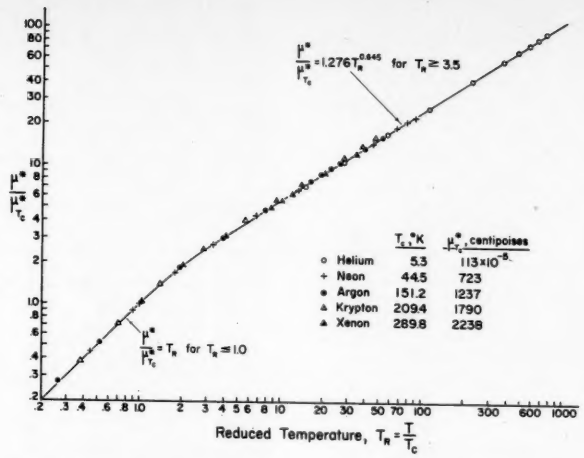

Fig. 3. Relationship of viscosity ratio and reduced temperature at moderate pressures (calculated with the Hirschfelder, Curtiss, and Bird equation).

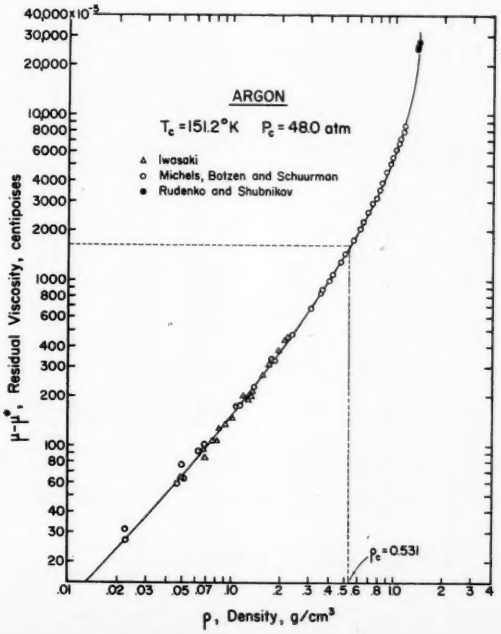

Fig. 4. Residual-viscosity–density relationship for argon in the gaseous and liquid states.

in extrapolating the relationship produced from the experimental values into the high-temperature region. Furthermore, these relationships are unique for the establishment of viscosities at any temperature, if limited to moderate pressures of less than 10 atm. For the treatment of viscosity at high pressures, the approach utilized for the thermal conductivity studies of the inert gases (*21*) has been applied to this study.

VISCOSITY AT HIGH PRESSURES

The equation of Enskog (*5*) for the calculation of viscosity at elevated pressures not only proves unwieldy and cumbersome to use but is found to be of limited accuracy and utility. To circumvent this situation in the comparable studies on thermal conductivities, Owens and Thodos (*21*) took advantage of the correlation proposed by Abas-Zade (*1*) to produce a single unique and continuous function for both gases and liquids when the residual thermal conductivity $k - k^*$ is correlated with ρ, the corresponding density of the substance. Following a parallel approach and utilizing the only available high-pressure data of Michels, Botzen, and Schuurman (*17*) and Iwasaki (*7*) for argon in the gaseous state, and those of Rudenko and Shubinkov (*23*) for the liquid state, the authors have developed a residual viscosity correlation involving $\mu - \mu^*$ and ρ, which is presented in Figure 4. As was shown to be the case for thermal conductivities, this viscosity correlation is also consistent and permits the calculation of viscosities at high pressures from the density of argon at the prevailing temperature and pressure conditions.

A residual viscosity at the critical point is readily available from Figure 4 and the critical density of argon $\rho_c = 0.531$ g./cc. The residual viscosity at the critical point, $(\mu - \mu^*)_c = 1620 \times 10^{-6}$ centipoises, in conjunction with the viscosity at atmospheric pressure and the critical temperature, $\mu_{T_c}{}^* = 1232 \times 10^{-6}$ centipoises, establishes the viscosity of argon at the critical point to be $\mu_c = 2{,}852 \times 10^{-6}$ centipoises. With these values, the ratio of $\mu^*/\mu_{T_c}{}^*$ becomes $(2{,}852 \times 10^{-6})/(1{,}232 \times 10^{-6}) = 2.315$ and thus establishes the constant applicable to this homologous series. Therefore, the relationship involving the viscosity at the critical point for the inert gases becomes

$$\mu_c = 2.315 \mu_{T_c}{}^* \qquad (7)$$

With the values $\mu_{T_c}{}^*$ presented in Table 1, critical viscosities have been produced with Equation (7) for the other inert gases, also presented in Table 1. With the critical viscosities defined for all the members of this series, all available high-pressure viscosity data found only for argon have been reduced to produce the high-pressure region of the correlation presented in Figure 5.

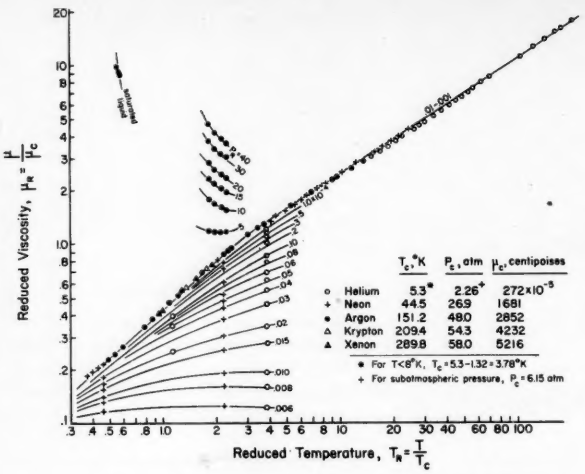

Fig. 5. Reduced-state correlation for the inert gases developed from available data.

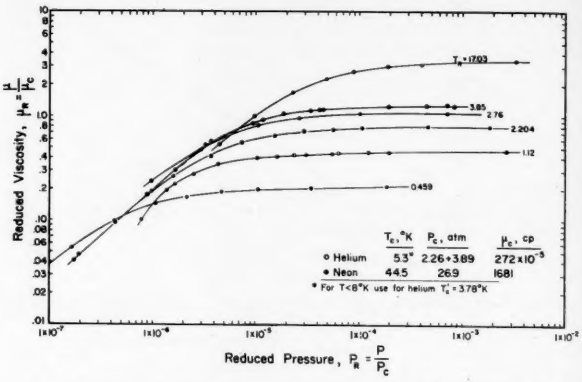

Fig. 6. Effect of subatmospheric pressures on the viscosity of helium and neon.

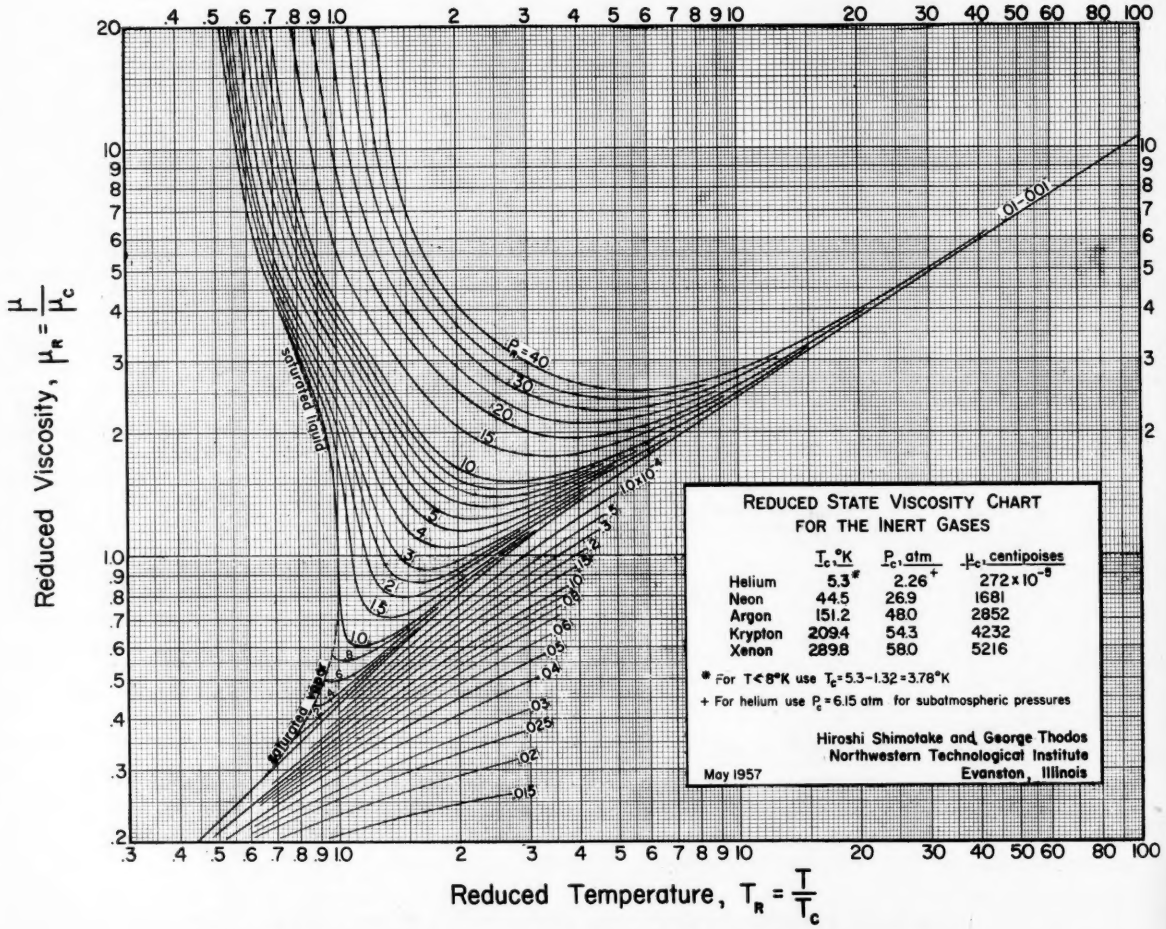

Fig. 7. Reduced-state viscosity correlation for the inert gases. (An 8-1/2-by 11-in. reproduction of this figure is available from the Chemical Engineering Department, Northwestern University, Evanston, Illinois.)

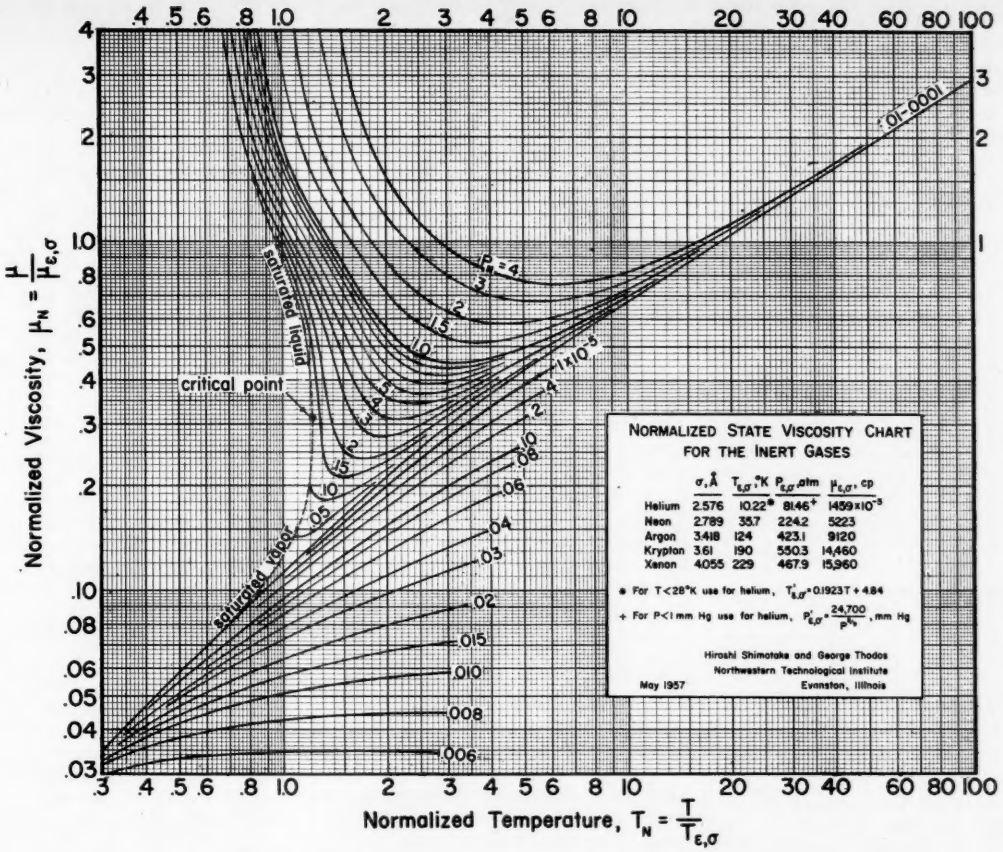

	σ, Å	$T_{\epsilon,\sigma}$, °K	$P_{\epsilon,\sigma}$, atm	$\mu_{\epsilon,\sigma}$, cp
Helium	2.576	10.22*	8146+	1459×10^{-5}
Neon	2.789	35.7	224.2	5223
Argon	3.418	124	423.1	9120
Krypton	3.61	190	550.3	14,460
Xenon	4.055	229	467.9	15,960

* For T<28°K use for helium, $T'_{\epsilon,\sigma} = 0.1923T + 4.84$

\+ For P<1 mm Hg use for helium, $P'_{\epsilon,\sigma} = \frac{24{,}700}{p^{5/4}}$, mm Hg

Fig. 8. Normalized-state viscosity correlation for the inert gases.

VISCOSITY AT LOW PRESSURES

The low-pressure viscosity data of van Itterbeek and van Paemel for neon (*12*) have been used as the basis to extend the correlation of Figure 5 in the low-pressure region. In this connection the low-pressure data for helium (*10, 12*) have also been incorporated to establish this region. The variation of viscosity with pressure for both neon and helium is presented for several fixed temperatures in Figure 6. The experimental data show that viscosity does not begin to decrease until the absolute pressure is reduced below 1 mm. of mercury. This effect, when translated into Figure 5 for both neon and helium, produces the subatmospheric-pressure region existing below the moderate-pressure isobar ($0.001 \leq P_R \leq 0.01$).

CONSTRUCTION OF REDUCED STATE CORRELATION

Residual viscosities $\mu - \mu^*$ produced from Figure 4 have permitted the construction of the high-pressure gaseous- and liquid-state regions of the reduced-state correlation presented in Figure 7. The construction of this figure was made possible by adopting the following procedure. For a defined temperature and pressure, the density of argon was obtained from an enlarged plot presented elsewhere (*21*) and applicable to both the gaseous and liquid regions. With this density value, the residual viscosity $\mu - \mu^*$, obtained from Figure 4 and used in conjunction with the corresponding moderate-pressure viscosity μ^*, obtained from Figure 2, produced the viscosity at the defined temperature and pressure. The critical viscosity for argon $\mu_c = 2852 \times 10^{-5}$ centipoises produces, for this calculated value, the reduced viscosity $\mu_R = \mu/\mu_c$. Reduced viscosities have been calculated for several isobars to produce the high-pressure region of the reduced-state correlation presented in Figure 7. The low-pressure region of Figure 7 is the same developed for Figure 5.

Table 2. Comparison of Viscosities Calculated from Reduced-State Correlation with Experimental Values for the Inert Gases

			Low-pressure region			Moderate-pressure region			High-pressure region			Liquid region		
	T_R	P_R	Experimental points	Deviation, % Maximum	Deviation, % Average	Experimental points	Deviation, % Maximum	Deviation, % Average	Experimental points	Deviation, % Maximum	Deviation, % Average	Experimental points	Deviation, % Maximum	Deviation, % Average
Helium	0.3 –100	8.9×10^{-6} – 0.425	65	27.60	13.4	61	9.00	2.31						
Neon	0.4 –25	0 0372	23	4.50	1.09	61	6.24	1.60						
Argon	0.4 –15	0.066–40				132	2.88	0.04	148	2.34	0.82	4	2.32	1.57
Krypton	1.3 –1.8	0.0185				4	0.765	0.49						
Xenon	0.95–1.9	0.0175				10	1.67	0.88						

NORMALIZED STATE VISCOSITY CORRELATION

The developments of Hirschfelder, Curtiss, and Bird (*9*) on transport properties extend into the dense-phase region through the introduction of reference states for temperature, pressure, and viscosity, defined as follows

$$T_{\epsilon,\sigma} = \frac{\epsilon}{\kappa} \tag{8}$$

$$P_{\epsilon,\sigma} = \frac{\epsilon}{\sigma^3} \tag{9}$$

$$\mu_{\epsilon,\sigma} = \frac{\sqrt{m\epsilon}}{\sigma^2} \tag{10}$$

The reference temperature $T_{\epsilon,\sigma}$ possesses the dimension of absolute temperature, in degrees Kelvin, and therefore can be used directly; however, the expressions defining the reference pressure $P_{\epsilon,\sigma}$ and reference viscosity $\mu_{\epsilon,\sigma}$ must be changed into the forms

$$P_{\epsilon,\sigma} = 0.9869 \times 10^{18} \frac{\epsilon}{\sigma^3}, \quad \text{atm.} \tag{11}$$

$$\mu_{\epsilon,\sigma} = 12.885 \times 10^5 \frac{\sqrt{M\epsilon}}{\sigma^2}, \quad \text{centipoises} \tag{12}$$

in order to define the pressure $P_{\epsilon,\sigma}$ in atmospheres and the viscosity $\mu_{\epsilon,\sigma}$ in centipoises. In Equations (11) and (12) ϵ and σ are the same Lennard-Jones potential parameters defining Equations (8), (9), and (10). The reference temperatures $T_{\epsilon,\sigma}$ and calculated values of $P_{\epsilon,\sigma}$ and $\mu_{\epsilon,\sigma}$ are presented in Figure 8 for the inert gases. Equations (8), (11), and (12) are used to define the normalized temperature, pressure, and viscosity as followed:

$$T_N = \frac{T}{T_{\epsilon,\sigma}} \tag{13}$$

$$P_N = \frac{P}{P_{\epsilon,\sigma}} \tag{14}$$

$$\mu_N = \frac{\mu}{\mu_{\epsilon,\sigma}}. \tag{15}$$

The dimensionless viscosity ratio $\mu/\mu_{\epsilon,\sigma}$ has been used to produce the normalized-state correlation of Figure 8. This was accomplished through the transformation of reduced-state values obtained from Figure 7 with Equations (13), (14), and (15). Therefore, Figure 8 is equivalent to Figure 7 and is presented in view of the current interest on transport properties defined in terms of the fundamental and basic potential parameters.

APPLICATION OF REDUCED-STATE CORRELATION

Viscosities have been calculated with the reduced correlation of Figure 7 and checked with the available literature values of the inert gases used in this study. Altogether, 152 viscosity values have been considered and produce an average deviation of less than 1% for argon in the liquid state and the gaseous high-pressure regions. In addition, the deviations for the low-pressure region are found to be 1.09% for neon and 13.4% for helium. A summary of the deviations resulting from the available data of the inert gases is presented in Table 2 for both the gaseous- and liquid-state regions. In these comparisons helium produces excessive deviations despite the fact that adjustments have been imposed on its critical temperature and pressure. This behavior indicates that helium must be treated by itself for the development of a viscosity correlation in which its actual critical constants are utilized. Inasmuch as high-pressure viscosity data for gaseous helium are not yet available, the construction of such a correlation will have to be postponed until this information becomes accessible.

The reduced-state correlation of Figure 7 has been applied to several diatomic and polyatomic gases. The high-pressure gaseous data of Michels and Gibson (*18*) and also those of Iwasaki (*13*), in conjunction with the high-temperature data of Vasilesco (*32*) at moderate pressures, have produced with Figure 7 an average deviation of 3.3% for nitrogen. Likewise, the high-pressure gaseous state data of Golubev (*7*) produced an average deviation of 3.1% for oxygen. A similar comparison with the high-pressure gaseous- and liquid-state data produced an average deviation of 11.5% for carbon dioxide (*25*). The high-pressure data for methane (*2*) and those for propane (*2*) produced average deviations of 4.1 and 16%, respectively. These results indicate that the reduced-state correlation of Figure 7 can be applied with good accuracy to the inert and diatomic gases but fails to produce reliable viscosity values for triatomic and polyatomic gases.

NOTATION

$f_\mu^{(k)}$ = viscosity correction factor for the kth approximation
m = mass of molecule, grams
M = molecular weight
T = absolute temperature, °K.
T_N = normalized temperature $T/(\epsilon/\kappa)$

Greek Letters

ϵ = characteristic energy for Lennard-Jones potential function, ergs
κ = Boltzmann constant, 1.38047×10^{-16} ergs/°K.
μ = viscosity, poises, g./(cm.)(sec.)
ϵ/κ = reference temperature, °K.
σ = characteristic length for Lennard-Jones potential function, Å
$\Omega^{(s,2)*}[T_N]$ = collision intergral function of the Lennard-Jones potential

LITERATURE CITED

1. Abas-Zade, A. K., *Zhur. Eksptl. i Teoret. Fiz.*, **23**, 60 (1952).
2. Bicher, L. B., and D. L. Katz, *Ind. Eng. Chem.*, **35**, 754 (1943).
3. Bonilla, C. F., S. J. Wang, and H. Weiner, *Trans. Am. Soc. Mech. Engrs.*, **78**, 1285 (1956).
4. Edwards, R. S., *Proc. Roy. Soc.* (*London*), **A119**, 578 (1928).
5. Enskog, David, *Kgl. Svenska Vetenskapsakad. Handl.*, **63**, No. 4 (1922).
6. Gille, Arthur, *Ann. Physik*, **48**, 799 (1915).
7. Golubev, I., dissertation (Russ.) Moscow, Nitrogen Inst. (1940).
8. Günther, P., *Z. physik. Chem.*, **110**, 626 (1924).
   Hirschfelder, J. O., C. F. Curtiss, and
9. R. B. Bird, "Molecular Theory of Gases and Liquids," p. 528, John Wiley and Sons, New York (1954).
10. Itterbeek, van, A., and W. H. Keesom, *Physica* **5**, 257 (1938).
11. Itterbeek, van, A., and O. van Paemel, *ibid.*, **5**, 1009 (1938).
12. *Ibid.*, **7**, 273 (1940).
13. Iwasaki, Hiroji, *Science Repts. Research Insts. Tohoku Univ. Ser. A.*, **6**, 296 (1954).
14. Iwasaki, Hiroji, private communication, Tohoku Univ., Sendai, Japan, (1957).
15. Johnston, H. L., and E. R. Grilly, *J. Phys. Chem.*, **46**, 948 (1942).
16. Kobe, K. A., and R. E. Lynn, Jr., *Chem. Revs.*, **52**, 117 (1953).
17. Michels, A., A. Botzen, and W. Schuurman, *Physica*, **20**, 1141 (1954).
18. Michels, A., and R. O. Gibson, *Proc. Roy. Soc.* (*London*), **A134**, 288 (1931).
19. Nasini, A. G., and C. Rossi, *Gazz. chim. ital.*, **58**, 433 (1928).
20. Nelson, L. C., and E. F. Obert, *Trans. Am. Soc. Mech. Engrs.*, **76**, 1057 (1954).
21. Owens, E. J., and George Thodos, *A.I.Ch.E. Journal*, **3**, 454 (1957).
22. Rankine, A. O., *Proc. Roy. Soc.* (*London*), **A83**, 516 (1910).
23. Rudenko, N. S., and L. W. Shubnikov, *Physik. Z. Sowjetunion*, **6**, 470 (1934).
24. Schultze, Hugo, *Ann. Physik*, **5**, 140 (1901).
25. Stakelbeck, H., *Z. ges. Kälte-Ind.*, **40**, 33 (1933).
26. Trautz, Max, and Robert Heberling, *Ann. Physik.*, **20**, 118 (1934).
27. Trauz, Max and Helmut Zimmerman *ibid.*, **22**, 189 (1935).
28. Trautz, Max and Robert Zink, *ibid.*, (5), **7**, 427 (1930).
29. Uehling, E. A., and E. J. Hellund, *Phys. Rev.*, **54**, 479 (1938).
30. Uyehara, Otto, and K. M. Watson, *Natl. Petroleum News*, Tech. Sec., **36**, R764 (October 4, 1944).
31. Vasilesco, Virgile, Doctoral thesis, Univ. Paris (1940).
32. ———, *Ann. phys.*, **20**, 292 (1945).
33. Wobser, R., and F. Müller, *Kolloid-Beih.*, **52**, 165 (1941).

Manuscript received July 29, 1957; revised Oct. 25, 1957; accepted Oct. 25, 1957.

Convergence Pressures for Close-boiling Nonideal Systems

J. M. LENOIR

C. F. Braun and Company, Alhambra, California

The unconventional behavior of equilibrium ratios and convergence pressures is illustrated for close-boiling systems with activity coefficients exceeding 1 throughout the two-phase region. Also presented is a correlation to predict convergence pressure, or the critical locus, of nonideal binary systems.

The behavior and correlation of convergence pressure for hydrocarbon mixtures (*1, 7, 15*) and the relation of equilibrium-ratios to convergence pressure have been presented in several articles (*9, 10, 13, 15*). Such methods do not apply to narrow-boiling mixtures that are nonideal throughout the two-phase region, and the convergence-pressure loci for such mixtures differ markedly from the conventional shape. In addition, the relationships between equilibrium-ratios and convergence pressure are often unusual. This paper presents an empirical procedure to evaluate convergence-pressure loci, and a qualitative analysis of the behavior of equilibrium ratios for nonideal close-boiling systems. Nonideal experimental phase equilibria form the basis of the studies (*2, 3, 4, 5, 8, 11, 14*).

The pressure-temperature diagram shown in Figure 1 typifies the phase areas for binary mixtures that behave ideally at low pressures. The curved arc, M to N, is the critical locus connecting the critical points of pure component M and pure component N. The projection at constant composition to the critical locus gives the critical pressure Pc for a two-phase condition, O. The isothermal projection to the critical locus produces the convergence pressure P_G. The identity of the components and the temperature define the convergence pressure for a binary system. Temperature, pressure, convergence pressure, and component identity determine equilibrium ratios. Typical equilibrium-ratio isotherms shown in Figure 2, illustrate the merging of the equilibrium-ratio curves at the convergence pressure. Two-phase mixtures exist at temperatures less than the minimum critical temperature. The isothermal projection to the curve CM on Figure 1 results in the point QP_G, the convergence pressure that correctly correlates equilibrium ratios at temperatures less than the minimum critical temperature. The point QP_G has been termed the quasiconvergence pressure (*1*). The curve CM represents the locus of quasiconvergence pressures (*7*). Figure 3 shows the behavior of equilibrium ratios under conditions where QP_G correlates the equilibrium ratios. The quasiconvergence pressure may be thought of as the pressure where convergence of the equilibrium ratios would occur if total condensation did not occur first when the pressure is raised. Quasiconvergence pressures are obtained by extrapolation of the equilibrium-ratio isotherms, and it is difficult to ascertain their exact numerical value.

The general phase behavior of close-boiling nonideal mixtures was first studied in the last part of the nineteenth century (*5, 14*) and the results were summarized by Kuenen (*6*) and Roozeboom (*12*). It is now desired to determine the convergence-pressure and equilibrium-ratio behavior. As a means of analysis, component M is defined as the component of a binary system with the higher critical pressure. Component N is the component with lower critical pressure. Figure 4 illustrates the behavior of convergence-pressure loci as the critical temperature of M increases relative to the critical temperature of N. Figure 4–1 shows the situation with the critical temperature of M roughly 100°F. less than the critical temperature of N. Region A, the two-phase area to the right of the critical temperature of M, represents conditions where the isothermal projection to the critical locus results in a real convergence pressure. Region B, to the left of M and below the vapor-pressure curve of M, represents conditions where the isothermal projection results in a quasiconvergence pressure.

In Figure 4–2, the critical temperature of M and N are closer together, with a smaller area A and a larger area B. With continued rise of critical temperature M,

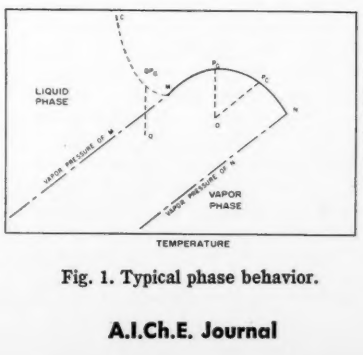

Fig. 1. Typical phase behavior.

Figure 4–3 shows region A still smaller and some additional peculiarities. The convergence-pressure locus has folded over in such a way that two convergence pressures are possible at the same temperature. A minimum temperature exists on the critical locus that is not the critical temperature of either component. A quasiconvergence-pressure locus exists in a real two-phase zone, and a two-phase

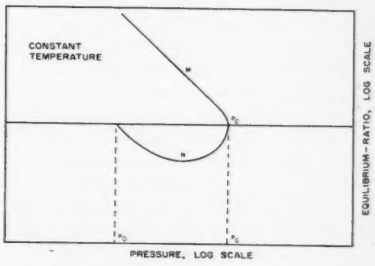

Fig. 2. Typical equilibrium-ratio behavior.

zone exists at higher pressures than the quasiconvergence pressure, a zone termed *region C*. Region C is bounded by the critical locus, the quasiconvergence pressure line, and either the vapor-pressure curve for component M or an azeotrope line, whichever is higher in pressure.

In Figure 4–4 a continuation of the folding process occurs. A new region A, denoted A_2, has appeared. The volatility relations in regions A and A_2 are reversed. In area A component M is more volatile. In area A_2 component N is more volatile. Azeotrope compositions can exist because the phase-boundary curves can lie outside the area bounded by the vapor-pressure curves (*2, 5, 6*). With Figure 4–5 the original A region has almost disappeared, and with Figure 4–6 has disappeared. Figures 4–4 and 4–5 show azeotropes. A locus of the type of Figure 4–6 may also show an azeotrope, as illustrated by Kay and Brice (*3*).

The curves of Figure 4 are not intended to represent quantitatively actual binary mixtures. Figure 4–1 approximates the acetylene-propane system (*8*). Figure 4–4 is similar to the propane-H_2S system (*4*), or the nitrous oxide-ethane system (*5*). Figure 4–6 is like the H_2S-ethane system (*3*) or the H_2S-pentane system (*11*).

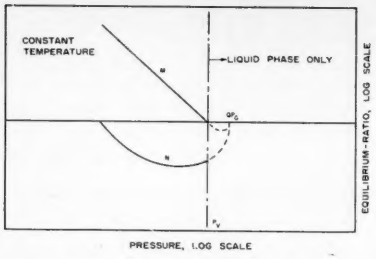

Fig. 3. Equilibrium-ratio behavior where quasi-convergence pressure applies.

The locus of the quasiconvergence pressure curves results from extrapolation of the isothermal equilibrium-ratio curves to the line where $K = 1$. Figure 5 shows the equilibrium ratios of H_2S and propane at a temperature of 178°F. where a real convergence pressure does not exist. Below 800 lb./sq. in. abs. the behavior of the equilibrium ratios is conventional, appearing to converge at some pressure between 800 and 900 lb./sq. in. abs. Extrapolation of the isotherms of Figure 5 with similitude to the shape of the equilibrium ratios for temperatures where a real convergence pressure exists gives the dashed line converging at 860 lb./sq. in. abs. This pressure is considered to be the quasiconvergence pressure. A study of the H_2S-propane system in this manner resulted in quasiconvergence pressures of 850 lb./sq. in. abs. at 170°F., 850 lb./sq. in. abs. at 175°F., and a real convergence pressure of 880 lb./sq. in. abs. at 184.2°F., the minimum critical temperature. The quasiconvergence pressure appears to be essentially constant in the two-phase area for the H_2S-propane system.

At pressures below the lower pressure convergence pressure and at pressures a reasonable pressure below the quasiconvergence pressure, the pattern of the isothermal-equilibrium-ratio curves appears conventional, permitting the development of a rational correlation of activity coefficients. At higher pressures the situation is more complex.

Figure 6 presents an empirical correlation to predict convergence pressures for close-boiling nonideal mixtures, dependent upon the measured values of the ethane-acetylene (*5*, *8*), propane-acetylene (*8*), propylene-acetylene (*8*), ethylene-acetylene (*8*), ethane-H_2S (*3*), propane-H_2S (*4*), pentane-H_2S (*11*), ethane–nitrous oxide (*5*), ethane-CO_2 (*5*), acetylene-CO_2 (*5*), and ethane-HCl (*14*) systems. The abscissa of Figure 6 is the operating temperature less the critical temperature of component N. The parameter is the difference in critical temperatures, $T_M - T_N$. The ordinate is $(P_G - P_N)/(P_M - P_N)$. It is possible to predict two convergence pressures for the same temperature. Composition considerations dictate the correct choice.

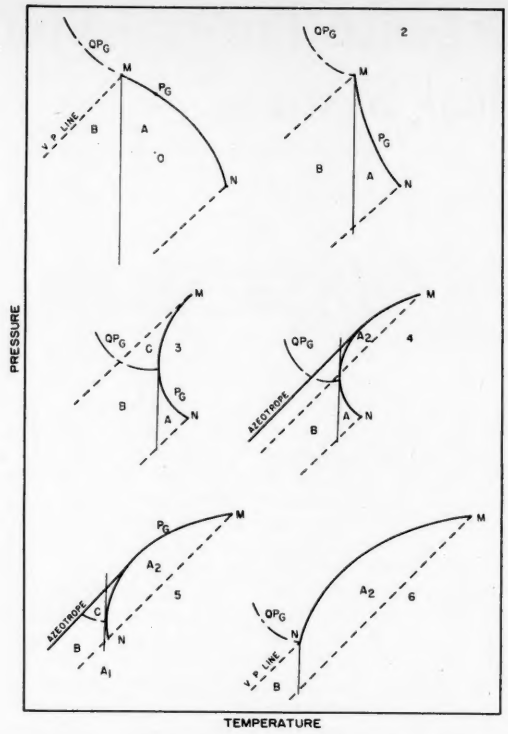

Fig. 4. Behavior of convergence-pressure loci for close-boiling mixtures.

Where quasiconvergence pressures are needed, a horizontal projection to the left from the minimum temperature point on the critical locus is suggested as the quasiconvergence-pressure line. Figure 6 is based on nonideal systems for the range of temperature between 50° and 213°F. and from 700 to 1,300 lb./sq. in. abs. convergence pressure, with mixtures having activity coefficients greater than 1.0. The correlation predicts the measured values of convergence pressure with an arithmetic deviation of 2.3% and a statistical deviation of 3.3%.

The unconventional behavior of equilibrium ratios is pictured by the curves of Figure 7 for a locus similar to that of Figure 4–4. Figure 7–1 shows the behavior for the case of an operating temperature above the minimum critical temperature. The customary behavior is shown for the equilibrium ratios in region A. For the A_2 region the volatility is reversed, and the equilibrium ratios converge at the azeotrope composition. As the pressure is reduced beyond the azeotrope, the equilibrium ratios spread apart and then converge again at the upper convergence pressure as the pressure is decreasing. Convergence takes place at three pressures, at the two convergence pressures and at the azeotrope pressure. Figure 7–2 shows equilibrium ratios where the temperature is the minimum critical temperature, resulting in a merging of the two convergence pressures. Figure 7–3 shows the situation just below the minimum critical temperature. As the pressure increases, the equilibrium ratios approach the quasiconvergence pressure but never quite converge to $K = 1$. Rather, with increasing pressure the equilibrium ratios tend to spread apart and then to converge at the azeotrope pressure.

It is not presumed that a knowledge of the convergence pressure for nonideal systems is all that is required to predict the equilibrium ratios. But the convergence-pressure locus outlines the two-phase area and indicates how the equilibrium ratios will behave. And this gives a degree of confidence in the prediction of activity coefficients in the high-pressure range, through the knowledge of the termination points of the equilibrium-ratio isotherms.

EXAMPLE: It is desired to find the convergence pressure of an H_2S-propane mixture at 188°F. The critical conditions are 213°F. and 1,306 lb./sq. in. abs. for H_2S, and 206°F. and 616 lb./sq. in. abs. for propane. Because propane has the lower critical pressure, it is component N.

$$T - T_N = 188° - 206° = -18°\text{F.}$$

$$T_M - T_N = 213° - 206° = 7°\text{F.}$$

From Figure 2 $(P_G - 616)/(1{,}306 - 616) = 0.25$ and 0.53.

$$P_G = 788 \text{ or } 982 \text{ lb./sq. in. abs.}$$

Kay and Rambosek (*4*) show values of 797 and 1,021 lb./sq. in. abs. The lower

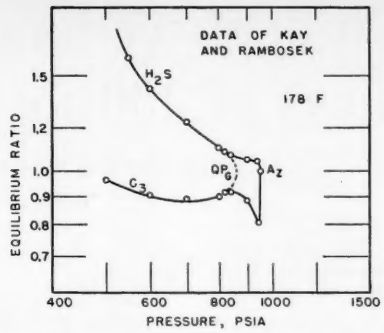

Fig. 5. Equilibrium-ratio behavior, quasiconvergence pressure in two-phase region.

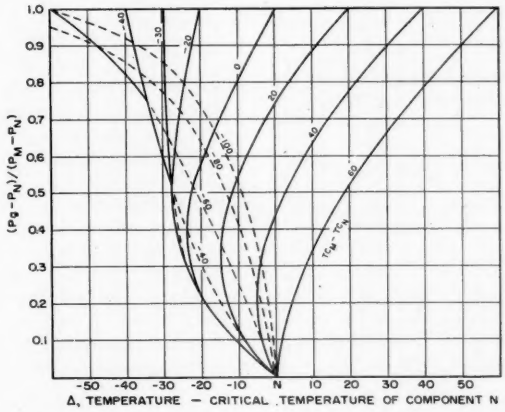

Fig. 6. Prediction of convergence pressure for close-boiling nonideal mixtures.

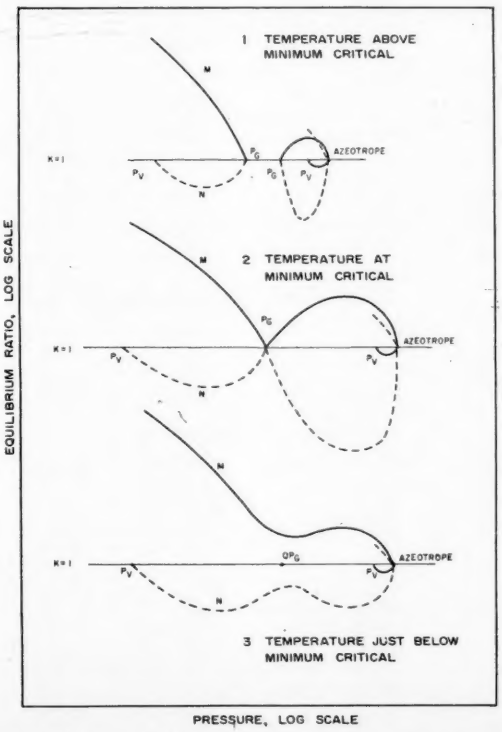
1 TEMPERATURE ABOVE MINIMUM CRITICAL
2 TEMPERATURE AT MINIMUM CRITICAL
3 TEMPERATURE JUST BELOW MINIMUM CRITICAL
AZEOTROPE
EQUILIBRIUM RATIO, LOG SCALE
PRESSURE, LOG SCALE

Fig. 7. Equilibrium ratios in the critical region for close-boiling nonideal mixtures.

pressure applies to the propane-rich mixture.

NOTATION

Az = azeotrope pressure, lb./sq. in. abs.
K = equilibrium ratio
M = component with higher critical pressure
N = component with lower critical pressure
Pc = critical pressure, lb./sq. in. abs.
P_G = convergence pressure, lb./sq. in. abs.
P_M = critical pressure of component M, lb./sq. in. abs.
P_N = critical pressure of component N, lb./sq. in. abs.
P_v = vapor pressure, lb./sq. in. abs.
QP_G = quasiconvergence pressure, lb./sq. in. abs.
T = temperature, °F.
T_M = critical temperature of component M, °F.
T_N = critical temperature of component N, °F.
Δ = temperature minus the critical temperature of component N, °F.

LITERATURE CITED

1. Hadden, S. T., *Chem. Eng. Progr. Symposium Ser.* No. 7, **49**, 53 (1953); *Chem. Eng. Progr.*, **44**, 135 (1948).
2. Haseldon, G. G., D. M. Newitt, and S. M. Shah, *Proc. Roy. Soc.* (*London*), **A209**, 1 (1951).
3. Kay, W. B., and D. B. Brice, *Ind. Eng. Chem.*, **45**, 615 (1953).
4. Kay, W. B., and G. M. Rambosek, *Ind. Eng. Chem.*, **45**, 221 (1953).
5. Kuenen, J. P., *Phil. Mag.*, (5), **40**, 173 (1895); (5), **44**, 174 (1897); *Z. f. Physik. Chemie*, **24**, 667 (1897).
6. Kuenen, J. P., "Theorie der Verdampfung und Verflussigung von Gemischen und der Fraktionierten Destillation," pp. 82–84, Barth, Leipzig (1906).
7. Lenoir, J. M., and G. A. White, *Petr. Refiner*, **32**, No. 10, 121 (1953); (in press).
8. McCurdy, J. L., and D. L. Katz, *Ind. Eng. Chem.*, **36**, 674 (1944); *Oil Gas J.* (March 17, 1945).
9. Myers, H. S., and J. M. Lenoir, *Petr. Refiner*, **36**, No. 2, 167 (1957).
10. Natural Gasoline Association of America, "Equilibrium-Ratio Data Book," Tulsa (1955).
11. Reamer, H. H., B. H. Sage, and W. N. Lacey, *Ind. Eng. Chem.*, **45**, 1805 (1953).
12. Roozeboom, H. W. B., "Die Heterogenen Gleichgewichte vom Standpunkte der Phesenlehre," pp. 89–93, Vieweg (1904).
13. Rzasa, M. J., E. D. Glass, and J. B. Opfell, *Chem. Eng. Progr. Symposium Ser.* No. 2, **48**, 28 (1952).
14. Von Quint, N., *Z. f. Physik. Chemie*, **39**, 14 (1902).
15. Winn, F. W., *Chem. Eng. Progr. Symp. Ser.* No. 2, **48**, 121 (1952).

Manuscript received Aug. 13, 1957; revision received Nov. 8, 1957; paper accepted Nov. 21, 1957.

Discharge Coefficients Through Perforated Plates at Reynolds Numbers of 400 to 3,000

P. L. SMITH, JR., and MATTHEW VAN WINKLE

University of Texas, Austin, Texas

The correlation of Kolodzie and Van Winkle (3) for predicting dry plate orifice coefficients through perforated plates originally covering a Reynolds number range of 2000 to 20,000 has been extended to apply to Reynolds numbers as low as 400. The correlation applies to column diameters ranging from 3 to 15 in.

Kolodzie and Van Winkle (3) reported experimental data and a correlation derived therefrom based on a study of perforated plate dry pressure drop with air as a fluid and the Reynolds numbers range of 2000 to 20,000. Because of possible interest in discharge coefficients and pressure drop through perforated plates at lower Reynolds numbers than those covered in the original work, this investigation was initiated to extend the data over the range down to Reynolds numbers of 400. Essentially, Reynolds numbers ranging from 400 to 3000 were studied in this work.

EQUIPMENT

The equipment arrangement was the same as that used by Kolodzie (3) and consisted mainly of flanged sections of 3-in. I.D. Pyrex glass pipe arranged horizontally so that perforated plates of various characteristics could be placed between the flanges. Details of the setup are given in (3).

The perforated plates studied were the same as those in the original work and the range of variables included in their design are shown in Table 1.

Table 1

Range of Plate Design Variables

Hole diameter, in.	1/16, 3/32, 1/8, 5/32, 3/16, 1/4
Hole pitch to diameter ratio	2, 3, 4
Plate thickness, in.	0.081, 0.125, 0.1875, 0.25
Plate thickness to hole diameter ratio	0.33 to 4.0
Plate free area, % of pipe cross-sectional area	2.33 to 15.8

All holes were drilled on a triangular pitch.

PROCEDURE

The experimental procedure was essentially that followed by Kolodzie but slightly modified to obtain greater accuracy in reading pressure drop data at the lower flow rates. These modifications included use of a more sensitive draft gauge with optical magnification of the scale and meniscus in the tube. Also the runs were started at the high flow rates and readings taken at decreasingly lower rates until the pressure drop was too small to be measured. This procedure enabled duplicate determinations to be made with a maximum absolute error of 5% and an average absolute error of approximately 2%.

ORIFICE COEFFICIENTS

The orifice coefficients shown on the figures were calculated by means of Equation (1)

$$w = CA_f Y \sqrt{\frac{2g_c \rho_1 \Delta P}{1 - \left(\frac{A_f}{A_D}\right)^2}} \qquad (1)$$

EXPERIMENTAL RESULTS

For each pitch to diameter ratio a plot was prepared showing the orifice coefficient as a function of Reynolds number with the thickness to diameter ratio as a parameter. Figures 1, 2, 3, and 4 present these data.

Sudden sharp decreases in pressure drop as the flow rate was gradually decreased were encountered in testing plates having a plate thickness to hole diameter of 0.75 to 0.80. Because of this, the experimental points were not as reproducible as in other situations. A number of points were taken and averaged to give the points from which the dashed curves shown on the figures were drawn.

Such instability in a study of a single orifice in approximately the same range of thickness-to-diameter ratio was reported by Lesem, *et al.* (4). They explained the phenomenon by postulating that for thick-plate orifices, the vena contracta lies between the upstream and downstream surfaces of the plate; for thin plate orifices the vena lies beyond the downstream surface of the plate; and that for orifices for intermediate plate thicknesses, the vena lies between the surfaces. In the

Table 2

Comparison of Experimental and Predicted Dry-Plate Pressure Drop

Fluid	Reynolds No.	t/d Ratio	P/d Ratio	ΔP, exp. in H_2O	ΔP, calc. in H_2O	% Difference
			Arnold, *et al.* (1) 15-in. column			
Air	1760	0.35	1.085	0.51	0.66	−16.6
	880			0.15	0.15	0.0
	400			0.04	0.04	0.0
	2500	0.49	1.14	2.80	2.70	0.4
	1880			1.70	1.66	0.2
	1252			0.70	0.68	0.3
	1096			0.50	0.50	0.0
	985	0.49	1.06	0.30	0.31	−0.1
	657			0.12	0.14	−0.2
	494			0.082	0.083	−0.2
			Mayfield, *et al.* (5) 6-in. column			
	2570	1.00	4.00	0.45	0.48	−6.2
	2380			0.40	0.42	−4.8
	1925			0.25*	0.28	−10.1
	1475			0.15*	0.17	−7.1
			Hunt *et al.* (2) 6-in. column			
Air	2820	1.00	4.00	0.166	0.162	4.9
	2000			0.083	0.082	1.2
	1260			0.033	0.033	0.0
	1395			0.166	0.164	2.4
	982			0.083	0.082	1.2
	624			0.033	0.033	0.0
Carbon Dioxide	2360	1.00	4.00	0.50	0.49	2.0
	1665			0.025	0.025	0.0
Methane	1835	1.00	4.00	0.046	0.045	2.1
	1160			0.0184	0.0183	0.0
Argon	2230	1.00	4.00	0.115	0.112	2.6
	1310			0.046	0.046	0.0

*extrapolated

P. L. Smith, Jr., is at present with C. F. Braun Co., Alhambra, California.

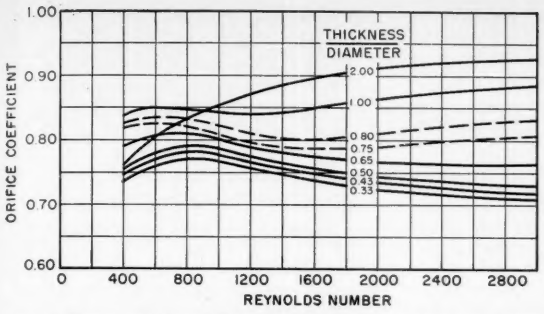

Fig. 1. Plot of orifice coefficient vs. Reynolds number for a pitch to hole diameter ratio of 2.0.

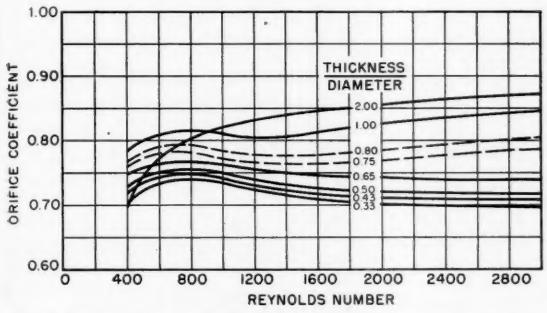

Fig. 2. Plot of orifice coefficient vs. Reynolds number for a pitch to hole diameter ratio of 3.0.

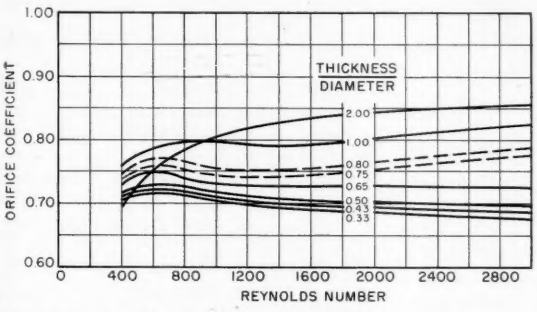

Fig. 3. Plot of orifice coefficient vs. Reynolds number for a pitch to hole diameter ratio of 4.0.

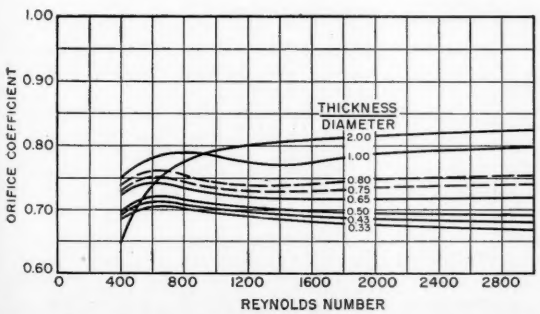

Fig. 4. Plot of orifice coefficient vs. Reynolds number for a pitch to hole diameter ratio of 5.0.

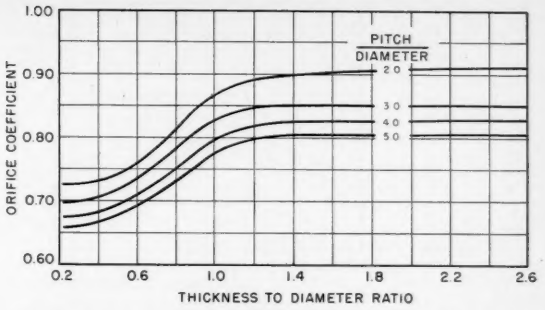

Fig. 5. Cross plot of Figures 1, 2, 3, and 4 at a Reynolds number of 2000.

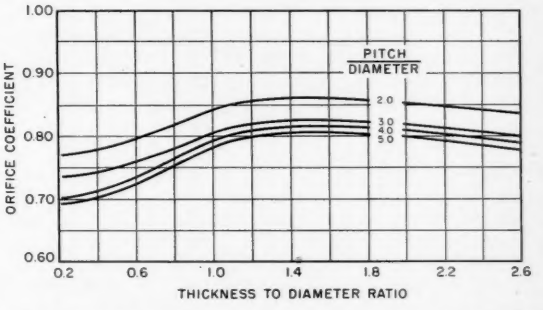

Fig. 6. Cross plot of Figures 1, 2, 3, and 4 at a Reynolds number of 1000.

first case, the jet is attached to the downstream edge. In the second, it is not attached to the surface. In the third case, the jet moves downstream as flow is increased or upstream as it is decreased; thus the jet attaches itself to or detaches itself from the surface and causes sharp changes in pressure drop. In all probability where perforated plates are concerned, this mechanism is intensified by interference action between adjacent holes at their downstream edges.

Figures 5, 6, and 7 are cross plots of Figures 1, 2, 3, and 4 at Reynolds numbers of 2000, 1000, and 600; these plots relate orifice coefficients to plate-thickness-to-hole-diameter ratio with parameters of hole-pitch-to-diameter ratio.

From these curves a plot of orifice coefficient vs. hole diameter-to-pitch ratio on log-log paper, Figure 8, indicated a series of parallel straight lines at each thickness-to-diameter-ratio. The average slope of the lines was 0.10. Equation (2) represents this family of lines.

$$\log C = \log k + 0.10 \log \frac{d}{P} \qquad (2)$$

Equation (2) may be rearranged in the form of Equation (3):

$$K = C\left(\frac{P}{d}\right)^{0.10} \qquad (3)$$

The curves in Figures 1 through 4 may be represented by one curve when K is plotted vs. the thickness-to-diameter ratio. K is a constant for any given thickness-to-diameter ratio.

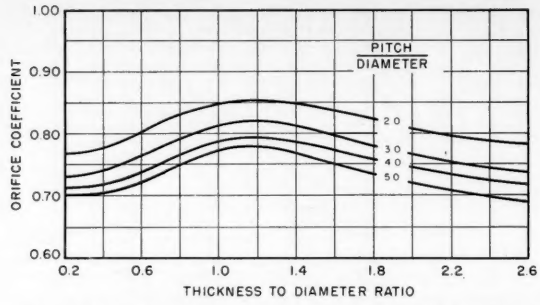

Fig. 7. Cross plot of Figures 1, 2, 3, and 4 at a Reynolds number of 600.

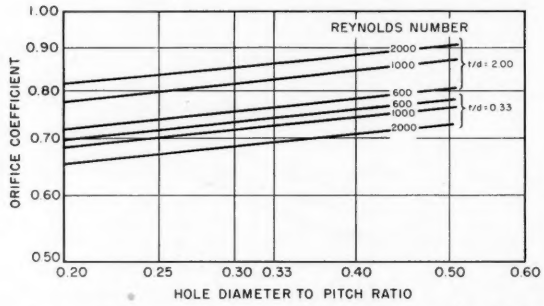

Fig. 8. Cross plot of Figures 5, 6, and 7 at two thickness to hole diameter ratios.

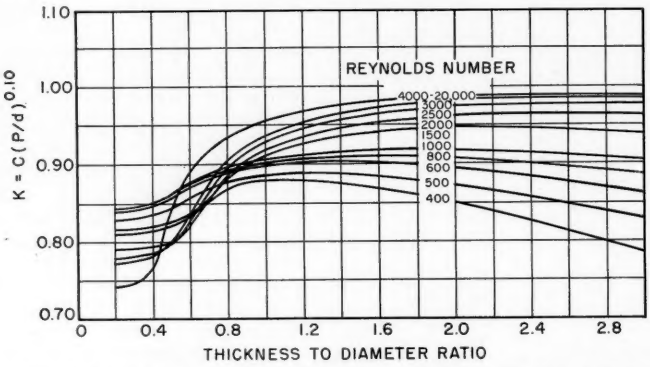

Fig. 9. A correlation relating perforated plate orifice coefficient with the physical characteristics of the plate and fluid.

Figure 9 is a plot of K vs. thickness-to-diameter ratio for the range of Reynolds numbers at parameters from 400 to 20,000. The single curve for Reynolds numbers of 4000 to 20,000 was taken directly from Kolodzie and Van Winkle (*3*).

DISCUSSION

The correlation shown in Figure 9 indicates that for Reynolds numbers above 4000 the orifice coefficient increases with increasing thickness-to-diameter ratio until the ratio reaches approximately 1.7. For t/d ratios greater than 1.7, the coefficient is practically independent of the t/d ratio. At Reynolds numbers below 2000 the coefficient increases with increasing t/d ratio to a maximum value at around $t/d = 1.0$. It then decreases. At the lower Reynolds numbers, the rate of decrease relative to t/d ratio is more rapid. The coefficient also decreases with increasing pitch-to-diameter ratio.

Figure 9 indicates that orifice coefficients increase with increasing Reynolds numbers only when the thickness-to-diameter ratio is above approximately 1.0. Below this value the orifice coefficient increases with increase in Reynolds number up to approximately 1000 and then decreases sharply until the minimum is reached for Reynolds numbers of 4000 to 20,000 at a thickness-to-diameter ratio below 0.4.

APPLICABILITY OF CORRELATION

Kolodzie (*3*) showed that the original correlation, based on Reynolds numbers of 2000 to 20,000, could predict other dry-plate pressure drop data reported in the literature (*1, 2, 5*) within an accuracy of 5%. The correlation, extended in Reynolds number range to 400 by this work, also predicts the available data to within an accuracy of 5% at the lower Reynolds numbers. Table 2 includes comparison of experimental pressure drop and predicted pressure drop selected at random.

Table 3 gives a summary of the range of variables in which this correlation has been shown to be accurate within 5%.

Table 3
Effective Range of Correlation

Variable	Minimum	Maximum
P/d ratio	2.0	5.0
t/d ratio	0.25	3.0
A_f/A_t ratio	0.60	1.00
Reynolds number	400	20,000
Column diameter	3 in.	15 in.

It applies to air, carbon dioxide, methane, and argon and covers a gas molecular weight range from 16 to 44.

Maximum orifice coefficients were obtained under the following conditions:

Reynolds number	1000 and greater	Less than 1000
t/d ratio	1.0 or greater	2.0 or less
P/d ratio	2.0 or less	2.0 or less

The correlation therefore has been shown to apply to dry-plate pressure drop through perforated plates at Reynolds numbers down to 400.

NOTATION

A_D = free cross-sectional area of duct, sq. ft.
A_f = total free area of holes on the plate, sq. ft.
A_t = maximum total free area of holes on the plate, sq. ft.
C = orifice coefficient
d = hole diameter, ft.
g_c = 32.2 (lb. force-ft.)/(lb. mass-sec.^{2})
K = constant
P = hole pitch (center to center distance), when used in ratio (P/d)
P = pressure drop across plate, lb./sq. ft.
ΔP = pressure drop, lb./sq. ft.
Re = Reynolds number
t = plate thickness
w = mass flow rate, lb./sec.
Y = expansion factor
ρ = density of fluid (air), lb./cu. ft.

LITERATURE CITED

1. Arnold, D. S., C. A. Plank, and E. M. Schoenborn, *Chem. Eng. Progr.*, **48**, 633 (1952).
2. Hunt, C. d'A., D. N. Hanson, and C. R. Wilke, *A.I.Ch.E. Journal*, **1**, 441 (1955).
3. Kolodzie, P. A., and Matthew Van Winkle, *A.I.Ch.E. Journal*, **3**, 305 (1957).
4. Lesem, L. B., J. J. McKetta, and G. H. Fancher, *J. Pet. Tech.*, **210**, No. 9, 61 (1957).
5. Mayfield, F. D., W. L. Church, A. C. Green, D. C. Lee, and R. W. Rasmussen, *Ind. Eng. Chem.*, **44**, 2238 (1952).

Manuscript received Dec. 30, 1957; revision received Jan. 23, 1958; paper accepted Jan. 25, 1958.

Regular Solution Theory for Gas-liquid Solutions

J. M. PRAUSNITZ, University of California, Berkeley, California

Regular-solution equations developed by Hildebrand and others are useful for obtaining semiquantitative estimates of phase equilibria in nonpolar systems. These equations, however, do not take into account the volume change on mixing and therefore require modification for solutions of gases in liquids. The required modifications are presented in this paper, and the resulting equations give reasonable estimates of the solubilities of gases and of the temperature coefficient of solubility. In the modified form the regular-solution theory may be used to estimate gas-liquid phase equilibria at high pressures.

The aim of solution theory is to predict the thermodynamic properties of a solution using only data for the pure components. No existing theory completely fulfills this aim, but various proposed theoretical treatments give good approximations in certain restricted cases. The most successful is the theory of regular solutions, and its most useful formulation for chemical engineering purposes is that of Hildebrand (*6*). This theory provides a simple method for estimating solubility and partial-pressure relationships for solutions of nonpolar liquids. The extension of Hildebrand's equations to solutions of nonpolar gases in nonpolar liquids is the subject of this paper. This extension provides a simple means for estimating the solubility of gases in liquids and for determining approximate values of the temperature coefficient of gas solubility.

IDEAL SOLUBILITY OF GASES

A rough estimate of the solubility of a gas, known as the ideal solubility, is given by Raoult's Law

$$x_1 = P_1/P_1^{\,0} \qquad (1)$$

where x_1 = mole fraction of gaseous solute in liquid solution.

The utility of Equation (1) has two serious limitations. First, Equation (1) implies that the ideal solubility of a given gas is the same in all solvents. Second, the method for extrapolating the vapor pressure beyond the critical temperature is nesessarily quite arbitrary. The usual procedure is to assume a linear relationship between the logarithm of the vapor pressure and the réciprocal temperature; consequently, Equation (1) also implies that the solubility of all gases must always decrease with rising temperature. These implications are, in general, contrary to the experimental facts.

REGULAR SOLUTION EQUATIONS

The regular-solution equations assume 1) that there are no orienting or chemical effects acting between the molecules of the solution, 2) that therefore the entropy of solution at constant volume is equal to that of an ideal solution, and 3) that the energy of interaction between two molecules of unlike species is given by the geometric mean of the energies of interaction for the two species of like molecules. Since data on the volume change in mixing are scarce and since volume changes are usually very small for liquids, a further assumption made is that mixing at constant temperature and pressure effects no change in the total volume. On the basis of these assumptions it was shown (*6*) that for a binary solution

$$RT \ln \gamma_1 = V_1 \phi_2^{\,2} (\delta_1 - \delta_2)^2 \qquad (2)$$

where the solubility parameter δ is given by $(\Delta E/V)^{1/2}$.

ΔE is the isothermal molar change in energy for a pure component in going from liquid to the ideal gas state. ΔE is essentially the molar energy of vaporization. Subscripts 1 and 2 refer respectively to components 1 and 2. The activity coefficient γ_1 is defined by

$$\gamma_1 = \frac{\bar{f}_1}{x_1 f_1^{\,L}}$$

Equation (2) cannot be applied to a gaseous solute in liquid solution for two reasons—1) the isothermal, isopiestic dissolution of a gas in a liquid is not a constant volume process since the volume of the gas decreases enormously; 2) the definitions of solubility parameter and activity coefficient as given cannot be applied readily to a component at a temperature above its critical. The regular solution equations as originally formulated are therefore not applicable to gas-liquid solutions.

ISOMETRIC MIXING OF GAS AND LIQUID

The difficulties encountered when applying regular-solution equations to solutions of gases in liquids can be overcome by considering the mixing process as an isothermal thermodynamic process in a series of three steps, the most important being the first:

1. Isothermal compression of the pure gas from its partial pressure and the pure liquid from its vapor pressure to the isometric mixing pressure. (At the isometric mixing pressure the pure gas has a volume equal to its partial molar volume in solution.)
2. Isothermal, isometric, and isopiestic mixing of the pure components at the isometric mixing pressure.
3. Isothermal expansion of the solution from the isometric mixing pressure to the equilibrium pressure.

For each step in this process it is possible to write an expression giving the molar free energy change of the gaseous component, designated by subscript 1:

Step 1

Isothermal compression of pure gas from P_1 to the isometer mixing pressure π.

$$\Delta F_1^{\,I} = \int_{P_1}^{\pi} V_1 \, dp = RT \ln \frac{f_1(\pi)}{f_1(P_1)} \qquad (3)$$

Step 2

Mixing at constant pressure, temperature, and volume.

The regular solution equation applies.

$$\Delta \bar{F}_1^{\,II} = \bar{V}_1 \phi_2^{\,2} (\delta_1 - \delta_2)^2 + RT \ln x_1 \qquad (4)$$

$\bar{V}_1$ = partial molar volume of gaseous solute at pressure π and mole fraction x_1

δ_1 = solubility parameter of gaseous solute = $(\Delta E_1/\bar{V}_1)^{1/2}$

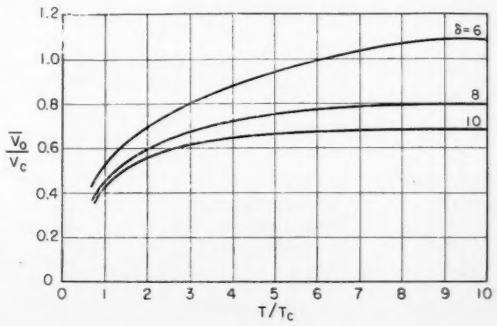

Fig. 1. Partial molar volumes of gases in nonpolar liquid solutions.

ΔE_1 = isothermal change in internal energy for the pure gas in going from molar volume $\bar{V}_1$ to the ideal gas state

ϕ_2 = volume fraction of liquid solvent = $(x_2\bar{V}_2)/(x_1\bar{V}_1 + x_2\bar{V}_2)$

$\bar{V}_2$ = partial molar volume of liquid solvent at pressure π

δ_2 = solubility parameter of liquid solvent at pressure π

At conditions remote from the critical, very little error is introduced by considering the solvent incompressible and by equating the partial molar volume of solvent to the molar volume of the pure component.

Step 3

Isothermal expansion of the solution at constant composition from π to P.

$$\Delta\bar{F}_1^{III} = \int_{\pi}^{P} \bar{V}_1\, dp \qquad (5)$$

If x_1 is the equilibrium composition corresponding to the partial pressure P_1 and if the excellent assumption is made that the Lewis fugacity rule holds for the gas at the low pressure, then the total free energy change for the gaseous component 1 is zero:

$$\Delta F_1^{I} + \Delta\bar{F}_1^{II} + \Delta\bar{F}^{III} = 0 \qquad (6)$$

Substitution of Equations (3), (4) and (5) into (6) yields

$$RT \ln \frac{f_1(P_1)}{x_1 f_1(\pi)} = \bar{V}_1\phi_2^2(\delta_1 - \delta_2)^2 - \int_{P}^{\pi} \bar{V}_1\, dp \qquad (7)$$

Equation (7) relates x_1 to $\bar{V}_1$. The pressure at which the pure gas has a molar volume equal to $\bar{V}_1$ is π. Computation of the solubility of a gas in a liquid solvent, therefore, requires information on the partial molar volume of the gas; once this is known, the thermodynamic properties of the pure gas and those of the pure solvent are sufficient for determining the other quantities in Equation (7).

PARTIAL MOLAR VOLUMES

Accurate measurements of partial molar volumes of gases in liquid solutions are scarce. Recent experimental work, however, has helped to establish the two conclusions that the partial molar volume of a gaseous component in liquid solution 1) is considerably larger than the liquid volume of that component at its normal boiling point and 2) tends to decrease as the internal pressure (solubility parameter) of the solvent increases. For estimation purposes all reliable data have been collected and correlated in the generalized plot shown in Figure 1. The reduced, partial molar volume at infinite dilution is plotted against the reduced temperature of the solute*; the effect of the solvent is indicated by lines of constant solubility parameter of the solvent at 25°C. This correlation reproduces the available reliable data with a standard deviation of about ±5%.

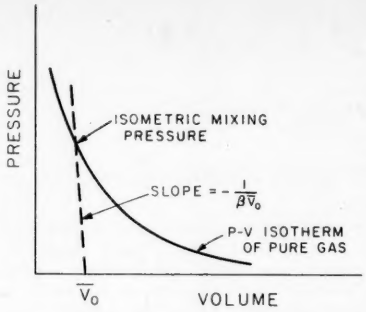

Fig. 2. Computation of isometric mixing pressure.

THE ISOMETRIC MIXING PRESSURE

The isometric mixing pressure is the pressure at which gaseous solute and liquid solvent mix isothermally and isopiestically without change of volume. To compute it the thermodynamic properties of the pure gas and an estimate of the partial molar volume are necessary. In general, the partial molar volume is itself a function of pressure, and since the isometric mixing pressure is large—usually in the vicinity of 1,000 atm.—this effect is not negligible. The correlation in Figure 1 gives the partial molar volume at very low pressure; this volume is smaller at high pressures. There are only a few experimental studies of the compressibility β of dissolved gases (*9, 10*), but these indicate that it is about the same as that observed for normal liquids; a good estimate for the compressibility, therefore, is $\beta \approx 10^{-4}$ atm.$^{-1}$. An approximate relation for $\bar{V}$, the partial molar volume of the gas at any pressure, is therefore given by

$$\bar{V} = \bar{V}_0[1 - \beta P] \qquad (8)$$

The isometric mixing pressure can be computed by finding the intersection of Equation (8) with the isothermal pressure-versus-volume curve for the pure gas as illustrated in Figure 2. Volumetric properties have been reported for numerous pure gases (*1, 4*) or may be estimated with fairly good accuracy from generalized correlations (*2, 11*). The uncertainty in β introduces considerable uncertainty in π. However, as shown later, for estimation purposes this uncertainty is not serious. Calculations presented below indicate that reasonable estimates of gas solubility can be made by using Equations (7) and (8) with Figure 1 and with thermodynamic properties of the pure gas under consideration.

SOLUBILITY PARAMETERS

The solubility parameter of the gaseous solute is computed from the thermodynamic properties of the pure gas at the temperature of the solution and at the isometric mixing pressure. When volumetric and enthalpy data for the gas are available, ΔE is found by

$$\Delta E = E(\text{at } P = 0) - E(\text{at } P = \pi)$$

or

$$\Delta E = \Delta H - \Delta(pv) = \Delta H - RT + \pi\bar{V}_1$$

where $\Delta H = H$ (at $P = 0$) $- H$ (at $P = \pi$), all at the temperature of the solution. Generalized charts for $\Delta E/T_c$ have been published by Lydersen *et al.* (*11*).

The solubility parameters of most common nonpolar solvents are tabulated, and their temperature dependence is discussed by Hildebrand and Scott (*6*). The effect of pressure is to increase somewhat the solubility parameter of the solvent. This increase can be calculated if the volumetric properties of the liquid solvent are known; it can be estimated

*Pseudocritical values were used for hydrogen as recommended by Newton (12); T_c = 41.3°K. and V_c = 47 cc./g.-mole.

Table 1. Solubility of Gases at 1-atm. Partial Pressure

Gas	Solvent	Temp., °C.	Solubility parameter of solvent, (cal./cc.)$^{1/2}$	Partial molar volume $\bar{V}_0$	Isometric mixing pressure, atm.	Solubility parameter of Gas, (cal./cc.)$^{1/2}$	Solubility: $x_1 10^4$ Equation (9)	Observed	Ref.
Nitrogen	*n*-Perfluoro heptane	25	5.7	67.5	545	2.9	29.1	39.1	*5*
Nitrogen	Carbon disulfide	25	10.0	52.2	1310	4.0	2.98	2.23	*5*
Krypton	Iso-octane	25	6.85	52.6	620	4.6	68.1	78.8	*1*
Krypton	Benzene	25	9.15	47.0	1130	5.8	29.9	27.3	*1*
Hydrogen	*n*-Heptane	0	7.80	38.1	1280	3.1	6.22	5.90	*3*
Hydrogen	Carbon tetrachloride	0	9.0	34.8	1760	2.9	3.15	2.60	*3*

Table 2. Entropies of Solution for Gases in Benzene at 25°C. and 1-atm. Partial Pressure

Gas	Solubility $x_1 10^4$ observed (8)	$\bar{V}_0\alpha$, cc./(g.-mole)(°K.)	π, atm.	Entropy of solution, cal./(g.-mole)(°K.) Equation (15)	Observed (8)
Nitrogen	4.42	0.058	1,050	2.9	3.3
Carbon monoxide	6.7	0.064	1,000	+1.0	+1.8
Ethane	148	0.131	1,450	−7.6	−7.5

roughly but not very accurately from Lydersen's charts. The simplest procedure is to consider the solvent as an incompressible liquid. For estimation purposes, the error introduced by this simplification is not very serious.

ESTIMATING THE SOLUBILITY OF GASES

Measured solubilities are available for a number of gases, the vast majority of such data having been taken at 25°C. and 1 atm. partial-gas pressure. Equations (7) and (8) have been used to estimate the solubilities of a few gases in several solvents. Table 1 gives a comparison of the calculated and observed results. At a partial gas pressure of 1 atm. the fugacity of the gas is very close to 1 atm., and the mole fraction of gaseous solute is so small that $\phi_2 = 1$. The equation used in these calculations, therefore, becomes

$$-RT \ln x_1 f_1(\pi) = \bar{V}_0(1 - \beta\pi)(\delta_1 - \delta_2)^2 - \bar{V}_0\pi\left[1 - \frac{\beta\pi}{2}\right] \quad (9)$$

Table 1 also gives the partial molar volume at low pressure as computed from Figure 1, the isometric mixing pressure, and the solubility parameter of the gaseous solute. In these calculations the value of β was 10^{-4} atm.$^{-1}$, and the solvents were considered incompressible.

MULTICOMPONENT SYSTEMS

The theory of regular solutions for binary systems is readily extended to multicomponent systems as discussed in detail by Hildebrand and Scott (6). For the estimation of the solubility of a gas in a mixture of n liquids Equation (7) is modified to

$$RT \ln \frac{f_1(P_1)}{x_1 f_1(\pi)} = \bar{V}_1(\delta_1 - \bar{\delta})^2 - \int_P^\pi \bar{V}_1\, dp \quad (10)$$

where

$$\bar{\delta} = \sum_{i=1}^{n+1} \phi_i \delta_i.$$

The symbol δ denotes an average solubility parameter. The average, taken on a volume fraction basis, comprises all components, including the gaseous solute.

TEMPERATURE COEFFICIENT OF SOLUBILITY

The solubility of gases in liquids is, in general, a strong function of temperature. In the vicinity of room temperature most gases become less soluble as the temperature is raised; there are, however, several exceptions, of which hydrogen is probably the best known. At higher temperatures many gases become less soluble with rising temperature. The temperature coefficient of solubility is directly related to the entropy of mixing, the exact relationship being

$$\frac{d \ln x_1}{d \ln T} = \frac{\Delta\bar{S}_1}{R\left(\frac{\partial \ln a_1}{\partial \ln x_1}\right)_T} \quad (11)$$

where $\Delta\bar{S}_1$ = entropy of solution = $\bar{S}_1 - S_1$.

In all cases $(\partial \ln a_1)/(\partial \ln x_1)$ is positive. The solubility therefore increases with temperature if the partial entropy change is positive and decreases with temperature if it is negative. In many cases the gaseous solute is sufficiently dilute to permit the assumption of Henry's Law. In that case $(\partial \ln a_1)/(\partial \ln x_1) = 1$, and Equation (11) becomes

$$R \frac{\partial \ln x_1}{\partial \ln T} = \Delta\bar{S}_1 \quad (12)$$

A three-step analysis analogous to that used to derive equations for the partial free energy also computes the partial entropy change of the gas $\Delta\bar{S}_1$. The equations for the entropy (per mole of gas) are

Step 1

Isothermal compression from P_1 to π

$$\Delta S_1^{\,I} = -\int_{P_1}^{\pi} \left(\frac{\partial V}{\partial T}\right)_P dP \quad (13)$$

Step 2

Isothermal, isopiestic, and isometric mixing

$$\Delta\bar{S}_1^{\,II} = -R \ln x_1 \quad (14)$$

Step 3

Isothermal expansion (in liquid solution) from π to P

$$\Delta\bar{S}_1^{\,III} = -\int_{\pi}^{P} \left(\frac{\partial \bar{V}_1}{\partial T}\right)_P dP \quad (15)$$

The partial molar entropy of solution $\Delta\bar{S}_1$ is then given by

$$\Delta\bar{S}_1 = \Delta\bar{S}_1^{\,I} + \Delta\bar{S}_1^{\,II} + \Delta\bar{S}_1^{\,III} \quad (16)$$

To compute $\Delta\bar{S}_1$ the isometric mixing pressure must first be estimated. The entropy change $\Delta S_1{}^I$ can then be found from the thermodynamic properties of the pure gas or from generalized charts. $\Delta\bar{S}_1{}^{II}$ is computed from the solubility, and $\Delta\bar{S}_1{}^{III}$, a relatively small term, can be found approximately by rewriting Equation (15)

$$\Delta\bar{S}_1^{\,III} \approx \bar{V}_0\alpha(\pi - P) \quad (17)$$

Experimental values of α are rare, but they can be estimated from the slopes of the generalized plots in Figure 1 by the relationship

$$\bar{V}_0\alpha \equiv \left(\frac{\partial \bar{V}_0}{\partial T}\right)_P = \frac{V_c}{T_c}\left[\frac{\partial \frac{\bar{V}_0}{V_c}}{\partial \frac{T}{T_c}}\right] \quad (18)$$

Table 2 compares observed entropies of mixing for nitrogen, carbon monoxide, and ethane with those calculated by Equation (16). The agreement is quite good. The calculated entropies show that at 25°C. the solubility of nitrogen in benzene rises considerably, that of carbon monoxide rises moderately, and that of ethane falls strongly as the temperature is increased.

To illustrate the use of entropies of solution consider the following problem: Cook *et al.* (3) have measured the solubility of hydrogen in benzene at 25°C. and 1-atm. partial pressure: $x_1 = 2.58 \times$

Table 3. Solubility and Entropy of Solution for Ethylene in Carbon Tetrachloride for Various Isometric Mixing Pressures

Isometric mixing pressure, atm.	Solubility Parameter for ethylene, (cal./cc.)$^{1/2}$	Solubility $x_1 10^4$ at 25°C. and 1-atm. partial pressure Calculated	Observed (8)	Entropy, cal./(g.-mole)(°K.) Calculated*	Observed (8)
400	6.2	128	145	−7.9	−7.9
600	6.6	158	145	−8.0	−7.9
900	7.1	196	145	−8.1	−7.9

*Based on the observed solubility.

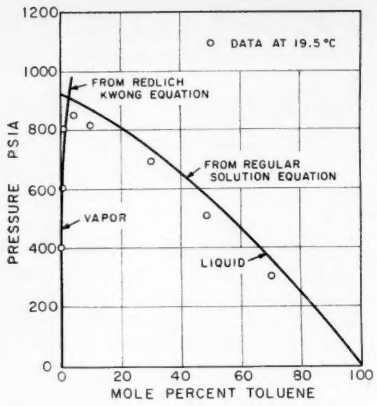

Fig. 3. Phase equilibria for toluene-ethylene system.

10^{-4}. Using this information estimate the solubility of hydrogen in benzene at 100°C. and at a partial pressure of 97 atm. To solve this problem the entropy of solution at 25°C. and 1 atm. is first computed by Equation (16) and found to be 4.9 cal./gmol. °K. At 1 atm., therefore, using Equation (12) and assuming the entropy of solution to be independent of temperature,

$$\ln \frac{x_1(100°\text{C.})}{2.58 \times 10^{-4}} = \frac{4.9 \ln \frac{373}{298}}{1.987}$$

This gives $x_1(100°\text{C.}) = 4.56 \times 10^{-4}$. At a partial pressure of 97 atm. a good estimate for the solubility is

$$x_1 = (97)(4.56 \times 10^{-4})$$

$$= 4.41 \times 10^{-2}.$$

The observed value (7) is 4.01×10^{-2}. The assumption of constant entropy of solution is good only for small temperature intervals. Also, Henry's Law is valid only at low solute concentrations.

UTILITY

Since the theory of regular solutions makes a variety of simplifying assumptions, it can only approximately describe the thermodynamic behavior of nonpolar solutions. The solubilities of gases and their temperature coefficients can therefore only be estimated by the given equations. The regular-solution equations as discussed here are not applicable for exact quantitative work. Rather, they should be regarded as first-order corrections to Raoult's Law.

One of the major computational difficulties in the application of regular-solution theory to gas-liquid solutions is the uncertainty of β for which almost no experimental results are available. The value of β has a large effect on π, but the effect of π on the computation of the solubility x_1 and the entropy $\Delta\bar{S}_1$ is not excessively serious. Thus a change in the isometric mixing pressure by as many as several hundred atmospheres usually produces in x_1 and $\Delta\bar{S}_1$ changes amounting to perhaps a factor of 2 or less. To illustrate this point solubilities and entropies for ethylene in carbon tetrachloride at 25°C. and 1 atm. have been calculated for several isometric mixing pressures. The results, given in Table 3, indicate that a very accurate value of the isometric mixing pressure is not required for estimation purposes. In fact, the simplest procedure is to assume $\beta = 0$ and to evaluate the isometric pressure using just the partial molar volume of the gas at low pressure. Solubilities based on this assumption, however, tend to be on the low side.

The main uses of these equations for chemical engineering purposes are to extend available data to new conditions and to make preliminary phase-equilibria estimates for nonpolar systems having no existing data. To illustrate, consider as a final example phase equilibrium in a system containing a gas near its critical temperature. (These systems have become interesting in connection with possible applications for fluid-liquid extraction.) The example chosen is the ethylene-toluene system, and, using only data for the pure components, a pressure-versus-composition diagram at 19.5°C. has been constructed. The liquid-phase equilibrium line is calculated from Equation (7) assuming that the partial molar volume of solvent is independent of composition. At high pressures P_1 must be replaced by a fugacity; at high pressures ϕ_2 is not unity, and therefore finding x_1 involves some trial-and-error algebra. The vapor-phase equilibrium line is computed from the Redlich and Kwong equation of state (*13*). The results, shown in Figure 3, are in better than qualitative agreement with the experimental values reported by Todd and Elgin (*14*).

ACKNOWLEDGMENT

The author is grateful to Professor J. H. Hildebrand for encouragement and for suggestions toward improvement of the manuscript.

NOTATION

a_1 = activity of gaseous solute
ΔE = change in internal energy
ΔF = change in free energy
f_1 = fugacity of pure gas
f_1^L = fugacity of pure component 1 as a liquid at the temperature and pressure of the solution
$\bar{f}_1$ = fugacity of component 1 in solution
ΔH = change in enthalpy
P = total pressure
P_1 = partial pressure of gas
P_1^0 = extrapolated vapor pressure of the gas
R = gas constant
S_1 = entropy of pure gas
$\bar{S}_1$ = partial molar entropy of gaseous solute
T = absolute temperature
T_c = critical temperature of gas
V = molar liquid volume of pure component
$\bar{V}_2$ = partial molar volume of liquid solvent
$\bar{V}_1$ = partial molar volume of gaseous solute
$\bar{V}_0$ = partial molar volume of gaseous solute at infinite dilution
V_c = critical volume of gas
x_1 = mole fraction of component 1 in liquid phase

Greek Letters

α = coefficient of thermal expansion
β = compressibility
δ = solubility parameter = $(\Delta E/V)^{1/2}$
γ = activity coefficient
ϕ = volume fraction
π = isometric mixing pressure

LITERATURE CITED

1. Clever, H. L., Rubin Battino, J. H. Saylor, and P. M. Gross, *J. Phys. Chem.*, **61**, 1078 (1957).
2. Comings, E. W., "High Pressure Technology," McGraw-Hill, New York, 1956.
3. Cook, M. W., D. N. Hanson, and B. J. Alder, *J. Chem. Phys.*, **26**, 748 (1957).
4. Din, Fazul, "Thermodynamic Functions of Gases," Vols. **1** and **2**, Butterworth, London, 1956.
5. Gjaldbaek, J. C., and J. H. Hildebrand, *J. Am. Chem. Soc.*, **71**, 3147 (1949).
6. Hildebrand, J. H., and R. L. Scott, "The Solubility of Non-Electrolytes," 3rd ed., Rheinhold, New York, 1950.
7. Ipatiev, V. V., and M. I. Levina, *J. Phys. Chem. (USSR)*, **6**, (1935).
8. Jolley, J. E., and J. H. Hildebrand, J. Am. Chem. Soc. **80**, 1050 (1958).
9. Krichevskii, I. R., and G. D. Efremova, *J. Phys. Chem. (USSR)*, **22**, 1116 (1948).
10. Lachowicz, S. K., D. M. Newitt, and K. E. Weale, *Trans. Faraday Soc.*, **51**, 1198 (1955).
11. Lydersen, A. L., R. A. Greenkorn, and O. A. Hougen, Univ. Wis. Eng. Expt. sta. (1955).
12. Newton, R. H., *Ind. Eng. Chem.*, **27**, 302 (1935).
13. Redlich, Otto and J. N. S. Kwong, *Chem. Rev.*, **44**, 233 (1949).
14. Todd, D. B., and J. C. Elgin, *A.I.Ch.E. Journal*, **1**, 20 (1955).

Manuscript received Oct. 25, 1957; revision received Dec. 16, 1957; paper accepted Dec. 16, 1957.

Drop Formation in Liquid-liquid Systems from Single Nozzles

HAROLD R. NULL and HOMER F. JOHNSON

University of Tennessee, Knoxville, Tennessee

Interfacial area is an important variable in mass transfer operations. In liquid-liquid extraction systems, where interfacial area comprises drop surfaces, the area can be computed if drop sizes are known. This work presents a new correlation which predicts volumes of drops formed from single nozzles to within 20% throughout the range of nozzle flow rates for which uniform drop sizes are obtained.

For years it has been the practice of experimenters in the field of liquid-liquid extraction to evaluate their data in terms of the product of the over-all mass transfer coefficient and the interfacial area available for mass transfer per unit volume of tower. Although the need for a basis by which to determine these two parameters separately has been recognized, the means for doing so have in most instances not been available.

In the case of a spray tower the area available for mass transfer is directly proportional to the average surface area of the individual drops, which, in turn, is a function of the volume and shape of the drops. A method of predicting static drop sizes is well established by the work of Harkins and Brown (*2, 3*), and a study has been made by Hayworth and Treybal (*4*) on the prediction of drop volumes for various flow rates of a dispersed phase into a static continuous phase from a single nozzle. This study was the logical first step toward predicting the interfacial area available for extraction, but Batson (*1*) was unable to verify the correlation obtained by Hayworth and Treybal. Batson found that for the system he studied, methyl isobutyl ketone dispersed in water, the drop volumes were all smaller than predicted and that two points of relative maximum were obtained when drop size was plotted vs. flow rate; whereas the correlation of Hayworth and Treybal gave only one maximum. Null (*6*) later obtained results in agreement with Batson, and the need for a more reliable method of predicting drop volumes from a single nozzle was established. It is the purpose of this paper to present a basic model for drop formation from single nozzles which may be used as the starting point in further search for a general method of predicting the interfacial area available in extraction towers.

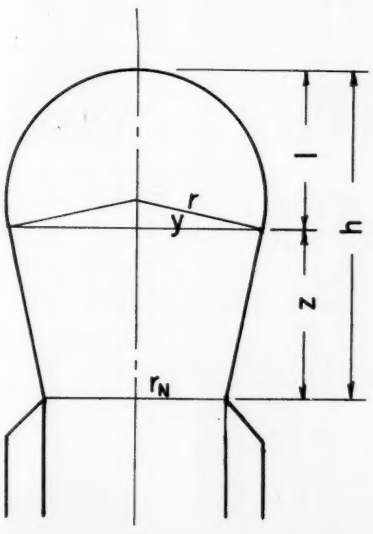

Fig. 1. Geometry of drop before break.

THEORY

The theoretical treatment of the drop-formation phenomenon is primarily one of geometry. The assumptions used are, for the most part, suggested by actual observation of drops with the aid of

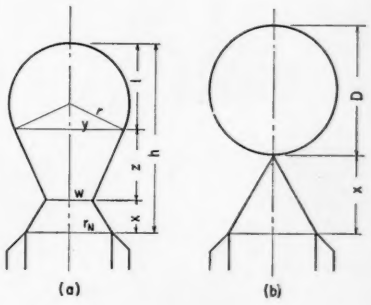

Fig. 2. Drop geometry during break period.

H. R. Null is now associated with the University of Dayton, Dayton, Ohio.

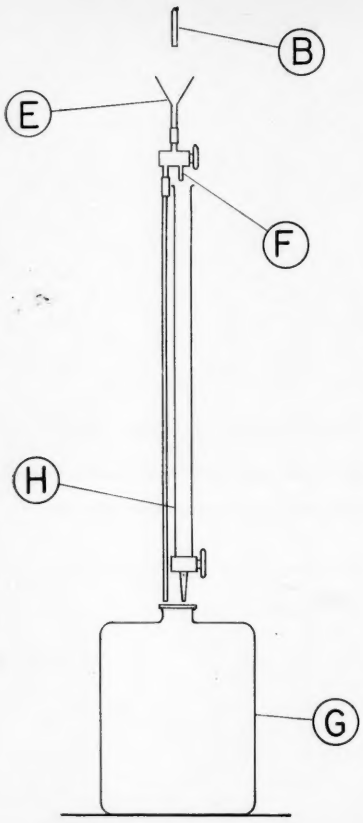

Fig. 3. Apparatus for flow measurement.

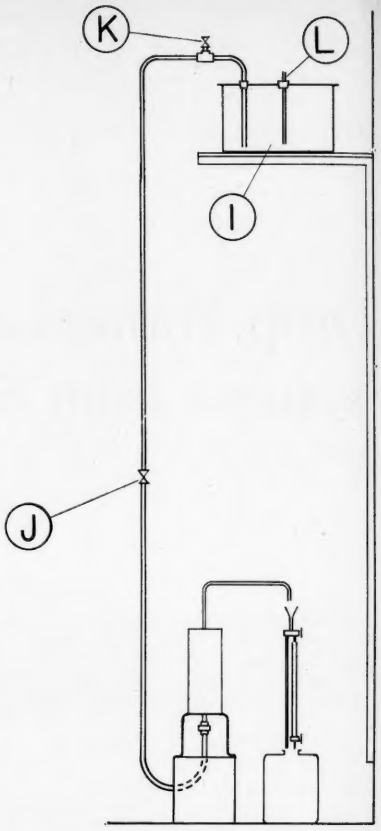

Fig. 4. Drop-dispersing apparatus.

stroboscopic light. Two distinct phases of the drop formation will be considered—the period of time during which the drop is growing but has not begun to break away from the nozzle and the period of time during which the process of breaking away is actually occurring. A more detailed treatment of the theory may be found in reference 5.

The model adopted for the period of drop growth before breaking is that of a sphere atop, and tangent to, a right-truncated cone passing through the circumference of the nozzle. This model and its dimensions are shown in Figure 1. The drop is assumed to grow with leading-edge velocity v constant. It will also be assumed that throughout this initial period the dimension l constantly increases. Eventually the assumption of constant v will no longer be compatible with increasing l; i.e., l will have reached a maximum characterized by $dl/dt = 0$,

Fig. 5. Photographs of drop formation.
(a) Cottonseed oil dispersed in water. D_N = 0.314 cm., V_N = 0.764 cc./sec.;
(b) Cottonseed oil dispersed in water. D_N = 0.263 cm., V_N = 0.0438 cc./sec.

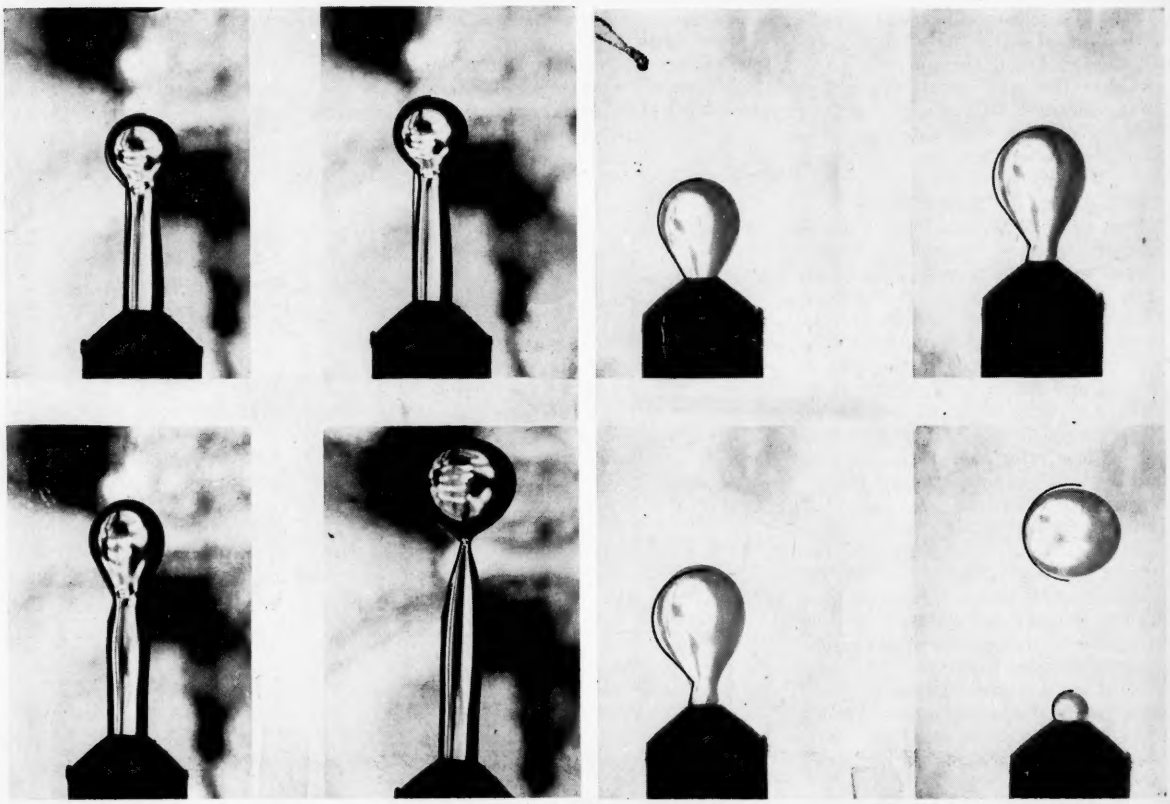

5a 5b

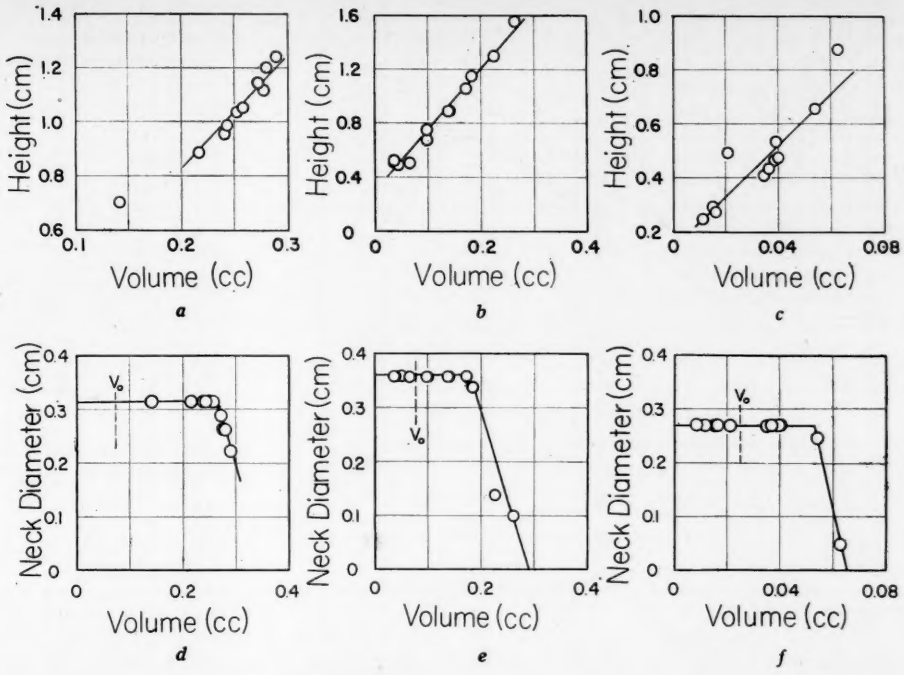

Fig. 6. Variation of drop dimensions.

a. Cottonseed oil in water.
b. Water in benzene.
c. Water in CCl_4.
d. Cottonseed oil in water.
e. Water in benzene.
f. Water in CCl_4.

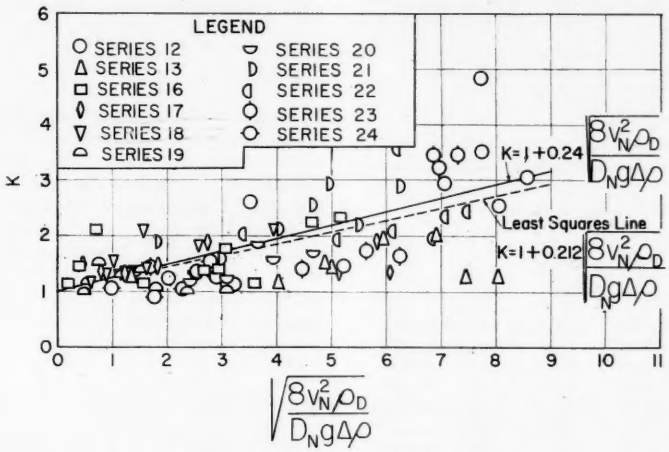

Fig. 7. Correlation of values of K.

when the period of simple drop growth will be assumed to end and the period of drop break away to begin. The geometry of the system coupled with constant flow rate and the condition $dl/dt = 0$ results in the following equation:

$$\frac{v}{v_N} = \frac{6(\beta^2 - 2\alpha^2\beta + \alpha^2)}{\beta^5 - \alpha^2\beta^3 + 2\beta^2 - 3\alpha^4\beta + 2\alpha^2} \quad (1)$$

and

$$\gamma = \frac{2\alpha\beta(\beta - 1)}{\alpha^2 - \beta^2} \text{ (from geometry)}$$

Equation (1) is valid whether v is considered constant or variable. The condition that v be constant leads to a condition that

$$\left.\frac{\partial\left(\frac{v}{v_N}\right)}{\partial y}\right]_0 = 0,$$

which in turn leads to the equation

$$3\beta^5 + (3\alpha - 8\alpha^2)\beta^4 + (6\alpha^2 - 8\alpha^3)\beta^3 + 6\alpha^3\beta^2 + (3\alpha^4 - 4\alpha^2)\beta + (3\alpha^5 - 4\alpha^3) = 0 \quad (2)$$

Equations (1) and (2) are sufficient to define α and β provided the value of v/v_N is known. The equations apply without modification to the cases $\alpha > 1$, $1 < \beta < \alpha$; $0 < \alpha < 1$, $\alpha < \beta < 1$; and $\alpha = \beta = 1$, which imply that the spherical segment in Figure 1 is respectively greater than, less than, and equal to a hemisphere. The volume of the drop at the beginning of the break V_o can be evaluated from geometric considerations which lead to

$$\frac{3V_o}{4\pi r_N^3} = \frac{\alpha}{8}(\alpha^2 + 3\beta^2) + \frac{\alpha}{4}(1 + \beta + \beta^2) \quad (3)$$

From the instant that the break begins until it is complete the configuration shown in Figure 2*a* is assumed with the limiting case for final break-away being as shown in Figure 2*b*. At this point it is necessary to define distinctly the terms *drop* and *jet* used in this discussion. During the break period the term drop is used to represent that portion of the fluid outside the nozzle but more remote from it than the distance x. The truncated cone having bases r_N and w is referred to as the jet. V designates the volume of the drop.

The total volume V_r represented in Figure 2*a* consists of the volume of the drop V, plus the volume of the jet:

$$V_r = V + \frac{\pi}{3} \times (r_N^2 + r_N w + w^2) \quad (4)$$

and

$$x = h_o + vt - l - z \quad (5)$$

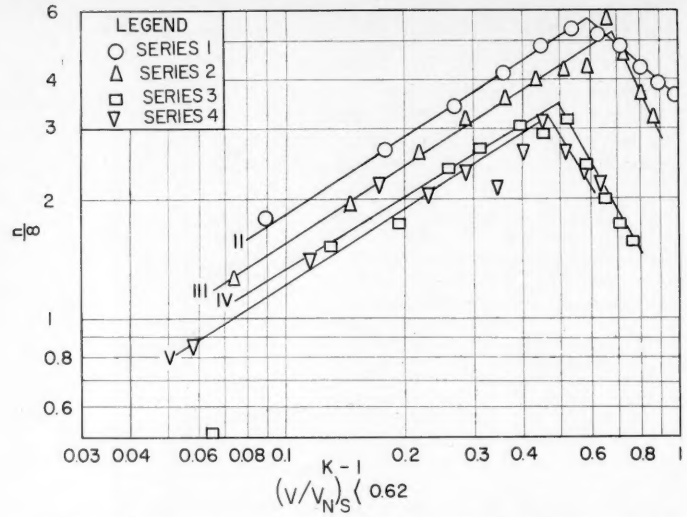

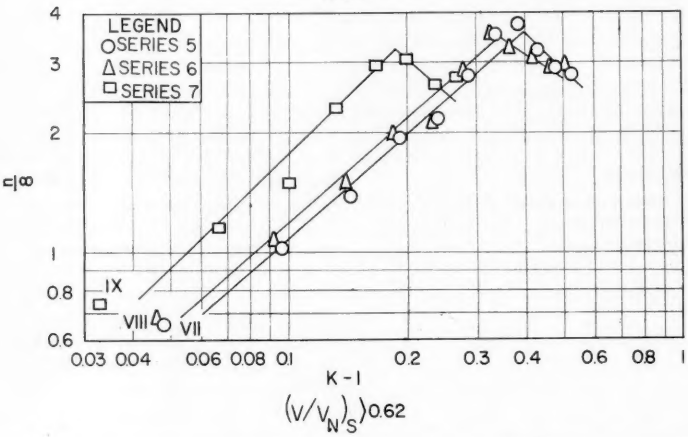

Fig. 8. Correlation of $n/8$ for the system methyl isobutyl ketone–water.

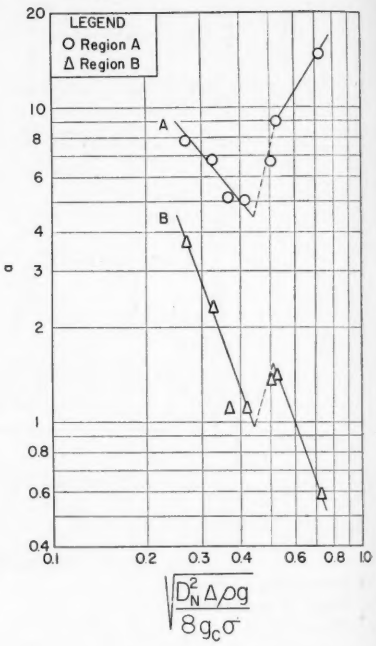

Fig. 9. Correlation of a of Equation (12).

TABLE 1. SUMMARY OF CONDITIONS OF DIFFERENT SERIES

Series	Table number of ref. 5	Dispersed phase*	Continuous phase	ρ_c, g./cc.	ρ_D, g./cc.	σ, dynes/cm.	D_N, cm.	$\sqrt{\frac{D_N^2 \Delta\rho g}{8 g_c \sigma}}$
1	II	MIK	Water	0.9984	0.8039	9.48	0.1691	0.269
2	III	MIK	Water	0.9982	0.8025	9.58	0.2071	0.326
3	IV	MIK	Water	1.0040	0.8014	9.52	0.2475	0.396
4	V	MIK	Water	1.0000	0.8022	9.56	0.261	0.416
5	VII	MIK	Water	1.0000	0.8040	9.21	0.3115	0.503
6	VIII	MIK	Water	0.9988	0.8015	9.67	0.3307	0.523
7	IX	MIK	Water	0.9983	0.7994	9.85	0.460	0.724
8	X	Benzene	Water	1.0000	0.8707	29.66	0.460	0.341
9	XI	Benzene	Water	0.9981	0.8694	26.89	0.3307	0.253
10	XII	Benzene	Water	0.9994	0.8691	30.4	0.3115	0.226
11	XIII	Benzene	Water	0.9982	0.8693	30.2	0.261	0.193
12	XV	Benzene	Water	0.9992	0.8646	31.6	0.201	1.1469
13	XVI	Benzene	Water	0.9972	0.8639	28.9	0.252	0.1891
14	XVII	EA	Water	0.9969	0.8884	4.5	0.269	0.462
15	XVIII	EA	Water	0.9966	0.8891	4.13	0.305	0.545
16	XIX	CSO	Water	0.9978	0.9113	24.2	0.314	0.208
17	XX	CSO	Water	0.9973	0.9099	23.8	0.263	0.176
18	XXI	Water	CTC	1.5728	0.9970	31.5	0.270	0.376
19	XXII	Water	CTC	1.5783	0.9993	33.8	0.348	0.504
20	XXIII	CTC	Water	0.9911	1.5808	19.21	0.280	0.405
21	XXIV	Water	Benzene	0.8710	0.9969	28.5	0.358	0.235
22	XXV	Water	Benzene	0.8693	1.0015	29.8	0.260	0.192
23	XXVI	Water	CSO	0.9110	0.9987	25.6	0.260	0.168
24	XXVII	Water	CSO	0.9110	0.9987	25.6	0.358	0.232

*Abbreviations: MIK = methyl isobutyl-ketone, EA = ethyl acetate, CSO = cottonseed oil, CTC = carbon tetrachloride.

where t is the time from the beginning of the break. When Equation (4) is differentiated with respect to time, the flow rate results. If the result is evaluated at the instant represented by Figure 2*b*, at which time drop growth ceases, the assumption $dV/dt = 0$ seems reasonable. When the differentiation is performed and evaluated at the completion of the break, and Equation (5) is substituted therein, the result simplifies to:

$$r_N^2 v_N = \tfrac{1}{3}(h_0 + v t_f - l - z)(r_N + 2w)\frac{dw}{dt}$$

$$+ \tfrac{1}{3}(r_N^2 + r_N w + w^2)\left(v - \frac{dl}{dt} - \frac{dz}{dt}\right) \quad (6)$$

where t_f is the time at the completion of the break.

Equation (6) may be simplified by first observing that $l = D$, the final drop diameter, at $t = t_f$, and applying two further assumptions, namely that z varies with time by

$$z = z_0\left[1 - \left(\frac{t}{t_f}\right)^n\right] \quad (7)$$

and w varies linearly with time:

$$w = r_N\left(1 - \frac{t}{t_f}\right) \quad (8)$$

These assumptions lead to

$$\left.\frac{dz}{dt}\right]_{t=t_f} = -\frac{nz_0}{t_f}$$

$$\left.\frac{dw}{dt}\right]_{t=t_f} = -\frac{r_N}{t_f} \quad \text{and}$$

$$\left.\frac{dl}{dt}\right]_{t=t_f} = \frac{nz_0}{2t_f}$$

The foregoing assumption can be used to reduce Equation (6) to

$$t_f = \frac{(D - h_0) + \frac{nz_0}{2}}{3v_N} \qquad (9)$$

There is still another relation available for determining t_f. If F denotes the frequency of drop formation,

$$\frac{1}{F} = \frac{D^3}{6r_N^2 v_N}$$

is the total time required for the drop to form and is equal to t_f plus the time required for the volume of the drop to increase from the jet volume of Figure 2*b* to the volume V_0 when the next drop begins to break away, or

$$\frac{D^3}{6r_N^2 v_N} = \frac{V_0 - \frac{\pi}{3}(h_0 + vt_f - D)r_N^2}{\pi r_N^2 v_N} + t_f \qquad (10)$$

Equations (9) and (10) combine to give

$$\left(\frac{D}{D_N}\right)^3 - A\left(\frac{D}{D_N}\right) - \left(B + \frac{n}{8}C\right) = 0 \qquad (11)$$

where

$$A = \frac{1}{2}\left(2 - \frac{1}{3}\frac{v}{v_N}\right)$$

$$B = \frac{3V_0}{4\pi r_N^3} - \frac{1}{4}\left(2 - \frac{1}{3}\frac{v}{v_N}\right)(\alpha + \gamma)$$

and

$$C = \gamma\left(1 - \frac{1}{3}\frac{v}{v_N}\right)$$

Equation (11), together with Equations (1), (2), (3), and the expression for γ, affords a means of computing drop sizes from a knowledge of only v/v_N and n.

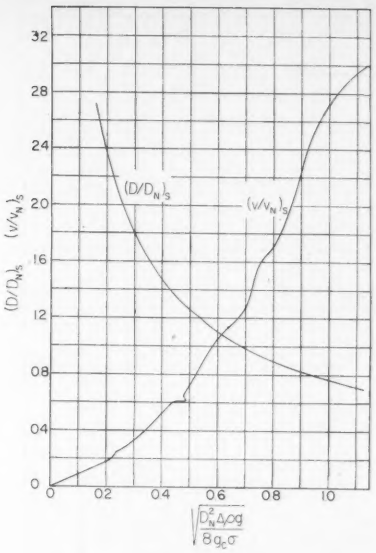

Fig. 10. Static drop parameters.

The simplest possible behavior for n would be for it to be zero for zero flow rate of dispersed phase and have a positive value for positive flow rates. It was observed in the theoretical portion of this work that v/v_N for positive dispersed phase flow rate is always greater than for static drop formation, or

$$K \equiv \left(\frac{v}{v_N}\right) \Big/ \left(\frac{v}{v_N}\right)_s \geq 1$$

where the subscript s designates static conditions. A simple form which suggests itself, then, is

$$\frac{n}{8} = a(K - 1)^b \qquad (12)$$

where a and b are to be determined experimentally. Equation (11) gives, for the static case,

$$\left(\frac{D}{D_N}\right)_s^3 - A_s\left(\frac{D}{D_N}\right)_s - B_s = 0 \qquad (13)$$

and since $(D/D_N)_s$ can be determined from the work of Harkins and Brown (*2, 3*) where the correction factor to Tate's law is given as function of $\sqrt{D_N^2 \Delta\rho g/8\sigma g_c}$, Equation (13) is seen to relate $(v/v_N)_s$ to $\sqrt{D_N^2 \Delta\rho g/8\sigma g_c}$.

The factors which influence the value of v/v_N are now to be further investigated. As indicated in Figure 2*b*, the vertex of the cone forming the jet will become the leading edge of the succeeding drop. If the point does not retract, the distance travelled by the leading edge of a drop during formation v/F is equal to D, the final drop diameter, or $v/FD = 1$. Actually, the point does retract, being supported by the impact force, P_I, and the buoyant force, P_B, and retracted by the surface tension P_T. Dimensional analysis of these factors results in

$$\frac{v}{FD} = \Phi\left(\frac{P_I}{P_T}, \frac{P_B}{P_T}\right)$$

which can lead to

$$K = f\left(\sqrt{\frac{D_N^2 \Delta\rho g}{8g_c\sigma}}, \sqrt{\frac{D_N v_N^2 \rho_D}{g_c\sigma}}\right) \qquad (14)$$

Evaluation of a and b of Equation (12) and determination of the form of f in Equation (14) are to be done experimentally.

The theoretical treatment has assumed a case of the drop forming at the top of the nozzle. Actually, the approach is also extended to the case where an extended jet appears at the nozzle by merely considering the jet as a cylinder of liquid with a cone at its end and considering the model developed herein as occurring at the end of the cylindrical portion of the jet. This model then becomes equivalent to the case illustrated in Figures 1 and 2.

APPARATUS AND PROCEDURE

The apparatus used for the experimental portion of the work is shown in Figures 3 and 4. The apparatus consisted of a square, stainless-steel column having two sides made of plate glass. The dispersed phase was admitted into the column through a nozzle and withdrawn through a tube at the other end. A drain was provided for the column. The holder for the nozzle was tapped to accommodate the ¼-in. feed line on the upstream side and the ⅛-in. pipe threads of the nozzle on the downstream side. Each nozzle consisted of a two-inch length of ⅜-in. rod through which the hole was drilled. One end was threaded with ⅛-in. pipe threads to fit the holder; the other end was chamferred away from the opening at a 45° angle to prevent spreading of the dispersed phase onto the metal around the opening. All nozzles were constructed of stainless steel or aluminum. Altogether sixteen inside nozzle diameters varying from 0.1691 to 0.460 cm. were studied. The discharge from tube B was directed into a funnel E (Figure 3) connected to a three-way stop cock, F which could be used to collect the dispersed phase in a burette H or a waste bottle G. Dispersed-phase

Table 2. Sample Experimental Data from Series 13.

Run	Dispersed-phase flow rate, cc./sec.	V, cc.	$\sqrt{\frac{D_N v_N^2 \rho_D}{g_c\sigma}}$	$\frac{6V}{\pi D_N^3}$	v, cm./sec.	$\frac{v}{v_N}$	K	$\sqrt{\frac{8v_N^2\rho_D}{D_N g \Delta\rho}}$
1	0.1472	0.1738	0.248	20.7	0.589	0.206	1.226	1.31
2	0.437	0.1683	0.763	20.1	2.17	0.190	1.131	4.03
3	0.646	0.1343	1.128	16.02	4.15	0.320	1.902	5.96
4	0.531	0.1518	0.925	18.10	2.70	0.253	1.502	4.89

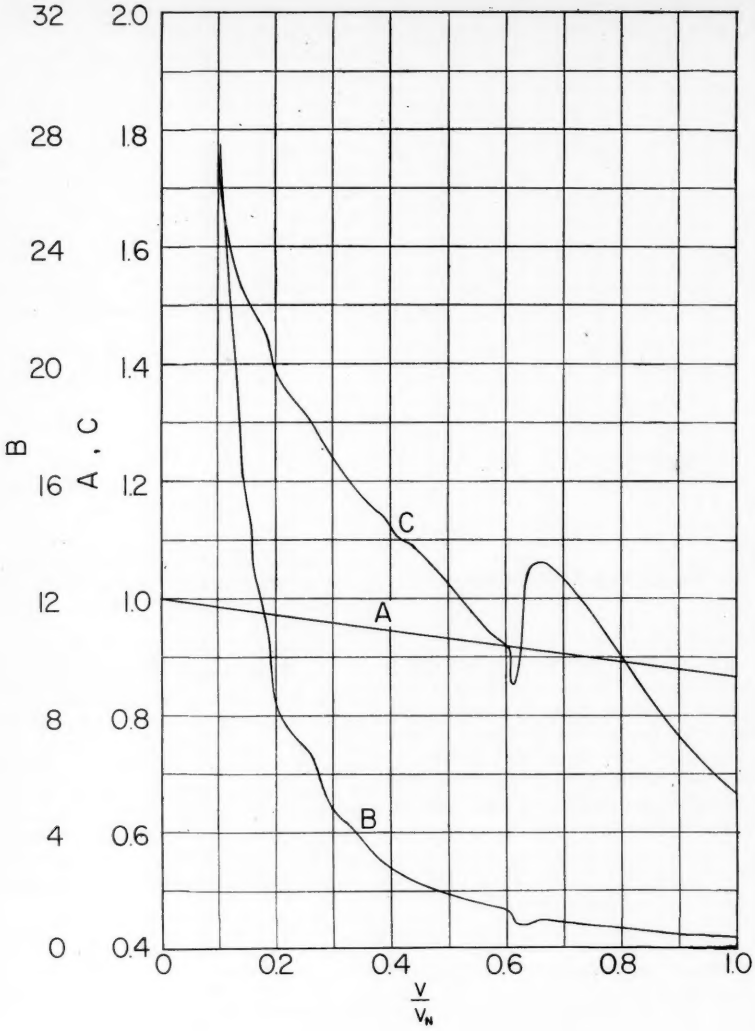

Fig. 11*a*. Coefficients of drop-volume equation.

flow was controlled by a needle valve J (Figure 4). The dispersed-phase head tank I was closed and equipped with a tube L to assure constant pressure of 1 atm. at the lower end of the tube. A valve K, was provided to bleed air out of the feed line.

Before a series of runs was made, the head tank was filled with the phase to be dispersed plus a layer of the continuous phase to maintain mutual saturation, and the column was filled with continuous phase containing a layer of the dispersed phase. This was normally done the day before the run was to be made. For a typical run the flow rate was adjusted and allowed to reach steady state. The frequency of the drop formation was then determined by adjusting a strobotac until the drop image at the nozzle tip appeared stationary. The dispersed-phase overflow was then directed into the burette for a period of time measured by a stopwatch to determine the flow rate. Photographs were then taken of the drop as it formed, after which a new flow setting was made. The photographs were taken with the aid of a strobolux acting as slave to the strobotac or with a strobolume as a single flash source. In either case the light source was shown through the column into the lens of the camera, an Exakta VX. For the earlier runs, an attempt was made to capture the drop image at the exact break-away instant, but when it later became apparent that a determination of drop front velocity during formation was important, several photographs were taken at each flow setting. From these photographs the height of the drop was measured directly and time was determined by graphical integration of the contour of the liquid outside the nozzle to determine total volume, which was in turn proportional to time. The accuracy of the graphical integration was found to be $\pm 3\%$ by comparing the volume found by integrating the outline of completely formed drops, such as appear in Figure 5*b*, with the volume determined by frequency and flow rate measurements. The average deviation from the lines determining frontal velocity v was not determined, but scatter was slight, as indicated in Figure 6*a*, *b*, and *c*. The results are based on the data of the systems and conditions enumerated in Table 1. Table 2 gives an example of the data obtained from one series of runs.

The density of each phase was measured at the end of each series of runs with a Westphal chain balance, and the interfacial tension was measured with a du Nuoy Tensiometer. The value of 19.21 dynes/cm. for the carbon tetrachloride-water system of Series 20 is abnormally low. This is believed to be due to contamination by the gasket material of the head tank; subsequently carbon tetrachloride was not used as dispersed phase.

RESULTS

Drop Appearance

The theoretical model adopted was based upon the actual appearance of the drop image observed by the authors. Figure 5 shows photographs of drops during various stages of formation with the assumed configuration superimposed. These photographs are typical of photographs of all systems and indicate the validity of the configuration assumed for the theoretical treatment. Complete original and calculated data are reported in reference 5.

Test of Assumptions

Figure 6 contains typical plots of leading edge height and neck radius as a function of total volume of dispersed phase outside the nozzle. Since for constant flow rate the total volume outside the nozzle is proportional to time, linearity of these plots indicates linearity with time. Constant leading edge velocity is indicated by Figures 6*a*, 6*b*, and 6*c*, although Figures 6*d*, 6*e*, and 6*f* leave considerable doubt as to the validity of the assumption of linearity of neck radius with time. The plots of neck diameter against total volume also have indicated on them values of V_0 for the runs from which the data were taken. Since the values of V_0 do not include the volumes of the extended jets, such as is shown in Figure 5*a*, V_0 should always be equal to or less than the total volume outside the nozzle at the beginning of the break period. This was universally true for all

values of V_0, and the greatest deviation from equality occurred in those systems exhibiting the longest extended jets.

Evaluation of Empirical Functions

When each set of data was taken individually, K was found to vary linearly with $\sqrt{D_N v_N^2 \rho_D / g_c \sigma}$, and the slopes of these plots varied inversely with $\sqrt{D_N^2 \Delta\rho g / 8 g_c \sigma}$. The resulting equation is

$$K = 1 + 0.24 \sqrt{\frac{8 v_N^2 \rho_D}{D_N g \Delta\rho}} \qquad (15)$$

where $\sqrt{8 v_N^2 \rho_D / D_N g \Delta\rho}$ is the ratio of the two dimensionless groups $\sqrt{D_N v_N^2 \rho_D / g_c \sigma}$ and $\sqrt{D_N^2 \Delta\rho g / 8 g_c \sigma}$. The combined plot of all the leading edge velocity data is shown in Figure 7 with the exception of the ethyl acetate-water system. This system is omitted because the two liquids involved are sufficiently soluble so that mutual saturation was never obtained. Therefore, some mass transfer occurred during drop formation, and the appropriate value of the interfacial tension was not known.

The data from which $n/8$ could be computed directly scattered too much for a and b of Equation (12) to be determined; a small error in v/v_N results in a large error in both γ and $3V_0/4\pi r_N^3$, and thus considerable precision in the measurement of v/v_N would be required. Therefore, in order to obtain a correlation for $n/8$, the smoothed curves representing the experimental drop size data for the system methyl-isobutyl ketone dispersed in water were used in Equation (11) to determine $n/8$. Equation (15) was employed to determine v/v_N and K. Values of $n/8$ and K thus obtained are plotted in Figure 8. The value of a versus $\sqrt{D_N^2 \Delta\rho g / 8 g_c \sigma}$ is shown in Figure 9, and the final correlation obtained is shown below

For $\left(\frac{v}{v_N}\right)_s < 0.62$, or $\sqrt{\frac{D_N^2 \Delta\rho g}{8 g_c \sigma}} < 0.49$

$$\left.\begin{aligned} &\text{A}\quad \frac{n}{8} = 1.85\left(\sqrt{\frac{D_N^2 \Delta\rho g}{8 g_c \sigma}}\right)^{-1.15} (K-1)^{\frac{2}{3}}, \quad K \le 1 + 0.25\left(\sqrt{\frac{D_N^2 \Delta\rho g}{8 g_c \sigma}}\right)^{-0.807} \\ &\text{B}\quad \frac{n}{8} = 0.092\left(\sqrt{\frac{D_N^2 \Delta\rho g}{8 g_c \sigma}}\right)^{-2.9} (K-1)^{-\frac{1}{3}}, \quad K \ge 1 + 0.25\left(\sqrt{\frac{D_N^2 \Delta\rho g}{8 g_c \sigma}}\right)^{-0.807} \end{aligned}\right\} \qquad (16)$$

For $\left(\frac{v}{v_N}\right)_s > 0.62$, or $\sqrt{\frac{D_N^2 \Delta\rho g}{8 g_c \sigma}} > 0.49$

$$\left.\begin{aligned} &\text{A}\quad \frac{n}{8} = 22.9\left(\sqrt{\frac{D_N^2 \Delta\rho g}{8 g_c \sigma}}\right)^{1.45} (K-1)^{0.9}, \quad K \le 1 + 0.108\left(\sqrt{\frac{D_N^2 \Delta\rho g}{8 g_c \sigma}}\right)^{-1.816} \\ &\text{B}\quad \frac{n}{8} = 0.334\left(\sqrt{\frac{D_N^2 \Delta\rho g}{8 g_c \sigma}}\right)^{-2.2} (K-1)^{-1}, \quad K \ge 1 + 0.108\left(\sqrt{\frac{D_N^2 \Delta\rho g}{8 g_c \sigma}}\right)^{-1.816} \end{aligned}\right\} \qquad (17)$$

Since Equations (16) and (17) do not coincide at $\sqrt{D_N^2 \Delta\rho g / 8 g_c \sigma} = 0.49$, a transition region is suggested, and the equations are not recommended for $0.47 \le \sqrt{D_N^2 \Delta\rho g / 8 g_c \sigma} \le 0.51$.

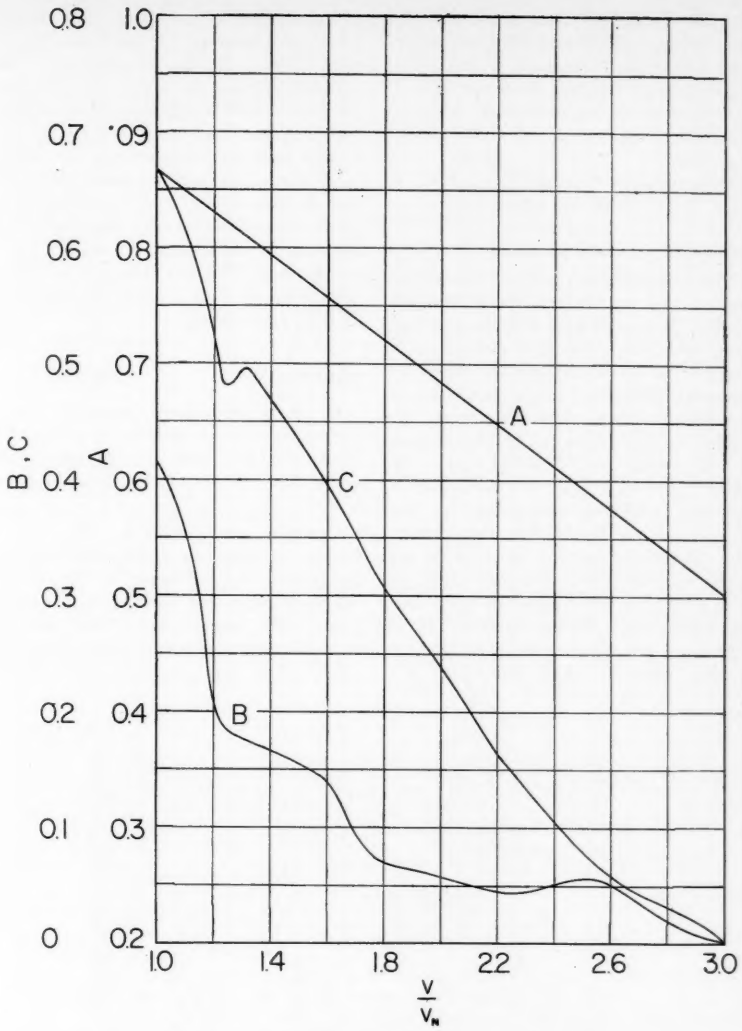

Fig. 11*b*. Coefficients of drop-volume equation.

Computation of Drop Volumes

A series of charts, Figures 10 to 14, have been prepared to aid in the computation of drop sizes based on the results of the current investigation. The steps in computing drop sizes are as follows:

1. Given the properties of the system, find the value of $\sqrt{D_N^2 \Delta\rho g / 8 g_c \sigma}$. This determines the values of $(D/D_N)_s$ and of $(v/v_N)_s$, which may be found from Figure 10, prepared from the work of Harkins and Brown, and solutions of Equation (13).
2. Compute the value of

$$\sqrt{8 v_N^2 \rho_D / D_N g \Delta\rho}$$

This determines K by the equation

$$K = 1 + 0.24 \sqrt{\frac{8 v_N^2 \rho_D}{D_N g \Delta\rho}} \qquad (15)$$

3. Compute $v/v_N = (v/v_N)_s K$.
4. Find the values of A, B, and C from Figure 11*a* or 11*b* which were prepared by solution of Equations (1) and (2) and the definitions of A, B, and C.
5. Find values of $n/8$ from Figures 12 and 13 prepared from Equations (16) and (17).

6. Compute $(n/8)C$ and $(B + (n/8)C)$.

7. Use A and $(B + (n/8)\ C)$ to determine D/D_N from Figure 14*a* or 14*b*, which represents solutions of Equation (11).

8. The drop volume may now be computed from

$$V = \frac{\pi}{6} D_N{}^3 \left(\frac{D}{D_N}\right)^3$$

Accuracy of Correlations

The computation of drop volumes has been carried out for each system studied. Typical plots of actual drop volume and computed curve volumes are given in Figure 15. The average deviation of experimental from computed values of drop volume has been calculated by the method of this paper and by the method of Hayworth and Treybal (4). The results are shown in Table 3, which indicates a better correlation by the present method for all but three series. The deviations on a volume basis are approximately three times as great as they would be on a diameter basis, but it is felt that the volume basis should be used since the equivalent diameter is a derived quantity. The deviations are quite acceptable for all systems except ethyl acetate-water, for which the phases were known to be unsaturated. The over-all average deviation was 20% for all runs; 15.5% when the ethyl acetate-water system was omitted; 7.55% for methyl isobutyl ketone-water, for which most data were taken; and 18.46% for the benzene-water system, which was used most extensively by Hayworth and Treybal. On the same bases the Hayworth and Treybal correlation gave deviations of 87.4%, 72.2%, 73.1%, and 27.47% respectively.

CONCLUSIONS

A model has been proposed which does satisfactorily describe liquid-liquid drop formation and predict drop volumes for flow rates in the range of $0 \leq \sqrt{D_N v_N{}^2 \rho_D / g_c \sigma} \leq 1.4$. It may be possible to refine the description further to obtain a more accurate prediction of drop volume by means of modification of the various assumptions used in the present derivation, but the over-all approach appears generally applicable. For example, the correlation obtained for n is far from conclusive, and the assumption that the neck radius varies linearly with time is not conclusively verified by the data. The high values obtained for n, in fact, are much greater than normally expected for physical phenomena obeying the type of law assumed for the variation of z. The value of n, however, may be greatly reduced by assuming the neck radius to vary as the square of time rather than linearly, all of which suggests that the most important assumption to be investigated in refining the approach outlined herein is the linearity of neck radius with time.

Further investigation will be necessary before the approach outlined can be extended to multiple nozzles, as encountered in liquid-liquid extraction.

NOTATION

A = parameter of drop-diameter equation, equal to $\frac{1}{2}(2 - \frac{1}{3}(v/v_N))$

B = parameter of drop-diameter equation, equal to $3V_0/4\pi r_N{}^3$

$$-\frac{1}{4}\left(2 - \frac{1}{3}\frac{v}{v_N}\right)\frac{h_0}{r_N}$$

C = parameter of drop-diameter equation, equal to $\gamma(1 - \frac{1}{3}(v/v_N))$

D = diameter of drop during and after formation

D_N = inside diameter of nozzle

F = frequency of drop formation

K = ratio of true value of v/v_N to the static value, $(v/v_N)_s$

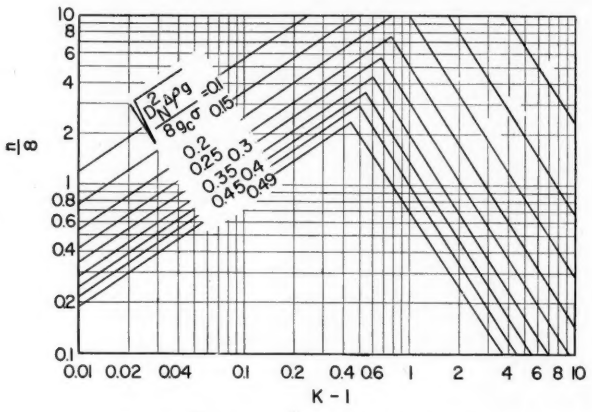

Fig. 12. Values of $n/8$ for $(v/v_N)_s < 0.62$.

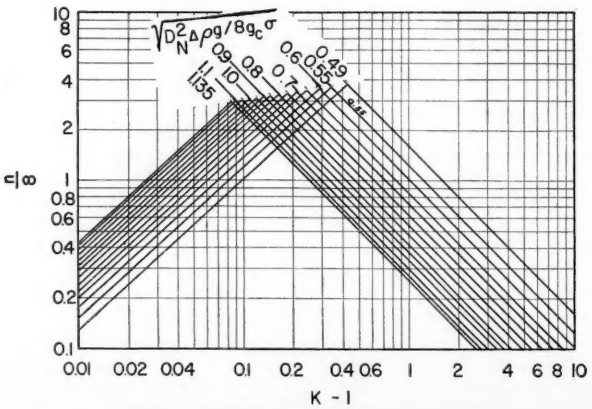

Fig. 13. Values of $n/8$ for $(v/v_N)_s > 0.62$.

Table 3. Deviations of Experimental from Calculated Drop Volumes

Series	Average percentage of deviation by proposed method	Average percentage of deviation from Hayworth and Treybal correlation
1	8.4	121.
2	5.0	94.
3	9.8	70.
4	7.5	65.
5	6.7	47.
6	6.8	37.5
7	7.5	28.8
8	16.7	18.0
9	30.5	9.5
10	12.2	28.4
11	11.4	20.2
12	21.6	61.
13	17.4	24.7
14	94.	377.
15	90.	325.
16	24.3	26.6
17	26.0	14.0
18	30.6	121.
19	22.3	130.
20	26.6	233.
21	14.6	53.
22	25.5	22.2
23	15.0	169.
24	55.	235.

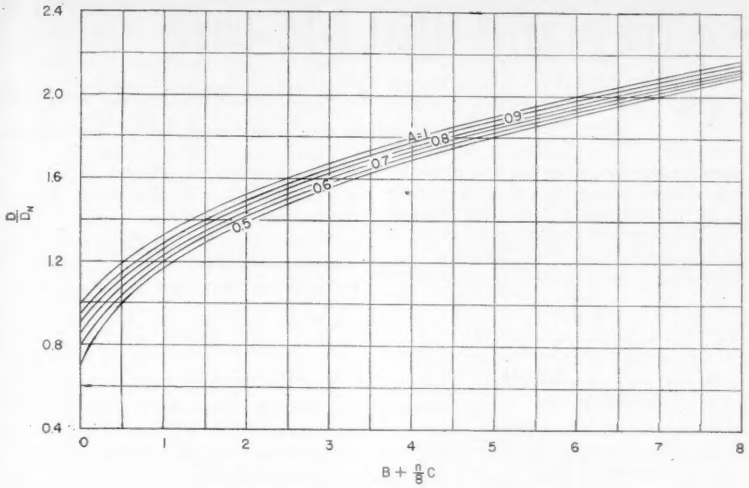

Fig. 14*a*. Solutions of drop-diameter equation.

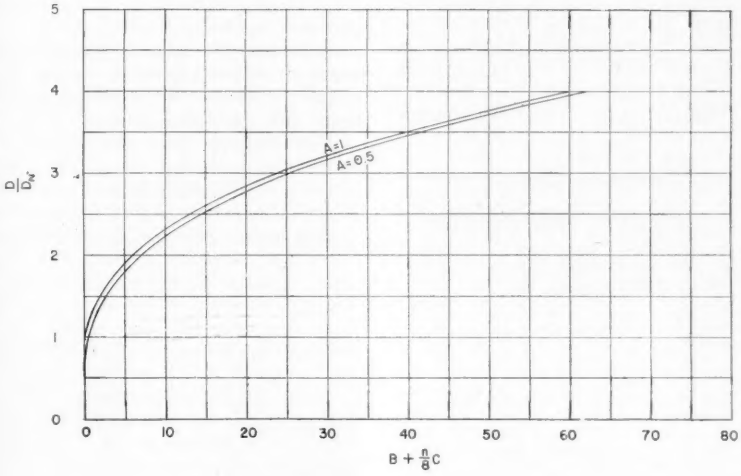

Fig. 14*b*. Solutions of drop-diameter equation.

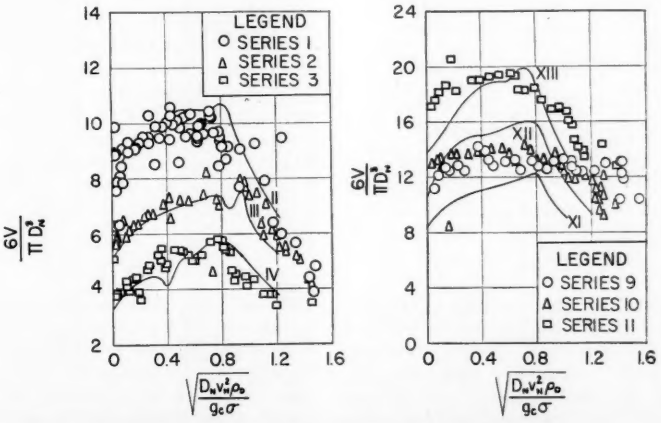

Fig. 15. Comparison of experimental data with theory.

P_B, P_I, P_T = buoyant, impact, and surface contraction forces on jet immediately after drop separation
V = volume of a drop during and after formation
V_N = volumetric flow rate of dispersed phase
V_s = drop volume for formation at zero dispersed phase flow rate
a = empirical constant
b = empirical constant
g = gravitational acceleration
g_c = conversion factor
h = distance from nozzle tip to leading edge of drop being formed
l = height of spherical segment portion of drop during formation
n = exponent representing the order of decrease of dimension z during drop break-away period
r = radius of spherical portion of the drop during formation
r_N = inside radius of nozzle
t = time
v = velocity of leading edge of drop during formation
v_N = velocity of dispersed phase flowing through the nozzle
w = radius of jet at its narrowest point during break-away period
x = height of jet during break-away period
y = radius of base of spherical-segment portion of drop during its formation
z = height of truncated-cone portion of drop during its formation

Greek Letters

α = dimensionless parameter l_0/r_N
β = dimensionless parameter y_0/r_N
γ = dimensionless parameter z_0/r_N
ρ = density
$\Delta\rho$ = absolute value of density difference between two phases
σ = interfacial tension

Subscripts

C = continuous phase
D = dispersed phase
f = conditions at final instant of drop separation
N = nozzle
0 = conditions at instant drop separation begins
s = static conditions

LITERATURE CITED

1. Batson, J. B., M.S. thesis, Univ. Tenn., Knoxville (1951).
2. Harkins, W. D., and F. E. Brown, *J. Am. Chem. Soc.*, **38**, 246 (1916).
3. *Ibid.*, **41**, 499 (1919).
4. Hayworth, C. B., and R. E. Treybal, *Ind. Eng. Chem.*, **42**, 1174 (1950).
5. Null, H. R., Ph.D. dissertation, Univ. Tenn., Knoxville (1955).
6. Null, H. R., M.S. thesis, Univ. Tenn., Knoxville (1951).

Manuscript received Sept. 5, 1956; revised Oct. 7, 1957; accepted Oct. 7, 1957.

Pulsations in Sieve-tray and Bubble-cap Distillation Towers

R. A. McALLISTER and C. A. PLANK

North Carolina State College, Raleigh, North Carolina

A periodic pulsation of the frothing mass of liquid and vapor on a sieve tray and a bubble-cap tray is reported. An equation is proposed which relates the frequency of the oscillation to the velocity of sound, the physical dimensions of the systems, and the flow rates of the gas and liquid. The equation is a modification of the acoustical analogy to the classical Helmholtz resonance in electrical circuits having both capacitance and inductance. The oscillation is shown to decrease back-mixing on the tray, and thus to result in an increase in the Murphree vapor efficiency.

Under certain velocities of flow of liquid and vapor in a bubble-cap and sieve tray, it was noticed that the froth and liquid mass on the tray would oscillate in a direction perpendicular to the flow of the liquid; that is, if the net liquid flow was from right to left, the oscillation would be established from front to back. The particular bubble-cap and sieve trays in question are shown diagrammatically in Figures 1 and 2. The vapor velocity at which the pulsations began was well defined, and further increase in it only increased the amplitude of the wave. The frequency of the oscillations was regular and reproducible and was noted to be a function of the vapor and liquid flow rates. The pulsation was found to occur in every binary-system run in the bubble-cap distillation tower, including several organic-organic and water-organic binary systems as well as steam-water. In the sieve tray only air-water was run, but the oscillation would be expected to occur for any vapor-liquid combination.

The oscillation was shown by Plank (*6*) to increase the number of well-mixed pools (*3*) existing on the tray. A well-mixed plate (unit well-mixed pools) implies back-mixing from the liquid-outlet to the liquid-inlet sides of the tray. Since the oscillations are perpendicular to such a path, the pulsations tend to decrease back-mixing and thus result in a closer approach to an unmixed plate. Such conditions increase the over-all plate efficiency.

For the bubble-cap tray, Figure 3 shows the number of well-mixed pools for several binary distillation systems under both pulsating and nonpulsating operating conditions. The number of well-mixed pools n was calculated from the expression from reference (*3*) relating the Murphree vapor efficiency E_{mv} to the point efficiency E_{OG} under conditions of partial mixing.

$$E_{mv} = B\left[\left(1 + \frac{E_{OG}}{nB}\right)^n - 1\right] \qquad (1)$$

The bubble-cap tray was constructed in such a manner that liquid samples could be obtained from any point along the length of liquid travel. Point efficiencies

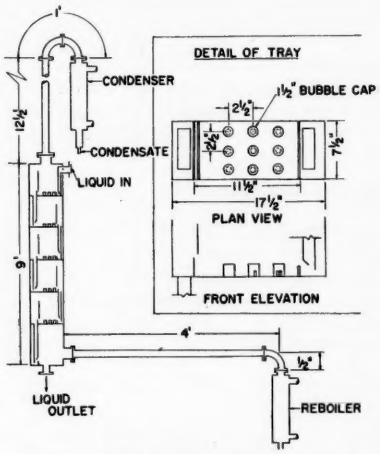

Fig. 1. Bubble-cap distillation tower.

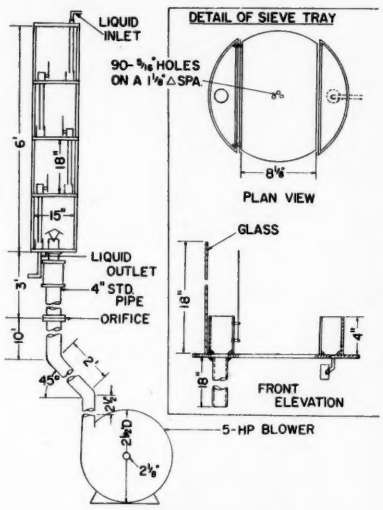

Fig. 2. Sieve-tray tower.

were calculated from the equation

$$E_{OG} = \frac{(y_n - y_{n-1})}{\left[\int_0^b y_{nb}^* \frac{db}{b} - y_{n-1}\right]} \qquad (2)$$

with liquid samples obtained by traverse along the tray floor in the direction of liquid travel. Such an efficiency has been successfully used by Anderson (*1*), Plank (*6*), and Winslow (*8*). Vapor efficiencies were measured and calculated in the normal way.

The abscissa of Figure 3, $t_L\sqrt{F_V}$, has been used by Plank (*6*) and Winslow (*8*) to correlate liquid mixing on the particular bubble-cap tray used in this investigation. The term t_L is called the *liquid contact time* and is calculated as

$$t_L = \frac{Z_c A}{L'} \qquad (3)$$

For the data of Figure 3, pulsation occurred in conjunction with the high F_V factor ($F_V = 1.3$) and is represented by the upper line. At the lower F_V factors pulsations did not occur, and these data are shown by the lower dashed line. Assumption of 1.1 well-mixed pools, when in fact $n = 1.6$ well-mixed pools, may result in errors greater than 100% in estimating Murphree vapor efficiencies from point efficiency by the methods described in (*3*).

Operation of a tower in the pulsating region, however, presents certain hydraulic problems. The sloshing of the liquid from front to back can become so violent that liquid from one tray can be thrown up into the tray above long before normal flooding is to be expected. Figure 4 shows successive frames of a motion picture taken of the bubble-cap tower and sieve tray when they are being operated in the pulsating range. The fact that liquid can be thrown up under the tray above is shown more clearly in the pictures of the bubble-cap-tray operation. The average froth height for these conditions is only about one half, or less, of the tray spacing.

Since the behavior was distinctly periodic, it was suspected that an acoustic phenomenon could account for the periodicity. Heath and Elliott (*4*) were able to predict by a simple equation the pulsation frequency in several duct systems used in their study. These had a centrifugal compressor which caused air to flow in the ducts. In a sense, a bubble-cap or sieve-tray distillation tower may be considered to be a duct system. The distillation towers are complicated by the existence of both the liquid and the gas phase, but still they are dynamic, fluid systems. The formula used to predict the frequency of pulsation in the duct systems (*4*) is

$$f = \frac{c}{2\pi}\sqrt{\frac{S'}{lV}} \qquad (4)$$

Richardson (*7*) developed Equation (4) by considering the acoustical analogy of a classical Helmholtz resonator. In an electrical circuit having impedance and capacitance but no resistance, the resonant frequency is described by the following familiar equation:

R. A. McAllister is with Lamar State College of Technology, Beaumont, Texas, and C. A. Plank with the University of Louisville, Louisville, Kentucky.

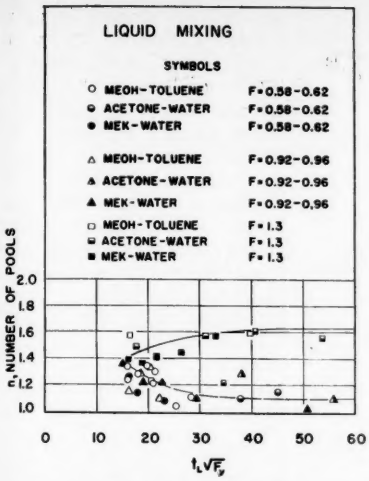

Fig. 3. Liquid mixing on bubble-cap tray.

$$2\pi f = \frac{1}{\sqrt{L_i C}} \qquad (5)$$

Equation (5) relates the resonant frequency in a classical Helmholtz resonator to the inductance and the capacitance. For an acoustical system the inertance is analogous to the inductance in an electrical circuit. Richardson (7) shows that the inertance can be represented as

$$\text{inertance} = \frac{\rho_V l}{S'} \qquad (6)$$

Likewise the capacitance is expressed by

$$\frac{1}{C} = \frac{\partial p}{\partial V} = \frac{c^2 \rho_V}{V} \qquad (7)$$

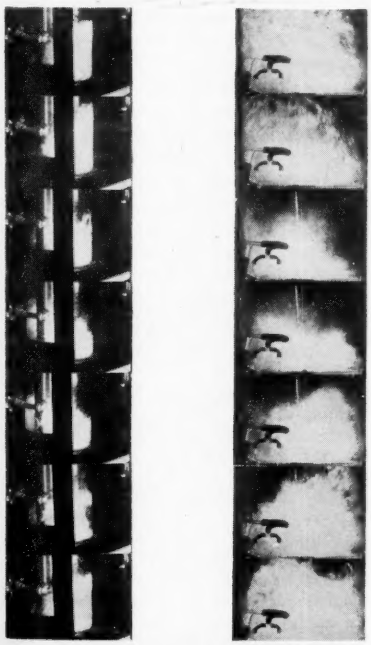

Sieve tray Bubble-cap tray

Fig. 4. Liquid pulsations on a bubble-cap and on a sieve tray.

Equation (4) is a combination of Equations (5), (6), and (7) and expresses the resonant frequency acoustically when all the inertance (inductance) is concentrated in a small duct and the capacitance is in the entire body of the vessel.

Equation (4) could not be expected to describe the pulsation frequency in a distillation tower because no account has been taken of the coupling action of the liquid and gas flow rates. In distillation towers the vapor while bubbling through the liquid transmits part of the kinetic energy to the liquid. For a simple harmonic oscillator, the frequency of vibration is directly proportional to the velocity of motion; therefore, the kinetic energy would be proportional to the square of the frequency. Conversely, the frequency would be proportional to the square root of the kinetic energy. Since a coupling action or transferring of kinetic energy exists between the liquid and gas phases, correction for this action might logically be made by use of a ratio of the kinetic energies of the two phases. Accordingly, if this action be looked upon as a capacitance or ratio of inertial forces, Equation (4) may be rewritten as

$$f = k \frac{c}{2\pi} \sqrt{\frac{S}{lV\left[\frac{(mu^2)_V}{(mu^2)_L}\right]}} \qquad (8)$$

or, written on a unit volume basis, as

$$f = k \frac{c}{2\pi} \frac{F_L}{F_V} \sqrt{\frac{S}{lV}} \qquad (9)$$

The term k in Equations (8) and (9) may be looked upon as a proportionality constant, the numerical value of which was found to be 2.5 ± 0.2.

EQUIPMENT AND PROCEDURE

The bubble-cap tower used for the frequency studies, shown diagrammatically in Figure 1, had five rectangular trays and nine 1½-in. bubble caps placed on a square spacing. The sieve-tray unit, shown in Figure 2, had three trays and was connected to a 5-hp. centrifugal blower. The tray perforations consisted of $\frac{5}{16}$-in.-diameter holes on 1⅛-in. triangular centers. The pertinent dimensions of the two towers are given in Table 1.

Table 1. Dimensions of Towers

	Bubble-gap tower	Sieve-tray tower
V	12.5 cu ft.	9.56 cu. ft.
l	27.0 ft.	37.5 ft.
S	0.124 sq. ft.	0.0477 sq. ft.
A	0.615 sq. ft.	0.815 sq. ft.
S/lV	0.000368, 1/sq. ft.	0.0001325, 1/sq. ft.

For the bubble-cap tower, steam-water and acetone-water (95 mole % acetone) were separately run in the pulsating region at several flow rates. The frequency, measured visually through the glass window, was observed to decrease with increasing gas and liquid velocities (or F factors). The column was run at total reflux, and hence the liquid and vapor flow rates were not independent of each other.

The sieve-tray tower was operated only on the air-water system. Here the liquid flow rate was maintained constant, and the air velocity was varied.

RESULTS AND DISCUSSION

Table 2 gives the results of the frequency measurements on the bubble-cap and sieve-tray towers. All the factors in Equation (9) were known or were measured, and the value of k was determined.

Calculation of the F factor for the liquid is based on a clear-liquid–height measurement. One leg of a manometer was mounted flush in the floor of the tray; the other leg was open to the vapor space above the tray. The manometer itself was filled with the liquid on the tray, and its reading was thus in terms of clear liquid (free from vapor bubbles). The manometer reading reduced the head of the total liquid and bubbling mass to an equivalent height if only clear liquid were traveling across the tray. The resulting value for F_L is very sensitive to the clear-liquid–height measurement. Furthermore, when the frothing mass on the tray is in oscillatory motion,

Table 2. Pulsation-frequency Tests

	u, ft./sec. (active area)	L, gal./min.	T, °C.	Z_c, ft. of liquid	F_V	F_L	c, ft./sec.	f, measured cycles/sec.	k
Bubble-cap tower									
Steam-water	5.24	0.87	104	0.20	0.99	0.12	1,585	1.66	2.7
	6.26	1.04	104	0.20	1.19	0.15	1,585	1.51	2.5
	7.30	1.21	104	0.21	1.39	0.16	1,585	1.42	2.5
	8.73	1.45	104	0.22	1.66	0.19	1,585	1.39	2.5
Acetone-water (95% acetone)	2.78	1.52	60	0.22	0.87	0.18	934	1.44	2.4
	3.30	1.81	60	0.23	1.03	0.21	934	1.37	2.3
	4.50	2.46	60	0.24	1.41	0.27	934	1.34	2.4
Sieve-tray tower									
Air-water	6.28	1.30	25	0.06	1.78	0.37	1,118	1.11	2.6
	6.45	1.30	25	0.06	1.82	0.37	1,118	1.09	2.7
	7.21	1.30	25	0.06	2.04	0.37	1,118	0.99	2.6

the manometer reading gives a damped average value for Z_e. The value for Z_e reported in Table 2 is a rather crude time-averaged clear-liquid height. The variation of k shown in Table 2 probably results from inaccuracy in the measurement of Z_e.

The agreement of the data with Equation (9), as shown by the constancy of k in Table 2, is striking in view of the range of variables studied, especially since two totally different pieces of apparatus were involved.

As yet it has not been possible to predict under what conditions the oscillations would be initiated; however, several qualitative observations can be made. The first is that the oscillations have not been observed at low mass-vapor rates [G = 700 lb./(hr.)(sq. ft.)] in either the sieve tray or the bubble-cap tray. Oscillations occurred at lower mass-vapor rates in conjunction with the bubble-cap tray than with the sieve tray, possibly because of the particular trays used. In a study of perforated-plate performance, McAllister, McGinnis, and Plank (*5*) found that the oscillation point was coincidental with the *weep* point for plate thickness of $\frac{1}{16}$ in. and greater. For thin plates, 0.029 in. thick, the oscillation point was at a gas velocity much higher than the weep point. The weep point here refers to the point where all the holes in the perforated plate become operative (*2*), and it is usually considered to be the beginning of the normal operating range of the sieve tray. The oscillation point refers to the minimum gas velocity at which the oscillation is sustained for a given liquid-flow rate. McAllister, et al. (*5*), also found that the mass-flow rate of the vapor at the oscillation point decreased as the clear-liquid height on the tray increased. Presumably, the tray dimensions, the relative vapor and liquid velocities (or F factors), and possibly some of the physical properties of the fluids would be among the variables expected to determine when the pulsations would begin.

Another observation that may be pertinent is that in both the columns studied the liquid flow on successive plates was reversed. For this type of system the oscillation was found to be one-half cycle out of phase on succeeding trays. If the flow pattern were such that the liquid flow was all in the same direction across the plate on successive plates, no prediction is offered as to how oscillations would occur. The pulsations, however, are to be expected. No prediction is offered for split-flow plates or other channel-flow plate designs.

Preliminary tests, with a small unit with perforated stages, have indicated that oscillating behavior also occurs in fluidized beds where solid and gas phases are in contact. The mechanism of correlation must be slightly different, however, since there is no actual flow of the solid phase. Further work along this line is forthcoming.

CONCLUSIONS

In plate towers oscillation of the frothing mass may occur with characteristic frequencies. The oscillation of the liquid on the tray is perpendicular to the direction of the flow of the liquid. The frequency of the pulsation is a function of the vapor and liquid F factors, the velocity of sound in the vapor, and the dimensions of the systems. The study reported here includes data on a bubble-cap tower operating as a distillation tower and on a sieve-tray contacting unit in which air is pumped through the system with a blower. The oscillating behavior of the system is thought to apply in any type of plate tower where the vapor is forced to bubble through the liquid. The oscillation on bubble-cap trays and sieve trays of the type studied here is a resonance which is fundamentally acoustic in nature.

ACKNOWLEDGMENT

The bubble-cap distillation tower described herein was employed for experiments carried out in connection with the American Institute of Chemical Engineer Research Project No. 1, "Tray Efficiencies in Distillation Columns." The sieve-tray tower was constructed in connection with a previous study supported by the Research Corporation. The support from both these sources is gratefully acknowledged.

R. W. Bondurant, Jr., and D. V. Knight, at one of the authors' suggestion, presented a preliminary paper on the subject of the pulsations in the sieve-tray and bubble-cap–tray towers during the Southern Regional Conference of Student Chapters of the A.I.Ch.E. at the University of Tennessee, Knoxville, on March 21 to 23, 1957.

Helpful suggestions, especially in the matter of coupling effects of the vapor and liquid kinetic energies, were made by Dr. F. W. Lancaster, Department of Physics, North Carolina State College, Raleigh.

NOTATION

A = active tray area, sq. ft.
B = ratio of the slope of the operating line to the slope of the equilibrium line
b = length of the liquid travel
C = capacitance
c = velocity of sound in the fluid, ft./sec.
f = frequency of pulsation, cycles/sec.

$$F_V = \sqrt{(\rho u^2)_V} = \sqrt{\left(\frac{mu^2}{v}\right)_V} = \sqrt{\left(\frac{K.E.}{v}\right)_V}$$

$$F_L = \sqrt{(\rho u^2)_L} = \sqrt{\left(\frac{K.E.}{v}\right)_L}$$

k = an empirical constant equal to 2.5 ± 0.2 (Table 2)
K.E. = kinetic energy, ft.-poundals
l = length of system, (*a*) sieve column: length of tower plus length of pipe plus twice the circumference of the blower; (*b*) bubble-cap column: length of reboiler to liquid level plus length of piping (containing vapor) plus tower length plus length of condenser
L = liquid rate, gal./min.
L' = liquid rate, cu. ft./sec.
L_i = inductance
m = mass, lb.
n = number of well-mixed pools (*3*)
p = pressure
ρ = density, lb. mass/cu. ft.
S = bubble-cap slot area, or hole area (sieve tray) per plate, sq. ft.
S' = cross-sectional area of small duct, sq. ft.
t_L = time of liquid contact, sec. [defined by Equation (3)]
u_L = average liquid velocity, ft./sec. $= L'/Z_eW$
u_V = superficial linear vapor velocity based on active tray area, ft./sec. $= w/\rho_V A$
v = volume of fluid, cu. ft.
V = total volume of distillation towers plus volume of vapor piping including condenser and reboiler, cu. ft.
W = width of tray perpendicular to liquid travel
w = weight rate of vapor flow, lb./sec.
y = vapor composition—mole fraction
y_{nb}^* = vapor composition in equilibrium with liquid samples taken at certain locations on the tray
Z_e = equivalent clear-liquid height of fluid on the active tray, ft.

Subscripts

L = liquid
V = vapor
n = plate number

LITERATURE CITED

1. Anderson, J. E., Sc.D. thesis, Mass. Inst. Technol., Cambridge (1954).
2. Arnold, D. S., C. A. Plank, and E. M. Schoenborn, *Chem. Eng. Progr.*, **48**, 633 (1952).
3. Gautreaux, M. F., and H. E. O'Connell, *ibid.*, **51**, 232 (1955).
4. Heath, W. R., and W. R. Elliot, *J. Appl. Mech.*, **13**, A-291 (1946).
5. McAllister, R. A., P. H. McGinnis, Jr., and C. A. Plank, *Chem. Eng. Sci.* **9**, 25 (1958).
6. Plank, C. A., Ph.D. thesis, N. Carolina State Coll., Raleigh (1957).
7. Richardson, E. G., "Technical Aspects of Sound," vol. 1, p. 13, Elsevier Publishing Company, New York (1953).
8. Winslow, C. E., Ph.D. thesis, N. Carolina State Coll., Raleigh (1955).

Manuscript received July 31, 1957; revised Dec. 30, 1957; accepted Jan. 6, 1958.

Combined Laminar Free- and Forced-convection Heat Transfer in External Flows

ANDREAS ACRIVOS

University of California, Berkeley, California

A method is presented for calculating the shear stress and the rate of heat transfer in external flows for combined laminar forced and free convection. The parameter Gr/Re^2 is of fundamental importance in such problems. Numerical results are reported for the heating and cooling of upward flow past a vertical flat plate for three Prandtl numbers. It is found that the transition from forced to free convection is gradual, especially at high Prandtl numbers. The influence of free convection on the separation point is also examined.

It is well known that forced and free convection play a predominant role in determining the rate of heat transfer from a surface to a fluid moving past it. To date, however, the theoretical and experimental studies on this subject have been restricted, with few exceptions, to cases where either, but not both, of the two mechanisms is taken into account. These investigations have been very successful, especially in regions where the flow is laminar, and have resulted in experimentally verified theoretical predictions for the rate of heat transfer in forced or in free convection.

In general, however, heat is transferred by both mechanisms acting simultaneously. It is therefore of some interest and importance to be able to predict how the rate of heat transfer is affected by the combined action of both forced and free convection and to know under what conditions it is permissible to neglect one mode of transfer for the other.

A few studies have been made in this direction. Experimental rates of heat transfer for air in turbulent forced and free convection in tubes have been reported by Eckert and Diaguila (*1*). Van der Hegge Zijnen (*12*) has proposed an empirical correlation, substantiated by his own experimental data, for predicting the rate of heat transfer from cylinders to air under conditions of combined natural and forced convection. Ostrach (*7*), Hallman (*3*), and Hanratty (*4*) have investigated the velocity and temperature distribution in vertical pipes and channels with low Reynolds numbers, where free-convection effects must be included.

This paper will present a theoretical treatment of combined laminar free- and forced-convection heat transfer in external flows. The general discussion will deal first with laminar-boundary-layer flows past an arbitrary two-dimensional surface; then the simple but representative flat-plate problem will be studied in detail.

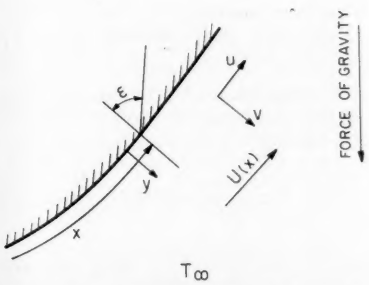

Fig. 1. The position directions of the coordinates x and y, the velocities u and v, and the angle ϵ.

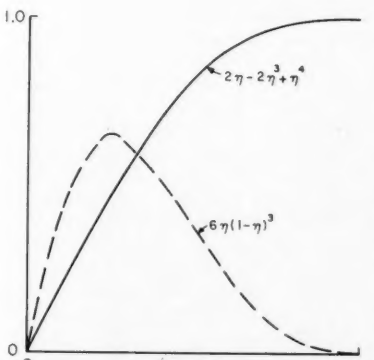

Fig. 2. The shapes of the two velocity profiles.

BASIC EQUATIONS AND THEIR INSPECTIONAL ANALYSIS

The laminar motion of a fluid at a temperature T_∞ past the arbitrary surface shown in Figure 1 will be considered. The surface temperature has the constant value T_w. It is well known that the basic equations which describe the behavior of this system, Navier-Stokes and energy, can be considerably simplified in many important cases by the use of Prandtl's boundary-layer theory. The resulting *boundary-layer equations* are generally used for such problems and can be found in the standard references (*2, 9, 10*). It is much more convenient, however, to start with the dimensionless form of the boundary-layer equations,

$$\left.\begin{aligned} u_1\frac{\partial u_1}{\partial x_1} + v_1\frac{\partial u_1}{\partial y_1} &= \pm\frac{Gr}{Re^2}\,\theta\sin\epsilon \\ &\quad + U\frac{dU}{dx_1} + \frac{\partial^2 u_1}{\partial y_1^2} \\ \frac{\partial u_1}{\partial x_1} + \frac{\partial v_1}{\partial y_1} &= 0 \\ u_1\frac{\partial\theta}{\partial x_1} + v_1\frac{\partial\theta}{\partial y_1} &= \frac{1}{Pr}\frac{\partial^2\theta}{\partial y_1^2} \end{aligned}\right\} \quad (1)$$

with

$$\left.\begin{aligned} u_1 &= \frac{u}{U_\infty}, \quad v_1 = \frac{v}{U_\infty}\sqrt{Re}, \\ x_1 &= \frac{x}{L}, \quad y_1 = \frac{y}{L}\sqrt{Re} \\ \theta &= \frac{T - T_\infty}{T_w - T_\infty}, \\ \beta_1 &= g\beta\,|T_w - T_\infty| \end{aligned}\right\} \quad (2)$$

$Re = U_\infty L/\nu$ (the Reynolds number)

$Gr = \beta_1 L^3/\nu^2$ (the Grashof number)

$Pr = c_p\mu/k$ (the Prandtl number)

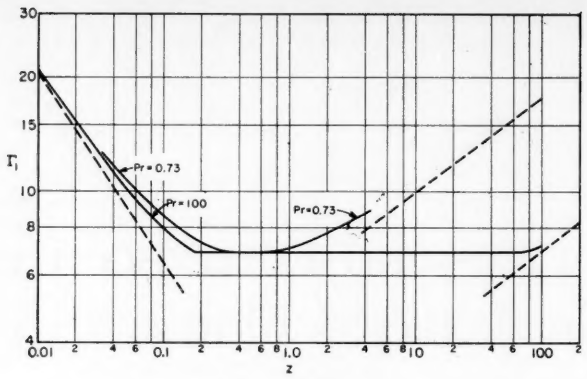

Fig. 3. Γ_1 heating vs. z.

β is the expansion coefficient of the fluid and is defined by

$$\frac{\rho_\infty}{\rho} = 1 + \beta(T - T_\infty) \qquad (3)$$

The boundary conditions are at

$$\left.\begin{array}{lll} x_1 = 0 & u_1 = U(0) & \theta = 0 \\ y_1 = 0 & u_1 = v_1 = 0 & \theta = 1 \\ y_1 = \infty & u_1 = U(x_1) & \theta = 0 \end{array}\right\} \qquad (4)$$

Although Equations (1) do not seem to have been given in this dimensionless form in the usual texts on the subject, they can readily be obtained from the boundary-layer equations by applying the transformations shown above. The buoyancy term $(Gr/Re^2)\theta \sin \epsilon$ is positive for the heating problem ($T_w > T_\infty$) and negative when $T_w < T_\infty$. It should be noted that terms usually of minor importance in low-speed flows—viscous dissipation and compression work—have been omitted from Equations (1), and that all the fluid properties except the density ρ are assumed constant.

For a given surface geometry the only parameters in the system of Equations (1) and (4) are the two dimensionless groups, Pr and Gr/Re^2. Therefore the expression for Nu becomes

$$Nu \equiv -L\left(\frac{\partial\theta}{\partial y}\right)_{y=0} = -\left(\frac{\partial\theta}{\partial y}\right)_{y_1=0} \cdot\sqrt{Re} = \sqrt{Re}\ \overset{(0)}{f_1}\left(Pr, x_1, \frac{Gr}{Re^2}\right)$$

where $\overset{(0)}{f_1}$ is a function of the indicated three variables only. However, in general one is interested in the mean Nusselt number for the surface, which is obtained from the foregoing expression by integrating with respect to x_1 from zero to a specified upper limit, which of course must not be past the separation point of the boundary layer, so that

$$Nu_m = \sqrt{Re}\, f_1\left(Pr, \frac{Gr}{Re^2}\right) \qquad (5)$$

Similarly one can show that $\overline{\tau_0}$ is given by

$$\frac{\overline{\tau_0}}{\rho U_\infty^{\,2}}\sqrt{Re} = f_2\left(Pr, \frac{Gr}{Re^2}\right) \qquad (6)$$

Naturally the functions f_1 and f_2, the form of which is determined by the surface geometry and the type of problem considered (heating or cooling), can be obtained only by solving Equations (1) and (4), but the two relations above should prove useful in correlating and interpreting experimental data. It is also clear that, aside from the Prandtl number Pr, the parameter (Gr/Re^2) is of fundamental importance in the study of combined natural and forced-convection heat transfer. Finally it can easily be shown that, as expected, Equations (5) and (6) reduce to the corresponding equations for forced- or free-convection heat transfer respectively as the parameter (Gr/Re^2) approaches zero or infinity. What has still to be determined for each surface geometry and type of problem (heating or cooling) is

1. The form of the functions f_1 and f_2 in Equations (5) and (6) respectively and in particular the variation between their limiting forms for $(Gr/Re^2) \to 0$ and $(Gr/Re^2) \to \infty$ respectively.

2. The way in which the separation point, if it exists, is affected by the parameters Gr/Re^2 and Pr.

These two questions will be discussed in some detail in the next section for the special geometry of a vertical flat plate. The method to be presented for solving the problem is however general and can be used for more complicated geometrical surfaces.

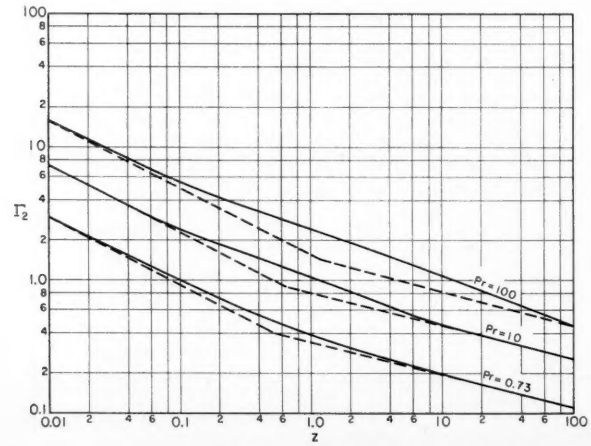

Fig. 5. Γ_2 heating vs. z.

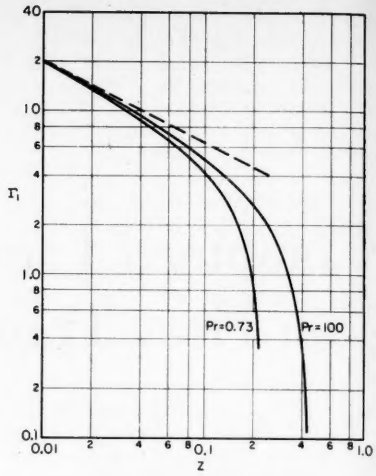

Fig. 4. Γ_1 cooling vs. z.

COMBINED LAMINAR FREE- AND FORCED-CONVECTION HEAT TRANSFER FROM A VERTICAL FLAT PLATE

For the flow past a vertical flat plate, $U = 1$ and $\sin \epsilon = 1$, and so Equations (1) become

$$u_1\frac{\partial u_1}{\partial z} + v_2\frac{\partial u_1}{\partial y_2} = \pm\theta + \frac{\partial^2 u_1}{\partial y_2^{\,2}} \qquad (7a)$$

$$\frac{\partial u_1}{\partial z} + \frac{\partial v_2}{\partial y_2} = 0 \qquad (7b)$$

$$u_1\frac{\partial\theta}{\partial z} + v_2\frac{\partial\theta}{\partial y_2} = \frac{1}{Pr}\frac{\partial^2\theta}{\partial y_2^{\,2}} \qquad (7c)$$

where

$$z = x_1 \frac{Gr}{Re^2},$$

$$y_2 = y_1 \sqrt{\frac{Gr}{Re^2}}, \qquad (8)$$

and

$$v_2 = v_1 \sqrt{\frac{Re^2}{Gr}}$$

Furthermore the boundary conditions are

At

$$z = 0 \quad u_1 = 1, \quad \theta = 0$$

$$y_2 = 0 \quad u_1 = v_2 = 0, \quad \theta = 1 \qquad (9)$$

$$y_2 = \infty \quad u_1 = 1, \quad \theta = 0$$

Also since the flat plate has no characteristic length, it is simpler to set $L = x$ and to base both the Grashof and the Reynolds numbers on x, the distance from the leading edge of the plate. Thus

$$Gr = \frac{\beta_1 x^3}{\nu^2} \cdot Re = \frac{U_\infty x}{\nu}, \text{ and } z = \frac{Gr}{Re^2}$$

The system of Equations (7), (8), and (9), which contains the Prandtl number Pr as a single parameter, can be solved exactly by a numerical procedure only and with considerable difficulty. Therefore the approximate Pohlhausen–von Karman momentum integral method (*2, 10*) will be used. It is recognized that this method has a serious disadvantage common to most "approximate" treatments; it is not possible to estimate the accuracy and reliability of the answers derived from it. However, for all the simple problems having exact solutions of the boundary-layer equations, the integral method usually gives very satisfactory results, except for extreme cases. The two momentum integrals are

$$\frac{d}{dz}\int_0^\infty u(u-1)\,dy_2 = \pm\int_0^\infty \theta\,dy_2 - \left(\frac{\partial u}{\partial y_2}\right)_{y_2=0} \qquad (10)$$

and

$$\frac{d}{dz}\int_0^\infty u\theta\,dy_2 = -\frac{1}{Pr}\left(\frac{d\theta}{dy_2}\right)_{y_2=0} \qquad (11)$$

The next step consists of assuming likely velocity and temperature profiles, each containing one parameter which is a function of z. These profiles are usually chosen to be polynomials which satisfy the boundary conditions, Equation (9), and certain compatibility relations. The profiles selected for this problem are

$$u_1 = (2\eta - 2\eta^3 + \eta^4) \pm \frac{\delta^2\eta}{6}(1-\eta)^3 \text{ for } \eta \le 1 \qquad (12)$$

$$u_1 = 1 \text{ for } \eta \ge 1 \text{ where } \eta = \frac{y_2}{\delta}$$

and

$$\theta = 1 - \frac{3}{2}\eta_T + \frac{\eta_T^3}{2} \quad \text{for} \quad \eta_T = \le 1$$

$$\theta = 0 \text{ for } \eta_T \ge 1 \quad \text{where } \eta_T = \frac{y_2}{\delta_T} \qquad (13)$$

δ and δ_T are both functions of z and must satisfy Equations (10) and (11) when the assumed profiles for u_1 and θ are substituted in them. It can readily be verified that these profiles satisfy Equation (9) and the following compatibility conditions:

$$\frac{\partial u_1}{\partial y_2} = \frac{\partial^2 u}{\partial y_2^2} = 0 \text{ at } y_2 = \delta \qquad (14a)$$

$$\frac{\partial \theta}{\partial y_2} = 0 \text{ at } y_2 = \delta_T \qquad (14b)$$

$$\frac{\partial^2 u}{\partial y_2^2} \pm 1 = 0 \text{ at } y_2 = 0 \qquad (14c)$$

[Equation (7*a*) is satisfied at the surface.]

$$\frac{\partial^2 \theta}{\partial y_2^2} = 0 \text{ at } y_2 = 0 \qquad (14d)$$

[Equation (7*c*) is satisfied at the surface.]

The actual selection of the profiles and the compatibility relations which they must satisfy is, to some extent, arbitrary. The ones above were chosen because they are relatively simple and also, as will be shown in the next section, because they lead to accurate predictions for the rate of heat transfer in forced or in natural convection, where a comparison with the results of exact calculations is possible. The temperature profile given by Equation (13) is quite standard and has been chosen before for other problems, and the velocity profile in Equation (23) can be broken up into two parts. The expression $(2\eta - 2\eta^3 + \eta^4)$ has been used to represent the velocity profile in forced convection. On the other hand the term $(\delta^2\eta/6)(1-\eta)^3$ could be taken as a velocity profile in natural-convection heat transfer, although it appears that a somewhat different form has usually been selected (*9, 11*). Therefore the velocity profile in Equation (12) is the sum of two terms, the velocity profile for forced convection and that for natural-convection heat transfer. This is shown schematically in Figure 2.

If Equations (12) and (13) are then substituted into Equations (10) and (11) one obtains the following two ordinary differential equations for the variables δ and Δ:

$$\frac{d\delta^2}{dz} = \frac{4 \mp \frac{\delta^2}{3}\left(\frac{9\Delta}{4} - 1\right)}{0.11746 \mp 3.1750 \times 10^{-3}\,\delta^2 - 5.51145 \times 10^{-4}\,\delta^4} \qquad (15)$$

and

$$\frac{d\Delta}{dz} = \frac{\frac{3}{Pr\Delta} - \left[H_1(\Delta) \pm \frac{\delta^2}{2}H_2(\Delta)\right]\frac{d\delta^2}{dz}}{2\delta^2\frac{dH_1(\Delta)}{d\Delta} \pm \frac{\delta^4}{3}\frac{dH_2(\Delta)}{d\Delta}} \qquad (16)$$

where Δ, $H_1(\Delta)$, and $H_2(\Delta)$ are defined below.

$$\Delta = \frac{\delta_T}{\delta}$$

$$H_1(\Delta) = \left(\frac{\Delta^2}{5} - \frac{3\Delta^4}{70} + \frac{\Delta^5}{80}\right) \text{ for } \Delta \le 1 \qquad (17)$$

$$H_2(\Delta) = \left(\frac{\Delta^2}{10} - \frac{\Delta^3}{8} + \frac{9\Delta^4}{140} - \frac{\Delta^5}{80}\right) \text{ for } \Delta \le 1$$

The initial conditions at $z = 0$ are

$$\delta = 0 \text{ and } \Delta H_1(\Delta) = \frac{0.088095}{Pr} \qquad (18)$$

since $d\Delta/dz$ must remain finite. Its value at $z = 0$ can be obtained from Equation (16) by a limiting process, so that

$$\left(\frac{d\Delta}{dz}\right)_{z=0} = \mp\frac{5.67569H_2(\Delta) + 1.2528H_1(\Delta) - 2.1284\Delta H_1(\Delta)}{\frac{dH_1}{d\Delta} + \frac{0.0293649}{Pr\,\Delta^2}} \qquad (18a)$$

If $\Delta > 1$, then $H_1(\Delta)$ and $H_2(\Delta)$ have different forms. However, it turns out that for Pr greater than about 0.6, which includes essentially most cases of interest except liquid metals, Δ remains less than 1 for all values of z. This is one of the reasons why Equations (12) and (13) were finally selected to represent the velocity and the temperature profiles respectively.

δ and Δ only intermediates in the determination of τ_0 and Nu. It is found that

$$\frac{6\tau_0}{\rho U_\infty^2}\sqrt{Re}\cdot\sqrt{\frac{Re^2}{Gr}} = \frac{12 \pm \delta^2}{\delta} = \Gamma_1 \qquad (19)$$

and

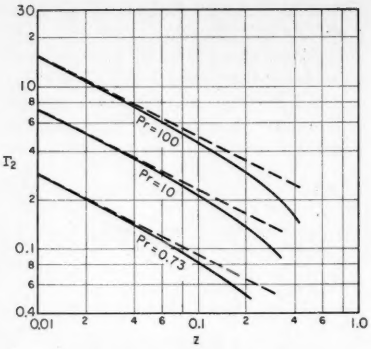

Fig. 6. Γ_2 cooling vs. z.

$$\frac{Nu}{\sqrt{Re}}\cdot\sqrt{\frac{Re^2}{Gr}} = \frac{1.5}{\delta\Delta} = \Gamma_2 \qquad (20)$$

from which τ_0 and Nu can be calculated once Equations (15) and (16) have been solved. It is interesting to note that for the heating problem τ_0 remains always positive, whereas for the cooling problem $\tau_0 = 0$ at $\delta^2 = 12$, which implies the existence of a separation point. This is expected from the equations of motion and the known result that, in laminar flow and in the absence of free convection, a separation point can exist when the term $U(dU/dx_1)$ in Equation (1) is negative (*10*). One can generalize therefore that (*a*) in the heating of upward flow over an arbitrary surface free convection will move the separation point away from the forward stagnation point, since the buoyancy term in Equations (1) is positive and (*b*), for the opposite reason, in the cooling of upward flow free convection will move the separation point toward the forward stagnation point. Thus it is easy to see that as $(Gr/Re^2) \rightarrow \infty$ Equations (5) and (6) reduce to the corresponding relations for natural-convection heat transfer for the heating problem only, for as $Gr/Re^2 \rightarrow \infty$ the separation point moves closer and closer to the forward stagnation point, and so, in general, the boundary-layer equations remain valid only over a smaller and smaller part of the surface.

HEATING PROBLEM FOR UPWARD FLOW OVER A VERTICAL FLAT PLATE

It is often advisable to compare, wherever possible, the results obtained by approximate methods with those derived from an exact solution of the mathematical equations. This is possible in the present problem for the two asymptotic regions only,

$z \rightarrow 0$ (natural convection is negligible,

and,

$z \rightarrow \infty$ (forced convection is negligible)

The comparison is shown below.

Case a: Asymptotic solution as $z \rightarrow 0$.

Since $\delta \rightarrow 0$ as $z \rightarrow 0$, it follows from Equations (15) and (16) that

$$\frac{d\delta^2}{dz} = 34.054$$

and

$$\Delta H_1(\Delta) = \frac{0.088095}{Pr} \qquad (21)$$

Therefore from Equation (19)

$$\frac{\tau_0}{\rho U_\infty^2}\sqrt{Re} = 0.343$$

which compares very favorably with the value 0.332 obtained from an exact solution of the Blasius equation (*10*). On the other hand, the expression for the Nusselt number depends on Pr. It is found that for

$$Pr = 0.73, \quad \frac{Nu}{\sqrt{Re}} = 0.291,$$

compared with the exact expression

$$\frac{Nu}{\sqrt{Re}} = 0.297$$

for

$$Pr \rightarrow \infty, \quad \frac{Nu}{\sqrt{Re}} = 0.338\,Pr^{\frac{1}{3}},$$

compared with the exact result

$$\frac{Nu}{\sqrt{Re}} = 0.339\,Pr^{\frac{1}{3}} \qquad (5)$$

Case b. Asymptotic solution as $z \rightarrow \infty$.

Since $\delta \rightarrow \infty$ as $z \rightarrow \infty$, Equations (15) and (16) have the asymptotic forms

$$\frac{d\delta^2}{dz} = \frac{604.8}{\delta^2}\left(\frac{9\Delta}{4} - 1\right)$$

and

$$Pr = \frac{6}{604.8H_2(\Delta)\left(\frac{9\Delta}{4} - 1\right)} \qquad (22)$$

respectively, which can also be derived by considering the free convection problem alone. One can easily show then that

$$\text{for } Pr = 0.73, \quad \frac{Nu}{(Gr)^{\frac{1}{4}}} = 0.342$$

and

$$\text{for } Pr \rightarrow \infty, \quad \frac{Nu}{(Gr)^{\frac{1}{4}}} = 0.480\,Pr^{\frac{1}{4}} \qquad (23)$$

These results are again in good agreement with those obtained by Schuh (*10*) and Ostrach (*8*) from the exact numerical solution of the boundary-layer equations for natural convection. Thus

$$\text{for } Pr = 0.73, \quad \frac{Nu}{(Gr)^{\frac{1}{4}}} = 0.358$$

and

$$\text{for } Pr \rightarrow \infty, \quad \frac{Nu}{(Gr)^{\frac{1}{4}}} = 0.503\,Pr^{\frac{1}{4}} \qquad (23a)$$

These comparisons between the momentum integral method and the exact solutions for the two cases $z \rightarrow 0$ and $z \rightarrow \infty$ are more than satisfactory. It is therefore not unreasonable to believe that Equations (19) and (20) will be sufficiently reliable for all values of z.

Equations (15) and (16) have been solved numerically for three values of the Prandtl number: $Pr = 0.73$, 10, and 100. The variables of primary interest Γ_1 and Γ_2 are shown plotted in Figures 3 and 5, together with their two asymptotes at $z = 0$ and $z = \infty$. These graphs show that the change from pure forced to pure free convection is gradual and that the mechanisms are nonadditive. It is seen also that the rule of McAdams (*6*) according to which, "If it is doubtful

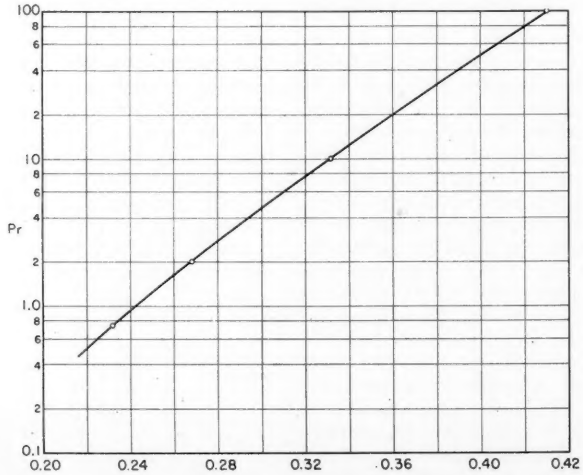

Fig. 7. z separation vs. Prandtl number.

whether forced or free convection flow applies, the heat transfer coefficient should be calculated using both the forced and the free convective relation and the larger one should be used," does not hold very well, especially for large Prandtl numbers.

The transition region, for which the two effects alone would be of the same order of magnitude, is most clearly seen in the plots of Γ_1 vs. z. It is interesting to note that according to Equations (15) and (16) Γ_1 is a minimum at $\delta^2 = 12$ and remains constant over a finite portion of the z axis, because the denominator in Equation (15) is zero at $\delta^2 = 12$ while the numerator is not. This unexpected result is due solely to the inherent inaccuracy of the momentum-integral method. It can be shown that, no matter which "reasonable" velocity profile is substituted in Equation (10), Γ_1 will have a minimum, approximately equal to 7.0, which will extend over a finite part of the z axis. It is believed, naturally, that if a more elaborate method for solving the boundary-layer equations is devised, one can obtain a smooth curve for Γ_1 vs. z, but it is improbable that the added accuracy thus arrived at would be significant. Therefore, in integrating Equations (15) and (16), one has to separate the z axis into three regions: (1) In the first region δ^2 increases from zero to 12, and Δ decreases from its initial value. (2) In the second region δ^2 remains constant at 12, but Δ increases, according to Equation (16), until it becomes equal to 8/9. (3) Finally Equations (15) and (16) are integrated for the third region, with initial conditions $\delta^2 = 12$ and $\Delta = 8/9$.

It is also clear from Figures 3 to 6 that it is very difficult to draw any specific conclusions which would allow one to predict, *a priori*, for what values of the parameter Gr/Re^2 forced or free convection alone would predominate. It is true that the influence of free convection is negligible for $z < 0.02$ for all Prandtl numbers; however, the value of z above which, for practical purposes, forced convection does not influence the shear stress or the rate of heat transfer depends on the Prandtl number. Thus for $Pr = 0.73$ this value of z is approximately 2; for $Pr = 100$ it is approximately 30. These inequalities are of course for the flat plate only. It is expected that somewhat different results would probably be reached for other surface geometries.

THE COOLING PROBLEM FOR UPWARD FLOW OVER A VERTICAL FLAT PLATE

The integration of Equations (15) and (16) is straightforward for the cooling problem, since they do not become singular for $0 < \delta^2 < 12$. When $\delta^2 = 12$, Γ_1 becomes equal to zero, which indicates the presence there of a separation point. Γ_1 and Γ_2 are plotted in Figures 4 and 6, and the separation point is shown as a function of the Prandtl number Pr in Figure 7. (This latter curve is based on four Prandtl numbers.) For most Prandtl numbers of interest the value of z at which separation occurs lies approximately between 0.2 and 0.5, but since it is known that the momentum-integral method cannot generally predict the separation point very accurately, the curve in Figure 7 should be considered only as an approximate one.

CONCLUSION

A method was presented for calculating the shear stress and the rate of heat transfer in external flows for combined laminar free and forced convection. The parameter Gr/Re^2 is of fundamental importance in such problems. Natural convection is negligible as $Gr/Re^2 \to 0$, and forced convection has little influence as $Gr/Re^2 \to \infty$. Numerical results were reported for the heating and cooling of upward flow past a vertical flat plate for three Prandtl numbers. It was found that the mechanisms of forced and free convection are nonadditive. The influence of free convection on the separation point was also examined, and it was shown that heating of upward flow stabilizes the boundary layer, whereas cooling hastens the appearance of the separation point.

The numerical results for the heating problem from a flat plate indicate, moreover, that the transition from a pure forced to pure free convection is gradual, especially at high Prandtl numbers. It is very difficult therefore to draw any specific conclusions concerning the values of the parameter Gr/Re^2 for which one of the above two mechanisms alone would predominate. It is observed that for the flat plate and for $z < 0.02$, free convection is negligible, whereas for $z > 100$ forced convection has little influence. It is expected however that somewhat different results would probably be reached for other surface geometries.

Sufficient experimental data do not exist to make a comparison with these theoretical deductions.

ACKNOWLEDGMENT

The Radiation Laboratory, University of California, provided the computing facilities for the numerical solution of Equations (15) and (16). John H. Duffin and Eugene J. Fenech assisted with the programming of the computer.

NOTATION

x = coordinate measured along surface from forward stagnation point

y = coordinate normal to surface

u, v = velocity components in x and y directions respectively

ρ = density

ρ_∞ = density outside boundary layer

g = acceleration due to gravity

ν = kinematic viscosity

$\epsilon(x_1)$ = angle between normal to surface and direction of force of gravity (See Figure 1.)

T = temperature

T_w = temperature at surface

T_∞ = temperature of the fluid outside the boundary layer

k, c_p = thermal conductivity and specific heat respectively

$U(x)$ = the velocity outside the boundary layer

β = coefficient of thermal expansion

U_∞ = characteristic velocity

L = characteristic length

$U(x_1)$ = dimensionless potential flow distribution

$u_1, v_1, x_1, y_1, \theta, \beta_1, Re, Gr, Pr$ = defined by Equation (2)

$|T_w - T_\infty|$ = absolute value of the temperature difference $T_w - T_\infty$

Nu = Nusselt number $= -L(\partial\theta/\partial y)_{y=0}$

Nu_m = average Nusselt number

$\tau_0, \overline{\tau_0}$ = shear stress and average shear stress respectively

z = $Gr/Re^2 = \beta_1 x/U_\infty^2$ (For the flat plate one can set $L = x$ and therefore $Gr = \beta_1 x^3/\nu^2$ and $Re = U_\infty x/\nu$.)

$\Delta, H_1(\Delta), H_2(\Delta)$ are defined by Equation (17)

Γ_1, Γ_2 are defined by Equations (19) and (20) respectively

LITERATURE CITED

1. Eckert, E. R. G., and A. J. Diaguila, *Trans. Am. Soc. Mech. Engrs.*, **76**, 497 (1954).
2. Goldstein, Sidney, "Modern Developments in Fluid Dynamics," **II**, Chapter XIV, Oxford 1938.
3. Hallman, T. M., *Trans. Am. Soc. Mech. Engrs.*, **78**, 1831 (1956).
4. Hanratty, T. J., E. M. Rosen, and R. L. Kabel, paper presented at the Christmas Symposium of the Am. Chem. Soc., Purdue Univ. (December, 1956).
5. Lighthill, M. J., *Proc. Roy. Soc. (London)*, **A202**, 359 (1950).
6. McAdams, W. H., "Heat Transmission," 2 ed., McGraw-Hill 1942, p. 207.
7. Ostrach, Simon, *Natl. Advisory Comm. Aeronaut., Tech. Note* 3141, 1954.
8. *Ibid.*, 2635, 1952.
9. Merk, J. H., and J. A. Prins, *Appl. Sci. Research*, **A4**, 11, 195, 207 (1954).
10. Schlichting, H., "Boundary Layer Theory," Chap. 14, McGraw-Hill Book Company, Inc., New York (1955).
11. Squire, H. B., in Sidney Goldstein, "Modern Developments in Fluid Dynamics," vol. 2, p. 641, Oxford Inversity Press, New York (1938).
12. Van der Hegge Zijnen, B. G., *Appl. Sci. Research*, **A6**, 129 (1956).

Manuscript received Sept. 5, 1957; revision received Dec. 20, 1957; paper accepted Dec. 28, 1957. Paper presented at the A.I.Ch.E. Montreal meeting, April, 1958.

Some Properties of the Poisson Distribution

A. S. SAID

College of Physicians and Surgeons, Columbia University, New York, New York

This paper lists various properties of the Poisson distribution and related functions which can be derived from elementary principles without reference to theories of probability or statistics. They are intended for use by persons who may have to deal with Poisson distributed variables but not from a satistical point of view. Limit values and sums of the Poisson distribution, the sums of related functions, and different relations between its sums and integrals are given.

Differential and difference equations which lead to solutions in the form of a Poisson distribution are discussed. The general elution equation is derived by setting up the differential-difference equation for plate n in a chromatographic column and showing that the Poisson distribution is a solution to this equation. The complete solution is then obtained by applying the boundary conditions of the process.

The function $e^{-u}(u^n/n!)$ where n is a positive integer and u is a positive quantity is called the *Poisson distribution*, and the function $\sum_{r=n}^{\infty} e^{-u}(u^r/r!)$ is called the *Poisson summation distribution*. In a previous paper by this author (*1*) it was shown that if a chromatographic column is regarded as equivalent to a finite number of equilibrium stages or theoretical plates, the distribution of a zone on these plates during its elution would be in the form of a Poisson or a Poisson summation distribution depending upon whether the initial zone occupied one or more than one plate.

Owing to its applications in chromatography and because it has many interesting properties and promises to be of help in solving other problems in chemical engineering unit operations, the Poisson distribution was further investigated, and in this paper some of its properties are summarized. It is also applied to the solution of the differential-difference equation which represents the solute-concentration distribution on a chromatographic column during elution. Such equations of the combined type may become useful in solving other chemical engineering problems, and this author feels that development of the mathematics needed for the solution of these equations may prove valuable to the chemical engineer.

If the function e^u is expanded in a Machlaurin series one gets

$$e^u = 1 + u + \frac{u^2}{2!} + \frac{u^3}{3!} + \frac{u^4}{4!} + \cdots$$

multiplying both sides by e^{-u}

$$\therefore\ 1 = e^{-u} + e^{-u}u + e^{-u}\frac{u^2}{2!} + e^{-u}\frac{u^3}{3!} + \cdots$$

$$= \phi_0{}^u + \phi_1{}^u + \phi_2{}^u + \cdots = \sum_{r=0}^{\infty} \phi_0{}^u = P_0{}^u$$

SOME LIMIT VALUES OF $\phi_n{}^u$ AND $P_n{}^u$

$$\phi_n{}^0 = 0 \text{ for } n > 0 \tag{1}$$

$$\lim_{u\to 0} \phi_0{}^u = 1 \tag{2}$$

$$\phi_0{}^u = e^{-u} \tag{3}$$

$$\phi_n{}^\infty = 0 \tag{4}$$

$$\phi_\infty{}^u = 0 \tag{5}$$

$$P_0{}^u = 1 \tag{6}$$

$$P_n{}^0 = 0 \text{ for } n > 0 \tag{7}$$

$$\lim_{u\to 0} P_0{}^u = 1 \tag{8}$$

$$P_n{}^\infty = 1 \tag{9}$$

$$P_\infty{}^u = 0 \tag{10}$$

$$\lim_{n\to\infty} n^{(m)}\phi_n{}^u = 0 \tag{11}$$

$$\lim_{u\to\infty} u^m\phi_n{}^u = 0 \tag{12}$$

$$\lim_{n\to\infty} n^{(m)}P_n{}^u = 0 \tag{13}$$

where

$$n^{(m)} = \frac{n!}{(n-m)!} = n(n-1)(n-2)\cdots(n-m+1)$$

Some of these relations can be proved directly, but others require the application of theories of limits. In Appendix 1* seven of these relations are deduced by means of theories of limits; the other six are simple and can be deduced directly by elementary principles.

FURTHER PROPERTIES OF THE POISSON DISTRIBUTION

The following properties can be proved by expanding and rearranging; detailed derivations are given in Appendix 2*

$$\sum_{n=1}^{\infty} P_n{}^u = u \tag{14}$$

$$\sum_{r=1}^{n} P_r{}^u = u(1 - P_n{}^u) + nP_{n+1}{}^u \tag{15}$$

$$\frac{d}{du}P_n{}^u = \phi_{n-1}{}^u \tag{16}$$

or

$$\int \phi_n{}^u\,du = P_{n+1}{}^u + C \tag{16a}$$

$$\sum_{r=0}^{n} \phi_r{}^{u_1}\phi_{n-r}{}^{u_2} = \phi_n{}^{u_1+u_2} \tag{17}$$

$$\sum_{r=1}^{n} P_r{}^{u_1}\phi_{n-r}{}^{u_2} = P_n{}^{u_1+u_2} - P_n{}^{u_2} \tag{18}$$

$$\sum_{r=1}^{n-1} P_r{}^{u_1}P_{n-r}{}^{u_2} = (n-1)(1 + P_n{}^{u_1} + P_n{}^{u_2} - P_n{}^{u_1+u_2}) - u_1P_{n-1}{}^{u_1} - u_2P_{n-1}{}^{u_2} + (u_1+u_2)P_{n-1}{}^{u_1+u_2} \tag{19}$$

when $u_1 = u_2 = u$ one gets

$$\sum_{r=0}^{n} \phi_r{}^u\phi_{n-r}{}^u = \phi_n{}^{2u} \tag{17a}$$

$$\sum_{r=1}^{n} P_r{}^u\phi_{n-r}{}^u = P_n{}^{2u} - P_n{}^u \tag{18a}$$

$$\sum_{r=1}^{n-1} P_r{}^uP_{n-r}{}^u = (n-1)(1 + 2P_n{}^u - P_n{}^{2u}) - 2u(1 - P_{n-1}{}^{2u}) \tag{19a}$$

RELATION BETWEEN THE INTEGRAL AND SUMMATION OF THE POISSON FUNCTION

Symbols and Definitions

For simplicity, the following symbols will be used:

1. $\int^{[1]} P_n{}^u \equiv \int_0^u P_n{}^u\,du$

*The appendices have been deposited as document 5717 with the American Documentation Institute, Photoduplication Service, Library of Congress, Washington 25, D. C., and may be obtained for $2.50 for photoprints or $1.75 for 35-mm. microfilm.

*See footnote in column 2.

and

$$\int^{[2]} P_n^u \equiv \int_0^u \left(\int^{[1]} P_n^u \right) du$$

and generally

$$\int^{[m]} P_n^u \equiv \int_0^u \left(\int^{[m-1]} P_n^u \right) du$$

$$\equiv \int_0^u \cdots \int_0^u P_n^u (du)^m$$

2. $$\sum^{[1]} P_n^u \equiv \sum_{r=n+1}^{\infty} P_r^u$$

and

$$\sum^{[2]} P_n^u \equiv \sum_{r=n+1}^{\infty} \left(\sum^{[1]} P_r^u \right)$$

and generally

$$\sum^{[m]} P_n^u \equiv \sum_{r=n+1}^{\infty} \left(\sum^{[m-1]} P_r^u \right)$$

$$\equiv \sum_{r_m=n+1}^{\infty} \cdots \sum_{r_2=r_3+1}^{\infty} \sum_{r_1=r_2+1}^{\infty} P_{r_1}^u$$

By means of integration and summation by parts, the following relations between the integral and sum of the Poisson function have been deduced. Details of the derivations are given in Appendix 3*.

a. $$\int_0^u P_n^u \, du = \sum_{r=n+1}^{\infty} P_r^u$$

$$= uP_n^u - nP_{n+1}^u \qquad (20)$$

or according to this notation

$$\int^{[1]} P_n^u = \sum^{[1]} P_n^u$$

$$= uP_n^u - nP_{n+1}^u \qquad (20)$$

and for $n = 0$

$$\int^{[1]} P_0^u = \sum^{[1]} P_0^u = u \qquad (20a)$$

b. $$\int_0^u uP_n^u \, du = \sum_{r=n+1}^{\infty} rP_{r+1}^u$$

$$= \frac{u^2}{2} P_n^u - \frac{n(n+1)}{2} P_{n+2}^u \qquad (21)$$

and for $n = 0$

$$\int_0^u uP_0^u \, du = \sum_{r=1}^{\infty} rP_{r+1}^u = \frac{u^2}{2} \qquad (21a)$$

c. $$\int_0^u u^m P_n^u \, du$$

$$= \sum_{r=n+1}^{\infty} (r+m-1)^{(m)} P_{r+m}^u$$

$$= \frac{u^{m+1}}{m+1} P_m^u - \frac{(n+m)^{(m+1)}}{m+1} P_{n+m+1}^u \qquad (22)$$

and for $n = 0$

$$\int_0^u u^m P_0^u \, du = \sum_{r=1}^{\infty} (r+m-1)^{(m)} \cdot P_{r+m}^u = \frac{u^{m+1}}{m+1} \qquad (22a)$$

d. $$\int^{[m]} P_n^u = \sum^{[m]} P_n^u = \frac{1}{m!} \cdot \sum_{r=0}^{m} (-1)^r C_r^m u^{m-r} (n+r-1)^{(r)} P_{n+r}^u \qquad (23)$$

and for $n = 0$

$$\int^{[m]} P_0^u = \sum^{[m]} P_0^u = \frac{u^m}{m!} \qquad (23a)$$

One also deduces the following:

1. when $m = 0$,

$$\int^{[0]} P_n^u = \sum^{[0]} P_n^u = P_n^u \qquad (24)$$

2. $$\frac{d}{du} \int^{[m]} P_n^u = \int^{[m-1]} P_n^u \qquad (25)$$

DIFFERENTIAL AND DIFFERENCE EQUATIONS LEADING TO SOLUTION IN THE FORM OF A POISSON DISTRIBUTION

The functions ϕ_n^u and P_n^u are functions of both u and n. They are continuous functions with respect to u and step functions with respect to n. In other words they are defined for any positive value of u whether integer or not, but they are defined only for values of n which are integer and positive.

If the symbol y is used to denote such a function, then $\partial y/\partial u$ represents the differential of y with respect to u, and n is kept constant; $\Delta_{(n)} y$ or simply Δy represents the first forward difference of the function y with respect to n with u held constant, and $\nabla_{(n)} y$ or ∇y represents the first backward difference of y

$$\Delta y = y_{n+1} - y_n$$

$$\nabla y = y_n - y_{n-1}$$

Also $\Delta_{(n)}{}^r y$ or $\Delta^r y$ represents the rth forward difference of the function y, and $\nabla_{(n)}{}^r y$ or $\nabla^r y$ represents the rth backward difference.

The subscript (n) is omitted when y is a function of n only, or, as in the case of the Poisson function, it is a step function of n only and a continuous function of the other variables. It is evident that the difference is always taken with respect to n

$$\Delta^r y = y_{n+r} - ry_{n+r-1} + \frac{r(r-1)}{2!} y_{n+r-2} - \cdots + (-1)^r y_n$$

$$= \sum_{S=0}^{r} (-1)^S C_S{}^{r-S+1} y_{n+r-S} \qquad (26)$$

and

$$\nabla^r y = y_n - ry_{n-1} + \frac{r(r-1)}{2!} y_{n-2} - \cdots + (-1)^r y_{n-r}$$

$$= \sum_{S=0}^{r} (-1)^S C_S{}^{r-S+1} y_{n-S} \qquad (26a)$$

Differentiating both the Poisson and the Poisson summation functions with respect to u, one gets

$$\frac{\partial}{\partial u} \phi_n^u = \phi_{n-1}^u - \phi_n^u = -\nabla \phi_n^u \qquad (27)$$

and

$$\frac{\partial}{\partial u} P_n^u = \phi_{n-1}^u$$

$$= P_{n-1}^u - P_n^u = -\nabla P_n^u \qquad (27a)$$

Differentiating again with respest to u, one finds that

$$\frac{\partial^2}{\partial u^2} \phi_n^u = \phi_{n-2}^u - 2\phi_{n-1}^u + \phi_n^u = \nabla^2 \phi_n^u \qquad (28)$$

and

$$\frac{\partial^2}{\partial u^2} P_n^u = \phi_{n-2}^u - \phi_{n-1}^u = P_{n-2}^u - 2P_{n-1}^u + P_n^u = \nabla^2 P_n^u \qquad (28a)$$

Generally by differentiating r times one can show that

$$\frac{\partial^r}{\partial u^r} \phi_n^u = (-1)^r \nabla^r \phi_n^u \qquad (29)$$

and

$$\frac{\partial^r}{\partial u^r} P_n^u = (-1)^r \nabla^r P_n^u \qquad (29a)$$

When y is a function of u only, then

$$\frac{d\phi_n^u}{du} = \phi_{n-1}^u - \phi_n^u = \phi_n^u \left(\frac{n}{u} - 1 \right) \qquad (30)$$

Similarly

$$\frac{dP_n^u}{du} = \phi_{n-1}^u$$

$$\frac{d^2 P_n^u}{du^2} = \phi_{n-2}^u - \phi_{n-1}^u$$

$$= \phi_{n-1}^u \left(\frac{n-1}{u} - 1 \right)$$

$$\therefore \frac{d^2 P_n^u}{du^2} + \frac{dP_n^u}{du} \left(1 - \frac{n-1}{u} \right) = 0 \qquad (31)$$

As a function of n only

$$\Delta \phi_n^u = \phi_{n+1}^u - \phi_n^u = \phi_n^u \left(\frac{u}{n+1} - 1 \right) \qquad (32)$$

*See footnote on page 290.

and

$$\nabla\phi_n^u = \phi_n^u - \phi_{n-1}^u = \phi_n^u\left(1 - \frac{n}{u}\right) \tag{33}$$

Similarly

$$\Delta P_n^u = P_{n+1}^u - P_n^u = -\phi_n^u$$

$$\Delta^2 P_n^u = P_{n+2}^u - 2P_{n+1}^u + P_n^u$$

$$= \phi_n^u - \phi_{n+1}^u = \phi_n^u\left(1 - \frac{u}{n+1}\right)$$

$$\therefore\ \Delta^2 P_n^u + \Delta P_n^u\left(1 - \frac{u}{n+1}\right) = 0 \tag{34}$$

and

$$\nabla P_n^u = P_n^u - P_{n-1}^u = -\phi_{n-1}^u$$

$$\nabla^2 P_n^u = P_n^u - 2P_{n-1}^u + P_{n-2}^u$$

$$= -\phi_{n-1}^u + \phi_{n-2}^u = \phi_{n-1}^u\left(\frac{n-1}{n} - 1\right)$$

$$\therefore\ \nabla^2 P_n^u + \nabla P_n^u\left(\frac{n-1}{u} - 1\right) = 0 \tag{35}$$

From these relations one deduces that $-\phi_n^u$ is a particular solution for the following total-differential, total-difference, and partial-differential-difference equations

1. $$\frac{dy}{du} = y\left(\frac{n}{u} - 1\right) \tag{36}$$

2. $$\Delta y = y\left(\frac{u}{n+1} - 1\right) \tag{37}$$

3. $$\nabla y = y\left(1 - \frac{n}{u}\right) \tag{38}$$

4. $$\frac{\partial^r y}{\partial u^r} = (-1)^r \nabla^r y \tag{39}$$

In Equation (36) y is a continuous function of u only. In Equations (37) and (38) it is a step function of n only, and in Equation (39) it is a function of both u and n. One also deduces that $-P_n^u$ is a particular solution to the following equations:

1. $$\frac{d^2y}{du^2} + \frac{dy}{du}\left(1 - \frac{n-1}{u}\right) = 0 \tag{40}$$

2. $$\Delta^2 y + \Delta y\left(1 - \frac{u}{n+1}\right) = 0 \tag{41}$$

3. $$\nabla^2 y + \nabla y\left(\frac{n-1}{u} - 1\right) = 0 \tag{42}$$

4. $$\frac{\partial^r y}{\partial u^{-2}} = (-1)^r \nabla^r y \tag{39}^*$$

More relations can also be deduced by combining two or more of these relations.

*Since it is understood that differentiation is always concerned with the continuous variable u only, Equation (39) can also be written in the form of a total–differential-difference equation and can be called simply a *differential-difference equation.*

From (36) and (37) and similarly from (37) and (38), for example, one deduces that ϕ_n^u is also a solution to the following two equations:

$$\frac{\partial y}{\partial u} + \left[\frac{\frac{n}{u} - 1}{1 - \frac{u}{n+1}}\right]\Delta y = 0 \tag{43}$$

and

$$\Delta y + \frac{\left(\frac{u}{n+1} - 1\right)}{\frac{n}{u} - 1}\nabla y = 0 \tag{44}$$

AN ALTERNATIVE DERIVATION OF THE GENERAL ELUTION EQUATION

In a previous paper (*1*) the general elution equation was derived by first obtaining the expression for plate 1 and then going to plate 2 to derive its elution equation, and then to plate 3, and so on until the form of the solution became evident, when the general equation was deduced. An alternative derivation would be to set up the partial–differential-difference equation for plate n, write the general solution, and, using the boundary conditions of the problem, obtain the values of the constants.

If it is assumed that at the beginning of the elution process the concentrations on plates 1, 2, 3, . . . n, . . . N are

$$y_1^0, y_2^0, y_3^0 \cdots y_n^0, \cdots y_N^0,$$

a differential material balance around plate n gives

$$(ky_n - ky_{n-1})\,dw = \frac{-S}{N}\,dy_n$$

$$\therefore\qquad k\nabla y_n\,dw = -\frac{S}{N}\,dy_n$$

Substitution of $x = wN/S$, $u = kx$ gives

$$\frac{dy_n}{du} = -\nabla y_n \tag{45}$$

According to Equation (39) both ϕ_n^u and P_n^u are particular solutions of this equation. A more general solution is

$$y_n = \sum_{n-m\geq 0} A_m \phi_{n-m}^u \tag{46}$$

m is an integer positive or negative such that $n - m \geq 0$. In order to evaluate the constants m and A_m, one substitutes the following boundary conditions:

1. $y_r = y_r^0$ when $u = 0$. Substituting in Equation (46) and making use of the fact that ϕ_{r-m}^0 is equal to 1 when $m = r$, is equal to 0 for $m < r$, and is undefined for $m > r$, one finds that $m = r$, $A_m = y_r^0$, and Equation (46) becomes

$$y_n = \sum_{n-r\geq 0} y_r^0 \phi_{n-r}^u \tag{47}$$

2. The second boundary condition is deduced from the fact that the concentration of solute in the eluent entering the first plate is equal to zero, and hence y_1 as a function of u can be deduced by a differential material balance around plate 1 resulting in

$$y_1 = y_1^0 e^{-u}$$

Substituting this boundary condition in Equation (47), one deduces that the solution is true only for values of r greater than or equal to 1, and the complete solution becomes

$$y_n = \sum_{\substack{n-r\geq 0 \\ r\geq 1}} y_r^0 \phi_{n-r}^u$$

or

$$y_n = \sum_{r=1}^{n} y_r^0 \phi_{n-r}^u \tag{48}$$

which is the general elution equation. This method can similarly be used to derive the elution equation for the special cases treated in the previous paper (*1*) and for deriving the deposition equation.

NOTATION

k = adsorption or exchange coefficient when it is neither a function of x nor a function of y_n; $k = \bar{y}_n/y_n$
N = total number of plates in column
n = plate number from top of column The top plate number $n = 1$ and the bottom plate number $n = N$.
P_n^u = $\sum_{r=n}^{\infty} \phi_r^u$ = Poisson exponential summation
R_n = y_n/y_0 or $\bar{y}_n/\bar{y}_0$
R_n^0 = y_n^0/y_0
S = total weight of adsorbent in the column
u = kx during the elution process
w = weight of eluent or solvent that has passed through any plate in the column
x = wN/S
y_n = concentration of solute on plate n, g. solute/g. adsorbent, for the elution process
$\bar{y}_n$ = concentration of solute in eluent in equilibrium with plate n during elution
$\bar{y}_0$ = concentration of solute in solvent before entering plate 1
y_0 = concentration of solute on adsorbent if in equilibrium with solvent containing the solute at concentration $\bar{y}_0$
ϕ_n^u = $e^{-u}u^n/n!$ = Poisson exponential function
Δ = first forward finite difference
Δ^r = rth forward finite difference
∇ = first backward finite difference
∇^r = rth backward finite difference

LITERATURE CITED

Said, A. S., *A.I.Ch.E. Journal*, 2, 477 (1956).

Manuscript received Sept. 19, 1957; revision received Jan. 16, 1958; paper accepted Jan. 18, 1958.

Phase Relations of Binary Systems that Form Azeotropes: I. The Ammonia–*n*-Butane System

WEBSTER B. KAY and HERBERT A. FISCH

Ohio State University, Columbus, Ohio

Binary systems that form azeotropes in the critical region of the system show a wide variation in their phase behavior. As part of an investigation of the factors responsible for this variation, the *P-V-T-x* relations of the ammonia-*n*-butane system were determined at the liquid-vapor phase boundaries from near room temperature to the highest temperature and pressure at which the liquid and vapor coexist. Ammonia and *n*-butane form an azeotrope whose composition varies from 81.7 mole % ammonia at 300 lb./sq. in. to 86.3 mole % at 1295 lb./sq. in. The critical locus possesses a minimum temperature point similar to other binary systems that form azeotropes in the critical region. The experimental results support the hypothesis that binary systems that form azeotropes exhibit a characteristic pattern of *P-T-x* relations in the critical region that is distinctively different from systems that do not form azeotropes.

In a previous paper (*2*) attention was called to the progressive change in the *P-T* critical loci of binary systems composed of hydrogen sulfide and the paraffin hydrocarbons, methane, ethane, and propane. This change, which ranged from a curve with a maximum pressure point in the case of the methane-hydrogen sulfide system to one with a minimum temperature point in the case of the propane-hydrogen sulfide system, was associated with the fact that hydrogen sulfide forms an azeotrope with ethane and with propane but not with methane. It was predicted, in the case of binary systems of hydrogen sulfide-hexane and higher members of the paraffin hydrocarbon series, that the critical locus would again possess a point of maximum pressure. This has been confirmed in part by the work of Reamer, Selleck, Sage and Lacey (*6*) on the hydrogen sulfide-decane system.

It was suggested that the relations exhibited by the binaries of hydrogen sulfide and the paraffin hydrocarbon series form a characteristic pattern of relations for binary systems composed of a compound termed an azeotropic agent and members of a homologous series of compounds. Within a certain temperature range wherein azeotropes are formed, a characteristic of the agent and the homologous series, the *P-T* critical loci will progress through a series of changes from a curve with a maximum pressure point, to one with a minimum temperature point, back to one with a maximum pressure point as the critical temperature of the agent changes from less than, to greater than, the critical temperature of the compound with which it is paired. The carbon dioxide-paraffin hydrocarbon systems studied by Poettmann and Katz (*5*) were cited as exhibiting this behavior.

To obtain further data for a test of this generalization and to investigate the variation in the form that the critical locus may take, the *P-V-T-x* relations of the ammonia-*n*-butane system were determined from 32°F. and 200 lb./sq. in. to the highest temperature and pressure at which the liquid and vapor phases can coexist. In this region the two components are miscible in all proportions.

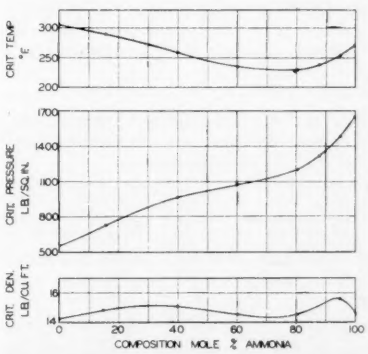

Fig. 1. Relations between composition and critical temperature, critical pressure and critical density; ammonia-*n*-butane system.

EXPERIMENTAL METHODS AND APPARATUS

The *P-V-T-x* relations of the ammonia-*n*-butane system at the liquid-vapor phase boundaries were obtained by the determination of the pressure-temperature border curves and temperature-density curves of a series of mixtures of known composition. The relations between any combination of the variables were derived by the construction of the appropriate cross plot of these curves.

The apparatus and experimental procedures for the preparation of mixtures of known composition and for the determination of the volume at different temperatures and pressures were the same as those employed in earlier investigations of a similar kind (*3*). The procedure was as follows:

A small air-free sample of the ammonia-*n*-butane mixture was confined over mercury in a thick-walled glass tube which was surrounded by a constant temperature bath. The tube was connected to a mercury-filled compressor with means for controlling the pressure on the sample. After the pressure had been properly adjusted and equilibrium attained by means of a magnetic stirrer, the volume of the sample was determined by measuring the length of the column of sample, this length having

H. A. Fisch is with U. S. Atomic Energy Commission, Schenectady, New York.

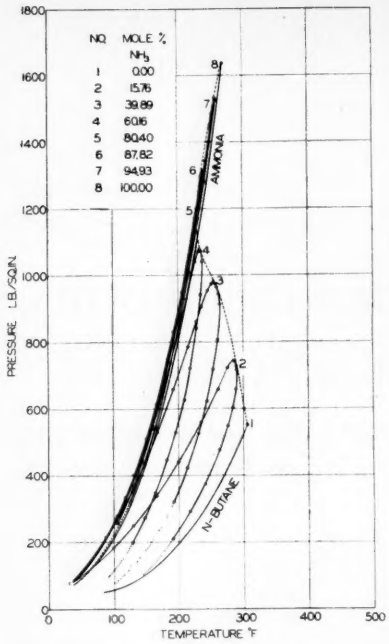

Fig. 2. The pressure-temperature-composition diagram; ammonia-*n*-butane system.

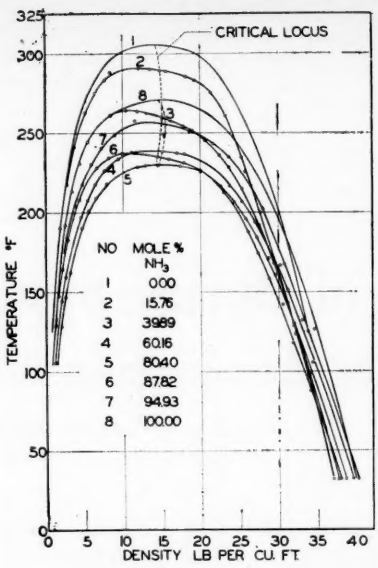

Fig. 3. The temperature-density-composition diagram; ammonia-*n*-butane system.

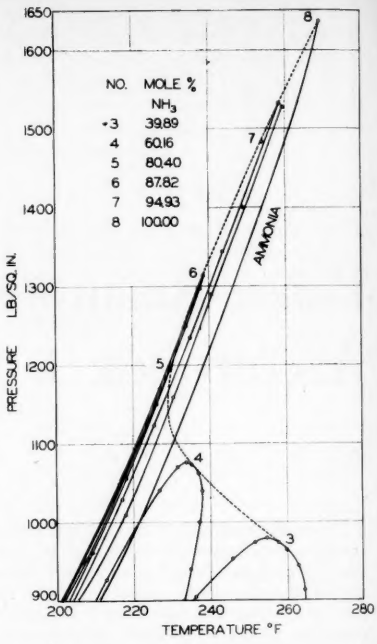

Fig. 4. Expanded *P-T-x* plot in the high-pressure region; ammonia-*n*-butane system.

been related to the volume by a prior calibration of the tube.

The temperature of the sample was measured to within 0.05°F. by means of a copper constantan thermocouple and a sensitive potentiometer. For the pressure, a dead weight gauge, similar to that previously described (*3*), was used. Its sensitivity was 0.02 lb./sq. in. The experimental tube in which the sample was confined was constructed of precision-bore capillary of approximately 2-mm. bore. It was carefully calibrated with mercury. By the use of a cathetometer, reading to 0.05-mm. and with a sample occupying a length never less than 15 mm. of the tube, the volume of the sample could be measured with a maximum error of about 0.6%. The methods employed in the calibration of the thermocouple, pressure gauge, and experimental tube have been described (*3*).

PREPARATION OF MATERIALS

The *n*-butane was furnished by Phillips Petroleum Company and was reported to be 99.78 ± .08 mole % *n*-butane. The ammonia was an anhydrous commercial sample, stated by the manufacturer to be better than 99 mole % ammonia.

Both the *n*-butane and ammonia were further purified by repeated distillation at low temperature and under high vacuum; the initial fraction and the residue were discarded, and the middle fraction was retained for the succeeding distillation. The deaerated *n*-butane and ammonia were then stored in the gaseous state by sealing them in glass ampoules (*3*).

Prior to their use, the *n*-butane and ammonia were tested for the presence of impurities by measuring, in the experimental apparatus, the difference between the bubble- and dew-point pressures at a constant temperature. The pressure change was 0.15 lb./sq. in. at 262.3°F. for *n*-butane and 1.4 lb./sq. in. for ammonia at 158.0°F.

Mixtures of ammonia and *n*-butane gas were prepared by first filling the experimental tube, under vacuum, with clean, freshly distilled mercury, then injecting into the tube a measured volume of each of the gases at a known temperature and pressure to make a mixture of the desired composition. The apparatus and procedure have been described (*3*). In the calculation of the amount of each gas, the deviation of the gas from the perfect gas law was taken into account. The composition arrived at in this way was accurate to within 0.05 mole %.

Table 1. Composition and Critical Constants of Mixtures of Ammonia and Normal Butane

Composition mole % ammonia	Composition wt. % ammonia	Critical temperature °F.	Critical pressure lb./sq. in. abs.	Critical density lb./cu. ft.
0.00	0.00	305.40	548.9	—
15.76	5.45	289.49	725.6	14.78
39.89	16.28	259.79	963.9	15.05
60.16	30.68	235.26	1072.4	14.48
80.40	54.58	229.84	1200.0	14.50
87.82	67.87	238.51	1313.7	15.15
94.93	84.59	253.94	1484.4	15.60
100.00	100.00	269.53	1637.1	—

RESULTS AND DISCUSSION

The pressure and specific volumes of the liquid and vapor at the bubble and dew points were determined for six different mixtures of ammonia and *n*-butane at temperatures ranging from near the ice point to the cricondentherm of each mixture. Experimental data on the pure components were limited to the purity checks previously described, except that the critical point of ammonia was determined. For butane, the vapor pressure and orthobaric density data reported by Kay (*1*) were used, for ammonia the vapor pressure and density data given in Landolt-Bornstein (*4*). The critical constants of the mixtures are listed in Table 1, and their relation to the composition is shown by the curves in Figure 1. Likewise, the pressure-temperature and density-temperature data for the mixtures and the pure components are shown graphically by the curves in Figures 2 and 3 respectively. For some of the mixtures the bubble- and dew-point curves in the low-pressure region were extrapolated by plotting the experimental data as the logarithm of the pressure against the reciprocal of the absolute temperature and extending the straight line through the points to the desired temperature and/or pressure. This region is indicated by the broken line curves in the diagrams.

Values of the temperature and density

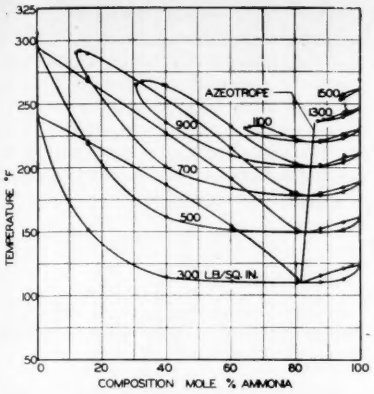

Fig. 5. Temperature-composition diagram; ammonia-*n*-butane system.

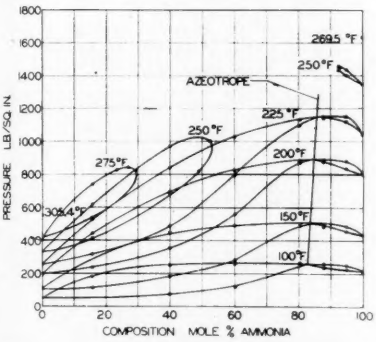

Fig. 6. Pressure-composition diagram; ammonia-*n*-butane system.

Table 2. Temperature-Composition Relations in *n*-Butane-Ammonia System at Constant Pressure

Ammonia mole %	Pressure 300 lb./sq. in. liquid °F.	vapor °F.	Pressure 500 lb./sq. in. liquid °F.	vapor °F.	Pressure 700 lb./sq. in. liquid °F.	vapor °F.	Pressure 900 lb./sq. in. liquid °F.	vapor °F.
0	241.0	241.0	295.0	295.0	—	—		
10	171	228.5	244.0	278.1	—	—		
12.2	—	—	—	—	289.5	289.5		
13.4	—	—	—	—	280.9	297.0		
20	140.9	214.9	202.6	261.0	255.7	285.0		
30	123.5	201.0	176.1	244.4	223.2	220.4		
30.7	—	—	—	—	—	—	264.5	264.5
33.6	—	—	—	—	—	—	250.5	268.0
40	114.2	186.5	161.2	227.1	200.6	253.6	235.9	264.2
50	111.6	171.4	154.7	209.7	190.0	235.7	220.8	250.5
60	110.5	154.5	151.5	191.5	183.8	215.7	210.2	232.5
70	110.0	135.4	150.0	171.4	180.3	194.4	204.3	214.7
80	109.8	113.8	149.5	152.0	178.3	180.5	201.5	203.4
81.7a	109.8	109.8	—	—	—	—		
83.1a	—	—	149.5	149.5	—	—		
84.1a	—	—	—	—	178	178		
84.8a	—	—	—	—	—	—	201.4	201.4
90	110.7	117.5	149.8	154.0	178.7	181.2	201.5	203.3
95	—	—	151.7	157.5	181.3	184.8	204.1	207.3
100	123.5	123.5	161.0	161.0	188.5	188.5	211	211

Ammonia mole %	Pressure 1100 lb./sq. in. liquid °F.	vapor °F.	Pressure 1300 lb./sq. in. liquid °F.	vapor °F.	Pressure 1500 lb./sq. in. liquid °F.	vapor °F.
64.4	230.7	230.7				
68	226.5	232.5				
70	225.0	232.0				
80	221.0	222.4				
85.6a	226.5	220.5				
87	—	—	236.6	236.6		
90	220.7	222.3	237.1	238.5		
94	—	—	—	—	254	254
95	223.0	220.3	239.7	242.7	—	—
96	—	—	—	—	256.0	258.7
98	—	—	—	—	258.7	260.2
100	230	230	246.5	246.5	261.2	261.2

at regular intervals of the pressure have been tabulated.*

The relations between pressure, temperature, and composition at the phase boundaries are represented by the *P-T-x* space diagram in Figure 2. Between approximately 80 mole % ammonia and pure ammonia the diagram is very narrow, and the liquid and vapor surfaces are curved and folded, a condition characteristic of a system whose components form a minimum boiling azeotrope. The nature of this portion of the diagram is more readily seen in Figure 4, which is an expanded view of the upper part of Figure 2.

The critical locus of the system possesses a point of minimum temperature. In this respect it differs from systems whose components are similar in chemical nature or whose critical temperatures are markedly different. For such systems the critical locus, in general, exhibits a point of maximum pressure.

The nonlinear relation between the density and composition is evident from an inspection of the temperature-density-composition space diagram (Figure 3). This is not surprising when one considers the difference in the chemical nature of the components.

The formation of an azeotrope with a minimum boiling temperature, which was indicated by the folding of the *P-T-x* space diagram, is clearly evident in the *T-x* and *P-x* diagrams shown respectively in Figures 5 and 6. The composition of the azeotrope is 81.7 mole % ammonia at 300 lb./sq. in., increasing to 86.3 mole % at 1295 lb./sq. in. The difference between the boiling point of the azeotrope and that of pure ammonia at 300 lb./sq. in. amounts to 13.5°F. and decreases to about 10°F. at 1295 lb./sq. in.

The effect of pressure on the vapor-liquid region is to be noted. Below 548.9 lb./sq. in. the *T-x* diagram extends from pure ammonia to pure *n*-butane; above this pressure the diagram terminates before the ordinate for pure *n*-butane is reached. For example, at 900 lb./sq. in. the *T-x* diagram terminates with a mixture of about 30.7 mole % ammonia, while at pressures above 1637 lb./sq. in. all mixtures are homogeneous regardless of the temperature. A summary of the *T-x* relations at equal intervals of the pressure is given in Table 2. These data were read from large scale plots of the curves in Figure 5.

The distribution of the components between the liquid and vapor phases at various pressures is shown by the curves in Figure 7 where the composition of the

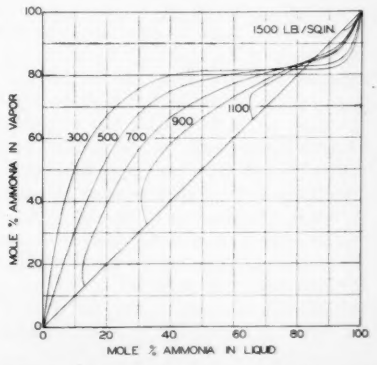

Fig. 7. Vapor-liquid composition diagram; ammonia-*n*-butane system.

*Tabular material has been deposited as document 5718 with the American Documentation Institute, Photoduplication Service, Library of Congress, Washington 25, D. C., and may be obtained for $1.25 for photoprints or $1.25 for 35-mm. microfilm.

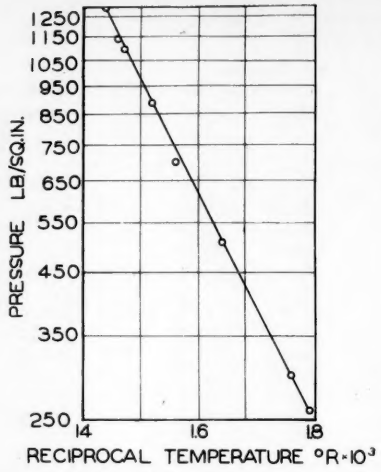

Fig. 8. Pressure-temperature relation for the ammonia-*n*-butane azeotrope.

vapor is plotted against the composition of the liquid. The existence of an azeotrope is indicated by the intersection of the curves with the diagonal where the compositions of the liquid and vapor phases are identical. With the aid of these curves, the composition of the azeotrope at different pressures (indicated in Table 2) was accurately determined.

Figure 8 shows a plot of the logarithm of the pressure vs. the reciprocal of the absolute temperature of the azeotropic point. From the linear form of the plotted curve it is evident that the relation between the pressure and temperature can be represented by the equation

$$\log p = A + B/T$$ as is the case for, a pure compound.

PHASE RELATIONS

The shape of the critical locus of the ammonia-*n*-butane system is in good agreement with the generalization deduced from a study of the critical loci of the carbon dioxide-hydrocarbon (*5*) and hydrogen sulfide-hydrocarbon systems. In accordance with this generalization, as the critical temperature of the component with the lower critical pressure increases relative to the critical temperature of the azeotropic agent, an inflection point develops in the critical locus near the critical point of the component with the lower critical pressure. As the difference in the critical temperatures becomes greater, the minimum critical temperature point disappears, and the inflection point gradually changes to a maximum critical-pressure point.

Since the critical temperature of *n*-butane is approximately 36°F. greater than the critical temperature of ammonia, it is to be expected that there will be an inflection point in the critical locus in the region of high butane content. The experimental results are in agreement with this prediction; as will be noted, a point of inflection occurs at about 50 mole % ammonia.

ACKNOWLEDGMENT

Grateful acknowledgment is made to Phillips Petroleum Company for furnishing the sample of *n*-butane.

LITERATURE CITED

1. Kay, W. B., *Ind. Eng. Chem.* **32**, 358 (1940).
2. Kay, W. B. and D. B. Brice, *Ind. Eng. Chem.* **45**, 615 (1953).
3. Kay, W. B. and G. M. Rambosek, *Ind. Eng. Chem.* **45**, 221 (1953).
4. Landolt-Börnstein, "Physikalisch-Chemische Tabellen," Berlin, Julius Springer.
5. Poettmann, F. H. and D. L. Katz, *Ind. Eng. Chem.* **37**, 847 (1945).
6. Reamer, H. H., F. T. Selleck, B. H. Sage, and W. N. Lacey, *Ind. Eng. Chem.* **45**, 1810 (1953).

Manuscript received July 22, 1957; revision received September 27, 1957, accepted October 24, 1957.

II. The Ammonia–Isooctane System

WEBSTER B. KAY and F. MORGAN WARZEL

Ohio State University, Columbus, Ohio

Because of the paucity of data on the phase behavior of binary systems that form azeotropes, the *P-V-T-x* relations of the ammonia-isooctane system were determined at the liquid-vapor boundaries from room temperature to the critical temperature of isooctane. Evidence of an azeotrope existing over a very limited pressure and temperature range was obtained. The system is unique in that the critical locus contains a minimum temperature point as well as a minimum and a maximum pressure point. These relations are shown to fit a general pattern of phase relations characteristic of binary systems that form azeotropes in the critical region. This pattern serves as an aid for the qualitative prediction of the *P-T-x* relations of such systems.

According to the hypothesis proposed for the phase relations of binary systems that form azeotropes (*7*), it would be expected that the greatest diversity in phase relations would occur in systems in which the difference in the volatility of the components is large, but still within the range necessary for the formation of an azeotrope. For some systems, it seems probable that as the critical temperature of the component with the lower critical pressure increases relative to the critical temperature of the other component, a stage might be reached wherein the critical locus would exhibit a minimum and a maximum pressure point as well as a minimum temperature point. Such a system, however, has not been observed heretofore.

For systems composed of ammonia and a paraffin hydrocarbon the above relations might be expected to exist in a system composed of ammonia and a heptane or an octane. To test the hypothesis, the *P-V-T-x* relations of the ammonia-isooctane system were determined at the liquid-vapor phase boundaries from 32°F. to the critical temperature of isooctane. Below 140.3°F. the ammonia and isooctane are only partially miscible. Data were obtained in this region from which the mutual solubilities of the liquids were determined.

F. Morgan Warzel is with Phillips Petroleum Company, Idaho Falls, Idaho.

EXPERIMENTAL

The apparatus and procedure were similar to those employed in the study of the ammonia-*n*-butane system (*6*). The dead-weight pressure gauge, thermocouple, and experimental tube were calibrated as previously described (*7*). Pressures and temperatures were measured to within ±0.1 lb./sq. in. and 0.05°C., whereas volume measurements varied in accuracy over a wide range, depending upon the length of the tube which a particular sample occupied. Expressed in terms of density, the uncertainty in the values was somewhere between 0.0015 g./cc. for the liquid and .00015 g./cc. for the vapor samples.

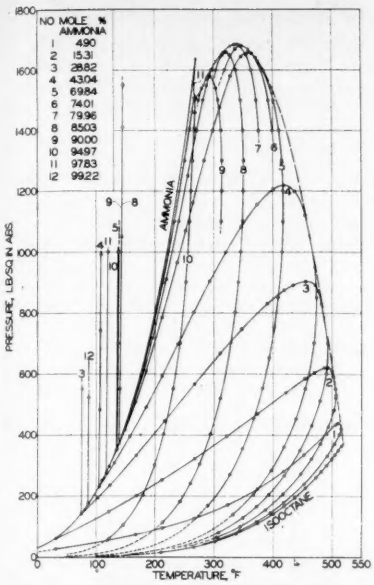

Fig. 1. Pressure-temperature diagram for ammonia-isooctane system.

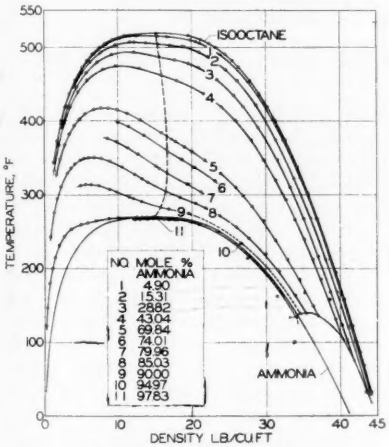

Fig. 2. Temperature-density diagram for ammonia-isooctane system.

PREPARATION OF MIXTURES

The ammonia was a sample of that purified and used in the study of the ammonia-*n*-butane system (*6*). The isooctane was from the same sample that was used for the determination of its vapor pressure and saturated liquid and vapor densities (*8*). It was furnished by Phillips Petroleum Company and was stated to be 99.87 ± 0.05 mole % isooctane. No further purification was undertaken except that possible traces of moisture were eliminated by distilling the sample in the presence of phosphorus pentoxide, into the degassing and loading train of the vapor-pressure apparatus.

Mixtures of ammonia and isooctane were prepared by loading the experimental tube with a sample of pure isooctane, calculating the weight from the measured volume and density and then adding a measured volume of ammonia gas at a known temperature and pressure to make a mixture of known concentration. The apparatus and procedure have been described in previous publications, (*4, 7*).

To determine if any decomposition of the ammonia occurred at the high temperatures to which the ammonia was subjected in the course of the measurements, a test sample of ammonia was loaded in the experimental tube and the bubble-point pressure determined at 158°F. before and after the sample was heated for about 13 hr. at 480°F. and 800 lb./sq. in. An increase of 3.7 lb./sq. in. was noted. Since 13 hr. represents the maximum period of time that any of the mixtures was heated at an elevated temperature, the error introduced into the data by the decomposition of the ammonia sample is believed to be insignificant.

Table 1. Composition and Critical Constants of Mixtures of Ammonia and Isooctane

mole % ammonia	Critical constants: pressure lb./sq. in.	temp. °F.	density lb./cu. ft.	Max. pres. pt.: pressure lb./sq. in.	temp. °F.	Max. temp. pts.: pressure lb./sq. in.	temp. °F.
0	371.9	519.22	15.2	—	—		
4.90	430.7	515.14	15.28	438	512 ± 1	424 ± 2	516
15.31	570.4	504.46	15.45	621	490 ± 1	530 ± 5	507
28.82	783.9	487.00	15.61	904	456 ± 3	670 ± 10	494
43.04	1055.3	461.98	15.91	1220	418 ± 2	830 ± 20	474
69.84	1630.5	375.55	17.23	1658	359 ± 1	1150 ± 20	418
74.01	1670.3	359.04	16.78	1681	348 ± 2	—	—
79.96	1680.1	329.05	16.68	1686	337 ± 2	—	—
85.03	1628.6	304.12	16.50	1660	320 ± 1	1280 ± 20	351
90.00	1550.3	282.51	15.74	1579	294.5	1270 ± 20	314
94.97	1514.8	268.57	14.87	1515	268.3	1508 ± 2	269.5
97.83	1557.6	266.72	13.96	1557	266.6	1558 ± 2	266.7
99.22	—	—	—	—	—	—	—
100.00	1637.1	269.53	14.76	—	—	—	—

RESULTS

The pressure-specific volume-temperature relations at the liquid-vapor phase boundaries of twelve different mixtures of ammonia and isooctane were determined in order to define the pressure-temperature-composition (P-T-x) and the temperature-density-composition (T-p-x) diagrams of the ammonia-isooctane system. The experimental data are represented by the curves in Figures 1 and 2, and a summary of the smoothed data at regular intervals of the pressure, read from large-scale plots of the curves was prepared.* The critical constants of the mixtures are listed separately in Table 1, and have been plotted in Figure 3 to show the relations with the composition.

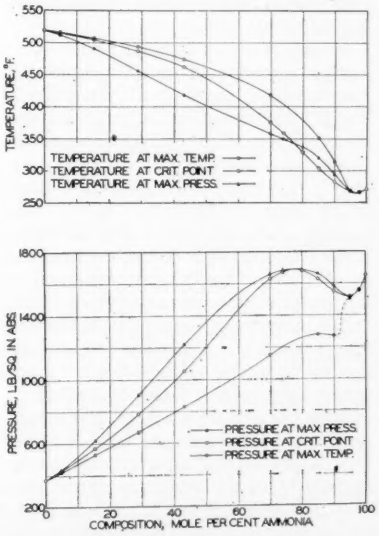

Fig. 3. Critical constants of mixtures of ammonia-isooctane system.

In the P-T-x space diagram, Figure 1, are shown the P-T border curves of the various mixtures, the critical locus, the vapor-pressure curves of the pure components, the three-phase vapor pressure curve and the curves defining the homogeneous and heterogeneous liquid regions.

As will be noted, the critical locus possesses three unique points: a minimum and a maximum pressure point and a minimum temperature point. The values of the pressure, temperature, and composition at each of the points are as follows:

Maximum pressure: 1688 ± 2 lb./sq. in. abs. at 342 ± 2°F. and 77.5 ± 1.0 mole % NH_3

Minimum pressure: 1513 ± 2 lb./sq. in. abs. at 270 ± 1°F. and 94.7 ± 0.3 mole % NH_3

Minimum temperature: 266 ± 0.7°F. at 1560 ± 10 lb./sq. in. abs. and 98.0 ± 0.5 mole % NH_3.

The critical temperature of ammonia was found to be 269.53°F. at 1637.1 lb./sq. in. abs.

The bubble-point curves of the mixtures in Figure 1 intersect the three-phase vapor pressure curve in the low temperature region. The points of intersection represent the conditions under which a liquid phase (composing the bulk of the sample and therefore having a composition very near the over-all mixture

*Tabular material has been deposited as document 5718 with the American Documentation Institute, Photoduplication Service, Library of Congress, Washington 25, D. C., and may be obtained for $1.25 for photoprints or $1.25 for 35-mm. microfilm.

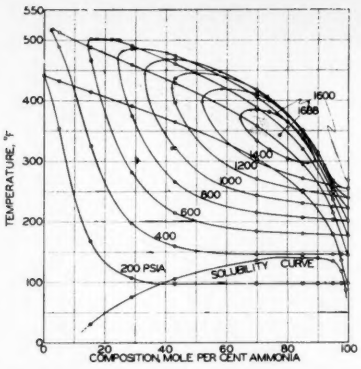

Fig. 4. Temperature-composition diagram of ammonia-isooctane system.

composition) is in equilibrium with a second liquid phase and a vapor phase. The second liquid phase and the vapor phase are present only in infinitesimal amounts. The three-phase vapor pressure curve very nearly coincides with the vapor pressure curve of ammonia, except in the region near the critical solution point, where it is situated slightly below that for ammonia (6 lb./sq. in. below, at the critical solution temperature, 140.27°F.) The fact that the three-phase curve is below rather than above the ammonia curve indicates that in this region the system is nonazeotropic.

The nearly vertical curves at the left in Figure 1, show the effect of pressure on the miscibility temperature of the various mixtures. These curves have a positive slope indicating that an increase in pressure decreases the mutual solubility of the two components over the range investigated. The experimental *P-V-T* data, including the points of intersection of the curves with the three-phase curve, are listed in Table 2.

Table 2. Pressure-Temperature-Density Relations at Miscibility Point, Ammonia-Isooctane System

Composition mole % NH_3	Pressure lb./sq. in. abs.	Temp. °F.	Density lb./cu. ft.	
28.82	141.5	75.07	41.88	SP
	551.4	76.24	41.88	L
43.04	228.9	105.10	40.43	SP
	481.8	106.30	40.29	
	741.4	107.49	40.46	
	991.8	108.55	40.58	
69.84	352.9	135.32	37.07	SP
	701.1	137.34	37.27	
	1000.8	139.12	37.38	
85.03	373.6	139.44	35.47	SP
	551.4	140.54	35.40	L
	1051.1	143.60	35.66	L
	1410.8	145.67	36.05	L
90.00	372.7	139.08	34.58	SP
	551.4	140.27	34.73	L
	1051.0	143.19	34.90	L
	1550.6	146.14	35.17	L
94.97	346.9	133.90	33.2	SP
	1000.9	137.73	33.2	L
97.83	278.0	117.39	33.85	SP
	1001.0	120.74	34.82	L
99.22	175.0	86.45	36.90	SP
	522.3	87.67	37.26	L

SP = tiny bubble of vapor + tiny drop of liquid with remainder in liquid phase.
L = tiny drop of liquid phase in presence of 2nd liquid phase.

Table 3. Temperature-Composition Relations at Constant Pressure

Mole % ammonia	Liquid °F.	Vapor °F.	Liquid °F.	Vapor °F.	Liquid °F.	Vapor °F.	Liquid °F.	Vapor °F.
	200 lb./sq. in. abs.		600 lb./sq. in. abs.		1000 lb./sq. in. abs.		1400 lb./sq. in. abs.	
0	441	441	—	—	—	—	—	—
4.90	353.7	431.6	—	—	—	—	—	—
15.31	167.6	414.0	465.6	501.9	—	—	—	—
28.82	107	391.0	281.0	490.6	—	—	—	—
43.04	96.5	364.2	214.2	460.5	320.8	467.6	—	—
69.84	96.5	302.8	183.5	387.8	242.8	416.1	298.0	410.5
74.01	—	—	—	—	—	—	—	399.4
79.96	—	—	—	—	—	—	—	376.1
85.03	96.5	248.3	179.4	319.8	229.9	346.0	271.1	349.6
90.00	—	—	—	—	—	—	—	312.5
94.97	96.5	178.6	177.3	235.2	223.8	256.3	258.8	267.0
97.83	96.5	134.9	—	—	—	—	—	—
100	96.5	96.5	176	176	221	221	254	254
	400 lb./sq. in. abs.		800 lb./sq. in. abs.		1200 lb./sq. in. abs.		1600 lb./sq. in. abs.	
0	(above critical)		—	—	—	—	—	—
4.90	488.8	512.6	—	—	—	—	—	—
15.31	325.1	487.9	—	—	—	—	—	—
28.82	197.0	458.8	374.0	485.5	—	—	—	—
43.04	159.1	428.2	265.3	474.0	396.2	437.1	—	—
69.84	145.6	357.7	214.4	405.9	269.9	417.6	333.1	384.0
74.01	—	—	—	—	—	—	318.8	380.8
79.96	—	—	—	—	—	—	304.3	364.0
85.03	144.8	293.8	206.2	336.0	251.0	350.4	296.4	338.1
90.00	—	—	—	—	—	314	—	—
94.97	144.8	214.2	202.7	248.4	242.4	261.9	—	—
97.83	144.8	—	—	—	—	—	—	—
100	143.8	143.8	200.2	200.2	238.3	238.3	268	268

The data for the construction of the vapor-pressure curve of ammonia are those taken from the literature (*3*), except the critical point which was experimentally determined. The vapor pressure data of isooctane are those reported from this laboratory (*8*).

In the T-ρ-x diagram, Figure 2, a point of maximum critical density is to be noted for a mixture of approximately 77 mole % ammonia which is the mixture that exhibits a maximum critical pressure. There is experimental evidence (not shown) to indicate that a point of minimum critical density exists for the mixture that exhibits the minimum critical temperature of the system. The region of two liquid phases appears as an area in the lower right side of the diagram.

The relations between temperature and the composition of the coexisting liquid and vapor phases (Figure 4) were determined graphically from crossplots of Figures 1 and 2. The temperatures corresponding to the points of intersection of the constant pressure line with the bubble and dew curves of the mixtures that were studied are listed in Table 3. Below the critical pressure of isooctane, 372 lb./sq. in., the T-x diagram extends from pure ammonia to pure isooctane. Above this pressure the liquid-vapor region terminates before the ordinate for pure isooctane is reached. For example, at 400 lb./sq. in., the T-x diagram on the isooctane-rich side terminates with a mixture containing 2.2 mole % ammonia. Up to 1513 lb./sq. in., the minimum pressure on the critical locus, the liquid-vapor region is represented by a single area. At higher pressures, however, this area splits into two separate areas. Thus, at 1600 lb./sq. in. one liquid-vapor area exists in the composition range from 64.4 to 89.0 mole % ammonia, the other between 99 and 100 mole % ammonia (too small to be shown). This ammonia-rich region diminishes with increased pressure and disappears when the critical pressure of ammonia is reached, leaving a single-liquid vapor region. The latter decreases as the pressure is further increased and finally disappears at 1688 lb./sq. in. Above this pressure the system is completely homogeneous.

In the region of high concentration of ammonia at pressures of 1400 lb./sq. in. and above, the vapor-liquid composition curves approach each other and appear to coincide. Such a condition indicates the presence of an azeotrope. Unfortunately, sufficient data to establish completely the curves in this region were not obtained. However, the fact that ammonia forms azeotropes with members of the paraffin series of lower molecular weight, leads to the prediction that ammonia would form an azeotrope with isooctane, provided that the difference in volatility of the components is not too great. That this difference is within the range for the

formation of an azeotrope is indicated by the existence of a point of minimum temperature on the critical locus. The latter relation is based on the observation that systems that possess a minimum temperature point in their critical locus show an azeotrope (*1, 7, 9–11*). It is estimated, therefore, that an azeotrope exists in mixtures of ammonia and isooctane between 98 and 100% ammonia at pressures above 1400 lb./sq. in.

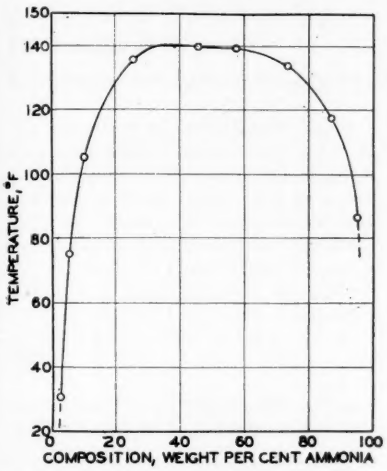

Fig. 5. Solubility curve for ammonia-isooctane at the three-phase pressure.

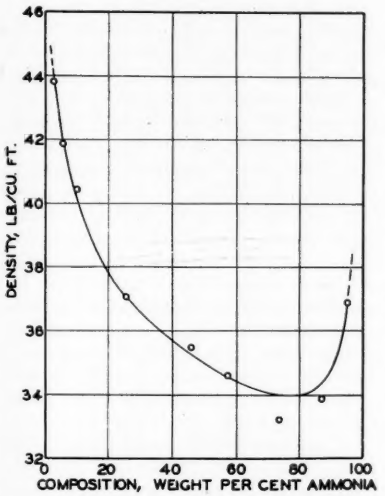

Fig. 6. Density of the saturated liquid phases in equilibrium with each other in ammonia-isooctane system.

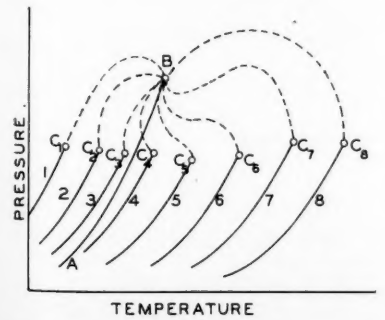

Fig. 7. Pattern of phase relations for binary systems that form azeotropes.

The solubility curve in the T-x diagram represents the mutual solubility of ammonia and isooctane at the 3-phase pressure. Since the effect of pressure on the solubility is very small, the variation of pressure along the curve may be ignored as far as its effect on the composition of the coexisting liquid phases is concerned. In Figure 5 the solubility is expressed in terms of weight percent. The critical solution temperature was found to be 140.27°F. and the composition 37 ± 5 wt. % ammonia (79 ± 4 mole % ammonia.) The critical solution temperature given in the literature for this system is 141.8°F. (*1*). The densities of the liquid phases as a function of the composition are given in Figure 6.

GENERAL PHASE RELATIONS WHEN AZEOTROPES ARE FORMED

The experimental data on the binary systems of ammonia with *n*-butane and with isooctane, as well as data on other systems (*5, 10*), indicate a general pattern which is illustrated schematically by the curves in Figure 7. Curves 1 through 8 represent the vapor pressure curves of similar kinds of compounds, such as members of an homologous series. Curve A, on the other hand, represents the vapor pressure curve of a compound whose chemical nature is sufficiently different so that it forms solutions with these compounds that deviate greatly from ideal solutions. Such mixtures are characterized by the formation of azeotropes which exist up to the critical region, provided the critical temperatures of the components do not differ greatly from each other. The broken line curves C_1B, C_2B, . . . C_8B represent the critical loci of the binary systems that A forms with each of the compounds 1 through 8. The curves C_1B and C_8B are those for systems whose components differ in their critical temperatures to such an extent that an azeotrope is not formed. These curves exhibit a maximum pressure point only.

For smaller differences in the critical temperatures, azeotropes are formed and the general shape of the critical locus depends to a large extent on whether the critical temperature of compound A is greater or less than the critical temperature of the compound with which it is mixed. When the critical temperature of A is greater, the locus may take the shapes illustrated by C_2B and C_3B. C_2B shows both a minimum-temperature and a maximum-pressure point whereas C_3B shows only a minimum temperature point. When the critical temperatures of both components are about the same, the locus is nearly symmetrical about a constant pressure line drawn through the minimum temperature point. As the critical temperature of the second component becomes greater than the critical temperature of the component A, the minimum temperature point moves toward the critical temperature of A and an inflection point in the curve appears near the critical point of the other component, as illustrated by curve C_5B. With a further increase in the difference between the critical temperatures, the inflection point moves toward the critical point of A and the locus may show minimum- and maximum-pressure points as well as a minimum-temperature point, (C_6B and C_7B), as in the case of the ammonia-isooctane system. Eventually, the difference between the critical temperatures becomes sufficiently great so that an azeotrope is not formed and the locus reverts to a simple curve with a maximum-pressure point.

These relations refer to systems in which minimum boiling azeotropes are formed. No experimental data are available on systems that form a maximum-boiling azeotrope in the critical region. However, it is presumed that the relations would be similar except that the point of minimum critical temperature would be replaced by a point of maximum critical temperature.

ACKNOWLEDGMENT

Grateful acknowledgment is made to the General Electric Company for financial aid in the form of a Gerard Swope Fellowship to F. M. Warzel, one of the authors, and to Phillips Petroleum Company for furnishing the sample of isooctane.

LITERATURE CITED

1. Caubet, F., *Z. physik. Chem.*, **49**, 101 (1904).
2. Francis, A. W., *Ind. Eng. Chem.*, **36**, 764 (1944).
3. Landolt-Börnstein, "Physikalisch-Chemische Tabellen, Berlin, Julius Springer, **I**, 272 (1923).
4. Kay, W. B., *J. Am. Chem. Soc.*, **68**, 1336 (1946).
5. Kay, W. B., and D. B. Brice, *Ind. Eng. Chem.*, **45**, 615 (1953).
6. Kay, W. B., and H. A. Fisch. To be supplied when printed.
7. Kay, W. B., and G. M. Rambosek, *Ind. Eng. Chem.*, **45**, 221 (1953).
8. Kay, W. B., and F. M. Warzel, *Ind. Eng. Chem.*, **43**, 1150 (1951).
9. Kuenen, J. P., *Z. physik. Chem.*, **24**, 667 (1897).
10. Poettmann, F. H., and D. L. Katz, *Ind. Eng. Chem.*, **37**, 847 (1945).
11. Quint Gzn, N., *Z. physik. Chem.*, **39**, 14 (1901).

Manuscript received July 22, 1957; revision received September 27, 1957; accepted October 24, 1957.

A Reactor-design Equation Based on a Proposed Distributed Boundary-layer Thickness

H. E. HOELSCHER

The Johns Hopkins University, Baltimore, Maryland

An empirical equation is developed which seems applicable to the general problem of fixed-bed catalytic-reactor design and relates the reaction rate (in a differential reactor) or conversion (through an integral reactor) to the surface reaction rate, the flow rate through the bed, and the physical properties of the system. The development is based on the assumption that there exists a film of stagnant fluid surrounding each catalyst particle, through which mass is transferred only by molecular motion, and that the thickness of this film varies throughout the bed from zero to some upper limit in a manner which is described by a distribution function. The equation involves two empirical constants: the multiplying constant and the exponent in the usual j_d-factor–Reynolds-number relationship.

The application of this equation is illustrated. It appears to provide a basis for evaluation of the contribution of diffusional steps in the over-all mechanism and to provide a means for predicting an expected conversion rate at any flow rate through the bed, provided only that the surface (chemical) reaction rate is known at the operating temperature. It also appears possible to calculate values of the surface-reaction-rate constant and the temperature coefficient from data taken from a reactor operating in the diffusion-controlled range.

The rational design of a fixed-bed catalytic reactor requires an understanding of the mass and heat transfer phenomena occurring, as well as of the chemical reaction kinetics. Of these, the detailed description of mass transfer rates between fluid phase and particle surface has received least attention to date.

There have been many studies of the gross nature of this problem. Over-all mass transfer coefficients, j factors, transfer-unit concepts, and other macroscopic analyses are common in chemical engineering literature. Such analyses gloss over the detailed point-to-point conditions in a packed bed and ascribe over-all behavior to averaged characteristics and properties.

It seems obvious that the catalyst surface area in a packed-bed reactor is not uniformly available. There must exist a film of fluid over the external particle surfaces which is essentially stagnant and through which reactant and product are transported by molecular motion only. It is furthermore obvious that the thickness of this film, for any flow rate through the bed, must vary from point to point over a given catalyst particle. This variation throughout the bed is between zero and some upper limit, which should be determined by the particle diameter and packing geometry.

At any specific location on the catalyst surface, the rate of diffusion of reactant to the surface will be determined by the film thickness at that point and by the concentration of reactant in the bulk of the fluid and at the surface. Furthermore, at this point, as at all points, the diffusion rate equals the rate of chemical reaction on the surface. The latter is determined by the concentration of reactant at the surface. The net rate of production of product by chemical reaction at the surface will vary with film thickness, as shown in Figure 1. Since the relationship between *rate* and *film thickness* is of a reciprocal nature, the following development will be expressed in terms of $1/\delta$.

For any real situation, it is obvious that the rate must continue to increase as $1/\delta \rightarrow \infty$ but in such a manner that $dr/d(1/\delta) \rightarrow 0$ as $1/\delta \rightarrow \infty$. Furthermore, the maximum rate, the value where $dr/d(1/\delta) = 0$, must be finite. Thus one may define a value of film thickness such that for $1/\delta \geq 1/\delta_c$ the measured rate is different from the maximum, or ultimate, value only by the probable error of measurement or less. This is shown schematically in Figure 1. For any value of $1/\delta > 1/\delta_c$ the surface reaction rate does not change appreciably. This is the *reaction-controlled* region. For $1/\delta < 1/\delta_c$ the surface concentration of reactant and, hence, the surface reaction rate is affected measurably by changes in $1/\delta$ and therefore by changes in flow rate. This is the *diffusion-controlled* region. Certainly this is oversimplified; however, it will serve to illustrate the physical meaning and significance of the critical *film thickness* δ_c.

It is assumed, then, that the bed surface areas can be divided into two kinds. The first are those surfaces over which $1/\delta > 1/\delta_c$, where the surface concentration of reactant will be essentially constant at a fraction of the free stream concentration approaching unity. The second types of surfaces are those over which $1/\delta < 1/\delta_c$, where the surface reaction rate will be fast by comparison to the rate of supply of reactant to the surface and the surface concentration of reactant will be low.

For convenience, a dimensionless film thickness is defined as

$$x = \frac{\delta}{\delta_{max}} \qquad (1)$$

where δ_{max} is the maximum possible film thickness in the particular bed under discussion. For the present, no attempt will be made to identify this in terms of bed geometry. However, it will be noted that $0 < x < 1$ at all points.

It will be interesting to seek a function of x to represent the distribution of x throughout the bed. The fraction of the bed area over which the dimensionless film thickness (as represented by x) is between two arbitrary values, say x_1 and x_2, may be represented by $(a)_{x_1/x_2}$.

Then the required function must be such that

$$(a)_{x_1/x_2} = \int_{x_1}^{x_2} f(x)\, dx \qquad (2)$$

Some of the properties of this function are obvious. First, as x_1 approaches zero and x_2 approaches unity, the function must yield a value of unity in Equation (2). Furthermore, the function must pass through a maximum in the interval $0 \leq x \leq 1$; the value of x at this maximum will be designated by x_m. The function must provide parameters which can be related to the performance of a packed-bed reactor. Thus, for example, as the mass rate of flow through the bed increases, all other variables remaining constant, the form of the $f(x) - x$ relationship must become sharply peaked about a value of $x_m \rightarrow 0$. As the mass rate of flow decreases, the relationship must become sharply peaked about a value of $x_m \rightarrow 1$. Between these two extremes, a single distribution must be available for all permissible sets of values of parameters such as the Reynolds number (based on particle diameter and flow rate through the empty tower), bed diameter, and possibly particle shape factors.

A function which seems to provide most of these characteristics is the beta distribution of beta density, a well-known distribution function in the field of statistics, of the following form:

$$f(x) = \frac{(\alpha + \beta + 1)!}{\alpha!\beta!}\, x^{\alpha}(1 - x)^{\beta} \qquad (3)$$

It is possible to show (5) that

$$\int_0^1 x^{\alpha}(1 - x)^{\beta}\, dx = \frac{\alpha!\beta!}{(\alpha + \beta + 1)!} \qquad (4)$$

and hence that

$$\int_0^1 f(x)\, dx = 1$$

Values of the incomplete beta function, defined as

$$\int_0^x \frac{(\alpha + \beta + 1)!}{\alpha!\beta!}\, x^{\alpha}(1 - x)^{\beta}\, dx \equiv B_x(\alpha, \beta) \qquad (5)$$

are tabulated for a wide range of the indicated parameters by Pearson (*8*). It will be noted that

$$B_x(\alpha, \beta) = 0 \text{ for } x \leq 0$$
$$0 < B_x(\alpha, \beta) < 1 \text{ for } 0 < x < 1 \quad (6)$$
$$B_x(\alpha, \beta) = 1 \text{ for } x \geq 1$$

The beta function represents a two-parameter family of distributions, yielding various forms for particular values of α and β. Figure 2 indicates the shape of this function for several sets of values of these parameters. Although there is no reason to expect the beta distribution function to be unique for the purpose of this work, many other functions have been tried without success, none having been found which yield the satisfactory results shown in the following development.

In a fixed-bed catalytic reactor a balance about a differential element taken perpendicular to the axis yields

$$-F\,dy = \left[\int_0^{a_c} r\,da\right] dV + \left[\int_{a_c}^{a} r_d\,da\right] dV \quad (7)$$

Noting then that the surface reaction rate is assumed essentially constant in the range $0 < \delta < \delta_c$ or for $0 < a < a_c$ (see Figure 1) and introducing the distribution function defined by Equation (3) one finds that Equation (7) becomes

$$-\frac{F\,dy}{dV} = r \cdot a \cdot \int_0^{x_c} f(x)\,dx + a\int_{x_c}^{1} r_d f(x)\,dx \quad (8)$$

Both of the integrals on the right-hand side of this equation are multiplied by a since the distribution function as previously defined represents a *fraction* of the total bed area and not the area itself. $dV = A\,dl$ and, approximately,

$$r_d = \frac{D}{\delta}(C_0 - C_i) \quad (9)$$

On the basis of the foregoing information, together with the previous assumption that C_i is negligible by comparison to C_0 for the areas over which $1/\delta_c > 1/\delta > 1/\delta_{max}$ plus Equations (5) and (9), Equation (8) can be transformed to the following:

$$-\frac{F\,dy}{aA\,dl} = rB_{x_c}(\alpha, \beta) + \frac{DC_0}{\delta_{max}}\int_{x_c}^{1}\frac{f(x)}{x}\,dx \quad (10)$$

In Equations (9) and (10) concentrations C are used rather than mole fractions y for dimensional reasons. Furthermore, $C/\rho = y$, where ρ is the average molal density. It can be shown that

$$\int_{x_c}^{1}\frac{f(x)}{x}\,dx = \frac{\alpha+\beta+1}{\alpha}\cdot[1 - B_{x_c}(\alpha - 1, \beta)] \quad (11)$$

and thus

$$-\frac{F\,dy}{aA\,dl} = rB_{x_c}(\alpha, \beta) + \frac{\rho D y_0(\alpha+\beta+1)}{\alpha\delta_{max}}\cdot[1 - B_{x_c}(\alpha - 1, \beta)] \quad (12)$$

This then is the final result. It should apply to a differential volume element of a fixed-bed catalytic reactor provided only that the true distribution of x over the area in that element can be represented by the beta distribution function and that the assumptions involved in the designation of $1/\delta_c$ are valid. The former involves only a curve fitting problem and the relating of the two arbitrary parameters to physically determinable variables. The assumption of a nonzero value of $1/\delta_c$ involves questions concerning the sensitivity with which the rate (or composition in the exit gases) can be measured for a specific problem to yield physically meaningful results and the shape of the relationship shown in Figure 1. The latter, in turn, depends upon the ratio of molecular diffusivity to surface reaction rate constant.

Two limiting cases will now be considered, namely, the form of Equation (12) resulting from setting x_c equal to the two permissible extreme values, 0 and 1. With $x_c = 0$, equivalent to $1/\delta = \infty$, the problem becomes one of pure diffusion involving a reaction at the surface which is infinitely fast (with zero energy of activation). Such a situation would be approximated by a gas-liquid adsorption process in a packed bed wherein the gas film controls. For this case, Equation (12) becomes

$$-\frac{F\,dy}{aA\,dl} = \frac{\alpha+\beta+1}{\alpha}\frac{\rho D y_0}{\delta_{max}} \quad (13)$$

For the other extreme, that is, with $x_c = 1$, it is apparent that $1/\delta_c = 1/\delta_{max}$ (indicating that the minimum permissible value of $1/\delta$ used in Figure 1 is properly nonzero). This case corresponds to a process which is reaction controlled throughout over all ranges of flow; that is, molecular diffusion is very fast by comparison to the chemical reaction at the surface, and Equation (12) should and does reduce to

$$-\frac{F\,dy}{aA\,dl} = r \quad (14)$$

The latter is the familiar result presented, for example, by Hougen and Watson (*2*).

Equation (13), being a diffusion equation, may be used to obtain some information concerning the relationship between α and β and the variables of importance in diffusion processes. If both parameters, flow rate, and density are assumed constant, this equation may be integrated

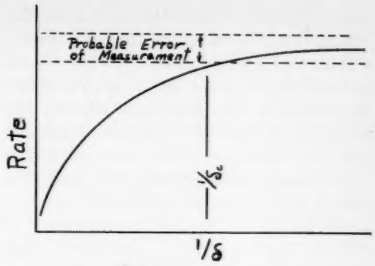

Fig. 1. Schematic rate curve.

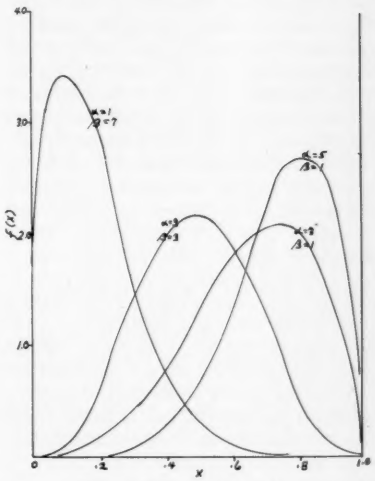

Fig. 2. The beta function.

to yield

$$\ln\frac{y_{0_1}}{y_{0_2}} = \frac{\rho D a A}{\delta_{max}}\cdot\frac{\alpha+\beta+1}{\alpha}\cdot\frac{L}{F} \quad (15)$$

This result is exactly analogous to the integrated equation for the design of gas-liquid packed-bed absorbers for the case where the gas film controls, provided only that

$$\frac{\rho D}{\delta_{max}}\cdot\frac{\alpha+\beta+1}{\alpha} = k_g \quad (16)$$

From gas-absorption theory, the mass transfer coefficient is defined as

$$k_g = \frac{DP}{RTB' y_{Bm}} \quad (17)$$

In this equation, B' (the symbol used in gas-absorption references to represent the film, or boundary-layer, thickness) is identical with δ as defined in this paper. Also, $P/RT = \rho$ from the ideal gas law. Thus Equation (16) becomes

$$\frac{\alpha+\beta+1}{\alpha} = \frac{\delta_{max}}{\delta y_{Bm}} \quad (18)$$

Empirically, k_g is related to the physical properties of the system and to flow rate through the usual j-factor relationship thus:

$$k_g = a'\frac{\mu}{d_p M_m} N_{Sc}^{-\frac{2}{3}} N_{Re}^{1+b} \quad (19)$$

where the constants a' and b are determined from experiment. There is little

question about the value of b since the experimental evaluation of this yields -0.51 with reasonable consistency. There is considerable question, however, about the value of a'. [See, for example, the summary of Ergun (*1*).] Some information can be obtained from the following relationship resulting from the combination of Equations (17) and (19):

$$\frac{\delta_{max}}{\delta y_{Bm}} = \frac{a' N_{Sc}^{\frac{1}{3}} N_{Re}^{\frac{1}{2}}}{(d_p/\delta_{max})} \qquad (20)$$

The left-hand side of this equation is obviously greater than unity, and, hence, the value of a' on the right must be large enough to make the right-hand side also greater than unity; it must also vary with N_{Re} and y_{Bm}. Thus, the value of a' must depend upon the physical and operational characteristics of the system. This seems wholly reasonable. For the present, a' will be considered an unknown empirically determined constant, and Equation (18) may be combined with Equation (20) to yield

$$\frac{\alpha + \beta + 1}{\alpha} = \frac{a' N_{Sc}^{\frac{1}{3}} N_{Re}^{\frac{1}{2}}}{(d_p/\delta_{max})} \qquad (21)$$

It is now necessary to identify α and β with the variables shown in Equation (21). This must necessarily be quite arbitrary and involve assumptions which are wholly *ad hoc*. It is assumed first that α is small compared to $\beta + 1$. Thus, $\alpha < \beta + 1$, and Equation (21) may be considered to be composed of two parts:

$$\alpha = \frac{d_p}{a' \delta_{max} N_{Sc}^{\frac{1}{3}}} = \frac{(\delta/\delta_{max}) y_{Bm}}{N_{Sc}^{\frac{1}{3}} N_{Re}^{\frac{1}{2}}} \qquad (22)$$

and

$$\beta + 1 = N_{Re}^{\frac{1}{2}}$$

These definitions are consistent with the characteristics previously required for α and β. The acceptability of these assumptions, or, better, these assignments, can be determined only by the success of the resulting equations. It is evident, however, that the accuracy of the previous statements will be best for large Reynolds numbers, large values of the Schmidt number, or both.

A further simplification of Equation (12) results from a consideration of the possible range of values of $B_{x_c}(\alpha - 1, \beta)$ in Equation (21). From Pearson's tables, it is evident that for $x_c > 0.05$ and $\alpha \leq 0.3$

$$B_{x_c}(\alpha - 1, \beta) \to 1$$

Examination of the variation of $B_{x_c}(\alpha - 1, \beta)$ with α indicates that as α decreases, the incomplete beta function rapidly approaches unity. For the problem considered in this paper, α is expected to be small. Thus, for such systems one may assume that

$$[1 - B_{x_c}(\alpha - 1, \beta)] \to 0$$

Equation 12 then becomes:

$$-\frac{F\,dy}{aA\,dl} = rB_{x_c}(\alpha, \beta) \qquad (23)$$

This result then is based on the implicit assumption that the fraction of the bed surface areas over which the surface reaction rate is controlling produces essentially all of the product and that the production rate from the remaining surface areas is negligible by comparison.

With the assumption that α is small, the beta function may be integrated and Equation (23) becomes

$$-\frac{F\,dy}{aA\,dl} = r[1 - (1 - x_c)^{\beta+1}] \qquad (24)$$

or if Equation (22) is introduced,

$$-\frac{F\,dy}{aA\,dl} = r[1 - (1 - x_c)^{\sqrt{N_{Re}}}] \qquad (25)$$

This may be written, for convenience, as

$$-\frac{N_{Re}\mu}{d_p M_m a}\frac{dy}{dl} = r[1 - (1 - x_c)^{\sqrt{N_{Re}}}] \qquad (26)$$

The left-hand side of Equation (24) is observed to be the *measured rate* at a point (or the measured rate in a differential reactor) and is equal to a fraction of the chemical reaction rate. The form of this result is shown in Figure 3. For the case of a first-order irreversible reaction at the catalyst surface, Equation (26) may be integrated to yield

$$\ln \frac{y_1}{y_2} = \frac{k\rho\, d_p M_m a}{\mu} \cdot \frac{[1 - (1 - x_c)^{\sqrt{N_{Re}}}]}{N_{Re}} \cdot L \qquad (27)$$

The form of this result is shown schematically on Figure 4.

The application of these results to a particular situation, that is, the application of Equations (12), (25), and (27), requires knowledge of x_c. Of course, with the required data, it is possible to compute a value of x_c to characterize the reaction.

For a first-order irreversible reaction, δ_c may be estimated from the Nernst equation (*6*) thus:

$$\delta_c \approx \frac{D}{k} \qquad (28)$$

From values of the molecular diffusivity and the chemical reaction rate constant k, δ_c may be estimated. Some values taken from the literature are shown in Table 1.

As in Equation (6), for $x_c \geq 1$, the incomplete beta function is unity, and Equation (12) reduces to the form for the reaction-controlled situation. It is apparent that except for very large operations, that is, large particle diameters, it is unlikely that diffusion will play a significant role in the reactions listed as *Set A* in Table 1. These reactions all show values of δ_c greater than 1 cm.; hence it appears that the particle diameter would have to be of this same order of magnitude before x_c becomes less than unity. For those cases listed as *Set B* one should expect some contribution from diffusion under certain conditions. Finally, for those reactions listed as *Set C*, it seems unlikely that rate-controlled situations will be observed in the laboratory since x_c is small. These conclusions are, in every case, in accord with the observations reported in the references cited.

There are a number of cases in the

TABLE 1

Reaction	Phase	Temp., °C.	k, cm./sec.	D, sq. cm./sec.	δ_c, cm.	Ref.
Set A						
1. Hydrogenation of ethylene	Gas	30	0.222	0.5	2.252	*1, 2*
2. Hydrogenation of ethylene	Gas	30	10^{-4}(approx.)	0.5	5(10^3)	*6*
3. Hydrogenation of propylene	Gas	30	0.053	0.5	9.433	*1, 2*
4. Hydrogenation of butene	Gas	30	0.104	0.5	4.807	*1, 2*
5. Decomposition of NH_3 on tungsten	Gas	631	.046	0.53	11.42	*4*
6. Dehydrogenation of ethyl benzene	Gas	30	0.0087	0.3	34	*7*
Set B						
7. Oxidation of carbon monoxide	Gas	299 319	28.4 58.3	0.675 0.717	0.023 0.012	*3* *3*
Set C						
8. Decomposition of HI on gold	Gas	705	0.64(10^4)	0.71	1.1(10^{-4})	*4*
9. Dissolution of zinc in acid	Liquid	27	6.2(10^{-3})	0.5(10^{-5})	8(10^{-4})	*5*

1. Weger, Eric, Dr. Eng. dissertation, The Johns Hopkins Univ., Balt. (1955).
2. ———, and H. E. Hoelscher, *A.I.Ch.E. Journal*, **3**, 153 (1957).
3. Langmuir, Irving, *Trans. Faraday Soc.*, **17**, 621 (1922).
4. Glasston, S., K. J. Laidler, and Henry Eyring, "The Theory of Rate Processes," p. 377, McGraw-Hill (1941).
5. Kiser, K. M., and H. E. Hoelscher, *Ind. Eng. Chem.*, **49**, 970 (June, 1957).
6. Wynkoop, Raymond, and R. H. Wilhelm, *Chem. Eng. Progr.*, **46**, 300 (1950).
7. Wenner, R. R., and E. C. Dybdal, *ibid.*, **44**, 275 (1948).

literature which apparently do not afford a check of these conclusions. For example, Smith and Fuzek (*9*) report on the hydrogenation of furan and furan derivatives over solid catalysts suspended in acetic acid as a solvent. From their data, values of k for two cases can be computed to be 0.04-cm./sec. and 0.12-cm./sec. respectively. Since the value of the molecular diffusivity in liquids is quite small (about 10^{-5} sq. cm./sec.), one would expect these reactions to be diffusion controlled, as x_c is small. The authors, however, treat the data as though it were rate controlled. Similarly, the vapor-phase catalytic dehydrogenation of ethylbenzene is reported to be rate controlled (*10*). However, from the data presented one may calculate a value of the rate constant of 0.04-cm./sec., which with a value of diffusivity of approximately 0.2 sq. cm./sec., yields a value of δ_c equal to 5 cm. Thus, one might expect a significant contribution from diffusion. In such cases it is possible that the analysis of the data taken during the experimentation may be faulty or that the value of δ_c calculated by the method indicated does not serve as a definitive criterion for these cases.

Equation (25), then, is the principal result of this effort. It is in reality an empirical equation based on many *ad hoc* assumptions. Its value, if any, can become apparent only from attempts to use it with experimental data. This is essentially a *curve fitting* type of operation and has been done for several sets of data taken from published work. The "fit" obtained has been surprisingly good in those cases tested. Two specific examples will be presented.

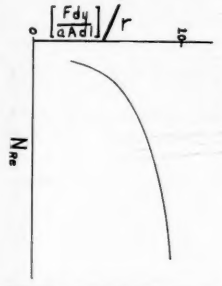

Fig. 3. Schematic representation of Equation (26).

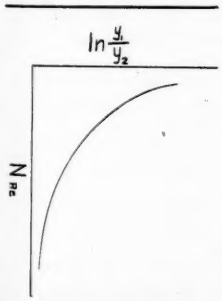

↑ **Fig. 4. Schematic representation of Equation (27).**

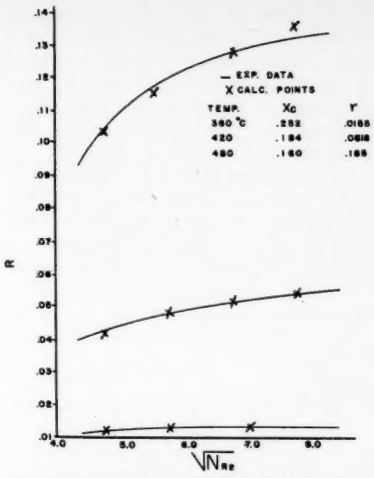

Fig. 5. Test of Equation (25) with data from reference 7.

In the paper by Olson, Schuler, and Smith (*7*) on the catalytic oxidation of sulfur dioxide over a platinum catalyst, it is shown that the reaction is diffusion controlled over the range of variables studied. The analysis in this article is based on this assumption and proves generally reasonable and sound. Figure 9 of Smith's paper presents a set of rate-flow rate curves of the form shown herein as Figure 1. R is the rate reported for any given mass velocity G in lb./(hr.)(sq. ft.) and r is the maximum. Then, since a differential reactor was used, Smith's Equation (25) indicates that

$$R = r[1 - (1 - x_c)^{\sqrt{N_{Re}}}] \qquad (29)$$

where r and x_c must be obtained from the data presented. (The values of G tabulated in the paper were converted to Reynolds numbers by means of the physical data presented.) The result is shown herein as Figure 5. The solid lines represent the experimental data, whereas the points were computed from the equation and constants shown on the figure. The latter were obtained by a curve fitting process, and the fit is seen to be quite good.

Since r should (physically) be equal to the surface or chemical reaction rate, it is possible to obtain a value of the energy of activation for the reaction. Values of r were plotted as the natural logarithm vs. the reciprocal of the absolute temperature and the slope determined to yield a value of 20,300 calories/mole for the energy of activation. This value is in reasonable agreement with previously reported values (*4* and *10*).

Finally, Hay, Coull, and Emmett (*2*) report on the catalytic isomerization of butene-1 and present data to indicate that the process is rate controlled. Specifically, Figure 7 of the reference paper presents a plot of space-time-yield vs. flow rate for several operating temperatures. The conversions reported by the authors are larger than those considered permissible in a differential reactor, and, hence, Equation (27) [the integrated form of (25)] was applied to these data. The result is presented herein as Figure 6. Again, the solid lines represent the experimental data, whereas the circumscribed points were computed from the equation and constants shown. The fit is again noted to be quite good. The values shown for x_c would again indicate that diffusion does play a significant role in the over-all mechanism, contrary to the statement of the authors. That this is true may be seen from an Arrhenius-type plot of the data (space-time-yield as the logarithm vs. $1/T$), the slopes of which yield values for an *over-all* energy of activation. Such a plot is shown in Figure 7. The effect of diffusion is evident in the variation of slopes on this figure. The variation of x_c with temperature is not unexpected in view of the temperature dependence of the terms comprising this constant.

From Equation (27) it is apparent that

$$C = \frac{k\rho\, d_p M_m a L}{\mu}$$

Hence, a value for the energy of activation of this reaction may be calculated from the temperature variation of C.

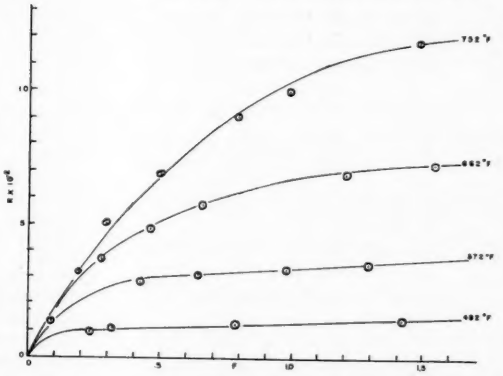

↑ **Fig. 6. Test of Equation (27) with data from reference 2. R = space-time-yield, S.T.Y., reciprocal hr.; F = butene flow rate, lb.-moles/(sq. ft.)(hr.); solid lines = experimental data from reference 2; points computed by use of Equation (27), viz:**

$$\ln y_1/y_2 = C\,\frac{[1 - (1 - X_c)^{\sqrt{N_{Re}}}]}{N_{Re}}$$

with the following values of the constants

$T°$, F.	X_c	C
482	0.397	1.025
572	0.678	1.980
662	0.450	4.550
752	0.390	8.000

This was done to yield a value of 12,500 cal./mole. At the highest flow rate and lowest temperatures shown on Figure 7 of this paper, a condition which is most likely to yield a reaction-controlled situation, the slope of the line yields a value of E of 12,360 cal./mole.

Finally, the authors present a plot of H_r vs. $1/T$ and indicate that the resulting straight line constitutes proof that the process is rate controlled. It may be seen, however, that the three data points at the highest temperatures may easily be interpreted as a portion of the curve yielding an increasing downward slope. This would correspond to an increasing influence of diffusion, in accordance with the definitions of H_r. The slope of the line through the low-temperature data yields a value for the energy of activation of the reaction studied of approximately 11,000 cal./mole, again in good agreement with the values calculated from flow-rate consideration and from the constant C.

SUMMARY AND CONCLUSION

A method has been developed for predicting the performance of a fixed-bed catalytic reactor when the surface (chemical) reaction rate is known or for predicting the surface rate when something of performance is known, even though the available data cover only the diffusion-controlled range of operation. The method is empirical and, like other such techniques, involves two empirical constants. Thus, the equations presented offer no advantage in the sense of degree of freedom. However, the method presented in this paper focuses attention on a property of packed beds which has been virtually neglected to date, namely the inescapable conclusions that the areas in a bed are *not* uniformly available to the fluid and that the film thicknesses throughout the bed vary according to some distribution law.

The basic idea of this paper is not restricted to the problem of a fixed-bed catalytic reactor but applies equally well to any problem involving contact of a fluid or fluid constituent with the surface of a solid in a packed bed. Such problems as adsorbers, absorbers, etc., should be amenable to treatment in much the same manner.

In a consideration of the applicability of this technique to reactors, it is highly possible that the major advantage of the method may become more apparent in reactions of higher orders than unity. The use of averaged and distributed film thicknesses yields essentially the same numerical over-all conversion rates for first-order reactions. A more detailed study of the present proposal for the case of higher ordered reactions is indicated.

The present method, therefore, is of interest chiefly because it initiates a way of looking at these problems, a method which demands consideration of the point-to-point variation of film thicknesses throughout the bed. While the method offers no dramatic advantage over more standard approaches for the case of a purely diffusion-controlled situation, it does permit computation of the surface-reaction-rate constants for the chemical step from data taken in the diffusion range. This is not possible by more "classical" approaches. In addition, significant advantages for the case of higher order reactions appear likely.

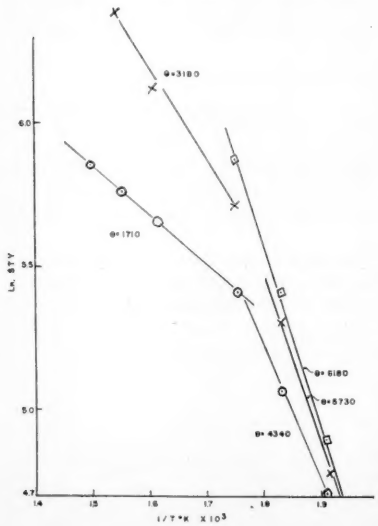

ACKNOWLEDGMENT

The author gratefully acknowledges the suggestions and interest of Professor R. H. Wilhelm and of Dr. Eliezer Naddor relative to the use of the beta distribution function.

NOTATION

A = cross sectional area of bed, sq. cm.
a = catalytic surface area per unit volume, sq. cm./cc.
a' = constant—defined by Equation (19), dimensionless
a_c = catalytic surface area per unit volume, over which $1/\delta_c < 1/\delta < \infty$, sq. cm./cc.
a_d = catalytic surface area per unit volume, over which $1/\delta_{max} < 1/\delta < 1/\delta_c$, sq. cm./cc.
B_x = incomplete beta function defined by Equation (5)
b = constant—defined by Equation (19), dimensionless
C_i = surface concentration of reactant, moles/cc.
C_0 = free stream concentration of reactant, moles/cc.
D = molecular diffusivity, sq. cm./sec.
dl = element of bed length
d_p = particle diameter, cm.
E = energy of activation, cal./mole
F = flow rate, moles/sec.
G = mass rate of flow; mass/(sq. cm.)(sec.)
j_d = j factor
k = reaction rate constant, cm./sec.
kg = mass transfer coefficient, moles/(sq. cm.)(sec.)
L = bed length cm.
Mm = mean molecular weight, g./mole
N_{Re} = Reynolds number based on empty cross sectional area of bed, dimensionless
N_{Sc} = Schmidt number, dimensionless
R = gas constant, cal./mole°
r = surface (chemical) reaction rate, moles/(sq. cm.)(sec.)
r_d = rate of diffusion of reactant to the surface; moles diffusing per unit time per unit of surface area
T = temperature, °K.
V = volume, cc.
x = dimensionless boundary layer thickness
y = mole fraction of reactant

Greek Letters

α = constant, defined by Equation (3), dimensionless
β = constant, defined by Equation (3), dimensionless
δ = boundary-layer thickness, cm.
δ_c = critical boundary-layer thickness cm.
δ_{max} = maximum boundary-layer thickness, cm.
ρ = average molal density, moles/cc.

Subscripts

0 = free stream condition
1 = inlet condition
2 = outlet condition

LITERATURE CITED

1. Ergun, S. K., *Chem. Eng. Progr.*, **48**, 227 (1952).
2. Hay, R. G., James Coull, and P. H. Emmett, *Ind. Eng. Chem.*, **41**, 2809 (1949).
3. Hougen, O. A., and K. M. Watson, "Chemical Process Principles," Pt. 3, John Wiley and Sons, New York (1947).
4. Hurt, D. M., *Ind. Eng. Chem.*, **35**, 522 (1943).
5. Mood, A. M., "Introduction to the Theory of Statistics," McGraw-Hill Book Company, Inc., New York (1950).
6. Nernst, Walter, "Theoretical Chemistry," 5 ed., Macmillan Company, Inc., New York (1923).
7. Olson, R. W., R. W. Schuler, and J. M. Smith, *Chem. Eng. Progr.*, **46**, 614, (1950).
8. Pearson, Karl, "Tables of the Incomplete Beta Function," Cambridge Univ. England (1934).
9. Smith, H. A., and J. F. Fuzek, *J. Am. Chem. Soc.*, **71**, 415 (1949).
10. Uyehara, O. A., and K. M. Watson, *Ind. Eng. Chem.*, **35**, 541, (1943).
11. Wenner, R. R., and E. C. Dybdal, *Chem. Eng. Progr.*, **44**, 275, (1948).
12. Wilke, C. R., and O. A. Hougen, *Trans. Am. Inst. Chem. Engrs.*, **41**, 445, (1945).

Manuscript received June 13, 1957; revised Dec. 30, 1957; accepted Jan. 6, 1958.

Fig. 7. Arrhenius plot of over-all data from reference 2. S.T.Y. = space-time-yield, reciprocal hr., T = temp., °K., ⊙ = data points for F = 0.2 lb.-moles butene/(sq. ft.)(hr.), x = data points for F = 0.5 lb.-moles butene/(sq. ft.)(hr.), ⊡ = data points for F = 1.6 lb.-moles butene/(sq. ft.)(hr.), ⊖ = E/R = slope.

Drainage of Packed Beds in Gravitational and Centrifugal-force Fields

EMILE NENNIGER, JR., and J. ANDERSON STORROW

University of Manchester, Manchester, England

The basic differential equations are developed for the prediction of saturation-time curves for the drainage of packed beds in either gravitational or centrifugal fields. The only mathematical solution existing at present, a series solution, is provided for these equations. A film drainage function is included to describe the movement of liquid along the surface of the particles when the main liquid level has passed through the pores of the bed. This method of analysis has been used successfully to predict the drainage of packed beds in a 9-in.-diameter hydroextractor. The important value of capillary suction head is best found from ancillary tests with Haines apparatus, but the value can be found with reasonable accuracy from the change in drainage rate as the liquid surface enters the upper surface of the packed bed. When these two rates are available, the permeability can also be found, and all the major variables are obtained from the drainage test on either the hydroextractor cake or the packed bed under gravity drainage.

Previous work (*35*) dealt with the problem of the movement of liquid through hydroextractor cakes in a centrifugal-force field (*16* to *21*, *23*, *24*) when the interstices of the packed bed were filled with liquid. For analysis of a complete hydroextraction cycle, it is necessary to obtain the equations governing the flow of liquid from a packed bed under drainage conditions when the voids are not filled with liquid. It should then be possible to integrate these two hydrodynamic processes over the appropriate portions of the cycle under the accelerating or decelerating fields while the cake is formed, washed, and "whizzed". The preliminary study of the spin-drying of cakes (*22*) showed that cake deformations and liquid distributions reduced the value of analyses based on samples cut from the hydroextractor cake. The two major problems were to measure the moisture content of a cake during spinning without liquid feed and to derive appropriate mathematical forms for analyses of experimental data. The solution to this problem has been provided (*31*) in the form of a series solution until the integrated form of the saturation-time function is available. The analysis has followed the necessary steps to apply functions for the bulk drainage of full pores and the film drainage across the walls of open pores toward the saturation limit at infinite time. This limit is set by the capillary suction head retaining a column of liquid that fills the pores at the base of the bed and the permanent liquid held by surface tension in the menisci at the interstitial contact points within the bed. The functions proposed have proved successful in both gravitational and centrifugal-force fields for a wide range of liquids and packed beds.

E. Nenniger is with Surveyer, Nenniger and Chênevert, Montreal, Canada, and J. Anderson Storrow with the Levington Research Station, Levington, Ipswich, England.

I. DRAINAGE OF PACKED BEDS IN A GRAVITATIONAL FIELD

LIQUID RETENTION IN PACKED BEDS

Liquid will be retained in a packed bed for any finite-force field, as (1) a saturated zone of capillary moisture stands above the datum of the outlet face of the bed, and (2) the drained portion of the bed will contain permanent residual liquid, i.e., liquid in menisci held at points of contact between bed particles.

Capillary Height in Packed Beds

The specification of capillary moisture depends on the statement of capillary height h_c of the vertical saturated column. The saturated zone due to capillary rise of liquid in packed beds, for instance in soil, and the time equations for upward infiltration from a lower source are known (*5*, *11*, *12*, *13*, *28*, *37*).

Haines (*14*, *15*), in applying surface-tension theory to spherical packing arrangements, predicted and found a difference in capillary height depending on whether the liquid was rising or falling within the bed. His experimental results for the latter in soils and those of Puri (*33*) for sands show an average value of $6\gamma/r$. Batel (*3*) suggested

$$h_c = C_1 \frac{2\gamma \cos \alpha}{\rho} \frac{1}{G} \left[\frac{d_m + d_h}{2} \right]^{1.2} \quad (1)$$

which includes particle-size distribution.

Dombrowski and Brownell (*8*) correlated capillary height h_c with a capillary drain number

$$Z = \left(\frac{K}{g} \right)^{\frac{1}{2}} \left[\frac{\rho G + \Delta P / L'}{\gamma / g \cdot \cos \alpha} \right]$$

finding a relation

$$h_c = 0.275/Z \quad (2)$$

Their data for gravity drainage from spherical particles and those of Uren and Difrawi (*36*) for capillary rise agree fairly well with Equation (2). The absence of the hysteresis mentioned by Haines may be a result of an overestimation of h_c due to the visual technique of Uren and Difrawi. The form of the capillary drain number has been confirmed by an analysis (*31*) based on Poiseuilles' equation for laminar motion in a capillary, Darcy's law, and the equation for capillary rise in a small tube. Recent experimental work (*31*) has shown good agreement with Equation (2) for beds of spherical particles and poor agreement for beds of kieselguhr and chalk. This leads to the conclusion that for spherical particles the Dombrowski

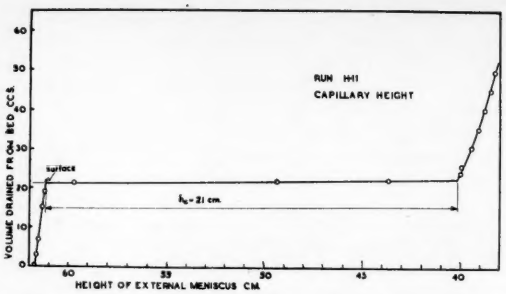

Fig. 1. Capillary height measured by Haine's technique.

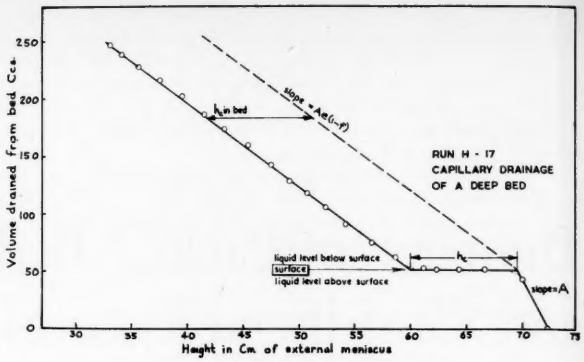

Fig. 2. Capillary drainage of a deep bed.

equation may be used, but for others h_c must be measured.

Experimental

The capillary height h_c for various packed materials was measured with a Haines apparatus for liquids of various surface tensions. Figure 1 shows a typical test for 0.036-cm.–diameter spheres with distilled water, the suction necessary to drag the liquid down into the bed being equivalent to a water-column h_c of 21 cm. A major premise in the development of the drainage equation is that h_c is a constant retarding force throughout the bed. Figure 2, which is the result of a Haines run on a deep bed, shows experimental proof of this. Moving from right to left as the liquid surface falls to the bed level, the slope corresponds to the area A of the open tube. As the liquid attempts to enter the bed, a suction of h_c is required. Thereafter the liquid falls through the bed following a line of constant slope which corresponds to the free pore volume of the drained bed. Since sufficient time elapsed between readings (30 min.) to eliminate dynamic effects, the residual moisture in the drained pores was constant, and, therefore, the capillary height h_c was constant and equal to the entry value of the bed.

Permanent Residual Liquid

The retention of liquid at contact points in a packed bed has not been analyzed in detail. Ferguson (*10*) has solved the case for a sphere in contact with a horizontal liquid surface, and Bashforth and Adams (*1*) have provided a lengthy step-by-step solution to the case of drops resting on a horizontal plane. Batel (*2*) has considered the problem for two spheres in horizontal contact, but a misapplication of the Laplace surface-tension equation seems to have been made, and his development is applicable only to two long cylinders in contact.

Brownell and Katz (*4*) correlated residual liquid (capillary liquid included) with the capillary number

$$Z_0 = \frac{K\Delta P}{g\gamma L'}$$

giving the equation

$$S_r = \frac{Z_0^{-0.264}}{86.3} \qquad (3)$$

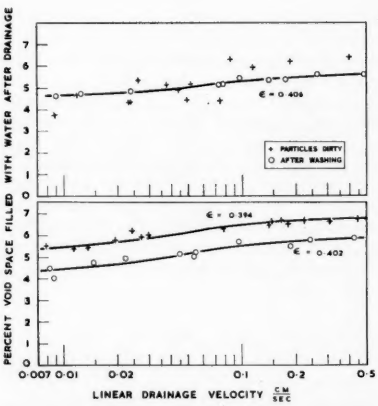

Fig. 3. Effect of drainage velocity on residual moisture in a packed bed of glass spheres with average particle diameter of 0.26 cm.

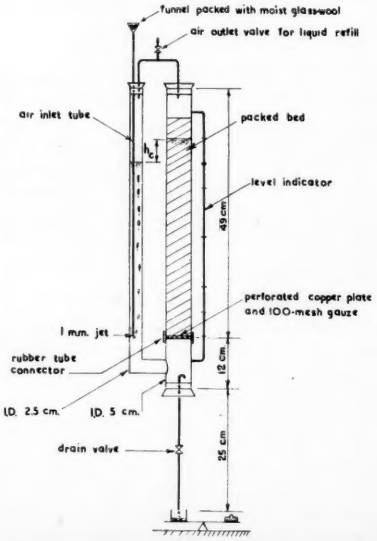

Fig. 4. Constant drainage-velocity apparatus for deep beds.

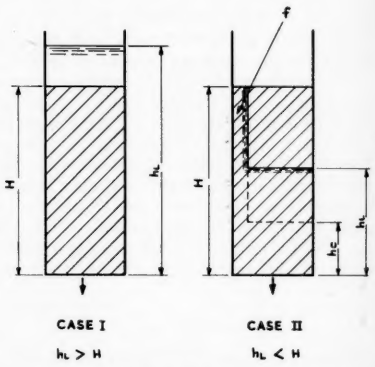

Fig. 5. Simple model of drainage mechanism in a packed bed.

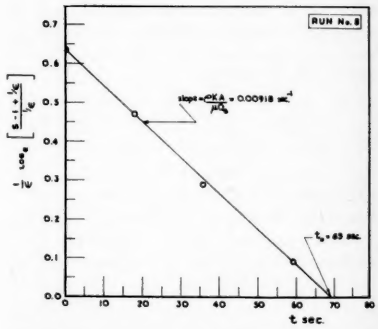

Fig. 6. Evaluation of permeability function in Equation (9).

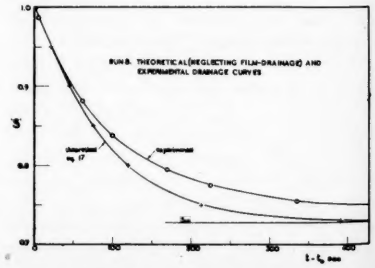

Fig. 7. Comparison of experimental drainage curves with theoretical equation (17), film drainage neglected.

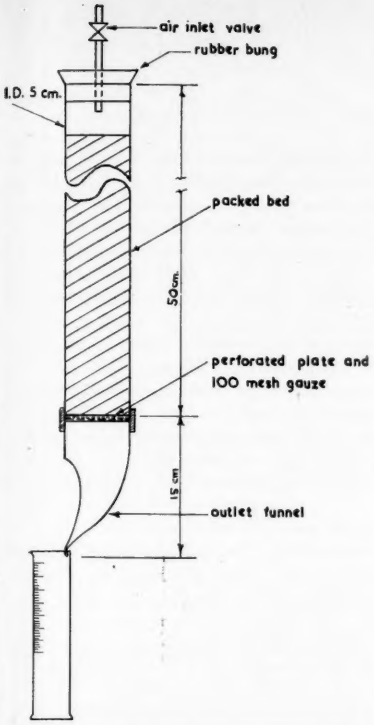

Fig. 8. Gravity drainage apparatus for deep beds.

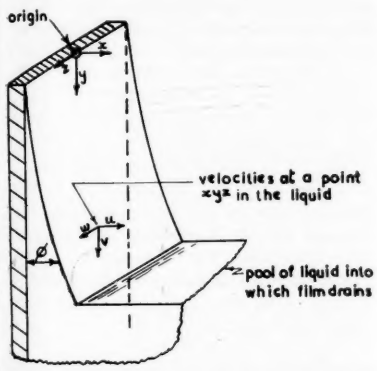

Fig. 9. Theoretical model of film drainage.

Dombrowski and Brownell (*8*) suggested that the permanent residual liquid never rises much above 7½% when Z_0 lies between 10^{-6} and unity, excluding moisture absorbed in the particles themselves. This is dubious. Keen (*27*), in an analysis of wedge moisture between spheres, showed that fusion would occur with an f value of 18.2 and 24.3% for the most open and closest packing arrangements respectively. This condition presumably must arise somewhere in the above-mentioned range of Z_0.

Batel (*3*) has suggested an equation which on analysis (*31*) reduces to

$$f = k_5 Z_0^{-0.25} \qquad (4)$$

This is similar to the Brownell equation (*3*) except that k_5 is an unknown function of porosity of the bed and sphericity of the particles. Experimental data are too few to allow a final choice between Equations (3) and (4).

Experimental

Observation of the meniscus formed between two 1-cm. glass spheres in vertical contact was made through a Vernier microscope. The volumes of the menisci formed from various liquids were measured by means of a corrected form of the equation stated by DallaValle (*7*). During these experiments a slight effect of formation velocity on meniscus size was noted. This effect was further tested by measuring the liquid retention in packed beds after lowering the liquid surface through a position of the bed at a fixed rate.

Constant Drainage-Velocity Apparatus

The apparatus in Figure 4 provided a constant pressure drop across the drain valve while the drainage of the bed proceeded, thus maintaining a constant drainage velocity for a given valve setting. An external level indicator showed an arbitrary level for the liquid in the bed, the indicated level differing from the actual level because of the difference of capillary effect in the bed and in the indicator tube. This difference was constant for a specific packed bed.

The permanent residual moisture in 39-cm.-deep beds of 0.26-cm.-diameter glass spheres and 33-cm.-deep beds of 1.00-cm.-diameter glass spheres was measured by weighing the drainage from the beds. The times allowed for drainage were generally considerably longer than the period from Equation (23) for the reduction of unstable-film drainage liquid to 0.1% of the void volume.

Results

Figure 3 shows data for 0.26-cm. glass spheres after drainage had ceased, the results being expressed as f, the fraction of the voids remaining filled. The influence of small amounts of dirt in the bed is shown by the lack of reproducibility. There was also a marked influence of changes in bed porosity.

DEVELOPMENT OF DRAINAGE EQUATIONS WITH FILM DRAINAGE NEGLECTED

The first steps in the formation of equations for the flow of liquid within the packed bed were based on the laminar movement of liquid as the liquid surface at h_L fell toward the upper surface of the bed at height H above the outlet datum (Figure 5), followed by a flow through the bed as h_L moved from H down to the final capillary height h_c. The pressure is taken as atmospheric at the surface h_L and at the datum of the outlet face.

Case when $h_L > H$

For laminar motion through the bed

$$-\frac{dQ}{dt} = \frac{h_L}{H}\frac{\rho K A}{\mu} \qquad (5)$$

$$Q = Q_s + (h_L - H)A \qquad (6)$$

whence

$$-\frac{dQ}{dt} = \left[\frac{Q - Q_s + HA}{HA}\right]\frac{\rho K A}{\mu} \qquad (7)$$

Expressing the moisture content as the fraction, $S = Q/Q_s$, of the voidage yields

$$-\frac{dS}{dt} = \left[\frac{S - 1 + 1/\epsilon}{1/\epsilon}\right]\frac{\rho K A}{\mu Q_s} \qquad (8)$$

Integrating this equation between the limits $S = S$ at $t = t$ and $S = 1$ when $t = t_0$ as the liquid level reaches the surface of the bed gives

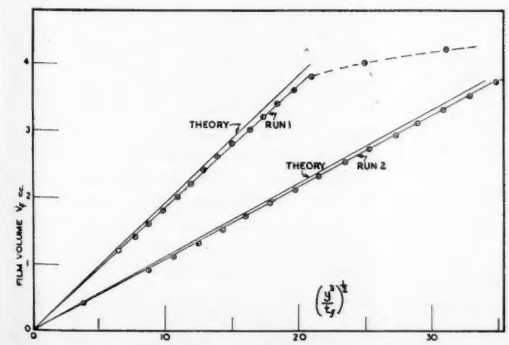

Fig. 10. Film drainage in a 50-ml. burette as a test of Equation (23).

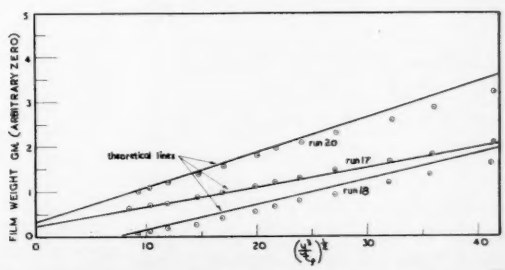

Fig. 11. Drainage of oil films from vertical strings of beads compared with Equation (23), with $L = \pi d$.

$$\log_e \left[\frac{S - 1 + 1/\epsilon}{1/\epsilon}\right] = \frac{\epsilon\rho KA}{\mu Q_s}(t_0 - t) \qquad (9)$$

This equation can be used to analyze data to give K, and to define t_0 as shown in Figure 6.

Case when $H > h_L > h_c$

Neglecting any film drainage on a surface exposed by the falling-liquid surface, one may base an equation for this case on the following assumptions:

1. K is constant for all positions in the submerged bed
2. The capillary force retards the drainage from the bed with a force equal to suction height h_c, which is constant for all positions of the liquid surface within the bed.
3. The permanent residual liquid in the bed above the liquid surface is of constant f throughout the drained portion of the bed
4. The equivalent of flow equation (5) applies to the moving fluid in the submerged part of the bed
5. Deceleration forces may be neglected in the slow changes of mean velocity in the liquid.

$$-\frac{dQ}{dt} = \left(\frac{h_L - h_c}{h_L}\right)\frac{\rho KA}{\mu} \qquad (10)$$

$$Q = h_L A\epsilon + (H - h_L)A\epsilon f \qquad (11)$$

whence

$$-\frac{dQ}{dt} = \left[\frac{Q - HA\epsilon f - h_c A\epsilon(1-f)}{Q - HA\epsilon f}\right]\frac{\rho KA}{\mu} \qquad (12)$$

The integration of Equation (12) may be simplified by substituting the terms Q_s, Q_c and Q_∞ for the values of saturated volume, capillary-height volume, and final liquid volume respectively, where

$$Q_\infty = (H - h_c)A\epsilon f + h_c A\epsilon \qquad (13)$$

$$Q_c = h_c A\epsilon \qquad (14)$$

$$Q_s = HA\epsilon. \qquad (15)$$

Integrating the expression between $Q = Q_s$ at $t = t_0$ and $Q = Q$ at $t = t$, when $t > t_0$ gives

$$Q_s - Q + Q_c(1 - f)\log_e\left[\frac{Q_s - Q_\infty}{Q - Q_\infty}\right] = \frac{\rho KA}{\mu}(t - t_0) \qquad (16)$$

or in terms of saturated fraction, S

$$1 - S + S_c(1 - f)\log_e\left[\frac{1 - S_\infty}{S - S_\infty}\right] = \frac{\rho KA}{\mu Q_s}(t - t_0) \qquad (17)$$

It may be observed that the gradient of the S, t curve is independent of f when the bed is saturated, that is, when $Q = Q_s$ and $S = 1$:

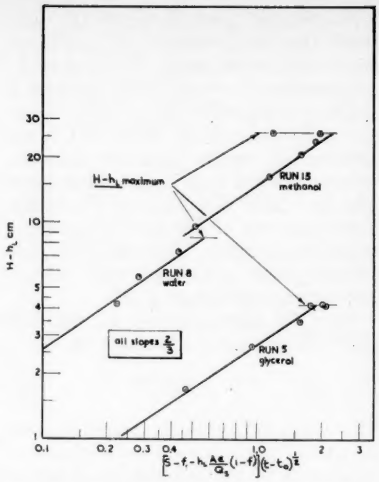

Fig. 12. Film-drainage test on gravity-drainage runs with packed beds.

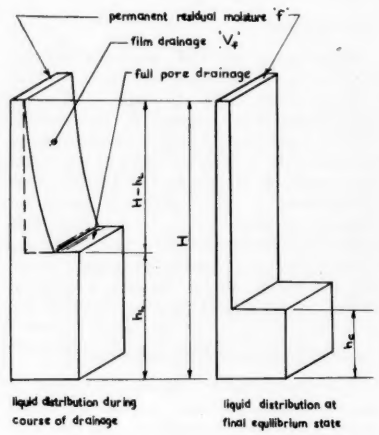
permanent residual moisture 'f'
film drainage 'V_f'
full pore drainage
liquid distribution during course of drainage
liquid distribution at final equilibrium state

Fig. 13. Models of liquid distribution in packed bed.

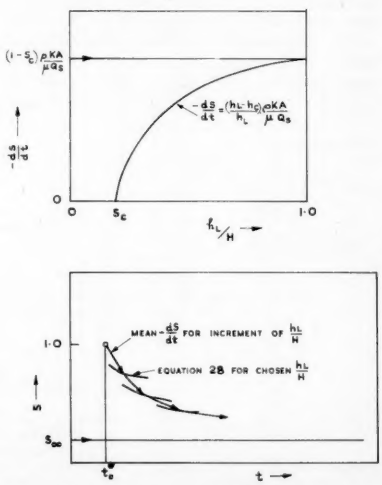

Fig. 14. Method of graphical integration combining Equations (24) and (28).

$$-\frac{dQ}{dt} = \left[\frac{Q_s - Q_c}{Q_s}\right]\frac{\rho KA}{\mu} \qquad (18)$$

$$-\frac{dS}{dt} = (1 - S_c)\frac{\rho KA}{\mu Q_s} \qquad (19)$$

Equations (18) and (19) may be used to evaluate the capillary suction height h_c from Q_c or S_c provided that it is a reasonable fraction of the bed and that the permeability K is known accurately.

Batel (3) also derived an equation similar to Equation (17) but discussed it only qualitatively. The foregoing equations were tested for drainage of water, water-glycerol solutions, ethyl alcohol, and methyl alcohol on various beds of glass spheres. The drainage rates when $h_L > H$ were analyzed by Equation (9), providing a measure of K and the time when the liquid reached the bed surface. The S, t function was drawn on a large scale and (dS/dt) found for $S = 1$ to evaluate h_c. The difference in dS/dt just above and below the limit $h_L = H$ is marked. Above the limit

$$-\frac{dS}{dt} = \frac{\rho KA}{\mu Q_s}, \text{ when } h_L \to H \qquad (20)$$

whereas a lower value from Equation (19) is obtained when h_L is just below H. The values for h_c compared within 5% with values found from Haines apparatus for beds of spheres 0.036 cm. in diameter. Although this drainage technique can be used for h_c determination, the Haines technique is more accurate. The permanent residual moisture f was found from Equation (13) and the S, t curve calculated from Equation (17). The deviation of the experimental data from this theoretical equation is exemplified in Figure 7. Calculation showed that it was justifiable to neglect the kinetic head change on the liquid entering the bed and that the flow regime was laminar. All tests showed the same discrepancies; the theoretical Equation (17) predicted a more rapid approach to the final state than was found.

There are two possible explanations for this: either variation in suction height h_c as the surface falls through the bed, or film drainage of liquid from the packing above the surface. Although the constancy of h_c with position in pure liquids has been proved experimentally, a very marked effect did occur in the presence of surface-active agents. It is well known that liquids containing surface-active agents display variations in surface tension under dynamic conditions, owing to the significant time required for molecular orientation at freshly formed surfaces. The variation in dynamic surface tension gives the effect of a false h_c, falling toward the value of h_c measured in the slow movements of a Haines test. In slow drainage tests at constant rate with surface-active agents, the variation in h_c is not observed, the value for h_c as

in Figure 2 remaining constant at all positions in the bed, with $h_c \propto 1/\gamma$ and having the same value as found at the bed surface.

This effect cannot be detected with pure liquids, and the explanation of the delay in bed drainage appeared to be the presence of film drainage over the exposed surfaces of the packing above the liquid surface. The effect was sufficiently significant to require a modification of Equation (17). The dynamic surface-tension problem need not be considered further in the present study, which is confined to liquids which did not contain active surface agents. The predominant deviating influence from the model (Figure 5) giving Equation (17) was undoubtedly the presence of film drainage of liquid across the surfaces of the packing after the liquid level had passed through the bed.

Gravity Drainage Apparatus

The apparatus used for run 5 consisted of a small cylindrical cell of diameter 4.9 cm. and depth 10 cm., with 100-mesh copper gauze used as a bed support. The cell was hung from a glass cantilever, the deflection of which was followed by a capacitance recorder.

Runs 7 to 16 were carried out on deeper beds in the simple apparatus shown in Figure 8, the outlet funnel being designed to minimize liquid holdup and to give smooth flow. The drainage-volume rate was obtained by timing the level in the volumetric measuring receiver through manual operation of an electrical marker on a fast ticker tape as the level passed calibration marks. Beds were made by dumping packing into the tube filled with liquid. Care was required to avoid disturbances of the tube contents which could favor a definite size distribution vertically in the bed, with consequent variations in h_c. To start a run it was necessary only to turn the air valve to the full open position.

DEVELOPMENT OF FILM DRAINAGE THEORY

A modifying function is required to include the effect of film drainage in the S, t function. Jeffreys (*26*) published an approximate solution to the Stokes-Navier equation for film drainage from a vertical plane. His expression for the liquid profile as a function of time may be integrated to give the volume of liquid in the film varying with time.

The Stokes-Navier equation for an incompressible fluid falling down a vertical plane reduces to

$$-\rho g = \mu \frac{\partial^2 v}{\partial x^2} \qquad (21)$$

if it is assumed that for the coordinates in Figure 9,

(1) no forces act horizontally along the z direction; $\partial v/\partial z = 0$, $\partial^2 v/\partial z^2 = 0$, $w = 0$

(2) velocity in the x direction is small; $u \rightarrow 0$

(3) change in vertical velocity with height is small; $\partial v/\partial y \rightarrow 0$, and its rate of change is small; $\partial^2 v/\partial y^2 \rightarrow 0$

(4) vertical acceleration is negligible except near the start of drainage; $\partial v/\partial t \rightarrow 0$, $t_f \neq 0$

Equation (21) has been applied as an approximation to similar problems by Nusselt (*32*) and by Kocatas and Cornell (*29*). The expression obtained by Jeffreys for the film thickness at a given level y is

$$\phi = \sqrt{\frac{\mu y}{\rho g t_f}} \qquad (22)$$

This expression may be integrated to give the volume of the film V_f at time t_f when y is the height of the top of the film above the pool into which it drains. For breadth of film L,

$$\partial V_f = L\phi \, \partial y$$

$$V_f = \frac{2}{3} L \sqrt{\frac{\mu y^3}{\rho g t_f}} \qquad (23)$$

Jeffreys did not test his equation (22). Morey (*30*) applied the form to evaluate the correction for wet gas meters and found better agreement with an exponent of 0.63 rather than 0.5. It seemed necessary to test these equations by the drainage of vertical surfaces.

The application to vertical walls is clear from the bases of derivation, with the expectation that the equations will fail in the initial stages of a film formation when accelerations are significant. The application to packed beds must rest on the assumption that the only major difference occurs in the interpretation of the significant breadth of film L.

Film-drainage Experiments

Initial experiments were conducted on the drainage of the wall of a 50-ml. glass burette, which effectively provided a plain wall. The liquid level in the burette was dropped rapidly from the top to the bottom graduation. The upward movement of the meniscus was then timed by observation through a traveling microscope. The results are shown in Figure 10 with V_f as a function of t_f and y. Run 1 for $\mu/\rho = 689$ centistokes shows the deviation from the equation expected by Jeffreys during the rapid acceleration period over a short time. The remaining points over periods up to hours fitted the gradient $\frac{2}{3} L(\mu/\rho g)^{1/2}$ within 3 to 4%. The experimental measurements gave the liquid drained from the film, and the first run was allowed to proceed for 60 hr. to obtain residual V_f for $t_f = \infty$, enabling the calculation of the true variable V_f value for each t_f. The data in run 2 showed similar agreement for a liquid of kinematic viscosity of 228 centistokes. Apart from a very short time at the start, the film drainage from a vertical plane agrees well with Equation (23).

Experiments were also made with vertical strings of spherical beads. The string was dipped in oils of various viscosities and immediately hung on a steel-rod cantilever. The deflection of this beam was followed by a high-frequency capacitance recorder, the record being available from calibration as a weight-time function for the drainage from the vertical string of beads. The mean effective breadth L of the vertical plane is difficult to specify, and equally so is the detailed function of the flow throughout the film draining over the beads. As an approximation, a value of L was taken as the mean surface area of the dry beads divided by the height of the string, that is, effectively πd. Results were analyzed by plotting an arbitrary weight against $(y^3/t_f)^{1/2}$, giving graphs such as in Figure 11. The rectilinearity of the plots confirmed the power of 0.5 and the near agreement with Equation (23). Data for eighteen runs with kinematic viscosities ranging from 150 to 700 centistokes showed an average agreement within 10% with Equation (23) and no significant variation with kinematic viscosity of the liquid. The variation of 10% around Equation (23) is not important in view of the fact that the drainage function is to be a modification to the main flow equation for liquid moving through the immersed voids. Hewitt (*25*), in allied work on the drainage of tower packing, has found agreement to 3 to 7% using a similar basis for L. He has used the initial condition as liquid flowing over the packing in a steady state. In the bead experiments the initial state is disturbed by the effective increase in gravitational field when the bead string is withdrawn rapidly from the oil. Again the form of Equation (23) appears satisfactory after a short initial period in the drainage.

Preliminary Test of Film Drainage in Packed Beds

In packed beds the presence of film drainage does not influence the driving-force Equation (10), which may be written

$$-\frac{dS}{dt} = \frac{\rho K A}{\mu Q_s} \frac{(h_L - h_c)}{h_L} \qquad (24)$$

but the material-balance Equation (11) must now accommodate the draining film:

$$Q = h_L A\epsilon + (H - h_L) f A\epsilon + \frac{Q_s B (H - h_L)^{\frac{1}{2}}}{\sqrt{t_f}} \qquad (25)$$

where B is a constant for a specific liquid and packing. From Equation (25), dividing through by Q_s and rearranging gives

$$\left[S - f - \frac{h_L A\epsilon(1 - f)}{Q_s}\right]\sqrt{t_f} = B(H - h_L)^{\frac{1}{2}} \qquad (26)$$

From the drainage run for a packed bed giving an S, t curve, the first derivative at any time allows the calculation of h_L and $(H - h_L)$ from Equation (24). These values, inserted in the groups of Equation (26), give the plot in Figure 12. Data for various liquids in a packing of glass spheres appear to conform to Equation (26), but it will be noticed that the data become more erratic at high $(H - h_L)$ values, where $h_L \to h_e$ and $t_f = (t - t_0) \to \infty$, owing to the difficulty of measuring dS/dt accurately. The agreement is such that the use of the Jeffreys form of film-drainage equation is justified in packed-bed analysis, despite its inadequacy for a short time after film drainage starts.

Complete Drainage Equation

The model now becomes as in Figure 13, with the conditions for Equation (11) modified by the presence of V_f expressed as

$$V_f = \frac{2}{3} L \sqrt{\frac{\mu(H - h_L)^3}{\rho g(t - t_0)}} \qquad (27)$$

$$L = s_0 A$$

and thus S at any time becomes

$$S = \frac{h_L}{H}(1 - f) + f + \frac{2}{3}\frac{s_0}{\epsilon}\sqrt{\frac{H\mu}{\rho g}}\sqrt{\frac{(1 - h_L/H)^3}{(t - t_0)}} \qquad (28)$$

This equation and Equation (24) form the bases for the complete drainage equation for the packed bed in a gravitational field.

Graphical Integration

The integration of these equations has not yet been solved, but two approaches have proved successful. A graphical integration was performed to test the equations for a specific run by plotting the quadratic equations for S against $(t - t_0)$ for various h_L/H. For decrements in S, starting from $S = 1$ at $t = t_0$, a mean slope from Equation (24) was used to draw a straight line to a (S, t) curve for the smaller value h_L/H; a progressive use of this approximation shown in Figure 14 provided the S, t curve. Figure 15 shows the comparison between the calculated and experimental data.

This method was tedious, but it served to show that the equations gave a satisfactory solution to the whole drainage problem.

Series Solution

In default of a successful integration, a series-solution method has been adopted. It is of advantage to simplify the equations for this purpose by letting

$$a = \frac{h_e}{H}\frac{\rho KA}{\mu Q_s} \qquad (29)$$

$$b = \frac{\rho KA}{\mu Q_s} \qquad (30)$$

$$p = (1 - f) \qquad (31)$$

$$k_1 = \frac{2}{3}\frac{s_0}{\epsilon}\sqrt{\frac{H\mu}{\rho g}} \qquad (32)$$

$$X = \left[1 - \frac{h_L}{H}\right] \qquad (33)$$

Substitution in Equations (24) and (28) leads to

$$\frac{dS}{dt} = \frac{a}{1 - X} - b \qquad (34)$$

$$S = 1 - pX + k_1\left[\frac{X^3}{t - t_0}\right]^{\frac{1}{2}} \qquad (35)$$

where all the terms are positive. It should be noted that Equations (34) and (35) are the two basic differential equations. For any specific case, a, b, p, and k_1 are constants.

To eliminate S and find X, the equations can be solved for the case when $k_1 = 0$, and then a correction introduced for the film drainage. The values of S can then be estimated.

Case when $k_1 = 0$

Combining Equations (34) and (35) and integrating with $X = 0$ when $t = t_0$ and with $X = X$ when $t = t$ gives

$$(t - t_0) = \frac{p}{b}\left[X - \frac{a}{b}\log_e\left(1 - \frac{bX}{b - a}\right)\right] = \psi_0(X) \qquad (36)$$

$\psi_0(X)$ can be expressed as a series

$$\psi_0(X) = a_1X + a_2X^2 + a_3X^3 + \cdots \qquad (37)$$

The values of a_1, a_2, etc., can be obtained by expanding the logarithm in Equation (36) and equating coefficients

$$a_1 = p/(b - a) \qquad (38)$$

$$a_2 = pa/2(b - a)^2 \qquad (38a)$$

$$a_n = \frac{apb^{n-2}}{n(b - a)^n} \quad (n \neq 1) \qquad (38b)$$

The solution to Equations (24) and (28) is now based on $\psi_0(X)$ and expressed as a series.

Case with $k_1 \neq 0$

Equation (36) may be adjusted to the case when $k_1 \neq 0$ by the addition of another series in X. Then, by manipulating the equations and equating the coefficients, a general solution of the film drainage equations is obtained.

If

$$(t - t_0) = \chi_0(X) + \chi_1(X) \qquad (39)$$

and

$$\psi_1 = b_1X + b_2X^2 + b_3X^3 + \cdots \qquad (40)$$

combining Equation (34) with the differential dS/dX from Equation (35) gives

$$\left[\frac{a - b + bX}{1 - X}\right][\psi_0{}^1(X) + \psi_1{}^1(X)] = -p + k_1\frac{d}{dX}\left[\frac{X^3}{\psi_0 + \psi_1}\right]^{\frac{1}{2}} \qquad (41)$$

and substituting the value of p, from the first derivative of Equation (36), in Equation (41) yields

$$\left[\frac{a - b + bX}{1 - X}\right][\psi_1{}^1(X)] = k_1\frac{d}{dX}\left[\frac{X^3}{\psi_0 + \psi_1}\right]^{\frac{1}{2}} \qquad (42)$$

It is an advantage to introduce a new series to reduce the right-hand side of Equation (42) to a form easier to handle.

If

$$\frac{X^3}{\psi_0 + \psi_1} = [c_1X + c_2X^2 + c_3X^3 + \cdots]^2 \qquad (43)$$

coefficients c_1, c_2, c_3 . . . must be evaluated in terms of a_1, a_2, a_3 . . . and b_1, b_2, b_3 . . . . Inserting Equations (37) and (40) in Equation (43) and equating coefficients of powers of X gives

$$c_1 = \sqrt{\frac{1}{a_1 + b_1}} \qquad (44)$$

and since $[X^3/(t - t_0)]^{1/2} > 0$, the positive root will be used.

$$c_2 = -\frac{a_2 + b_2}{2(a_1 + b_1)^{\frac{1}{2}}} \qquad (44a)$$

$$c_3 = \frac{3}{8}\frac{(a_2 + b_2)^2}{(a_1 + b_1)^{5/2}} - \frac{a_3 + b_3}{2(a_1 + b_1)^{\frac{1}{2}}} \qquad (44b)$$

From Equation (42) it is possible to write

$$(a - b + bX)(b_1 + 2b_2X + 3b_3X^3 + \cdots) = k_1(1 - X)[c_1 + 2c_2X + 3c_3X^2 + \cdots] \qquad (45)$$

Equating coefficients again gives the terms of the ψ_1 series as functions of the original constants in the basic equations.

Constant b_1

$$(a - b)b_1 = k_1c_1 \qquad (46)$$

and from Equations (38) and (44)

$$(b - a)^2b_1{}^3 + (b - a)pb_1{}^2 - k_1{}^2 = 0 \qquad (47)$$

where

$$(b - a) > 0$$

TABLE 1. SUMMARY OF PACKED-BED AND LIQUID PROPERTIES FOR GRAVITY DRAINAGE RUNS ON BEDS OF GLASS SPHERES

Run	d_m, cm.	H, cm.	A, sq. cm.	ϵ	Liquid	ρ, g./cc.	μ, poise	γ, dyne./cm.	h_c, cm.	f
5	0.26	6.2	18.9	0.415	Glycerol	1.25	4.72	66	2.08*	0.048
8	0.036	29.6	19.7	0.405	Water	1.00	0.010	73	21.1*	0.052
9	0.036	34.5	19.7	0.400	Water	1.00	0.010	73	20.5*	0.116
15	0.036	34.0	19.7	0.396	Methanol	0.796	0.00606	22.8	8.00†	0.146
16	0.036	33.6	18.8	0.408	Ethanol	0.793	0.0123	22	7.65†	0.127

*Measured in drainage apparatus, from Equation (19), by use of measured $-dS/dt$ at h_L just below H.
†Measured in similar bed in separate Haines capillary suction-height apparatus.

Constant b_2

$$b_2\left[2(a-b)+\frac{k_1}{(a_1+b_1)^{\frac{1}{2}}}\right] \quad (48)$$
$$=-bb_1-\frac{k_1a_2}{(a_1+b_1)^{\frac{1}{2}}}-\frac{k_1}{(a_1+b_1)^{\frac{1}{2}}}$$

Constant b_3

$$b_3\left[3(a-b)+\frac{3}{2}\frac{k_1}{(a_1+b_1)^{\frac{1}{2}}}\right]$$
$$=-2bb_2+\frac{9}{8}\frac{k_1(a_2+b_2)^2}{(a_1+b_1)^{5/2}}$$
$$-\frac{3}{2}\frac{k_1a_3}{(a_1+b_1)^{\frac{1}{2}}}+\frac{k_1(a_2+b_2)}{(a_1+b_1)^{\frac{1}{2}}} \quad (49)$$

More terms may be evaluated but in most cases only b_1 and b_2 are necessary to obtain an equation of accuracy comparable to the constants a, b, p, etc.

A slight problem arises in the calculation of the first term of the ψ_1 series, b_1. It requires the solution of a cubic equation (47), only one of the three roots being correct. The correct root is easy to select, and the limits of this root can be established.

The correct root b_1

The general pattern of Equation (46) is

$$\theta(b_1)=(b-a)^2{b_1}^3+(b-a)p{b_1}^2-{k_1}^2 \quad (50)$$
$$(b-a)>0$$

now

$$\theta(\infty)=\infty$$
$$\theta(-\infty)=-\infty$$
$$\theta(0)=-{k_1}^2$$
$$\theta[-p/(b-a)]=-{k_1}^2$$

The first derivative

$$\frac{d\theta}{db_1}=3(b-a)^2{b_1}^2+2(b-a)pb_1 \quad (51)$$

Now $d\theta/db_1=0$, when $b_1=0$

$$\frac{d\theta}{db_1}=0, \quad \text{when} \quad b_1=-\frac{2}{3}\frac{p}{b-a}$$

The second derivative

$$\frac{d^2\theta}{{db_1}^2}=6(b-a)^2b_1+2(b-a)p \quad (52)$$

and

$$\frac{d^2\theta}{{db_1}^2}=0 \quad \text{when} \quad b_1=\frac{1}{3}\frac{p}{b-a}$$

Thus there is a pattern with

(1) a point of inflection at $b_1=\frac{1}{3}p/(b-a)$
(2) a maximum at $b_1=-\frac{2}{3}p/(b-a)$
(3) a minimum at $b_1=0$

and the maximum value of θ is

$$\theta\left[-\frac{2}{3}\frac{p}{b-a}\right]=\frac{4}{27}\left(\frac{p^3}{b-a}\right)-{k_1}^2 \quad (53)$$

From Equation (46), b_1 must be negative since $(b-a)>0$ and $c_1>0$. It is therefore necessary to choose between the two negative roots for b_1 where $\theta(b_1)=0$. This can be done by considering Equation (47) for small values of k_1.

As $k_1\to 0$, then $\theta(b_1)\to(b-a)^2{b_1}^3+(b-a)p{b_1}^2\to 0$ which has roots $b_1=0$ and $b_1=p/(b-a)$. But as $k_1\to 0$, $\psi_1\to 0$, and, from Equation (39), then $b_1\to 0$, $b_2\to 0\ldots$. Thus the correct root for b_1 lies between $-\frac{2}{3}p/(b-a)$ and zero in all cases.

An interesting variation arises when there is no real root for b_1 between these limits. This means that ${k_1}^2>4/27\,(p^3)/(b-a)$. Analysis of this situation, including the Kozeny equation

$${s_0}^2=k_4\frac{\epsilon^3}{5}\frac{g}{K} \quad (54)$$

shows that in this case

$$\frac{(1-f)^3}{(1-S_c)}>\frac{3}{5}$$

which is not a clear conclusion. It is tacitly assumed that this occurs when ${k_1}^2$ is large compared with the other variables, that is, when the film drainage is the dominant problem and the permeability is large, the level h_L approaching h_c in a very short time. In this event X will quickly assume its final value $(1-h_c/H)$ or $(1-S_c)$, and Equation (35) become

$$S=1-p(1-S_c)+k_1\left[\frac{(1-S_c)^3}{t-t_0}\right]^{\frac{1}{2}} \quad (55)$$

or

$$S=S_\infty+k_1\left[\frac{(1-S_c)^3}{t-t_0}\right]^{\frac{1}{2}} \quad (56)$$

Thus, when ${k_1}^2>4/27\,(p^3)/(b-a)$, Equation (56) may be used alone to describe the S, t function, with the caution that it does not hold when $(t-t_0)$ approaches zero.

Summary of Mathematical Solution

The mathematical solution gives the two simultaneous equations

$$(t-t_0)=\frac{p}{b}\left[X-\frac{a}{b}\log_e\left(1-\frac{bX}{b-a}\right)\right]+b_1X+b_2X^2+b_3X^3 \quad (57)$$

$$S=1-pX+k_1\left[\frac{X^3}{t-t_0}\right]^{\frac{1}{2}} \quad (35)$$

If $k_1=0$, then $b_1, b_2\ldots=0$, and the combination of these equations gives Equation (17). This solution for zero film drainage from the wetted packing is only a limit, all actual cases having $k_1>0$ and significant film drainage. Knowing the constants enumerated above makes it possible to find the relationship between t and X from Equation (57) and the S, t function by substitution in Equation (35).

EXPERIMENTAL RESULTS

Drainage in a Gravitational Field

The data for run 16 were calculated in this way and the results are plotted on Fig. 15. They show very good agreement with the experimental results. Another typical experimental result is shown in Figure 16, confirming the success of the proposed Equations (35, 57). The S, t curves with film drainage neglected are shown by plotting Equation (17), an indication of the significance of the film-drainage correction.

Experimental data for various liquids (Table 1) showed excellent agreement with the analysis proposed and appear to confirm the validity of both the series functions and the drainage model postulated. Until a suitable integrated solution is available for S, the series solution seems adequate. This method of solution may appear complicated, but the following example shows the method of procedure.

Example of drainage calculation

The conditions of the chosen problem correspond to those of run 5 except that the residual saturation $100f$ is taken as 7% instead of the experimental value of 5% to demonstrate that a small change in f will remove the discrepancy between the calculated and experimental values on

Figure 16 and give an exact fit. This adjustment is within the limit of experimental error in this case, as the permanent residual moisture $f = 0.05$ was measured on the electronic weighing balance after standing for several hours.

PROBLEM

Calculate the saturation of a bed with time when it is allowed to drain from fully saturated to the final equilibrium state. The capillary drain height h_c of this bed with the liquid used is 2.08 cm., the bed permeability K is 0.0647 cc./sec.^{2}, and the permanent residual moisture f is equivalent to 7%.

DATA

Bed

Type	glass ballotini
area, A	18.9 sq. cm.
Depth, H	6.2 cm.
Average particle size, d	2.6 mm.
Sphericity	1.0
Total void volume, Q_s	48.6 cc.
Voidage, ϵ	0.415
Liquid	glycerine and water
Density, ρ	1.25 g./cc.
Viscosity, μ	472 centipoise
Surface tension, γ	66 dynes/cm.

X	ψ_0	b_1X
0.0	0	0
0.1	21.6	−6.95
0.2	44.5	−13.9
0.3	69.7	−20.8
0.4	98.6	−27.8
0.5	135	−34.7
0.6	193	−41.7
0.64	244	−44.5
0.66	331	−45.8
0.663	395	−46

CALCULATION

(a) Calculation of Constants a, b, p, k_1, X_∞, a_1, a_2

From Equation (29), $a = 0.00224$ sec.$^{-1}$
From Equation (30), $b = 0.00668$ sec.$^{-1}$
From Equation (31), $p = 0.93$
From Equations (32) and (54), with k_4 taken as unity, $k^1 = 3.65$ sec.$^{1/2}$
From Equation (33), with $h_L = h_c$, $X_\infty = 0.664$
From Equation (38), $a_1 = 210$ sec.
From Equation (38a), $a_2 = 53$ sec.

X	$t - t_0 = \psi_0 + \psi_1$	pX
0.0	0	0
0.1	14.6	0.093
0.2	30.4	0.186
0.3	48.6	0.279
0.4	69.8	0.372
0.5	98.8	0.465
0.6	149	0.559
0.64	197	0.596
0.66	283	0.614
0.663	346	0.617

(b) Test for the Significance of Permeability

Equation (53) will be used to see whether there is a real value of b_1. If b_1 is imaginary, the simplified Equation (56) will be used for S. If b_1 is real, as in this case, the series solution will be used. Quantity b_1 is real since $4/27(p^3)/(b - a) - k_1^2 = 13.5$; i.e., > 0.

(c) Calculation of b_1, the First Term of the Series

The cubic equation (47) is solved for the root b_1, within the limits of zero and $-\frac{2}{3}(p)/(b - a) = -140$. The solution is $b_1 = -69.5$ sec.

(d) Calculation of b_2, the Second Term of the Series

From Equation (48) and the preceding value of b_1, the value of b_2 becomes −6.0 sec.

(e) Calculation of the X, t Curve

A number of X values are chosen between $X = 0$ and $X = X_\infty$, and for each of these t is calculated from Equation (57), which is more easily handled as

$$t - t_0 = \frac{p}{b}\left[X + S_c \log_e\left(\frac{X_\infty}{X_\infty - X}\right)\right] + b_1X + b_2X^2 + \cdots \qquad (57a)$$

With $t_0 = 0$, at the time the liquid leaves the surface, the following values result:

b_2X^2	ψ_1	$t = \psi_0 + \psi_1$
0	0	0
−0.06	−7.0	14.6
−0.24	−14.1	30.4
−0.36	−21.1	48.6
−0.96	−28.8	69.8
−1.5	−36.2	98.8
−2.2	−43.9	149
−2.5	−47	197
−2.6	−48	283
−2.6	−49	346

$$\psi_0 = \frac{p}{b}\left[X + S_c \log_e \frac{X_\infty}{X_\infty - X}\right]$$

These values show that it is sufficient to take the first two terms of the series, as the second term correction, $b_2 X^2$, amounts to only about 1% of the total time.

(f) Calculation of the S, t Curve

The saturation for any value of time and X calculated above may be obtained from Equation (35) by inserting the simultaneous values of X and $t - t_0$.

$1 - pX$	$k_1[X^3/t]^{1/2}$	S
1.00	0	1.00
0.907	0.030	0.937
0.814	0.059	0.873
0.721	0.086	0.807
0.628	0.111	0.739
0.535	0.129	0.664
0.441	0.139	0.580
0.404	0.133	0.537
0.386	0.116	0.502
0.383	0.106	0.489

The curve of saturation with time is shown in Figure 17. It is interesting to note that the largest value of X chosen for the calculation is very nearly that of the final value, and if it is required to extend the curve further in time, Equation (56) may be used alone. The agreement between experimental data and the calculated S, t function is shown to be satisfactory in Figure 17. The influence of the change of f from 5 to 7% is seen by comparison with Figure 16.

II. HYDROEXTRACTION: DRAINAGE OF PACKED BEDS IN CENTRIFUGAL FIELD

DRAINAGE IN A CENTRIFUGAL FIELD

A detailed analysis of the problem of drainage from a centrifuge cake would involve allowance for the variation with radial position of both centrifugal force and cross sectional area normal to the force. As the cake thickness is usually a small fraction of the basket radius, the use of constant mean values of the quantities will be sufficiently accurate:

$$A_m = \pi(r_c + r_0)Y \qquad (58)$$

$$G = \frac{2\pi^2 n^2 (r_c + r_0)}{g} \qquad (59)$$

The depth of cake perpendicular to the direction of flow and the location of liquid level may be expressed in terms of radii (Figure 18). Thus Equation (24) becomes

$$-\frac{dS}{dt} = \left[\frac{(r_0 - r_L) - h_c}{(r_0 - r_L)}\right]\frac{G\rho KA}{\mu Q_s} \qquad (60)$$

and Equation (28) becomes

$$S = \left(\frac{r_0 - r_L}{r_0 - r_c}\right)(1 - f) + f + \frac{2}{3}\frac{s_0}{\epsilon}\left[\frac{\mu(r_0 - r_c)}{\rho g G}\right]^{\frac{1}{2}} \cdot \left[\frac{\left[1 - \left(\frac{r_0 - r_L}{r_0 - r_c}\right)\right]^3}{t - t_0}\right]^{\frac{1}{2}} \qquad (61)$$

Equations (60) and (61) are of the same form as Equations (24) and (28), and the same series solution will apply.

$$a_c = \frac{h_c}{r_0 - r_c}\frac{G\rho KA}{\mu Q_s} \qquad (62)$$

$$b_c = \frac{G\rho KA}{\mu Q_s} \qquad (63)$$

$$p = (1 - f) \qquad (31)$$

$$k_c = \frac{2}{3}\frac{s_0}{\epsilon}\sqrt{\frac{(r_0 - r_c)\mu}{G\rho g}} \qquad (64)$$

$$X_c = 1 - \left(\frac{r_0 - r_L}{r_0 - r_c}\right) \qquad (65)$$

with these groups Equations (61) and (62) become

$$\frac{dS}{dt} = \frac{a_c}{1 - X_c} - b_c \qquad (66)$$

$$S = 1 - pX_c + k_c\left[\frac{X^3}{t - t_0}\right]^{\frac{1}{2}} \qquad (67)$$

and the series solution is

$$(t-t_0)=\frac{p}{b_c}\left[X_c-\frac{a}{b}\log_e\frac{X_\infty}{X_\infty-X_c}\right]$$
$$+b_1X_c+b_2X_c^2+b_3X_c^3+\cdots \quad (68)$$

where b_1, b_2 . . . are defined as before.

EXPERIMENTAL RESULTS

Experiments were carried out on a 9-in.-diameter vertical-wall perforated-basket centrifuge with beds of chalk and of kieselguhr formed on duck-weave cloth (Table 2). Each cake was formed slowly from a dilute slurry maintained at constant concentration by recirculation to a feed tank to keep the particle-size distribution constant through the cake. The cake thickness was made uniform by disturbance of the adjacent liquid, and the permeability was measured by a probe technique as described previously (*16*). The method involves the measurement of the time Δt required for the liquid surface at $r_L < r_c$ to move from r_{L_1} to r_{L_2}, whence

$$\log_e\left[\frac{r_0^2-r_{L_1}^2}{r_0^2-r_{L_2}^2}\right]=\frac{4\pi^2n^2\rho K\Delta t}{\mu g\log_e r_0/r_c} \quad (69)$$

To measure the drainage, the cakes were allowed to drain to equilibrium at a constant centrifuge speed, the moisture content being found by stopping the centrifuge at intervals and weighing the whole basket and contents to determine the liquid loss. The permanent residual moisture was found in each run by the gravimetric analysis of a sample from the inner surface of the cake. This enabled the calculation of a capillary-drain height by a material balance on the final equilibrium state. The capillary suction height for the chalk material was very high, and consequently the cakes scarcely drained at all.

In Figure 19 the data for three tests on chalk show reasonable agreement with the series solution despite the crude method of obtaining the experimental S, t data. The specific surface per unit volume of bed was obtained for these cakes from the Kozeny Equation (54) without any correction factor, that is, $k_4 = 1$, ϵ ranging from 0.548 to 0.665. The drainage on curve 1C (Figure 19) is so small that h_c may have been greater than the cake thickness ($r_0 - r_c$). The small moisture loss of 1½% could have been due to the slight contraction of the cake as the liquid level penetrated the surface, although the probe survey did not show contraction within 1%.

The kieselguhr cakes had lower h_c values than the chalk and drained to lower S_∞ values, improving the accuracy of the tests. In each case the data showed that with the high permeability the film drainage was dominant. Thus the S, t curves were adequately expressed by

$$S = S_\infty + k_c\left[\frac{(1-S_c)^3}{t-t_0}\right]^{\frac{1}{3}} \quad (70)$$

A problem arose in the calculation of specific surface of these cakes owing to their high porosities of 0.825 to 0.840. Rose (*34*) suggests a correction factor of 9 or 10 on k_4 in Equation (54) when determining S_0 by the gas permeability method for porosities of this range. The calculated values in Figure 20 show good agreement with the experimental results when using a correction factor of 1.3 to the specific surface determined from liquid permeability.

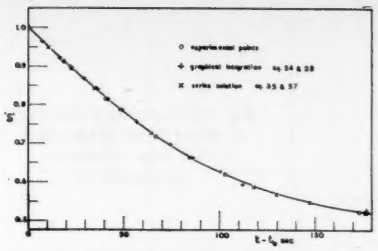

Fig. 15. Graphical integration and series solution for run 16.

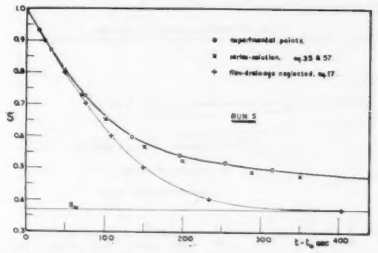

Fig. 16. Gravity drainage of glycerol from a packed bed.

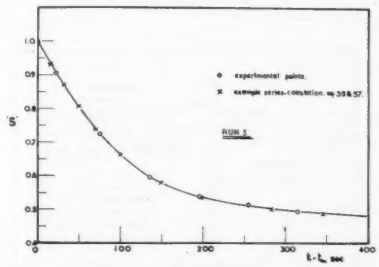

Fig. 17. Example of series calculation on data from run 5 with f equivalent to 7% for comparison with the data from f = 5% in Fig. 16.

CAPACITANCE APPARATUS

Capacitance Cell

The cell shown in Figure 21 consisted essentially of a 4-cm. length of 2.48-cm.-internal-diameter Perspex tube with a 100-mesh copper gauze fixed at the outer end to act as an earthed plate and as a support for the 0.036-cm.-diameter ballotini. A further copper gauze was fitted firmly over the bed with a Perspex slip ring to act as the live plate of the condenser. This gauze was in contact with the Fielden-Drimeter capacitance recorder through the mercury-pool contact in the Perspex centerpiece fixed to the axis of the hydroextractor bowl. The earthed contact through the aluminum basket was made by a brass screw to the gauze, and a rubbing ring was fitted to the top of the bowl. Care was taken in the construction to ensure that atmospheric pressure obtained at the outer gauze face of the cell, that is, at radius r_0 in Figure 21.

The constancy of calibration of the cell is shown in Figure 22*a*, which indicates the weight changes involved in a cell of dry weight 48.4 g. The corresponding saturation calibration curve is shown in Figure 22*b*.

Capacitance Method with Hydroextractor

This research ends the series of studies undertaken on hydroextraction problems. Thus it may be of interest to describe briefly the partial success of the attempt

TABLE 2. SUMMARY OF CAKE DATA FOR 9-IN.-DIAMETER HYDROEXTRACTOR DRAINAGE RUNS

Outer radius of cake, r_0 = 11.3 cm.

Height of cake, Y = 11.8 cm.

Run	Material	r_c, cm.	Q_s, cc.	ϵ	$K \times 10^7$, cc./sec.^{2}	N, rev./min.	G	f
1*C*	Chalk	9.58	736	0.548	0.421	1,820	—	—
2*C*	Chalk	8.81	1,226	0.665	1.12	1,820	372	0.53
3*C*	Chalk	8.87	1,119	0.620	0.995	2,380	637	0.445
4*C*	Kieselguhr	8.94	1,481	0.840	12.6	1,400	224	0.465
5*C*	Kieselguhr	9.46	1,173	0.825	13.0	1,440	240	0.57
6*C*	Kieselguhr	8.61	1,633	0.825	7.9*	875	85.5	0.50†

*This cake was made from reused kieselguhr and was circulated for several hours through the mixing-pump system; changes in particles may have occurred.

†Estimated value from Brownell-Katz correlation, Equation (3); all other f values measured.

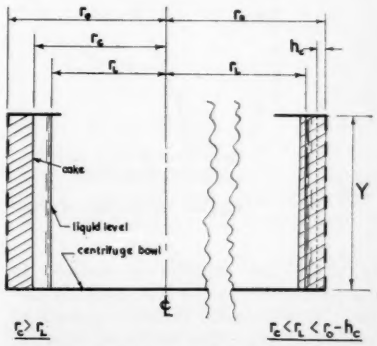

Fig. 18. Sketch of hydroextractor cake.

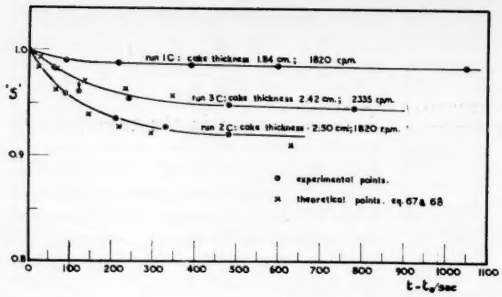
run 1C: cake thickness 1.84 cm.; 1820 rpm.
run 3C: cake thickness 2.42 cm.; 2335 rpm.
run 2C: cake thickness 2.50 cm; 1820 rpm.
experimental points.
theoretical points. eq. 67 & 68
S
t - t₀, sec

Fig. 19. Centrifugal drainage of water from chalk cakes in a 9-in.–diameter hydroextractor.

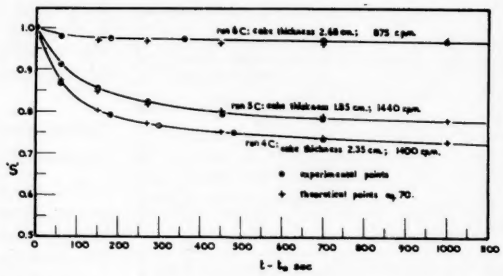
run 6C: cake thickness 2.68 cm.; 875 rpm.
run 5C: cake thickness 1.85 cm.; 1440 rpm.
run 4C: cake thickness 2.35 cm.; 1400 rpm.
experimental points
theoretical points eq. 70.
S
t - t₀, sec

Fig. 20. Centrifugal drainage of water from kieselguhr cakes in a 9-in.–diameter hydroextractor.

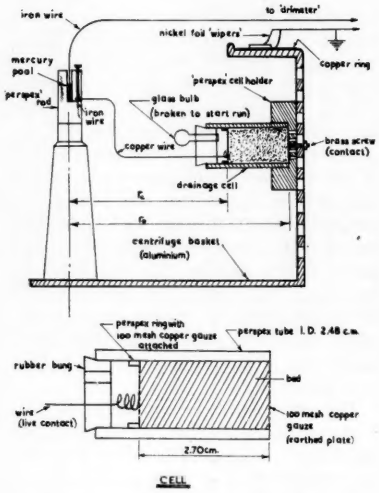

Fig. 21. Small capacitance cell held in hydroextractor for drainage of glycerol through glass ballotini.

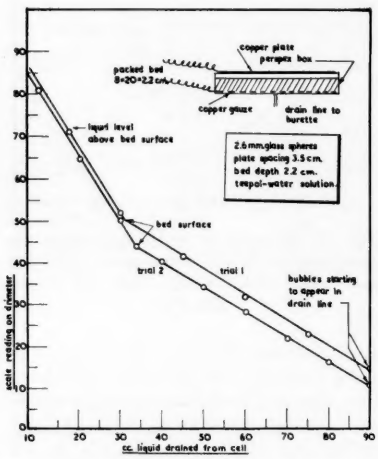
copper plate perspex box
packed bed 8·20×2.2 cm.
copper gauze
drain line to burette
liquid level above bed surface
2.6 mm glass spheres plate spacing 3.5 cm. bed depth 2.2 cm. teepol-water solution.
bed surface
trial 2
trial 1
bubbles starting to appear in drain line
scale reading on drimeter
cc. liquid drained from cell

Fig. 23. Capacitance apparatus for gravity drainage from packed bed.

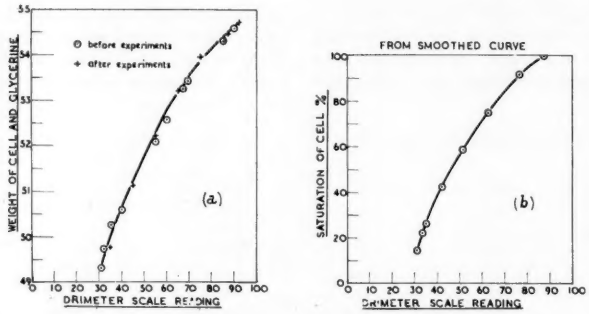

Fig. 22. Calibration of small-capacitance cell with glycerol.

to apply the capacitance method to complete cakes in the 9-in. hydroextractor. A fundamental problem appears to need solution. The electrical method proved successful in a small drainage cell (Figure 21) as it had done for drainage from beds of large particles in a gravitational field (Figure 23), giving clear indication of the point where the liquid level entered the surface of the bed and of the porosity relationship above and below the bed. The cell principle in Figure 21 was applied to the hydroextractor (Figure 24). The drainage curve from the Drimeter chart was as exemplified in Figure 25. The $S = 1$ position was indefinite and was found by extrapolation. The S, t curve for $S < 1$ was very shallow and fitted neither Equation (17), adjusted for G, to represent zero film drainage at the beginning of drainage just after $S = 1$, nor Equation (70) for purely film drainage toward the end of the drainage. It is clear that no fit could be obtained with the series solution which uses the limiting functions shown.

Although the chalk cake was spun for ten minutes at $N = 2{,}500$ rev./min. while submerged before the drainage test, shrinkage may be the problem when $S < 1$. Another possibility of error lies in the assumed proportionality between Drimeter scale reading and S over the range from $S = 1$ found by extrapolation in Figure 25*a* to fix t_0 and the measured value S_∞ after long spinning of the cake. This electrical method of following the S, t history of the cake requires further investigation as it does offer a possible method for following the chronological series of operations in a batch hydroextraction operation. If successful, it could then provide the major experimental method for the final functions proposed for the analysis and control of either batch or continuous operation.

Procedure and Results of Capacitance Cell

The procedure in a drainage run consisted of saturating the cell with an aqueous solution of glycerine and sealing the end with a small glass bulb. The cell was fixed in the centrifuge, and, when the basket had attained the desired constant speed, the bulb was broken. As the liquid level then moved toward the bed, the drainage started with $r_L < r_c$. Figures 26, 27, and 28 show data from runs at different speeds with glycerine-water solutions of various kinematic viscosities.

The curves drawn were calculated from values of capillary suction height h_c and permanent residual moisture f obtained from the Dombrowski-Brownell correlation, with a permeability K from the Kozeny equation. Actual measurements showed the estimated h_c as 2% high and the estimated K as 4% low. These discrepancies would have small effect on the S curve and show the value of the estimations. The estimated f values were not checked, as the long time required to attain S_∞ also allowed significant pick-up of atmospheric moisture by the glycerine. It is clear that in run 2*G* (Figure 27) f has been underestimated, but the series solution gives a reasonable prediction of the S, t function. It is also clear that the simpler equation (70) for film drainage alone gives a fair approximation.

CONCLUSIONS

The experimental results appear to confirm the value of the drainage equations proposed. Packed beds are expected

to fall into three general cases, depending on the properties of the system:

1. For fine particulate material, such as chalk, the beds have low permeability, and it is necessary to use the series solution to predict the moisture content variation with time.

2. For beds of intermediate permeability where there is no negative root for b_1 in Equation (50), such as the kieselguhr cakes, it is possible to use the simplified expression such as Equations (56) and (70) where film drainage is dominant.

3. For beds of fairly large crystals, the permeability will be high, and the capillary drain height may be an insignificant fraction of the cake thickness. In this event the expression $[4/27(p^3/(b-a)) - k_c^2]$ will approach an infinite value, and the root b_1 of Equation (50) will be indeterminate. Obviously the drainage of the full pores will be rapid; Equation (70) will reduce to Equation (71), and S_∞ will be small. The strings of beads may be taken as an extreme example, equivalent to

$$S = S_\infty + \frac{k_c}{(t - t_0)^{\frac{1}{2}}} \qquad (71)$$

The present studies of the drainage mechanisms have confirmed the need for consideration of the allied fields of capillary suction height, permanent residual moisture, and film drainage. The equations derived have been successful in application to the problems of drainage in a gravitational and in a centrifugal-force field, but the important correlations of capillary suction height and permanent residual moisture are still inadequate. The drainage equations warrant further study, particularly in their application to spin-drying, but much depends on finding a satisfactory method of measuring the moisture content of a moving hydroextractor cake.

The correlation of capillary drain height with capillary drain number proposed by Dombrowski and Brownell seems valuable, although wide deviations exist for nonspherical particles, emphasizing the need for further study of the effects of porosity and sphericity. These factors are not adequately represented by the inclusion of permeability in the capillary drain number, as their influences on flow characteristics are not necessarily the same as those on the capillary properties of the bed. Where applicable, the capillary drain height is best determined with a Haines apparatus and may then be assumed constant throughout a uniformly packed bed. When Haines's method cannot be used, an estimate of h_c can be found from the change of gradient on the S, t curve as the liquid surface enters the packing.

The correlation for permanent residual moisture requires further study, and benefit should result from a detailed solution to the problem of the maximum moisture retained at the contact point of two spheres. The velocity of drainage has only a minor effect on the retention.

Within these reservations on the accuracy of the values available for h_c and f, the series solution provides a saturation curve which applies to the drainage of beds for wide ranges of permeabilities and particle shapes. For beds of high permeability it is likely that the simple Equation (70) will apply. The relationships proposed have all depended on the assumption of a laminar flow regime, and this was found correct with the present materials. If with coarse particles in a centrifugal field, the flow in submerged pores becomes semiturbulent,

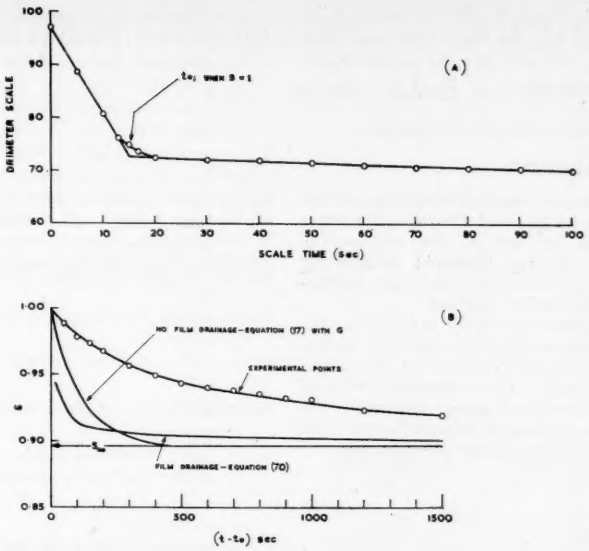

Fig. 25. Drainage test using capacitance measurement for water in chalk cake with N = 2,030, r_0 = 11.30 cm., r_c = 10.23 cm., ϵ = 0.615, K = 0.872 × 10^{-7} cc./sec.², S_∞ = 0.896 h_c = 0.87 cm., f = 0.20.

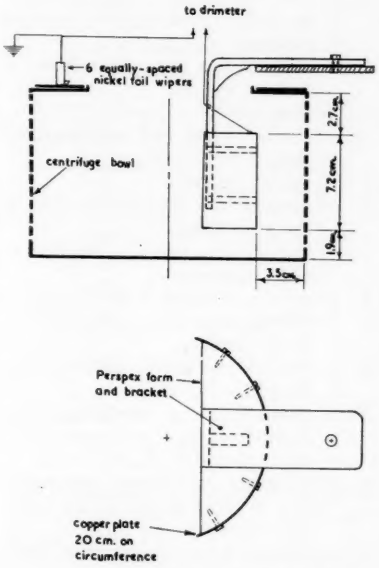

Fig. 24. Condenser arrangement in 9-in.-diameter hydroextractor, showing necessary earthing contact to copper ring pinned to the aluminum bowl.

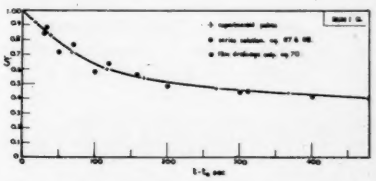

Fig. 26. Centrifugal drainage of glycerine solution from small cell, with N = 520 rev./min. and μ/ρ = 562 centistokes.

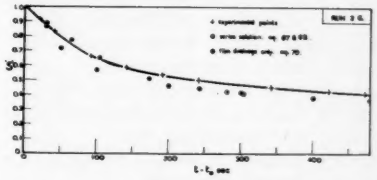

Fig. 27. Centrifugal drainage of glycerine solution from small cell, with N = 610 rev./min. and μ/ρ = 800 centistokes.

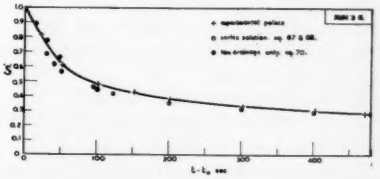

Fig. 28. Centrifugal drainage of glycerine solution from small cell, with N = 800 rev./min. and μ/ρ = 736 centistokes.

it is highly probable that drainage from the voids will be very fast and that Equation (70) will be valid for the major flow mechanism.

ACKNOWLEDGMENT

The research described above was carried out under an Imperial Chemical Industries Fellowship by one of the authors (E. Nenniger) in the Chemical Engineering Laboratory, Faculty of Technology, University of Manchester, England.

The authors are deeply indebted to Dr. L. R. Shenton, Senior Lecturer in Mathematics in the same Faculty, for his interest in this work. The successful solution obtained for the drainage equations was the result of tests of series solutions with various properties under his guidance.

NOTATION

A = area of packed bed normal to flow, sq. cm.

A_m = mean area of centrifuge cake, sq. cm.

a = constant for a given gravity-drainage run $a = h_c\rho KA/H\mu Q_s$ sec.$^{-1}$

a_c = constant for a given centrifuge run $a_c = h_c\rho KA/(r_0 - r_c)\mu Q_s$ sec.$^{-1}$

$a_1, a_2, a_3 \ldots$ etc. = series terms

B = film-drainage constant for a given run

b = constant for a given gravity drainage run $b = \rho KA/\mu Q_s$ sec.$^{-1}$

b_c = constant for a given centrifuge run $b_c = G\rho KA_m/\mu Q_s$ sec.$^{-1}$

$b_1, b_2, b_3 \ldots$ etc. = series terms

C_1 = constant in Batel's (*3*) correlation of capillary drain height

$c_1, c_2, c_3 \ldots$ etc. = series terms

d = particle diameter, cm.

d_m = mean particle diameter, cm.

d_h = diameter of maximum frequency in size distribution, cm.

f = permanent residual moisture as a fraction of voidage

G = acceleration force divided by g g./g.

g = acceleration of gravity—980 cm./sec.^{2}

H = depth of bed, cm.

h_c = capillary drain height, cm. fluid

h_L = height of liquid level above bottom of bed, cm.

K = bed permeability cc./sec.^{2}

k_1 = constant for a given gravity drainage run $= 2[s_0/3\epsilon]\sqrt{h\mu/\rho g}$

k_c = constant for a given centrifuge run $= 2[s_0/3\epsilon]\sqrt{(r_0 - r_c)\mu/G\rho g}$

k_4 = correction factor to Kozeny equation

k_5 = function of sphericity and voidage

L' = depth of bed in Dombrowski and Brownell (*8*) and Brownell and Katz (*4*) equations

L = equivalent horizontal width of draining film, cm.

N = revolutions per minute, min.$^{-1}$

n = revolutions per second, sec.$^{-1}$

ΔP = pressure drop across bed

p = constant for a given drainage, $p = (1 - f)$

Q = total volume of liquid above bottom of bed, cc.

Q_c = capillary-height volume $= h_c A\epsilon$, cc.

Q_s = total volume of voids in bed, cc.

Q_∞ = final volume of moisture content in drained bed, cc.

q = flow rate of liquid through the bed, cc./sec.

r_c = radius of inner face of centrifuge cake, cm.

r_L = radius of liquid level in centrifuge, cm.

r_0 = radius of outer face of centrifuge cake, cm.

S = total volume of liquid above base of bed divided by pore volume, i.e., $S > 1$ when $h_L > H$ and $S < 1$ when $h_L < H$

S_c = capillary height volume divided by total pore volume; $S_c = h_c/H$

S_r = total final residual moisture in Brownell and Katz (*4*) correlation $(= S_\infty)$

S_∞ = final volume of moisture content in drained bed divided by pore volume

s_0 = surface area per unit volume of bed, sq. cm./cc.

t = time, sec.

t_0 = time at which bed was saturated (i.e., $S = 1$), sec.

t_f = age of film, sec.

u = velocity of a point in the fluid in the x direction

v = velocity of a point in the fluid in the y direction

V_f = volume of liquid in the film, cc.

w = velocity of a point in the fluid in the z direction

X = variable in a gravity drainage run, $X = [1 - h_L/H]$

X_c = variable in a centrifuge run $X_c = [1 - (r_0 - r_L)/(r_0 - r_c)]$

X_∞ = final value of X, $X_\infty = 1 - S_c$

x = horizontal co-ordinate perpendicular to plane of wall where drainage is occurring

Y = vertical depth of centrifuge bowl, cm.

y = vertical coordinate measured downwards from top of film

z = horizontal coordinate parallel to wall where drainage is occurring

z_0 = capillary number

Greek Letters

α = contact angle

γ = surface tension, dynes/cm.

ϵ = void fraction

θ = function of b_1

μ = liquid viscosity, poise

ρ = liquid density, g./cc.

ρ_s = solid density, g./cc.

ϕ = film thickness, cm.

ψ_0 = solution to drainage equation neglecting film drainage in terms of t, sec.

ψ_1 = correction to t accounting for film drainage, sec.

LITERATURE CITED

1. Bashforth, Francis and Adams, J. C., "Capillary Action," Cambridge Univ. Press, (1883).
2. Batel, W.; *Chem. Ing. Tech.*, **26**, 497 (1954).
3. *Ibid.*, **27**, 497 (1955).
4. Brownell, L. E., and Katz, D. L., *Chem. Eng. Progr.*, **43**, 601 (1947).
5. Buckingham, Edgar, *U. S. Bur. Chem. and Soils Bull.*, **38** (1907).
6. Burak, Nathan, and Storrow, J. A., *J. Soc. Chem. Ind.*, **69**, 8 (1950).
7. Dallavalle, J. M., "Micromeritics," Pitman Pub. Co., New York, 220 (1943).
8. Dombrowski, H. S., and Brownell, L. E., *Ind. Eng. Chem.*, **46**, 1207 (1954).
9. Fisher, R. A., *J. Agr. Sci.*, **16**, 492 (1926).
10. Ferguson, Allan, *Phil. Mag.*, **26**, 925 (1913).
11. Gardner, Willard, and Widstoe, J. A., *Phys. Rev.*, **18**, 206 (1921).
12. Green, W. H., and Ampt, G. A., *J. Agr. Sci.*, **4**, 1 (1911).
13. Hackett, F. E., *Trans. Faraday Soc.*, **17**, 260 (1921).
14. Haines, W. B., *J. Agr. Sci.*, **17**, 264 (1927).
15. *Ibid.*, **20**, 96 (1930).
16. Haruni, M. M., and Storrow, J. A., *Ind. Eng. Chem.*, **44**, 2751 (1952).
17. *Ibid.*, 2756.
18. *Ibid.*, 2764
19. ———, *Chem. Eng. Sci.*, **1**, 154 (1952).
20. *Ibid.*, **2**, 108 (1953).
21. *Ibid.*, 164.
22. *Ibid.*, 204.
23. Haruni, M. M., and Storrow, J. A., *Chem. Eng. Sci.*, **3**, 43 (1954).
24. Haruni, M. M., J. A. Storrow, and K. H. Todhunter, *ibid.*, **3**, 87 (1954).
25. Hewitt, G. F. (Chem. Eng. Lab., Faculty of Technol. Univ. Manchester), Private communication (1956).
26. Jeffreys, Harold, *Proc. Cambridge Phil. Soc.*, **26**, 204 (1930).
27. Keen, B. A., *J. Agr. Sci.*, **14**, 177 (1924).
28. King, F. H., *U. S. Geol. Survey, 19 Ann., Rpt.*, II, 59 (1899).
29. Kocatas, B. M., and David Cornell, *Ind. Eng. Chem.*, **46**, 1219 (1954).
30. Morey, F. C., *Natl. Bur. Standards J. Research*, **25**, 385 (1940).
31. Nenniger, Emile, Ph.D. thesis, Univ. Manchester, (1956).
32. Nusselt, W., *Z. Ver. deut. Ing.*, **60**, 541 (1916).
33. Puri, A. N., "Soils—Their Physics and Chemistry," Reinhold Pub. Co., New York, 346 (1949).
34. Rose, H. E., *J. Appl. Chem.*, **2**, 511 (1952).
35. Storrow, J. A., *A.I.Ch.E. Journal*, **3**, 528 (1957).
36. Uren, L. C., and Difrawi, A. H., "Petroleum Development and Technology in 1926," Pet. Div. Am. Inst. Mining Met. Engrs.
37. Washburn, E. W., *Phys. Rev.*, **17**, (2nd Ser.), 273 (1921).

Manuscript received July 10, 1957; revised Nov. 27, 1957; accepted Nov. 29, 1957.

Freezing Points of Binary Mixtures of Methane

JEROME BREWER and FRED KURATA

University of Kansas, Lawrence, Kansas

The experimental freezing-point data of the methane–*n*-hexane and the methane–*n*-octane binaries are presented and compared with the methane–carbon dioxide system investigated by Donnelly and Katz. A step-by-step variation of the freezing point in the paraffin homologous series is exploited to provide reasonably accurate extrapolation of the experimental data on the two binaries and scattered freezing-point data on the methane–*n*-butane mixture to other paraffin hydrocarbon mixtures of methane in which the heavier constituent ranges from ethane to *n*-nonane, inclusive.

A composite graph of the freezing points of the various binaries with methane, from ethane to *n*-nonane, is presented.

Recently the purification of natural gas as well as other petroleum hydrocarbons by low-temperature separation processes has received increasing attention, owing to the technical and economic attractiveness of the possibilities of effecting such a separation by physical rather than chemical means. An example of such an application has been the removal of ethane and ethylene from natural and refinery gases by low-temperature distillation.

To exploit the possibilities of such processes for the petrochemical industries, basic information must first be obtained in the form of low-temperature phase and volumetric properties of the hydrocarbon mixtures involved. With such fundamental information, processes may be designed to evaluate the feasibility of these proposed low-temperature processes as compared with existing procedures for effecting purification. Were it not for the lack of basic knowledge in this field, applications of the low-temperature–process technique would no doubt be more widespread than they are today.

Sage (*1*) has summarized the present knowledge of the physical properties of binary systems of the paraffin hydrocarbons from methane through decane. Deschner, *et al.* (*2*), and Mullins, *et al.* (*3*), have proposed that nitrogen be separated from natural gas by distillation at low temperatures. P. C. Davis, *et al.* (*4*), have contributed data on the phase and volumetric studies of natural gas. Aroyan and Katz (*5*) have investigated the low-temperature equilibria in the hydrogen–*n*-butane binary, and Brown and Stutzman (*6*, *7*) reported on the low-temperature equilibrium constants for the nitrogen-methane-ethane system.

This paper presents the experimental data of Beck (*8*) on the freezing points of the methane–*n*-hexane binary and those of Papahronis (*9*) on the freezing points of the methane–*n*-octane system. In addition, these data are compared with those of Donnelly and Katz (*10*) on the methane–carbon dioxide binary, together with extrapolated values of those other paraffin hydrocarbon mixtures of methane in which the heavier constituent ranges from ethane to nonane, inclusive.

The work of Beck (*8*) and Papahronis (*9*) was carried out in the apparatus previously described by Kohn and Kurata (*11*).

DATA USED

The experimental freezing-point determinations of the methane–*n*-hexane binary as measured by Beck (*8*) are presented in Table 1.

Table 1. Freezing Point of CH_4–nC_6H_{14} Mixtures

Mole fraction nC_6H_{14}	Freezing point, °F.
1.00	−138.0
0.90	−141.6
0.80	−145.0
0.70	−149.2
0.60	−153.0
0.50	−157.6
0.40	−161.8
0.30	−169.0
0.20	−181.8
0.10	−207.4
0.05	−236.0
0.0	−296.0

The freezing-point data of Papahronis (*9*) on the methane–*n*-octane system are given in Table 2

Table 2. Freezing Point of CH_4–nC_8H_{18} Mixtures

Mole fraction nC_8H_{18}	Freezing point, °F.
1.00	− 70.3
0.92	− 71.9
0.895	− 73.0
0.835	− 74.5
0.762	− 77.2
0.643	− 81.5
0.56	− 84.0
0.0	−296.0

A summary of the freezing point data of Donnelly and Katz (*10*) concerning the methane-carbon dioxide binary is presented in Table 3.

Table 3. Freezing Point of CH_4–CO_2 Mixtures

Mole fraction CO_2	Freezing point, °F.
1.00	− 72
0.90	− 74
0.80	− 77
0.70	− 81
0.60	− 83.5
0.543	− 86
0.50	− 86.5
0.18	−117
0.0	−296

Table 4. Freezing Points of Paraffin Hydrocarbons

Compound	Freezing point, °F.	Difference in freezing point, °F.
C_2H_6	−298	
C_3H_8	−306	8
nC_4H_{10}	−217	
nC_5H_{12}	−201.5	−15.5
nC_6H_{14}	−138	
nC_7H_{16}	−131.5	− 6.5
nC_8H_{18}	− 70.3	
nC_9H_{20}	− 64	− 6.3

Table 5. Freezing Points of Paraffin Hydrocarbons

Compound	Freezing point, °F.	Difference in freezing point, °F.
C_3H_8	−306	
nC_4H_{10}	−217	−89
nC_5H_{12}	−201.5	
nC_6H_{14}	−138	−63.5
nC_7H_{16}	−131.5	
nC_8H_{18}	− 72	−59.5

EXTRAPOLATED FREEZING POINTS OF OTHER METHANE MIXTURES

When the freezing points of the pure paraffin hydrocarbons are tabulated and paired as in Tables 4 and 5, some interesting observations may be made.

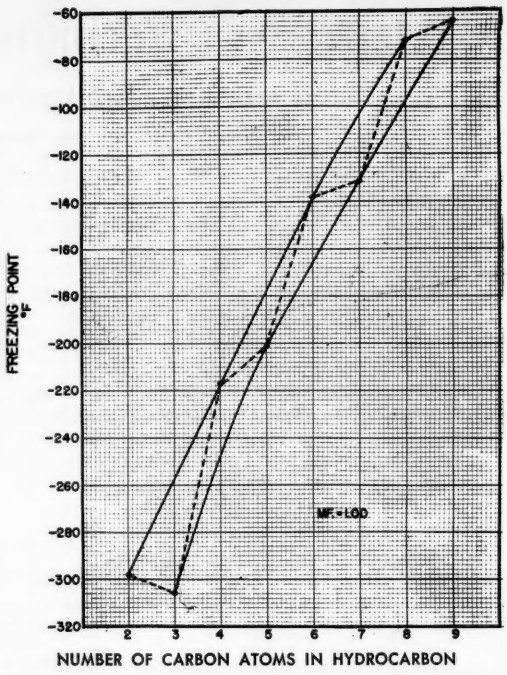

Fig. 1. Step-by-step variation in freezing points of hydrocarbons.

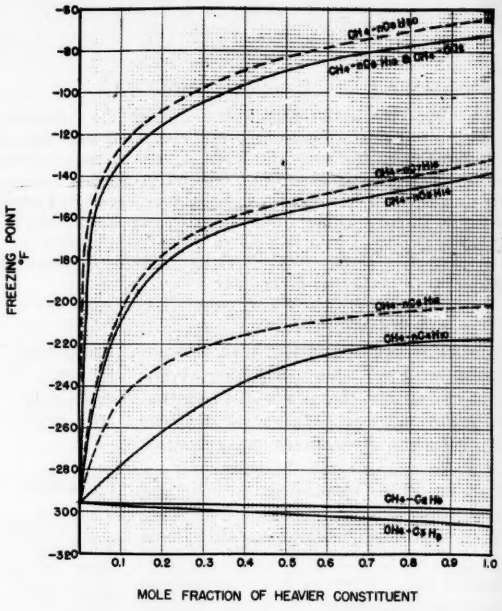

Fig. 2. Freezing point of methane mixtures.

It is evident from Table 4 that the freezing point increases as the paraffin series advances, with the sole exception of that for C_3H_8. Furthermore the freezing points of the hydrocarbons do not increase smoothly as the series progresses but appear to increase by steps. This is illustrated analytically in the comparison of Tables 4 and 5. In Table 4 the hydrocarbons are paired beginning with C_2H_6, and in Table 5 the paired hydrocarbons start with C_3H_8. The differences in the freezing points of the various pairs of hydrocarbons are shown in the last entries of the two tables.

When the hydrocarbons are paired, as in Table 4, the average difference in the freezing points of the pairs is about 10°F. On the other hand, when the compounds are paired, as in Table 5, the average difference in the freezing points is seen to be much higher, about 70°F. This characteristic is shown graphically in Figure 1, in which the freezing points of the paraffins are plotted against the number of carbon atoms in the hydrocarbon. In this graph the dotted curve connects successive members of the paraffin series from ethane to *n*-nonane, inclusive, and illustrates the step-by-step nature of the variation in the freezing points. However when the series is divided into two groups containing those members having an even number and those having an odd number of carbon atoms, each of these groups separately shows a smooth change in the freezing point. The two solid curves in Figure 1 illustrate this.

These observations indicate that the freezing point of a given paraffin hydrocarbon depends a great deal upon whether the number of carbon atoms in that hydrocarbon is odd or even.

Since an arrangement of the pairs of hydrocarbons like that of Table 4 gives a low value for the difference in freezing points for the pairs, it suggests that reasonably accurate values for the freezing points of methane–*n*-nonane mixtures, for example, can be had by simple extrapolation of the methane–*n*-octane data. Likewise the freezing points of the methane–*n*-heptane mixtures can be had by extrapolation of the methane–*n*-hexane data.

Since the freezing points of ethane and propane are nearly the same as the freezing point of methane, it is believed that a plot of the freezing point of their methane mixtures as a function of concentration can be taken as a simple, straight line with reasonable accuracy. With this information and additional scattered data of the freezing points of the methane–*n*-butane binary, the freezing-point curve of the methane–*n*-pentane binary was found from a series of cross plots of the foregoing data at various mole fractions.

An item of note is that the freezing-point curves of the binaries methane–*n*-octane and methane–carbon dioxide are reasonably coincident over that portion of the experimental data presented in Tables 2 and 3.

The final results are given in Figure 2, a composite graph of the freezing points of the various binary mixtures with methane from ethane to *n*-nonane, inclusive. In this graph the solid curves were plotted from experimental data and the dotted curves were obtained by extrapolation, as described above.

Figure 2 should be of value in approximating the freezing points of the various binary mixtures of methane and other paraffins and in approximating the maximum concentrations of the higher hydrocarbon which can be tolerated in methane before the solids begin to form.

LITERATURE CITED

1. Sage, B. H., *Ind. Eng. Chem.*, **42**, 631 (1950).
2. Deschner, W. W., and W. W. Bodle, *J. Oil & Gas*, **46**, No. 50, 76; No. 51, 92, 112 (1948).
3. Mullins, P. V., and R. W. Wilson, *Am. Gas Assoc. Proc.*, (1948), **30**, 601.
4. Davis, P. C., A. F. Bertuzzi, T. L. Gore, and Fred Kurata, *Trans. Am. Inst. Mining Met. Engrs.*, Petroleum, T. P. 3917.
5. Aroyan, H. J., and K. I. Katz, *Ind. Eng. Chem.*, **43**, 185 (1951).
6. Brown, G. M., and L. F. Stutzman, *Chem. Eng. Progr.*, **45**, 142 (1949).
7. Stutzman, L. F. and F. M. Brown, *ibid.*, **45**, 139 (1949).
8. Beck, L. A., M.S. thesis, Univ. Kansas, Lawrence (1956).
9. Papahronis, B. T., M.S. thesis, Univ. Kansas, Lawrence (1954).
10. Donnelly, H. G., and D. L. Katz, "Phase Equilibria in the Carbon Dioxide-Methane System," Research Conference, Phase Behavior of the Hydrocarbons, Univ. Mich. (July 1 & 2, 1953).
11. Kohn, J. P., and Fred Kurata, *Petroleum Processing*, **11**, No. 12, 57 (1956).

Manuscript received Sept. 17, 1957; revision received Jan. 17, 1958; paper accepted Jan. 22, 1958.

Heat Transfer in Forced Convection with Internal Heat Generation

H. L. TOOR

Carnegie Institute of Technology, Pittsburgh, Pennsylvania

A solution to the problem of heat transfer with simultaneous heat generation in viscous tubular flow is presented. The temperature profiles and heat transfer coefficients which are obtained apply to compressible as well as incompressible Newtonian and power-law non-Newtonian fluids with constant physical properties and to systems in which the heat generation is an arbitrary function of radius. An example of heat transfer with frictional heat generation in a non-Newtonian fluid is also presented, and the solution to the problem in which a fluid enters a tube in laminar flow with an arbitrary temperature profile is given, with a consideration of a first approximation to the case of heat transfer in a turbulent fluid in which heat is being generated.

Heat may be generated or absorbed in a fluid by various mechanisms. In cases such as a chemical reaction or fluid flow under a large pressure gradient the heat generation or absorption is incidental to the main operation, and it would be desirable to be able to determine the effect of the generation on the system. In the flow of very viscous liquids, such as high polymers, the frictional heat generation may be quite large, and one would like to know the temperature history and mean exit temperature of the material when it is forced through a hot or cold conduit.

Although a number of viscous-flow heat-generation problems have been analyzed, the general solution to the Graetz problem with simultaneous heat generation is not available. Gee and Lyon (*5*) have worked out one particular solution on a digital computer; Topper (*14*) has solved the problem with a generation term which is constant across the tube; and Brinkman (*3*), Bird (*1*), and others (*13*) have considered the special case where the inlet temperature equals the wall temperature and heat is generated by friction. A number of solutions to related problems are also available (*4, 6, 7, 12*).

In this paper the general solution to the Graetz problem with heat generation will be obtained for Newtonian and certain types of non-Newtonian fluids by an extension of the methods used by Brinkman and Bird. The solution will not exclude compressibility effects, but, as an example, heat transfer coefficients and temperature profiles will be calculated for an incompressible non-Newtonian fluid in which heat is generated by friction. The solution to the problem in which a fluid in laminar flow enters a tube with an arbitrary temperature profile will also be obtained as a by-product. Since physical properties will be assumed constant and the velocity profile will be taken as fully developed, the solutions must be considered as approximations to the real case in the same sense as the Graetz equation is an approximation to the case of no heat generation (*10*).

In turbulent flow, in addition to the well-known example of high-velocity gas flow (*10*), the case of constant heat generation with a constant wall heat flux in a long tube has been investigated (*11*), and a first approximation to the problem in which the wall temperature is specified will be considered here.

TURBULENT FLOW

In a steady, well-developed turbulent flow entering a uniform channel at a temperature T_0, where the wall temperature is constant at T_w, the local rate of heat transfer to the fluid in the absence of heat generation is given by

$$dq = h(T_w - T_m)P\,dx \qquad (1)$$

If the equation is interpreted in terms of the idealized film theory, all resistance to transfer lies in a thin laminar film at the wall, and the central core of fluid is completely mixed. With this model, then, there would be negligible interaction between the heat transfer coefficient and the heat generation, since practically all the heat is generated in the turbulent core where mixing is immediate. In addition, the particular manner in which the heat generation varies with radial position is immaterial as long as a significant fraction of the generation does not take place in the film. Thus the following heat balance can be written in the presence of heat generation,

$$wc_p\,dT_m = h(T_w - T_m)P\,dx + WA_x\,dx \qquad (2)$$

and if the film theory is a suitable approximation, h has the same value it would have if there were no heat generation. Rearranging (2) gives

$$\frac{dT_m}{dx} = \frac{hP}{wc_p}\left[\left(T_w + \frac{WA_x}{hP}\right) - T_m\right] \qquad (3)$$

If the group in the inner parentheses is considered to be T_{we}, and since the inlet temperature is T_0, both with and without heat generation, it is clear that heat generation causes the system to act as if the wall temperature were higher than the actual value by the amount WA_x/hP, which is $WR/2h$ for a tube. This result differs from high-velocity flow, as that particular case has been excluded from the analysis on the assumption that the heat generation is not concentrated near the wall. The solution to Equation (3) for a conduit of constant area and shape with W, h, and Cp constant, is

$$\frac{T_{we} - T_m}{T_{we} - T_0} = e^{-hPx/wc_p} \qquad (4)$$

and Equation (4) shows that the effective wall temperature, T_{we}, is the temperature attained by the fluid in flowing through a long conduit. If Equation (4) is put in the usual design form, then

$$q = wc_p(T_m - T_0) = hA_s(T_{we} - T_m)_{lm} \qquad (5)$$

and q is not the total thermal energy transferred across A_s but, as defined by Equation (5), is the net thermal energy supplied to the fluid by convection and generation.

If WA_x/hP varies with x or T_m, the problem is equivalent to one with no heat generation and a varying wall temperature. If W varies linearly with T_m, Equation (5) still holds, and the mean driving force is the log mean of $(T_{we} - T_m)$ at both ends of the conduit.

The foregoing analysis can be considered only a first approximation, and, when resistance to transfer in the turbulent core is a significant fraction of the total resistance, the heat transfer coefficient will be altered by the heat generation. The analysis would be expected to increase in accuracy as the Prandtl number and the ratio of the heat transfer through the wall to the heat generation

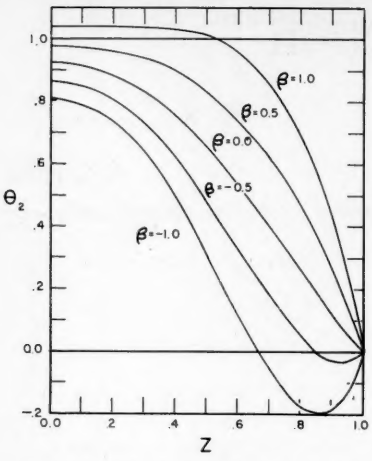

Fig. 1. Temperature profiles at $N_{Gz} = 31.4$; frictional heat generation with $n = 3$.

increase. The interaction between the coefficient and generation, for a constant flux in a long tube, can be obtained by analogy from available calculations (*11*) and might be used to estimate h in the problem considered here. When the interaction between the coefficient and generation is a predominate factor, the situation is of the same type as encountered in laminar flow.

LAMINAR FLOW

The energy equation for laminar flow is (*12*)

$$\rho c_p \frac{dT}{d\theta} = k\nabla^2 T + \frac{\epsilon'}{J}\frac{dp}{d\theta} + \Phi \qquad (6)$$

The last term on the right is the volumetric rate of heat generation, and the adjacent term is minus the rate at which heat is removed by fluid expansion.

Considered here is a fluid at a constant temperature T_0 entering a tube with a fully developed laminar velocity profile which is constant along the tube; that is, u is a function of r only and there are no radial velocity components. The wall is at a constant temperature T_w, and heat is generated (or consumed) at a rate depending only upon radial position. The physical properties are independent of temperature, and the flow has existed long enough for the temperature at all points to be independent of time. Equation (6) then reduces to

$$\rho c_p u \frac{\partial T}{\partial x} = k\frac{1}{r}\frac{\partial}{\partial r}\left(r\frac{\partial T}{\partial r}\right) + \frac{\epsilon' u}{J}\frac{\partial p}{\partial x} + \Phi(r) \qquad (7)$$

when axial conduction is neglected. To include non-Newtonian as well as Newtonian fluids the stress-rate-of-strain curve is assumed to be given by a power law,

$$\frac{\partial u}{\partial r} = -A\tau^{n-1} \qquad (8)$$

For $n = 2$ this is the equation of a Newtonian fluid, and for $n > 2$ the equation approximately describes the rheological properties of many high polymers. The velocity profile then becomes (*12*)

$$\frac{u}{u_m} = \frac{n+2}{n}\left[1 - \left(\frac{r}{R}\right)^n\right] \qquad (9)$$

$$u_m = \frac{AR^n}{n+2}\left(-\frac{dp}{2dx}\right)^{n-1} \qquad (10)$$

and Equation (7) can be written as

$$\rho c_p u_m \frac{n+2}{n}\left[1 - \left(\frac{r}{R}\right)^n\right]\frac{\partial T}{\partial x} = k\frac{1}{r}\frac{\partial}{\partial r}\left(r\frac{\partial T}{\partial r}\right) + Wf(r) \qquad (11)$$

where W is defined by

$$W = \frac{2}{R^2}\int_0^R r\left[\frac{\epsilon' u}{J}\frac{\partial p}{\partial x} + \Phi\right]dr = \frac{\epsilon' u_m}{J}\frac{\partial p}{\partial x} + \frac{2}{R^2}\int_0^R r\Phi\, dr \qquad (12)$$

and $f(r)$ describes the manner in which the net generation varies wih radius.

The following transformations:

$$\Theta = \frac{T - T_w}{\frac{1}{a}\frac{R^2 W}{k}} \qquad (13)$$

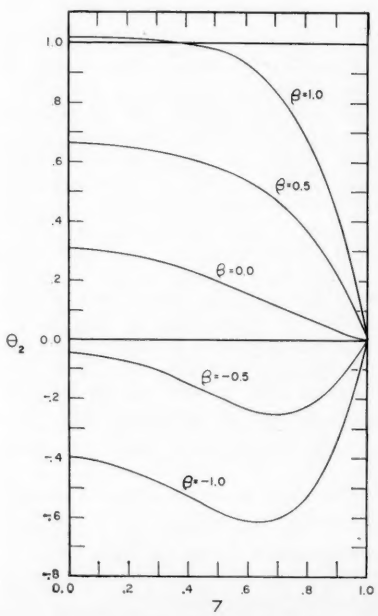

Fig. 2. Temperature profiles at $N_{Gz} = 7.85$; frictional heat generation with $n = 3$.

$$Z = \frac{r}{R} \qquad (14)$$

$$X = \frac{n}{n+2}\frac{\alpha x}{R^2 u_m} = \frac{n\pi}{n+2}(N_{GZ})^{-1} \qquad (15)$$

make Equation (11) dimensionless,

$$(1 - Z^n)\frac{\partial\Theta}{\partial X} = \frac{1}{Z}\frac{\partial}{\partial Z}\left(Z\frac{\partial\Theta}{\partial Z}\right) + af(Z) \qquad (16)$$

The dimensionless number a is included merely for convenience.

The boundary conditions of the problem are

$$\Theta(0, Z) = \Theta_0 = \frac{T_0 - T_w}{\frac{1}{a}\frac{R^2 W}{k}} \qquad (17a)$$

$$\Theta(X, 1) = 0 \qquad (17b)$$

$$\frac{\partial\Theta(X, 0)}{\partial Z} = 0 \qquad (17c)$$

For large X the temperature profile is independent of X, and Equation (16) reduces to

$$\frac{1}{Z}\frac{d}{dZ}\left(Z\frac{d\Theta_s}{dZ}\right) + af(Z) = 0 \qquad (18)$$

Conditions (17*b*) and (17*c*) are unchanged, and Equation (18) yields the temperature profile for large X,

$$\Theta_s = a\int_z^1 \frac{1}{Z'}\int_0^{Z'} Zf(Z)\, dZ\, dZ' \qquad (19)$$

Following previous procedures (*3*, *1*, *13*) the solution to Equation (16) is assumed to be

$$\Theta = \Theta_s + \Theta_1 \qquad (20)$$

and by substituting this into Equation (16) one removes the generation term,

$$(1 - Z^n)\frac{\partial\Theta_1}{\partial X} = \frac{1}{Z}\frac{\partial}{\partial Z}\left(Z\frac{\partial\Theta_1}{\partial Z}\right) \qquad (21)$$

The boundary conditions now are

$$\Theta_1(0, Z) = \Theta_0 - \Theta_s \qquad (22a)$$

$$\Theta_1(X, 1) = 0 \qquad (22b)$$

$$\frac{\partial\Theta_1(X, 0)}{\partial Z} = 0 \qquad (22c)$$

Except for condition (22*a*) the problem is identical to the Graetz problem (*10*) when $n = 2$ and to the non-Newtonian generalization treated by Bird (*2*) for other values of n. It has been shown (*2*) that the solution to Equation (21) is

$$\Theta_1 = -\sum_{i=1}^{\infty} B_i\varphi_i(Z)e^{-a_iX} \qquad (23)$$

and the eigenfunctions $\varphi_i(Z)$ and the eigenvalues a_i are tabulated for various n (2).

From Equation (22a) and (23) at $X = 0$,

$$\Theta_0 - \Theta_s = -\sum_{i=1}^{\infty} B_i\varphi_i(Z) \qquad (24)$$

and since the $\varphi_i(Z)$ satisfy the orthogonality condition

$$\int_0^1 (1 - Z^n)Z\varphi_i(Z)\varphi_j(Z)\,dZ = 0 \quad i \neq j \qquad (25)$$

multiplication of Equation (24) by $\varphi_j(Z)Z(1 - Z^n)\,dZ$ and integration allows determination of the B_i,

$$B_i = B_i^* - \Theta_0 B_i' \qquad (26)$$

where

$$B_i^* = \frac{\int_0^1 \Theta_s(1 - Z^n)Z\varphi_i(Z)\,dZ}{\int_0^1 Z(1 - Z^n)\varphi_i^2(Z)\,dZ} \qquad (27)$$

$$B_i' = \frac{\int_0^1 (1 - Z^n)Z\varphi_j(Z)\,dZ}{\int_0^1 Z(1 - Z^n)\varphi_i^2(Z)\,dZ} \qquad (28)$$

From Equations (20), (23), and (26) the solution to the original problem is

$$\Theta = \Theta_s(Z) - \sum_{i=1}^{\infty} B_i^*\varphi_i(Z)e^{-a_iX} + \Theta_0 \sum_{i=1}^{\infty} B_i'\varphi_i(Z)e^{-a_iX} \qquad (29)$$

Dividing Equation (29) by θ_0 gives a more convenient form:

$$\Theta_2 = \beta\left[\Theta_s(Z) - \sum_{i=1}^{\infty} B_i^*\varphi_i(Z)e^{-a_iX}\right] + \sum_{i=1}^{\infty} B_i'\varphi_i(Z)e^{-a_iX} \qquad (30)$$

where

$$\Theta_2 = \frac{T - T_w}{T_0 - T_w} \qquad (31)$$

$$\beta = \frac{1}{\Theta_0} \qquad (32)$$

If $1/a$ is defined to be the value of the double integral in Equation (19) at some reference point, say at the center line,

$$\frac{1}{a} = \int_0^1 \frac{1}{Z'}\int_0^{Z'} Zf(Z)\,dZ\,dZ' = \frac{T_{sc} - T_w}{R^2W/k} \qquad (33)$$

then θ_s is 1.0 at $Z = 0$; the denominator of Equation (13) becomes $T_{sc} - T_w$, and from Equation (32),

$$\beta = \frac{T_{sc} - T_w}{T_0 - T_w} \qquad (34)$$

where T_{sc} is the center-line temperature at $X = \infty$, given by Equation (33).

The term in brackets in Equation (30) now rises from 0 at $X = 0$ to a maximum value of 1.0 in the tube center at $X = \infty$, while the term on the right decreases from 1.0 at $X = 0$ to 0 at $X = \infty$. β may take on values ranging from $-\infty$ to $+\infty$, and, when the absolute value of β is small, heat generation may be neglected.

β also has another interpretation. With the earlier assumptions, an energy balance over an adiabatic conduit yields

$$wc_p(T_{ma} - T_0) = W\pi R^2 x \qquad (35)$$

combining this with Equation (32) gives

$$\beta = \frac{1}{a}\frac{N_{GZ}}{\pi}\beta' \qquad (36)$$

where β' is the ratio of the adiabatic temperature rise to the inlet temperature difference.

When there is no generation or expansion, $\beta = 0$, and Equation (30) reduces to

$$\Theta_2' = \sum_{i=1}^{\infty} B_i'\varphi_i(Z)e^{-a_iX} \qquad (37)$$

This is the solution to the generalized Graetz problem for which the θ_2' are tabulated (2). [For a Newtonian fluid Equation (37) is Graetz's solution.]

When $T_0 = T_w$, Equation (29) yields

$$\Theta_2^* = \Theta_s - \sum_{i=1}^{\infty} B_i^*\varphi_i(Z)e^{-a_iX} \qquad (38)$$

the solution to the problem in which the inlet temperature equals the wall temperature.

Thus from Equations (30), (33), (37), and (38),

$$\Theta_2 = \beta\Theta_2^* + \Theta_2' \qquad (39)$$

or

$$\frac{T - T_w}{T_0 - T_w} = \frac{T^* - T_w}{T_0 - T_w} + \frac{T' - T_w}{T_0 - T_w} \qquad (40)$$

and so the reduced temperature at any point in a tube is equal to, in the general case, the reduced temperature which would be obtained with heat generation if the inlet temperature were equal to the wall temperature, plus the reduced temperature which would be obtained in the absence of heat generation.

Since the a_i, $\varphi_i(Z)$, and B_i' are known for various n (2), specifying $f(Z)$ fixes θ_s by Equation (19), and Equation (27) allows the B_i^* to be determined. Numerical values may then be obtained from Equation (30). (It should be noted that the n used in this paper is $[1 + n]$ in Bird's notation [1, 2]).

MEAN TEMPERATURE CHANGE AND HEAT TRANSFER COEFFICIENT

The mean temperature across a tube is defined by

$$\Theta_{2m} = 2\int_0^1 Z\frac{u}{u_m}\Theta_2\,dZ \qquad (41)$$

and the average of Equation (39) shows that the mean reduced temperatures are additive in the same sense as the reduced point temperatures. It follows that the total thermal energy change of the fluid is the sum of the change due to normal conduction without generation and the change due to the net effect of heat generation in a tube where the wall temperature equals the inlet temperature. The former term is available, and the latter can be calculated once $f(Z)$ is specified.

Alternately an arithmetic mean heat transfer coefficient can be defined to give the effects of conduction and heat generation by

$$q = wc_p(T_m - T_0) = 2\pi Rh_a x\left[\frac{(T_w - T_0) + (T_w - T_m)}{2}\right] \qquad (42)$$

This leads to the usual equation for h_a (10),

$$\frac{h_aD}{k} = \frac{2}{\pi}\left(\frac{wc_p}{kx}\right)\frac{1 - \Theta_{2m}}{1 + \Theta_{2m}} \qquad (43)$$

and from Equations (39) and (41) and the definitions of Nusselt and Graetz numbers,

$$N_{Nu} = \frac{2}{\pi}N_{GZ}\left[\frac{1 - \Theta_{2m}' - \beta\Theta_{2m}}{1 + \Theta_{2m}' + \beta\Theta_{2m}}\right] \qquad (44)$$

When $T_w > T_0$, β is negative and N_{Nu} is increased by generation and when $T_w < T_0$, β is positive and N_{Nu} is decreased by generation.

FRICTIONAL HEAT GENERATION—LAMINAR FLOW

An example of the application of the foregoing equations is frictional heat generation in an incompressible fluid. Here

$$W = -\frac{u_m}{J}\frac{dp}{dx} \qquad (45)$$

and

$$f(Z) = \frac{n + 2}{2}Z^n \qquad (46)$$

Equation (33) gives

$$a = 2(n + 2) \qquad (47)$$

and the profile for large (X) is given by Equations (19) and (46),

$$\Theta_s = 1 - Z^{n+2} \qquad (48)$$

The equations for $f(Z)$ and θ_s are available if the fluid is compressible (*12*). From Equations (45), (32), and (36),

$$\beta' = \frac{\Delta p/\rho c_p}{J(T_0 - T_w)} \tag{49}$$

and $\Delta p/\rho c_p$ is the mean adiabatic temperature rise of an incompressible fluid, $(T_{ma} - T_0)$.

With θ_s known, the B_i* may be obtained from Equation (27). Since these calculations have already been carried out in studies of frictional heat generation (*1, 13*) in which the inlet temperature equals the wall temperature, the temperature profiles shown in Figures 1 and 2 were obtained by calculating θ_2* from Equation (38) and adding these to the tabulated (*2*) values of θ_2'.

θ_{2m}* was obtained by numerically integrating Equation (41) by use of the preceding values of θ_2*, and, with Bird's (*2*) values of θ_{2m}', θ_{2m} was obtained from Equations (39), and (41). All these calculations apply only for $n = 3$.

The series for θ_{2m}' converges slowly at high Graetz numbers, but the asymptotic form has been determined by Lévêque (*8*) for Newtonian fluids and can be obtained from Marshall and Pigford (*9*) for non-Newtonian fluids. The value of θ_{2m}* at high Graetz numbers is known only for the adiabatic case, but as the series in Equation (38) converges more rapidly than the one for θ_{2m}', θ_{2m} could be extended to Graetz numbers of about 200 without too great an error.

Figure 3 shows $1 - \theta_{2m}$, which is the reduced temperature rise of the fluid, as a function of Graetz number for various values of β and β'. When the inlet fluid is warmer than the tube wall, β is positive, and the temperature change of the fluid is decreased as β increases, since the heat generation partly compensates for the heat loss through the tube wall. When β is negative, the conduction and generation are both in the same direction, and the temperature change is increased as the magnitude of β increases.

At low values of the Graetz number the temperature attains its steady value, which from Equations (30), (41), (9), and (48) is found to be

$$\frac{T_{ms} - T_0}{T_w - T_0} = 1 - \frac{n+3}{n+4}\beta \tag{50}$$

This is $1 - 6/7\beta$ for $n = 3$, and it is clear that when β is negative the mean temperature rises above the wall temperature when the Graetz number is small. From Figure 3, the point at which the mean temperature reaches the wall temperature depends upon β and N_{GZ}. For $\beta = -1$ the mean temperature reaches the wall temperature at a Graetz number of 20 and exceeds it for lower Graetz numbers.

When β is positive, Equation (50) shows that the mean temperature may fall below the wall temperature for large enough values of β.

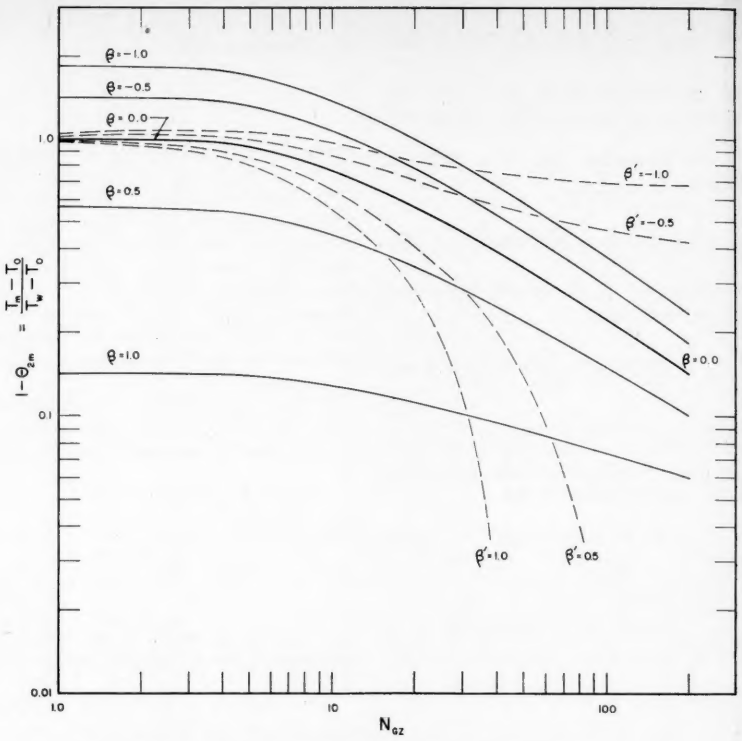

Fig. 3. Mean temperature rise with frictional heat generation; $n = 3$.

The lines of constant β' of Figure 3 apply to operation at a constant ratio of the adiabatic temperature rise to the inlet temperature difference. They would correspond to operation with one fluid at at a constant pressure drop with a varying tube length. Although the heat generated per unit mass of fluid is constant along a line of constant β', all the lines converge to the $\beta = 0$ line at low Graetz numbers and diverge increasingly from this line as β' and N_{GZ} increase.

The results in Figure 3 are shown in Figure 4 in terms of the arithmetic mean heat transfer coefficient, defined by Equation (44). The asymptote at small Graetz numbers, when the steady temperature is attained, is from Equations (44) and (50)

$$N_{Nu} = \frac{2}{\pi}\left[\frac{(n+4) - \beta(n+3)}{(n+4) + \beta(n+3)}\right]N_{GZ} \tag{51}$$

HEAT TRANSFER WITH INLET TEMPERATURE A FUNCTION OF RADIUS: LAMINAR FLOW

The solution can be obtained from the earlier results, if the generation and expansion terms are dropped from Equation (7), the reduced coordinates (14) and (15) are used, and (13) is replaced by

$$\Theta_3 = \frac{T - T_w}{T_{m0} - T_w} \tag{52}$$

where T_{m0} is the mean inlet temperature. The differential equation is

$$(1 - Z^n)\frac{\partial \Theta_3}{\partial X} = \frac{1}{Z}\frac{\partial}{\partial Z}\left(Z\frac{\partial \Theta_3}{\partial Z}\right) \tag{53}$$

the boundary conditions are

$$\Theta_3(0, Z) = I(Z) \tag{54a}$$

$$\Theta_3(X, 1) = 0 \tag{54b}$$

$$\frac{\partial \Theta_3(X, 0)}{\partial Z} = 0 \tag{54c}$$

and $I(Z)$ is the reduced inlet temperature.

This problem is formally identical to the one defined by Equations (21) and (22) if $I(Z) = \theta_0 - \theta_s$. From Equations (23) to (28) the solution to the present problem is

$$\Theta_3 = \sum_{i=1}^{\infty} e^{-a_i X}\varphi_i(Z) \cdot \frac{\int_0^1 I(Z)Z(1 - Z^n)\varphi_i(Z)\,dZ}{\int_0^1 Z(1 - Z^n)\varphi_i^2(Z)\,dZ} \tag{55}$$

The generalization to the case in which heat is being generated follows readily.

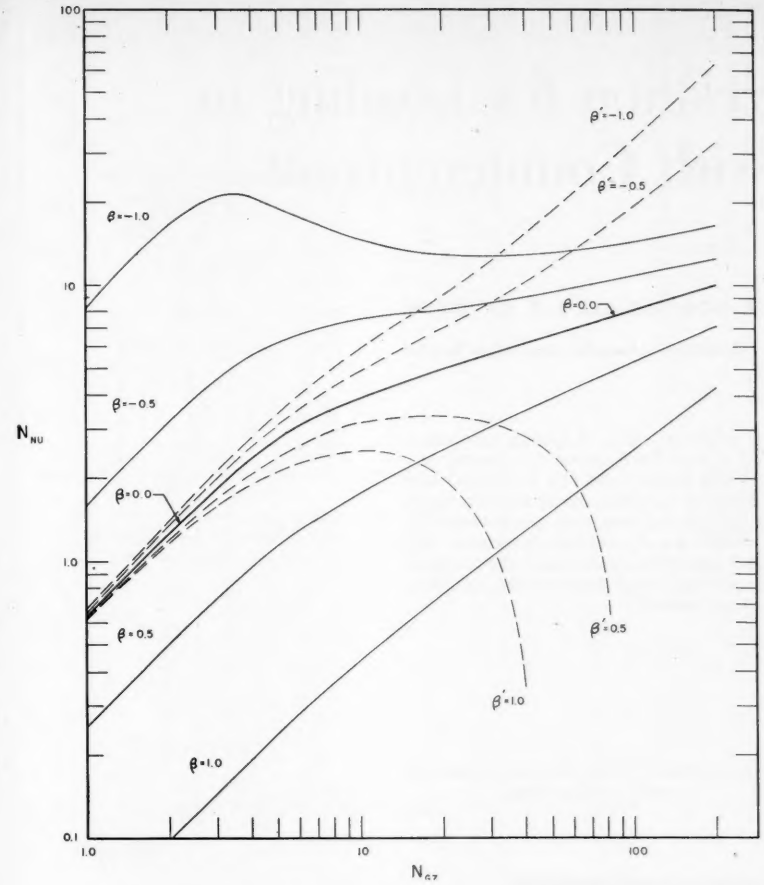

Fig. 4. Nusselt number with frictional heat generation; $n = 3$.

NOTATION

a = dimensionless constant, Equation (33)
a_i = eigenvalues
A = constant relating stress and rate of strain, 1/hr. × (lb. force/sq. ft.)$^{1-n}$
A_s = surface area for heat transfer, sq. ft.
A_x = cross-sectional area, sq. ft.
B_i = dimensionless coefficient, Equation (23)
B_i^* = dimensionless coefficient, Equation (27)
B_i' = dimensionless coefficient, Equation (28)
c_p = heat capacity at constant pressure, B.t.u./(lb.-mass)(°R.)
D = diameter, ft.
f = dimensionless function which describes variation of heat generation with position
h = local heat transfer coefficient, B.t.u./(hr.)(sq. ft./°F.)
h_a = arithmetic mean heat transfer coefficient, B.t.u./(hr.)(sq. ft./°F.)
I = reduced inlet temperature
J = conversion factor = 778 ft.-lb.-force/B.t.u.
k = thermal conductivity, B.t.u./(hr.)(ft./°F.)
n = dimensionless constant, Equation (8)
N_{Nu} = Nusselt number, h_aD/k
N_{Gz} = Graetz number, wc_p/kx
p = pressure, lb.-force/sq. ft.
Δp = pressure drop, lb.-force/sq. ft.
P = perimeter, ft.
q = net rate of heat input, B.t.u./hr.
r = radius vector, ft.
R = tube radius, ft.
T = temperature, °R.
T_{ma} = mean adiabatic temperature, °R.
T_{we} = effective wall temperature, °R.
T' = temperature in absence of heat generation, °R.
T^* = temperature if $T_0 = T_w$, °R.
u = velocity, ft./hr.
w = mass flow rate, lb.-mass/hr.
W = mean net volumetric rate of heat generation across tube B.t.u./(hr.)(cu. ft.)
x = axial distance, ft.
X = reduced axial distance = $[n/(n+2)]\,\alpha x/(R^2u_m)$
Z = reduced radial distance = r/R

Greek Letters

α = thermal diffusivity, sq. ft./hr.
β = dimensionless parameter, $1/\theta_0$
β' = dimensionless parameter, $(T_{ma} - T_0)/(T_0 - T_w)$
ϵ' = mean value of absolute temperature times coefficient of thermal expansion
θ = time, hr.
Θ = reduced temperature = $(T - T_w)/(1/a)(R^2W/k)$
Θ_1 = reduced temperature = $\Theta - \Theta_s$
Θ_2 = reduced temperature = $(T - T_w)/(T_0 - T_w)$
Θ_3 = reduced temperature = $(T - T_w)/(T_{m0} - T_w)$
Θ_2' = reduced temperature = $(T' - T_w)/(T_0 - T_w)$
Θ_2^* = reduced temperature = $(T^* - T_w)/(T_{ac} - T_w)$
ρ = density, lb.-mass/cu. ft.
τ = shear, stress, lb./force/sq. ft.
φ_i = eigenfunction
Φ = volumetric rate of heat generation, B.t.u./(hr.)(cu. ft.)

Subscripts

c = center line
i, j = indexes
m = mean
lm = logarithmic mean
0 = initial value, $X = 0$
s = steady value, $X = \infty$
w = wall temperature
∇^2 = Laplacian operator
$\frac{d}{d\theta}$ = derivative following the motion of the fluid

LITERATURE CITED

1. Bird, R. B., *Soc. Plastics Engineers' J.*, **11**, 35 (September, 1955).
2. ———, *Chem. Eng. Sci.*, **6**, 35 (1956).
3. Brinkman, H. C., *Appl. Sci. Res.*, **A2**, 120 (1950).
4. Chambré, P. L., *ibid.*, **A6**, 393 (1957).
5. Gee, R. E., and J. B. Lyon, *Ind. Eng. Chem.*, **49**, 956 (1957).
6. Hausenblas, H., *Ing.-Arch.*, **18**, 151 (1950).
7. Hersey, M. D., *Physics*, **7**, 403 (1936).
8. Lévêque, M. A., *Compt. rend.*, **185**, 1190 (1927).
9. Marshall, W. R., Jr. and R. L. Pigford, "The Application of Differential Equations to Chemical Engineering Problems," p. 140, Univ. Delaware, Newark (1947).
10. McAdams, W. H., "Heat Transmission," McGraw-Hill Book Company, Inc., New York (1954).
11. Poppendiek, H. F., *Chem. Eng. Progr. Symposium Ser. No.* **11**, **50**, 93 (1954).
12. Toor, H. L., *Ind. Eng. Chem.*, **48**, 922 (1956).
13. ———, *Trans. Soc. of Rheology*, **1**, 177 (1957).
14. Topper, Leonard, *Chem. Eng. Sci.*, **5**, 13 (1956).

Manuscript received Dec. 11, 1957; revision received Feb. 2, 1958; paper accepted Feb. 24, 1958.

Generalized Correlation for Loading in Packed Towers with Countercurrent Gas-liquid Flow

J. E. HOWKINS and J. F. DAVIDSON

Cambridge University, Cambridge, England

Experiments in which a liquid film runs over a vertical string of spheres surrounded by a concentric tube through which air is blown upward have shown that loading in a packed tower is due to the formation of standing waves on the liquid film. In the ball-and-tube system a wave is formed just below the equator of each ball, owing to the pressure gradient within the air stream as it accelerates through the narrowing gap between the ball and the tube. Interfacial shear and surface tension are of secondary importance. The similarity between the characteristics of the ball-and-tube system and those of the randomly packed tower suggests that loading in the latter system is also due to wave formation. With this concept of loading, a correlation has been derived.

The importance of loading and flooding in the design of packed towers for countercurrent gas-liquid flow is well known, and numerous correlations for the prediction of these phenomena have been proposed (*1* to *4*), but none of them are based on a clear understanding of the detailed mechanism of loading and flooding. In a previous paper (*5*) the authors suggested that loading is due to the formation of standing waves on the liquid film within the packing. The present paper gives further support to this idea, which has been used as the basis for a correlation to predict the loading point with countercurrent gas-liquid flow.

The proposed mechanism involves a balance between the forces shown in Figure 1, which depicts an element of liquid running down the packing in a region where the gas is accelerating as it moves upward. The acceleration is due to contraction of the flow area available to the gas, and it follows from Bernoulli's theorem that there must be a pressure gradient within the gas stream and that consequently the pressure at P is greater than at Q, giving a net upward force on

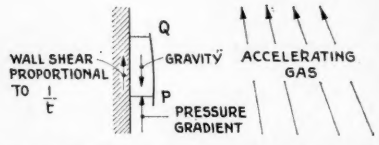

Fig. 1. Forces on an element of the liquid film of thickness *t*.

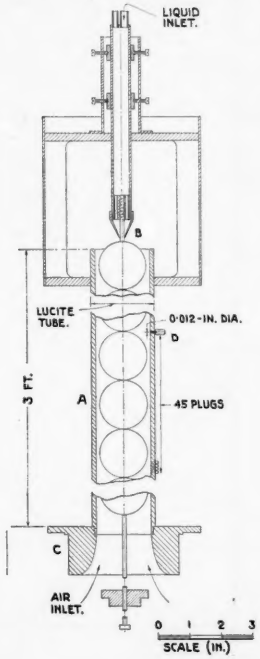

Fig. 2. Sectional scale drawing of the ball-and-tube apparatus.

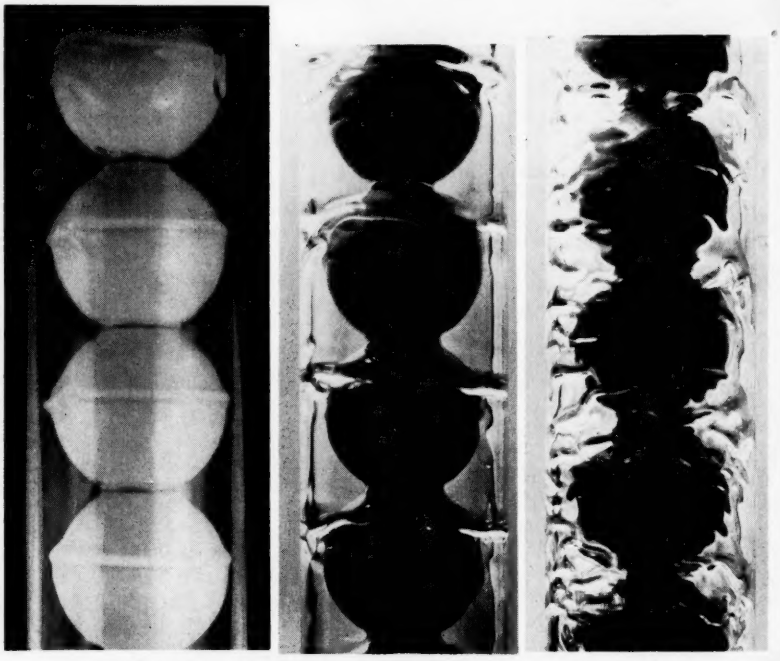

A *B* *C*

Fig. 3. Liquid paraffin ($\mu \simeq$ 300 centipoises) flowing over 1.49-in.-diameter balls inside 1.75-in.-diameter tube.

	(*A*) Loading	(*B*)	(*C*) Flooding
Liquid rate cc./min. =	6	6	6
Air rate cu. ft./min. =	4.31	4.87	6.06

J. E. Howkins is with Standard Oil Company, Sarnia, Ontario, Canada.

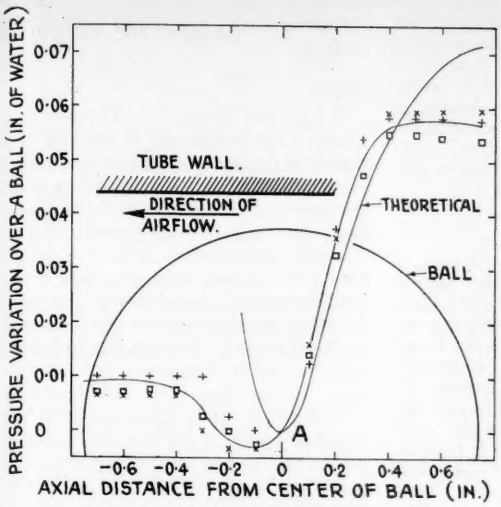

Fig. 4. The pressure distribution along the tube beside three successive balls: first, ⊡; second, ×; third, +.

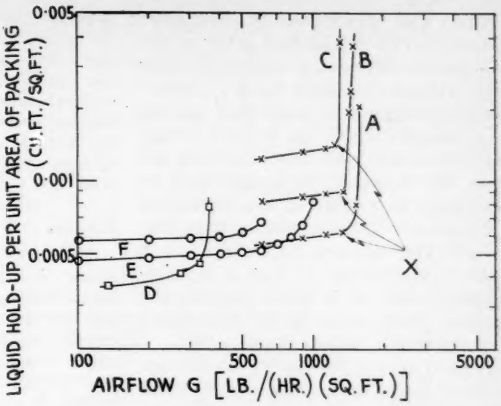

Fig. 6. Variation of holdup with air flow. *A*, *B*, *C*: 1.49-in. balls in 1.75-in. tube with water rates of 117, 860, and 3,410 lb./(hr.)(sq. ft.); *D* (*12*): 0.5-in. balls (random) in 2.89-in. column with water rate of 3,170 lb./(hr.)(sq. ft.); *E*, *F* (*13*): 0.5-in. rings in 10-in. column with water rates of 1,000 and 3,500 lb./(hr.)(sq. ft.)

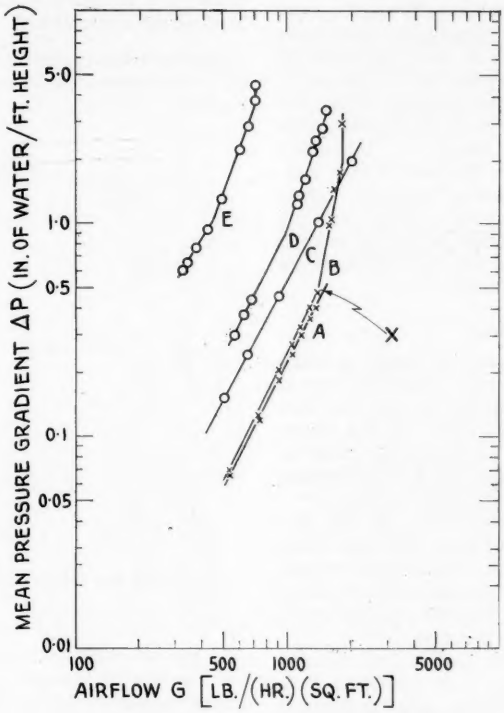

Fig. 5. Variation of mean pressure gradient with air flow. 1.49-in. balls in 1.75-in. tube: *A* = no liquid, *B* = water rate of 117 lb./(hr.)(sq. ft.); 8.66-in. column with 1-in. ceramic rings (*9*): *C* = no liquid, *D* = water rate of 1,250 lb./(hr.)(sq. ft.), *E* = water rate of 12,500 lb./(hr.)(sq. ft.).

the element of liquid. As the gravity force is balanced by the sum of the pressure gradient and wall shear forces and since the latter force is inversely proportional to the film thickness t, the accelerating gas flow must increase t. It can easily be seen that there must be a maximum gas flow beyond which the film cannot run down, because at a certain gas flow the pressure-gradient force will balance the gravity force and the film thickness must become very large if the viscous force is to be small. This kind of instability is thought to give an explanation of the phenomenon of loading and was investigated by the authors (*5*), using an apparatus specially designed for studying the instability rather than for simulating the behavior of packed towers.

This paper is a detailed study of what is thought to be a good, though simplified, model of a packed tower. The model consists of a vertical string of spheres covered by a liquid film and surrounded by a concentric tube through which gas is blown upward. At a certain gas flow a small wave is formed on the liquid film just below the equator of each sphere. The forces in Figure 1 account for the appearance of the waves, which form, as would be expected, near the point of maximum gas acceleration and pressure gradient. Measurements of pressure variation up the tube, together with theoretical calculations, make it clear that the wave formation is due to the pressure gradient balancing the gravity forces.

That the wave formation corresponds to loading in a packed tower is clear from a study of the holdup and pressure-drop characteristics and a comparison of them with the corresponding characteristics for packed towers. This comparison of characteristics shows that the ball-and-tube system is a good model of a packed

tower. The coincidence of the wave formation with the loading point for the ball-and-tube system, as determined from the pressure-drop and holdup characteristics, suggests strongly that loading in a packed tower is due to wave formation within the interstices. This being the case, the dimensionless groups used in the theory for predicting wave formation are applicable to the correlation of loading points. The resulting correlation is not entirely satisfactory in that it is semiempirical and for a given packing the loading points have to be determined experimentally at two liquid rates.

This concept of loading due to pressure-gradient forces rather than to interfacial shear accords with the calculations of Chilton and Colburn (*6, 7*), who showed that with single-phase flow in a packed tower the over-all pressure drop is due largely to repeated accelerations and that wall friction is of secondary importance.

APPARATUS AND PROCEDURE

The ball-and-tube apparatus, shown in Figure 2, was designed to fit into the air distributor and liquid separator described in the previous paper (*5*). A string of table-tennis balls of 1.49-in. diameter was held concentrically within a Lucite tube A of 1.75-in. bore. Water was fed onto the top ball through the annular gap between the end of the conical nozzle B and the ⅛-in.-diameter rod carrying the balls. Adjacent to the liquid inlet at the top of the apparatus was a small outlet tube, normally blanked off, which was used to eliminate air. The water ran uniformly in a thin film over the outside of the spheres and was removed at the bottom by the ⅛-in.-diameter rod which passed through the centers of the spheres. Air after being uniformly distributed passed through the Lucite orifice C, up the tube between the inner wall and the balls, and out to atmosphere at the top.

The pressure variation was measured over the whole column and across three balls in the middle of a string of twenty. This number was enough to counteract end effects, as shown by the similar pressure profiles across each of the three middle balls (Figure 4). The pressure tappings were formed by forty-six holes of equal diameter, drilled at 0.1-in. pitch in a straight line down the tube. Because of the sharp variations in pressure, the final tapping was 0.012 in. in diameter. The holes were normally plugged, but, when a measurement of the pressure was required, a plug was replaced by the tapping D, which was connected to a Chattock gauge measuring the pressure to ±1%. In Figure 2 the top tapping is ready for use and the forty-five holes below are plugged.

Balls and tubes of other diameters (without pressure tappings) were used to investigate the effect of size and voidage on the loading velocities. Orifice C was changed, but the general layout of the apparatus was the same as in Figure 2. Liquid paraffin was used in place of water to find the effect of higher viscosity.

Liquid holdup on the 1.49-in. balls was measured by recirculating the liquid and fixing all the volumes in the system except the volume of a graduated tank into which the liquid flowed from the column. Changes in level within the tank gave changes in holdup, and the total holdup was obtained by adding the initial holdup with zero airflow, obtained from data of Cullen (*8*), who used a weighing technique.

Behavior

The general behavior of the system is shown in Figure 3. Low air rates have a small effect on the liquid film and merely increase the amplitude of moving ripples, which are present at all but very low liquid rates. At a critical air rate the stationary waves shown in Figure 3*A* are formed, the initial formation being just below the equator of each ball. With water the wave breaks into spray as soon as it is formed; with liquid paraffin the wave is stable and is blown up above the equator, as in Figure 3*A*. At higher air rates the motion shown in Figures 3*B* and *C* is induced, the tube as well as the balls being covered with liquid. Ultimately flooding is reached, when liquid will not run out of the base of the apparatus.

RESULTS: LOADING DUE TO WAVE FORMATION

Pressure Variation over a Single Ball

Figure 4 shows the results from the forty-six tappings in the wall of the 1.75-in.-diameter tube, with 1.49-in. balls and no liquid flow. The results from the three successive balls have been made to agree at point A, and their similarity at other points shows that end effects are small. In the accelerating region the results agree, as would be expected, with simple theory based on Bernoulli's theorem, uniform flow across each horizontal section being assumed. Downstream there is a small pressure recovery, followed by a constant-pressure wake in the same way as with an infinite stream flowing past a sphere.

Over-all Pressure Drop

Figure 5 shows the mean pressure gradient as a function of air flow, both in the dry ball-and-tube system and with a constant liquid rate, and the results from randomly packed towers given by Sarchet (*9*) are also shown. The following points of similarity may be noted:

1. With no liquid flow, ln ΔP is a linear function of ln G, the slope being about 1.9 for the ball-and-tube system and for the randomly packed tower, where ΔP is the mean pressure gradient and G is the superficial gas rate.

2. With liquid flowing, the relation between ΔP and G is similar in both systems. The loading point is followed in each case by a line of increased slope. For the ball-and-tube system it is known from visual observation that the loading point X is coincident with the wave formation shown in Figure 3*A*; it therefore seems likely that loading in a randomly packed tower is due to wave formation in the converging parts of the packing.

Holdup

It has been found (*10, 11*) for packed towers that holdup is a function primarily of the liquid rate up to the loading point and that above the loading point the holdup increases sharply with gas flow. The ball-and-tube system behaves similarly, as shown in Figure 6, where holdup is plotted as a function of air flow at constant liquid rates. The point at which standing waves are formed is marked by an X. The increase in holdup after loading is sharper for the ball-and-tube system than for the randomly packed tower, as is consistent with the idea that loading is due to wave formation within the interstices. In the randomly packed tower, wave formation would be expected first in the most serious restrictions, and holdup would increase in these regions (in the manner of Figure 3*B*) before wave formation had begun in the other parts of the tower. The loading process would not be complete until wave formation had begun in all parts of the packing. With the ball-and-tube system, loading occurs all at once throughout the tower and the increase in holdup is therefore sharper.

THEORETICAL DEVELOPMENT OF THE GENERALIZED CORRELATION

The basic assumptions for the generalized correlation are as follows. (*See* Figure 7.)

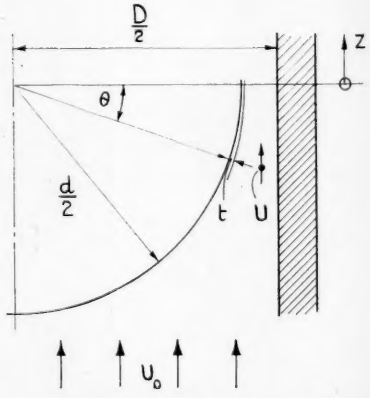

Fig. 7. Ball and tube with liquid film.

1. The viscosity of the air is neglected and its velocity across any horizontal section is assumed uniform. This assumption is justified by the agreement between theory and experiment in Figure 4. From continuity

$$U = \frac{U_0}{1 - \frac{d^2}{D^2}\cos^2\theta - \frac{4dt}{D^2}\cos^2\theta} \quad (1)$$

From Bernoulli's theorem

$$\frac{dp}{dz} = -\rho_G U \frac{dU}{dz} \qquad (2)$$

2. The liquid-film thickness is calculated from a balance between the forces in Figure 1. The velocity is assumed to be a parabolic function of distance measured normal to the surface, and since the surface of the ball is nearly vertical where the wave is formed, $\cos\theta \simeq 1$. The film thickness is therefore calculated by neglecting the kinetic energy of the liquid in the same way as in reference *5*:

$$t = \left[\frac{3\mu D^2 L}{4d\rho_L(\rho_L g + dp/dz)}\right]^{\frac{1}{3}} \qquad (3)$$

From Equation (3) it is clear that $-dp/dz$ cannot exceed $\rho_L g$, and in the previous paper (*5*) it was shown that wave formation occurs when

$$\frac{-dp}{dz} = \alpha\rho_L g \qquad (4)$$

where α is less than unity and varies from system to system. α can be predicted theoretically by relaxation methods (*5*), but in the present paper it will be left as an unknown parameter.

To give dp/dz at the wave crest, Equation (1) is differentiated, with the simplification that $dt/dz = 0$ at the wave crest. In Equation (1) it is also permissible to put $t\cos^2\theta \simeq t$ since the wave is formed near the equator, and using the resulting expression for dU/dz with Equations (2) and (4) gives the condition for loading:

$$\frac{4U_0{}^2 d\sin\theta}{D^2\left(1 - \frac{d^2}{D^2}\cos^2\theta - \frac{4dt}{D^2}\right)^3} = \frac{\alpha\rho_L g}{\rho_G} \qquad (5)$$

TABLE 1. LOADING CORRELATION

[Equation (9)]

Reference		Ball and tube: Ball diam., in.	Ball and tube: Tube diam., in.	A	B	ϵ	$\alpha = \frac{1.195A}{(1-\epsilon)^{1/2}(3\epsilon-1)^{5/3}}$
		1.49	1.75	0.032	26	0.51	0.27
		1.00	1.22	0.058	14	0.55	0.31
		0.50	0.63	0.064	5.9	0.58	0.25
		1.96	2.50	0.066	21	0.60	0.23
		1.49	2.00	0.11	21	0.64	0.26
		1.49	2.50	0.16	21	0.77	0.20
(*14*)	Quartz, 2 in. Serrated grids			0.015	63	0.46	0.27
(*14*)	2 in.			0.16	77	0.83	0.18
(*14*)	1.5 in. Stacked rings			0.10	41	0.89	0.10
(*14*)	3-in. stoneware Random rings			0.058	31	0.76	0.075
(*13*)	0.5-in. stoneware			0.024	16	0.61	0.075
(*14*)	1-in. carbon			0.018	23	0.66	0.039
(*13*)	1-in. carbon			0.032	22	0.70	0.055
(*13*)	1.5-in. stoneware			0.028	28	0.72	0.044
(*13*)	1.0-in. stoneware			0.032	25	0.73	0.048
(*14*)	1.0-in. stoneware			0.030	19	0.80	0.035
(*14*)	0.5-in. metal			0.024	13	0.87	0.024
(*14*)	2.0-in. metal			0.033	31	0.92	0.034

This equation can be generalized by writing d and D in terms of the voidage, ϵ, and a, the wetted area per unit volume:

$$\left.\begin{aligned}\epsilon &= 1 - \frac{2d^2}{3D^2}\\ a &= \frac{4d}{D^2}\end{aligned}\right\} \qquad (6)$$

The wave will be formed where $-dp/dz$ is maximum, and to find the angle where this occurs it is necessary to put $d^2p/dz^2 = 0$. Using Equations (1), (2), and (6), with $t = 0$ and $2z = -d\sin\theta$, gives the angle for maximum pressure gradient:

$$\sin^2\theta = \frac{3\epsilon - 1}{15(1-\epsilon)} \qquad (7)$$

This equation gives the angle for maximum pressure gradient in the absence of the liquid film and will therefore be applicable only at very low liquid rates. Eliminating t, dp/dz, θ, d, and D from Equations (3) to (7) gives the final condition for loading:

$$\frac{G^2 a}{\alpha\rho_G\rho_L g}\left[\frac{3\epsilon-1}{15(1-\epsilon)}\right]^{\frac{1}{3}}\left[\frac{5}{3(3\epsilon-1)}\right]^3 = 1 - \frac{5}{3\epsilon-1}\left[\frac{3La^2\mu}{(1-\alpha)\rho_L{}^2 g}\right]^{\frac{1}{3}} \qquad (8)$$

This may be written in the form

$$\frac{1}{A}\left(\frac{G^2 a}{\rho_G\rho_L g}\right) = 1 - B\left(\frac{La^2\mu}{\rho_L{}^2 g}\right)^{\frac{1}{3}} \qquad (9)$$

where A and B are functions which are given in terms of the packing dimensions by Equation (8) for the ball-and-tube system but have to be determined experimentally for other packings. The area a has not been included in the constants A and B to keep them dimensionless.

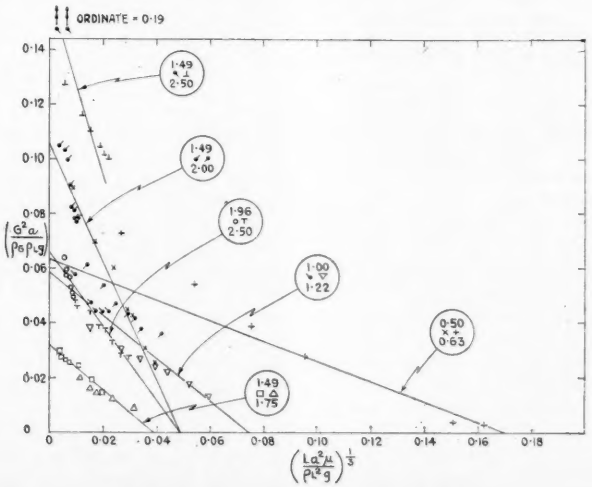

Fig. 8. Determination of A and B, Equation (9), for the ball-and-tube systems. In each circle the upper and lower numbers are the ball and tube diameters. The left-hand symbol is for air-water; the other is for air–liquid paraffin.

APPLICATION OF THE CORRELATION

To get A and B in Equation (9), $G^2a/\rho_G\rho_L g$ at loading is plotted as a

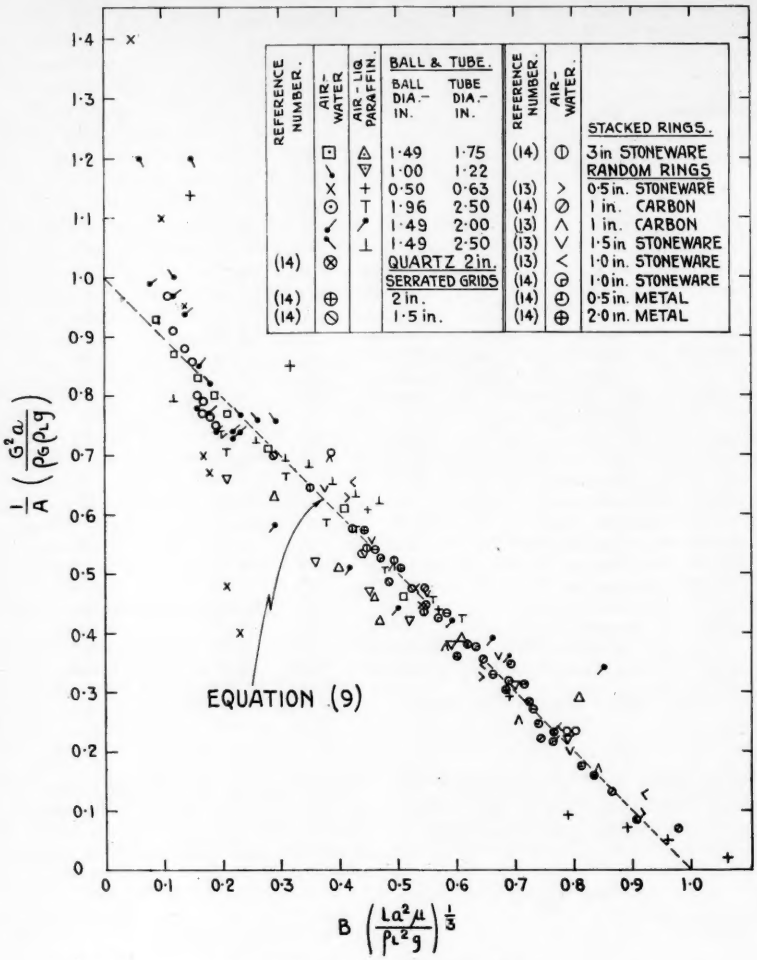

Fig. 9. Generalized loading correlation.

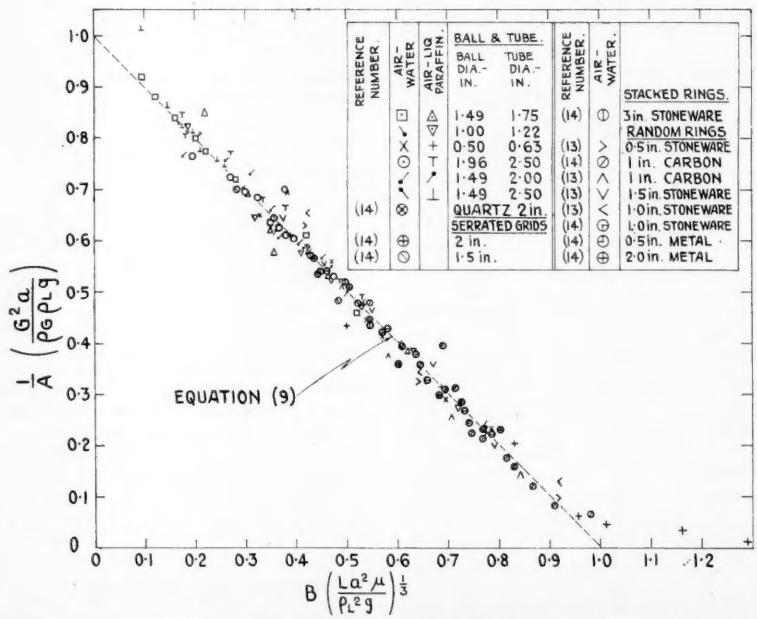

Fig. 10. Nongeneralized loading correlation.

function of $(La^2\mu/\rho_L{}^2g)^{1/3}$ and A and B are determined from the best straight line through the points. Figure 8 shows the results for the ball-and-tube system, and similar graphs were plotted by means of the data for various packed towers of Shulman, Ullrich, and Wells (*13*) and Morris and Jackson (*14*). Table 1 shows the resulting values of A and B, which were used to replot all the results in Figure 9. The points from references *13* and *14* were selected from smoothed experimental data as the original data were not available. It is not certain whether the original data would give a better or worse scatter than is shown in Figure 9.

Validity of the Correlation

In Figure 8 the agreement between the results with water and liquid paraffin for the same system is satisfactory except in the case of the 0.50-in. balls, where the poor correlation is thought to be the effect of surface tension, which was not allowed for in the derivation of Equation (9) and is magnified with smaller packing.

The agreement between experiment and theory in Figure 9 indicates that the mechanism of loading in the ball-and-tube system is similar to the mechanism in the other packings.

A further check on the validity of the theory is given in Figure 10, which is similar to Figure 9, but with different values of A and B for each liquid. To get Figure 10, Figure 8 was redrawn, the behavior of each ball-and-tube system being represented by two straight lines, one for water and one for liquid paraffin. Essentially, Figure 10 is a plot of G^2 against $L^{1/3}$, since A, B, a, ρ_L, ρ_G, and μ are fixed for any one system, and it shows very good agreement with theory. The fact that Figure 10 is a better correlation than Figure 9 indicates that the constants A and B are not entirely independent of liquid viscosity for a particular system. This is further indicated in Figure 8, where for any ball-and-tube system the results are somewhat scattered around the fitted straight line; Figures 8 and 9, nevertheless, correlate the results reasonably well and justify the assumption that, to a first approximation, A and B are independent of liquid viscosity for each packing.

The theory can also be checked by calculating α, which is a measure of the maximum pressure gradient within the packing, in terms of liquid head. It should be somewhat less than unity, and its significance will be discussed later, with reference to interfacial shear. α can be calculated for the ball-and-tube system, because in this case Equations (8) and (9) should be identical. A and B can therefore be related to α and ϵ, and, the latter being known, two values of α are calculable, one from A and one from B. In the derivation of Equations (7) and (8), however, it was assumed that the

liquid-film thickness t was negligible. It would therefore be expected that the constant A, which depends upon the loading-gas rate at L and t being equal to zero, would give reasonable values of α. B, which gives a measure of the variation in the loading-gas rate due to finite liquid-film thicknesses, would not be expected to give a reasonable estimate of α. These assumptions are confirmed by calculation; Table 1 shows values of α calculated from the experimental values of A, but values of α calculated from B are nearly unity and in one case negative and have not been included.

Factors Affecting Loading

1. *Liquid Viscosity.* The viscosity of the liquid paraffin was about 300 times that of water, and the agreement obtained between the two sets of results for the ball-and-tube systems indicates that the final correlation, Equation (9), could be used for an approximate prediction of the behavior of randomly packed towers with any liquid when the air-water results are used. This method could not be applied to small packings.

2. *Interfacial Shear.* The approximate dependence of A and B on ϵ and the relative constancy of α (Table 1) indicate that the neglect of interfacial shear in deriving Equation (8) is justified. As was explained above, α may be thought of as the maximum pressure gradient within the packing in feet of liquid per foot of height and cannot exceed unity. In reference *5* α was about 0.6 and the difference from unity was attributed partly to interfacial shear and partly to interaction between the water film and the air stream. In Table 1, α is about 0.25 for the ball-and-tube system, and simple boundary-layer calculations showed that the lower value is due to interfacial shear.

Strictly, it is not possible to calculate α for the other packings, since its relation to A is not known. However, the values in Table 1, calculated from the ball-and-tube formula, indicate interesting trends. The serrated grids show, as might be expected, the greatest similarity to the ball-and-tube system. For the random packings it is not clear whether the low values of α are due to the packing geometry or to interfacial shear; however, the success of Equation (9) in correlating all the results indicates that shear is of secondary importance in randomly packed towers.

3. *Surface Tension.* In Figures 8 and 9, the results for the 0.50-in. balls are extremely scattered, probably because of surface tension, which would affect the loading point by stabilizing the wave and by altering the shape of the interstitial meniscus. Both these effects would be magnified for smaller packings and would be different for water and liquid paraffin, the surface tension of the latter being approximately 30 dynes/cm.

4. *Voidage* ϵ. The effect of increasing voidage is to move the point of wave formation. Table 2 shows the angle below the equator for maximum pressure gradient, calculated from Equation (7). It was difficult to observe the position of the initial waves on the balls, because as soon as the waves were formed they were pushed above the equator as in Figure 3*A*. At very high voidages, however, a wave formed on the lowest ball of the series at a point well below the equator, as would be expected from Table 2; a detailed

Table 2. Angle for Wave Formation

[Equation (7)]

ϵ	0.333	0.4	0.5	0.6	0.7	0.8
θ degrees	0	9	15	21	30	43

treatment of this special case is given elsewhere (*15*). It is interesting to note that in the present experiments the 1.49-in. balls in the 2.50-in. tube loaded by wave formation on the bottom ball with air and water, and that therefore the resulting points on Figure 9 have a large deviation from Equation (9).

CONCLUSIONS

1. Loading in a packed tower is caused by the formation of standing waves on the liquid film at points within the packing where the pressure gradient, due to acceleration of the gas, is maximum. In a randomly packed tower loading is thought to be a gradual process, the wave formation occurring over a small range of air flows, although the evidence for this is not direct.

2. At large voidages loading will start at the bottom, and the practice of putting larger, and possibly graded, packing at the bottom is a good one.

3. Interfacial shear has a secondary effect on loading and is most important at large voidages.

4. Surface tension has a secondary effect on loading, although it is quite important for small sizes of packing.

5. Equation (9), which is a linear relation between the dimensionless velocity head in the gas and the dimensionless liquid-film thickness, is suitable for correlating loading points. The correlation is semiempirical, because constants A and B have to be determined for each packing by measuring the loading point at two liquid rates. The loading point at other liquid rates, and for different gases and liquids, can then be predicted.

ACKNOWLEDGMENT

J. E. Howkins wishes to acknowledge the support given by a Gas Council Scholarship to enable him to carry out this work.

NOTATION

A = packing constant
$$= \alpha\left[\frac{15(1-\epsilon)}{3\epsilon-1}\right]^{\frac{1}{3}}\left[\frac{3(3\epsilon-1)}{5}\right]^{3}$$
for the ball-and-tube system

a = interfacial area, sq. ft./cu. ft.

B = packing constant
$$= \frac{1}{(1-\alpha)^{\frac{1}{3}}}\left[\frac{5\times 3^{\frac{1}{3}}}{3\epsilon-1}\right]$$
for the ball-and-tube system

D = tube internal diameter, ft.

d = ball diameter, ft.

G = superficial gas rate, lb./(hr.)(sq. ft.)

g = acceleration of gravity

L = superficial liquid rate, lb./(hr.)(sq. ft.)

ΔP = mean pressure gradient, in. water/ft. height

p = pressure, lb./(ft.)(hr.^{2})

t = liquid-film thickness, ft.

U = gas velocity at any section, ft./hr.

U_0 = gas velocity in the empty tube, ft./hr.

z = axial distance, ft.

Greek Letters

α = fraction defined by Equation (4)

ϵ = voidage

θ = angle indicated in Figure 7

μ = liquid viscosity, lb./(ft.)(hr.)

ρ_G = gas density, lb./cu. ft.

ρ_L = liquid density, lb./cu. ft.

LITERATURE CITED

1. Sherwood, T. K., G. H. Shipley, and F. A. L. Holloway, *Ind. Eng. Chem.*, **30**, 765 (1938).
2. Bain, W. A., and O. A. Hougen, *Trans. Am. Inst. Chem. Engrs.*, **40**, 29 (1944).
3. Dell, F. R., and H. R. C. Pratt, *J. Appl. Chem. (London)*, **2**, 429 (1952).
4. Hoffing, E. H., and F. J. Lockhart, *Chem. Eng. Progr.*, **50**, 94 (1954).
5. Davidson, J. F., and J. E. Howkins, *Proc. Roy. Soc. (London)*, **240A**, 29 (1957).
6. Chilton, T. H., and A. P. Colburn, *Ind. Eng. Chem.*, **23**, 913 (1931).
7. ———, *Trans. Am. Inst. Chem. Engrs.*, **26**, 178 (1931).
8. Cullen, E. J., Ph.D. thesis, Univ. Cambridge, England (1956).
9. Sarchet, B. R., *Trans. Am. Inst. Chem. Engrs.*, **38**, 283 (1942).
10. Leva, Max, "Tower Packings and Packed Tower Design," p. 35, United States Stoneware Co., Akron, Ohio (1953).
11. Piret, E. L., C. A. Mann, and Thomas Wall, *Ind. Eng. Chem.*, **32**, 861 (1940).
12. Elgin, J. C., and F. B. Weiss, *Ind. Eng. Chem.*, **31**, 435 (1939).
13. Shulman, H. L., C. F. Ullrich and N. Wells, *A.I.Ch.E. Journal*, **1**, 247 (1955).
14. Morris, G. A., and J. Jackson, "Absorption Towers," pp. **24**, **25**, **38**, **39**, Butterworths, London, (1953).
15. Howkins, J. E., and J. F. Davidson, *Chem. Eng. Sci.*, **7**, 235 (1958).

Manuscript received Aug. 14, 1957; revised Jan. 20, 1958; accepted Feb. 6, 1958.

Shape Factors for Conductive Heat Flow

JULIAN C. SMITH, JOHN E. LIND, JR., and DAVID S. LERMOND, Cornell University, Ithaca, New York

Application of shape factors to problems of conductive heat flow eliminates the need for lengthy calculations by numerical approximation methods. Shape factors for several systems, determined by electrical analogues, are given in the accompanying article.

In differential form the Fourier equation for conductive heat flow is

$$dq = -k(dt/dx)\,dA \qquad (1)$$

When the conductivity k is constant, Equation (1) may be integrated for steady flow between one boundary at temperature t_1 and another at t_2 to give

$$q = -k(\bar{A}/\bar{x})(t_2 - t_1)$$

$$= -kF_L(t_2 - t_1) \qquad (2)$$

Here F_L is the Langmuir *shape factor* (*4*, *5*), the ratio of the average cross-sectional area for heat flow to the average effective distance for travel. Equation (2) is valid for any system in which k is constant, each boundary is at a uniform temperature, and there is no production or absorption of heat between the boundaries of the system. The rate of heat flow may then be calculated from the conductivity and total temperature drop, provided the shape factor F_L is known.

Rigorous calculation of F_L is easy for a few simple shapes, possible but difficult for certain others, and impossible for a great many. Even a simple problem such as two-dimensional flow between concentric squares defies rigorous mathematical analysis. Several methods have been devised for estimating shape factors for such systems, including numerical approximation methods, graphical methods, and electrical and fluid-flow devices (*3*, *6*).

Unfortunately the methods are often tedious and inconvenient to use in practical problems. Once the shape factor for a given system has been accurately established, however, and presented in an equation or chart, it can be used directly to compute rates of transfer. The tedious calculations or measurements are no longer needed. Langmuir, *et al.* (*5*), presented empirical equations for two- and three-dimensional flow through bodies bounded by rectangular prisms or right-rectangular parallelepipeds, with corresponding inner and outer surfaces parallel and, in any given system, the same distance apart. Equations for several other shapes are given by McAdams (*6*). Andrews (*1*) derived equations for a number of shapes and checked them experimentally.

This study was undertaken to establish shape factors for several systems of industrial importance which have received little or no attention in previous work.

MEASUREMENT OF SHAPE FACTORS

Shape factors were measured by the method described by Andrews (*1*) for two-dimensional figures. This involves measurement of the electrical resistance of the figure and comparison with the resistance of a standard reference figure of known shape factor. The conducting medium was a sheet of Teledeltos Recording Paper Type L. The figures were carefully outlined with General Cement Silver Print, a silver paint made for use in printed circuits. Electrical connections were made with spade lugs cemented to the boundaries of the figures with an excess of silver paint. The reference figure consisted of two concentric circles.

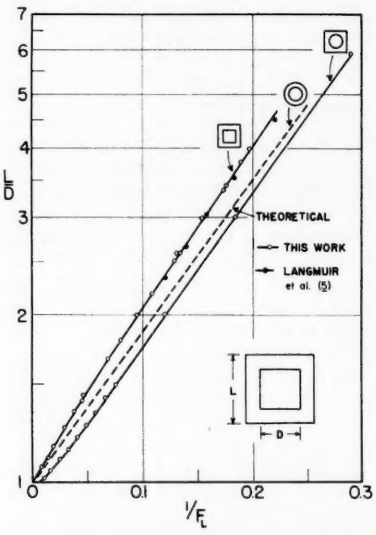

Fig. 1. Shape factors for concentric squares, concentric circles, and a circle within a square.

The conductivity of the paper was not entirely constant but varied with direction and from region to region. The resistivity, on the average, was 11% greater in the direction of the width of the roll of paper than in the direction of its length. The standard deviation of the resistivities from region to region in the longitudinal direction was 1.7%; in the transverse direction it was 2.0%. In addition, the resistivity varied with the humidity of the surrounding air: it rose by about 10% when the relative humidity changed from 20 to 80%. The effect of these variations on the results was very small because in most of the tests both the unknown and the reference figures were symmetrical about several axes and comparison with a standard figure eliminated the effect of changes in humidity.

The figures tested were concentric squares, a circle inside a square and concentric with it, and a circle inside and concentric with a rectangle. The first might be applied to heat flow through the walls of a tall square chimney of uniform wall thickness; the second two might represent a cylinder or pipe enclosed in a square or rectangular duct, filled with a conducting or insulating medium. In the studies of a circle within a rectangle, the figure was drawn with its longest sides at an angle of 45 deg. with the longitudinal direction of the roll of conducting paper. With each figure sets of runs were made, with the relative sizes of the inner and outer boundaries varied: in one set the outer boundary was kept constant and the inner boundary varied; in a second set the reverse was true. In most of the last set of runs the long side of the rectangle was 1.2 times as long as the short side, and the diameter of the circle was varied. In a few runs the diameter of the circle was held at half the length of the short side, and the length of the other side of the rectangle was varied.

RESULTS

The results for concentric squares and for a circle within a square are shown in Figure 1. The ratio of the length of one side of the outer square L to the side or diameter of the inner boundary D is plotted against the reciprocal of the shape factor $1/F_L$. The theoretical graph for concentric circles, where L is now the diameter of the outer circle, is included for comparison. Shape factors for a circle within a rectangle are given in Figures 2 and 3. These shape factors are all for two-dimensional flow in a system of unit length in the third dimension.

Concentric Squares

The graph for concentric squares (Figure 1) consists of two linear branches joined by a short section of gentle curvature. At values of L/D greater than 1.7 the line is straight and nearly parallel to that for concentric circles. In this region it is defined by the empirical equation

$$F_L = \frac{a}{\log \frac{L}{D} - b} \qquad (3)$$

where

$$a = 2.92 \pm 0.05$$

$$b = 0.0233 \pm 0.0007$$

The values of a and b were found by the method of least squares, the uncertainties being computed at the 90% confidence limits. The corresponding correlation coefficient is 0.999950.

The theoretical equation for concentric circles is

John E. Lind, Jr., is at Yale University, New Haven, Connecticut, and David S. Lermond with E. I. duPont de Nemours and Company, Wilmington, Delaware.

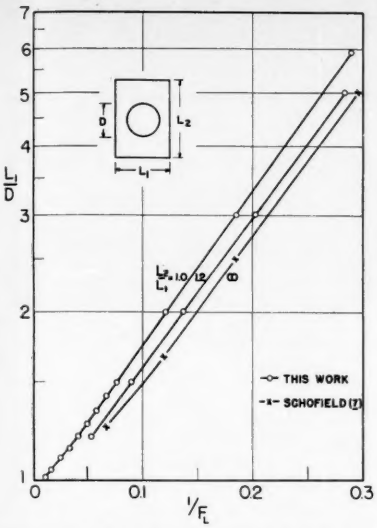

Fig. 2. Shape factors for a circle inside and concentric with a rectangle.

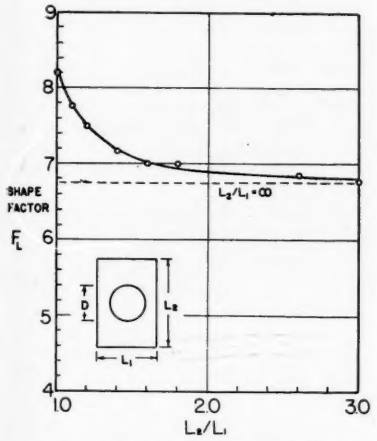

Fig. 3. Variation of shape factor with L_2/L_1 for a circle within a rectangle, ($L_1/D = 2$).

$$F_L = 2\pi/\ln (L/D)$$
$$= 2.728/\log (L/D) \qquad (4)$$

When L/D for concentric squares is less than 1.35 the distance between the squares is small, and the flow approximates that between plates of equal area. The measured shape factors for this region agree closely with those calculated on the basis of the logarithmic mean of the perimeters of the inner and outer boundaries of the figure and are given by the equation

$$F_L = 3.47/\log (L/D) \qquad (5)$$

When L/D is between 1.35 and 1.7, neither Equation (3) nor (5) exactly describes the graph, but the maximum error in using either one when L/D is 1.4 is about 6%. Equation (3) should be used when L/D is greater than 1.4 and Equation (5) when it is smaller than 1.4.

Data given by Langmuir, *et al.* (*5*), for concentric squares are shown in Figure 1 as solid circles. The points are slightly below the graph defined by Equation (3). They were obtained by measuring the electrical conductivity of a copper sulfate solution and are believed to be somewhat less accurate than those reported here. To check the accuracy of the present work, the shape factors for two values of L/D were calculated by the relaxation method (*2*), with an IBM 650 computer. The results are given in Table 1. The present measurements are thus believed to be accurate to within 0.5%.

Table 1. Comparison of Computed and Measured Shape Factors

L/D	Number of points in network	F_L computed by relaxation	F_L from Eq. (3)	Difference, %
2.0	144	10.59	10.51	1.0
2.0	240	10.49	10.51	0.1
3.5	216	5.58	5.61	0.5

Circle Within a Square

The graph for a circle within a square, also in Figure 1, is almost straight and parallel with that for concentric circles when L/D exceeds 1.2. It is below the graph for concentric circles, instead of above it as is the graph for concentric squares. The linear portion is described by the empirical equation

$$F_L = \frac{c}{\log \dfrac{L}{D} + d} \qquad (6)$$

where

$$c = 2.79 \pm 0.010$$

$$d = 0.0360 \pm 0.0007$$

The uncertainties in c and d were also estimated at the 90% confidence limits. The correlation coefficient is 0.999985.

At low values of L/D the graph bends toward the origin, slowly at first, and then very sharply. The shape factor becomes infinite when L/D reaches 1, that is, when the inner circle touches the sides of the square.

Circle Within a Rectangle

Figures 2 and 3 show the results for a circle inside a rectangle, with the center of the circle at the intersection of the diagonals. Figure 2 applies to systems in which the long sides of the rectangle are 1.2 times the short sides ($L_2/L_1 = 1.2$). Also shown are the graphs for a circle within a square ($L_2/L_1 = 1.0$) and for a circle midway between infinite parallel plates ($L_2/L_1 = \infty$). This last graph is based on the calculations of Schofield (*7*) and represents the midpoints of the ranges he estimated for the shape factors. The graph for $L_2/L_1 = 1.2$ is straight and almost parallel with that for the circle within a square but is surprisingly close to that for a circle between infinite plates. This similarity is borne out by Figure 3, which shows how fast the shape factor diminishes as L_2/L_1 increases. Here D, the diameter of the circle, is always half the short side of the rectangle L_1. Once the long side of the rectangle is twice the short side, the shape factor is only about 2% greater than the asymptotic value for infinite parallel plates.

NUMERICAL EXAMPLE

The example used by Emmons (*2*) to illustrate the relaxation method will be solved by the equations presented above. The problem is to compute the heat loss per foot of height through the walls of a square chimney when the inner opening is 24 in. on a side, and the walls are 10 in. thick. The inside surface is at a uniform temperature of 500°F.; the outside surface is at 100°F. The conductivity of the walls is k B.t.u./(hr.)(sq. ft.)/(°F./ft.).

Solution.

$D = 24$ in. $\quad L = 24 + 20 = 44$ in.

$$L/D = 1.833$$

From Equation (3),

$$F_L = 2.92/(\log 1.833 - 0.0233) = 12.17$$

Thus

$$q = 12.17k(500 - 100) = 4868k \text{ B.t.u./hr.}$$

The result Emmons obtained by the relaxation method was $4{,}848k$ B.t.u./hr.

NOTATION

- a = empirical constant in Equation (3)
- A = area normal to direction of flow, sq. ft.; $\bar{A}$ = effective mean area
- b = empirical constant in Equation (3)
- c, d = empirical constants in Equation (6)
- D = diameter or side of inner boundary, ft.
- F_L = Langmuir shape factor, $\bar{A}/\bar{x}$
- k = thermal conductivity, B.t.u./(hr.)(sq. ft.)/(°F./ft.)
- L = length of side or diameter of outer boundary, ft.; L_1 = length of short side of rectangle; L_2 = length of long side of rectangle
- q = rate of heat flow, B.t.u./hr.
- t = temperature, °F.; t_1 of hot boundary; t_2 of cold boundary
- x = distance in direction of transfer, ft.; $\bar{x}$ = mean effective distance for transfer

LITERATURE CITED

1. Andrews, R. V., *Chem. Eng. Progr.*, **51**, 67-F (1955).
2. Emmons, H. W., *Trans. Am. Soc. Mech. Engrs.*, **65**, 607 (1943).
3. Jakob, Max, "Heat Transfer," vol. 1, John Wiley and Sons, New York (1949).
4. Langmuir, Irving, *Trans. Am. Electrochem. Soc.*, **23**, 299 (1913).
5. ———, E. Q. Adams, and G. S. Meikle, *ibid.*, **24**, 53 (1913).
6. McAdams, W. H., "Heat Transmission," 3 ed., Chap. 2, McGraw-Hill Book Company, Inc., New York (1954).
7. Schofield, F. H., *Phil. Mag.*, **12**, 329 (1931).

Manuscript received Oct. 2, 1957; revised received Dec. 12, 1957; accepted, Dec. 14, 1957.

Local Shell-side Heat Transfer Coefficients in Baffled Tubular Heat Exchangers

T. W. AMBROSE and J. G. KNUDSEN

Oregon State College, Corvallis, Oregon

An experimental study of local heat transfer coefficients in a baffled tubular heat exchanger for five baffle spacings and two tube spacings ($2\frac{3}{16}$-in.-pitch, four-tube bundle, and $1\frac{1}{4}$-in.-pitch, fourteen-tube bundle) is reported. Shell-side air-flow rate was constant for all runs. The variation of the local heat transfer coefficient around the tubes and along the length of the tubes for each tube spacing and baffle spacing was investigated. Average shell-side heat transfer coefficients were evaluated from local values and were found to agree with average values reported in the literature. These average values varied with the six-tenths power of the mass velocity in the heat exchanger. The average Nusselt number and the pressure drop across the exchanger each increased at about the same rate as the number of baffles was increased from two to ten. The average heat transfer rate decreased with decreased tube spacing. This effect was evident from the local heat transfer coefficients, and it is explained on the basis of the mechanism of flow around tubes. An eddy flow zone was detected between the baffles. Average heat transfer rates in the eddy and cross-flow zones were almost equal and were about 15% below the average rate in the longitudinal-flow zone. The variation of the average heat transfer coefficient along a tube definitely showed the effects of baffles. High coefficients occurred in the baffle holes and in the baffle windows.

Baffled tubular-heat exchangers are widely used where heat transmission by forced convection is desired between two fluids. In heat exchangers, the shell side is generally the most difficult to design, because of the shortage of fundamental information concerning flow patterns and associated heat transfer rates on the shell side of heat exchangers. Research conducted on the shell side of heat exchangers has been directed toward the measurement of average shell-side heat transfer coefficients. Although this type of data is useful in the design of similar heat exchangers, it gives little information as to the actual dynamics of flow in the exchanger shell or the effect of flow on heat transfer rates.

The shell-side heat transfer coefficient is dependent upon the geometry and dimensions of the exchanger, as well as upon the properties of the fluid. Variables which describe the exchanger geometrically are baffle type, baffle spacing, baffle size, tube size, tube spacing, and the various clearances between the parts of the heat exchanger. The most common baffle type is the segmental baffle, the type employed in this investigation. The height of segmental baffles is generally 75% of the inside diameter of the shell (*6*); however, various other segmental baffle cuts have been investigated (*2*). A decrease in baffle spacing causes the local velocities and the number of passes across the tube bank to increase. The effects of tube size and tube spacing are difficult to separate, as the effectiveness of a tube is dependent upon the clearance between tubes. An increase in tube spacing causes an increase in heat transfer rate (*3*). The clearances between various parts of the exchanger significantly affect the heat transfer coefficient. The fluid that flows between the baffles and the shell is ineffective, as it does not touch any heat transfer surfaces. As a result, increasing the baffle to shell clearance causes a decrease in the heat transfer rate (*2*). The other major leakage zone is the clearance between the tubes and baffle. As a result the cross flow will be decreased and the flow through the baffle increased.

The purpose of the present investigation was to determine local shell-side heat transfer coefficients in a baffled tubular heat exchanger. From the local coefficients obtained it was possible to (1) compare average shell-side heat transfer coefficients with literature values, (2) evaluate the effect of baffles, (3) evaluate the effect of tube spacing, (4) detect the various flow zones that exist on the shell-side of a heat exchanger, (5) evaluate the heat transfer rate in these zones, and (6) determine the direction of future research of this nature.

EXPERIMENTAL EQUIPMENT

The major components of the experimental equipment included a model heat exchanger, a sensing probe, a direct-current power source, an emf. metering arrangement, and an air source.

The model shell and tube heat exchanger had an effective length of 45-in. The shell was a 6-in.–O.D. cast Lucite plastic tube. The tube bundle was made up of 1-in. aluminum condenser tubes, steel tie-rods, and plastic baffles and tube sheets. A photograph of the tube bundle is shown in Figure 1. The shell had an entrance and exit so air could be provided to the shell-side. The tube bundle had no provision for handling a tube-side fluid. The baffles were $\frac{1}{8}$-in.–thick plastic sheets. Table 1 shows the dimensions and tolerances of the shell, tubes, and baffles.

Table 1. Dimensions of Heat Exchanger Components In.

Shell	
Inside diameter	5.72 ± 0.03
Outside diameter	5.94 ± 0.03
Inside length	45
Tubes	
Outside diameter	1.000 ± 0.001
Baffles	
Baffle diameter	5.594 ± 0.002
Height at cut	4.290 ± 0.002
Drilled holes	1.063 ± 0.010

A sensing probe was constructed to measure local heat transfer coefficients. An electrically heated resistance ribbon in contact with a cooling fluid assumes a temperature which is related to the heat transfer coefficient, the cooling-fluid temperature, and the power supplied to the ribbon. An energy balance on the ribbon gives an expression relating these variables [Equation (1)].

A drawing of the sensing probe is shown in Figure 2. It was fabricated from a 6-in. piece of 1-in.–O.D. Lucite plastic rod, drilled with a $\frac{1}{2}$-in. hole along its longitudinal axis. A 1-in. section at each end of the tube was machined and threaded. Three 1-in.–wide by 0.002-in.–thick pieces of resistance ribbon were wrapped around the plastic bar as shown in Figure 3. The resistance ribbon used was Tophet *C*, having a resistance of 0.271-ohm/ft. and a thermal conductivity of 7.63-B.t.u./(hr.)(sq. ft.)(°F./ft.). The ribbons were held in place by copper bus bars embedded in the plastic, which also served to supply electric power to the resistance ribbons. Power leads were soldered to the lower connecting bar in such a manner that the three ribbons were in series. The leads were brought into the plastic piece through the holes along its horizontal axis. Seven iron-constantan thermocouples were located in a groove under the center ribbon, as shown in Figure 2. The thermocouple junctions were electrically insulated from the ribbon by a layer of Saran wrap. At the opposite end from the power leads the thermocouple leads entered the probe, which was supported between two pieces of aluminum condenser tubing with plastic adapters threaded to the plastic piece. The thermocouple leads were connected to a multiple-junction selector switch attached to one of the support tubes. A photograph of the sensing probe attached to one support tube is shown in Figure 3. Direct current was supplied by passing alternating current through a voltage stabilizer and a selenium rectifier. The emf.'s of the various thermocouples were measured with a Leeds and Northrup precision potentiometer.

The above-described sensing-probe assem-

T. W. Ambrose is with General Electric Company, Richland, Washington.

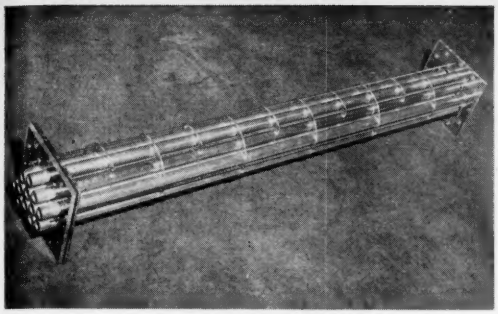

Fig. 1. Assembled tube bundle.

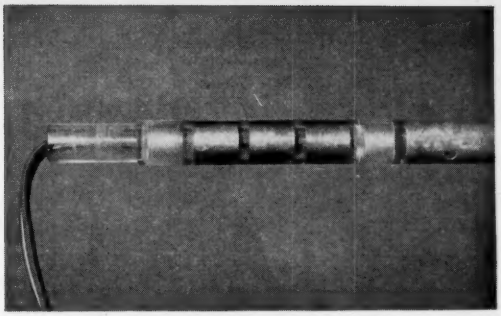

Fig. 3. Sensing probe attached to one support tube.

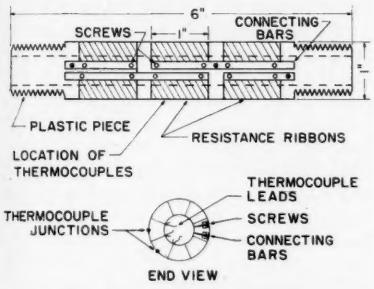

Fig. 2. Detail of sensing probe.

bly could replace any of the aluminum condenser tubes in the bundle or could be located at any given point along the length of the exchanger. In this manner, it was possible to determine local heat transfer coefficients at any location in the tube bundle.

The shell-side fluid was air supplied by a Roots-type blower rated at 280 cu. ft./min. at 3½ lb./sq. in. gauge. The air from the blower passed through a 2-in. pipe to the coolers and then to the model heat exchanger. Sharp-edged orifices equipped with manometers were used to determine the air flow rate, and the pressure drop across the exchanger was measured with a manometer. The air temperature was measured by a thermocouple located in the heat exchanger outlet. A schematic drawing of the air flow system is shown in Figure 4.

EXPERIMENTAL DATA

Five baffle spacings and two tube spacings were investigated. Original data are available (*1*). The air flow rate was maintained constant at 60 cu. ft./min. (60°F., 1 atm.) throughout the study. Shell-side air temperature was usually quite close to room temperature. In all, about 7,000 local heat transfer coefficients were obtained. The data are summarized briefly in Table 2.

Various baffle spacings were studied by varying the number of baffles in the exchanger; zero, two, four, six, and ten baffles equally spaced in the 45-in. shell. The number of positions investigated along each tube for the five baffle spacings was limited to the locations shown to scale in Figure 5. (Reference should be made to Figure 5 in subsequent discussions regarding locations in the heat exchanger.) These locations are at the inlet, outlet, and center of the model heat exchanger, as well as in each baffle hole and 2 in. on each side of the baffle. In the four- and six-baffle cases, the region downstream from the center line of the exchanger was not investigated, as it was assumed to be symmetrical with the upstream region. The same reasoning was used in the ten-baffle case, where only the first three spaces were studied.

One-inch outside-diameter tubes in two triangular pitches: a $2\frac{3}{16}$-in. tube pitch, which comprised a four-tube bundle, and a $1\frac{1}{4}$-in. tube pitch, which comprised a fourteen-tube bundle. As may be seen in Figure 6, the tube spacing of the four-tube bundle is identical with that of the same four tubes in the fourteen-tube bundle. The tube and thermocouple numbering system is also shown in Figure 6.

CALCULATION OF THE LOCAL HEAT TRANSFER COEFFICIENT

To calculate local heat transfer coefficients, required data were the current

Table 2. Summary of Experimental Data

No. of baffles	No. of positions studied along tube	Total No. of local coefficients measured	Air flow rate, cu. ft./min. cfm (60°F., 1 atm.)
	Four-tube bundle		
0	7	196	59.5
2	11	308	59.1
4	10	280	59.5
6	12	336	59.5
10	9	252	59.1
	Fourteen-tube bundle		
0	7	686	59.3
2	11	1,078	59.1
4	10	980	59.3
6	12	1,176	59.4
10	9	882	59.4

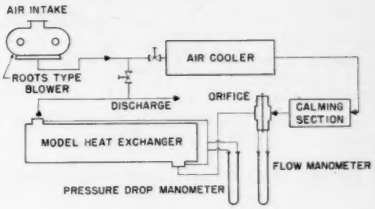

Fig. 4. Air flow system.

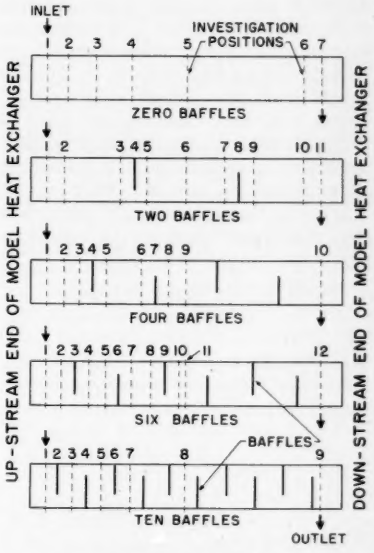
INLET
INVESTIGATION POSITIONS
1 2 3 4 5 6 7
ZERO BAFFLES
1 2 3 4 5 6 7 8 9 10 11
TWO BAFFLES
1 2 3 4 5 6 7 8 9 10
FOUR BAFFLES
1 2 3 4 5 6 7 8 9 10 11 12
SIX BAFFLES
BAFFLES
1 2 3 4 5 6 7 8 9
TEN BAFFLES
OUTLET
UP-STREAM END OF MODEL HEAT EXCHANGER
DOWN-STREAM END OF MODEL HEAT EXCHANGER

Fig. 5. Baffle spacings and positions investigated.

in the resistance ribbon and the millivolt readings from the seven sensing-probe thermocouples and the air thermocouple.

A general expression for the local heat transfer coefficient is developed by making an energy balance around a differential length of resistance ribbon. The following equation results, as shown by Giedt (*5*):

$$h = \frac{\frac{i^2R}{W} + \frac{kZ}{Wr^2}\frac{d^2t}{d\theta^2} - \frac{q_{rad}}{A} - \frac{q_{cond}}{A}}{t - t_a} \quad (1)$$

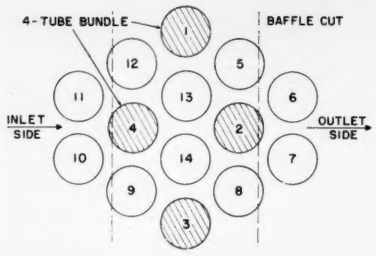

Fig. 6a. Tube arrangements numbered at up-stream end of exchanger.

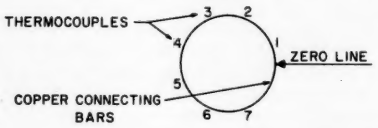

THERMOCOUPLES NUMBERED AT THE UP-STREAM END OF SENSING PROBE

Fig. 6b. Thermocouple numbering system.

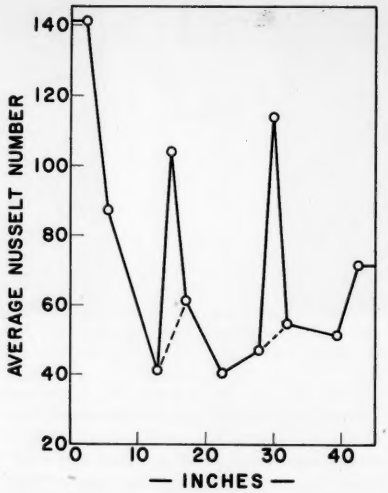

Fig. 7. Plot for determination of average Nusselt number for model heat exchanger
———— high Nusselt number
---------- low Nusselt number

The radiation term was neglected in calculating the local heat transfer coefficients, it being assumed to be negligible in the majority of cases. This assumption is in agreement with other investigators who have used this method (*3, 4*). The rate of conduction of heat into the plastic probe was also assumed to have a negligible effect on the local heat transfer coefficient. This assumption was justified by a maximizing type of calculation (*1*). Neglecting the radiation and conduction term and substituting in the numerical constants, one can write Equation (1) as

$$h = \frac{11.10i^2 + 2404(d^2t/d\theta^2)}{t - t_a} \qquad (2)$$

Equation (2) was used to calculate the local heat transfer coefficients. The second derivative was evaluated with a Milne three-point method (*9*). The actual calculation of the local heat transfer coefficients was performed on a digital computer. An average heat transfer coefficient was evaluated at each position from the arithmetic average of the seven local coefficients around the circumference of the tube. A Nusselt number for each position was calculated by means of this average heat transfer coefficient.

EXPERIMENTAL RESULTS

Average Shell-side Nusselt Numbers

The average shell-side heat transfer rates for the heat exchanger were determined and compared with those of Williams and Katz (*13*) and Donohue (*2*). Two values of the average Nusselt number were calculated. In each, the average Nusselt number at each cross section (including all tubes) was plotted vs. exchanger length as shown in Figure 7. The high average Nusselt number for the heat exchanger was obtained by integrating the plot in Figure 7 and dividing by the heat-exchanger length. At each baffle a maximum in the Nusselt number is observed. The low average Nusselt number was obtained by neglecting these high peaks, as shown by the broken lines. The difference between the high and low average Nusselt numbers indicates the effect of the high heat transfer coefficients at the baffle holes. The effect could be obtained more accurately by a detailed study of local coefficients in the vicinity of the baffle.

The term $(hd/k)(C_p\mu/k)^{-1/3}$ was calculated from the average Nusselt number and the Prandtl number of air, which was taken as 0.7 in all cases. In Figure 8 the term $(hd/k)(C_p\mu/k)^{-1/3}$ is plotted against the weighted Reynolds number (dG_e/μ). Also plotted are two curves from Williams and Katz (*13*). The two remaining curves were obtained by Donohue (*2*) on the basis of data of Short (*11*). All the curves shown in Figure 8 are for segmental baffled heat exchangers with triangular tube pitches.

The curves representing the high values of average Nusselt numbers are above those of the other workers. However, a straight line with a 0.6 slope is obtained. The curves representing the low average heat transfer coefficients lie very close to the data of Williams and Katz, particularly for the fourteen-tube case, which is most nearly like the exchangers studied by these investigators. The slope of the curve, however, is less than 0.6.

The method used to evaluate the high Nusselt numbers was thought to overweight the heat transfer coefficients at the baffles. It is believed, however, that the high average values are closer to the true average than the low average values. The contribution of the high heat transfer coefficients at the baffles is greater for the ten-baffle case than for the two-baffle case. This is apparent when the low average values are compared with the high average values. For the two-baffle case the difference between the two average Nusselt numbers is about 5%, and for the ten-baffle case about 25%. This also accounts for the curve representing the low values having a slope of less than 0.6. The true curve is thought to pass between the high and low points for the two-baffle case and to have a 0.6 slope.

The results in Figure 8 show good agreement of the present work with that of other investigators. These results are always somewhat high, but this is expected because of the large tube size used. All other investigators have studied tube diameters no greater than $\frac{3}{4}$-in., while the present results are based on a 1-in.–O.D. tube.

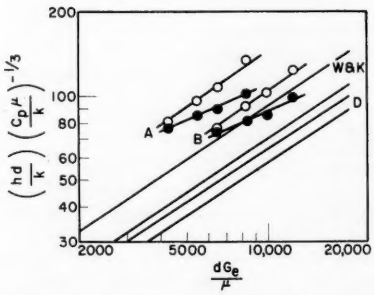

Fig. 8. Correlation of shell-side heat transfer data, ○ high values, ● low values

Curve

A	Ambrose & Knudsen	(6″ shell, 1″ tubes, 2-3/16″ tube pitch)
B	Ambrose & Knudsen	(6″ shell, 1″ tubes, 1-1/4″ tube pitch)
W & K	Williams & Katz	(6″ shell, 5/8″ tubes, 3/4″ tube pitch)
	Williams & Katz	(8″ shell, 1/2″ tubes, 5/8″ tube pitch)
D	Donohue	(8″ shell, 5/8″ tubes, 3/4″ tube pitch)
	Donohue	(6″ shell, 5/8″ tubes, 7/8″ tube pitch)

Effect of Baffles

The addition of baffles to the tube bundle increased the shell-side heat transfer rate. This effect is shown in Figures 8 and 9. In Figure 9 average shell-side Nusselt numbers for the four- and fourteen-tube cases are plotted against the number of baffles. The curve for the four-tube bundle is always higher than that for the fourteen-tube bundle with the exception of the no-baffle case. This reversal at the no-baffle case was expected, since the mass flow rate was increased by the addition of tubes. After the addition of two baffles, the rate of increase in the Nusselt number by adding baffles is nearly the same for both four- and fourteen-tube cases.

The addition of baffles to the tube bundle increased the pressure drop across the shell-side of the heat exchanger. Figure 10 shows a plot of the pressure drop (inches of water) vs. the number of baffles present. The points lie very nearly on a straight line with similar slopes for both the four- and fourteen-tube bundles. It can be seen from Figures 9 and 10 that increasing the number of baffles from two to ten increases the heat transfer rate and the pressure drop. The rate of increase of each is about the same as the number of baffles is increased.

Effect of Tube Spacing

As shown in Figure 9, the 2 $\frac{3}{16}$-in. pitch arrangement had a higher heat transfer rate than the 1¼-in. pitch for all baffle cases, despite the fact that velocities are higher in the latter case. The tube area for the smaller pitch was only 93.5 to 95.5% as effective as that for the greater tube pitch. This effect was noted in Short's (*11*) data, which show that, for a heat exchanger with ⅜-in. tubes on a ½-in. triangular tube pitch, the area was from 92.9 to 93.8% as effective as when the tubes were spaced on a $1\frac{1}{16}$-in. tube pitch for three, seven, eleven, fifteen and nineteen baffles.

When the tube pitch was decreased by the addition of tubes, the clearances between the tubes were greatly decreased (Figures 6 and 11). The decreased flow area caused an increase in local velocities throughout the heat exchanger. Generally, increased heat transfer rates are associated with increases in the local mass velocities; however, in the results cited above, just the reverse was true for the average heat transfer coefficients.

A comparison of the four tubes, which had the same location in each tube arrangement, indicated that tubes in the four-tube bundle always had higher local heat transfer coefficients than the same tubes in the fourteen-tube bundle. This effect is explained by examining the characteristics of the flow past the tubes. When only the four tubes were in the shell, as in Figure 11*A*, the area behind the lead tube was characterized by a turbulent wake almost as wide as the tube and

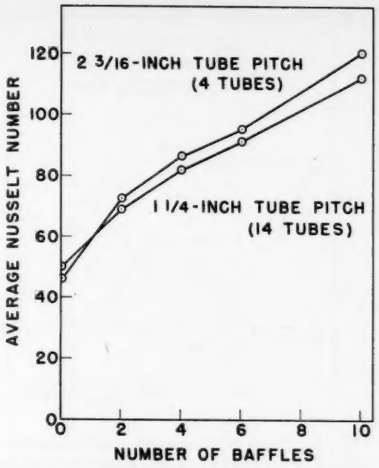

Fig. 9. Effect of baffles on the heat transfer rate.

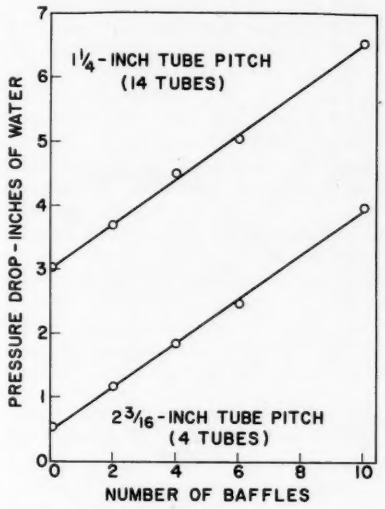

Fig. 10. Effect of baffles on pressure drop.

probably extending to the next tube (*12*). This turbulent wake has the effect of producing a high heat transfer coefficient on the trailing tube. Although the local velocity of the stream was lower when compared with the fourteen-tube bundles, the turbulence caused higher local coefficients. The fluid leaving the trailing tube had to flow around the baffle cut before striking the lead tube in the next baffle space. This fluid was also in a highly turbulent state, and the local coefficients on the lead tube were even higher than those on the trailing tube.

With fourteen tubes there were two lead tubes instead of one, as shown in Figure 11*B*. All tubes were located quite close to each other. Owing to the close spacing of the tubes, the turbulent wake was confined to a narrow region behind the tubes and did not extend to the

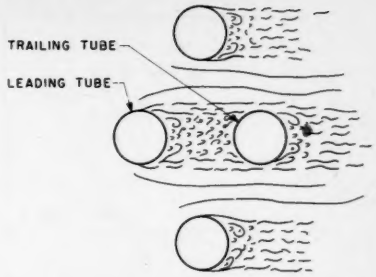

Fig. 11*a*. Flow pattern across tube bank (four tube bundle).

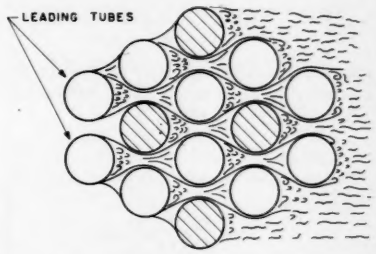

Fig. 11*b*. Flow pattern across tube bank (fourteen tube bundle).

downstream tube (*12*). This is illustrated in Figure 11*B*. For this reason, local heat transfer coefficients are lower than in the four-tube case.

The local heat transfer coefficients for each position were plotted vs. the angle θ, measured counterclockwise around the tube when the sensing probe was observed from the upstream end. The 0-deg. point was arbitrarily set on the outlet side of the exchanger, as shown in Figure 6. Thermocouple 1 was located at 22½ deg. from the zero point and a thermocouple located every 45 deg. thereafter until thermocouple 7 was reached at 292½ deg. from the zero point. The position at 337½ deg. was the region occupied by the connecting bars.

Parts *A* and *B* of Figure 12 show a comparison of the local heat transfer coefficients at position 3 for tubes 2 and 4 for the four- and fourteen-tube bundles and the ten-baffle case. The lead tube in the four-tube case (tube 2) was noted to have a greater heat transfer rate at $\theta = 0$ deg. when compared with the trailing tube (tube 4), owing to high turbulence in the fluid coming around the baffle. At $\theta = 180$ deg. the heat transfer rates for the lead tube were slightly lower than those of the trailing tube. For both tubes 2 and 4, the heat transfer coefficients for the fourteen-tube case were considerably less than for the four-tube case. This is consistent with the explanation outlined above.

Flow Zones

Gupta and Katz (*7*) visually detected two flow zones in the space between

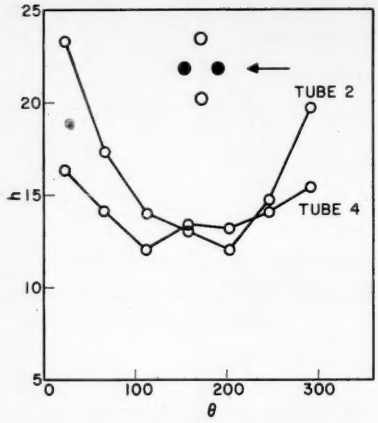

Fig. 12*a*. Local heat transfer coefficients for position 3 in exchanger with 10 baffles and 4 tubes.

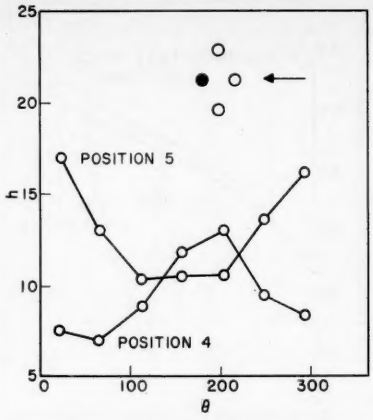

Fig. 13*a*. Local heat transfer coefficients for tube 4 in exchanger with 6 baffles and 4 tubes.

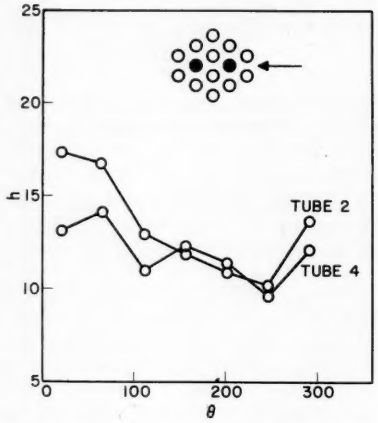

Fig. 12*b*. Local heat transfer coefficients for position 3 in exchanger with 10 baffles and 14 tubes.

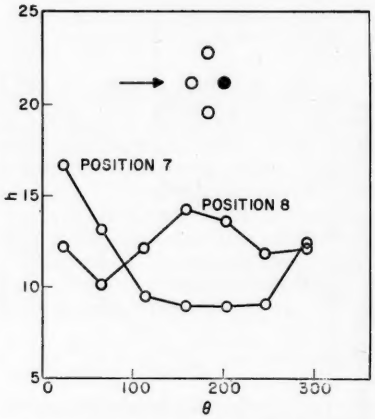

Fig. 13*b*. Local heat transfer coefficients for for tube 2 in exchanger with 6 baffles and 4 tubes.

baffles: an eddy zone located behind a baffle and a cross-flow zone located in the region in front of the next baffle. These observations were made in a glass heat exchanger which had no clearance between tubes and baffles or between baffles and shell. Eddy zones were shown by Gunter, Sennstrom, and Kopp (*6*) to exist behind solid baffles.

In both these investigations no leakage occurred through the baffle, and the eddy zone was not disturbed by flow through or around the baffle, nor was the effect of leakage on the eddy zone determined. From the present investigation, sufficient data were available for the regions between baffles to permit the detection of the eddy zones and the determination of the heat transfer rates in these localities.

In the case of the fourteen-tube bundle, the eddy zone was present but was not so pronounced as in the four-tube case.

Evidence of the eddy zone is shown by the local heat transfer coefficients. In the four-tube bundle, positions 5 and 8 were located in the cross-flow zone and were used as a basis of comparison. Figure 13*A* shows that at position number 5 the local heat transfer coefficient for tube 4 has a definite maximum near $\theta = 0$. For position 4 the local heat transfer coefficient for tube 4 has a minimum in the region of $\theta = 0$. The complete reversal of these two curves indicated that the fluid was approaching tube 4 in a different direction at position 5 than at position 4. This can be explained if position 4 lies in an eddy zone. This same effect is shown in Figure 13*B* for the region between baffles 2 and 3. Here the trailing tube is tube 2. Tubes 1 and 3 show this same reverse type of curve for position 4 as compared with position 5 and for position 7 as compared with position 8. Thus the eddy zone was large enough to cover the entire bundle at the downstream side behind the baffle. For the fourteen-tube, six-baffle case, the data for position 7 and tubes 1 to 5 and 8, 9, 12, 13, and 14 indicated that tubes 2, 5, and 8 showed evidences of the eddy zone; tubes 4, 9, and 12 had the normal type of curve, that is, the high coefficients near the leading edge; tubes 1 and 3 showed evidences of the eddy zone; and tubes 13 and 14 indicated neither a maximum nor minimum, yielding heat transfer rates which were nearly the same completely around the tube.

Evidence of the eddy zones was noted at positions 2 in. behind the baffles in both the two- and four-baffle spacings; however, insufficient data prevented detailed examination of the eddy zones. In the ten-baffle arrangement a single examination point was located midway between baffles (2 in. on each side of the baffles). No evidence of an eddy zone was noted at any of the tubes in either the four- or fourteen-tube bundles. A study of more locations between the baffles would allow a more thorough analysis.

Heat Transfer Rates in Various Zones

The heat transfer rates in the longitudinal flow zone, the cross-flow zone, and the eddy zone were compared for the fourteen-tube case and six-baffle arrangement. The longitudinal flow zone between baffles 1 and 3 through the window of baffle 2 had an average heat transfer coefficient of 13.93 B.t.u./(hr.)(sq. ft.)(°F.). The longitudinal-flow zone was considered as the region enclosed by the shell between baffles 1 and 3 and two imaginary planes extending from the cut of baffle 2 to the base of baffles 1 and 3 respectively. The average heat transfer coefficients of the cross-flow and of the eddy zones were taken as the average of the local coefficients on the transverse section through these zones. The average heat transfer coefficients in the cross-flow zones at positions 5 and 8 were 11.61 and 11.36 respectively. The average heat transfer coefficients in the eddy zones at positions 4 and 7 were 11.01 and 11.57. The average coefficients of the two zones do not seem to be significantly different when compared on the basis of the variation between cross-flow and eddy zones. The average of these four values is 11.40, which is about 18% lower than the value for longitudinal flow. Insufficient data were taken for the two, four, and ten baffles for a comparison of the heat transfer rates in various zones.

Heat Transfer Rates Along the Length of the Heat Exchanger

The heat transfer coefficients along the length of the heat exchanger varied considerably. To show this variation, the average Nusselt numbers at each position on a tube were plotted vs. distance from the upstream end of the exchanger. Figure 14 shows the distribution of the average Nusselt number at each position along tube 10 for the fourteen-tube bundle.

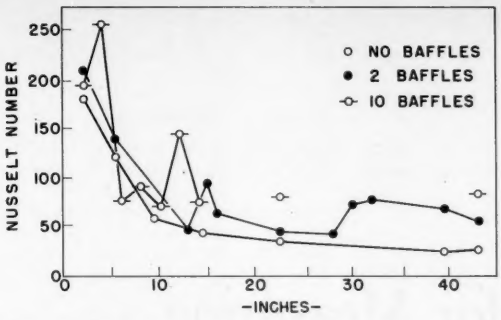

Fig. 14. Average local Nusselt numbers along tube 10.

High Nusselt numbers were observed at the entrance, and these showed small variation with the number of baffles in the exchanger. With no baffles present, the Nusselt number decreased rapidly with length and became constant after the midpoint of the exchanger. The constant value was about one sixth of the value at the entrance.

For the two-baffle case, the Nusselt number decreases with length, then increases to a maximum where the tube goes through the first baffle. The Nusselt number then decreases and increases again to a maximum at the point in the baffle window where the tube passes the baffle. Similar phenomena are observed for all baffle spacings. A large increase is noted in the Nusselt number as the tube passes through the hole in the baffle. These results indicate semiquantitatively that a small clearance between the tube and baffle has the effect of producing a high Nusselt number at this point. The baffle also affects the tube in the baffle window in that a moderate increase occurs in the Nusselt number at the point in the baffle window where the tube passes the baffle.

Heat Transfer Rates Around a Single Tube

True cross flow through the tube bundle was most nearly obtained in the region between baffles in the ten-baffle case. At points midway between the baffles, the lead tubes all showed similar circumferential variation of the local heat transfer coefficients. This pattern is characterized by a high heat transfer coefficient at the leading edge of the tube. The local coefficient decreased with increasing distance away from the leading edge until a minimum was reached near the trailing edge of the tube. The trailing tube in the bundle had a lower heat transfer coefficient at the leading edge when compared with the lead tube, but it had a higher coefficient on the trailing side of the tube than did the lead tube. About a twofold decrease in heat transfer rate around tubes in cross flow was observed. The variation around the tubes in the bundle was considerably different from that observed on a single cylinder in cross flow.

CONCLUSIONS

Local heat transfer coefficients were determined on the shell side of a baffled tubular heat exchanger. Baffle spacing and tube spacing were varied, but volumetric flow rate was held constant. An average Nusselt number for the shell side was calculated from these local coefficients, both including and neglecting the high values at the baffles. It is believed that the average Nusselt number which includes the high value at the baffles is closer to the true Nusselt number. These average values calculated from the measured local coefficients agree fairly well with those of other investigators.

Addition of baffles caused an increase in the average Nusselt number and the pressure drop at a constant flow rate. The average Nusselt number and the pressure drop across the exchanger each increased at about the same rate as the number of baffles was increased from two to ten.

Increasing the tube spacing from $1\frac{1}{4}$ to $2\frac{3}{16}$ in. at constant flow rate increased the average heat transfer coefficient for all baffle arrangements except the zero-baffle case.

Between baffles a cross-flow and eddy zone were detected from the variation of local coefficients on the tubes. The eddy zone was detected for all but the ten-baffle case, for which insufficient data were available. For the fourteen-tube, six-baffle case there was little difference in the average rate of heat transfer in the longitudinal-flow, cross-flow, and eddy-flow zones.

The variation of average heat transfer coefficient along a tube definitely showed the effect of baffles in a heat exchanger. Large values are obtained in baffle holes, and moderately large values occur in the baffle window where the tube passes the baffles.

ACKNOWLEDGMENT

Appreciation is expressed to the National Science Foundation for a grant to support the research described here.

NOTATION

A = area, sq. ft.; A_c, cross flow area in tube bank; A_w, baffle window area
C_p = specific heat at a constant pressure, B.t.u./(lb.)(°F.)
d = diameter of tube, ft.
G_e = weighted mass velocity, lb./(hr.)(sq. ft.) = $w/\sqrt{A_w A_c}$
h = heat transfer coefficient, B.t.u./(hr.)(sq. ft.)(°F.)
i = current, amp.
k = thermal conductivity, B.t.u./(hr.)(sq. ft.)(°F.)/ft.
$q_{cond.}$ = heat conducted into plastic specimen, B.t.u./hr.
$q_{rad.}$ = heat radiated from ribbons, B.t.u./hr.
R = resistance of ribbon, ohms/ft.
r = radius, ft.
t = temperature, °F.; t_a, air temperature
W = width of resistance ribbon, ft.
w = mass flow rate, lb./hr.
z = thickness of resistance ribbon, ft.

Greek Letters

θ = angle measured from leading edge of a tube, deg.
μ = viscosity, lb./(ft.)(hr.)

LITERATURE CITED

1. Ambrose, Tommy W., Ph.D. thesis, Oregon State Coll., Corvallis (1957), available from University Microfilms, Ann Arbor, Mich.
2. Donohue, Daniel A., *Ind. Eng. Chem.*, **41**, 2499 (1949).
3. Drake, R. M., Jr., *J. Appl. Mechanics*, **16**, 3 (March 1949).
4. ———, et al., Am. Soc. Mech. Engrs. paper 52-A-59 (1952)
5. Giedt, W. H., *Trans. Am. Soc. Mech. Engrs.*, **71**, 375 (1949).
6. Gunter, A. Y., H. R. Sennstrom, and S. Kopp, paper presented at the annual meeting of the Am. Soc. Mech. Engrs., Atlantic City, N. J., (December, 1947).
7. Gupta, Rajeshwar, K., and Donald L. Katz, *Ind. Eng. Chem.*, **49**, 998 (1957).
8. Kern, Donald Q., "Process Heat Transfer," p. 130, McGraw-Hill Book Company, Inc., New York (1950).
9. Milne, William E., "Numerical Calculus," p. 96, Princeton Univ. Press (1949).
10. Short, B. E., *Trans. Am. Soc. Mech. Engrs.*, **64**, 780 (1942).
11. ———, *Univ. Texas Publ.* 4324, pp. 1–55 (1943).
12. Wallis, R. P., *Engineering*, **148**, 423 (1934).
13. Williams, Richard B., and Donald L. Katz, *Trans. Am. Soc. Mech. Engrs.*, **74**, 1307 (1952).

Manuscript received Aug. 12, 1957; revised Dec. 10, 1957; accepted Jan. 13, 1958.

Electrolytic Methods for Measuring Water Velocities

WILLIAM E. RANZ

The Pennsylvania State University, University Park, Pennsylvania

A convection-controlled mass transfer process in which the rate of mass transfer results in an electrical signal should have certain advantages as the working principle for a velocity- and turbulence-measuring device. The velocity can be read at a remote place as a calibrated electrical signal. Compensation for phase shift and amplitude attenuation of a fluctuating signal should be small because the measuring probe would have no capacity for the transferred quantity. In water, such processes are possible whenever electrolysis occurs under conditions of *concentration polarization*, and they exist in relatively uncomplicated form as the *limiting currents* of polarographic analysis. The investigation reported here was intended as a survey and evaluation of electrolytic methods for measuring water velocities.

The series of experiments that was performed showed that a working instrument could be designed on the principle of convection-controlled electrolysis, but that the chemical reactions involved were unreliable for consistent trouble-free results. Practical instruments appear to be possible only after long development and considerable study of chemical mechanisms.

EXAMPLE SYSTEM

A variation of an experiment in polarography (*2, 7*) illustrates what happens when the mass transfer rate controls an electrolytic reaction and shows how the phenomenon can be used to measure velocities. The cell components shown in Figure 1 are (*a*) a platinum *indicator* electrode, (*b*) a silver and silver chloride *reference* electrode (S.S.C.E.) immersed in saturated potassium chloride and in contact with the electrolyte through an agar plug, and (*c*) an aqueous electrolyte of 0.1 M potassium chloride containing naturally dissolved oxygen as the electroactive species. The cell is attached to a polarograph instrument that can vary the potential of the indicator electrode with respect to the reference electrode. The current flow through the cell is read on a suitable recorder.

The electrolyte is now made to flow past the indicator electrode at various velocities v_0, and the curves of current vs. voltage are plotted as shown in Figure 2. The current *plateaus* are called *limiting currents*. The existence of limiting currents and the fact that different curves are plotted for different values of v_0 are evidences of a convection-controlled electrochemical reaction. Current values at constant voltage are obviously a measure of velocity at nearly every voltage setting at which finite currents are realized. Voltage values at constant current are also a measure of velocity when the constant current is not a limiting current.

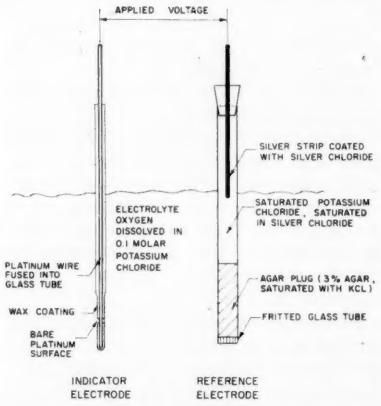
APPLIED VOLTAGE
SILVER STRIP COATED WITH SILVER CHLORIDE
SATURATED POTASSIUM CHLORIDE, SATURATED IN SILVER CHLORIDE
ELECTROLYTE OXYGEN DISSOLVED IN 0.1 MOLAR POTASSIUM CHLORIDE
PLATINUM WIRE FUSED INTO GLASS TUBE
AGAR PLUG (3% AGAR, SATURATED WITH KCL)
WAX COATING
FRITTED GLASS TUBE
BARE PLATINUM SURFACE
INDICATOR ELECTRODE
REFERENCE ELECTRODE

Fig. 1. Electrolysis cell which can be used for velocity measurements.

The random current fluctuations shown in Figure 2 probably resulted from turbulence in the test medium. The electrolyte was contained in a plastic basin, which was rotated at various speeds (*5*). The cylindrical electrode was immersed near the outer circumference with its axis perpendicular to the flow. The probe traveled in its own wake and detected the turbulence of this wake, the eccentricity of the rotating system, and the stirring action of the reference electrode, which was also immersed in the electrolyte. Figure 2 is a direct copy of the chart record taken on a Leeds and Northrup Electro-chemograph, type *E*, which applied a voltage change at a constant rate. The voltage scale is also a time scale, and the recorder gave a time record within the limits of its response rate.

EFFECT OF MASS TRANSFER ON THE OVER-ALL RATE OF ELECTROLYSIS

A brief discussion of electrochemical reactions and associated rate phenomena is necessary to explain Figure 2.

As the potential of the probe was brought into a range where dissolved oxygen was reduced to hydrogen peroxide (and possibly to water), the current increased exponentially with increasing negative potential. (There may be evidence in Figure 2 that the reaction occurred in two steps, the second reaction beginning at a slightly different potential.) When the reaction rate was sufficiently high to reduce the concentration of oxygen next to the surface to a value negligibly small compared with the ambient concentration, the curve exhibited constant current over a range of potentials between −0.65 and −0.85 volt.

*Supplementary material has been deposited as document 5714 with the American Documentation Institute, Photoduplication Service, Library of Congress, Washington 25, D. C., and may be obtained for $2.50 for photoprints or $1.75 for 35-mm. microfilm.

Table 1. Experimental Conditions for the Curves Shown in Figure 3

Curve (Fig. 3)	Electroactive Species: Type	Electroactive Species: Concentration	Electrolyte: Type	Electrolyte: Temperature, °C.	Probe: Type	Probe: Diameter, mm.	Probe: Length, mm.	Probe: Base, mm.	Probe: Height, mm.	Applied voltage vs. S.S.C.E.	Cell resistance, ohms
1	$Fe(CN)_6^{-3}$	$1.994 \times 10^{-3}M$	1.0M KCl	25	Cyl.	4.432	4.736			0.00	< 500
2	O_2 (dissolved)	Saturated by air at 732 mm. Hg	0.1M KCl	25	Cyl.	0.449	5.310			−0.75	< 500
3	O_2 (dissolved)	Saturated by air at 737 mm. Hg	Sea water	25	Cyl.	0.449	5.310			−0.95	—
4	$Fe(CN)_6^{-3}$	$2.057 \times 10^{-3}M$	1.0M KCl	25	Pencil			1.19	2.04	0.00	< 300
5	O_2 (dissolved)	Saturated by air at 737 mm. Hg	0.1M KCl	25	Pencil			1.21	1.41	−0.75	400
6	$Fe(CN)_6^{-3}$	$2.003 \times 10^{-3}M$	1.0M KCl	25	Pencil			1.19	2.04	−2.00	12,000*
7	O_2 (dissolved)	Saturated by air at 736 mm. Hg	0.1M KCl	25	Pencil			1.21	1.41	−0.95	< 800
8	O_2 (dissolved)	Saturated by air at 734 mm. Hg	0.5M Na_3PO_4	33–34	Pencil (mercury plated)			1.19	2.04	−0.81	1,000

*Total resistance in cell circuit containing an oscillograph in parallel with the resistance.

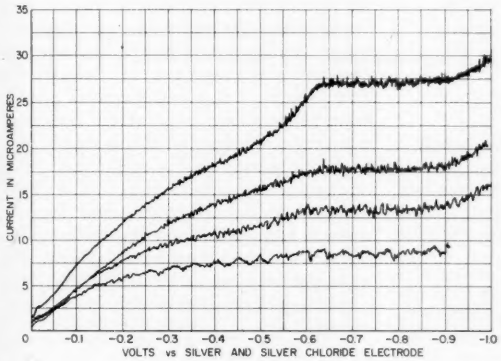

Fig. 2. Effect of applied voltage on electrolytic currents at four flow velocities.

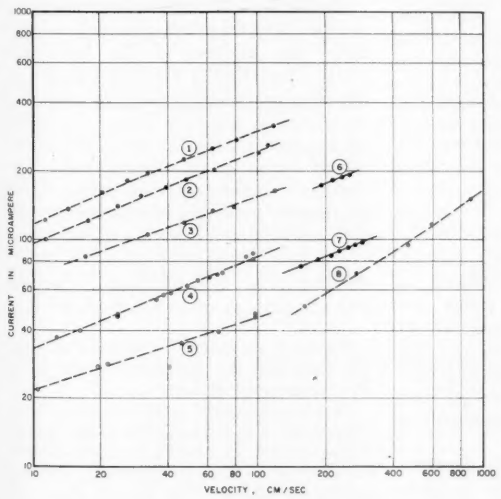

Fig. 3. Limiting current vs. velocity for a variety of experimental conditions.

In the region of constant current, where the reaction rate did not depend on the reaction constant but on the rate at which dissolved oxygen could be brought to the surface by convection and diffusion, the current was not affected by changes in the applied voltage. Finally, when a potential was reached at which hydrogen was evolved, the current again rose exponentially with increasing negative potential.

The over-all rate of electrolysis, as measured by the electric current, depends on three interrelated processes which occur in series (*5, 10*): (1) mass transfer of reactants to the electrode surface, (2) electrochemical reaction, and (3) mass transfer of reaction products from the electrode surface. Diffusional rate equations can be written for processes 1 and 3. A chemical rate equation can be written for process 2. An over-all rate equation, of the form of Figure 2, results when the unknown surface concentrations of reactants and products are eliminated from the three equations (*5, 10*).

When only the oxidized form of the electroactive species is contained in the main flow and when limiting current conditions are reached, the rate equation reduces to a form which involves only mass transfer by convection and diffusion

$$I_1 L/nFA_i C_{Ox0} D_{Ox} = N_{Sh}(Lv_0/\nu, \nu/D_{Ox}) \qquad (1)$$

POSSIBLE ELECTROLYTIC REACTIONS FOR MEASURING WATER VELOCITIES

Because dissolved oxygen is contained in nearly all natural water, much of the attention of this survey was devoted to the use of the oxygen reaction. In principle, an electrolytic probe operating with oxygen currents can be used in fresh waters if sufficient potential is applied to overcome the high electrical resistance of the cell. Boyer and Lonsdale's device (*1*) for measuring low water velocities appears to have worked on such a principle. Here the negative potentials of the probe were relatively small and the currents were not limiting currents.

Sea water contains a ready-made "indifferent" electrolyte; therefore, the oxygen current can be observed directly with applied potentials in the same range as those of laboratory experiments.

In test facilities a noncorrosive electrolyte, such as sodium phosphate, might be added to the water to decrease the cell resistance and to create chemical con-

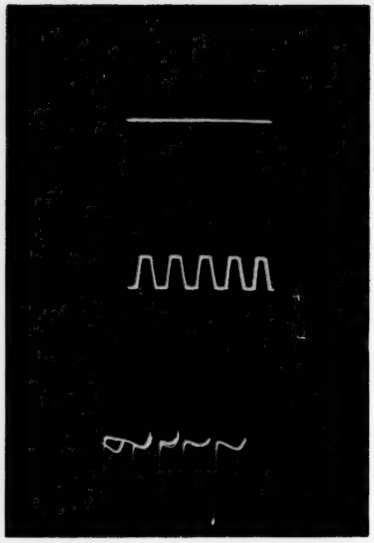

Fig. 4. Oscillograph record of the response of an electrolytic probe; average limiting current = 170 μa., resistance across oscillograph = 12,000 ohms.

ditions that stabilize the oxygen current readings.

Only a few other substances, notably the ferricyanide ion, can be used as the electroactive species in the presence of dissolved oxygen. Suitable ions for such conditions give limiting currents at potentials that are less negative than those for the oxygen reaction. Such ions may be desirable in test waters because the chemical reaction can be simpler and the applied potentials are less likely to evolve hydrogen.

When the test water is deoxygenated, a very large number of electrolytic reactions (7) can, in principle, be applied to give electric currents that are a measure of water velocity.

EXPERIMENTAL APPARATUS

Three types of flow systems were used to obtain the experimental data for the curves shown in Figure 3. The experimental conditions for these data are listed in Table 1.

In system 1, described in reference (5), the indicator electrode was immersed in a rotating basin of electrolyte.

In system 2, probes were mounted in the free-liquid jet issuing from a 0.50-cm. nozzle at the bottom of a 10-cm.-diameter glass tube. A flow free from turbulence was obtained by allowing the liquid to drain from a height of about 60 cm.

In system 3, probes were mounted in a free-liquid jet issuing from a 3-in.-diameter, sharp-edged orifice. To obtain data at high velocities a 300-gallon circulating system was constructed. The liquid jet was deflected by a cone into a 3-ft.-diameter by 5-ft.-deep tank and returned overhead through a 450-gal./min. pump into an 8-ft.-long, 18-in.-diameter standpipe containing two bundles of flow-straightening tubes. The orifice was located at the bottom of this standpipe. Both the probe and the reference electrode were mounted in the free jet.

In principle many types of probes and electrodes can be used for velocity measurements. In the experiments reported here platinum was used as the indicator electrode material, and the S.S.C.E. (silver and silver chloride reference electrode) shown in Figure 1 was used as the anode. Short platinum wires were fused into the ends of narrow glass tubes to form cylindrical probes, the ends of which were ground to form a "pencil point" of platinum on the end of a glass cone. In the case of the 300-gal. system a special mount to hold the indicator probe and a deceleration tube to protect the reference electrode were constructed.

EXPERIMENTAL RESULTS

Figure 3 shows typical plots of measured current vs. velocity for a variety of experimental conditions in which the applied voltage appeared to be in a range of limiting currents. In every case the current is a function of the velocity and does not appear to have a well-defined form, being about the ½ power of the velocity.

The probes were extremely sensitive to low velocities and could measure flows of 1 cm./sec. to two significant figures. Although no velocities greater than 9 meters/sec. were measured, there seemed to be no upper limit to the velocity which could be measured.

The shorter the period of time in which the data were obtained, the more consistently the points fell on a single curve; for example, the data for curves 6 and 7 were taken within 2 min. and show no scatter. Data taken over periods of hours show scatter, and, if the data were rerun after a period of days, another curve would be obtained that would be displaced from the original curve.

Curve 3 was obtained with a sample of sea water. Since curves 2 and 3 were taken with the same probe under nearly equivalent chemical conditions, they should be nearly alike. The large difference in current between these two curves could have been caused by the gradual masking of active surface area by contaminating materials in the sea water. Indeed, the limiting currents in this case showed a gradual decrease with time.

Flow system 2 was constructed to show the stability of the current and to indicate the time response of the probe. A 12,000-ohm resistor was placed in series with the cell and in parallel with an oscillograph. A glass stirring rod with six short spokes or knobs on its end was rotated at 600 rev./min. so that the knobs would pass through the edge of the jeb and interrupt or disturb the flow. Figure 4 shows the results of this experiment. The undisturbed flow had a turbulence intensity of less than 0.5%, and the probe easily responded to a 60 cycles/sec. disturbance. The data showed fine scale variations in the disturbance to frequencies at least ten times that of the major frequency. No attempt was made to determine the phase lag or attenuation of the fluctuating signal.

CHEMICAL ASPECTS

The time sensitivity of the calibration of an electrolytic probe appears to depend upon the fraction of the geometric surface area that is actively engaged in the chemical reaction and the nature of the chemical reaction itself (as characterized by changes in the values of the standard-reaction potential and rate constant). Surface reactions such as these are notably fickle and have a memory for their previous history and chemical experiences. Moreover, there is always the possibility that additional reactions will appear and confuse the situation.

Figure 5 represents a convenient basis for discussing the chemical aspects of an electrolytic-velocity meter.

Figure 5*a* shows the current-voltage curve when a ferricyanide ion is the electroactive species. The curve is cleanly drawn, has a well-defined limiting current, and is in accord with theory. The limiting current at 0.0 volt was found to be proportional to ion concentration over a wide range (the chemical test for a true limiting current), but the velocity dependence of the limiting current (curve 4, Figure 3) did not follow exactly the ½-power relationship expected from theory (4) and from experimental correlations.

Figure 5*b* shows the current-voltage curve for oxygen of the air dissolved in 0.1M potassium chloride. The oxygen reaction

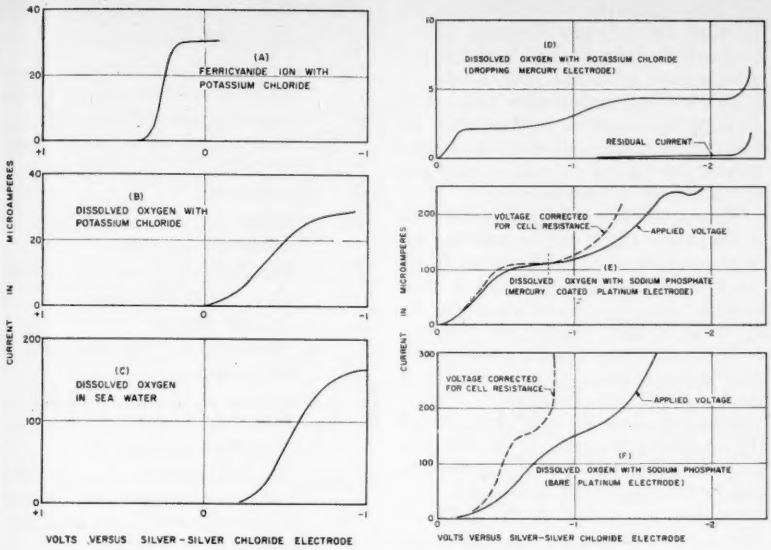

Fig. 5. Current-voltage curves.

occurs at a higher negative potential than does the ferricyanide reaction and would have appeared as an added step on Figure 5*a* had more negative voltages been explored. Figure 5*b* was taken with a newly made probe. After several days of use the limiting-current plateau would disappear and could be restored only by such drastic chemical treatment as soaking the probe in nitric acid and evolving hydrogen from its surface.

Figure 5*c* shows a similar curve for oxygen dissolved in a sample of sea water. Unaccountably the voltage at which the wave appears has become more negative, indicating a change in the nature of the reaction. The limiting currents, which were much less than would be expected from a completely active surface, gradually decreased with time.

Figure 5*d* shows the chemical features of the oxygen reactions in terms of the current-voltage curve of a dropping mercury electrode where the electrode surface is always a newly created liquid surface. The curve shown is an average of the saw-tooth curve drawn by the recorder. Two reactions are involved. The first reaction has been interpreted (*7*) as a two-electron reaction in which dissolved-oxygen molecules are converted to hydrogen peroxide; the second reaction has been interpreted as a four-electron reduction of oxygen molecules to two molecules of water. It should be noted that the second limiting current is nearly twice the first limiting current and that the current rises again only at a relatively high negative potential (−2.2 volts vs. the S.S.C.E.). The final current rise is due to the reduction of potassium ion to form potassium amalgam.

Figure 5*d* shows the so-called "residual current." When the electrolyte is deoxygenated, a small current of a few tenths of a microampere may appear at voltages where hydrogen evolution does not occur. These currents are attributed, in part, to capacity and double-layer effects, and they should be subtracted from an apparent limiting current to obtain a true limit current.

Figure 5*e* shows the current-voltage curves for oxygen of the air dissolved in sodium-phosphate electrolyte taken with a mercury-coated, platinum electrode. It appears that a two-electron oxygen reaction occurred but at a larger negative potential than in the case of Figure 5*d*. Higher in the curve there is a discontinuity at a voltage where a four-electron reaction should be expected. When an attempt was made to repeat the data of Figure 5*e*, which was taken with a newly plated probe, current values were found to be much less, the dip disappeared, and hydrogen was evolved at less negative potentials. To establish current-velocity curve 8 of Figure 3, the applied voltage on the platinum probe, newly electroplated with mercury, was always kept less negative than −0.9 volt.

Figure 5*e* also indicates the effect of cell resistance at relatively high-current levels. The current-voltage curve is stretched out along the abscissa, and the region of limiting currents is less apparent.

Figure 5*f* shows the current-voltage curve for the newly ground and polished probe of Figure 5*e* before it was mercury coated. Apparently a convection-controlled oxygen reaction occurred, but the limiting current was poorly defined. Comparisons with the limiting currents of curve 8 of Figure 3 and consideration of relative velocities indicated that the reaction required four electrons for each oxygen molecule* and occurred at a surprisingly low negative potential. Although the resistance of the cell (2,500 ohms) was not known accurately enough to plot the exact electrode potentials, the onset of the hydrogen reaction has moved to less negative potentials, overcoming much of the effect of the oxygen reaction.

Evolution of hydrogen by electrolytic decomposition of water is a major difficulty to be resolved in the application of electrolysis to velocity measurement. Ordinary dirt and contaminants appear to promote hydrogen evolution, and the reaction itself is unpredictable. Since the oxygen reaction concerns recent studies of cathodic corrosion protection, and since the hydrogen reaction continues to receive much attention from electrochemists interested in hydrogen overvoltage, there is some hope for eventual understanding and control of both reactions.

MASS TRANSFER RATES: COMPARISON WITH THEORY

Limiting current can be predicted by transfer correlations. In many recent research investigations (such as those in references *3* and *8*) the limiting current has been used to measure mass transfer rates and to establish correlations, one type of which is given in functional form by Equation (1). The chief difficulties associated with establishing or using a generalized correlation lie in the paucity of data on diffusivities and in the marked effect of small temperature variations on viscosity and diffusivity.†

Figure 6 is a generalized plot of curves

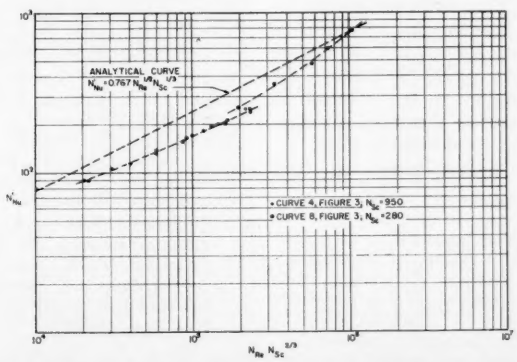

Fig. 6. Mass transfer to conical probe. Comparison with theory.

*A possible explanation of this unusual result is that the dissolved oxygen first undergoes a two-electron electrolytic reaction forming hydrogen peroxide. The hydrogen peroxide then undergoes a further reaction forming water and oxygen. Since one out of every two oxygen molecules reappears in the second reaction, the over-all result is a four-electron transfer.

†Diffusivity and oxygen-solubility values used for correlation were taken from references *6* and *7*.

4 and 8 of Figure 3. Here the characteristic dimension of the electrode surface is taken to be the slant height of the platinum cone. The theoretical solution for a laminar boundary layer (4) is superimposed. While theory predicts the proper order of magnitude of the limiting current under most conditions, the agreement is not very good. Similar correlations of the other curves shown in Figure 3 are in as much agreement with theory and independent correlation as Figure 6. Reasons for disagreement are numerous and beyond the scope of the limited experimental results obtained. As a ½-power relationship between current and velocity would have permitted the circuitry of hot-wire anemometers to be directly applicable to the analysis of fluctuating currents, it was particularly disappointing that this simple relationship did not exist.

EVALUATION

Beyond purely chemical limitations, which require further study, there are other factors to be considered in evaluating the practical potentialities of electrolytic flow meters.

In water the active area of a useful probe will have to be about 10^{-2} to 10^{-3} sq. cm. to prevent dirt particles from making serious changes in calibration. An increase in size is also dictated by a need for mechanical strength sufficient to withstand the hydrodynamic forces. Turbulence-scale measurements would, of course, be limited to the size of the probe, and frequency measurements would be limited to a value equal to the flow velocity divided by the size of the probe.

It is natural to compare the response of an electrolytic probe to the response of a hot-wire probe which has been successfully adapted to measurements in water by Ling and Hubbard (9). They developed a wedge-shaped probe of glass thinly coated with a platinum resistance element. The active area is sufficiently large (1 mm. wide with a slant height of 0.2 mm. on each side) to satisfy the requirement for an area of such size that calibration would not be destroyed by a few dirt particles. The platinum coating is thin enough (a few angstrom units) to give rapid response to fluctuating velocities, and the temperature of the film is always well below the boiling point of the water. The construction is sturdy enough to withstand hydrodynamic forces at velocities as high as 80 ft./sec., and resistance of the probe is about 5 ohms.

The hot-film probe can also be used as an electrolytic probe. As designed, it works on a heat transfer principle. As an electrolytic probe it would work on a mass transfer principle. A comparison of performance can be predicted by considering the Nusselt number and the mass-transfer number N_{Sh} for a thin wedge at various values of the Reynolds, Prandtl, and Schmidt numbers. Such a comparison under normal operating conditions leads to several conclusions.

The hot-film anemometer gives mean currents measured in milliamperes; the electrolytic instrument with an oxygen current gives mean currents of only tens and hundreds of microamperes.

Because electrical dissipation into heat is proportional to I^2 and because the rate of electrolysis is proportional to I, the the hot-film anemometer gives a mean current that is proportional to the ¼ power of the velocity, and the electrolytic instrument gives a mean current that is approximately proportional to the ½ power of the velocity.

Fluctuations in velocity give $dI/I = (\frac{1}{4})\ dv_0/v_0$ in the case of the hot-film anemometer, and $dI/I = (\frac{1}{2})\ dv_0/v_0$ in the case of the electrolytic instrument.

A rough comparison of the ability to respond to fluctuations in convection conditions can be obtained by comparing the product of the thermal diffusivity of the fluid and the ⅔ power of the Prandtl number with the product of the diffusivity of the electroactive species and the ⅔ power of the Schmidt number. A larger value indicates a better response rate. The value for the hot-film anemometer is about 5×10^{-3} sq. cm./sec.; the value for the comparable electrolytic instrument using the oxygen reaction is about 1.5×10^{-3} sq. cm./sec. The hot-film anemometer also has a response lag because of the thermal capacity of the film and the glass wedge; the electrolytic instrument is not subject to a similar kind of response lag because it has no capacity for the transferred component.

It is not possible to make a complete comparison between the response rates of the two probes. It is probable, however, that the response rates are comparable for the smallest size of probe and that the response rate of the electrolytic probe becomes relatively much better as the bulk of the probe is increased.

On the basis of survey experiments, it appears that applications of electrolysis to the problem of measuring water velocities can be made, but practical success will require a development comparable to that which was needed for the hot-wire anemometer. Because of the many chemical unknowns, further chemical studies would be required for a full evaluation of the electrolytic method and for its successful development into a practical velocity meter.

ACKNOWLEDGMENT

This study was sponsored by the Ordnance Research Laboratory of The Pennsylvania State University, University Park, Pennsylvania. Experiments were performed by R. A. Javick, D. L. Sullivan, and J. V. Maizel. Technical assistance and consultation were provided by Dr. Joseph Jordan, Department of Chemistry.

NOTATION

A_i = interfacial area of electrode

C_{Oxo} = main-stream concentration of oxidized form of electroactive species

ΔC = concentration difference of electroactive species across the transfer path

D = diffusivity

D_{Ox} = diffusivity of oxidized form of electroactive species

F = Faraday's constant = 96,500 amp. sec./g. equivalent

I_1 = limiting current

L = characteristic dimension of electrode surface

n = number of electrons involved in reduction of each molecule or ion of electroactive species

N_{Sh} = Sherwood number, mass transfer number analogous to Nusselt number for heat transfer: $N_{Sh} = r_{ai}L/\Delta CD = N_{Sh}(N_{Re}, N_{Sc})$

N_{Re} = Reynolds number; $N_{Re} \equiv Lv_0/\nu$

N_{Sc} = Schmidt number; $N_{Sc} \equiv \nu/D$

r_{ai} = average rate of mass transfer (or rate of reaction) of electroactive species/unit area of electrode interface

v_0 = flow velocity

ν = kinematic viscosity

LITERATURE CITED

1. Boyer, M. C., and E. M. Lonsdale, *Third Midwestern Conference on Fluid Mechanics*, Univ. Minn. (March 23–25, 1953).
2. Delahay, Paul, "New Instrumental Methods in Electrochemistry," Interscience Publishers, Inc., New York (1954).
3. Eisenberg, M., C. W. Tobias, and C. R. Wilkie, *J. Electrochem. Soc.*, **101**, 306 (1954).
4. Johnson, H. A., and M. W. Rubesin, *Trans. Am. Soc. Mech. Engrs.*, **71**, 447 (1949).
5. Jordan, Joseph, *Anal. Chem.*, **27**, 1708 (1955); Jordan, Joseph, R. A. Javick, and W. E. Ranz, *J. Am. Chem. Soc.* (to be published).
6. Jordan, Joseph, Eugene Ackerman, and R. L. Berger, *J. Am. Chem. Soc.*, **78**, 2979 (1956).
7. Kolthoff, I. M., and J. J. Lingane, "Polarography," Interscience Publishers, Inc., New York (1952).
8. Lin, C. S., E. B. Denton, H. S. Gaskill, and G. L. Putnam, *Ind. Eng. Chem.*, **43**, 2136 (1951).
9. Ling, S. C., and P. G. Hubbard, *J. Aeronaut. Sci.*, **23**, 890 (1956).
10. Ranz, W. E., Document 0000, ADI Auxiliary Publications Project, Photoduplication Service, Library of Congress, Washington 25, D. C.
11. Sherwood, T. K., and R. L. Pigford, "Absorption and Extraction," 2 ed., McGraw-Hill Book Company, Inc., New York (1952).

Manuscript received Dec. 3, 1957; revised Jan. 27, 1958; accepted Jan. 28, 1958.

Diffusion in a Pore of Varying Cross Section

E. E. PETERSEN

University of California, Berkeley, California

The ratio of the effective to the normal diffusivity of a material diffusing within porous solids is less than unity. In the simple theory the porosity and tortuosity, or labyrinth, factors are used to explain the magnitude of this ratio and to account respectively for the reduced cross-sectional area and the increased diffusion distance. However, abnormally large values of the tortuosity factor are obtained from experimentally measured effective diffusivities within pelleted or extruded porous solids. This work is concerned with the quantitative effect of periodic pore constrictions on the effective diffusivity. The pore model assumed for this study is a hyperbola of revolution giving a pore constriction at the vertex of the hyperbola. Solutions to the steady state diffusion equation in a pore of this shape were obtained at various values of β, the ratio of the maximum to the minimum cross-section in the pore. Comparison of the rate of diffusive transport in this pore and an equivalent cylindrical pore indicates that δ, the ratio of the effective to the normal diffusivity, is about 0.33 at $\beta = 25$ for large pores. At the same value of β, δ would be smaller for diffusion in the Knudsen region.

The effective diffusivity D_e of a gas being transported within a porous solid by a diffusive mechanism is smaller than the normal diffusion coefficient D_b. Efforts to relate the ratio D_e/D_b quantitatively to the variables characterizing the porous medium can be broadly classified into two types. The more fundamental method begins with the derivation of an expression for the value of D_e/D_b in dilute suspension of particles of simple geometric shapes. Maxwell (*5*) considered uniform spheres and Rayleigh (*7*) infinite cylinders normal to the direction of flow, leading to the following equations, respectively:

$$\frac{D_e}{D_b} = \frac{2\epsilon}{3 - \epsilon} \tag{1}$$

$$\frac{D_e}{D_b} = \frac{\epsilon}{2 - \epsilon} \tag{2}$$

where ϵ = volume fraction voids. Using a continuum model, Bruggeman (*1*) extended the range of validity of the Maxwell expression to higher values of ϵ, to obtain the equation

$$\frac{D_e}{D_b} = \epsilon^{\frac{3}{2}} \tag{3}$$

De La Rue and Tobias (*3*) found excellent agreement between the Bruggeman equation and their experimental values of the electrical conductivity of suspensions of spheres in the range of porosities from 1.0 to 0.5. Hoogschagen's (*4*) experimental values of D_e/D_b for randomly packed beds of glass spheres in the porosity range from 0.35 to 0.4 lie between the values predicted by the Maxwell and Bruggeman equations, although slightly closer to the latter.

The other commonly used method is to relate D_e/D_b to the porosity and a labyrinth, or tortuosity, factor τ by the following expression:

$$\frac{D_e}{D_b} = \frac{\epsilon}{\tau} \tag{4}$$

Equation (4) is essentially a defining equation for τ. From a geometrical point of view, this form appears reasonable because ϵ allows for the reduced area for diffusive flow and τ accounts for the fact that the actual diffusion path between two points within a porous medium is generally greater than the distance between points. For loose powders and randomly packed glass spheres the labyrinth factors range from 1.42 to 1.58 (*4*), an indication that the actual diffusion path is $\sqrt{\tau}$, or from 1.19 to 1.26 times longer than the distance in the direction of net flow. The ratio of the channel length to the geometric depth in a system of closely packed uniform spheres is 1.304 (*2*).

Both these methods appear to be invalid when applied to tableted or extruded porous media, wherein labyrinth factors from 5 to as high as 300 are obtained with values of 10 to 12 being common (*4*). Interpreting such high values of the labyrinth factors simply as an increased diffusion length is hard to justify physically. In this investigation diffusion in a pore of varying cross section is compared with that in an "equivalent" cylindrical pore in order to determine whether periodic constrictions in the pore channel may reasonably account for unusually high labyrinth factors. In the model adopted, no account will be taken of the porosity or tortuosity factor, only of constrictions in the channel cross sectional area; moreover, the analysis will not directly apply when the Knudsen diffusivity must be used.

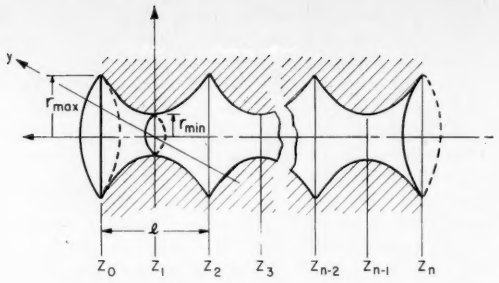

Fig. 1. Model of pore with periodic pore constrictions.

MODEL

The shapes of pores formed within porous media pelleted or extruded from particulate material are complex especially if the particles are deformed in the process. However, it seems reasonable that the network of channels formed by the interconnected interstitial spaces between particles will vary in cross section. The extent of variation will depend in part upon the amount of compaction and the shape of particles comprising the aggregate. It is proposed herein to study diffusion in an idealized model (Figure 1) of a pore which retains the property of variable cross section along its length. The pore walls are hyperbolas of revolution about the Z axis. A pore of any length is made from repeating units represented by Z_0, Z_2, Z_2Z_4 . . . $Z_{n-2}Z_n$. It is clear that if the concentration in the xy planes at Z_0 and Z_n are held at C_0 and C_n, respectively, where $C_0 > C_n$, then a net transport of material will take place from Z_0 to Z_n. Moreover, if the fluid in the pore is held at constant temperature and total pressure and if D_b is assumed to be independent of concentration, symmetry demands that the concentration will drop in equal increments in the xy planes at Z_1, Z_2 . . . Z_{n-1} at steady state. Therefore, the problem is simplified to solving Laplace's equation for the region between Z_0 and Z_1.

A pore of this shape can be most conveniently described in oblate spheroidal coordinates (*6*). The origin for the coordinate system will be taken at Z_1 along the Z axis as shown in Figure 1 and in greater detail in Figure 2. Since angular symmetry has been assumed, two coordinates will be needed which will describe a mutually orthogonal set of hyperbolas and ellipses with focuses at $x = \pm 1.0$. The coordinates ξ and η are defined as

$$\frac{x^2}{(1+\xi^2)} + \frac{Z^2}{\xi^2} = 1 \qquad (5)$$

for the ellipses and

$$\frac{x^2}{(1-\eta^2)} - \frac{Z^2}{\eta^2} = 1 \qquad (6)$$

for the hyperbolas.

The walls of the pore are defined by the hyperbolas asymptotic to lines $x = \pm Z$, and correspond to setting $\eta = 0.707$ in Equation (6). This choice seemed most appropriate to describe a constriction formed from roughly spherical particles.

The concentration profile in the pore is given by the solution to the Laplace equation

$$\nabla^2\psi = 0 \qquad (7)$$

where ψ is a dimensionless concentration in terms of the concentrations at the boundaries Z_0 and Z_1 as defined below.

$$\psi \equiv \frac{C(Z) - C(Z_1)}{C(Z_0) - C(Z_1)} = \frac{C(Z) - C(0)}{C(Z_0) - C(0)} \qquad (8)$$

when the origin is taken through Z_1. The boundary conditions are

$$\psi(Z_0) = 1 \quad \left(\frac{d\psi}{d\eta}\right)_{\eta=0.707} = 0$$
$$\psi(0) = 0 \quad \left(\frac{d\psi}{d\eta}\right)_{\eta=1} = 0 \qquad (9)$$

As the first boundary condition $\psi(Z_0) = 1$ introduces mathematical difficulties, it is proposed to solve the Laplace equation twice for each ratio of r_{max} to r_{min}: one solution subject to the boundary condition $\psi(\xi_0) = 1$ where ξ_0 characterizes the ellipse going through the point $\eta = 0.707$, Z_0; and the other solution subject to the boundary condition $\psi(\xi_0') = 1$ where ξ_0' characterizes the ellipse going through $\eta = 1$, Z_0. These solutions are readily obtained and the desired solution lies between them.

In oblate spheroidal coordinates

$$\nabla^2\psi = \frac{1}{(\xi^2+\eta^2)}\left\{\frac{\partial}{\partial\xi}\left[(1+\xi^2)\frac{\partial\psi}{\partial\xi}\right] + \frac{\partial}{\partial\eta}\left[(1-\eta^2)\frac{\partial\psi}{\partial\eta}\right]\right\} = 0 \qquad (10)$$

Defining $\psi(\xi, \eta) = E(\xi)M(\eta)$ causes the equation to separate into

$$(1-\eta^2)\frac{d^2M}{d\eta^2} - 2\eta\frac{dM}{d\eta} - \lambda^2 M = 0 \qquad (11)$$

and

$$(1+\xi^2)\frac{d^2E}{d\xi^2} + 2\xi\frac{dE}{d\xi} + \lambda^2 E = 0 \qquad (12)$$

To satisfy the boundary condition, $(dM/d\eta)_{\eta=1} = 0$, clearly λ^2 in Equation (11) must be set equal to zero in order to avoid a trivial solution. If the separation constant $\lambda^2 = 0$, then in order to satisfy all boundary conditions, $M = 1$ and

$$\psi(\xi) = \frac{\tan^{-1}\xi}{\tan^{-1}\xi_0} \qquad (13)$$

The diffusive flow is always normal to the ξ = constant lines and the net transport N through the pore is

$$N = [C(\xi_1) - C(0)] \iint_s \frac{D_b}{h_\xi}\left(\frac{d\psi}{d\xi}\right) ds \qquad (14)$$

$$= [C(\xi_1) - C(0)] \int_0^{2\pi} d\phi \cdot \int_{\eta_1=0.707}^{1} D_b\left(\frac{d\psi}{d\xi}\right)\frac{h_\phi h_\eta}{h_\xi}\, d\eta \qquad (15)$$

where

$$h_\phi = \sqrt{(\xi^2+1)(1-\eta^2)}$$
$$h_\eta = \sqrt{\frac{(\xi^2+\eta^2)}{(1-\eta^2)}} \qquad (16)$$
$$h_\xi = \sqrt{\frac{\xi^2+\eta^2}{\xi^2+1}}$$

Substituting, simplifying, and integrating gives

$$N = \frac{2\pi[C(\xi_1) - C(0)](1-\eta_1)D_b}{\tan^{-1}\xi_0} \qquad (17)$$

The rate of transport in a channel of varying cross section is given in Equation (17). A question of interest may now be raised. If the hyperbolic-shaped pore is replaced by an equivalent system of cylindrical pores, what values of the diffusivity D_e should be used in order to compute the correct rate of diffusive transport?

If there are m cylindrical pores of radius r_{avg} and of length Z_0, the rate of diffusive transport is

$$N = \frac{D_e\pi r_{avg}^2 m[C(Z_0) - C(0)]}{Z_0} \qquad (18)$$

the radius r_{avg} is generally obtained from the volume and surface area of the true pore system by the equation

$$r_{avg} = \frac{2V}{S} \tag{19}$$

Equation (19) is correct if the pores are smooth, cylindrical, and separate. The number of pores m must be chosen so that the total pore volume of the equivalent pore system is equal to the true pore volume; therefore

$$m = \frac{V}{\pi r_{avg}^{\,2} Z_0} \tag{20}$$

Substituting Equations (19) and (20) into (18) and simplifying gives

$$N = \frac{[C(Z_0) - C(0)]D_e V}{Z_0^{\,2}} \tag{21}$$

where V = volume of the hyperbolic pore model

$$= \pi(1 - \eta_1^{\,2})\left[Z_0 + \frac{Z_0^{\,3}}{3(\eta_1^{\,2})}\right] \tag{22}$$

and $\eta_1 = 0.707$. The desired ratio D_e/D_b is obtained by setting N of Equation (21) equal to its correct value, obtained from Equation (17), which upon rearrangement is

$$\frac{D_e}{D_b} = \frac{1.172 Z_0^{\,2}}{\left(Z_0 + \dfrac{Z_0^{\,3}}{1.5}\right)\tan^{-1}\xi_0} \tag{23}$$

The parameter ξ_0 takes the two values (ξ_0 and ξ_0') described previously under boundary conditions. The D_e/D_b ratio is plotted in Figure 3 as a function of the A_{max}/A_{min} ratio, which will be referred to hereafter as β where A_{max} refers to the maximum cross-sectional area at the entrance to the pore and A_{min} refers to the minimum cross-sectional area at the pore constriction. The lower curve corresponds to the boundary condition $\psi(\xi_0) = 1$, whereas the upper curve corresponds to $\psi(\xi_0') = 1$. The dashed curve is an interpolated curve going through the point $D_e/D_b = 1$ at $\beta = 1$ and represents a reasonably accurate solution to the original problem. It should be pointed out that the D_e/D_b ratio is not particularly sensitive to pore shape; for example a pore unit having about twice the length-to-diameter ratio of the pore shown in Figure 2 is bounded by the hyperbola corresponding to $\eta = 0.9$ and $\beta = 25$ and has a value of D_e/D_b equal to 0.39 instead of 0.33 at $\eta = 0.707$ and the same value of β.

If the ratio of D_e/D_b in Equation (23) is defined as equal to δ, the convergence factor, that is, a factor which accounts for reduction in D_e due to constrictions in the pore along its length. If the δ factor is taken into account, Equation (4) can be redefined as

$$\frac{D_e}{D_b} = \frac{\epsilon\delta}{\tau} \tag{24}$$

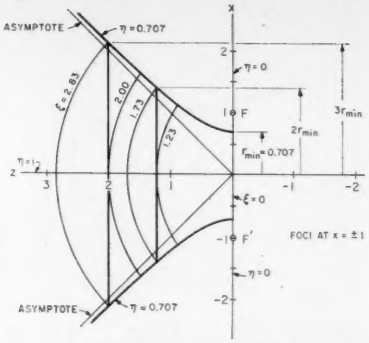

Fig. 2. Detail of pore repeating unit for cases of R_{max}/R_{min} equal to 2 and 3.

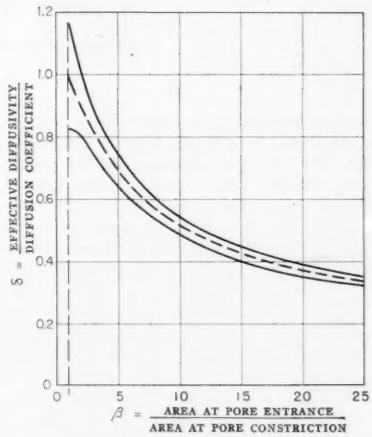

Fig. 3. Effective diffusivity as a function of convergence ratio, shown by the dashed curve. The upper curve is for $(\xi_0') = 1$ and the lower for $(\xi_0) = 1$.

For porosities greater than about 0.4, corresponding to the region from dilute dispersions to loosely packed beds, the Bruggeman form is applicable where $\tau \propto \epsilon^{-1/2}$ and $\delta = 1$.

When solids are compacted owing to pelleting or extruding, it is postulated that constrictions are produced within the solid and δ becomes less than unity. The ratio of D_e/D_b, therefore, is less than predicted by the Bruggeman equation. Postulating pore constrictions and the δ factor forms a more satisfactory explanation for the greatly reduced values of D_e than attempting to interpret them on the basis of a tortuosity factor alone. Estimation of the magnitude of δ factors by the model assumed in this paper are not valid if under the conditions of the diffusion process the mean free path of the gas molecules is of the same order of magnitude as the diameter of pores. In this region the Knudsen form of the diffusion coefficient must be used where D_k is a function of the pore radius. It is clear, however, that in the Knudsen region the magnitude of δ would be smaller for a given value of the β than the values plotted in Figure 3.

Although the concept of pore constrictions in compacted materials provides the basis for a reasonably attractive explanation of abnormally high tortuosity factors, unfortunately there appears to be at present no satisfactory experimental technique to characterize independently the structure of pores within compacted materials in sufficient detail to test the method presented here.

NOTATION

A_{max} = maximum cross-sectional area of pore
A_{min} = minimum cross-sectional area of pore
C = concentration
D_b = normal diffusion coefficient
D_e = "effective" diffusion coefficient
h_η, h_ξ, h_ϕ = scaling factors in oblate spheroidal coordinate system defined by Equation (16)
N = rate of diffusive transport through the pore
r_{avg} = radius of equivalent cylindrical pore
r_{max} = maximum radius of pore
r_{min} = minimum radius of pore
S = pore wall surface
V = volume of pore
X = Cartesian coordinate
Y = Cartesian coordinate
Z = Cartesian coordinate
Z_0 = pore length

Greek Letters

β = A_{max}/A_{min}
δ = convergence factor
ϵ = porosity
η = oblate spheroidal coordinate
λ = separation constant
ξ = oblate spheroidal coordinate
τ = tortuosity or labyrinth factor
ψ = dimensionless concentration
∇^2 = Laplacean operator

LITERATURE CITED

1. Bruggeman, D. A. G., *Ann. Physik*, **24**, 636 (1935).
2. Dalle Valle, J. M., "Micrometrics," 2 ed., p. 131, Pitman Publishing Company, New York (1948).
3. De La Rue, R. E., and C. W. Tobias, "Conductivities of Random Dispersions." Presented at 107 Meeting of the Electrochemical Society, Cincinnati (1955).
4. Hoogschagen, Jan, *Ind. Eng. Chem.*, **47**, 906 (1955).
5. Maxwell, J. C. "Treatise on Electricity and Magnetism," p. 365, Oxford (1873).
6. Morse, P. M., and Herman Feshback, "Methods of Theoretical Physics," vol. 1, p. 662, and vol. 2, p. 1292, McGraw-Hill Book Company, Inc., New York (1953).
7. Rayleigh, J. W., *Phil. Mag.*, **34**, 481 (1892).

Manuscript received Dec. 3, 1957; revised Feb. 3, 1958; accepted Feb. 5, 1958.

The Formation of Interfacial Area in Immiscible Liquids by Orifice Mixers

L. S. SCOTT, W. B. HAYES, III, and C. D. HOLLAND

Agricultural and Mechanical College of Texas, College Station, Texas

This paper deals with the dispersion of one immiscible liquid in another (water in kerosene) by means of an orifice mixer. The degree of mixing was determined by measuring the area per unit volume of the dispersed phase. The area was measured with a photoelectric device, which had been calibrated photographically. The interfacial area formed at high Reynolds numbers (10,000 to 45,000, based on the diameter of the orifice) was found to increase with increases in both the volume fraction of water in the water-kerosene mixture and the change in kinetic energy across the orifice. In addition, other aspects such as the rate of coalescence of the dispersed phase downstream from the orifice are treated.

Orifices are commonly used for the dispersion or mixing of immiscible liquids. An example is the sweetening process, one step of which is the dispersion of an aqueous solution of caustic soda in a petroleum fraction such as kerosene. When the two liquids are passed through the orifice plate, an interfacial area is formed which increases the rate of reaction between the caustic and the mercaptans and other compounds in the petroleum fraction.

Two investigations are described here; in the first the formation of interfacial surface area of the dispersion, water in kerosene, was determined as a function of the volume fraction, flow rate, and the orifice diameter. The area was measured by a photoelectric device, which had been calibrated photographically. In the second set of experiments the rate of coalescence of the dispersed phase was determined as a function of the downstream distance from the mixing orifice, of the total rate of flow, and of the volume fraction. The diameter of the pipe was held constant for all experiments.

The use of orifice mixers and their applications in petroleum refining was discussed several years ago by Morrel and Bergman (*5*). Recently a number of articles dealing with mixing have appeared (*6, 7, 8*), among them Rushton and Oldshue's discussion (*8*) of the application of the ideas and principles of fluid mechanics to the mixing of fluids. Much of the recent literature pertains to the characteristics of mixing impellers. The production of interfacial area by turbine impellers has been described by Rodger, Trice, and Rushton (*6*), who for the measurement of the surface area used the photoelectric method, reported by Trice and Rodger (*11*). Vermeulen and coworkers (*12*) have also used this method for measuring the interfacial area of dispersed liquid-liquid systems. These workers as well as Wesselhoft (*13*) and the present authors found a quantitative relationship between light transmission and interfacial surface area.

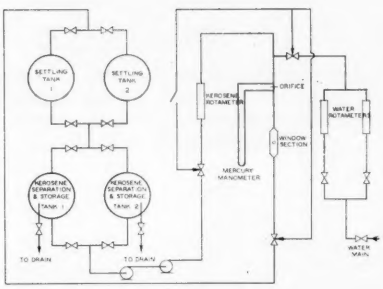

Fig. 1*a*. Flow diagram of equipment.

EXPERIMENTAL EQUIPMENT AND PROCEDURE

Equipment

The equipment consisted of four 55-gal. drums, two centrifugal pumps, three rotameters, a set of orifice plates, a manometer, a General Radio microflash unit, a camera, photoelectric equipment, and a specially designed window section. The arrangement of the equipment, which was also used by R. D. Wesselhoft and R. V. Andrews (*13*), is shown in Figure 1.

Two of the drums were used for settling tanks and the other two for the storage of kerosene. To prevent the formation of rust, the insides of the drums were coated with a suitable resin. The kerosene and water streams were metered separately through appropriate rotameters which had been calibrated gravimetrically.

The orifice plates were of the square-edge type. The pressure drop across the orifice was measured with a mercury manometer having a maximum reading of 60 in. The manometer was connected to the orifice taps through two mercury traps. Water, being the heavier liquid employed in the mixing investigations, was used to fill the volume bounded by the mercury levels in the manometer and the orifice taps.

The kerosene-water mixture flowed through a flattened section of pipe (Figure 1*c*) located downstream from the orifice.

L. S. Scott and W. B. Hayes, III, are with E. I. du Pont de Nemours and Company, Inc., Charleston, West Virginia.

The original data upon which this paper is based has been deposited as document 5712 with the American Documentation Institute, Photoduplication Service, Library of Congress, Washington 25, D. C., and may be obtained for $1.25 for photoprints or $1.25 for 35-mm. microfilm.

The pipe, which provided a means of photographing the mixture, was constructed of aluminum and tapered from a circular cross section at each end to an approximate rectangular cross section in the middle. It was designed so that the cross-sectional area remained constant throughout its length and was equal to the cross-sectional area of a 1-in. Pyrex-glass pipe; this ensured a constant linear velocity of the mixture throughout its length. Two glass windows (*3*) utilized for the photographic method of counting droplets and later for the photoelectric method, were placed opposite each other in the flattened section, 7 in. from the inlet end. The distance between the windows was 0.5 in.

Photographs of the dispersion were taken with a $2\frac{1}{4} \times 3\frac{1}{4}$ Speed Graphic Camera equipped with a box extension 32 in. long, which was used to enlarge the projection of the image on the negative (Figure 1*c*). With this arrangement sharp images of droplets as small as 0.01 mm. in diameter could be obtained.

A Federal Enlarger was used to magnify the negatives so that the droplets might be measured and counted. For illumination a General Radio microflash unit with a flash duration of approximately two-millionths of a second was used. This unit was equipped with a microphone which was connected so that the microflash might be actuated by sound.

The photoelectric equipment consisted of a pen lamp, phototube, galvanometer, and Ayrton shunt. This equipment was connected electrically according to two circuits: a light-source circuit and a phototube circuit (Figure 2*a*). The light-source circuit consisted of a 2.2-volt pen lamp (G. E. 222), four 1.5-volt dry-cell batteries, and a 4.5-ohm variable resistor. The output voltage from the dry cell was reduced to fewer than 2.2 volts by the suitable adjustment of the variable resistor. The pen lamp was located on one side and the phototube on the opposite side of the window section. It was encased in a brass tube attached directly to the window section.

The phototube circuit consisted of a 90-volt dry-cell battery, a galvanometer equipped with an Ayrton shunt, and a phototube. The phototube was encased in a brass tube similar to that used for the pen lamp and attached to the window section directly opposite the lamp to pick up any light passing through the window section. The output of the phototube was measured by a Leeds and Northrup Type E 243OD moving-coil galvanometer with a current sensitivity of 0.000035 μa./mm. of scale deflection. The Ayrton shunt was used to adjust the sensitivity of the galvanometer and to supply a constant external damping resistance of 25,000 ohms to the galvanometer. Special glass filters of Corning type-4,600 glass were placed in front of the pen lamp and in front of the phototube (IP41). In addition, a red filter was used to absorb the light having the shorter wave lengths. As discussed by Trice and Rodger (*11*), the light transmission is independent of the precise particle-size distribution, provided that the wave length of the incident light is much less than the diameter of the smallest particles.

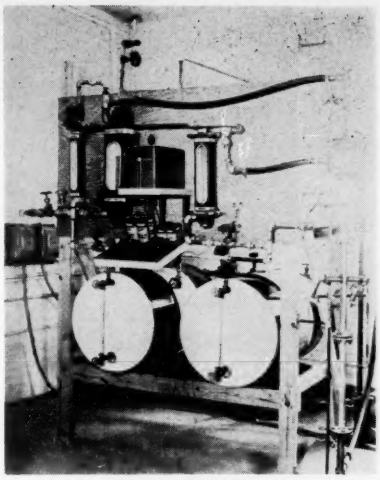

Fig. 1*b*. Experimental equipment.

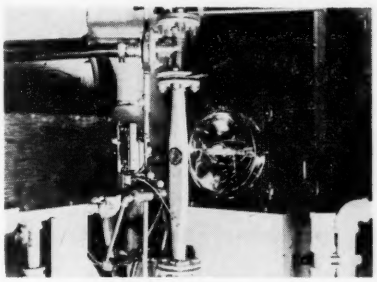

Fig. 1*c*. Window section, camera, microflash.

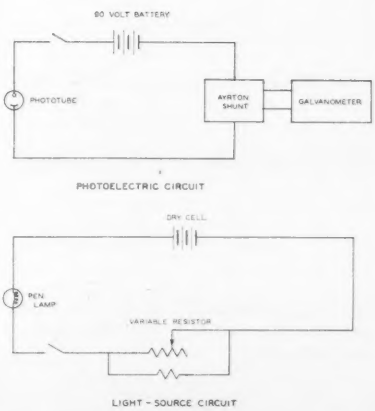

Fig. 2*a*. Photoelectric circuits.

Experimental Procedure

The surface area of the dispersed phase (per unit volume of mixture) was measured directly with the photographic equipment mentioned. The camera equipped with the extension tube was placed in front of the window section and properly aligned and focused.

The lamp unit of the microflash was placed as close as possible to the window opposite the camera. A microphone of the sound-tripping device was placed against the camera-shutter housing so that the shutter noise produced by tripping the shutter of the camera set off the microflash. This method of synchronization of the photographic operations proved so effective that pictures virtually free of background haze could be taken. Proper adjustment of the lens opening and shutter speed and use of a very fast film gave satisfactory photographs of the highly dispersed mixtures.

Kerosene and water were passed through the orifice. After sufficient time had elapsed for the mixing to come to a steady state, two or more photographs of the dispersion were taken at each set of operating conditions. The Federal Enlarger was used to give a final magnification of 100 times the actual bubble diameter. The droplets were then traced on a sheet of paper and counted with respect to size. Increments of 1 mm. were used in the classification. From these data the volume-surface diameter was calculated by Equation (1), and then the interfacial area was calculated by Equation (4). A typical drop-size–distribution curve is shown in Figure 3.

The first step in the photoelectric procedure consisted of attaching the pen lamp and the phototube to the window section. The pipe was then filled with kerosene. Prior to the performance of an experiment a period of 20 min. was allowed for the circuits to come to a steady state temperature. The voltage across the pen lamp was adjusted so that a reading of 5 cm. was obtained on the galvanometer at a particular Ayrton shunt setting. After the instruments had been properly adjusted, the flow rates of the kerosene and water were set at the desired values, and the corresponding galvanometer and manometer readings were recorded. The combination of these readings and the corresponding areas obtained photographically gave the calibration curve (Figure 4). This curve reflects the fact that the intensity of the light passing through the mixture was a function only of d_{ss}, or the interfacial area, over the range of flow rates, orifice diameters, and volume fractions used in the experiments. Each calibration run was repeated several times and on different days. It was found that the reproducibility of the photoelectric method was better than $\pm 1\%$ and that of the photographic was $\pm 5\%$.

After any given series of experiments had been completed, the resulting water and kerosene mixture was placed in an empty storage drum and the water allowed to settle out. A settling time of about 14 hr. was required for complete separation of the dispersion.

In the experiments pertaining to the coalescence of dispersions the same general procedure was employed. In these experiments the window section was located, and

the readings were taken at each of several positions directly below the mixing orifice.

INTERPRETATION OF EXPERIMENTAL RESULTS

Adequate representations of the data were obtained by the empirical correlations stated below. The formation of the interfacial area of water dispersed in kerosene was determined as a function of three variables: flow rate, orifice size, and volume fraction of water in kerosene; the pipe diameter was held constant for all experiments. Flow rates (water plus kerosene) within the range of 3 to 18 gal./min. were used at each of the following orifice diameters: 0.3125, 0.375, 0.4375, 0.5, 0.625, 0.6875, and 0.75 in. The interfacial areas corresponding to the volume fractions of 0.02, 0.05, 0.10, 0.15, and 0.2 at each flow rate and orifice diameter were determined. In addition, the pressure drop across the mixing orifice for each experiment was measured. These data are available*. The correlation was based on the postulate that the surface area formed by an orifice mixer is a power function of the volume fraction and the change in kinetic energy across the orifice. These present data, demonstrating the formation of interfacial area, were also correlated by Scott (*9*) as power functions of the groups obtained by a dimensional analysis. It was necessary to use two equations in order to correlate all these data; each equation contained identical groups, but the powers to which they were raised differed. Among others, Vermeulen and associates (*12*) and Rodger and coworkers (*6*) have correlated the interfacial area formed by turbine impellers by use of the associated dimensionless groups.

The coalescence of the dispersed phase as a function of the downstream distance from the mixing orifice, flow rate, and volume fraction of water dispersed in kerosene was investigated, and it was found that the decline in the interfacial area (a measure of coalescence) with respect to the distance downstream from the mixing orifice was proportional to the interfacial area raised to a power either equal to or slightly greater than unity.

Relationships Used in the Correlations

All of the correlations as well as the calibration curve were based on the mean volume-surface diameter (*2, 6*), which is defined as follows:

$$d_{vs} = \frac{\sum_i n_i d_i^3}{\sum_i n_i d_i^2} \qquad (1)$$

This definition permitted the calculation of the surface area corresponding to a given volume fraction and volume surface diameter. In any one of the present experiments ϕ was fixed, and the corresponding value of $\sum_i n_i d_i^3$ was determined experimentally. On this basis f was defined by

$$\phi = f \frac{\sum_i n_i \pi d_i^3}{6} \qquad (2)$$

*See footnote on page 346.

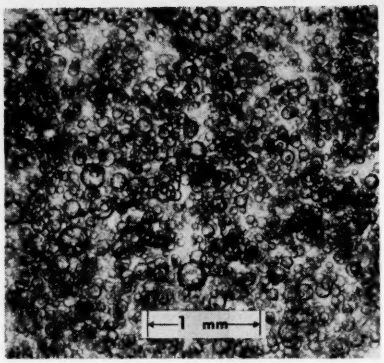

Fig. 2b. Drop-size distribution. $V = 6.0, \phi = 0.1, D_0 = 0.375$ in.; downstream distance = 7.0 in.

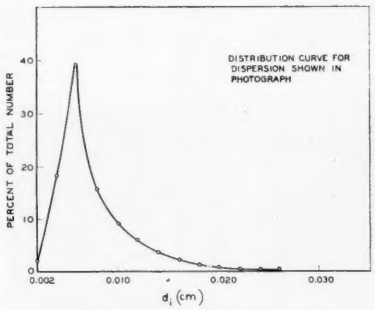

Fig. 3. Drop-size distribution curve.

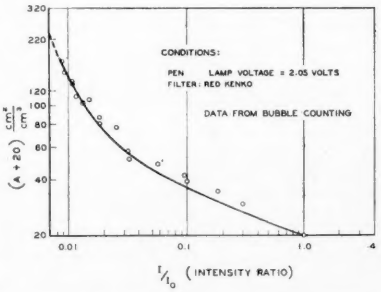

Fig. 4. Calibration curve for phototube.

When the drops are perfect spheres, a state very nearly approached by the water-kerosene systems, and when very small increments of diameter are used in the classification of the drops, f approaches unity. The volume-surface area, referred to as specific area and interfacial area, is defined by

$$A = f \sum_i n_i \pi d_i^2 \qquad (3)$$

The equations are readily combined to give

$$A = \frac{6\phi}{d_{vs}} \qquad (4)$$

Correlation of the Formation of Interfacial Surface Area

When a single-phase fluid passes through an orifice, it emerges with what might be thought of as an excess of kinetic energy. As the fluid proceeds downstream from the orifice, part of this excess kinetic energy is converted back to a *pressure head* and the remainder of it is converted into heat. In the case of a two-phase mixture, water dispersed in kerosene, the possibility of the formation of surface represents an additional degree of freedom with respect to the dissipation of the excess kinetic energy. Thus it is reasonable to postulate that the surface area produced by an orifice mixer is a function of the change in kinetic energy across the orifice. Also the amount of surface formed is a function of the volume fraction of the dispersed phase, which follows from the fact that when the volume fraction of the dispersed phase is zero, the surface formed is, of course, zero.

The energy required to form A is given by the product $A\sigma$. The energy available to effect this is taken to be some function of ΔK.E. across the orifice. The preceding postulates are summarized in concise form:

$$A\sigma = F[(\Delta\text{K.E.})(\rho_m) f(\phi)] \qquad (5)$$

The product $(\Delta\text{K.E.})\ (\rho_m)$ has the units of foot-pounds per cubic foot of mixture. $\rho_m = (1 - \phi)\rho_k + \rho\phi$. Since $A = 0$ at $\phi = 0$, the function F must also be equal to zero at $\phi = 0$. One form of F which satisfies these conditions is a product function of $(\Delta\text{K.E. } \rho_m)$ and $f(\phi)$, where $f(\phi)$ approaches zero as ϕ approaches zero. It was found that the experimental results could be represented by taking F to be a power function of the following form:

$$A\sigma = f(\phi)(\Delta\text{K.E. } \rho_m)^\alpha \qquad (6)$$

The logarithmic form of Equation (6) is

$$\log A = \alpha \log \Delta\text{K.E.} + \log \frac{f(\phi)\rho_m{}^\alpha}{\sigma} \qquad (7)$$

Furthermore it was found that the change in kinetic energy of the water-kerosene

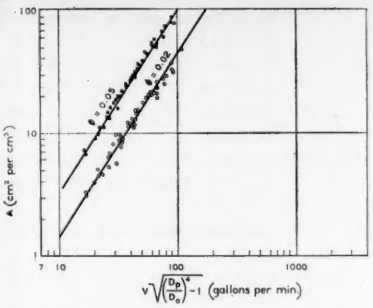

Fig. 5. Variation of interfacial area with flow rate, $\phi = 0.02$ and 0.05.

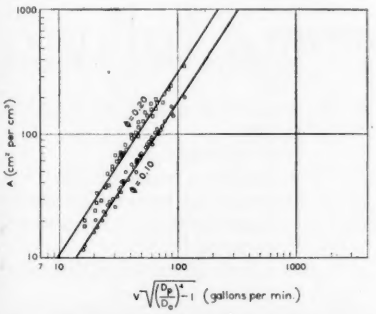

Fig. 6. Variation of interfacial area with flow rate, $\phi = 0.10$ and 0.20.

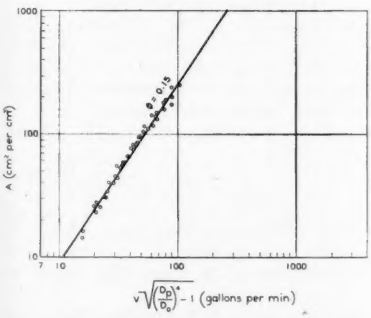

Fig. 7. Variation of interfacial area with flow rate, $\phi = 0.15$.

mixture across the orifice could be represented accurately by the conventional orifice equation

$$\frac{u_0^2 - u_p^2}{2g_c} = \frac{C_0^2\,\overline{\Delta P}}{\rho_m} = \Delta\text{K.E.} \qquad (8)$$

For the range of Reynolds numbers covered in this investigation Tuve and Sprenkle (*10*) have shown that the orifice coefficient for a single-phase system varies little with flow rate and orifice diameter. Orifice coefficients were calculated (on the basis of the experimental values of flow rates and corresponding pressure drops) for the two-phase system by use of the conventional orifice equation and found to be of the same order of magnitude as those shown by Tuve and Sprenkle.

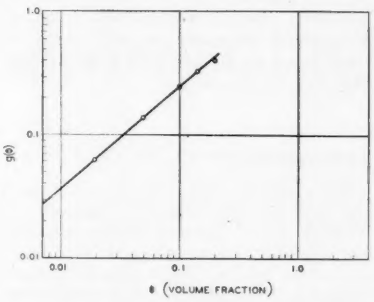

Fig. 8. Variation of the volume fraction function, $g(\phi)$, with ϕ.

Since liquids are for all practical purposes incompressible, $u_0 S_0 = u_p S_p$. This relationship permits one to write the preceding equation in the form

$$u_p\sqrt{\left(\frac{D_p}{D_0}\right)^4 - 1} = C_0\sqrt{\frac{2g_c\,\overline{\Delta P}}{\rho_m}} = \sqrt{\Delta\text{K.E.}\ 2g_c} \qquad (9)$$

Since V was measured in gallons per minute, this expression was written in the following form:

$$V\sqrt{\left(\frac{D_p}{D_0}\right)^4 - 1} = 7.48 S_p C_0\sqrt{\frac{2g_c\,\overline{\Delta P}}{\rho_m}} = 7.48 S_p\sqrt{(\Delta\text{K.E.})(2g_c)} \qquad (10)$$

In the left-hand member of the expression the product $7.48\,U_p S_p$ has been replaced by its equivalent V. In view of the equality given by Equation (10), Equation (7) may be stated as follows:

$$\log A = 2\alpha \log V\sqrt{\left(\frac{D_p}{D_0}\right)^4 - 1} + \log g(\phi)\left(\frac{\rho_m}{\rho}\right)^{\alpha} \qquad (11)$$

where

$$g(\phi) = \frac{f(\phi)\rho^{\alpha}}{(7.48 S_p)^{2\alpha}(2g_c)^{\alpha}\sigma}. \qquad (12)$$

It is to be observed that the first logarithmic term on the right-hand side of Equation (11) is independent of the volume fraction and that the second is independent of the volumetric rate of flow and the diameter of the orifice. Plots of the experimentally determined interfacial surface areas versus

$$V\sqrt{\left(\frac{D_p}{D_0}\right)^4 - 1}$$

are shown in Figures 5, 6, and 7. The straight line drawn through the points was determined in the following manner. The slope 2α of each line was determined at each of the volume fractions: $\phi = 0.02$, 0.05, 0.1, 0.15, and 0.20 by the method of least squares. The slopes of the curves in the order of the volume fractions stated were 1.420, 1.450, 1.485, 1.507, and 1.491, respectively. The corresponding correlation coefficients were all greater than 0.98. If the lines are parallel, the slope as determined by the method of least squares is 1.469.

With the slope of each curve taken as 1.469, the intercept $g(\phi)(\rho_m/\rho)^{\alpha}$ was determined for each value of ϕ. From these intercepts the corresponding values of $g(\phi)$ were calculated.

It was found by trial that $g(\phi)$ was of the form

$$g(\phi) = C\phi^{\beta}, \text{ or } g(\phi) = 1.668\phi^{0.847} \qquad (13)$$

A plot of $g(\phi)$ vs. ϕ is shown in Figure 8, where the solid line represents Equation (13). The values of C and β were also determined by the method of least squares. When the numerical values of the constants are substituted in Equation (11), one obtains

$$A = 1.668\phi^{0.847}(\rho_m/\rho)^{0.735}\left[V\sqrt{\left(\frac{D_p}{D_0}\right)^4 - 1}\right]^{1.47} \qquad (14)$$

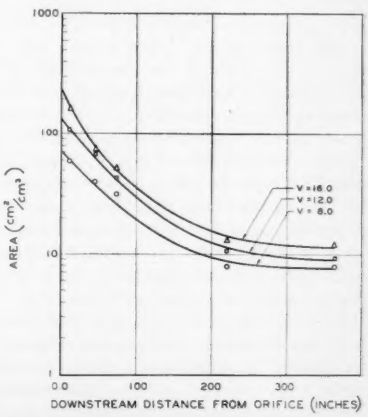

Fig. 9. Coalescence, $D_0 = 0.4375$ in.; $\phi = 0.10$.

The correlation coefficient for the complete expression was 0.993. The average deviation of the experimental values of the areas from the corresponding ones calculated by use of Equation (14) was 9.0%. It is to be observed that when this expression for A is substituted in Equation (4), one finds that d_{vs} is proportional to $\phi^{0.153}\,(\rho/\rho_m)^{0.735}$. Although the latter relationship indicates that d_{vs} has zero as the limit as ϕ approaches zero, this is not necessarily the correct limit, since data for volume fractions less than 0.02 were not obtained. It should also be noted that the coefficient 1.668 is a function of the cross-sectional area of the pipe, which was held constant for all experiments.

Since the relationship between

$$V\sqrt{\left(\frac{D_p}{D_0}\right)^4 - 1}$$

and $\overline{\Delta P}$ is given by Equation (7), it is readily shown that an alternate statement of Equation (14) is

$$A = 282\phi^{0.847}[C_0^2\,\Delta P]^{0.735} \qquad (15)$$

In the indicated derivation of this expression cancelations of the terms involving the density of the mixture and the cross-sectional area of the pipe were obtained, the coefficient 282 being left inversely proportional to the interfacial tension at the water-kerosene interface. Furthermore, since the permanent head loss for single-phase flow is related to the pressure drop across the orifice, Equation (15) suggests a direct relationship between the formation of interfacial area and the power required for pumping.

Coalescence of the Dispersed Phase

The coalescence of the dispersed phase was demonstrated by the experiments shown in Figure 9. The areas were measured at selected positions located vertically downstream from the mixing orifice, because it was discovered in the process of the experimentation that changes in direction of the piping produced a significant amount of coalescence.

An inspection of these curves shows that essentially all the coalescence for this particular system occurs between the orifice and a position 220 in. downstream from it. For the curve corresponding to a rate of 8 gal./min. the line connecting the first four points is nearly straight, an indication that the change in the interfacial area with respect to the downstream distance is proportional to the first power of the interfacial area. For those curves corresponding to flow rates of 12 and 16 gal./min. the slopes decrease with an increase in downstream distance, evidence that the change in the interfacial area with respect to the downstream distance is proportional to the interfacial area raised to a power greater than unity. Clay (*1*) has also considered the phenomenon of coalescence and, in describing it, he took a kinetic approach which was similar to the kinetic theory of gases.

CONCLUSIONS

As a result of this experimental investigation it can be concluded that for the particular system considered the interfacial area formed in the water-kerosene mixture in passing through an orifice was proportional to the 0.735 power of the change in kinetic energy across the orifice. Also the interfacial area was found to increase with increases of the volume fraction of water in kerosene. The interfacial area formed at the orifice decreased rapidly owing to coalescence as the mixture flowed downstream from the orifice.

ACKNOWLEDGMENT

The project was supported by the Humble Oil and Refining Company through the Texas A. & M. Research Foundation. This aid is gratefully acknowledged. The assistance given by the Engineering Experiment Station in the preparation of this manuscript is appreciated.

NOTATION

A = interfacial area of dispersed phase, measured at a given distance downstream from mixing orifice, (cm.)^2(cm.)$^{-3}$

C = proportionality constant defined by Equation (13), dimensionless

C_0 = coefficient of discharge defined by Equation (8), dimensionless

d_i = diameter of particle i, cm.

d_{vs} = mean volume-surface diameter defined by Equation (1), cm.

D_0 = diameter of orifice, in.

D_p = internal diameter of the pipe, in. For all experiments shown here $D_p = 1.049$ in.

f = factor required to give an equality between the volume fraction of water in kerosene as determined volumetrically and photographically; defined by Equation (2)

F = function of kinetic energy and volume fraction defined by Equation (5)

$f(\phi)$ = function of volume fraction

$g(\phi)$ = function of volume fraction defined by Equations (12) and (13)

g_c = standard gravitational constant, (ft.)(min.)$^{-2}$

I/I_0 = intensity ratio. I_0 corresponds to the intensity indicated by the phototube at zero volume fraction, and I represents the intensity at any volume fraction ϕ

ΔK.E. = change in the kinetic energy of the mixture across the orifice, (ft.)(lb.)(lb.)$^{-1}$

n_i = number of water droplets in 1 cc. of dispersion having a diameter of d_i cm. in size interval

$\overline{\Delta P}, \Delta P$ = pressure drop across the orifice (lb.)(ft.)$^{-2}$ and (lb.)(in.)$^{-2}$, respectively

S_0 = cross-sectional area of orifice, sq. ft.

S_p = cross-sectional area of pipe, sq. ft.

u_0 = linear velocity at which mixture passes through orifice, (ft.)(min.)$^{-1}$

u_p = linear velocity at which mixture passes through the pipe, (ft.)(min.)$^{-1}$

V = volumetric rate of flow, (gal.)(min.)$^{-1}$

Greek Letters

α = constant defined by Equation (6)

β = constant defined by Equation (13)

π = 3.1416 radians

ρ = density of water (lb.)(ft.)$^{-3}$

ρ_k = density of kerosene (lb.)(ft.)$^{-3}$

ρ_m = density of mixture of water and kerosene (lb.)(ft.)$^{-3}$

σ = interfacial tension of the water-kerosene interface

$\sum$ = sum over all components indicated

ϕ = volume fraction of water in water-kerosene mixture

LITERATURE CITED

1. Clay, P. C., *Proc. Roy. Acad. Sci.* (Amsterdam), **43**, 852 (1940).
2. Dallavalle, J. M., "Micromeritics," Pitman Pub. Co., New York, 47 (1948).
3. McNair, Howard, and P. G. Murdock of the Dow Chemical Company, personal communication.
4. Mie, G., *Ann. Physik.* (14), **25**, 377 (1908).
5. Morrell, J. C., and D. J. Bergman, *Chem. & Met. Eng.*, **35**, 210 (1928).
6. Rodger, W. A., V. G. Trice, Jr., and J. H. Rushton, *Chem. Eng. Progr.*, **52**, No. 12, 515 (1956).
7. Rushton, J. H., *Ind. Eng. Chem.*, **49**, 530 (1957).
8. ———, and J. Y. Oldshue, *Chem. Eng. Progr.*, **49**, 161 (1953).
9. Scott, L. S., M.S. thesis, Texas Agr. and Mech. Coll., College Station (1957).
10. Tuve, G. L., and R. E. Sprenkle, *Instruments*, **6**, 201 (1933).
11. Trice, V. G., Jr., and W. A. Rodger, *A.I.Ch.E. Journal*, **2**, 205 (1956).
12. Vermeulen, Theodore, G. M. Williams, and G. E. Langlois, *Chem. Eng. Progr.*, **51**, 85 (1955).
13. Wesselhoft, R. D., M.S. thesis, Texas Agr. and Mech. Coll., College Station (1955).

Manuscript received Sept. 17, 1957; revision received Dec. 6, 1957; manuscript accepted Dec. 9, 1957

An Improved Experimental Reactor for Applied Kinetic Studies

THOMAS K. PERKINS and HOWARD F. RASE

University of Texas, Austin, Texas

A recirculation type of reactor has been designed and tested on a rapid reaction which characteristically causes difficult temperature-control problems and high diffusional resistances (hydrogenation of propylene on nickel catalyst). Descriptions of the reactor and its operation are given, together with an assessment of errors and the advantages and disadvantages of the recirculation technique. A rate equation and rate constants are determined so that the data will be more readily comparable with the work of other investigators.

Chemical-reactor design must be based on four processes—chemical reaction kinetics and the transfer of mass, heat, and momentum. For practical purposes idealized models for a given system may be selected and the approximate effects of these four processes determined simultaneously. The advent of the digital computer has made such calculations feasible.

At the present stage of development the effects of these four processes on the ultimate rate of production must often be determined experimentally. It is of primary importance, however, that these effects be studied independently, to minimize or eliminate the dependence of the data on the type and size of bench-scale or pilot plant equipment. Too often data which are assumed to represent the kinetics of a reaction have been obtained with an experimental reactor in which temperature and diffusional gradients are large. Correction by computational methods leads to data of doubtful value. The preferred procedure is to eliminate such gradients experimentally with a reactor designed for independent study of each variable. A recirculation type of reactor has been designed to meet the criteria for experimentation and has been successfully applied in the study of the kinetics of a typical rapid reaction, the catalytic hydrogenation of propylene.

RECIRCULATION TYPE OF REACTOR FOR EXPERIMENTATION

A recirculation type of differential reactor reduces some of the experimental difficulties usually encountered in determining precise reaction-rate data. This type of reactor has been mentioned by Hougen (*4*), but little work has been published describing successful applications. The outstanding feature of such a system is the recirculation of most of the reactor effluent stream, a small feed stream being continuously added and a small net-product stream continuously removed. A sketch of this arrangement is included in Figure 1.

Advantages

Perhaps the greatest advantage of this reactor is its ability to control catalyst temperatures more accurately. Recirculation rates ten to fifteen times larger than fresh feed rates, for instance, would give an adiabatic temperature rise of approximately one tenth to one fifteenth of that which would occur in an ordinary adiabatic differential reactor operating with the same over-all conversion. Hence, combining recirculation and good heat transfer to or from the catalyst bed usually provides excellent control of temperatures.

High recirculation rates also permit high gas velocities past the catalyst particles without the use of excessive

Thomas K. Perkins is with The Atlantic Refining Company, Dallas, Texas, and Howard F. Rase with The University of Texas, Austin, Texas.

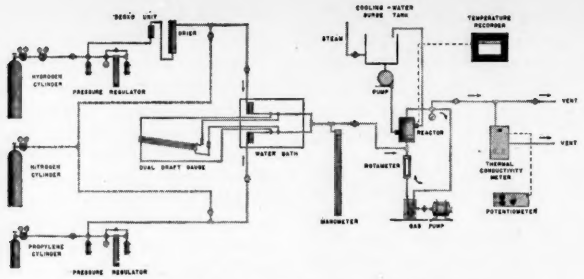

Fig. 1. Flow diagram of the experimental system.

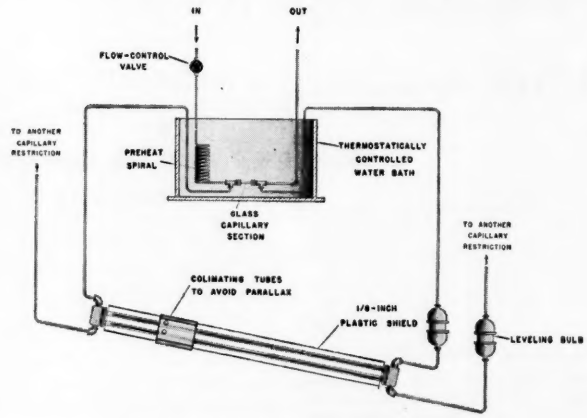

Fig. 2. Sketch of capillary flow meters.

quantities of reactants. Theoretically mass transfer could be reduced until, even for reactions occurring at a very rapid rate, the rate of mass transfer would no longer influence the over-all rate of reaction. Possibly recirculation can provide an effective experimental means of showing when mass transfer effects are absent. On the assumption that the over-all rate of reaction is being limited at low recirculation rates by the rate of mass transfer, then, as the recirculation rate is increased, the total conversion increases and approaches an asymptotic value. If there is an experimental means of varying the recirculation rate, it is necessary to show only that experimental conditions are such that a change in recirculation rate has no effect on the conversion. This method would circumvent the necessity of knowing exact activity levels of several different catalyst charges as is required when mass transfer effects are determined by the usual method (*5*) of varying catalyst weight at constant values of W/F (reciprocal space velocity).

High recirculation rates and the associated low conversions per pass also give more uniform compositions throughout the reactor. All this can be accomplished without limiting the total conversion to very low values, which would introduce errors through analysis.

Disadvantages

Although such an experimental arrangement presents these very definite advantages, there are also some disadvantages. Not every reaction can be studied in this way; in some cases various side reactions may be promoted, owing to the admixture of products to the fresh feed. Another possible difficulty is the length of time required for the recirculating portion of the system to reach steady state operation. This time can be reduced by increasing the recirculation rate and decreasing the volume of the recirculation system.

Experimental pressure drops across the reactor may be higher than those usually observed in ordinary differential beds. It is necessary to a compromise between high-pressure drop across the bed and high gas velocity past the catalyst. These can be varied independently of the total recirculation rate by varying the free area for gas flow.

Owing to the transient period after the change of any expermental variable, one must have a continuous method of analysis when using this type of reactor.

For the most part these disadvantages can be overcome by careful design of the experimental equipment. It may be concluded that a carefully designed recirculation differential-reactor system will permit precise control of experimental conditions within the catalyst bed.

EXPERIMENTAL INVESTIGATION

To investigate the merits of this type of experimental arrangement, a recirculation differential reactor system was constructed and operated to obtain reaction-rate data for the hydrogenation of propylene. Many studies (*3, 7, 10*) have shown that the hydrogenations of light olefins proceed in a straightforward manner, which simplifies study and analysis by the accepted kinetic theories.

Equipment was designed so that recirculation rates ten to fifteen times larger than the fresh feed rates might be attained. A brief résumé of operating characteristics follows:

1. A maximum temperature rise of 6°F. was observed. Closer control undoubtedly could have been attained by spacing the catalyst in such a manner as to give more heat transfer area between each particle.

2. Gas velocities past the catalyst particles of approximately 200 ft./sec. were achieved. Calculations and comparison with other data from these laboratories in which feed rate was varied independently of W/F show that the effects of mass transfer were negligible. Recirculation rates were not varied but were held at the maximum possible values.

3. The change in the percentage of hydrogen across the reactor was in each case less than 0.1%.

4. There was only one primary reaction, and difficulties with side reactions were not encountered.

5. Analyses of hydrogen-propylene mixtures were made by continuously measuring thermal conductivities. Conversions were calculated from the changes in percentage of hydrogen.

6. The time required for the recirculation system to reach a steady state could not be detected because it was less than the time required for the thermal conductivity meter to reach a constant reading.

EXPERIMENTAL EQUIPMENT AND MATERIALS

Feed System

Calculations of conversions from changes in percentage of hydrogen require inordinate accuracy in the gas-stream analyses. Furthermore it was necessary that compositions of the feed stream be held constant for some time. Consequently an unusually stable feed system and an accurate analytical technique were developed in addition to the

reactor itself. Figure 1 shows a flow diagram of the complete system.

High-pressure hydrogen from a cylinder passed through two pressure-regulating valves, in series, where the pressure was dropped to approximately 30 lb./sq. in. gauge. It then passed through one chamber of a pressure-balancing device to control upstream pressures accurately and then through a Deoxo unit and a bed of activated alumina to remove trace quantities of oxygen and water. The hydrogen finally passed through a flow-control valve and through a glass capillary tube. The capillary-tube and draft-gauge arrangement is shown in Figure 2. After metering, the hydrogen stream was mixed with propylene from the olefin feed stream. Liquefied propylene from a 1-gal. cylinder was vaporized and passed through a similar pressure control and capillary measuring system.

The two gases entered a common back-pressure control valve where the absolute pressure on both capillary tubes was adjusted to 1,140 mm. Hg ± 0.3 mm. The combined feed stream was then fed into the recycle stream of the reactor system. A product stream was removed from the reactor and passed through the reactor-pressure control valve. The product stream was then split, a portion of it being sent to the thermal-conductivity meter for analysis and the remainder vented to the atmosphere.

Water to absorb the heat of reaction was circulated through the reactor jacket by means of a centrifugal pump. The water was maintained at the proper operating temperature by bleeding low-pressure stream into the water surge tank.

Calculations showed that for precise control of the flow rate it was necessary that the pressure upstream from the flow-control valves be held constant to within ±0.2 in. of water. A system was designed which allowed the balancing of the flowing-stream pressure against a static pressure. The equipment consisted essentially of two chambers connected by a light-oil–filled manometer with a by-pass line between the two chambers. When the system was brought on stream, the by-pass line was at first opened, and the control valve was adjusted until the gas was flowing at the desired rate and the indicated pressure on both chambers was approximately 20-lb./sq. in. gauge. When all pressures had reached constant values, the by-pass valve was closed. Any slight change in the pressure of the flowing stream was indicated rapidly by the manometer, and manual adjustment was made by the control needle valve. It was found possible to control the flowing stream pressure to within ±0.2 in. of oil (±0.17 in. of water), which was within limits that could be tolerated without a detectable change in flow rates.

Flow rates of the two reactants were determined by measuring the pressure drop across a section of 6-mm. by 1-mm. glass capillary tubing. The gas to be metered first flowed through a stainless steel needle valve, then through a preheat spiral, and finally through the capillary restriction. The capillary section and preheat spiral were immersed in a constant-temperature bath regulated to 110° ± 0.45°F.

Pressure drops across the restrictions were measured with 37-in.–long draft gauges made from heavy-wall glass tubing.

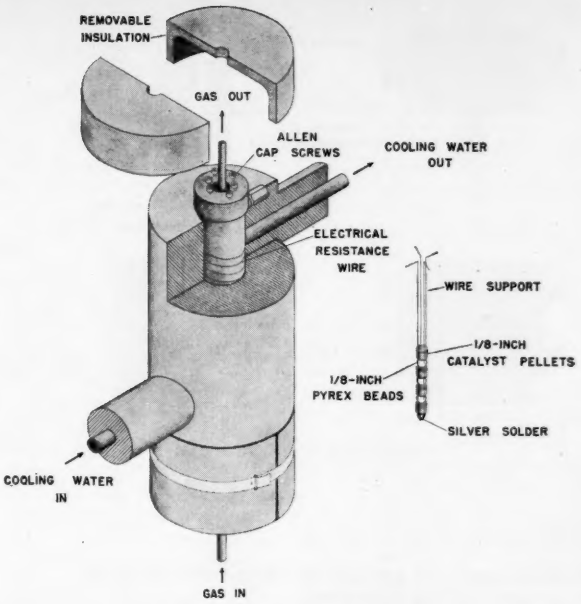

Fig. 4. The assembled reactor.

The Reactor

The reactor, Figures 3 and 4, consists of four separate tubes which can be used either individually or in parallel. For all runs reported in this work catalyst pellets were placed in only one of the tubes, and the other three were blocked with stainless steel plugs. The tubes were attached to a *floating head* at the bottom to prevent excessive stress when the reactor was raised to a high temperature during reduction of the catalyst. The outside of the water jacket was wrapped with electrical resistance wire for heating of the reactor during the reduction period. The complete reactor was surrounded with 2-in.–thick magnesia insulation.

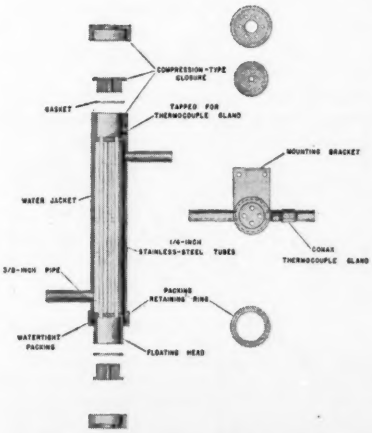

Fig. 3. The experimental reactor.

A gas recirculation pump with a capacity of 1 to 3 cu. ft./min. was required. It was imperative that there was no leakage of the hydrogen-propylene mixture, and a low holdup of gas was desired in order that the system might reach equilibrium rapidly.

After an extensive survey of commercially available equipment and special research equipment had not uncovered a pump meeting the desired requirements, a four-cylinder diaphragm-type pump was constructed (Figure 5). Diaphragms were made from 1/32-in. fabric-reinforced neoprene. No appreciable leakage was detected, and after many hours of operation little or no wear of the diaphragms could be observed. The pump was powered by a 2-hp., 220-volt, 3-phase induction motor, with a rated operating speed of 1,730 rev./min. Two of the cylinders were exhausting at all times during operation, and the rotameter indicated no pulsation of the gas stream. Holdup in the pump was very small, as was the clearance volume, and the pump operated efficiently. Lines before and after the pump were jacketed so that the gas might be cooled with water.

Thermal Conductivity Meter

A Leeds and Northrup model 7802-D-A9 thermal-conductivity meter with a reference cell filled with 70% hydrogen and 30% nitrogen was used for analysis. The following modifications were made to attain the desired accuracy. The heater circuit for the constant-temperature cabinet was separated from the electrical circuit for the measuring

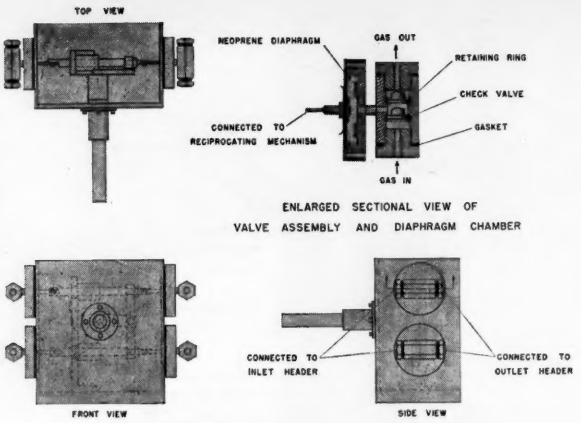

Fig. 5. The recirculation pump.

bridge. The bridge circuit was preceded by an auxiliary constant-voltage transformer. A shunt (a 50-ohm and a 10,000-ohm manganin resistor in series) was placed across the output of the selenium rectifier in order that the exact voltage to the bridge might be measured during runs. A powerstat in series with this circuit allowed precise control of the bridge voltage to an arbitrarily selected value.

The thermal-conductivity meter was calibrated by use of known compositions metered with the flow meters. The unbalance of the thermal-conductivity meter bridge is a unique function of the gas composition. As suggested by Wynkoop and Wilhelm (*10*) the data were fitted to an equation of the form

$$\log (\%H_2) = A(\text{mvr}) + B$$

Sussman and Potter (*7*) found no effect of the saturate if the hydrogen concentration was maintained above 30% (as was the case for all runs in this work).

Catalyst

To show the advantages of the recirculation type of reactor, a catalyst giving a high rate of reaction was desired. Fair (*3*) used a supported nickel catalyst and reported high rates of reaction and consequently appreciable temperature gradients in an ordinary differential reactor. The same catalyst (Harshaw Ni-0101 T 1/8) was selected for use in this investigation. A typical analysis of the unreduced catalyst, which is supplied as 1/8-in. pellets, is

	Weight %
Nickel (elemental)	44
SiO_2	16
Carbon	4
Nickel compounds	36
	100

Reactants

Electrolytic hydrogen (99.5% H_2, 0.5% O_2) "pure"-grade propylene of 99% purity (principal impurity-propane) were used.

OPERATING PROCEDURE

After the catalyst particles had been weighed they were spaced between Pyrex-glass cylinders (Figure 4). The supporting frame and catalyst were then lowered into the reactor tube, and the thermocouple was adjusted to touch the upper catalyst particle. After the reactor had been closed and the pressure tested, the system was purged with nitrogen and then with hydrogen. Pressure on the reactor was adjusted to 4 lb./sq. in gauge with hydrogen gently flowing through the reactor. The temperature of the catalyst was raised to 600°F. ± 15°F. and maintained for 6 hr. At the end of this time the reactor was again thoroughly purged with hydrogen, placed under 5 lb./sq. in. gauge hydrogen pressure, and allowed to cool.

Before rate data was taken, the activity of the catalyst was stabilized by adjustment of the temperature of the catalyst to 90° to 100°F. admission of propylene and hydrogen at low flow rates, and turning on of the recirculation pump. These conditions were held constant for several hours, when the reactor was purged with hydrogen and maintained under hydrogen pressure.

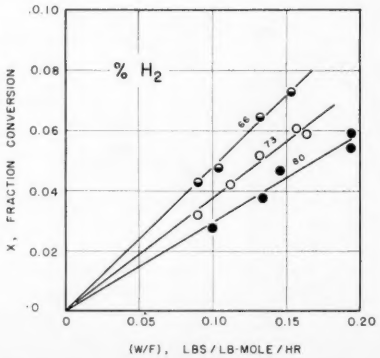

Fig. 6. Corrected conversions vs. (*W*/*F*), 110°F.

To ensure thermal equilibrium in the feed-metering system, the constant-temperature bath surrounding the capillary tubes was brought up to temperature and maintained for at least 1 hr. before each series of runs. At the beginning of the runs the reactor cooling water was brought up to the maximum desired temperature and circulated through the water jacket; then the cooling-water rate to the recirculation pump was adjusted. All equipment other than the reactor was purged with nitrogen. The reactor was by-passed, and the desired flow rates of gases were set. Gauge pressures on the manual pressure controllers were maintained at 20 lb./sq. in., and the back pressure on the flow meters was adjusted to 1.5 atm. abs. A check reading was taken on the thermal-conductivity meter. When all conditions had reached equilibrium, the gas stream was diverted through the reactor, and the recirculation pump was turned on. When a constant effluent analysis reading was reached on the thermal-conductivity meter, it was recorded, and the temperature of the cooling water was adjusted to a new value. Each point of data required 10 to 15 min.

After several series of runs the activity of the catalyst was checked by repeating some of the earlier runs. The activity was calculated in the manner described by Hougen and Watson (*5*).

The activity of the reactor alone was also investigated. Pyrex glass cylinders were charged in the same manner as the catalyst, and the usual reduction procedure was followed. Runs at a maximum water temperature, with and without the recirculation pump, showed no measurable conversion.

RESULTS

To complete the evaluation of this reactor, a rate equation was selected as described by Hougen and Watson (*5*) and applied by others (*6*, *7*, *8*). Experimental data were obtained at five temperatures in the range of 110° to 190°F. and at three hydrogen partial pressures. Complete data and plots showing a comparison of experimental and calculated conversions are available (*5a*). See Figure 6.

Examination of the complete data indicated that, within experimental accuracy and over the range investigated, the propane formed had no effect. Thus p_u terms (partial pressure of propane) were eliminated in all rate equations considered; terms involving the reverse reaction were also omitted because of the high equilibrium constant.

Preliminary graphical interpretation of all possible rate equations indicated the following as the most consistent:

Rate Equation (1)

$$R = \frac{aK_hp_up_h}{(1 + K_hp_h)^2}$$

Rate Equation (2)

$$R = \frac{aK_hp_up_h}{(1 + \sqrt{K_hp_h})^3}$$

Values of the constants for the two rate equations were determined by an iterative procedure on an IBM-CPC computer and are given in Table 1.

Table 1. Constants For The Rate Equations

General equation

$$\ln \text{constant} = -m/T + n$$

where T = °K.

	m	n
Rate Equation (1)		
a	1,715	1.68×10^{3}
K_h	−1,381	5.25×10^{-3}
Rate Equation (2)		
a	2,003	1.27×10^{4}
K_h	−1,833	6.72×10^{-4}

Both rate equations are based on the surface reaction between adsorbed propylene and adsorbed hydrogen, molecular hydrogen in Equation (1) and atomic hydrogen in Equation (2). The average deviations for Equations (1) and (2) were ±3.3% and ±3.5%, respectively; maximum deviations were in both cases 9.1%.

Owing to the similarity of the equations and the limited range of variables investigated in this work, it is not possible to recommend one of the equations more strongly than the other, each having been reported by previous investigators for the hydrogenation of light olefins. There is much evidence in the literature indicating adsorption of both reactants, as suggested here, and some to the contrary for similar reactions on nickel films (*1, 9*).

ASSESSMENT OF ERRORS

A careful assessment of errors was made to complete the evaluation of the reactor system, and the results are given in Table 2.

Table 2. Tabulation Of Errors

Measured variable	Maximum error
Feed composition	±0.4% H_2 at 66% H_2 ±0.02% H_2 at 80% H_2
Product composition	±0.002% H_2
Catalyst weight	Negligible
Reaction temperature	Maximum temperature rise was 6°F.
Reactor pressure	Maximum pressure drop was 1 to 2 in. Hg

The consistency of any one set of experimental points is better than the over-all accuracy owing to the order in which data were taken. For any one set of points flow rates were held constant while the temperature was varied. Hence uncertainties due to errors in flow rates were the same for each point of data in the given series. In a correlation of the various series of runs it is estimated that the maximum probable error in the calculated over-all conversion in no more than ±10%.

CONCLUSIONS

A recirculation differential reactor eliminates many of the experimental difficulties encountered in determining rate data for highly exothermic or endothermic reactions occurring at rapid rates. By proper design of the reactor, temperature gradients in the catalyst section can be maintained within acceptable limits. High gas velocities in the reactor prevent interfering mass transfer effects. Owing to the small conversion per pass, gas compositions within the reactor are more uniform than those encountered in ordinary differential reactors. All reactions, however, may not lend themselves to treatment in this type of equipment, as admixture of products to the feed may promote secondary reactions.

The free volume of the recirculation system must be small to reach steady state rapidly. Because of the transient period occurring after the change of any variable, a continuous method of analysis is desirable; measurement of the thermal conductivity has proved to be a good method of analyzing hydrogen and propylene mixtures.

The recirculation type of reactor permitted the determination of accurate initial-rate data for the vapor-phase hydrogenation of propylene over nickel-kieselguhr catalyst. It was, therefore, possible to conclude that the data can be represented equally well with two equations over a range of reaction conditions of 110° to 190° F., 1-atm. pressure, and 65 to 80% hydrogen. Both equations are based on the surface reaction as the controlling step, in one case with reaction between adsorbed propylene and adsorbed molecular hydrogen and in the other with reaction between adsorbed propylene and hydrogen adsorbed as atoms.

These conclusions can be made with some confidence because the measurements were carried out with a good degree of accuracy and with negligible temperature and differential gradients. In a nonrecirculation type of reactor the temperature and diffusional gradients for this rapid reaction would have been high and the results uncertain.

ACKNOWLEDGMENT

The authors are grateful to the Ethyl Corporation for a fellowship and gifts of certain supplies and equipment; to Carbide and Carbon Chemical Corporation for a fellowship; to Jefferson Chemical Corporation for gifts and loans of equipment and supplies; and to Anthony L. Pozzi for his generous assistance.

NOTATION

- a = an empirical constant which includes the over-all effectiveness factor and the reaction-velocity constant
- F = feed rate, g.-moles of propylene/sec.
- K = an adsorption-equilibrium constant
- m = constant, °K.
- mvr = millivolt reading of the potentiometer
- n = constant, lb./moles/(lb. unreduced catalyst)(hr.)(atm.)^2
- p = partial pressure, atm.
- R = reaction rate, lb.-moles of propane produced/(hr.)(lb. of unreduced catalyst)
- S = corrected scale reading on flow meters
- T = absolute temperature, °K.
- W = weight of catalyst, lb.
- x = fraction of propylene reacted

Subscripts

- h = hydrogen
- u = propylene
- 1 = upstream conditions
- 2 = downstream conditions

Other

- log = logarithm to base 10
- ln = logarithm to base e

LITERATURE CITED

1. Beeck, Otto, *Revs. Mod. Phys.*, **17**, 61 (1945).
2. Binder, R. C., "Fluid Mechanics," 2 ed., Prentice-Hall, Inc., New York (1952).
3. Fair, J. R., Ph.D. dissertation, Univ. Texas, Austin (1955).
4. Hougen, O. A., Reaction Kinetics in Chemical Engineering, Chem. Eng. Progr. Monograph Ser., **47**, No. 1 (1951).
5. ———, and K. M. Watson, "Chemical Process Principles," Part III, John Wiley and Sons, New York (1947).

5a. Perkins, T. K., Ph.D. dissertation, Univ. Texas, Austin (1957); available from University Microfilms, Ann Arbor, Michigan, Microfilm Mic 57-4081, $2.00.

6. Potter, Charles, and Seymour Baron, *Chem. Eng. Progr.*, **47**, No. 9, 473 (1951).
7. Sussman, M. V., and Charles Potter, *Ind. Eng. Chem.*, **46**, 457 (1954).
8. Tschernitz, J. L., Sidney Bornstein, and R. B. Beckmann, *Trans. Am. Inst. Chem. Engrs.*, **42**, 883 (1946).
9. Twigg, G. H., *Trans. Faraday Soc.*, **35**, 934 (1939).
10. Wynkoop, Raymond, and Richard H. Wilhelm, *Chem. Eng. Progr.*, **46**, 300 No. 6 (1950).

Manuscript received Dec. 3, 1957; revision received Feb. 5, 1958; paper accepted Feb. 6, 1958.

Critical Temperatures and Pressures of Hydrocarbons

J. CHARLES FORMAN and GEORGE THODOS

The Technological Institute, Northwestern University, Evanston, Illinois

A method has been developed for the calculation of van der Waals' constants both a and b for hydrocarbons usually encountered, including the aliphatic, naphthenic, and aromatic types. With these constants critical temperatures and pressures can be calculated directly.

Methods recently made available (*12, 13, 14, 15*) allow the calculation of these constants through the use of substitution values involving the replacement of hydrogen atoms by methyl groups in a definitely prescribed pattern. In this study van der Waals' constants are directly calculated from a consideration only of the molecular structure of the hydrocarbon. This approach has become possible through the assignment of group contributions to different types of carbon atoms, which can be combined in any manner to produce the van der Waals' constants representative of the molecular structure of the hydrocarbon.

Several methods have been presented which permit the evaluation of critical constants of organic compounds (*2, 4, 5, 7, 8, 9, 12* to *17*). For their successful application most of these methods require certain physical properties of the substances; for example, the method of Watson (*17*) requires the use of the normal boiling point and corresponding liquid density, that of Wan (*16*) utilizes molar refraction for the calculation of the critical temperature, Meissner and Redding (*7*) and Herzog (*4*) introduce the use of the parachor in conjunction with the normal boiling point for the calculation of critical constants of a number of hydrocarbons, and density and viscosity measurements are required for the calculation of the critical density according to Boas (*2*).

The first attempt to eliminate the use of physical properties was that of Riedel (*8, 9*), later extended and improved by Lydersen (*5*). These methods are fundamentally alike and permit the calculation of critical constants from structural-group contributions and only the normal boiling point. In their attempts, Riedel and Lydersen minimized the dependence of critical-constant calculations on physical properties and chose to use the normal boiling point, which is usually readily available. Although their methods constitute an improvement, they are not completely independent of physical properties and, in addition, do not permit differentiation between structural isomers.

The calculation of critical constants without recourse to physical properties was introduced by Thodos and was applied to several classes of hydrocarbons (*12* to *15*). His method utilizes substitution values for the calculation of van der Waals' constants, which in turn permit the calculation of the critical temperature, pressure, and volume. To produce these van der Waals' constants, a successive building up of the molecular structure is employed involving the replacement of hydrogen by methyl groups along a definite prescribed pattern of substitutions, which must be rigorously adhered to in order to produce reliable values. Unless this replacement procedure is carefully followed over the entire course of structural development, considerable confusion can result.

This investigation was undertaken to develop a method for calculating van der Waals' constants which would not require recourse to a pattern for building molecular structures.

FUNDAMENTAL RELATIONSHIPS

As utilized previously (*12* to *15*), the van der Waals' constants a and b are again employed as the fundamental basic quantities with which critical temperatures and pressures can be calculated from the relationships

$$T_c = \frac{8a}{27Rb} \tag{1}$$

$$p_c = \frac{a}{27b^2} \tag{2}$$

Conversely, from the simultaneous solution of Equations (1) and (2), the van der Waals' constants can be evaluated from available critical temperatures and pressures:

$$a = \frac{27R^2T_c^{\,2}}{64p_c} \tag{3}$$

$$b = \frac{RT_c}{8p_c} \tag{4}$$

By means of Equations (3) and (4), both van der Waals' constants were evaluated from the literature data on seventy-five saturated and unsaturated aliphatic, naphthenic, and aromatic hydrocarbons and constitute the basic values for the development of the method presented here.

Earlier attempts to relate the van der Waals' constants with structure have produced a linear relationship with the number of carbon atoms of the normal paraffins for values of $a^{0.626}$ and $b^{0.76}$ (*13*). The exponents 0.626 and 0.76 have been assumed valid for other types of hydrocarbons (*12* to *15*) and have been applied successfully to produce van der Waals' constants for saturated and unsaturated aliphatic, naphthenic, and aromatic hydrocarbons.

A reconsideration of the exponents for both van der Waals' constants indicated essentially the same linear relationship for values of $a^{2/3}$ and $b^{3/4}$, and accordingly these exponents have been adopted in this study in place of the awkward previous values, $a^{0.626}$ and $b^{0.76}$. The approach adopted here for the determination of values of a and b is entirely different from that utilized previously. The concept of substitution values has been discarded, and in its place a method has been devised utilizing group contributions specific to various types of carbon atoms. These group contributions are added to produce the van der Waals' constants of the hydrocarbon from its structure alone and do

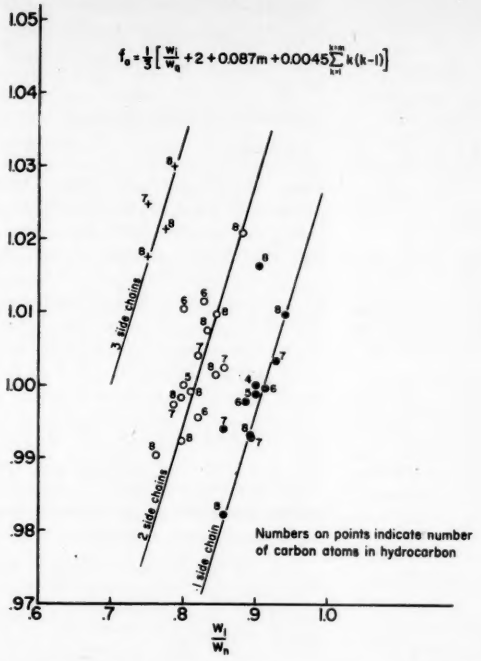
$f_a = \frac{1}{3}\left[\frac{w_i}{w_n} + 2 + 0.087m + 0.0045\sum_{k=1}^{k=m} k(k-1)\right]$
3 side chains
2 side chains
1 side chain
Numbers on points indicate number of carbon atoms in hydrocarbon
$\frac{w_i}{w_n}$

Fig. 1. Relationship of isomer factor, f_a, and Wiener number ratio.

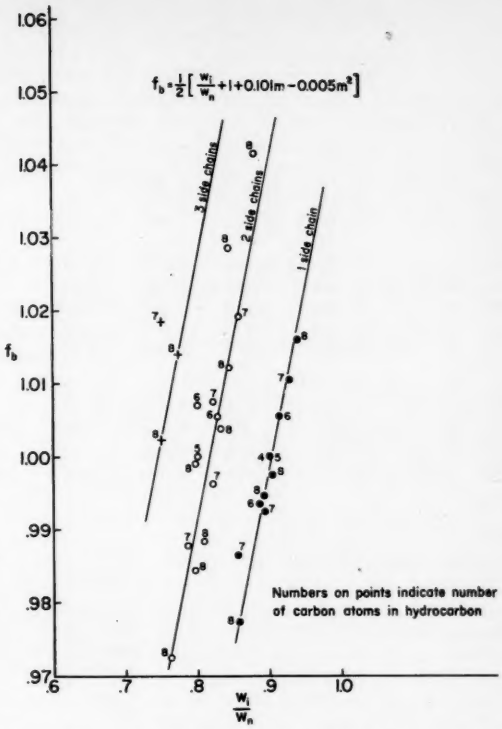
$f_b = \frac{1}{2}\left[\frac{w_i}{w_n} + 1 + 0.101m - 0.005m^2\right]$
3 side chains
2 side chains
1 side chain
Numbers on points indicate number of carbon atoms in hydrocarbon
f_b
$\frac{w_i}{w_n}$

Fig. 2. Relationship of isomer factor, f_b, and Wiener number ratio.

not involve the replacement procedures adopted in the earlier work.

SATURATED ALIPHATIC HYDROCARBONS

The paraffins represent the largest group of hydrocarbons for which experimental data are available and consequently were used as the basis of study for the aliphatic series. In this study the notation of Andersen, Beyer, and Watson (*1*) was used to differentiate types of carbon atoms. For the saturated aliphatic series four different types of carbon atoms are possible:

Type	1	2	3	4
Structure	—CH(H)(H)	—C(H)(H)—	—C(H)(—)—	—C(—)(—)—

and can be recognized by the number of carbon-carbon (as contrasted with carbon-hydrogen) bonds.

The basis of analysis was the establishment of constant group-contribution values of $\Delta a^{2/3}$ and $\Delta b^{3/4}$ for the type-2 methylene-group carbon by taking the difference in $a^{2/3}$ and $b^{3/4}$ of normal paraffins differing in size by a single methylene group. For the normal paraffins between *n*-octane and *n*-butane, these differences are essentially constant and their average values

$$\Delta a^{\frac{2}{3}} = 13{,}678 \quad \text{and} \quad \Delta b^{\frac{3}{4}} = 6.262$$

have been taken as the contribution for the type-2 carbon.

The normal paraffins were also used to establish the group contributions for the type-1 (methyl group) carbon. Subtracting the contribution of the methylene groups in each normal paraffin established the contribution due to the two end methyl groups, and when this was divided by two it produced the methyl-group contribution in each compound. For the van der Waals' constant *a*, these group contributions were not constant and decreased with the size of the molecule. The variation of $\Delta a^{2/3}$ for the type-1 carbon can be expressed as a function of the total number of carbon atoms in the molecule *n* as

$$\Delta a^{\frac{2}{3}} = \frac{2168}{n} + 14{,}493 \qquad (5)$$

On the other hand, the methyl-group contribution for *b* was found to be constant as $\Delta b^{3/4} = 11.453$.

The isomeric paraffins, in conjunction with the above-determined group contributions for types-1 and -2, permitted the establishment of the group contributions for types-3 and -4 carbons. Fortunately, almost all the isomeric hydrocarbons available contained either type-3 or type-4 carbons, but not both. This situation permitted the direct evaluation of these group contributions, which were also found to be dependent on the number of carbon atoms in the molecule. The average values for $\Delta a^{2/3}$ and $\Delta b^{3/4}$ within each isomeric group (that is, octanes, heptanes, hexanes, etc.) similarly were found to vary as follows with the total number of carbon atoms in the compound:

Type-3 ($n \geqq 5$)

$$\Delta a^{\frac{2}{3}} = \frac{27{,}560}{n} + 5677 \qquad (6)$$

$$\Delta b^{\frac{3}{4}} = \frac{23.55}{n} - 3.824 \qquad (7)$$

Type-4

$$\Delta a^{\frac{2}{3}} = \frac{36{,}013}{n} - 1022 \qquad (8)$$

$$\Delta b^{\frac{3}{4}} = \frac{52.00}{n} - 15.337 \qquad (9)$$

For convenience, values of group contributions for both $\Delta a^{2/3}$ and $\Delta b^{3/4}$ have been calculated for paraffin hydrocarbons up to $n = 15$ and are presented in Table 1 for the four types of carbon atoms.

Up to this point the adopted procedure fails to differentiate between isomeric hydrocarbons containing the same types of carbon atoms but differing in structural arrangement. For example, 2-methylheptane, 3-methylheptane, 4-methylheptane, and 3-ethylhexane produce the same calculated van der Waals' constants, since they contain the same number of types-1, -2, and -3 carbon atoms.

In order to account for these isomeric differences, van der Waals' constants calculated with the group contributions from Table 1 were divided into the corresponding constants resulting from the critical values in the literature to produce

TABLE 1. GROUP CONTRIBUTIONS, $\Delta a^{2/3}$ AND $\Delta b^{3/4}$ FOR THE SATURATED ALIPHATIC HYDROCARBONS

	Type-1		Type-2		Type-3		Type-4	
n	$\Delta a^{2/3}$	$\Delta b^{3/4}$	$\Delta a^{2/3}$	$\Delta b^{3/4}$	$\Delta a^{2/3}$	$\Delta b^{3/4}$	$\Delta a^{2/3}$	$\Delta b^{3/4}$
1								
2	15,577	11.453						
3	15,216	11.453	13,678	6.262				
4	15,035	11.453	13,678	6.262				
5	14,927	11.453	13,678	6.262	11,189	0.886	6,181	− 4.937
6	14,854	11.453	13,678	6.262	10,270	0.101	4,980	− 6.670
7	14,803	11.453	13,678	6.262	9,614	−0.460	4,123	− 7.909
8	14,764	11.453	13,678	6.262	9,122	−0.880	3,480	− 8.837
9	14,734	11.453	13,678	6.262	8,739	−1.207	2,979	− 9.559
10	14,710	11.453	13,678	6.262	8,433	−1.469	2,579	−10.337
11	14,690	11.453	13,678	6.262	8,182	−1.683	2,252	−10.160
12	14.674	11.453	13,678	6.262	7,974	−1.862	1,979	−11.004
13	14,660	11.453	13,678	6.262	7,797	−2.012	1,748	−11.337
14	14,648	11.453	13,678	6.262	7,646	−2.142	1,550	−11.623
15	14,638	11.453	13,678	6.262	7,514	−2.254	1,379	−11.870

the isomer factors defined by the expressions

$$a_{actual}^{\frac{2}{3}} = f_a a_{group}^{\frac{2}{3}} \qquad (10)$$

and

$$b_{actual}^{\frac{3}{4}} = f_b b_{group}^{\frac{3}{4}} \qquad (11)$$

Attempts to correlate the isomer factors f_a and f_b proved successful when the Wiener number ratio w_i/w_n was used as the correlating variable. The Wiener number w is defined as "the sum of distances between any two carbon atoms in the molecule in terms of carbon-carbon bonds" (*18*). This is calculated by multiplying the number of carbon atoms on one side of each carbon-carbon bond by the number of carbons on the other side of the bond and then adding all the contributions from each carbon-carbon bond in the molecule; for example, for the compound 2-methylbutane, the procedure is as follows

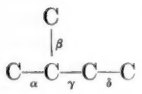

$$\alpha = 1 \times 4 = 4$$
$$\beta = 1 \times 4 = 4$$
$$\gamma = 3 \times 2 = 6$$
$$\delta = 4 \times 1 = 4$$
$$w = 18$$

The Wiener number ratio w_i/w_n is defined as the quotient of the Wiener number of the isomeric hydrocarbon and the corresponding normal paraffin (that is, with the same number of carbon atoms). Figures 1 and 2 represent the resulting correlation, in which the number of side chains m in the isomer is the third correlating parameter. The variation of f and w_i/w_n can be expressed linearly for each group having the same number of side-chain constituents. The linear relationships can be collectively expressed as follows:

$$f_a = \frac{1}{3}\left[\frac{w_i}{w_n} + 2 + 0.087m + 0.0045\sum_{k=1}^{k=m} k(k-1)\right] \qquad (12)$$

$$f_b = \frac{1}{2}\left[\frac{w_i}{w_n} + 1 + 0.101m - 0.005m^2\right] \qquad (13)$$

As an example, the critical temperature and pressure of 2-methyl-3-ethylpentane are calculated by the procedure adopted in this study:

Structure

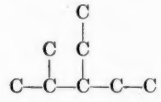

Calculation of $a_{group}^{2/3}$ and $b_{group}^{3/4}$

The isomer 2-methyl-3-ethylpentane contains a total of eight carbon atoms ($n = 8$) and also two side chains ($m = 2$). In this hydrocarbon there are four type-1, two type-2, and two type-3 carbon atoms. From the group-contribution values presented in Table 1, $a_{group}^{2/3}$ and $b_{group}^{3/4}$ are calculated as follows:

Number		$a^{2/3}$	$b^{3/4}$
4	Type-1	4(14,764) = 59,056	4(11.453) = 45.812
2	Type-2	2(13,678) = 27,356	2(6.262) = 12.524
2	Type-3	2(9,122) = 18,244	2(−0.880) = −1.760
		$a_{group}^{2/3}$ = 104,656	$b_{group}^{3/4}$ = 56.576

Calculation of Isomer Correction

By the procedure already developed, the Wiener numbers are calculated to be for

2-methyl-3-ethylpentane, $w_i = 67$

n-octane, $w_n = 84$

The Wiener-number ratio becomes $w_i/w_n = 67/84 = 0.798$. Substituting this value and $m = 2$ into Equations (12) and (13) yields the isomer corrections

$$f_a = \frac{1}{3}\left[0.798 + 2 + 0.087(2) + 0.0045\sum_{k=1}^{k=2} k(k-1)\right] = 0.9940$$

$$f_b = \tfrac{1}{2}[0.798 + 1 + 0.101(2) - 0.005(2)^2] = 0.9900$$

Calculated van der Waals' Constants and Critical Temperature and Pressure

The calculated values given above are substituted into Equations (10) and (11) to produce the following actual van der Waals' constants:

$$a_{actual}^{\frac{2}{3}} = 0.9940(104{,}656) = 104{,}028$$

$$b_{actual}^{\frac{3}{4}} = 0.9900(56.576) = 56.010$$

From these values, the following calculated van der Waals' constants are produced:

$a = 33.552 \times 10^6$ (cc./g.-mole)^2 atm.

$b = 214.30$ cc./g.-mole

to give the following critical temperature and pressure from Equations (1) and (2):

$$T_c = \frac{8(33.552 \times 10^6)}{27(82.055)(214.30)} = 565.4°\text{K.}$$

$$p_c = \frac{33.552 \times 10^6}{27(214.30)^2} = 27.06 \text{ atm.}$$

Kobe and Lynn (*6*) report values of 568.2°K. and 27.4 atm. for 2-methyl-3-ethylpentane.

Similarly, the critical temperatures and pressures for the thirty-nine saturated aliphatic hydrocarbons used in this study were calculated, and they produced average over-all absolute deviations of 0.61% for the critical temperature and 1.06% for the critical pressure.

UNSATURATED ALIPHATIC HYDROCARBONS

Both critical constants available in the literature for nine monoolefins, one diolefin, and two acetylenes were used to calculate the van der Waals' constants for these unsaturated aliphatic hydrocarbons. Differences of these van der Waals' constants $a^{2/3}$ and $b^{3/4}$ and those of the corresponding paraffin hydrocarbons were accepted as representative of the particular type of unsaturation present. Thus, these differences represent the removal of a hydrogen from each of

two adjacent carbon atoms to produce the corresponding olefinic linkage and the removal of two hydrogens from each of two adjacent carbons to produce the acetylenic triple bond.

The principle utilized in this method has been used previously (*12*) and was adopted here since the literature data on the unsaturated aliphatics were limited and did not permit an extensive treatment for the establishment of group contributions specific to unsaturated carbon atoms in a manner similar to that already developed for the paraffins. If extensive data had been available for isomeric unsaturated hydrocarbons, a method of analysis similar to that used above could have been developed. Since this was not the case, the extensive background of group contributions and isomer corrections developed for the paraffinic hydrocarbons, when combined with these difference contributions for unsaturated linkages, should produce reliable van der Waals' constants.

The difference contributions $\Delta a^{2/3}$ and $\Delta b^{3/4}$ are characterized by the type of saturated carbon atoms existing before the introduction of the unsaturated linkage; for example, the difference contribution for the establishment of the double bond in ethylene is designated as 1-1 since both carbon atoms of the corresponding paraffin, ethane, were of type-1. Likewise, the double bond in 1-butene and other end-of-chain olefins was designated as 2-1. Other types of differences are 2-2, 3-1, 3-2, and 3-3 contributions. Difference contributions accounting for *cis* and *trans* forms of the olefinic linkages cannot be included until reliable critical values become available for these structural isomers.

TABLE 2. DIFFERENCE CONTRIBUTIONS FOR THE CALCULATION OF VAN DER WAALS' CONSTANTS OF UNSATURATED ALIPHATIC HYDROCARBONS

	$\Delta a^{2/3}$	$\Delta b^{3/4}$
First double bond		
1—1	−3,868	−2.021
2—1	−3,154	−1.895
2—2	−2,551	−2.009
3—1	−1,548	−1.706
3—2	− 928	−1.820
3—3	− 540	−1.930
Second double bond		
3—1	− 828	−1.259
3—2	− 496	−1.343
3_u—1	−1,332	−1.745
3_u—2	−1,324	−1.862
3_u—3	−1,316	−1.979
3_u←2—1	−1,687	−1.399
3_u←2—1	− 910	−1.485
Triple bond		
1—1	−4,269	−3.680
1—2	−1,934	−3.008
2—2	−1,331	−3.122

NOTE: Arrow points away from the carbon atom involved in the formation of unsaturated bonds and toward the type of carbon atom adjacent to it (to be used in conjugated systems only).

The introduction of a second double bond to form diolefins necessitated the definition of an additional type of carbon atom to account for existing adjacent and conjugated unsaturation. An extension of the Andersen, Beyer, and Watson nomenclature (*1*) suggests the designation of the following additional type of carbon atom:

Type	Structure
3_u	H =C—

which must already be present before the introduction of the second bond.

The development of difference contributions for the triple bond is identical to that already presented for the first double bond and includes types 1-1, 1-2, and 2-2.

Because the data were limited, it became necessary to utilize the available information generally, in order to produce as many difference contributions as possible. Considerable interpolation and extrapolation of the available difference contributions was found necessary to produce the values presented in Table 2.

As an illustration of the procedure, the calculation of the critical temperature and pressure for 3-methyl-1-butene (isoamylene) is presented:

structure 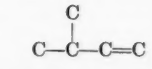

Calculation of van der Waals' Constants and Critical Temperature and Pressure

Values of $a^{2/3}$ and $b^{3/4}$ for the corresponding paraffin, 2-methylbutane, have been calculated by the method presented in the previous section:

2-methylbutane	69,370	41.320
Difference contribution, first double bond (2–1)	−3,154	−1.895
	$a^{2/3} = 66{,}216$	$b^{3/4} = 39.425$

$a = 17.033 \times 10^6$ (cc./g.-mole)^2 atm.

$b = 134.19$ cc./g.-mole

Substituting these values into Equations (1) and (2) yields the following calculated critical temperature and pressure:

$T_c = 458.3°\text{K.}$ and $p_c = 35.03$ atm.

Kobe and Lynn (*6*) report values of 464.8°K. and 33.9 atm.

In the same way critical temperatures and pressures have been calculated for several unsaturated aliphatic hydrocarbons, including all those used in this investigation. This group includes values calculated for hydrocarbons for which only the critical temperature is presented in the literature. Altogether, critical temperatures have been calculated for eleven monoolefins, three diolefins, and five acetylenes, for which critical temperatures are reported. For these the over-all average deviation was 1.21% for the critical temperature. The comparison of critical pressures was limited to nine monoolefins, one diolefin, and two acetylenes used to produce the difference contributions. In these comparisons excessive deviations were noted for an undefined pentene and 2-pentene. If these two values are disregarded, the average absolute deviation becomes 1.37% for the critical pressure. The average critical-temperature deviation for the remaining ten compounds is 0.53%.

NAPHTHENIC HYDROCARBONS

Group contributions $\Delta a^{2/3}$ and $\Delta b^{3/4}$ for the carbons in naphthenic rings were developed from data on cyclopentanes and cyclohexanes. Differences of $a^{2/3}$ and $b^{3/4}$ between cyclohexane and cyclopentane produced values which were taken as the group contributions for the group–CH_2– in a naphthenic ring. When these contributions were used to construct the cyclopentane and cyclohexane molecules, the additional values of $\Delta a^{2/3} = 2{,}658$ and $\Delta b^{3/4} = 9.073$ were necessary to duplicate the van der Waals' constants derived from critical values. Therefore, these values contribute to the formation of naphthenic rings and have been designated as the *naphthenic-ring contributions.*

To obtain group contributions for type-3 and -4 carbon atoms in naphthenic rings, the previously outlined method for paraffin hydrocarbons was applied to the alkyl side chains of substituted naphthenes. These alkyl group contributions, combined with the values calculated above, permitted calculation of the type-3 and -4 group contributions. In order to differentiate these carbon atoms from types present in other classes of hydrocarbons, the notation of Andersen, Beyer, and Watson was extended to include the carbon atoms present in naphthenic rings, as follows:

Type	2_n	3_n	4_n
Structure	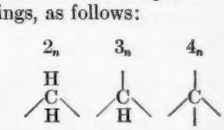		

The group-contribution values resulting from this study are summarized in Table 3.

Additional data (*10*) on five disubstituted cyclopentanes permitted the establishment of position contributions of the *cis* and *trans* type for 1,2 and 1,3 disubstituted naphthenes. Lack of further data on disubstituted naphthenes prevents an extension of these position contributions beyond the 1,2 and 1,3 types presented in Table 3. For substitutions involving other position types the 1,3 position contribution can be used. Further lack of data prevents a rigorous analysis of position contributions for polysubstituted hydrocarbons. Until such data become available, the 1,2 and 1,3 position con-

tributions can be applied in multiple sequence. These position contributions are also presented in Table 3.

Table 3, in conjunction with Tables 1 and 2, makes possible the establishment of van der Waals' constants for alkyl naphthenes with side chains of considerable size and complexity. In order to establish the values for the alkyl side chains, the total number of carbon atoms in the alkyl naphthene must be used to obtain the group-contribution values from Table 1. To illustrate this method, the critical temperature and pressure of 1-ethyl-3, *cis*-*n*-propylcyclopentane are calculated as follows:

Structure

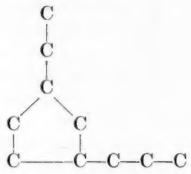

A. Naphthenic Ring		
Three Type-2_n carbons	$3(12,535) =$ 37,605	$3(5.338) =$ 16.014
Two Type-3_n carbons	$2(\ 9,910) =$ 19,820	$2(0.023) =$ 0.046
Naththenic-ring contribution	2,658	9.073
Position contribution, *cis*-1, 3	−2,525	−1.493
B. Ethyl Side Chain (n = 10)		
One Type-1 carbon	14,710	11.453
One Type-2 carbon	13,678	6.262
C. n-Propyl Side Chain (n = 10)		
One Type-1 carbon	14,710	11.453
Two Type-2 carbons	$2(13,678) =$ 27,356	$2(6.262) =$ 12.524
	$a^{2/3} =$ 128,012	$b^{3/4} =$ 65.332

$$a = 45.801 \times 10^6 (\text{cc./g.-mole})^2 \text{ atm.}$$

$$b = 263.12 \text{ cc./g.-mole}$$

From Equations (1) and (2)

$$T_c = \frac{8(45.801 \times 10^6)}{27(82.055)(263.12)} = 628.6°\text{K.} \qquad p_c = \frac{45.801 \times 10^6}{27(263.12)^2} = 24.50 \text{ atm.}$$

Critical constants are not available for this hydrocarbon, and consequently no direct comparisons can be made.

This procedure was applied to the calculation of critical temperatures and pressures of the ten available naphthenic hydrocarbons (*6, 10*). Average absolute deviations of 0.11% for the critical temperature and 0.20% for the critical pressure were obtained, but these low deviations should not be construed as representative of this class of compounds since the group contributions presented in Table 3 were established directly from these hydrocarbons.

AROMATIC HYDROCARBONS

The same type of analysis was applied to cover the aromatic series or the remaining class of hydrocarbons, including polynuclear aromatics and alkyl derivatives of benzene and polynuclear compounds. In this connection, the notation of Andersen, Beyer, and Watson (*1*) was further extended to define the following additional types of carbon atoms specific to the aromatic series:

Type 3_a 4_a

Structure

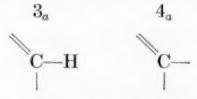

Group contributions for the type-3_a carbon were directly obtained by dividing by six the van der Waals' constants $a^{2/3}$ and $b^{3/4}$ for benzene. Because aromatic rings consist of six carbon atoms, no ring contribution is necessary. With the group contributions for type-3_a as a basis, in conjunction with the contributions due to alkyl side chains, the group-contribution values for the type-4_a carbon were established from the monoalkyl benzenes. As pointed out for alkyl-naphthenic hydrocarbons, the total number of carbon atoms in the alkyl benzene must be used to obtain group contribution values from Table 1 for the alkyl side chains.

Position contributions for polysubstituted aromatic hydrocarbons were obtained by using the group-contribution values of the type-3_a and -4_a carbons already established, in conjunction with the values of the alkyl side chains. Position-contribution values of the types 1-2, 1-3, 1-4, 1-5, and 1-6 were established. These position types designate the location of the side chains with reference to the carbon atoms in the aromatic nucleus. In using these position contributions, any convenient side chain can be selected as a reference point. The ring is then traversed in a clockwise or counterclockwise direction, any side-chain constituents being accounted for along the path until the reference point is reached again. Thus for *o*-xylene, two position contributions are utilized: the 1-2 contribution for the immediately adjacent methyl group and the 1-6 contribution continuing from the second methyl group back to the starting point. Likewise, *m*-xylene requires a 1-3 and a 1-5 position contribution, and *p*-xylene utilizes two 1-4 contributions. A similar procedure is followed for polyalkyl benzenes.

In order to construct polynuclear aromatic hydrocarbons, fused bridge carbons must be used to join the aromatic nuclei. This carbon atom is of type 4 and for purposes of differentiation has been designated as type-4_p. The critical temperature and pressure reported by Schröer (*11*) for naphthalene made possible the establishment of this group-contribution value. Group-contribution values for this type of carbon were produced from the van der Waals' constants $a^{2/3}$ and $b^{3/4}$ for naphthalene through the subtraction of eight type-3_a carbons. The resulting difference when divided by two produced the type-4_p group contribution. All these group and position contributions for the aromatic series are presented in Table 4.

Table 3. Group and Position Contributions, $\Delta a^{2/3}$ and $\Delta b^{3/4}$, for Naphthenic Rings

Type	Structure	$\Delta a^{2/3}$	$\Delta b^{3/4}$
A. Group contributions			
2_n		12,535	5.338
3_n		9,910	0.023
4_n		2,066	−8.094
Naphthenic-ring contribution		2,658	9.073
B. Position contributions			
cis-1,2		− 427	−0.866
-1,3		−2,525	−1.493
trans-1,2		−2,525	−1.493
-1,3		−4,195	−2.494

Table 4. Group and Position Contributions, $\Delta a^{2/3}$ and $\Delta b^{3/4}$ for Aromatic Rings

Type	Structure	$\Delta a^{2/3}$	$\Delta b^{3/4}$
A. Group contributions			
3_a		11,646	5.991
4_a		11,144	1.043
4_p		11,561	1.634
B. Position contributions			
1–2		−830	−1.253
1–3		−1,597	−0.806
1–4		155	0.212
1–5		279	0.254
1–6		488	0.525

As an illustration of the application of this method, the procedure for calculating the critical temperature and pressure for 1-methyl-3-ethylbenzene becomes

Structure 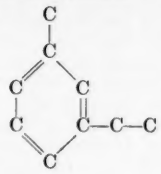

		a	b
A. Aromatic Ring			
Four Type-3_a carbons	$4(11,646) =$	$46,584$	$4(5.991) = 23.964$
Two Type-4_a carbons	$2(11,144) =$	$22,288$	$2(1.043) = 2.086$
Position contributions:			
1–3		$-1,597$	-0.806
1–5		279	0.254
B. Methyl Side Chain ($n = 9$)			
One Type-1 carbon		$14,734$	11.453
C. Ethyl Side Chain ($n = 9$)			
One Type-1 carbon		$14,734$	11.453
One Type-2 carbon		$13,678$	6.262
		$a^{2/3} = 110,700$	$b^{3/4} = 54.666$

$$a = 36.832 \times 10^6 (\text{cc./g.-mole})^2 \text{ atm.}$$

$$b = 207.47 \text{ cc./g.-mole}$$

From Equations (1) and (2)

$$T_c = \frac{8(36.832 \times 10^6)}{27(82.055)(207.47)} = 641.0°\text{K.}$$

$$p_c = \frac{36.832 \times 10^6}{27(207.47)^2} = 31.69 \text{ atm.}$$

Kobe and Lynn (*6*) report critical values of 636.2°K. and 31 atm. for 1-methyl-3-ethylbenzene.

In the same way the critical temperatures and pressures of nineteen aromatic hydrocarbons for which data were available were calculated, and they produced over-all average-absolute deviations of 0.43% for the critical temperature and 2.29% for the critical pressure. In these comparisons questionable literature values have been included, and consequently these deviations represent conservative expectations. This is further substantiated from the excellent agreement resulting from the comparison of actual and calculated critical values for diphenyl and diphenylmethane. Critical constants for these hydrocarbons were obtained from Guye and Mallet (*3*) and were not utilized for the establishment of group contributions presented in Table 4; yet for both hydrocarbons the average deviation was found to be less than 0.5% for the critical temperature and pressure.

CONCLUSIONS

The method of this investigation has been applied to the calculation of critical temperature and pressure of a number of hydrocarbons of all classes. The resulting calculated critical values have been compared with those in the literature to produce the following results:

	Number	Deviation T_c, %	Deviation p_c, %
Saturated aliphatics	36	0.61	1.06
Unsaturated aliphatics	10	0.53	1.37
Naphthenes	10	0.11	0.20
Aromatics	19	0.43	2.29
	75	0.49	1.30

In view of these results, it is felt that this method is capable of producting critical values with an expectancy of less than 1% deviation for the critical temperature and less than 2% for the critical pressure.

Critical constants for these hydrocarbons have been produced by the methods of Riedel (*8, 9*) and Lydersen (*5*) and have been presented elsewhere (*12* to *15*). Comparisons of the critical values resulting from these methods have been made with literature values and were found to be in good agreement with the results of this investigation. Specifically, the over-all deviations resulting from this study were found in general to be somewhat less than those resulting from the methods of Riedel and Lydersen.

It should be noted that the exponents applied to the van der Waals' constants a and b for the saturated aliphatic hydrocarbons were adapted to those of the unsaturated, naphthenic, and aromatic hydrocarbons. This approach was adopted since the data on these classes of hydrocarbons are not sufficiently extensive for individual investigation. Because of these limitations and in order to make this pattern consistent throughout, the general behavior of the van der Waals' constants for the other classes of hydrocarbons was assumed to follow that of the saturated aliphatics. The validity of this assumption is borne out by the good agreement found to exist for classes of hydrocarbons other than the saturated aliphatics.

NOTATION

- a = pressure van der Waals' constant, (cc./g.-mole)^2 atm.
- b = volume van der Waals' constant, cc./g.-mole
- f_a = isomer factor for pressure van der Waals' constant, Equation (10)
- f_b = isomer factor for volume van der Waals' constant, Equation (11)
- m = number of side chains in isomeric paraffin
- n = total number of carbon atoms in hydrocarbon
- p_c = critical pressure, atm.
- R = gas constant, 82.055 (atm.)(cc.)/(g.-mole)(°K.)
- T_c = critical temperature, °K.
- w_i = Wiener number for isomeric paraffins
- w_n = Wiener number for normal paraffins
- Δ = difference

Subscripts for types of carbon atoms

- a = for aromatic ring carbons
- n = for naphthenic ring carbons
- p = for polynuclear aromatic bridgehead carbons
- u = for unsaturated aliphatic hydrocarbons

LITERATURE CITED

1. Andersen, J. W., G. H. Beyer, and K. M. Watson, *Natl. Petroleum News*, Tech. Sec., **36**, R476 (July 5, 1944).
2. Boas, Arnold, *Ind. Eng. Chem.*, **40**, 2202 (1948).
3. Guye, P. A., and Ed. Mallet, *Compt. rend.*, **133**, 1287 (1901).
4. Herzog, Robert, *Ind. Eng. Chem.*, **36**, 997 (1944).
5. Hougen, O. A., K. M. Watson, and R. A. Ragatz, "Chemical Process Principles," p. 87, John Wiley and Sons, New York (1954).
6. Kobe, K. A., and R. E. Lynn, Jr., *Chem. Rev.*, **52**, 117 (1953).
7. Meissner, H. P., and E. M. Redding, *Ind. Eng. Chem.*, **34**, 521 (1942).
8. Riedel, L., *Z. Elektrochem.*, **53**, 222 (1949).
9. Riedel, L., *Chem. Ing. Tech.*, **24**, 353 (1952).
10. Rossini, F. D., K. S. Pitzer, R. L. Arnett, R. M. Braun, and G. C. Pimental, "Am. Petroleum Inst. Project 44," Carnegie Press, Pittsburgh (1953).
11. Schröer, Erich, *Z. physik. Chem.*, **B49**, 271 (1941).
12. Thodos, George, *A.I.Ch.E. Journal*, **1**, 165 (1955).
13. *Ibid.*, 168.
14. *Ibid.*, **2**, 508 (1956).
15. *Ibid.*, **3**, 428 (1957).
16. Wan, S. W., *J. Phys. Chem.*, **45**, 903 (1941).
17. Watson, K. M., *Ind. Eng. Chem.*, **23**, 360 (1931).
18. Wiener, Harry, *J. Am. Chem. Soc.*, **69**, 17 (1947).

Manuscript received Sept. 5, 1957; revision received Dec. 30, 1957; paper accepted Jan. 6, 1958.

The Viscosity of Acetone-water Solutions Up to Their Normal Boiling Points

KATHERINE S. HOWARD and R. A. McALLISTER

North Carolina State College, Raleigh, North Carolina

The viscosity of acetone-water liquid solutions has been measured over the entire concentration range at temperatures from 20°C. to generally within 1° to 10°C. of the normal boiling point. A capillary suspended-level viscometer was used, and the authors estimate that the results are accurate to ±0.2%. Both kinematic and absolute viscosities are given, and the results have been extrapolated to the boiling point of the solutions. The calibration of the Cannon-Ubbelohde viscometer is discussed in detail.

One of the aims of Research Project 1, Tray Efficiencies in Distillation Columns, sponsored by the American Institute of Chemical Engineers, was the determination of the effect of the physical properties of binary liquid systems on distillation efficiency. The viscosity of the system is required for the calculation of the liquid-phase diffusivity by the method of Wilke and Chang (*18*) and for the calculation of the liquid-phase Schmidt group. The physical properties are required at the boiling point, where the mass transfer is occurring, in order to relate the efficiency and the physical properties.

The viscosity of binary systems has been widely reported in the literature of the past sixty years, usually in connection with an attempt to devise equations for the prediction of the viscosity of mixtures, based on the viscosities of the pure components. Much of this work, however, is subject to errors resulting from the failure to apply the necessary corrections to the viscometer, for example, corrections for surface-tension effects or for kinetic-energy effects. In addition, not until recently (*15*) has there been available an accurate value for the viscosity of water for use as a primary standard for viscosity. With rare exseptions, viscosities of binary systems are not available at temperatures above 45°C.; for estimation of the boiling-point viscosity, an extrapolation of 15° to 60°C. would be required.

This investigation was designed to provide accurate liquid viscosity data for the acetone-water system over the entire concentration range. The investigation was carried out at temperatures from 20°C. to within 1° to 10° of the boiling point of the solution, and these data allowed estimation of the boiling-point viscosity with a high degree of accuracy.

EQUIPMENT AND PROCEDURE

Viscometer

General. After a survey of the various types of available viscometers and preliminary investigation of several, the Cannon-Ubbelohde viscometer was selected as best suited for this work, and two (size 25) were used. The instrument is of the "suspended-level" type, a modification the design of Ubbelohde (*17*). Its advantages include no significant variation of viscometer constant over the temperature range used, as well as no kinetic-energy correction for viscosities greater than 0.3 centistoke, and exact control of the filling volume is not required. It is capable of high precision ($< \pm 0.1\%$ deviation) in routine use, with the precautions specified below.

The viscometer is shown in Figure 1. Sufficient sample (about 11 ml.) was introduced into tube A to fill bulb D to the lower filling line. This level was never higher than the upper filling line when the viscometer was mounted in the vertical position at the temperature of measurement. The viscometer, supported in the bath by rubber stopper cut to fit closely around tubes A and B, was aligned vertically and allowed to reach thermal equilibrium. In preliminary work the time required for the sample to flow between the two calibrated marks of bulb F was recorded at intervals to determine the minimum equilibration

R. A. McAllister is at Lamar State College of Technology, Beaumont, Texas.

time. Entirely reproducible efflux times were obtained at all temperatures after 20 to 30 min., and 30 min. was adopted as the minimum equilibration time.

After the viscometer had been in the constant-temperature bath for the required time, tube C was closed by a small rubber tube attached to a 5-ml. glass syringe, and slight suction was applied to tube B by means of a rubber tube attached to a 50-ml. glass syringe. With some liquids it was necessary to draw the sample about halfway up tube H to prevent the entrance of air through the tube. When the liquid meniscus had traveled through bulb F and had about half-filled bulb E, suction was released, and tube C was opened, in that order, so that the sample dropped away from the lower end of the capillary and bulb G was emptied. The time required for the liquid meniscus to travel between the marks at the upper and lower ends of bulb F was recorded as the sample efflux time. Experiments which investigated the effect of filling bulb E to various levels failed to demonstrate any difference in efflux time, regardless of the initial level in E. Experiments in which the sample was forced up by slight pressure on tube A, designed to reveal any differences caused by application of pressure rather than suction to the sample, failed to show any difference in efflux time. Samples which were aerated before running had the same efflux time as nonaerated samples. The speed with which the sample was drawn up, as long as bubble formation in the liquid was avoided, had no detectable effect on efflux time. Allowing the sample to stand for 10 min. before running, after it had been drawn up into bulb E in an effort to dissipate any induced static charge, did not change the efflux time. Since the suction method was more convenient, it was used in all the following work.

At least three, and usually four, separate observations of efflux time were made with each sample. For the calibration runs, at least six observations were made. These multiple runs always agreed within ±0.1% and usually showed even less variation. More reproducible results were obtained when the viscometer walls were wet by the sample prior to the recorded runs.

Samples for analysis were obtained by inserting the tip of a 6-in. 20-gauge stainless-steel hypodermic syringe needle into the center of bulb F, Figure 1, and withdrawing about 1 ml. with a 5-ml. glass syringe. A sample was withdrawn and analyzed prior to the first run, once during the series of runs, and following the final run in order to detect any change in sample concentration during the run. No appreciable differences in concentration were found, even at the highest temperatures used, and the average of these analyses was reported.

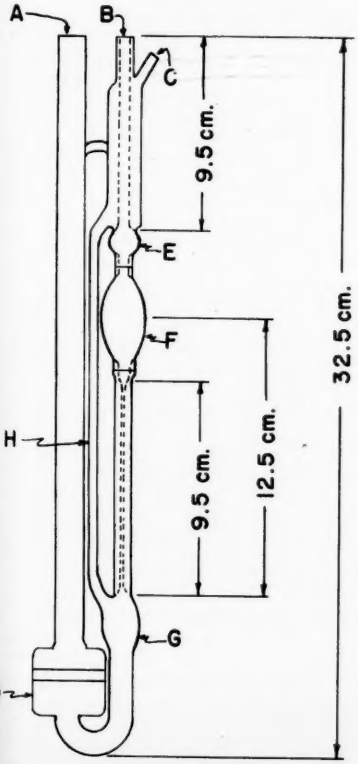

Fig. 1. Cannon-Ubbelohde viscometer.

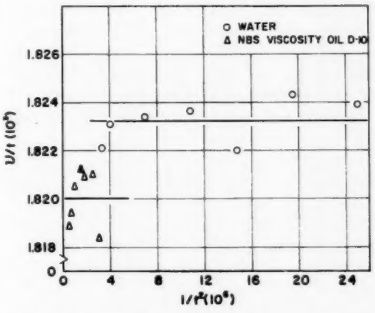

Fig. 2. Calibration curve, viscometer A19.

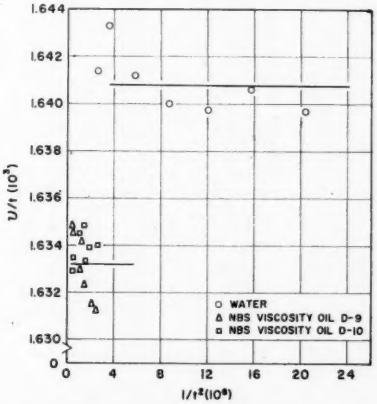

Fig. 3. Calibration curve, viscometer A43.

Temperature Control. Very careful temperature control is required for accurate and reproducible results. For temperatures between 20° and 40°C., a Model A Fisher Isotemp Bath provided control within ±0.005°C. Cooling was provided by a four-coil copper tube attached to a refrigerated water-methanol line. For temperatures between 50° and 90°C., an 18-liter water bath equipped with a circulating pump and heating coils and a tungsten-mercury thermoregulator attached to a relay provided control within ±0.02°C. The latter bath was illuminated by a circular fluorescent lamp.

Temperatures were measured during each run by a mercury-in-glass thermometer graduated in 0.1°C. intervals; the temperature was estimated to 0.01°C. by the use of a cathetometer. The true bath temperature and the thermometer in use were checked daily by reference to a thermometer which had been calibrated by the National Bureau of Standards and compared with at least one other N.B.S.-calibrated thermometer. The ice-point readings of these thermometers were checked at intervals.

Timing. Some of the efflux times were measured with stopwatches graduated in 0.2-sec. intervals; later, stopwatches graduated in 0.1-sec. intervals became available, and they were used for all subsequent work, including the calibrations runs. All stopwatches were calibrated against the National Bureau of Standards time signal, and no correction larger than 0.05% was required. While the efflux time was noted, the meniscus was observed through a cathetometer telescope in order to provide magnification and to avoid parallax.

Cleaning. Maintaining a scrupulously clean surface within the viscometer was essential. During every run the drainage characteristics of bulbs E, F, and G were carefully observed, and if any irregularities were noted in drainage or in reproducibility of results, the sample was discarded, and the viscometer was removed for cleaning. If both the sample and the viscometer were free from grease and dirt, the liquid drained from bulbs E, F, and G in a completely smooth and uniform film. Any rivulets or drops that formed during or after drainage resulted in erratic efflux times and required a thorough cleaning of the viscometer and a fresh, clean sample.

The cleaning procedure which proved most satisfactory consisted in soaking the viscometer for 24 hr. in concentrated cleaning solution (concentrated sulfuric acid, saturated with potassium dichromate), followed by rinsing eight times with conductivity water and soaking for 24 hr. in conductivity water to remove adsorbed chromic acid. Drying overnight in an air oven at 105°C. completed the process. This cleaning procedure was routinely carried out at least once a week. The viscometer was cleaned daily by multiple rinses with conductivity water and dried at 105°C.

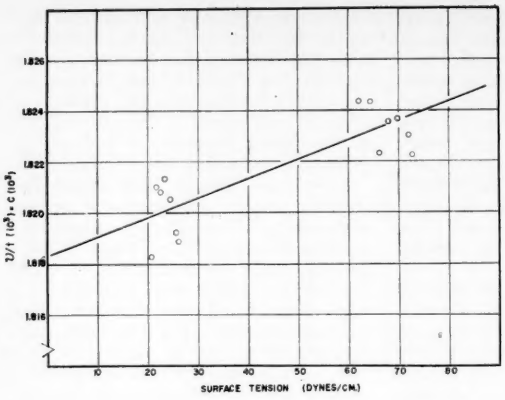

Fig. 4. Variation of viscometer constant with surface tension, viscometer A19.

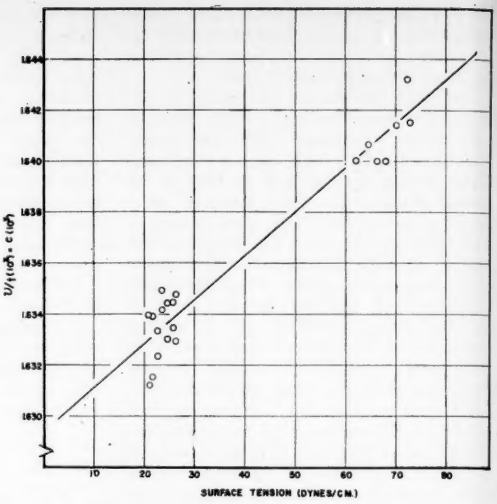

Fig. 5. Variation of viscometer constant with surface tension, viscometer A43.

Solvents

The water used as a calibration standard and for preparation of aqueous samples was daily prepared from once-distilled water (Barnstead still) by redistillation in an all-quartz still equipped with an air-cooled condenser, the middle cut (one-third the starting volume) being retained. Such water had a specific conductance of 1×10^{-6} reciprocal ohms at most and is referred to as *conductivity water*.

The acetone was analyzed by refractive index, and its density was determined. From these data the actual composition of the starting material was found (*16*) to be 99.54 mole % acetone, 0.45 mole % water. Distillation of the material in a fractional-distillation column packed with ⅛-in. Pyrex helices (packing 1 × 90 cm.) showed a boiling range of 56.1° to 56.2°C. (747 to 750 mm.).

For calibration in the high-viscosity range (0.9 to 2.5 centistokes), samples of standard viscosity oil *D* (calibrated at six to eight temperatures over the range 20° to 100°C.) were obtained from the National Bureau of Standards. Benzene, acetic acid, and toluene were purified for use in comparing results obtained with the two viscometers.

Calibration

With routine capillary viscometers, viscosity is usually calculated from the modified Poiseuille equation

$$\nu = Ct - \frac{B}{t} \qquad (1)$$

where

ν = kinematic viscosity, centistokes
t = efflux time, sec.
C, B = viscometer constants, dependent on the Reynolds number

Discussion of the derivation of this simplified equation may be found in Cannon and Fenske (*5*) and Swindells, Hardy, and Cottington (*15*). Calibration of the Cannon-Ubbelohde viscometer consists in the evaluation of C and B. Although C and B vary with Reynolds number (*4*), the design of most commercial viscometers is such that for most of their useful range (efflux time greater than 200 sec.) C is constant, and $B = 0$. Thus Equation (1) reduces to

$$\nu = Ct \qquad (2)$$

To define this range and to evaluate the quantities B and C, one can rewrite Equation (1):

$$\frac{\nu}{t} = C - \frac{B}{t^2} \qquad (3)$$

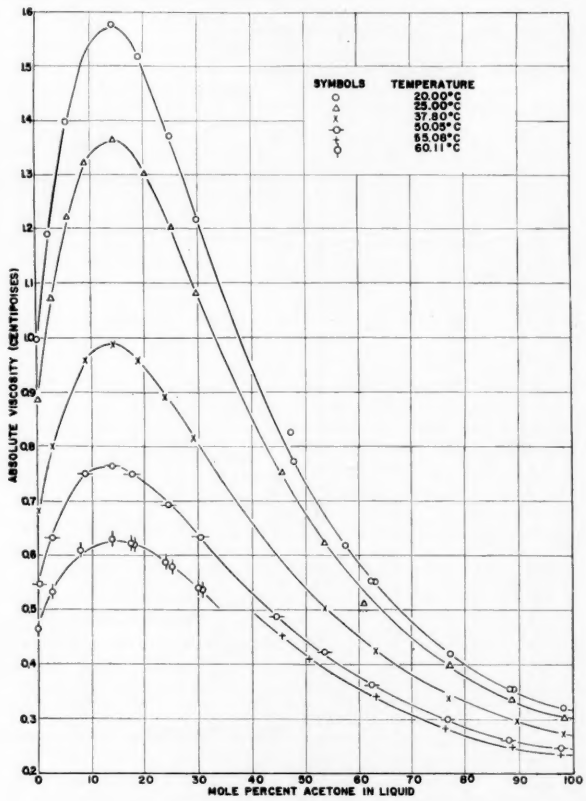

Fig. 6. Viscosity of acetone-water solutions.

The efflux times of liquids of different known viscosities are measured (in this case water at several temperatures and N.B.S. calibrated oil at several temperatures). The quantity ν/t is then plotted vs. $1/t^2$; B is the slope of the tangent to the curve at a given value of $1/t^2$, and C is the intercept of the tangent at a value of $1/t^2 = 0$. Where $B = 0$, a horizontal line results, and C is constant.

Conductivity water and N.B.S. viscosity oil D were the calibration standards used here. At every temperature six efflux-time observations were made on each of at least two samples of each standard. Deviation in efflux time between repeated runs seldom amounted to more than 0.3 sec. in up to 1,500 sec., and was never greater than 0.1%. The viscosities and average efflux times for each standard in the two viscometers, $A19$ and $A43$, are available from the American Documentation Institute (*1*); Figures 2 and 3 show the resulting curves. The deviation of the experimental points from the horizontal lines drawn through their averages was 0.04 to 0.06%. It is evident that B may be neglected over the range of t indicated. An efflux time of 200 sec. is the arbitrary minimum recommended by the A.S.T.M. (*2*). No efflux time less than 199.3 sec. was observed in the calibration.

Since the oil and water calibration points (Figures 2 and 3) did not fall on the same straight line, it was assumed that a surface-tension correction must be applied. The surface tension of oil D was measured by the capillary-height method (*8*) at the temperatures at which the viscometers were calibrated; the surface tension of water at these temperatures is well known (*8*). Figures 4 and 5 show ν/t [from Equation (2) it is seen that $\nu/t = C$ over the range of t used here] plotted as a function of surface tension. The cluster of points at the lower end of each line represents the oil runs, and the points at the higher end of the line represent the water calibration runs. Figures 4 and 5 were considered to be the calibration curves in this work. Figures 2 and 3 were useful only to demonstrate that $B = 0$. As long as the surface tension is known to 2 or 3 dynes/cm., any possible error in C due to the surface-tension correction will be within the precision of the C constant determination itself. The surface tension of all the acetone-water solutions the viscosities of which are reported here has been determined (*8*). From the surface tension, a C constant was selected from Figures 4 and 5, and the kinematic viscosity was calculated by means of Formula (2).

Comparison of Viscosities. When a series of purified solvents (benzene, toluene, acetic acid, and acetone) was run at several temperatures for each solvent in both viscometers, comparative results, calculated from the constants of Figures 4 and 5, did not differ from one another by more than ±0.15%. The average difference in calculated viscosity when the two viscometers were used was ±0.06%. The viscometers were used interchangeably throughout the investigation.

Discussion of the Calibration. The results of the calibrations reported here demonstrate the inadequacy of Equation (1) to describe the conditions of flow in the Cannon-Ubbelohde viscometers used. Only when the surface-tension correction was made in the manner described here could the calculated viscosities measured with different Cannon-Ubbelohde viscometers be made to agree to better than ±0.5 to 1.0%, although the results with either viscometer could be reproduced to better than ±0.05%. Although the calibration method presented here may be lacking in theoretical rigor, it was the only method found that would give the same viscosity for a particular sample with two different viscometers.

In later runs a third Cannon-Ubbelohde viscometer having approximately twice the capillary diameter of A19 and A43 was calibrated in the same manner as described here. The results of all three viscometers could be brought into agreement only by using a surface-tension correction of the type presented here.

TABLE 1. VISCOSITY OF LIQUID ACETONE-WATER SOLUTIONS

Mole % acetone	ρ^* g./cc.	ν, cs.	η, cp.	Mole % acetone	ρ^*, g./cc.	ν, cs.	η, cp.
20.00°C.				25.00°C.			
0	0.9982053	1.0038	1.0020	0	0.9970470	0.8931	0.8905‡
2.51	0.9886	1.2125	1.1987	2.92	0.9852	1.0954	1.0792
5.87	0.9766	1.4415	1.4077	5.83	0.9743	1.2596	1.2272
14.63	0.9477	1.6702	1.5828	9.13	0.9625	1.3809	1.3291
18.07	0.9367	1.6531	1.5485	14.57	0.9444	1.4541	1.3733
25.25	0.9159	1.5044	1.3779	20.14	0.9262	1.4133	1.3090
30.55	0.9022	1.3577	1.2249	25.08	0.9140	1.3259	1.2119
47.7	0.8621	0.9593	0.8270	30.1	0.8980	1.2123	1.0886
48.4	0.8607	0.9018	0.7762	46.2	0.8603	0.8749	0.7527
58.2	0.8431	0.7393	0.6233	53.8	0.8455	0.7389	0.6247
63.0	0.8352	0.6619	0.5528	61.6	0.8323	0.6133	0.5104
63.6	0.8343	0.6588	0.5496	77.5	0.8097	0.4896	0.3964
77.5	0.8150	0.5169	0.4213	89.4	0.7953	0.4219	0.3355
89.2	0.8010	0.4412	0.3534	99.2	0.7851	0.3860	0.3030
90.1	0.8000	0.4410	0.3528	(100)	0.7844	(0.3840)†	(0.3012)†
99.2	0.7970	0.4024	0.3207				
(100)	0.7899	(0.3985)†	(0.3148)†				
37.80°C.				50.05°C.			
0	0.99304	0.6857	0.6809‡	0	0.98781	0.5530	0.5464‡
2.97	0.9797	0.8221	0.8054	2.87	0.9739	0.6521	0.6351
9.12	0.9546	1.0101	0.9643	9.10	0.9464	0.7860	0.7439
14.47	0.9349	1.0635	0.9943	14.49	0.9249	0.8259	0.7639
19.05	0.9190	1.0496	0.9646	18.20	0.9111	0.8228	0.7497
24.20	0.9025	0.9944	0.8974	24.90	0.8889	0.7841	0.6970
29.9	0.8860	0.9247	0.8193	30.7	0.8715	0.7320	0.6379
45.6	0.8484	0.7029	0.5963	45.6	0.8347	0.5842	0.4876
53.8	0.8326	0.6070	0.5054	54.2	0.8182	0.5138	0.4204
63.9	0.8153	0.5202	0.4241	63.5	0.8025	0.4497	0.3609
77.6	0.7949	0.4286	0.3407	77.5	0.7807	0.3818	0.2981
90.5	0.7790	0.3766	0.2934	89.3	0.7655	0.3422	0.2620
99.2	0.7705	0.3494	0.2692	99.0	0.7528	0.3241	0.2440
(100)	0.7698	(0.3465)†	(0.2690)†	(100)	0.7550	(0.3235)†	(0.2442)†
55.08°C.				60.11°C.			
46.3	0.8273**	0.5467	0.4523	0	0.98243**	0.4738	0.4658‡
50.9	0.8185**	0.5012	0.4102	2.92	0.9729**	0.5506	0.5357
63.9	0.7961**	0.4302	0.3425	8.03	0.9434**	0.6441	0.6083
77.0	0.7753**	0.3669	0.2845	14.38	0.9172**	0.6891	0.6320
89.4	0.7593**	0.3298	0.2504	17.74	0.9044**	0.6896	0.6237
98.9	0.7500**	0.3105	0.2329	18.11	0.9031**	0.6894	0.6226
(100)	0.7488**	(0.3095)†	(0.2318)†	24.20	0.8811**	0.6650	0.5859
				25.32	0.8774**	0.6587	0.5779
				30.3	0.8627**	0.6264	0.5404
				31.4	0.8598**	0.6257	0.5380

*Interpolated from the results of Thomas and McAllister (*16*) measured on the same acetone lot. The water densities were calculated from those reported by J. H. Perry, "Chemical Engineers Handbook," McGraw-Hill Book Company, Inc., New York (1950), p. 175.

†Extrapolated by extension of the experimental results.

‡The viscosities of water were calculated by the modified Cragoe equation (J. F. Swindells, personal communication):

$$\log_{10}\frac{\eta_t}{\eta_{20°}} = \frac{1.3272(20 - t) - 0.001053(20 - t)^2}{t + 105}$$

where t = temperature, °C., and with the accepted [Swindells, J. F., J. R. Coe, Jr., and T. B. Godfrey, *J. Research, Natl. Bur. Standards*, **48**, 1 (1952)] value for $\eta_{20°H_2O} = 1.0020$ cp. Absolute viscosity was then converted to kinematic viscosity by the relationship

$$\nu = \frac{\eta}{\rho}$$

**Extrapolated from the results of Thomas and McAllister (*16*).

Table 2. Viscosity of Liquid Acetone-water Solutions at Their Normal Boiling Points

Mole % acetone	B.P.*, °C.	ρ†, g./cc.	η, cp.
0	100.0	0.95835	0.282
1.0	93.0	0.9567	0.329
2.0	86.5	0.9551	0.370
3.0	81.3	0.9533	0.407
4.0	77.6	0.9500	0.437
5.0	75.0	0.9472	0.462
6.0	72.8	0.9435	0.486
7.0	71.0	0.9400	0.510
8.0	69.5	0.9364	0.532
9.0	68.1	0.9331	0.543
10.0	66.7	0.9298	0.560
12.5	65.7	0.9202	0.576
15.0	63.4	0.9119	0.597
17.5	62.7	0.9030	0.595
20.0	62.2	0.8949	0.591
30.0	61.0	0.8623	0.539
40.0	60.4	0.8368	0.473
50.0	59.8	0.8155	0.403
60.0	59.3	0.7983	0.340
70.0	58.8	0.7823	0.304
80.0	58.2	0.7678	0.268
90.0	57.4	0.7560	0.246
100.0	56.2	0.7476	0.231

*These temperatures were obtained from the data of A. S. Brunjes and M. J. P. Bogart [*Ind. Eng. Chem.*, **35**, 258 (1954)], D. F. Othmer and R. F. Benenati [*ibid.*, **37**, 299 (1945)], and J. C. Chu ["Distillation Equilibrium Data," Reinhold Publishing Corporation, New York (1950), p. 24]. More weight was given the data of Brunjes and Bogart, since they showed more internal consistency.

†Thomas and McAllister (*16*).

Analytical Procedure

All analyses were made by determining the refractive index (n_D^{25}) of the solution with a Bausch and Lomb Precision Refractometer and reading the acetone concentration from a standard curve of refractive index vs. mole percentage of acetone. The standard curve was prepared by determining the refractive indices of solutions which had been prepared by mixing weighed samples of acetone and water. All weights used in calculating the compositions of the solutions were the corrected vacuum weights. The chain, the rider, and the brass weights used in the analytical balance were checked against National Bureau of Standards calibrated weights, and corrections were noted.

The refractive index–composition curve has a maximum at 40 to 42 mole % acetone and, for this reason, refractive index alone is not a suitable analysis in the region of 35 to 45 mole % acetone. The accuracy of the analysis is within 0.02 to 0.05 mole % in the region of 0 to 26 and 98 to 100 mole % acetone; the accuracy is within 0.1 mole % for the remainder of the curve. The refractive index found for solutions between 0 and 100 mole % acetone may be obtained from the American Documentation Institute (*1*).

RESULTS

The viscosity of the acetone-water system at various temperatures is given in Table 1. The absolute viscosities were calculated from the measured kinematic viscosities and the liquid densities. The surface tensions of the solutions, used for the selection of the proper C constant, were those reported by Howard and McAllister (*8*). The absolute viscosity results are shown graphically in Figure 6.

From the data of Table 1, viscosity-vs.-temperature curves were prepared and extrapolated to the normal boiling points. The average extrapolation required was 9°C., but from 8 to 100 mole % acetone the extrapolation covered less than 9°C. The viscosities at the boiling points are given in Table 2.

DISCUSSION

Two factors impede comparison of these viscosities with those found in the literature. In 1953 a new value for the viscosity of water at 20°C. (1.002 centipoise) was adopted (*15*) as the primary standard for viscosity determinations, and all work carried out prior to that time had been based on higher values (1.005, 1.009 centipoise). This error cannot be corrected by multiplying observed viscosities by the ratio of the two 20°C. values; correction would require recalculation of the calibration constants of the viscometers used, and, in most cases, sufficient data for this correction have not been reported. An error of greater magnitude has been introduced by the failure of earlier workers to use anhydrous acetone. Only within the past decade (*16*) has the density of absolutely anhydrous acetone been available for comparison. A comparison of the reported viscosity and density of the "100%" acetone of various investigators (*3, 7, 9, 10, 11, 12, 14*) is given in reference *1*. The densities indicate that the starting material of these workers was not anhydrous, and on the assumption that the only contaminant was water, the compositions ranged from 99.3 to 96.7 mole % acetone. It is apparent from these results that the acetone concentrations which were reported would be subject to increasingly large errors as the acetone percentage increased. For these reasons a tabular comparison of the viscosities found by earlier workers (*3, 6, 10, 13, 14*) and those found here is not presented. In general, however, the values from 0 to 50 mole % acetone agree within about 1.0% with those reported here; previous work in the range of 50 to 100 mole % acetone may be from 2 to 5% high. An exception is the work reported by Sandonnini (*14*); these viscosities are from 40 to 80% higher than those reported here. The viscosities reported in Table 1 are thought to have an absolute accuracy of ±0.2%. The viscosities reported in Table 2 are given to three significant figures only, because the boiling temperature at the given composition is not known to greater accuracy than ±0.1°C., and hence the boiling-point viscosity is no more accurate than shown.

ACKNOWLEDGMENT

This work was carried out in connection with Research Project 1, Tray Efficiencies in Distillation Columns, sponsored by the American Institute of Chemical Engineers. The authors gratefully acknowledge the support and encouragement of the A.I.Ch.E. Research Committee during the course of this investigation.

In addition, helpful suggestions which aided materially in the calibration of the viscometers were made by Dr. R. E. Manning, Technical Director, Cannon Instrument Company, and J. F. Swindells, National Bureau of Standards.

LITERATURE CITED

1. Tabular material has been deposited as Document 5716 with the American Documentation Institute, Photoduplication Service, Library of Congress, Washington 25, D. C., and may be obtained for $1.25 for photoprints or $1.25 for 35-mm. microfilm.
2. *Am. Soc. Testing Materials Standards*, Part 5, p. 195, Am. Soc. for Testing Materials, Philadelphia, Pa. (1955).
3. Barr, Guy, and L. L. Bircumshaw, "International Critical Tables," vol. 5, p. 22, McGraw-Hill Book Company, Inc., New York (1929).
4. Bell, J. D., M.S. thesis, Penn. State Coll., State College, Pa. (1947).
5. Cannon, M. R., *Ind. Eng. Chem.*, Anal. ed., **16**, 708 (1944); Cannon, M. R., and M. R. Fenske, *ibid.*, **10**, 297 (1938).
6. Davis, P. B., Horatio Hughes, and H. C. Jones, *Z. Physik. Chem.*, **85**, 513 (1913).
7. Dunstan, A. E., and T. P. Hilditch, *Z. Elektrochem.*, **18**, 186 (1912).
8. Howard, K. S., and R. A. McAllister, *A.I.Ch.E. Journal*, **3**, 325 (1957).
9. Hughes, O. L., and Harold Hartley, *Phil. Mag.* (7), **15**, 610 (1933).
10. Jones, H. C., and E. C. Bingham, *J. Am. Chem. Soc.*, **34**, 481 (1905).
11. Jones, H. C., and E. G. Mahin, *ibid.*, **41**, 440 (1909).
12. Kendall, James, and Elizabeth Brakeley, *ibid.*, **43**, 1827 (1921).
13. Muchin, G. E., *Z. Elektrochem.*, **19**, 819 (1913).
14. Sandonnini, Carlo, *Atti. accad. Lincei*, [vi], **1**, 448 (1925).
15. Swindells, J. F., R. C. Hardy, and R. L. Cottington, *J. Research Natl. Bur. Standards*, **52**, 105 (1954).
16. Thomas, K. T., and R. A. McAllister, *A.I.Ch.E. Journal*, **3**, 161 (1957).
17. Ubbelohde, L. K. E., *J. Inst. Petroleum Technol*, (London), **19**, 376 (1933); **22**, 32 (1936); **23**, 427 (1937).
18. Wilke, C. R., and Pin Chang, *A.I.Ch.E. Journal*, **1**, 264 (1955).

Manuscript received Aug. 13, 1957; revised Nov. 18, 1957; accepted Nov. 18, 1957.

Axial Dispersion of Mass in Flow Through Fixed Beds

J. J. CARBERRY and R. H. BRETTON

Yale University, New Haven, Connecticut

The axial dispersion of water flowing through fixed beds was determined by measuring and recording the dispersion of a pulse input of dye at one or two points downstream of the injection site. Dispersion coefficients at various flow rates were obtained in systems of 1/2-, 1-, 3-, and 5-mm. spheres and 2- and 6-mm. rings each packed in a 1.5-in. I.D. column. Data were also obtained with 3-mm. spheres in a 1-in. I.D. column. Bed length was varied from 6 to 36 in. Void fractions of from 0.365 to 0.645 were represented by the systems studied. One gas system was studied at Reynolds numbers below unity.

The results of the water study indicate that the dispersion coefficient increases linearly with the Reynolds number in the range of $Re = 0.5$ to 100. Beyond that point the Reynolds number exponent decreases through 0.85 to a value of about 0.25 at a characteristic breakpoint in the region of $Re = 350$ to 400. Pressure-drop data secured for the systems studied clearly indicate that the cited breakpoint in dispersion behavior is identical with the well-known region of flow transition as characterized by the friction-factor–Reynolds-number relationship within a given system.

The dispersion values for the 5- and 6-mm. particles, while obeying this Reynolds-number functionality, are of lower magnitude.

A theory based upon bed-void cell-mixing efficiency is developed, and this efficiency is shown to be directly proportional to the Peclet number, which at the condition of perfect void-cell mixing should attain a value of about 2.

Anomalous behavior was noted in two respects: (1) the pulse amplitude change between two stations is greater than that predicted by either diffusion or cell-mixing theory, lending strong support to a bed-capacitance effect, and (2) short-bed studies revealed unusually high dispersion coefficients, reflecting short-circuiting, that is, poor cell-mixing efficiencies in these shallow beds, presumably owing to entrance effects, yet independent of the mode of pulse injection.

The dispersion of a pulse of air injected into a stream of helium flowing through a gas chromatographic column was briefly investigated. At $Re < 1$, E was found to be about equal to the calculated molecular diffusivity of this gas system.

In view of the key position occupied by fixed-bed processes in the chemical and allied industries, it follows that much attention should be focused on the fundamental aspects of heat, mass, and momentum transfer in these systems. Such studies are particularly important where heat and/or mass transfer occur simultaneously with one or more chemical processes. Ion exchange and catalyst regeneration constitute unsteady state examples, and any heterogeneously catalyzed reaction may be cited as a steady state case, in which the chemical kinetic picture is usually rendered more complicated by the transfer as well as the distribution of heat and mass.

With regard to mass transport there are aspects to be considered other than transfer or diffusion through a film to the surface of another contacting phase. There is the problem of fluid mixing across a packed bed (radial dispersion) and that of mixing in the axial or longitudinal direction of the bed.

Wilhelm and coworkers (*5*) initiated the experimental studies of radial dispersion of mass in packed columns, with the assumption, however, that the axial dispersion term in the basic differential equation could be neglected. This assumption was necessitated by a unique lack of data on axial dispersion, which is reflected in the fact that, to date, the design of fixed-bed reactors has been based upon the assumption that piston flow prevails in the system. The effect of axial dispersion in any reactor system is to damp the concentration gradient existing between bed inlet and outlet. As reaction or mass transfer rates generally depend upon the concentrations of reacting species at a point (for example, reactant concentration at the catalyst surface), it is apparent that axial dispersion reduces the conversion per pass simply because point concentrations are lower than those predicted on the assumption of piston flow. While designers are aware that packed beds exhibit axial mixing characteristics which lie between piston flow and those of perfect mixing, such as occurs in a well-stirred autoclave, the quantitative generalizations do not exist to permit the inclusion of the axial dispersion factor into rational design methods.

EXPERIMENTAL APPROACH

An experimental study of axial dispersion implies immediately that the fluid employed be tagged at some point. The tagged portion of fluid is then the input signal to the system under study. Events which occur within the system (the packed column in this case) alter the input signal so that the character of the resulting output signal represents the response to the system.

The usual approach to the problem is essentially that of proposing a mathematical model *a priori* and then solving the basic equation for rational boundary conditions. The solution to this mathematical model for the signal imposed is then tested for agreement with the experimental results. If agreement is satisfactory, suitable constants or a particular coefficient are then obtained. Correspondence between the data and the theoretical equation does not necessarily prove that the model truly represents the physical system. Rather it may only demonstrate that the theoretical relation reproduces a result which is due to a reality more complicated than or even quite different from the assumed model. A classic example of this situation is the two-film theory of mass transfer. While it undoubtedly is a good working model in that field, radically different models are equally justified by mass transfer data at this time.

Of the three types of input signals (the step, pulse, and sine wave) which might be employed in a dispersion study, the pulse input was chosen in this work by virtue of the relative simplicity of equipment required. Further, both Kramers and Alberda (*13*) and Raseman and Bretton (*6*) have noted apparent discrepancies in the results acquired in the use of a sinusoidal signal.

In the present work the mathematical model chosen is one which has been used by other investigators. It is assumed that dispersion can be expressed by a simple diffusion type of equation. This model and one involving void-cell mixing are more fully discussed later in this paper. Strong evidence indicates that this diffusion model does not adequately describe the axial-dispersion phenomenon, however, the anomalous behavior observed may be due to necessary oversimplifications as well as to the choice of boundary conditions. Boundary conditions are quite critical, particularly in the case of short-bed studies. Further work is needed to define axial dispersion for short beds. Until such knowledge is secured, the data presented in this paper should be utilized with regard to the assumptions implicit in the model.

PREVIOUS STUDIES

Experimental studies of axial dispersion are of very recent origin, owing perhaps to the fact that rapidly responding measuring techniques are required in order to obtain an accurate account of the response of a system to an imposed signal.

Liquid Studies

Rafai (*15*) studied the dispersion of salt in water in laminar flow through sand beds ($Re < 1$), using a step input of salt solution and measuring the dispersion of the front directly in the bed at various bed lengths both chemically and by electric conduc-

J. J. Carberry is with E. I. du Pont de Nemours and Company, Inc., Wilmington, Delaware.

tivity. The breakthrough data were treated by trial and error by the simple approximation which holds beyond several mixing lengths

$$C/C_0 = \tfrac{1}{2}[1 - \text{erf}\ (X - vt)/2(Et)^{\frac{1}{2}}] \qquad (1)$$

The two methods of measurement gave significantly different results, and arguments presented indicate that the electric-conductivity measurements made in the bed are not reliable.

Beran (*4*), who made a theoretical and limited experimental study of axial dispersion in a sand-packed column, showed that theoretically, for a pulse input, the dispersion coefficient could be obtained from the standard deviation of a measured Gaussian response, that is, if the dispersed pulse exhibits Gaussian character, its standard deviation σ is related to the Peclet number, column height L, and particle diameter D_p by the equation

$$\sigma = \sqrt{(2LD_p)(1/Pe)} \qquad (2)$$

Beran showed that this relationship applies when molecular diffusivity is insignificant. He reports the results of seven experimental runs in which a pulse of radioactively-tagged solution was injected into water flowing through a packed column (Re = 0.2 to 4.5). In the range of variables investigated he found the Peclet number to be a constant.

The first published result on axial dispersion in a packed bed appears to be that of Danckwerts (*8*). Although the paper is devoted largely to a theoretical discussion of residence-time distribution in flow systems, a single experiment is briefly described in which a step input of tracer was introduced into a bed packed with ⅜-in. Raschig rings. The fluid flowing was water at Re = 40. Danckwerts analyzed the breakthrough curve by means of the same equation employed by Rafai, that is, Equation (1).

Kramers and Alberda (*13*) followed Danckwerts's study with a theoretical and experimental investigation of axial dispersion as determined by the response of a packed column to a sinusoidal input signal. Theirs is the first discussion of the problem of axial dispersion in which an analogy is explicitly stated to exist between a packed bed and a series of mixing vessels. Relationships for the amplitude change and phase shift were obtained both for this model and also for the model based on a diffusion mechanism. It was shown that for a large number of mixers the two solutions gave the same frequency-response diagram. Experimentally, Kramers and Alberda investigated the dispersion in water flowing through a column packed with 1-cm. Raschig rings at Re = 100 and 200. In commenting upon the experimental results, they note that the phase-shift data indicate a lower value of n ($= Lv/2E$) than do the amplitude-change data. They describe the discrepancy as probably "being caused by a certain amount of trapping in the interior of the rings" (*13*). Their amplitude- and phase-shift data yield dispersion coefficients which differ by 50 to 100%.

Klinkenberg and coworkers (*12, 19*) have published two papers devoted to factors which affect residence-time distribution in vessels. Their discussion is confined to cases where the resulting distribution curves are Gaussian; that is, a large number of stages are involved. They attempt to treat cases where several events such as absorption, reaction, and mixing contribute to the net dispersion of a pulse. Klinkenberg (*12*) also cites the results of axial-dispersion measurements for flow in a sand bed made with the step-input technique ($Re < 1$).

Gas Studies

McHenry and Wilhelm (*14*) report axial-dispersion data for gas flowing through a bed packed with 3-mm. spheres. They used a sinusoidal-input signal and determined values of E from the amplitude change. A value of the Peclet number equal to about 2 was found in a Reynolds-number range of from 26 to 1,000, this value as has been shown (*2, 7*), being the limiting one corresponding to a mixing efficiency of 100% in each void cell of the bed.

In a recent theoretical discussion Aris and Amundson (*2*) demonstrate that the dispersion of a mathematical pulse by turbulent diffusion and dispersion by cell-mixing mechanisms are identical when complete cell mixing is assumed. A comparison of these distribution functions led them to conclude that the limiting value of the Peclet number at high Reynolds numbers should be about 2. One of the present authors (*7*) has shown that the Peclet number itself is a direct measure of void cell-mixing efficiency and that, while a value of Pe = 2 represents perfect void-cell mixing, values of Pe much less than 2 can be anticipated in the usual range of packed-bed–flow rates.

The results of the cited experimental investigations are discussed and noted graphically later in this paper. It is sufficient to note here that whereas the work of McHenry and Wilhelm (*14*) on gas dispersion embraced a wide range of flow rates, the data secured by others for liquid systems are confined to limited regions of the Reynolds number. Therefore, it was the purpose of this research to ascertain the behavior of the dispersion coefficient for water over a wider range of flow rates in beds of various particle size, length, and diameter. In addition, it was deemed important to determine the dispersion characteristics of a gas system in the Reynolds-number range below that studied by McHenry and Wilhelm (*14*).

THEORY

Ergun (*9*) provided substantial evidence for the existence of near-perfect mixing in some fixed-bed studies.

The other extreme, that of piston flow in any packed bed (E = 0), is virtually nonexistent. This may be shown as follows. Any packed bed must consist of a series of randomly arrayed void cells. The behavior of a pulse input imposed upon such a series of cells, each of holding time θ_n, will be considered.

The concentration-time behavior in the effluent of the nth perfect mixing cell is given by

$$C = \frac{G}{\theta_n{}^n} \frac{t^{n-1}e^{-t/\theta}}{(n-1)!} \qquad (3)$$

where G is the transform of an impulse function.

For several beds of the same total retention time T, the cell-holding time is obviously $\theta_n = T/n$. Equation (3) has been solved for equal total-volume beds composed of 2, 4, and 12 perfect mixers. The resulting dispersions are plotted in Figure 1. It is apparent that the least dispersion occurs when n is largest. The limit is the case of n approaching infinity. Since any real bed consists of a finite number of cells, it is clear that even in the limiting case of perfect mixing in each void cell there exists, nevertheless, a finite axial dispersion; hence, for a bed of many perfect mixing cells the axial dispersion of matter corresponds to a finite value of E.

One may infer that E is inversely related to cell mixing efficiency, which is a function of turbulence and retention time for a given fluid. Since fluid velocity and cell size may control mixing efficiency, as an approximation it may be assumed that

$$E = kD_pv \qquad (4)$$

The ratio $D_pv/E = 1/k$ is defined as the Peclet number, Pe.

Imperfect mixing may be viewed profitably as the result of by-passing or short-circuiting and dead-space retention. This simply states that of a given number of particles entering a void cell, a fraction pass through the cell in a time much shorter than the holding time, while another fraction is retained for a period much greater than this holding time. Obviously a distribution of retention times results, which is characterized by a dispersion coefficient E.

Drawing an analogy between this mechanism of imperfect mixing and Einstein's kinetic diffusion model, one of the authors showed (*7*) that

$$n = \frac{Lv}{2E} \qquad (5)$$

and consequently the height of a mixing unit is

$$\text{HMU} = 2E/v \qquad (6)$$

In a bed in which each cell is a perfect mixer, the length of each perfect mixing cell, according to the work of Aris and Amundson (*2*), will be some fraction γ of particle diameter D_p. This fraction γ will be about unity or less, depending on the packing arrangement. Thus the number of perfect mixers is $n_p = L/(\gamma D_p)$. For any bed one may define a cell-mixing efficiency as the ratio of actual mixers n to the limiting number in the perfect-mixing–cell case n_p:

Mixing efficiency, $\epsilon = n/n_p$; thus

$$\epsilon = (Lv/2E)/(L/\gamma D_p) = \gamma D_pv/2E$$

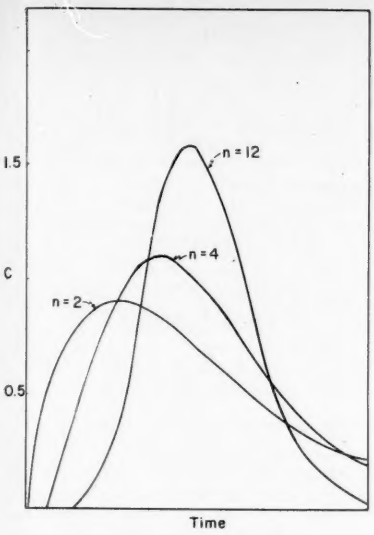

Fig. 1. Pulse dispersion in n perfect mixers. Equal total holding time.

or

$$\epsilon = (\gamma/2)Pe \qquad (7)$$

As γ is a constant for a given fixed bed the Peclet number is a direct measure of cell-mixing efficiency.

Further, the limiting value of the Peclet number is easily predicted from the foregoing argument, for as each void approaches the perfect-mixer ideal, $\epsilon \rightarrow 1$ and

$$Pe = 2/\gamma \qquad (8)$$

Since γ is approximately 1, the limiting value of the Peclet number is about 2.

Mathematical Model

This mixing-cell concept would imply that the spread of an injected tracer as a result of passage through a packed bed could be described by Equation (3). The application of this equation to experimental concentration-time data for a determination of n, and thus $E(= Lv/2n)$, would clearly be a most difficult task with beds of any reasonable length. For example Dankwerts (*8*) in a study of axial dispersion in a column packed with Raschig rings found n to be about 40.

An alternative approach is one employed by others who have studied the general problems of turbulent dispersion, that is, considering the problem in terms of Fick's Second Law of Diffusion:

$$E\frac{\partial^2 C}{\partial Z^2} = \frac{\partial C}{\partial t} \qquad (9)$$

where E, a dispersion coefficient, replaces the molecular diffusion coefficient.

Clearly, mass dispersion does not depend upon the concentration gradient as stated in Equation (9). Briefly, the justification for the use of Fick's Law is that its solution is identical with the solution of the more complex equations derived from statistical considerations of turbulence at points removed some distances from the injection site. Beeton (*3*) has treated this problem by developing from theoretical considerations a general expression governing the turbulent diffusion of mass from a point source. He shows that the distribution at points some distance downstream of the source can be reduced to a relatively simple equation, which is the solution of Fick's second-law expression. Beeton states, "In comparison with the accurate values obtained by graphical integration of this expression [the rigorous solution], the approximate equation is found to give better than 1 percent accuracy at all points beyond about 5 mixing lengths downstream of the source (*3*)."

As Aris and Amundson (*2*) have demonstrated the equivalence of the cell-mixing and turbulent-diffusion models at large values of n, then the use of a diffusion model for beds of many mixers satisfies the demands of both the statistical-turbulence and the cell-mixing theories.

Mathematical Treatment

In a differential segment of bed length, dX, through which a tracer of concentration, C, is being transported by a fluid flowing at a constant average velocity v and dispersed in the axial direction only at a rate governed by a mixing coefficient E, by material balance

$$E\frac{\partial^2 C}{\partial X^2} - v\frac{\partial C}{\partial X} = \frac{\partial C}{\partial t} \qquad (10)$$

If

$$Z = X - vt$$

and

$$t = t$$

then

$$E\frac{\partial^2 C}{\partial Z^2} = \frac{\partial C}{\partial t} \qquad (11)$$

Boundary Conditions

$$C(Z, 0) = 0 \begin{cases} 0 < Z < \infty \\ 0 > Z > -\infty \end{cases} \qquad (12)$$

and at $Z = 0$ there is an ∞ pulse of zero thickness.

$$\lim_{Z\rightarrow\infty} C(Z, t) = 0 \quad t > 0 \qquad (13)$$

and

$$Q = \pi r^2 f \int_{-\infty}^{\infty} C(Z, t)\, dZ \qquad (14)$$

where Q is the amount of tracer injected at $X = 0$ across a bed of cross-sectional area πr^2 and void fraction f. Equation (14) merely states that at any time for an infinite bed the total mass injected must be present in the bed. Boundary condition (13) implies that the bed is long or that the behavior at the end of a finite bed is the same as at a point L in an infinite bed. Equation (12) assumes a bed extended to $-\infty$. The final solution of Equation (11) with the boundary conditions given is

$$C(Z, t) = \frac{Q}{2\pi r^2 f\sqrt{\pi E t}}\, e^{-Z^2/4Et} \qquad (15)$$

Letting $K' = Q/(2\pi r^2 f)\sqrt{\pi}$ one obtains

$$C = \frac{K'}{\sqrt{Et}}\, e^{-Z^2/4Et} \qquad (16)$$

For a given E, the concentration-time profile is described by

$$C = \frac{K}{\sqrt{t}}\, e^{-Z^2/4Et} \qquad (17)$$

where

$$K = K'/\sqrt{E}$$

The time at which the maximum occurs is obtained by setting the first derivative dC/dt equal to zero. One obtains for t_m, the time at which C_{max} appears,

$$t_m = -E/v^2 + E/v^2(1 + (Xv/E)^2)^{\frac{1}{2}} \qquad (18)$$

when

$$(Xv/E)^2 \gg 1$$
$$t_m = X/v - E/v^2 \qquad (19)$$

As X/v is the nominal holding time, then as a result of dispersion the dispersed-pulse maximum actually arrives at the point of observation earlier than the residence time by an amount governed by E/v^2.

Discussion of Assumptions Implied in the Mathematical Model

It is clear that Equation (10) and its solution, Equation (15), involve the assumptions of (1) absence of radial gradients, (2) absence of bed capacitance, and (3) injection of a mathematical pulse, that is, a pulse of tracer of virtually zero thickness.

Radial Gradients

Smith and coworkers (*17*) have demonstrated that unusual radial-velocity profiles are encountered in the flow of gases through packed beds. They attributed these apparent anomalies to variation of void fraction with radial position in the beds studied. Thus it is to be expected that radial gradients of some magnitude will inevitably be present. However it is argued that if radial gradients are severe, one would then not expect the experimental concentration-time curves, at the observation points, to agree with the theoretical equation [Equation (15)], which is based upon the assumption of the

absence of such gradients. This is not to argue that a good fit of the data by the use of the theoretical equation is proof of the absence of radial gradients; rather it is to submit that a good agreement between data and theory simply means that whatever contribution radial gradients may make to axial dispersion is in fact well described by the dispersion coefficient E.

Bed Capacitance

Two stations of observation will be considered and Equation (15) applied to each and solved for E.

$$E = \frac{1}{4}\frac{(Z_1^2/t_1 - Z_2^2/t_2)}{\ln \sqrt{t_2/t_1} - \ln (C_1/C_2)} \qquad (20)$$

Now when Z_1 and $Z_2 = 0$

$$C_1/C_2 = (t_2/t_1)^{\frac{1}{2}} \qquad (21)$$

Thus the pulse amplitude should decrease as a function of the square root of time in the absence of capacitance effects, since the implication of Equation (20) is the equality $K_1 = K_2$. Two possible interpretations of an inequality of K_1 and K_2 are (1) variation of E with distance or (2) a decrease in Q due to column holdup or capacitance. The latter states that the signal entering bed 2 in a two-station system is not identical in total tracer mass Q to that which entered the preceding bed, since a finite capacitance in bed 1 withholds a fraction of the original signal. This does not necessarily imply a permanent adsorption on, or complete removal by, the packing but rather a trapping of fluid in low-velocity or stagnant areas from which removal occurs by a much slower mechanism than the primary dispersion one. This phenomenon should be evidenced by the existence of a long "tail" in the concentration-time profile.

Actually one can verify whether an abnormal amplitude ratio is due to variation in E or capacitance by use of two-station experimental data. Consideration of Equation (15) at $Z_1 = 0$ gives at the first station

$$C_1 = K_1/(t_1)^{\frac{1}{2}}$$

and at the second station

$$C_2 = K_2/(t_2)^{\frac{1}{2}}$$

from which values of K are directly obtained. If then the station 1 data are fitted for a particular value of E

$$C_1 = \frac{K_1}{(t_1)^{\frac{1}{2}}} e^{-Z_1^2/4E_1t_1} \qquad (22)$$

and the same value of E fits the data of station 2 with

$$C_2 = \frac{K_2}{(t_2)^{\frac{1}{2}}} e^{-Z_2^2/4E_1t_2} \qquad (23)$$

where

$$K_2 < K_1$$

Then it is clear that the inequality of K values must be a reflection of differing input signals due to capacitance. For if station 2 data were treated by use of a value of $E_2 > E_1$ in order to account for the inequality of K values, then

$$C_2 = \frac{K_1}{(t_2)^{\frac{1}{2}}}\left[\frac{E_1}{E_2}\right]^{\frac{1}{2}} e^{-Z_2^2/4E_2t_2} \qquad (24)$$

would be the correlating relationship. Evidently Equations (23) and (24) yield different concentration-time distributions.

Pulse Injection

A consideration of the boundary conditions employed in the solution of the basic differential equation suggests the injection of a mathematical pulse input, that is, a pulse of zero thickness. Such an input signal cannot be physically realized; rather, any injected pulse will be of finite thickness. A solution to Equation (11) based upon a "thick" pulse input will, then, be considered. For a pulse of thickness $2a$ the boundary conditions are

$$C(Z, 0) = C_0 \quad -a < Z < +a$$

$$C(Z, 0) = 0 \quad \begin{cases} -\infty < Z < -a \\ +a < Z < +\infty \end{cases} \qquad (25)$$

$$\lim_{Z\to\infty} C(Z, t) = 0 \quad t > 0 \qquad (26)$$

$$Q = \pi r^2 f 2aC_0$$

$$= \pi r^2 f \int_{-\infty}^{\infty} C(Z, t)\, dZ \qquad (27)$$

Equation (11) is satisfied by the expression

$$C = \frac{1}{2(\pi Et)^{\frac{1}{2}}} \cdot \int_{-\infty}^{\infty} F(Z')e^{-(Z-Z')^2/4Et}\, dZ' \qquad (28)$$

since the integral does converge. The solution to these systems of equations is

$$C = -\frac{C_0}{2}\operatorname{erf}\left[\frac{(Z-a)}{2(Et)^{\frac{1}{2}}}\right] + \frac{C_0}{2}\operatorname{erf}\left[\frac{(Z+a)}{2(Et)^{\frac{1}{2}}}\right] \qquad (29)$$

or

$$C = \frac{Q'}{4a}\left(\operatorname{erf}\left[\frac{Z+a}{2(Et)^{\frac{1}{2}}}\right] - \operatorname{erf}\left[\frac{Z-a}{2(Et)^{\frac{1}{2}}}\right]\right)$$

where

$$Q' = \frac{Q}{\pi r^2 f}$$

If Q' is allowed to remain constant as $a \to 0$, then by L'Hospital's Rule,

$$C = \frac{Q'}{2(\pi Et)^{\frac{1}{2}}} e^{-Z^2/4Et}$$

which is identical to Equation (15).

In a consideration of the behavior of Equation (29) in view of establishing the conditions under which it will reduce to Equation (15) for a given input pulse of thickness $2a$, Equation (29) at $Z = 0$ becomes

$$C = \frac{Q'}{2a}\operatorname{erf}\frac{a}{2(Et)^{\frac{1}{2}}} \qquad (30)$$

If the error function is expanded in a series and only the first term of the series is used, Equation (30) becomes

$$C = Q'/[2(\pi Et)^{\frac{1}{2}}] \qquad (31)$$

Equation (31) is the same expression obtained from Equation (15) at $Z = 0$. Thus for finite-width pulse injection one merely has to provide enough time (distance) between injection point and initial station of observation to render the second and succeeding terms in the series expansion of the error function insignificant and thus justify the use of the simpler Equation (15) in treatment of the experimental data.

EQUIPMENT AND MATERIALS

The test column consisted of sections of Dow-Corning glass pipe joined as required by a standard Corning bolt-and-flange assembly. The test section itself comprised an injector bolted between flanges and seated immediately atop the first packed test section of the bed, as well as the items described below. Between the end

Table 1. Characteristics of Systems Studied

Key: I.D. = nominal inside diameter of column, in.
f = percentage void volume of bed

System	I.D.	A	f	X_1	X_2
A-3 3-mm. spheres	1.5	11.4	37	61.3	91.8
B-5 5-mm. spheres	1.5	10.4	39	61.3	91.8
C-½ ½-mm. spheres	1.5	11.4	37	15.3	46
D-6 6-mm. rings	1.5	10.4	64.5	61.3	91.8
E-2 2-mm. rings	1.5	11.4	42.7	15.5	
F-1 1-mm. spheres	1.5	11.4	36.5	15.5	
G-3 3-mm. spheres	1.5	11.4	37.2	15.6	
H-3 3-mm. spheres	1.5	11.4	37.2	31.1	
I-3 3-mm. spheres	1	5.02	39	31.1	

(bottom) of the first bed and top of the second bed a ½-in.–high, clear-glass spacer was inserted, serving as the unpacked gap required for station 1 dye detection. An identical spacer was bolted between the bottom of the second bed and the downstream sections of unpacked pipe. The second spacer served as an optical window for station 2. Piping above the injector and test section provided the head requirement.

A constant-head weir was provided atop the entire column assembly. Water was supplied from the sink tap and conveyed by plastic garden hose up to the inner bowl of the weir assembly. Overflow was returned through four drain hoses to the laboratory sink. Downstream of the test section a horizontal run of pipe led to the sink. Volumetric flow rates were measured and regulated at this point.

An auxiliary line served as a means to fill and backwash the column. Backwashing was required to remove any trapped air from the packing. Packing in the test section was secured between support screens. Thus the beds were fixed and could not expand even under backwashing. This was done to ensure constancy of void fraction as originally determined upon initial packing of the sections.

Figure 2 is a schematic diagram of the experimental equipment. The pulse injector was designed to facilitate pulse injection either when the fluid was at rest (static injection) or when flow prevailed (dynamic injection). While static injection was employed in most of the runs, several dynamic injection runs were made to demonstrate that the results are independent of the mode of injection. In essence the technique consisted of rotating of *wafer* of dye solution into a small chamber between two packed sections.

Two 150-watt projector lamps were employed as light sources. Power was supplied to the lamps from a Variac in series with a voltage stabilizer. The lamp-lens system was modified empirically to obtain parallel light beams. Each lamp was placed upon a shelf mounted upon a wood frame surrounding the column. The heights of the two shelves were adjustable to accommodate various station positions. The light beam from each lamp focused directly upon the spacer at the respective stations. The lamp side of each spacer was masked so that a beam of light about 3-mm. thick and 25-mm. wide was transmitted through the gap at each station. Directly behind the column, in line with the light beam and on the same shelf with the lamp, the photocell box was located. A 929 RCA photocell was mounted in each of the two boxes. A window in each box (3 mm. high and 13 mm. wide) permitted passage of the light from the column gap to the photocell.

Photocell output was amplified by use of a simple cathode follower circuit, the output being impressed upon a dual channel Brush oscillograph.

Tap water was the liquid investigated with du Pont Pontamine Blue dye employed as tracer material. The molecular diffusivity of this dye is reported to be 5×10^{-6} sq. cm./sec. (*10*).

In the gas runs helium as a carrier gas was tapped directly from a high-pressure cylinder, and air, injected by a hypodermic needle, served as the tracer substance.

A gas chromatographic column several meters in length was employed for the gas studies, and a standard thermal conductivity cell detected the air pulse.

The essential characteristics of the systems studied are summarized in Table 1.

TREATMENT OF DATA

Early in the investigation analysis of two-station data clearly revealed that the maximum in the concentration-vs.-time plot

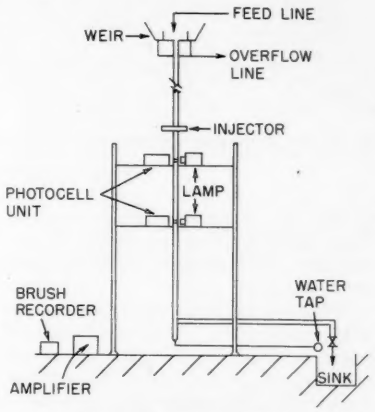

Fig. 2. Equipment layout.

did not decrease with an increase in bed length as predicted; in fact the amplitude decrease was greater than predicted. This fact, coupled with clear evidence of long "tails" in the concentration-time profile, suggested a capacitance effect which could not be accounted for by any single mechanism over the range of variables studied. Individual treatment of data at each of two stations did indicate that Equation (17) could be fitted to the data with success and that the same value of E fitted both station data provided the constant K was determined at each station.

With a previously determined calibration curve the Brush pen position at various chart positions was translated into dye concentration and chart position was converted to time coordinates by the known chart speed. The resulting concentration-time curve at a given station then had to be treated further with respect to the time axis. Two time corrections are involved, (1) a correction for residence time outside the bed and (2) a correction resulting from the shift in the maximum of the pulse due to the dispersion; that is, the maximum occurs not at the time $t = X/v$ but at $t_m = X/v - E/v$. An estimate of E is required, therefore, before one may treat the concentration-time curve for a final determination of E. Such an estimate can be obtained by use of an approximation valid for a Gaussian distribution (*18*). With the expression for C as a function of t for a given X and v [Equation (17)], one calculates a C-vs.-t curve for a specific value of E and the corrected t values. The coefficient K is readily determined from the original data, since at $X = vt'$ or $Z = 0$

$$K = C\sqrt{t'}$$

If a poor fit is obtained with the initially chosen value of E, another choice is made, the time values are recorrected in conformity with the corrections demanded by the term E/v^2, and another series of C-vs.-t values is calculated.

RESULTS

The method of presentation of data and results is:

1. The nine systems studied are designated by the letters A to I inclusive. Thus system A-3 refers to the experiments with the 3-mm. spheres in the 1.5-in. I.D. column. Table 1 summarizes the characteristics of each system.
2. Typical experimental results are

Table 2. Typical Experimental Data and Results

System	Run	v	E	Re	Pe
A-3	13	3.32	2.3	100	0.435
	32	11.3	5.8	340	0.59
	39	0.71	0.5	21	0.42
	51	16.4	6.5	490	0.76
B-5	63	20.7	8	1035	1.3
	66	15	7.2	750	1.04
	68	10.3	6.1	515	0.85
	70	5.1	4	254	0.64
	74	0.88	0.8	44	0.55
C-½	96	1.4	0.21	7.1	0.34
	102	3	0.45	15	0.33
	115	0.09	0.009	0.44	0.49
D-6	124	3.13	2.3	187	0.81
	128	0.57	0.44	34	0.78
	139	7.25	4.25	435	1
	143	19.7	10	1180	1.2
E-2	145	7	5.75	140	0.2
	147	1.4	1	28	0.28
	152	18.5	10	370	0.37
	155	0.45	0.2	8.9	0.44
F-1	164	0.14	0.038	1.4	0.37
	167	4.7	2	47	0.235
	171	10	4.5	103	0.23
G-3	182	0.67	0.5	20	0.4
	183	23	13	690	0.53
H-3	190	9	7.5	270	0.36
	191	2.84	2.8	85	0.3
	193	0.38	0.24	11	0.46
I-3	219	22.2	13	665	0.51
	221	7.9	7.25	240	0.33
He-air		0.3	0.4	0.046	0.015
		2.7	0.5	0.42	0.1

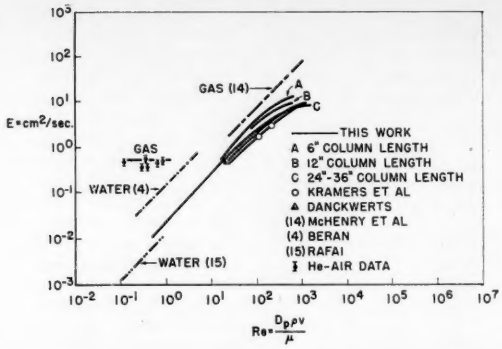

Fig. 3. Axial dispersion coefficient E, vs. Reynolds number.

given in Table 2.* Included are the run numbers in each system and particle diameter specified by the number following the system letter. For each run Table 2 lists bed velocity v, axial dispersion coefficient E, and Peclet and Reynolds numbers.

3. A complete graphical description of the results of this study as well as those of previous investigators is given in Figure 3 as a log-log plot of E vs. Re. A similar but more limited plot showing a portion of the data points for this work is given in Figure 4.

4. In Figure 5 the relationship between Pe and Re, for this and previous investigations is shown on logarithmic coordinates.

5. In Figures 6 and 7 both the experimental and theoretical concentration-time profiles for a few typical runs are reproduced.

6. Friction factor data are plotted vs. Reynolds number in Figure 9.

7. A photograph of original Brush recorder charts for runs 210 and 211 is presented in Figure 8. The chart record for one of the gas runs is also found in Figure 8.

DISCUSSION

Effects of Equipment Parameters and Operating Techniques

Before any discussion of the effects of various parameters upon the results of this study, the reproducibility of these results for a given system and Reynolds number should be noted. For four different runs, all at a Reynolds number of 422-3, the values of E found were 6.2, 6.3, 6.3, and 6.2. Static injection was employed in all the runs.

Figure 8 is a photograph of the original Brush recorder charts for runs 210 and 211, System I-3, at a Reynolds number of 485. Run 210 was made under conditions of static injection, and dynamic injection of the dye pulse was employed in 211. The profiles are virtually identical. Reproducibility was apparently realized for the experimental conditions and methods used.

When one has established that results were reproducibile and independent of injection technique, the effect of changes in the unpacked observation gaps must be considered. To ascertain the importance of the gap, experiments in system A-3 were subdivided into (1) runs in which the light beam at station 1 passed through the column at a point 1.2 cm. below bed 1 and (2) runs in which the first station-light beam was situated 0.1 cm. below the first bed. No difference in determined coefficients resulted. Further, runs were made in system B-5 in which gap 1 was removed entirely and gap 2 served as the initial observation point. Thus X_1 was 3 ft. in these runs. Since the resulting dispersion coefficients so obtained agreed with those found with the first unpacked gap in its position between beds 1 and 2, it may be concluded that any mixing which could occur in these gaps is insignificant compared with bed mixing. When it is realized that a 2-ft. section of packed bed causes a pulse dispersion equivalent to that of about sixty perfect mixers, it is not surprising that the presence of unpacked gaps, each only 2 cm. high, contributes in no way to pulse dispersion.

In addition the 3-ft.–bed experiments would suggest that the packing method used in this work is a reproducible one for spheres, in that identical dispersion data are obtained when two independently packed beds are joined to form a 3-ft.–bed unit.

Bed Capacitance and Length

Initial two-station experiments with system A-3 revealed immediately that the amplitude ratio between stations 1 and 2, C_1/C_2, did not equal the square root of the time ratio $(t_2/t_1)^{1/2}$ as predicted by both the diffusion and cell-mixing models. The same deviation was noted in systems B-5, C-½, and D-6. Further, the magnitude of the inequality $(K_1 \neq K_2)$ increased with decreasing particle size. Since theory predicts that K_1 equals K_2, the ratio K_1/K_2 as found in two-station experiments, is the indication of deviation from theory. This ratio, as a function of particle sizes studied, is listed below. These tabulated values are virtually independent of the Reynolds number.

Example	System	D_p	K_1/K_2
Run 124	D-6	6-mm. rings	1.1
67	B-5	5-mm. spheres	1.15
37	A-3	3-mm. spheres	1.23
96	C½	½-mm. spheres	2.3

The noted inequality could be explained either by an increase in E with distance or by a bed-capacitance effect which withholds a fraction of the original signal in the first bed. The evidence found to support the bed capacitance theory is:

1. The same value of E fits both station data for a given run provided one uses a value of $K_2 < K_1$ in applying Equation (17).

2. If a larger value of E is applied to station 2 data to account for the abnormal amplitude change, the resulting predicted concentration-time profile does not fit the experimental profile so well as the expression based upon constancy of E and bed capacitance. (For example, see Figure 6.)

3. Experiments with beds of ½- and 1-ft. lengths indicate that the dispersion coefficient increases with decreasing bed length. These data, when considered with the system B-5 data obtained at 2- and 3-ft.–bed lengths, which indicate constancy of E at each length, would refute the possibility of an increasing dispersion coefficient with increasing length.

4. All the data revealed the presence of long tails at each station. (For example, see Figure 7.) This would suggest a hold-back of tracer which is only slowly removed from the bed through which the pulse has just passed.

5. Gas-dispersion studies demonstrate obedience to the theoretical amplitude-length relationship, presumably because the high molecular diffusivity of the gas minimizes capacitance.

Bed Length

While these arguments tend to preclude the viewpoint of an increasing E with bed length *in the bed*, the short-bed studies might seem to point to an explanation of the amplitude discrepancy other than the bed-capacitance hypothesis. Studies of 3-mm. spheres in ½- and 1-ft. beds reveal that E decreased with bed height in the following fashion ($Re = 240$):

System	X, ft.	E, sq. cm./sec.
G-3	½	9
H-3	1	7
A-3	2	4.8
A-3	3	4.8

*Complete tabular material has been deposited as document 5715 with the American Documentation Institute, Photoduplication Service, Library of Congress, Washington 25, D. C., and may be obtained for $1.25 for photoprints or $1.25 for 35-mm. microfilm.

In other words the short-column data indicate an entrance effect, independent of the mode of injection as shown in Figure 8, which might be manifested when a dispersed pulse enters the second of a two-bed system. Hence an entrance effect or a reentrance effect in two-station studies may reasonably account for the discrepancy in amplitude-ratio data. With reference to Figure 4, however, it is noted that abnormally high dispersion coefficients are obtained in the ½- and 1-ft.-bed studies only at Reynolds numbers above about 20. Below this value all the data appear to align themselves with long-bed data (*A*-3) and the ½-mm. data (*C*-½). These ½-mm. data obtained in a ½-ft. bed very successfully bridge the data of systems *A*-3 and those data of Rafai (*15*) obtained in a 4-ft.-long bed as shown in Figure 3. One may conclude that in this region of flow bed length has no effect. Yet *within this region* serious discrepancies in amplitude ratio were noted in the data of the ½-mm. sphere. Thus the bed-capacitance hypothesis is not excluded by the evidence of entry effects. In addition the short-bed data suggest that E increases with decreasing bed length in the same manner for 3-, 2-, and 1-mm. particles, while the noted amplitude discrepancy is clearly a function of particle size.

It is suggested that the short-bed results are due either to the rapid acceleration of a fluid upon entering a system restricting flow, such as a packed bed, or to the inapplicability of boundary-condition equation (13) for short beds.

Consideration was given to the fact that perhaps the diffusion law cannot be applied to short beds for the reasons cited by Beeton (*3*). As discussed under Theory, the diffusion model can be applied beyond five mixing lengths. However the ½-ft. bed consists of more than five mixing lengths measured in terms of particle diameters. Even in terms of n where

$$n = Lv/2E \qquad (5)$$

the lowest value found in the ½-ft. bed studies was 8.

Influence of Controlled Variables

The effect of the Reynolds number upon the axial dispersion coefficient is immediately evident in Figures 3 and 4. When one confines his attention to the ½-, 3-mm., and Rafai's data it appears that E varies linearly with Reynolds number in the range of 0.1 to about 100. Between 100 and about 350 to 400 the exponent of the Reynolds number changes from unity to about 0.8 and then to about ¼ beyond the *break point*. This *break point* phenomenon is exhibited by all systems studied in the higher Reynolds-number range, with the exception of the 6-mm. ring system (*D*-6) where such a change in slope is not clearly evident. From a general consideration of packed-bed friction-factor characteristics and particularly with reference to the friction data determined in this study (Figure 9), it is quite clear that the *break point* in the $E - Re$ relationship occurs in the very same Reynolds-number range as does the transition from *laminar* to *turbulent* friction-factor behavior in the $f - Re$ relationship.

As shown in Figure 5, the cell mixing efficiency, that is, $(\gamma/2)Pe$, is independent of Reynolds number up to the transition region. The height of a mixing unit (HMU = $2E/v$) is a constant for a given system until the friction-factor–Reynolds-number transition region, at which point the intraparticle turbulence reduces the HMU value rapidly. The limit of the Peclet number, corresponding to perfect-void cell mixing, would then approach at a Reynolds number of perhaps 2,500 to 3,000. This prediction is made on the basis of Figure 5, where an extrapolation of the $Pe - Re$ relationship to a Peclet number value of 2 brings one into the cited Reynolds-number range.

Particle Size and Shape

The effect of particles size and shape upon the dispersion coefficient is most interesting. While the data for ½-, 1-, 2-, and 3-mm. particles are apparently uniquely correlated (excluding those data for short beds) as a function of the Reynolds number, those of the 5-mm. spheres and 6-mm. rings fall below these data. When it was suspected that these 5- and 6-mm. data might be the result of a pipe-to-particle diameter ratio, a study was made of the dispersion characteristics of 3-mm. spheres in a 1-in. I.D. column. This system (*I*-3) exhibited identical dispersion characteristics with

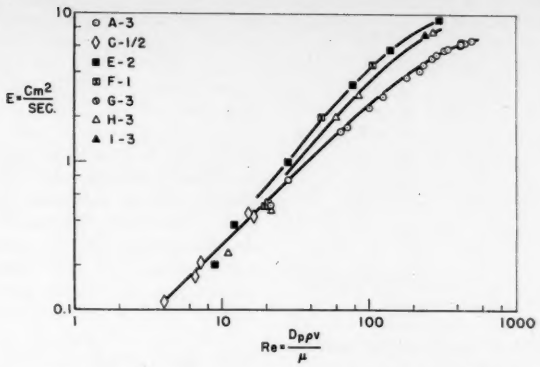

Fig. 4. E vs. Re for 1/2, 1, 2, and 3 mm. particles.

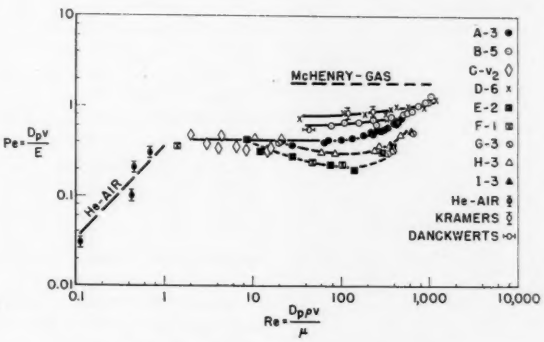

Fig. 5. Peclet number vs. Reynolds number.

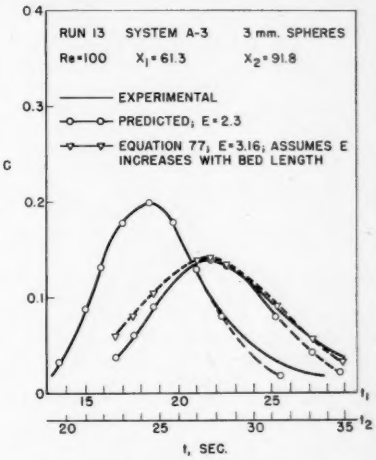

Fig. 6. Experimental and predicted profile, run 13.

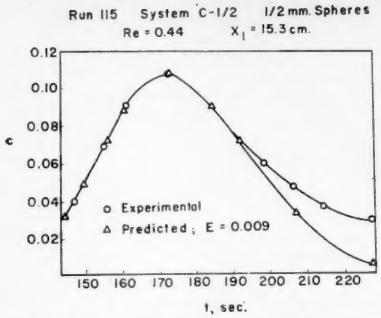

Fig. 7. Predicted and experimental profile—run 115.

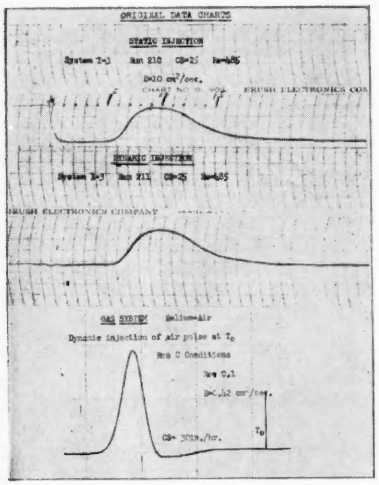

Fig. 8. Original data charts.

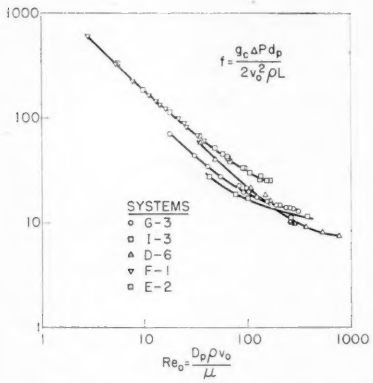

Fig. 9. Friction factor, f, vs. Reynolds number.

that of 3-mm. spheres in a 1.5-in. I.D. column (H-3) of equal length (1 ft.). An alternative explanation is the possibility that γ is smaller for the 5- and 6-mm. systems than for the others studied. Granting the 3-mm. sphere system an arbitrary value of $\gamma = 1$, the following values of γ result for the other systems on the basis of experimental Peclet numbers:

System	γ
½, 1, 2, 3 mm.	1
5 mm.	0.73
6 mm.	0.6

While this is an attractive hypothesis, it is difficult to see why 5-mm. spheres should pack in a manner radically different from other spheres and the 2-mm. *doughnut* rings. On the other hand the 6-mm. rings may well pack in such a fashion as to present more than one perfect mixer per particle length ($\gamma < 1$).

Referring to Figure 5, one notes that while the mixing efficiency for 6- and 5-mm. particles is greater (higher Peclet number) throughout most of the Reynolds-number range, the respective Pe values converge in the *turbulent* region.

It is interesting to note the similarity of the log E vs. log Re plot to a mixing-time correlation for agitated tanks and jets presented by Fox and Gex (*11*). These authors determined the time required to achieve uniformity of composition in the above-cited systems. Though their systems are radically different from those presented here, their final correlation is of note in that two regions of mixing are found, both *laminar* and *turbulent*, as noted in the present work.

In another study of miscible liquid mixing Van de Vusse (*20*) measured the mixing-time requirement in a simple tank by a pulse-injection technique and found that the mixing time varied inversely with the 0.85 power of fluid velocity. These experiments were carried out *in the absence of mechanical stirring*. Only one vessel size was investigated by Van de Vusse in this aspect of his study; thus nothing can be inferred concerning cell size. However the 0.85 exponent on flow rate applied over a thirtyfold range.

In view of these findings it is conceivable that void-cell size affects mixing efficiency in a manner more complex than is indicated by specifying cell dimension simply in terms of a particle diameter. This is to argue that the available mixing time per cell is not uniquely specified once particle diameter and bed velocity are cited, especially in the case of irregular particles such as Raschig rings. In the correlation of Fox and Gex (*11*), for example, a number of geometric factors required specification for a reasonable correlation of the data.

Pressure Drop

The pressure-drop data and friction factors calculated therefrom simply reveal the identity of transition regions for both E and f as a function of Reynolds number. No correlation between systems as far as dispersion is concerned is possible by a comparison of their respective friction-factor–Reynolds-number behavior. This point is emphasized by a comparison of the friction-factor data for 3-mm. spheres for the 1- and 1.5-in. tube systems. A change in D/D_p value results in an alteration of the $f = Re$ relationship, but no difference is noted in the dispersion characteristics of the two systems.

Previous Data

As shown in Figures 3 and 5, the results of this work are in very good agreement with the data of Rafai (*15*) and those of Kramers and Alberda (*13*). Berans's (*2*) data are very much higher than any result found in this study. Danckwerts's (*8*) value for 10-mm. Raschig rings (the same packing studied by Kramers and Alberda) falls in line with the 5-mm.-sphere results of this investigation. Values of the Peclet number reported by Klinkenberg (*12*) at Reynolds numbers "less than unity" agree well with those found in this work.

The discrepancy between phase-shift and amplitude-ratio data found by Kramers and Alberda (*13*) is interesting in that the results of the present work on amplitude-change discrepancies point to capacitance effects which would certainly cause anomalies in sinusoidal-input studies.

Gas Data

Results of the gas dispersion experiments are of an approximate nature since the dispersed pulse profiles were evaluated for the determination of E by using an approximate equation suitable for a Gaussian distribution. However, since the profiles were very nearly Gaussian, the E values so derived should not be in serious error. The Peclet numbers as determined in five experiments are plotted against the Reynolds number in Figure 5, and the gas correlation of McHenry and Wilhelm (*14*) is likewise shown there. In Figure 3 the measured E values for the present study are plotted vs. the Reynolds number. Within the limits of accuracy of the method of estimation the dispersion coefficients for an air pulse injected into a helium stream flowing through a packed tube appear constant. Indeed the measured values are well within the range of the molecular diffusivity of the mixture. Since an experimental value is lacking, the air-helium diffusivity was calculated by use of the Gilliland equation (*16*). On the basis of the atomic volume of helium found in a paper by Andrussow (*1*), the diffusivity of helium-air so calculated is 0.51 sq. cm./sec.

Figure 5 shows that the constancy of E in this system results in a linear relationship between Pe and Re. These data and those of McHenry and Wilhelm (*14*) would indicate that Pe must continue to increase with Re and gradually approach the near-limiting values found at higher Reynolds numbers by McHenry and Wilhelm.

A most interesting consequence of these limited gas studies is the indication that, at values of $Re < 1$, a value of the

molecular diffusivity of the component gas of interest in sufficient to define the dispersion characteristics of the system.

CONCLUSIONS

This study clearly demonstrates that the axial dispersion of a liquid in flow through fixed beds is of significant magnitude in the Reynolds number region below 200 to 300. With the ratio of the dispersion coefficient to average bed velocity expressed as the height of a mixing unit (HMU = $2E/v$), the data indicate constancy of this value until the flow transition regime is reached, as characterized by the packed-bed friction-factor–Reynolds-number relation. Thus the analyses of packed-bed processes (for example, ion exchange) characterized by low liquid-flow rates are rendered more complicated by this dispersion phenomenon.

The void-cell mixing model appears to substantiate the results in that low values of the Peclet number (low void-cell mixing efficiency) would be predicted in the flow region preceding fully developed void-cell turbulence, while a limiting value of Pe equal to about 2 is indicated by the model at higher Reynolds numbers. The region beyond which the height of a mixing unit decreases quite rapidly toward relative insignificance is now defined.

The Peclet number ($D_p v/E$) herein shown to be a direct measure of void-cell mixing efficiency may, with suitable modification, find useful application in stirred-tank mixing efficiency studies.

Finally the void-cell mixing model suggests that liquid kinematic viscosity effects should affect axial dispersion only insofar as the Reynolds number is modified; that is, the $E - Re$ relationship should be independent of viscosity. This point, however, requires experimental verification.

The gas data of this research and those of McHenry and Wilhelm appear to be unique in that near-perfect void-cell mixing efficiency is apparently achieved at a very low Reynolds number (about 26). However, given that the molecular diffusivity of a gas is many orders of magnitude greater than that of a liquid, it is not surprising that the ultimate in cell-mixing efficiency is achieved even at low Reynolds numbers. Indeed the data of McHenry and Wilhelm indicate an HMU $\cong$ 0.3 cm. for a bed packed with 0.3-cm. spheres. Thus in gas systems void-cell mixing is a function both of turbulence, as characterized by the Reynolds number, and of molecular diffusivity. It follows that one may expect a molecular-diffusivity contribution in liquid systems at extremely low Reynolds numbers. Indeed the data of von Rosenberg (*21*) on the displacement of benzene by *n*-butyrate from columns packed with Ottawa sand indicate dispersion coefficients about equal to liquid-molecular diffusion coefficients at flow rates of about a few feet a day.

Though data are now available over a wide range of conditions for both gases and liquids, the chief problem, namely that of mathematically defining the precise physical events which contribute to dispersion, remains unsolved. Even the simple void-cell mixing model employed here is very complex in that the ancient problem of mixing efficiency still demands rigorous mathematical description.

ACKNOWLEDGMENT

This research was supported in part by a grant from the Petroleum Research Fund administered by the American Chemical Society. Grateful acknowledgment is made to the donors of the fund. The authors are equally grateful for support provided by the Allied Chemical and Dye Corporation and the Yale Garland Fund.

William E. Kirst and Clyde O. Davis, Director and Assistant Director, respectively, of the Eastern Laboratory, Explosives Department, E. I. du Pont de Nemours and Company, most generously made this research possible by their loan of the Brush Oscillograph. George Kopperl, Edgar Slocum, and Joseph Jaffer deserve specific citation for their contributions to the design of the photocell amplifier circuit.

Richard H. Wilhelm of Princeton University very generously provided the author with the 1-mm. glass spheres employed during this study, and Martin Saunders of the Yale Chemistry Department very kindly provided the facilities for the gas dispersion study.

NOTATION

a = half-thickness of finite pulse, cm.
A = cross-sectional area of column, sq. cm.
C = tracer concentration, ml. standard/ml. of solution
D_p = particle diameter, cm.
D = nominal column diameter, cm.
D_m = molecular diffusivity, sq. cm./sec.
ϵ = cell mixing efficiency = $(2/\gamma)Pe$.
E = axial dispersion coefficient, sq. cm./sec.
f = packed bed friction factor
f = void fraction
HMU = height of a mixing unit, cm.
I.D. = inside diameter of column, cm.
k = proportionality constant
K = coefficient of Equation (17)
K' = coefficient, $K' = K\sqrt{E}$
L = bed length, cm.
n = number of mixers, $Lv/2E$
n_p = number of perfect mixers $L/\gamma D_p$
Pe = Peclet number, $D_p v/E$
Q = quantity of tracer injected
r = column radius, cm.
Re = Reynolds number, $D_p v\rho/\mu$
t = time, sec.
T = total retention time
t_m = actual time of pulse maximum, $X/v - E/v^2$, sec.
v = average bed velocity, cm./sec.
v_0 = superficial velocity, cm./sec.
X = packed bed distance, cm.
Z = change of variable = $X - vt$, cm.

Greek Letters

γ = fraction of a particle diameter equal to a perfect mixing length
ρ = density, g./cc.
θ = holding time, sec.
θ_n = cell holding time, sec.
σ = standard deviation, cm.
μ = viscosity, g./(cm.)(sec.)
erf = error function

Subscripts

1, 2 = observation point references

LITERATURE CITED

1. Andrussow, Leonid, *Z. fur physik. chem.*, **199**, 314 (1952).
2. Aris, Rutherford and Neal R. Amundson, *A.I.Ch.E. Journal*, **3**, No. 2,280 (1957).
3. Beeton, A. B. P., *Brit. Natl. Gas Turbine Establishment, Report* R 152 (March, 1954).
4. Beran, M. J., Ph.D. dissertation, Harvard Univ., Cambridge, Mass. (May, 1955).
5. Bernard, Robert A., and Richard H. Wilhelm, *Chem. Eng. Progr.*, **46**, No. 5, 233 (1950).
6. Bretton, R. H., personal communication (September, 1956).
7. Carberry, J. J., *A.I.Ch.E. Journal*, **4**, 13M (1958).
8. Danckwerts, P. V., *Chem. Eng. Sci.*, **2**, 1 (1953).
9. Ergun, Sabri, *Chem. Eng. Progr.*, **48**, No. 5, 227 (1952).
10. Ferrell, J. K., *et al.*, *Ind. Eng. Chem.*, **47**, No. 1, 29 (1955).
11. Fox, E. A., and V. E. Gex, *A.I.Ch.E. Journal*, **2**, No. 4, 539 (1956).
12. Klinkenberg, A., and F. Sjenitzer, *Chem. Eng. Sci.*, **5**, No. 6, 258 (1956).
13. Kramers, H., and G. Alberda, *Chem. Eng. Sci.*, **2**, 173 (1953).
14. McHenry, K. W., and R. H. Wilhelm, *A.I.Ch.E. Journal*, **3**, No. 1, 83 (1957).
15. Rafai, Mohamed N. E., Ph.D. dissertation, Univ. Calif., Berkeley (1956).
16. Sherwood, T. K., and R. L. Pigford, "Absorption and Extraction, p. 10, McGraw-Hill Book Company, Inc., New York (1952).
17. Smith, J. M., *et al.*, *Ind. Eng. Chem.*, **45**, 1209 (1953).
18. Taylor, G. I., *Proc. Roy. Soc.*, **A225**, 473 (1954).
19. Van Deemter, J. J., *et al.*, *Chem. Eng. Sci.*, **5**, No. 6, 271 (1956).
20. Van de Vusse, J. G., *ibid.*, **4**, 209 (1955).
21. Von Rosenberg, D. U., *A.I.Ch.E. Journal*, **2**, No. 1, 55 (1956).

Manuscript received Sept. 4, 1957; revision received Jan. 28, 1958; paper accepted Jan. 30, 1958.

Heat Transfer to a Liquid Fluidized Bed

ROBERT LEMLICH and ISIDORO CALDAS, JR.

University of Cincinnati, Cincinnati, Ohio

An experimental study of the rate of heat transfer from the retaining wall to a fluidized bed of solids was carried out for liquid water and glass spheres. The independent variables included mass velocity, particle size, bulk temperature, and wall temperature. Significant increases in heat transfer were observed, owing to the presence of the suspended solids, even to the extent of tripling the coefficient. For each of several particle sizes, the coefficient passed through a maximum corresponding to a particular mass velocity. The behavior of the bed at velocities below and above those for maximum coefficient was studied and categorized. Tentative correlations for both regions are offered.

Much work in recent years has dealt with heat transfer in fluidized beds. However, published data dealing with heat transfer from the retaining wall to the bed appear to be limited to systems wherein the fluid itself is a gas. Virtually nothing could be found for the case of a liquid. Accordingly, the present investigation was undertaken in an effort to study the transfer of heat from a vertical cylindrical retaining tube to a fluidized bed consisting of solid spheres suspended in water. The independent variables included mass velocity, particle diameter, wall temperature, and, to a lesser extent, bulk temperature and bed height.

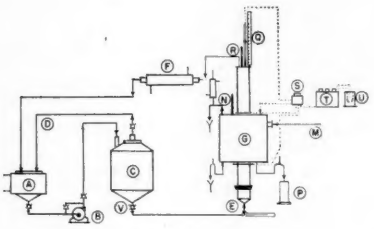

Fig. 1. Apparatus.

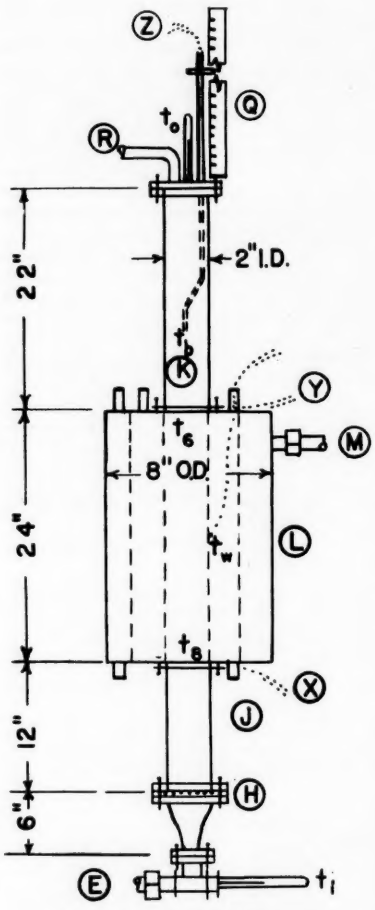

Fig. 2. Details of fluidizing unit.

EXPERIMENTAL

Materials

The solid particles employed were six closely sized groups of Scotchlite glass beads, ranging from 0.0019 to 0.027 in. in average diameter. Upon microscopic examination the beads appeared generally spherical with but little variation in diameter within any one group.

The diameter for each group was taken as the arithmetic mean of microscopic measurements on a representative sample of fifty to sixty beads from the particular group. The average diameters so obtained agreed closely with those specified by the manufacturer.

Absolute particle density for each bead size was determined by water displacement. Combining their value with bulk density measurements yielded an average value for the void fraction in the settled bed of about 0.43 with a standard deviation of about ±2% for all six bead sizes. Comparison with values offered by Brown (*1*) for randomly packed beds of solids indicates a sphericity of nearly unity, which is in accord with the high degree of sphericity observed microscopically.

The physical properties of the six groups of beads are summarized in Table 1.

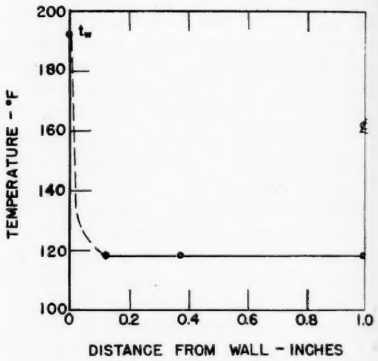

Fig. 3. Typical radial temperature profile in the fluidized bed.

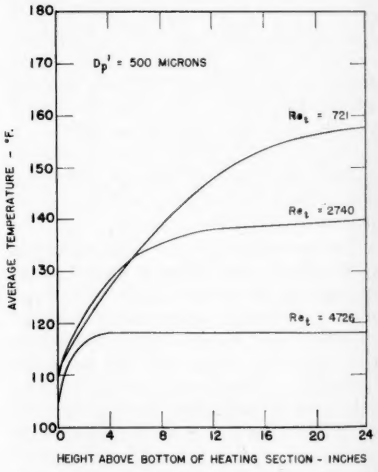

Fig. 4. Typical axial temperature profile in the fluidized bed.

The physical properties of the six groups of beads are summarized in Table 1.

Isidoro Caldas, Jr., is with Antibioticos S. A., Leon, Spain.

Table 1. Physical Properties of Glass Beads

Average measured diameter, μ	Standard deviation in diameter, ±%	Particle density, lb./cu. ft. Absolute	Bulk
685	2.4	154	90
500	4.4	156	89
292	4.4	157	88
219	8.4	155	90
125	5.5	158	91
49	25	152	88

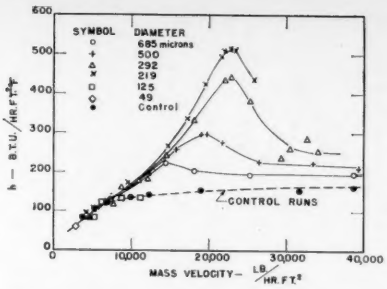

Fig. 5. Effect of flow rate and particle diameter on heat transfer coefficient, with steam as the heating medium.

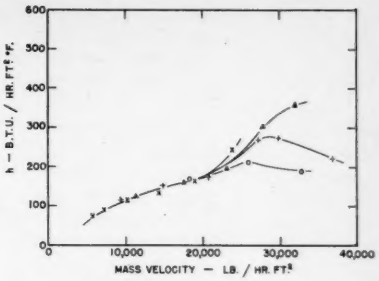

Fig. 7. Effect of flow rate and particle diameter on heat transfer. (Symbols are identified in Figure 5.)

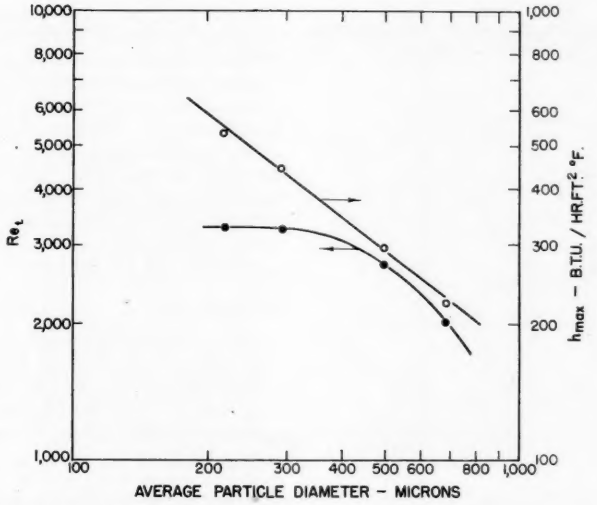

Fig. 6. Approximate transition between low- and high-velocity fluidization.

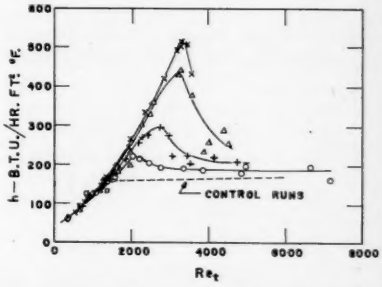

Fig. 8. Over-all results, showing effect of Reynolds number (based on tube diameter) and particle diameter on heat transfer coefficient. (Symbols are identified in Figure 5.)

The heating medium employed was a condensing vapor. For most of the work this was the general laboratory supply steam which was first passed through a moisture separator. For some runs, however, rectified methanol vapor was employed instead, in order to extend (downward) the temperature range.

Apparatus

An over-all schematic diagram of the equipment is shown in Figure 1. Distilled water from the jacketed circulating tank A was pumped B into the upper section of the ballast tank C. Any air entrapped in the liquid separated in this tank and escaped through the upper vent D. Water from the ballast tank under a slight positive pressure was admitted at a controlled rate to the bottom of the fluidizing column E passing upward through the bed of suspended solids and out through the water cooler F to the circulating tank.

The fluidizing unit itself G is a modification of that used by Dow and Jakob (*3*) in their work with air as the fluidizing medium. It is shown schematically in Figure 2. A 325-mesh copper screen H supported on a 40-mesh screen was used to support the bed of solids at the lower section of the column. A straight 1-ft. section of Pyrex-glass tubing J served as a straightening section and as a means for observing conditions in the lower part of the fluidized bed. A 2-ft. section of similar tubing K was used above the heating unit L and served as a disengaging section and as a means for observing the upper portion of the bed.

The heat transfer surface consisted of a 24-in.–long, 2-in.–I.D., 0.06-in.–thick copper tube surrounded by a double steam jacket. The outer steam jacket virtually eliminated any steam loss to the surroundings from the inner jacket. To further minimize heat losses, the entire unit was covered with asbestos paper and aluminum foil, except for narrow slits on the glass sections to permit visual observation. Vapor M was admitted at such a rate as to maintain a slight stream from the upper vent N. Condensate from each jacket was continuously drained P and collected separately.

Mercury thermometers measured the inlet water temperature t_i and the outlet water temperature t_o. A third thermometer measured the condensing vapor temperature. The wall temperature t_w was determined by means of a calibrated, glass-insulated, 20-gauge iron-constantan thermocouple welded in a groove approximately 1-in. long midway up the length of the copper heating tube. This groove was then filled with liquid solder and ground smooth and level with the rest of the condensing surface. Similar thermocouples X and Y were located at the center line of the inner tube at the entrance and exit to the heating section. In addition, a moving and rotatable thermocouple probe Z equipped with a calibrated scale Q was used to measure bed temperature t_b at various locations (to within ⅛ in. of the wall) and thus to determine longitudinal and radial temperature profiles throughout the fluidized bed. All thermocouples were connected via an ice-water cold junction U and a multiple contact switch S to a potentiometer, the precision of which was ±0.2°F.

Generally speaking, about 1½ to 2 hr. was required for the system to come to steady state after initial startup.

RESULTS

Control runs without solids, as well as fluidization runs with solids, were carried out. Detailed data and curves are available (*2*). At very low velocities some air bubbles appeared at the wall. Such runs were omitted.

Control Runs

Temperature-profile measurements for the control runs indicated virtually no radial variation in temperature at any level in the tube, even at Reynolds num-

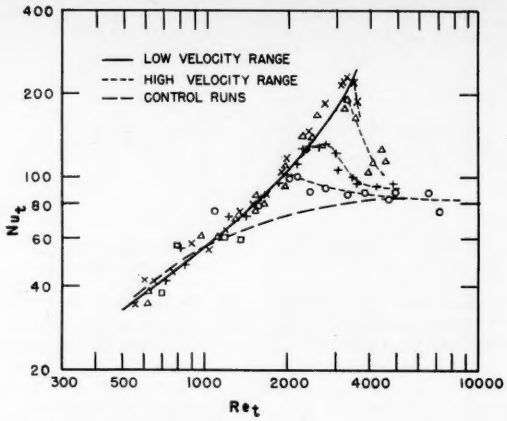

Fig. 9. Over-all results, showing relationship between Nusselt number and Reynolds number, both based on tube diameter. (Symbols are identified in Figure 5.)

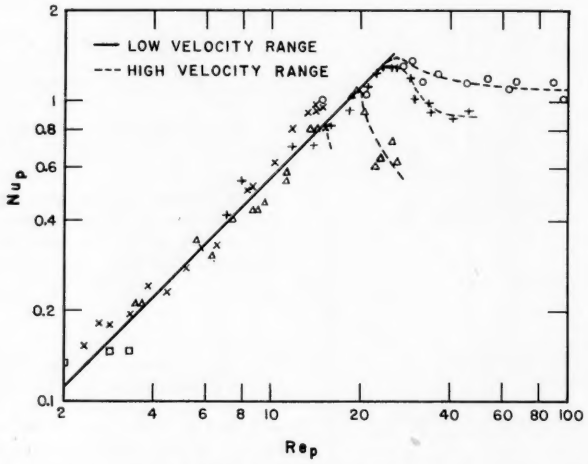

Fig. 10. Fluidation results, showing correlation for low-velocity regime. (Symbols are identified in Figure 5.)

bers Re_t (based on tube diameter) below 2,100. In other words, the temperature drop between wall and fluid was essentially confined to within $\frac{1}{8}$ in. of the wall. Furthermore, small quantities of ink introduced into the flowing stream at various levels were quickly dispersed, even at Re_t as low as 300 and with the walls unheated. This inherent mixing action is attributed to entrance effects and the relatively low ratio of tube length to diameter.

The heat transfer coefficient h for each run was computed from Equation (1). The quantity q was determined from the measured rise in temperature for a given rate of water flow. Comparison with q calculated from the measured rate of steam condensation from the inner jacket yields an average deviation of $\pm 5\%$, indicating a satisfactory heat balance.

$$h = \frac{q}{\int \Delta t \, dA} \qquad (1)$$

Table 2. Approximate Transition Between Low- and High-velocity Fluidization

Average particle diameter, μ	Reynolds number Based on tube diameter	Reynolds number Based on average particle diameter	Void fraction	Coefficient of heat transfer, B.t.u./(hr.)(sq. ft./°F.)	Increase in coefficient due to presence of particles, %
685	2020	27.3	0.542	224	57
500	2740	26.7	0.660	298	92
292	3260	18.8	0.816	442	178
219	3280	14.2	0.930	518	225

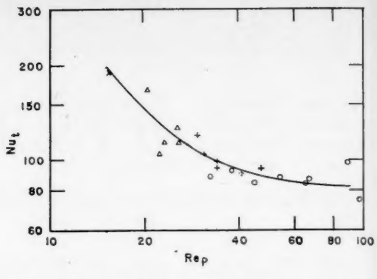

Fig. 11. Correlation for high-velocity regime. (Symbols are identified in Figure 5.)

The quantity $\int \Delta t \, dA$ was computed by graphical integration of the longitudinal profile. Results for the control runs are indicated as the broken curves in Figures 5 and 8. Some additional control runs (not shown), for which no temperature-profile measurements were taken but for which Δt was taken instead as constant at its arithmetic mean between inlet and outlet, were also carried out. The trend of these runs proved to be in fair agreement with the others.

Fluidization Runs

By and large little radial variation in temperature was observed for the runs with a fluidized bed. As with the control runs, radial variation in temperature appeared to be essentially confined to within $\frac{1}{8}$ in. of the wall, an indication that the major resistance to heat flow lies within this layer, in accordance with the usual film concept of resistance to convective heat transfer. A typical radial temperature profile is shown in Figure 3.

At high flow rates little longitudinal temperature variation was observed either, an indication of thorough mixing throughout the bed. Analogous results have been reported by others, such as Mickley and Trilling (*6*) in their work with air in the lean fluidization range. However, at lower flow rates longitudinal variation in temperature became pronounced, suggesting less vertical mixing. Figure 4 shows some longitudinal temperature profiles. Thus there are two general regimes, one for high flow rates and little vertical variation in temperature and a second for low flow rates and considerable vertical variation in temperature. In a limited sense, these two regimes may be considered analogous to lean and dense fluidization respectively in gas-solid systems. For the present liquid-solid system, the region of transition between the two regimes is, of course, not clearly defined; however, it does appear to be a function of particle size. It also falls in the usual Re_t transition range between viscous and turbulent flow.

Values for h were computed from

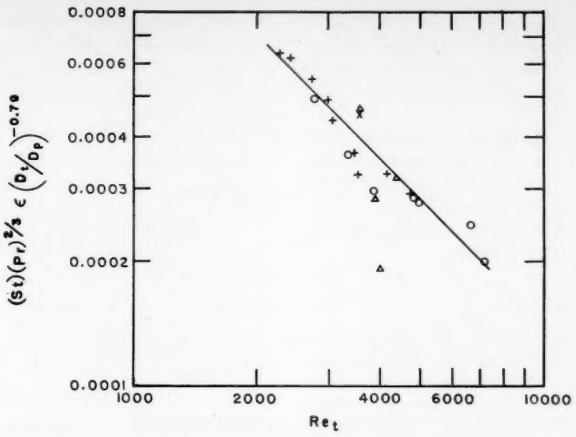

Fig. 12. Alternative correlation for high-velocity regime. (Symbols are identified in Figure 5.)

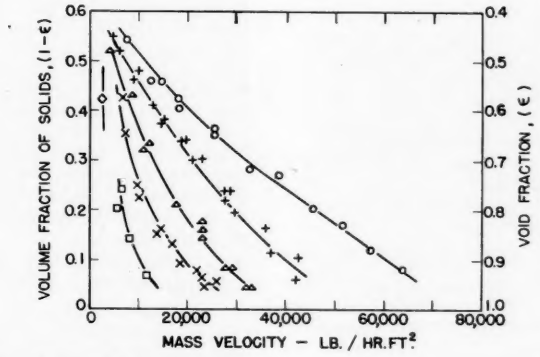

Fig. 13. Effect of mass velocity and particle size on solid fraction and void fraction. (Symbols are identified in Figure 5.)

Equation (1) and plotted against the mass velocity G in Figure 5 for runs with steam as the heating medium. The results show a marked improvement in h due to the presence of the fluidized particles, even to the extent of more than tripling the coefficient that would obtain in their absence. The maxima in h correspond approximately to the region of transition between these two regimes and are listed as such in Table 2. These maxima decrease with particle diameter as shown in Figure 6. (Carryover prevented attainment of sufficient mass velocity to yield a maximum h for the two smallest particle sizes of 49 and 125 μ. By the same token, the relatively sparse data obtained for these two smallest sizes are likely to be somewhat less reliable than the more extensive data taken for the four larger sizes.)

Maxima have been reported by others for gas-fluidized systems (*5*, *6*, *8*). Fitting this plot in Figure 6 with a straight line yields Equation (2) for the effect of particle diameter D_p' in microns on maximum h.

$$h_{max} = 34{,}400(D_p')^{-0.77} \qquad (2)$$

Similar results, shown in Figure 7, were obtained with condensing methanol as the heating medium. However, the corresponding curves are shifted downward and to the right as compared with those of Figure 5. By means of Re_t, both sets of data have been combined in Figure 8. Reasonable agreement is shown in this way between the data for the high-temperature levels of condensing steam and the data for the low-temperature levels of condensing methanol.

Improvement in h due to the presence of the solids in gas-fluidized systems has been ascribed (*7*) in part to the ability of the solids to carry heat. Compared to that of a gas under usual conditions, the volumetric heat capacity of a solid is very large; however, in the present work with water the volumetric heat capacity of the solid particles is actually less than half that of the fluid. Nevertheless, considerable increase in h has been obtained. It would thus appear likely that for liquid-fluidized systems, such as in the present investigation, convective transport by the solids is relatively slight and some other mechanism controls.

Low-velocity Fluidization

Figure 9 shows the effect of Re_t on Nu_t, the Nusselt number based on tube diameter, for all the data. Plotted in this way, all the results for the low-velocity regime cluster well about a common curve indicating the absence of any appreciable effect due to particle size. However, as the previously mentioned maximum h is approached, the results for the high-velocity regime appear to break away from the trend and to decrease along a different curve for each particle size. At the upper and lower extremes of Re_t the curve for the control runs is approached, and so extrapolation is possible at either end.

The analogous plot of Nusselt number based on particle size Nu_p vs. Reynolds number based on particle size Re_p is shown in Figure 10. As with the previous figure, the data for low-velocity fluidization follow a clear trend, while those for high-velocity fluidization branch off near the maximum. If the slight curvature in the low-velocity fluidization trend is disregarded, a straight line may be drawn through the data and fitted by the following simple equation:

$$Nu_p = 0.055 Re_p \qquad (3)$$

No significant effect on h was found for the modest variation in bed height. Equation (3) fits the low-velocity fluidization data with a standard deviation of $\pm 13\%$. This relation can be readily transformed into Equation (4) where μ and k are the viscosity and thermal conductivity of the liquid respectively.

$$h = 0.055 \frac{k}{\mu} G \qquad (4)$$

Direct comparison with results of previous investigators, such as the recent correlation of Wen and Leva (*8*) for dense fluidization, is difficult, owing to the wide differences in physical properties between water and gases.

Thermal properties for these relationships are evaluated at the bulk temperature. Use of the arithmetic-mean film temperature did not appear to correlate the data any better.

High-velocity Fluidization

The data for high-velocity fluidization appear to scatter more than those for the low-velocity regime. Particle size has a definite effect, an increase in D_p' at constant G causing a decrease in h. Figure 11 shows Nu_t vs. Re_p, a method of plotting which allows for variation in particle size.

An alternative method of correlation is based on a modified Colburn-type j factor following an approach somewhat similar to that of Gamson (*4*). By a technique of successive cross plots, Figure 12 was prepared. Both particle size and void fraction ϵ are included here. A straight line was drawn and fitted by Equation (5)

$$j=(St)(Pr)^{\frac{2}{3}}=1.4(D_t/D_p)^{0.79}/Re_t\epsilon \quad (5)$$

All properties were evaluated at bulk temperature. The standard deviation for Equation (5) is ±19%. The effects of G and D_p' on ϵ are shown for both regimes in Figure 13. (Variation in temperature with attendant variation in fluid properties accounts for some of the scatter in this figure.)

SUMMARY OF CONCLUSIONS

1. The presence of fluidized solids can increase the rate of heat transfer from retaining wall to liquid considerably, a tripling of the coefficient having been obtained.

2. The behavior of the liquid-fluidized bed can be divided into two regimes, with the maximum coefficient for a given particle size occurring approximately at the transition.

3. The first regime at lower velocities is characterized by an appreciable vertical temperature gradient, which indicates limited axial mixing; by an increase of coefficient with mass velocity; and by a lack of any appreciable effect of particle size on coefficient. Within the limits of the experiment, results in this regime are correlated by Equations (3) or (4).

4. The second regime at higher velocities is characterized by little or no vertical temperature gradient, which is an indication of considerable axial mixing; by a decrease of coefficient with mass velocity; and by a decrease in coefficient with an increase in particle size. Within the limits of the experiment, results in this regime are correlated by Figure 11 or Equation (5).

5. In view of the low volumetric heat capacity of the solids in comparison with that of the liquid, it would appear that heat carried by the solids is not an important factor in determining the increase in heat transfer.

ACKNOWLEDGMENT

The authors wish to express their appreciation to Schenley Laboratories, Inc., of Lawrenceburg, Indiana, for the use of their facilities. The authors also thank William Licht and Chad Gottschlich for reviewing the original manuscript and Stuart Willins, Richard Lasure, and Chungkong Hwu for assistance in preparing the figures.

NOTATION

A = heat transfer surface, sq. ft.
c = heat capacity, B.t.u./(lb.)(°F.)
D = diameter, ft.
D' = diameter, μ
G = mass velocity, lb./(hr.)(sq. ft.)
h = coefficient of heat transfer, B.t.u./(hr.)(sq. ft.)(°F.)
k = thermal conductivity B.t.u./(hr.)(sq. ft.)(°F./ft.)
Nu = Nusselt number = hD/k, dimensionless
Pr = Prandtl number = $c\mu/k$, dimensionless
q = rate of heat transfer B.t.u./hr.
Re = Reynolds number = DG/μ, dimensionless
St = Stanton number = h/cG, dimensionless

Greek Letters

Δt = temperature difference, °F.
ϵ = void fraction, dimensionless
μ = viscosity, lb./(ft.)(hr.)

Subscripts

max. = maximum
p = particle
t = tube

LITERATURE CITED

1. Brown, G. G., "Unit Operations," p. 214, John Wiley and Sons, New York (1950).
2. Caldas, Isidoro, Ph.D. dissertation, Univ. Cinn. (1955), available from University Microfilms, Ann. Arbor, Mich.
3. Dow, W. M., and Max Jakob, *Chem. Eng. Progr.*, **47**, 637 (1951).
4. Gamson, B. W., *ibid.*, **47**, 19 (1951).
5. McAdams, W. H., "Heat Transmission," 3 ed., p. 303, McGraw-Hill Book Company, Inc., New York (1954).
6. Mickley, H. S., and C. A. Trilling, *Ind. Eng. Chem.*, **41**, 1135 (1949).
7. Van Heerden, C., A. P. P. Noble, and D. W. Van Krevelen, *Ind. Eng. Chem.*, **45**, 1237 (1953).
8. Wen, Chin-Yung, and Max Leva, *A.I.Ch.E. Journal*, **2**, 482 (1956).

COMMUNICATIONS TO THE EDITOR

Flow Measurement with Ball Flow Meters

H. L. SHULMAN and K. A. VAN WORMER, JR., Clarkson College of Technology, Potsdam, New York

The measurement of the rate of fluid flow is an essential part of control in almost all chemical plants. A wide variety of metering devices have been developed for this purpose ranging from relatively simple direct reading meters, such as the rotameter, to elaborate instrumentation for metering, recording, and controlling. Recently Gradishar (*2*) used a simple direct reading meter for gaseous hydrogen fluoride which avoided the difficulties encountered with the glass tubes used in rotameters. The reading meter consisted essentially of a section of Saran tubing in the shape of a quarter of a circle and a ball to serve as a quantitative indicator of the flow rate.

Shulman, Stieger, and Leist (*3*) modified this meter by employing a semicircular tube (Figure 1). This modification makes flow-rate measurements possible in either direction without the use of auxiliary valves and piping. In addition, the symmetry of the meter makes it possible easily to check the levelness of the installation because the ball should rest at the zero reading when there is no fluid flowing through the meter.

A ball flow meter can easily be constructed of a piece of transparent or translucent tubing and a ball which has a density greater than that of the fluid to be metered. If translucent tubing is employed, it should be mounted so that light may pass through it to facilitate locating the ball. Suitable tube materials include glass, vinyl, Tygon, Saran, and polyethylene. Balls can be metallic: steel, aluminum, and brass or nonmetallic: glass, nylon, sapphire, etc. The wide range of materials available and the ease of constructing this type of meter should make it very useful for laboratory, pilot plant, and exploratory work.

DERIVATION OF THE BALL-FLOW-METER EQUATION

For many applications ball flow meters can be calibrated experimentally with a trial-and-error procedure employed for the selection of the tube and ball. When toxic, corrosive, inflammable, or volatile fluids are to be metered, experimenta calibration is difficult or impossible. To aid in the selection of the tube and ball and in the prediction of calibration curves, an analytic and experimental study was undertaken to determine the factors influencing the design of ball flow meters.

An equation suitable for the prediction of calibration curves can be developed. When a fluid is flowing through the meter the ball comes to rest at a position indicative of the flow rate. This position is most conveniently measured by the angle which a radius of the circle extended through the center of the ball makes with the vertical (Figure 1). The ball remains in its position because there are two equal and opposite forces acting upon it. The first is the total drag of the fluid on the ball, which tends to move the ball up the tube. The second is the force due to the component of the weight of the ball which is acting parallel to the tangent at the point of contact of the ball and tube and which tends to move the ball down the tube. Goldstein (*1*) has

K. A. Van Wormer, Jr., is with Tufts University, Medford, Massachusetts.

collected data indicating that the total drag on a sphere τ can be related to fluid velocity u by

$$\tau = \frac{C_d \rho_f u^2}{2g_c} \quad (1)$$

where C_d is a function of only a Reynolds number, $D_b \rho_f u/\mu$, if the flow pattern of the fluid around the sphere is not influenced by the presence of a boundary.

The force opposing the drag on the ball is a component of the net weight of the ball per unit of projected area.

$$\frac{V_b(\rho_b - \rho_f) \sin \theta}{A_b} \quad (2)$$

If $W/\rho_f A_f$ is substituted for u and the forces of Equations (1) and (2) are equated, one obtains

$$W = A_f \left[\frac{2g_c v_b(\rho_b - \rho_f)(\rho_f) \sin \theta}{C_d A_b} \right]^{\frac{1}{2}} \quad (3)$$

If a new coefficient C is equal to $1/(C_d)^{1/2}$, the ball flow meter equation is obtained in its final form:

$$W = C A_f \left[\frac{2g_c v_b(\rho_b - \rho_f)(\rho_f) \sin \theta}{A_b} \right]^{\frac{1}{2}} \quad (4)$$

A correlation for the ball flow meter coefficient must be obtained from experimental data rather than determined from the data in the literature for C_d as given by Goldstein (*1*) because the fluid-flow patterns around the ball in a ball flow meter are influenced by the presence of the tube wall. Employing the usual dimensional-analysis methods and assuming C is a function of D_b, D_t, ρ_f, u, and μ one finds that C is a function of two dimensionless groups, a ratio of diameters (D_b/D_t) and a Reynolds number $(D_t \rho_f u/\mu)$. The final correlation of the experimental data indicates that the best correlation is obtained if C is taken as a function of (D_b/D_t) and a modified Reynolds number (Deq. G/μ).

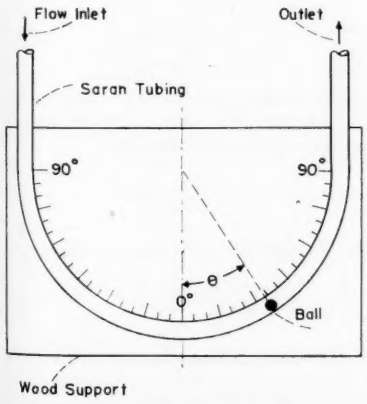

Fig. 1. Diagram of ball flow meter.

APPARATUS AND PROCEDURE

The apparatus employed for the experimental determination of the meter coefficient, shown in Figure 1, consists of a loose ball in a piece of Saran tubing of uniform circular cross section. The tube is supported in a semicircular groove of 7-in. radius milled in a sheet of plywood and backed by glass and a light to facilitate reading of the position of the ball with the attached protractor.

The diameter of the tubing is checked for uniformity and calculated from the weight of water required to fill a measured length of tubing. Ball diameters are measured with a micrometer, the balls are weighed, and the densities are calculated.

The meter is leveled by bringing the ball to an angle of 0 deg. with no fluid flowing. Water flow from a constant-head tank or air flow from a compressed air line is maintained at a constant rate through the meter by the use of a screw clamp on a section of rubber tubing attached to the inlet side of the Saran tubing. When constant conditions are establishsd, the temperature of the fluid, the meter reading in degrees, and the flow rate are noted and recorded. When water is used, flow rates are determined by noting the time required to collect a given weight in a galvanized container placed on a platform scale; when air is used, the volume is measured with calibrated wet and dry gas meters.

To calculate C from the experimental data, Equation (4) was modified by substituting for A_b, A_f, and v_b their respective equivalents $(\pi/4)(D_b^2)$, $(\pi/4)(D_t^2 - D_b^2)$, and $(\pi/6)(D_b^3)$, with appropriate conversion factors to obtain the working equation

$$C = \frac{W}{0.01029[(\rho_b - \rho_f)(\rho_f)(D_b')(\sin \theta)]^{\frac{1}{2}}(D_t'^2 - D_b'^2)} \quad (5)$$

Data were obtained for three tube diameters (0.1565, 0.268, and 0.419 in.) with two fluids (air and water), three ball materials (aluminum, brass, and nylon), and various ball diameters as tabulated on Figure 2.

Meter readings were kept between 9 and 60 deg. Above 60 deg. the erratic behavior of the balls makes it difficult to obtain reliable data.

CORRELATION OF DATA

Several methods of correlation were attempted, but the best results were obtained when $C(D_b/D_t)^{-0.15}$ was plotted vs. a Reynolds number (Deq. G/μ). Figure 2 shows the data obtained with three different tube diameters, a variety of balls, and air and water as the metered fluids. Data for a total of 199 runs are shown to define one smooth curve. At the higher Reynolds numbers the data fit the curve so well that it is impossible to distinguish the individual points. The excellent correlation obtained for such a wide variety of conditions indicates that Equation (4) and the correlation should be reliable for the prediction of calibration curves for ball flow meters for conditions other than those covered by the experimental work. The data presented were obtained with a 7-in.–radius meter. Additional work done with meters of radii up to 48 in. showed no effect of varying radius. In the construction of these meters it would be wise to avoid radii which are short enough to cause flattening of the tube.

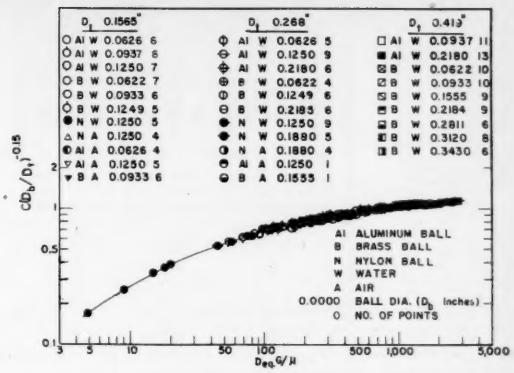

Fig. 2. Correlation of experimental data.

DESIGN OF BALL FLOW METERS

The design of a ball flow meter involves the selection of a ball and tube and the calculation of a calibration curve. The selection of the proper materials of construction will be omitted here because it is similar to the choice of materials for any other piece of equipment handling the same fluid. To illustrate the use of the ball-flow-meter equation, a solution for a typical design will be outlined.

The specifications call for the design of a ball flow meter to meter water at 25°C. flowing at a rate of about 70 lb./hr. For this service a brass ball with a density of 528 lb./cu. ft. and a diameter 0.5 of the tube diameter will be used. Any transparent or translucent plastic tube will be suitable for this service. As an approximation C will be assumed equal to 1.0, and an angle of 25 deg. will be used as a midscale reading to allow for readings on either side of 70 lb./hr. Since $D_t' = 2D_b'$, Equation (5) can be solved for D_b' to give

$$D_b' = 0.127 \text{ in.}$$

In order to employ standard sizes a ball with a 0.125-in. diameter and a tube with a 0.250-in. internal diameter will be used. To prepare a calibration curve for this ball and tube several values of W are selected,

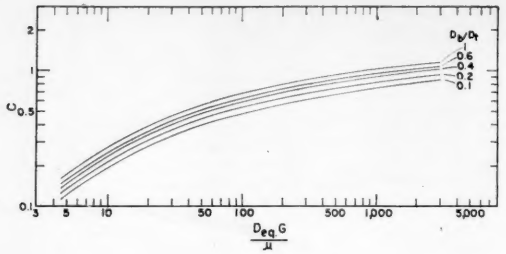

Fig. 3. Design chart for ball flow meters.

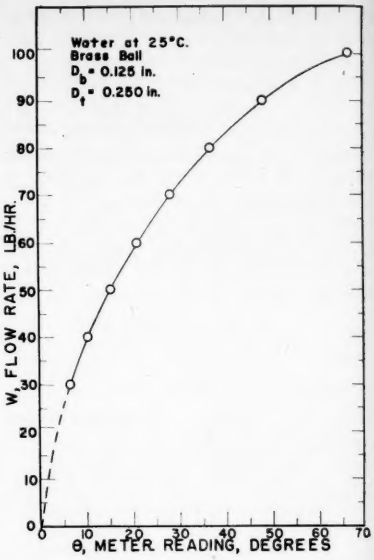

Fig. 4. Calibration curve for sample design.

and the corresponding values of Deq. G/μ are calculated. From Figure 3 the values of C, corresponding to a D_b/D_t of 0.5 and the appropriate values of Deq. G/μ, are obtained. Equation (4) or (5) may now be used to obtain values of sin θ, from which θ is obtained. The calibration curve is shown on Figure 4.

NOTATION

A_b = projected cross-sectional area of ball, sq. ft.
A_f = free area for flow of fluid between ball and tube, sq. ft.
C = ball-flow-meter coefficient, dimensionless
C_d = drag coefficient for spheres, dimensionless
D_b = ball diameter, ft.
D_b' = ball diameter, in.
Deq. = equivalent diameter for use in the Reynolds number, $(D_t - D_b)$, ft.
D_t = tube diameter, ft.
D_t' = tube diameter, in.
G = mass flow rate based on free area (A_f), lb./(sec.)(sq. ft.)
g_c = conversion factor, (lb.-mass)(ft.)/(lb. force)(sec.)(sec.)
T = temperature of fluid, °C.
u = fluid velocity, ft./sec.
v_b = volume of ball, cu. ft.
W = fluid flow rate, lb./sec.

Greek Letters

θ = meter reading, angle from vertical, deg.
μ = fluid viscosity, lb./(ft.)(sec.)
ρ_b = ball density, lb./cu. ft.
ρ_f = fluid density, lb./cu. ft.
τ = drag on sphere per unit of projected area, lb.-force/sq. ft.

LITERATURE CITED

1. Goldstein, S., ed., "Modern Developments in Fluid Dynamics," Oxford Univ. Press, London (1938).
2. Gradishar, F. J., *Chem. Eng.*, **57**, No. 10, 122 (1950).
3. Shulman, H. L., F. M. Stieger, and A. R. Leist, *ibid.*, **60**, No. 2, 173 (1953).

Absorption into an Accelerating Film

L. E. SCRIVEN and R. L. PIGFORD

University of Delaware, Newark, Delaware

If the velocity field in the neighborhood of the gas-liquid interface is not uniform in a steady state apparatus such as a wetted-wall column or a jet, then the rate of absorption is no longer given by the simplest form of the so-called "penetration" theory, in which the local absorption rate is assumed to be the stagnant-liquid absorption rate. Rather, a more general form of the diffusion equation must be employed in which it may not be especially convenient to replace contact distance by contact time. Since this matter does not seem to have been fully allowed for by the author of a recent communication (*3*), a brief discussion is given here. For the purpose of illustration, the magnitude of the acceleration end effect in a short wetted-wall column is estimated from the equations presented herein. Such an end effect was suggested by Vivian and Peaceman (*4*) as a possible explanation of the discrepancy between experimental and theoretical absorption rates in their columns.

The equation governing ordinary diffusion in a binary system, for constant diffusivity and mass density, is

$$\frac{\partial c}{\partial t} + (\mathbf{u}\cdot\nabla)c = D\nabla^2 c \qquad (1)$$

For a short wetted-wall column or jet it is generally permissible to regard the absorbing liquid as two dimensional with infinite depth and to neglect diffusion in the direction of flow; at steady state Equation (1) then reduces to

$$u\frac{\partial c}{\partial x} + v\frac{\partial c}{\partial y} = D\frac{\partial^2 c}{\partial y^2} \qquad (2)$$

where c is concentration in mass per unit volume, x and u are distance and the velocity component parallel to the interface respectively, y and v are distance and the velocity component normal to the interface respectively, and D is the diffusivity. The appropriate boundary conditions are

$$c = c_0 \quad \text{for} \quad x < 0, \quad y \geq 0$$

$$c = c_0 \quad \text{for} \quad x > 0, \quad y = \infty$$

$$c = c_e \quad \text{for} \quad x \geq 0, \quad y = 0$$

where interfacial equilibrium and absence both of heat effects at the interface and of gas-phase diffusional resistance have been assumed. At the interface $(\partial u/\partial y)_{x,0}$ will be very nearly zero (the adjoining gas exerts negligible drag upon the liquid surface), and so u may be replaced by the surface velocity u_s, provided that the penetration depth of solute gas molecules is sufficiently small. From the equation of continuity

$$v = -\int_0^y \frac{\partial u}{\partial x}\,dy \qquad (3)$$

Hence in the region of interest, close to the interface, the normal component of velocity is approximated by

$$v = -y\frac{du_s}{dx} \qquad (4)$$

and the diffusion equation becomes

$$u_s\frac{\partial c}{\partial x} - y\frac{du_s}{dx}\frac{\partial c}{\partial y} = D\frac{\partial^2 c}{\partial y^2} \qquad (5)$$

If the liquid is being accelerated in the x direction, liquid elements are stretched in the x direction and suffer a corresponding shrinkage in the y direction; this causes a bulk flow of liquid toward the surface, which in the case of absorption opposes the mass flux due to the concentration gradient, but at the same time results in a steepening of the concentra-

CHEMICAL REACTION ENGINEERING

Edited by Dr. K. Rietema, Secretary, European Federation of Chemical Engineers

This volume contains the thirteen papers presented at a symposium held in Amsterdam under the auspices of the European Federation of Chemical Engineers, which was attended by over 200 participants from all over Europe. Each paper is preceded by an abstract in English, French and German. Topics covered are flow phenomena, mass and heat transfer, and reaction kinetics—and their relation and interaction.

Price $12.50

★

PHYSICAL CHEMISTRY

By E. A. MOELWYN-HUGHES, D.Sc. (Liverpool), D. Phil. (Oxon), Sc.D. (Cantab), University Lecturer in Physical Chemistry, Cambridge, England

This carefully planned, critical and scholarly work covers the whole of physical chemistry, first from the experimental angle and next from the standpoint of the partition function. Equal emphasis is placed on experiment and theory, and the notation is uniform throughout. The book, containing 1,200 pages of text and numerous diagrams, is based on the author's lectures at Cambridge, and although primarily written to meet the needs of students taking Part II of the Natural Sciences Tripos at this University, will also be most useful to research workers, teachers and all who desire to be conversant with modern mid-century physical chemistry.

Price $15.00

★

CHEMICAL ENGINEERING in the COAL INDUSTRY

Edited by Dr. Forbes W. Sharpley

This volume contains the papers presented at the symposium held at the National Coal Board Research Establishment. The subjects covered were: Controlled oxidation of coal; Fluidized oxidation of coal; Investigations of the carbonization of briquettes in Germany; Hot briquetting; Semicarbonization in a fluid bed; Study of tars obtained in fluidized carbonization; Industrial treatment of low-temperature of carbonization tars. Also included is a review of the conference by Dr. J. Bronowski.

Price $8.50

★

TETRAHEDRON

The International Journal of Organic Chemistry

FOUNDED BY SIR ROBERT ROBINSON

Assisted by an International Honorary Editorial Advisory Board under the co-chairmanship of Sir Robert Robinson and Prof. R. B. Woodward.

Tetrahedron covers all aspects of organic chemistry, whether theoretical or practical, analytical or synthetic, physical or biological, including papers on applied chemistry which have a pure organic chemical content. The Journal publishes original memoirs, preliminary communications and notes.

SUBSCRIPTION PRICE:

(A) $17. per volume (Postage included) for institutes, libraries, firms, government offices and similar organizations. Volumes 2, 3, 4 in 1958.

(B) $15. per annum (Postage included) for individual subscribers certifying that they require the journal for their private use only.

★

Write for fully descriptive leaflets

PERGAMON PRESS

New York • London • Paris • Los Angeles

122 East 55th Street, New York 22, N. Y.
4 & 5 Fitzroy Square, London, W.1.
24 rue des Ecoles, Paris Ve.
P.O. Box No. 47715, Los Angeles 47, California

Just Published!

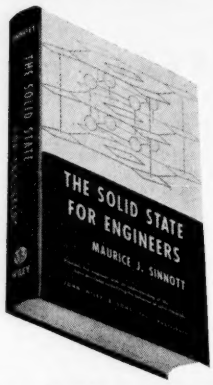

1. THE SOLID STATE FOR ENGINEERS

By MAURICE J. SINNOTT, University of Michigan

An accurate and convenient reference to problems concerning the choice and use of materials. Surveys the basic principles underlying the behavior of solid materials. Problems illustrating the principles are included, *plus* examples of how to apply them to practical problems.

Check these information-packed chapters:

The Structure of Matter. Crystallography. X-Ray and Electron Defraction. Equilibrium. Rate Processes. Metallic Solids. Ionic Solids. Covalent Solids. Molecular Solids. Elastic and Plastic Deformation. Theory of Dislocations. Polycrystalline Solids. Mechanical Properties. Thermal Properties. Electron and Zone Theories. Electrical Conduction. Electronic Properties. Magnetic Properties. Dielectrics and Related Properties. Optical Properties. Miscellaneous and Surface Properties. 1958. 522 pages. 325 illus. $12.50

2. ION EXCHANGE RESINS, Second Edition

By ROBERT KUNIN, Rohm & Haas Company

Describes the nature and preparation of all kinds of ion exchange resinous materials. Shows you how to synthesize an ion exchange resin, evaluate the product, and employ it for major and minor applications. 1958. 466 pages. Illus. $11.00

3. AUTOMATIC PROCESS CONTROL

By DONALD P. ECKMAN, Case Institute of Technology

A comprehensive treatment of the important principles of automatic control, using the modern approach with block diagrams and frequency techniques. 1958. 368 pages. Illus. $9.00

4. CERAMIC FABRICATION PROCESSES

Edited by W. D. KINGERY, M.I.T. with 22 contributors.

Information on ceramic research, development, and production, based mainly on 1956 M.I.T. Special Summer Program in Ceramics. A Technology Press Book, M.I.T. 1958. 235 pages. Illus. $9.50

5. CHEMICAL PROCESS ECONOMICS

By JOHN HAPPEL, New York University

Deals with the application of technical information to economic design and operation of chemical-process plants. Uses the same basic, mathematically-developed relationships to handle all problems. 1958. 291 pages. Illus. $8.50

Mail this coupon TODAY for ON-APPROVAL copies!

JOHN WILEY & SONS, INC. **AICE-98**
440 Fourth Ave., New York 16, N. Y.

Please send me a copy of the book(s) circled below to read and examine ON APPROVAL. Within 10 days I will either return the book(s), and owe nothing, or I will remit the full purchase price(s), plus postage.

1 2 3 4 5

Name .....

Address .....

☐ SAVE POSTAGE! Check here if you ENCLOSE payment, in which case we will pay postage. Same return privilege, of course.

tion gradient. The second term in Equations (2) and (5) represents the net effect of bulk flow normal to the surface.

In the special case of constant surface velocity Equation (5) reduces to

$$u_s \frac{\partial c}{\partial x} = D \frac{\partial^2 c}{\partial y^2} \qquad (6)$$

With the substitution of $\theta = x/u_s$ this becomes the familiar equation for diffusion in a stagnant liquid, corresponding to which the local absorption rate per unit area is

$$N_A^* \quad \Delta c \sqrt{\frac{D u_s}{\pi x}} = \Delta c \sqrt{\frac{D}{\pi \theta}} \qquad (7)$$

Toor (*3*) considered the case in which

$$u_s = a x^m, \quad -1 < m < 1 \qquad (8)$$

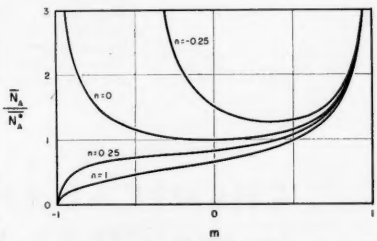

Fig. 1. Average absorption rates for varying surface velocity [Equation (15)].

and attempted to evaluate the effect of variable perimeter and surface velocity on average absorption rate from

$$\overline{N_A} = \frac{\int_0^X N_A(x) P(x)\, dx}{\int_0^X P(x)\, dx} = \frac{\int_0^\theta N_A P u_s\, d\theta}{\int_0^\theta P u_s\, d\theta} \qquad (9)$$

His result appears to be incomplete, inasmuch as he made use in Equation (9) of N_A^* calculated from Equation (6) instead of the true value, N_A, from Equation (5). The correct result is obtained by substituting Equation (8) in (5) and solving by a method given in reference *2* to obtain

$$N_A = \Delta c \sqrt{\frac{a(1+m)D}{\pi x^{1-m}}} \qquad (10)$$

$$= \sqrt{(1+m)/(1-m)}\, N_A^*(\theta) \qquad (11)$$

In an evaluation of N_A^* according to Equation (7), the time θ is taken as

$$\theta = \int_0^x u_s^{-1}\, dx \qquad (12)$$

If the perimeter $P(x)$ varies according to

$$P = b x^n, \quad n > -(1+m)/2 \qquad (13)$$

the average absorption rate, if use is made of Equation (9), is

$$\overline{N_A} = \Delta c \frac{2(1+n)}{(1+m+2n)} \cdot \sqrt{\frac{a(1+m)D}{\pi(X)^{1-m}}} \qquad (14)$$

$$= \frac{1+n}{1+m+2n} \cdot \sqrt{\frac{1+m}{1-m}}\, \overline{N_A{}^*(\theta')} \qquad (15)$$

where $\overline{N_A{}^*(\theta')}(= 2\Delta c\sqrt{D/\pi\theta'})$ is the average absorption rate into a film of constant perimeter moving at constant velocity over the same total distance. The ratio $\overline{N_A}/\overline{N_A{}^*}$ is shown in Figure 1.

In flow down a wetted-wall column like the columns employed by Vivian and Peaceman (*4*) the film surface must accelerate from zero velocity at the inlet slot and approach the final steady velocity downstream. In the past it has been assumed that the final velocity is attained immediately at the inlet slot. For the purpose of estimating the effect on average absorption rate of the acceleration end effect, it will be assumed that the outermost portion of the film accelerates downward under the influence of gravity alone until it reaches the final steady velocity, with which it continues to move thereafter. During the acceleration period ($0 < x \leq x_a$) the surface velocity is approximately the free-fall velocity,

$$u_s = \sqrt{2g_L}x^{1/2} \qquad (16)$$

and the local absorption rate, from Equation (10), is

$$N_{Aa} = \Delta c\sqrt{\frac{3D}{\pi}}\left(\frac{g_L}{2x}\right)^{1/4}, \quad 0 < x \leq x_a \qquad (17)$$

At the end of the acceleration period the concentration within the film is given by (*1*)

$$c = c_0 + \Delta c\ \mathrm{erfc}\left[\frac{y}{2}\sqrt{\frac{3}{D}}\left(\frac{g_L}{2x_a}\right)^{1/4}\right] \qquad (18)$$

$$x_a = u_f{}^2/2g_L \qquad (19)$$

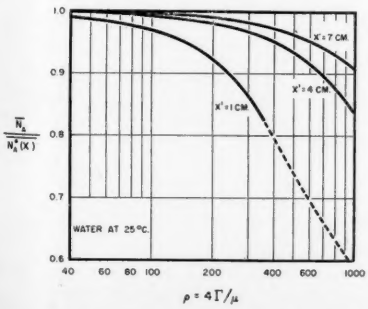

Fig. 2. Influence of acceleration end effect on average rate of absorption in short wetted-wall columns [Equation (24)].

Built by HEVI-DUTY specialists in electric heat

Temperatures to 250° C. (480° F.)

Improved Temperature Uniformity with Hevi-Duty's "circle-of-heat" design has no cold corners. Heaters, fastened to the outside of the aluminum chamber, give uniform heat distribution.

Fast Heat-Up with new "circle-of-heat" diffusion enables oven to reach 200° C. in less than one hour.

Low-Cost Operation on either 115 or 230 volts is made possible by a selector switch which permits high or low input to enclosed heating elements.

Durable Double-Wall Construction. Steel outer shell is prime coated on both sides to prevent corrosion.

Accurate Temperature Control by sensitive bulb-type thermostat permits little lag or overshoot. Control knob is located on a sloped panel for easy reading and adjustment.

Ventilation is provided through fresh air intake at bottom and top exhaust port.

For complete information on this new Hevi-Duty oven, write for Bulletin 458.

PRICE $169.00

Hevi-Duty Laboratory Oven, Model HK

15" diameter, 13" deep work chamber • Over-all dimensions, 20" wide, 18" deep, 23" high • 115 or 230 volts AC, 60 cycles, rated 600 watts • Three-wire, rubber-coated cord and plug with adapter for conventional outlets • Three perforated aluminum shelves removable for easy cleaning.

HEVI-DUTY ELECTRIC CO.
Milwaukee 1, Wisconsin

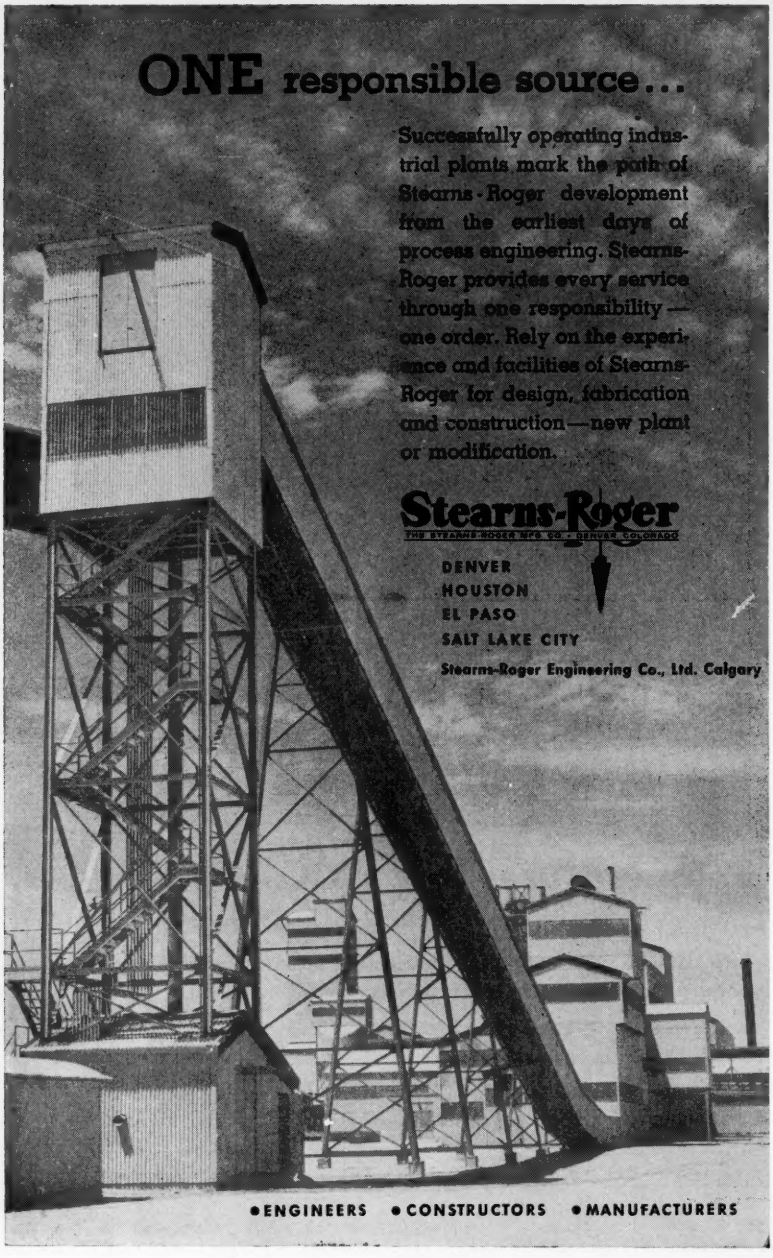
ONE responsible source...
Successfully operating industrial plants mark the path of Stearns-Roger development from the earliest days of process engineering. Stearns-Roger provides every service through one responsibility — one order. Rely on the experience and facilities of Stearns-Roger for design, fabrication and construction—new plant or modification.
Stearns-Roger
THE STEARNS-ROGER MFG. CO. • DENVER, COLORADO
DENVER
HOUSTON
EL PASO
SALT LAKE CITY
Stearns-Roger Engineering Co., Ltd. Calgary
• ENGINEERS • CONSTRUCTORS • MANUFACTURERS

where u_f is the final steady velocity (4). At the end of a fictitious distance x_a' the concentration within the film, if it moved with constant velocity u_f, would have been

$$c = c_0 + \Delta c \operatorname{erfc}\left(\frac{y}{2}\sqrt{\frac{u_f}{Dx_a'}}\right) \qquad (20)$$

Thus, as far as subsequent absorption is concerned, the free-fall distance x_a can be replaced by an equivalent distance x_a' given by

$$x_a' = u_f^2/3g_L \qquad (21)$$

The average absorption rate over the entire contact distance X is found by means of Equation (9):

$$\overline{N_A} = (X)^{-1}\int_0^{x_a} N_{Aa}\,dx + (X)^{-1}\int_{x_a'}^{x_a'+X-x_a} N_A^*(x)\,dx \qquad (22)$$

$$= 2\Delta c\sqrt{\frac{Du_f}{\pi X}\left(1 - \frac{x_a}{3X}\right)}, \qquad x_a \leq X \qquad (23)$$

Comparison of this result with the average absorption rate if it is assumed that the final velocity is immediately attained leads to (1)

$$\frac{\overline{N_A}}{N_A^*(X)} = \sqrt{1 - \left(\frac{4\Gamma}{\mu}\right)\frac{\delta}{32X}}, \qquad \left(\frac{4\Gamma}{\mu}\right)\frac{\delta}{32X} \leq \frac{1}{3} \qquad (24)$$

where Γ is the mass flow rate of liquid per unit perimeter, δ the film thickness, and μ the liquid viscosity.

This analysis indicates that the error in assuming that (7) applies to short wetted-wall columns 1 to 6 cm. long may lead to much too high predictions of absorption rates when the Reynolds number $4\Gamma/\mu$ exceeds 200 to 500 (see Figure 2; operation has generally been in the range 100 to 1,200). The simplifying assumptions which have been made here are of course open to question. For instance, the shear force exerted by the supporting wall will cause the surface to accelerate a little more slowly than in free fall, but on the other hand the flow and geometry of the film near the inlet may be such that the initial downward velocity of the surface is greater than zero.

LITERATURE CITED

1. Scriven, L. E., Ph.D. thesis, Univ. Delaware, Newark (1956).
2. ———, and R. L. Pigford, to be published.
3. Toor, H. L., *A.I.Ch.E. Journal*, 2, 578 (1956).
4. Vivian, J. E., and D. W. Peaceman, *ibid.*, 437.

INDEX OF ADVERTISERS

Atlas Powder Company 5S
Eimco Corporation 6S
Electronic Associates, Inc. 248
Hevi-Duty Electric Company 9S
Hunt Machine Co., Rodney ..Inside Back Cover
Mixing Equipment Company Outside Back Cover
Pergamon Press 7S
Stearns Roger Mfg. Company 10S
United Nations 4S
Wiley & Sons, Inc., John 8S
York Co. Inc., Otto H .....Inside Front Cover

Advertising Offices

New York 36—Lansing T. Dupree, Adv. Mgr.; John M. Gaede, Asst. Adv. Mgr.; Paul A. Jolcuvar, Dist. Mgr.; Donald J. Stroop, Dist. Mgr.; 25 W. 45th St., Columbus 5-7330.

Chicago 4—Martin J. Crowley, Jr., Dist. Mgr.; Robert Kliesch, Dist. Mgr.; 53 W. Jackson Blvd. Harrison 7-0382.

Cleveland 15—Eugene B. Pritchard, Dist. Mgr., 1836 Euclid Ave., Superior 1-3315.

Pasadena 1—Richard P. McKey, Dist. Mgr., 465 East Union St., Ryan 1-8779.

Dallas 18—Richard E. Hoierman, Dist. Mgr., 9006 Capri Drive, Diamond 8-1229
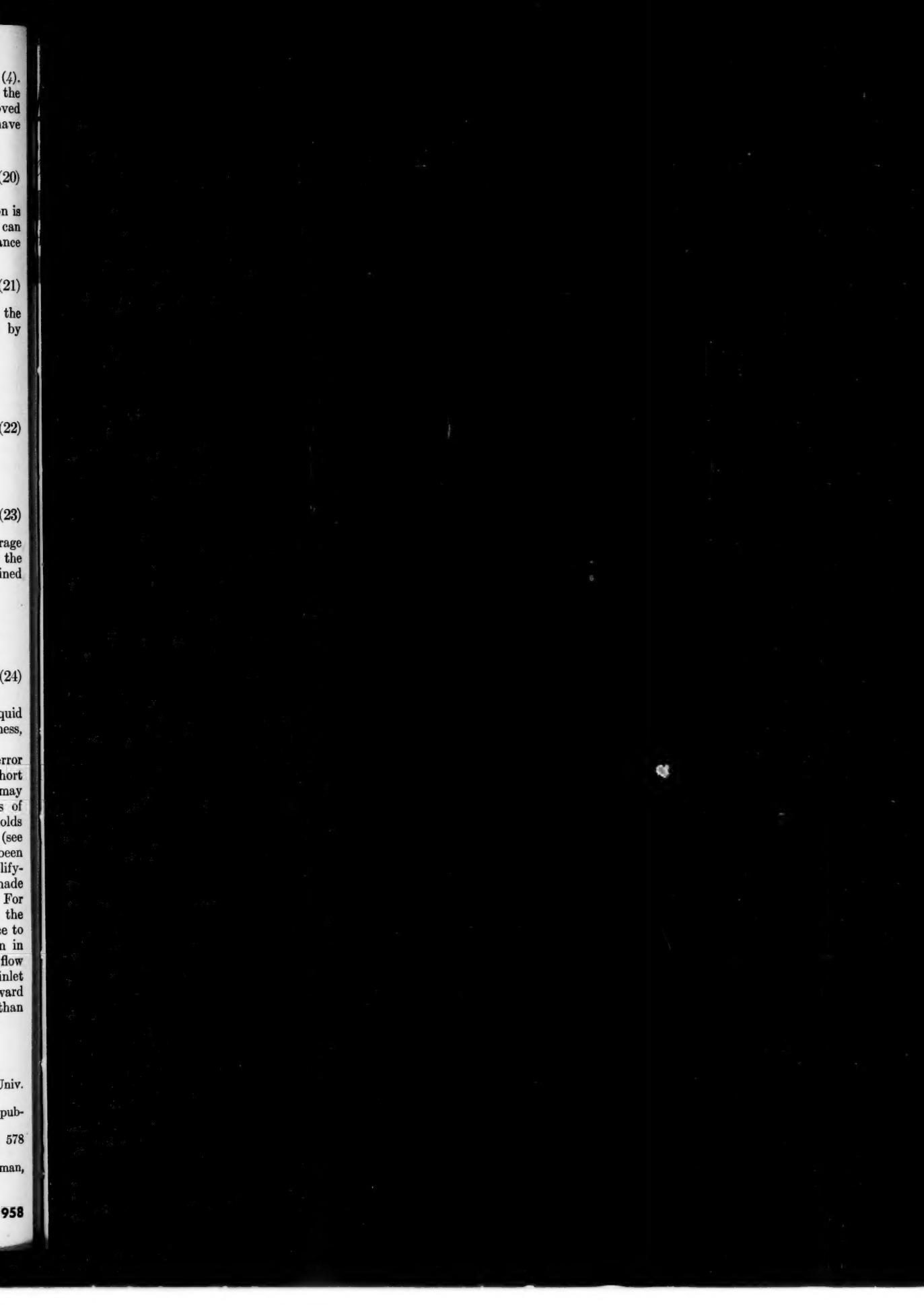
Birmingham 9, Ala.—Fred W. Smith, Dist. Mgr., 1201 Forest View Lane—Vesthaven, Tremont 1-5762.